UNIVERSITY OF ENGINEERING AND TECHNOLOGY
VIETNAM NATIONAL UNIVERSITY, HANOI

INSTITUTE OF MECHANICS
VIETNAM ACADEMY OF SCIENCE AND TECHNOLOGY

PROCEEDINGS OF THE 6TH INTERNATIONAL CONFERENCE ON

ENGINEERING MECHANICS AND AUTOMATION

(ICEMA 2021)

VIETNAM NATIONAL UNIVERSITY PRESS, HANOI

We would like to thank the Asia Research Centre, Vietnam National University Hanoi (VNU-ARC) for their kind financial support to aid with the organization of the 6th International Conference on Engineering Mechanics and Automation. VNU-ARC was established on 23 November 2001 by VNU's President in accordance with the Agreement between the Korea Foundation for Advanced Studies and Vietnam National University, Hanoi. For more information, please visit http://arc.vnu.edu.vn.

Proceedings of the 6th International Conference on Engineering Mechanics and Automation (ICEMA 2021)

ISBN: 978-604-342-918-3

Published by

Vietnam National University Press, Hanoi

16 Hang Chuoi, Pham Dinh Ho, Hai Ba Trung, Hanoi, Vietnam

Tel: (024) 39714899 Fax: (024) 39729436

Email: nxb@vnu.edu.vn Website: http://press.vnu.edu.vn/

Printed in Vietnam

Engineering Mechanics and Automation plays a vital role in nearly every industry, from aerospace and automotive to energy, manufacturing, robotics, and biotechnology. In the past decade, Engineering Mechanics and Automation have experienced substantial improvements with a change of focus in terms of scale, span, and applications. Besides, new requirements in terms of design efficiency have become more and more important, pushing to relevant improvements in terms of new methods and advanced approaches. In such circumstance, the 6th International Conference on Engineering Mechanics and Automation (ICEMA - 2021) will be organised at University of Engineering and Technology on November 14, 2021.

The aim of the conference is to provide an international forum for scientific researchers in the technologies and applications of Engineering Mechanics and Automation. The Conference also aims to provide a chance for exchange of experiences and international collaboration in these fields. The scope of the conference includes, but not limited to, the following topics:

- Fundamental Issues of Fluid Mechanics
- Mechanics with Climate Change and Environment
- Industrial and Environmental Fluid Mechanics
- River and Sea Dynamics
- Fundamental Issues of Mechanics of Solids
- Mechanics of Composite Materials and Structures.
- Fracture Mechanics and Fatigue
- Mechanics of Soil, Rocks and Porous Medium
- Technical Diagnostics
- Linear and Nonlinear Oscillations
- Dynamics of Multi-body Systems
- Nonlinear Dynamics and Chaos
- Mechanics of Machines and Mechanism
- Computational Mechanics
- Industrial Automation
- CAD/CAM/CNC Systems
- Control Strategies and Algorithms
- Design Automation
- Intelligent Systems
- Machine Tools and Machinery
- Manufacturing Process Control
- Mechatronics Engineering
- Rapid Prototyping
- Civil Engineering and Transportation Technology

Steering Committee

Nguyen Viet Ha, Nguyen Tien Khiem, Dinh Van Manh

Program Committee

Chairman: Nguyen Dong Anh
Vice Chairman: Nguyen Dinh Duc, Dinh Van Manh

Dao Huy Bich, Nguyen Van Diep, Nguyen Tien Khiem, Tran Ich Thinh, Duong Ngoc Hai, Seung Chul Jung (Korea), Nguyen Van Khang, Cheol-Koo Hahn (Korea), Pham Manh Thang, Tran Ngoc Hung, Tran Anh Quan, Jae Woo Wie (Korea), Tran Van Lien, Dinh Van Phong, Pham Chi Vinh, Tran Minh Tu, Bui Dinh Tri, Pham Anh Tuan, Nguyen Thi Viet Lien, Doan Minh Chung, Nguyen Phong Dien, Nguyen The Duc, Dang The Ba, Nguyen Tien Cuong, Luong Xuan Binh, Phan Le Binh, Le Van Canh, Nguyen Xuan Hung, Ngo Nhu Khoa, Nguyen Ngoc Linh, Do Tran Thang, Truong Tich Thien, La Duc Viet, Nguyen Viet Khoa, Nguyen Thoi Trung.

Organising Committee

Chairman: Chu Duc Trinh
Vice Chairman: Nguyen Dinh Duc, Pham Manh Thang, Nguyen Viet Khoa
Dang The Ba, Dao Nhu Mai, Nguyen Ngoc An, Le Huy, Pham Thi Thu Lan, Luong Viet Nguyen

Secretariat

Chairman: Dao Nhu Mai
Dinh Tran Hiep, Nguyen Ngoc Linh, Phan Thi Cam Ly, Chu Thi Minh

TABLE OF CONTENT

SESSION 1. MECHATRONICS AND AUTOMATION

SESSION 2. FLUID MECHANICS

SESSION 3. SOLID MECHANICS

SESSION 1
MECHATRONICS AND AUTOMATION

3D Printed Micro nozzle-based Mixer with Integrated Capacitive Sensor toward High Precision Mixing Applications

Cuong Nguyen Nhu
VNU University of Engineering and Technology
Hanoi, Vietnam
cuongnn241@vnu.edu.vn

Luan Le Van
VNU University of Engineering and Technology
Hanoi, Vietnam
luanlv@vnu.edu.vn

Lam Bao Dang
Hanoi University of Science and Technology
Hanoi, Vietnam
lam.dangbao@hust.edu.vn

Van Thanh Dau
School of Engineering and Built Environment, Griffith University
Brisbane, QLD 4222, Australia
v.dau@griffith.edu.au

Tung Thanh Bui
VNU University of Engineering and Technology
Hanoi, Vietnam
tungbt@vnu.edu.vn

Trinh Chu Duc
VNU University of Engineering and Technology
Hanoi, Vietnam
trinhcd@vnu.edu.vn

***Abstract*: Fluid delivery and mixing process are both indispensable parts in many Micro Total Analysis Systems - µTAS. In this work, we presented a micropump/mixer actuated by the PZT diaphragm with capacitive sensing electrodes integrated into the device. It can be fabricated by a low-cost 3D additive manufacturing process and is capable of both pumping and mixing simultaneously. Both the device is first studied using the finite element method and by experiments with prototypes. Both studies demonstrate the working principles of the devices. Experiments with the sensing electrodes show that they are able to detect the change in pumping liquid by measuring the change in capacitance.**

Keywords: micropump, micromixer, capacitive sensing.

I. Introduction

In recent years, the advances in microelectromechanical systems (MEMS) and sub-millimeter and microscale technology have resulted in micro total analysis systems (µTAS). These systems integrate multiple devices of different functions on a single platform. µTAS plays a vital role in developing low-cost, rapid, and point-of-care (POC) testing or assays [1]. When it comes to components of microfluidic devices or µTAS, micropumps are regarded as the heart of microfluidics systems because they provide the moving fluids for such devices to work. The practice of controlling the internal flow in the pumping and mixing device usually involves the use of the microvalve structure[2]–[4]. However, valves have the tendency to be suffered from wear and fatigue. This negatively affects the durability and reliability of the devices. Apart from pumping devices, many microfluidic systems also require micro-mixers, this leads to the development of micromixers [5]–[8]. Usually, the pumping and mixing processes are needed to occur simultaneously. Unfortunately, micropumps and micromixers are two separate devices. In other words, a micromixer needs to be accompanied by other micropumps. In addition, in mixing applications, it is often required that the concentration or mixing ratio is precise and monitorable. However, current micromixers, especially passive micromixers usually lack these abilities.

In this paper, based on our previous work on the valveless micropump [9], we continue to develop the proposed device with an integrated capacitive sensor for mixing applications. The device is capable of both pumping and mixing simultaneously. For this purpose, the device is comprised of two inlets connecting to the pumping chamber, which is driven by the PZT diaphragm. Interestingly, capacitive electrodes were embedded along the outlet channel so that the device is capable of measuring the concentration of the mixed solution by monitoring the capacitance of the capacitor formed at the outlet.

II. Structure of the 3D Printed Mixer

A. Design

The proposed device for the mixer consists of a mixing chamber that serves as the source of driving force for the devices; two inlets connected to the fluid sources and one outlet channel where the mixed fluid is conveyed through. The inlet and outlet channels are connected with the mixer chamber to form a nozzle/diffuser structure at the center of the device as shown in Fig. 1 (a). The mixer chamber is actuated by a PZT membrane provided by Murata Manufacturing Co., Ltd [10]. It is comprised of a brass plate and a piezoelectric material plate. The piezoelectric plate is smaller and is firmly bonded onto the brass plate. The wires are connected to this silver-plated PZT and the brass plate.

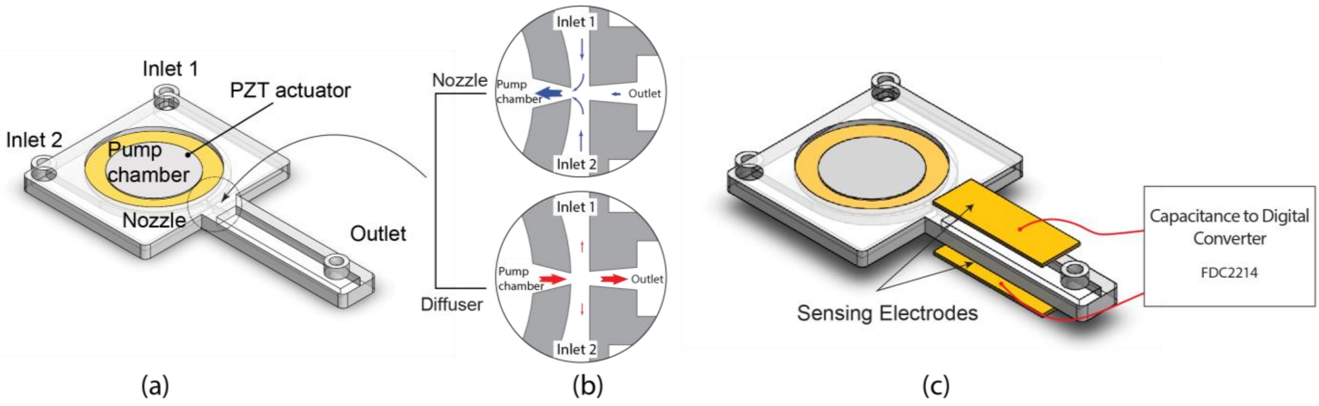

Fig. 1. (a) Design of the micropump with the zoom-in shows dimensions at the nozzle rectifier (b) Illustration of nozzle/diffuser structure and the pumping behavior (c) Set-up for the integration of capacitance sensing

The PZT diaphragm is then connected to the external voltage source. Because of the piezoelectric effect, the PZT material part will contract or expand according to the polar of the applied voltage. The magnitude of deflection will depend on the magnitude of the said voltage. The mechanical stress produced by the PZT under electrical stress is proportional to the voltage magnitude. The voltage magnitude is, therefore, a parameter in controlling the behavior of the PZT diaphragm.

The mixer does not use valves to control the flow. Therefore, in order to mitigate the undesired backward fluid flow in the mixer, the device integrates the nozzle/diffuser structure, which is illustrated in Fig. 1 (b). It is simple to fabricate but efficient when it comes to flow rectification. This simple structure allows it to easily integrate into the device, which makes the device simple in structure, and thus, helps reduce the fabrication time and cost. The diffuser/nozzle component has the ability to work with high frequency, and fast response time [11].

B. *Capacitive Sensing*

The device is further enhanced by embedding sensing electrodes along the outlet channel. This sensor is expected to measure the capacitance along the outlet channel for different fluid materials and mixing ratios in real-time and set the foundation to build a closed-loop pumping/mixing system. A capacitor is formed when at least two electrical conductors, often in the form of metallic plates or surfaces are separated by a dielectric medium. The capacitance of a capacitor is a function of the geometry of the design including the area of the plates and the distance between them and the permittivity of the dielectric material, which is the measure of the electric polarizability of a dielectric. Two electrodes of equal size of 20×7 mm were added to the top and bottom face of the outlet channel as in Fig. 1 (c). These two electrodes create a parallel-plate capacitor with the dielectric material being the fluid inside the outlet channel. The capacitance of a capacitor constructed from two parallel plates is given by:

$$C = \frac{\epsilon A}{d}$$

in which C is the capacitance (F), A is the area of overlap of the two electrodes (m^2), ε_0 is the permittivity of the dielectric material between two plates (F/m) and d is the separating distance between two plates (m).

Since the area of the plates and separation between the plates is constant, the capacitance of the created capacitor depends on the material between the plates i.e., the permittivity of the fluid at the outlet channel. Thus, the capacitor would give different capacitance for different liquids due to the difference in their permittivity values. Therefore, by embedding two electrode plates, the device is expected to be able to detect the liquid being mixed or the ratio of the mixing solution by measuring the capacitance between the integrated electrodes. Each electrode was then connected to the capacitive sensor. The capacitance to digital converter FDC2214 provided by Texas Instruments [12], which is a multi-channel, noise-resistant, high resolution, high/speed capacitance-to-digital converter, was used. The sensor has a resolution as high as 28 bits with a fast sample rate of 4.08 ksps. This makes it easy to be implemented on applications that involve fast-moving targets. The sensor is capable of measuring a wide capacitance with a maximum value of up to 250 nF.

III. Numeral Simulation

A. *Simulation Setup*

A simulation was conducted to verify and study the characteristics of the proposed device. The simulation was carried out on COMSOL Multiphysics©, a finite element analysis, solver, and Multiphysics simulation package. The mixer was modeled by multi-physics simulation in which the transient flow and piezoelectric analyses were coupled as in Fig. 2. The transient flow models model the velocity and pressure profiles of the fluid while the piezoelectric took into account the two-way conversion between electricity and displacement of the piezoelectric material. The motion of fluids is governed by the Navier-Stokes equations. In the case of an incompressible Newtonian fluid flow, the equation yields:

$$\rho(\partial u/\partial t + u \cdot \nabla u) = -\nabla p + \nabla \cdot \mu \nabla u$$

where u is the velocity, p is the pressure, ρ is the density, and μ is the dynamic viscosity of fluid flow.

This equation is accompanied by the continuity equation which represents the conservation of mass:

$$\nabla \cdot u = 0$$

The fluid-wall condition was considered to be no-slip:

$$u = 0$$

The stress and deformation on the diaphragm, which are generated by the voltage applied on the piezoelectric diaphragm, are expressed by the following stress-strain relations:

$$T = c_E S + e^T E$$
$$D = eS + \epsilon_S E$$

where T and S are the stress and strain matrices, respectively; E the electric field and D the electric deformation and c_E, e,ϵ_S the elasticity, coupling, and permittivity matrices, respectively.

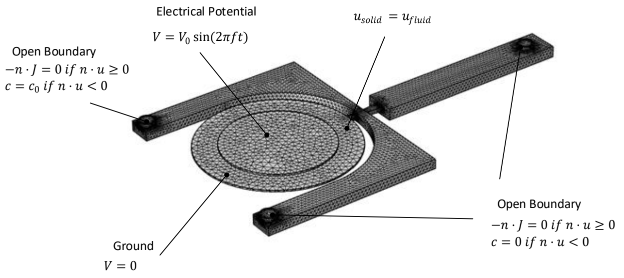

Fig. 2. Boundary condition set-up for the mixing simulation

TABLE I. TABLE TYPE STYLES

Properties	Values	Unit
Density of water	1000	kg/m^3
Viscosity of water	0.8	mPa
Density of copper	8960	kg/m^3
Young's modulus of copper	110×10^9	Pa
Poisson's ratio of copper	0.35	1
Diffusion coefficient	1.412×10^{-9}	m^2/s
Concentration	150	mol/m^3

The PZT diaphragm clamped at its edge is actuated by an applied voltage $V_{app} = V_o sin(2\pi f t)$, where v_0 is the amplitude of the voltage, f is the driving frequency. The fluidic response inside the pump was simulated using the fluid-structure interaction (fsi) and the displacement of the piezo diaphragm by coupling piezoelectric (solid) and electrostatics (es) modules. To study the mixing process of the proposed structure, the Chemical reaction module was added. Due to the dilution, properties of the mixture such as density and dynamic viscosity can be assumed to correspond to those of the solvent. The mixing simulation modeled the transport of chemical species through the process of diffusion and convection. The diffusion of the solute, dilute mixtures, or solution is governed by Fick's law:

$$\frac{\partial c}{\partial t} + \nabla \cdot J = 0$$

in which, c is the concentration of the species (mol/m^3), D is the diffusion coefficient (m^2/s), and J is the mass flux diffusive flux vector (mol/(m^{2}s)).

The inlets and the outlet of the model were defined as open boundaries. This established the mass transport across the boundaries where both convective inflow and outflow can occur. When the fluid flows into the domain, an exterior species concentration is defined as:

$$c = c_0$$

In contrast, when the fluid flows out of the domain, the boundary condition is equivalent to the outflow:

$$n \cdot D\nabla c = 0$$

One inlet was set with a species concentration of 150 mol/m^3 while the concentration at the other inlet was set to zero. Properties used in the simulation model are listed in Table I.

B. *Simulation Results*

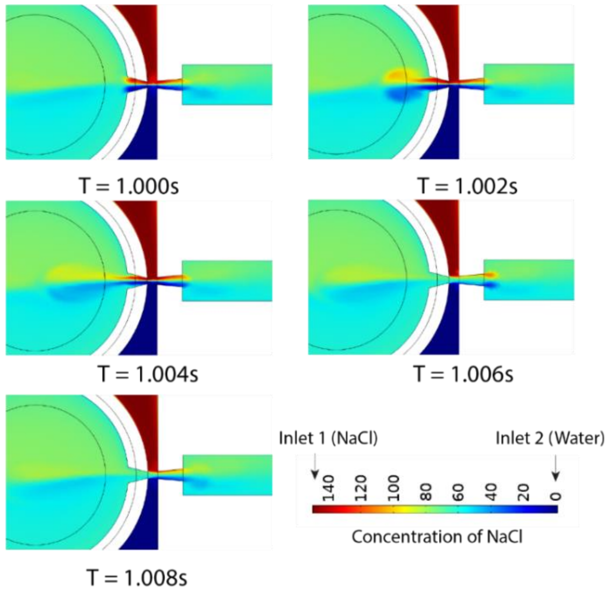

Fig. 3. The evolution of the mixing process in one period at 100Hz

Fig. 3 presents the simulation results on the evolution of the mixing process in one period of the applied driving voltage. The driving frequency chosen in the simulation was 100 Hz. The color represents the concentration of sodium chloride (NaCl). Similar to the pumping process [9], the mixing process also involved two phases, namely the suction phase and the discharge phase. During the suction phase, the currents from two inlets, which are closer to the pump nozzle than the outlet, are sucked into the mixer chamber. Since two inlet flows are collinear and opposite in direction, they will collide directly, and the mixing process starts. In addition, the inlet channels are perpendicular to the outlet ones, the coming flow from the inlet blocks the backflow by the outlet at the crossing. In addition, the diffuser on the outlet channel also limits the liquid returning from the outlet to the mixer chamber. For the discharge phase, the liquid concentrated surrounding the nozzle of the mixing chamber moves through the nozzle. Thus, the suction and pumping phases successively occur and push the mixed liquid from inlets to the outlet. Fig. 4. provides a closer look at the mixing process captured at discharged phase. The lines present the streamline of the fluid flow. It represents the path of the fluid flow inside the device at one instance. It can be seen that the circular shape of the chamber and the fact that two inlet channels were designed facing each other facilitated the mixing process. When the suction phase starts, the liquids from two inlets were drawn into the chamber, the two flows met at the intersection between the inlets and the nozzle/diffuser structures. Because the two flows were then opposing each other, they collided, and the mixing process started. When liquids were already drawn into the chamber, the circular shape of the chamber caused each liquid flow to move along the circular wall of the chamber. They eventually met at the line of symmetry of the chamber. In addition, vortices were also created when the liquids were drawn into the chamber, this further helped improve the mixing process.

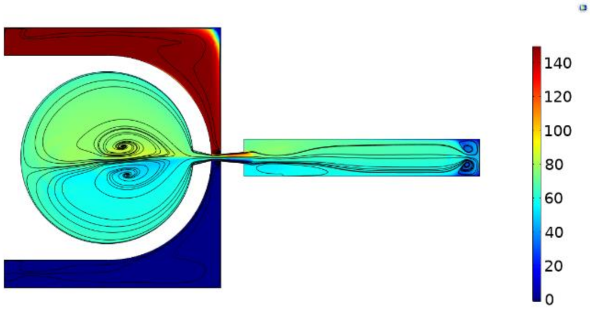

Fig. 4. The concentration and velocity streamline of the fluid at 100 Hz

The frequency of the simulation was then set to vary from 50 Hz to 150 Hz. The concentration at the outlet was obtained to get an average value. Fig. 5 shows the average concentration at the outlet for different driving frequencies. As can be seen from the graph, the average concentration increased with the frequency. When the voltage of 50 Hz, the concentration was the lowest, at 43.13 mol/m^3. At 100 Hz, the average concentration increased to 48.89 mol/m^3 while the figure was the highest, at 52.86 mol/m^3 when the 150 Hz voltage was applied. It can be concluded that the concentration of the liquid at the outlet can be changed by changing the frequency to the appropriate value.

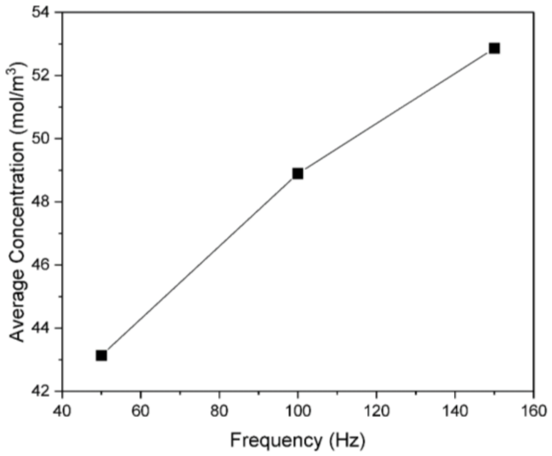

Fig. 5. The average concentration at the outlet at different frequencies

IV. Experimental Results

A. Mixing Process

The prototypes were fabricated using a 3D printing system (Conex3 Objet500, Stratasys) and were used in the experiments to demonstrate the mixing ability of the device. The set-up is shown in Fig. 6 (a). Dyed waters of blue and red colors are injected into the inlet channels 1 and 2, respectively. The mixing efficiency was determined for two cases of voltage. The experiments were conducted with the applied voltage of 220V and two different driving frequencies of 10 Hz and 100 Hz. A glance at the mixing results in Fig. 6 (b) and (c) reveals that the mixing efficiency was much better in terms of mixing speed and mixing outcomes when the voltage was applied and when the device operated at a higher frequency. With the presence of the driving voltage of 10 Hz, the mixing did not occur strongly. The colors of the fluid in two halves of the nozzle/diffuser structure and the beginning end of the outlet were still very different. The difference was, however, reduced with the applying of the 100 Hz – 220V voltage. Especially, the mixing liquid achieved homogeneity in color as in Fig. 6 (c). Two colored liquids were evenly mixed right at the nozzle/diffuser structure.

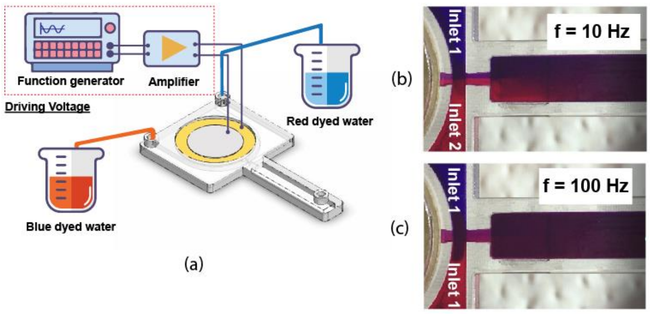

Fig. 6. Micropump in mixing mode with two colored liquids: (a), (b) & (c): Color of mixed liquid in the outlet channel with the applied voltages of 220V-10Hz and 220V-100Hz, respectively

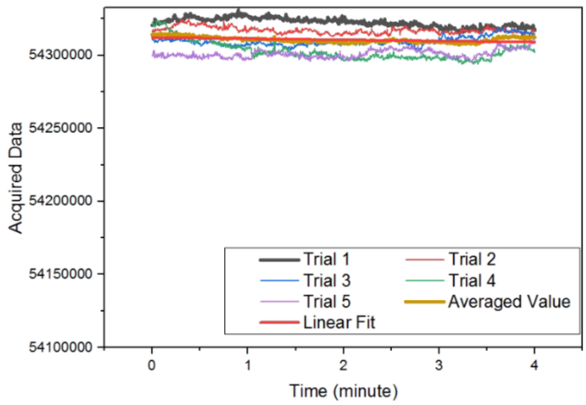

Fig. 7. Acquired data for 4 minutes with the outlet channel filled with water

V. Capacitance Sensing

The experiments with different liquids and its concentration were conducted. The data acquired from the sensor was converted to decimal numbers and stored on the connected computer for further analysis. Fig. 7 presents the data acquired from the sensor for 5 trials. In all the trails, the outlet channel was filled with water, and in each measurement, the data was acquired for 4 minutes. The data acquired from 5 trials were shown in Fig. 7. The value which represented that capacitance value was inevitably influenced by noise from the surroundings and the values measured for each trial were slightly different. However, it can be seen that in each trial, a fairly straight averaged line was observed. In addition, the measured values had the tendency to converge with time. Overall, the measurement with a fully filled water outlet channel returned an average value of 54310000. The experiment with the capacitive sensor was continued with the solution of sodium chloride at 20% (wt:wt%) as another test liquid at the outlet. Five trials, which measured the capacitance of the outlet channel for 4 minutes, were carried out and the obtained data were compared with the previous results with water. The comparison between the acquired data from the experiments with water and Sodium chloride is presented in Fig. 8. The medium data were plotted with the color bands indicating the 95% confidence intervals. It can be seen from the graph that the measured values for water and Sodium chloride solution were quite distinct. To be more specific, the value for Sodium chloride solution fluctuated around 53900000 while the figure for water was higher, at 54310000. The ranges for each case were quite distinct. There was no overlap between the confidence interval of data for water and sodium chloride solution. This shows that the chosen capacitive senor along with its acquired data can be used to distinguish the solution inside the microchannel or in this case, the outlet channel.

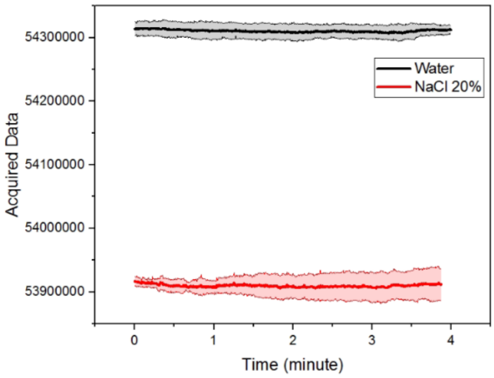

Fig. 8. Acquired data for 4 minutes with the outlet channel filled with water and the solution of sodium chloride 20%

The experiments with two types of water, namely drink water and distilled water, and sodium chloride solution with three different concentrations from 10% to 30% (wt:wt%) was then set up and carried out. The experiment with each liquid was carried out 3 three times each. The obtained data were shown in Fig. 9. The data for drinking water was the highest at 54005015. At the same time, the figure for distilled water was slightly slower, at 53919340. Meanwhile, the numbers for Sodium chloride solutions were much lower, ranging from 53539273 to 53662450. Interestingly, there is a recognized relationship between the concentration and the received data. The values of the obtained data decreased with the increase in the concentration of the sodium chloride solution. The data for Sodium chloride solution of 10% concentration was the highest, at 53662450. The figure for 20% Sodium chloride solution was lower, at 53623773. The data obtained for the experiment with 30% sodium chloride solution was 53539273. It can be implied from the given data that by measuring the capacitance between electrode plates embedded along the outlet channel, not only can we detect different liquids being mixed or conveyed through the outlet channel, but we can also detect the ratio or the concentration of the mixed liquid.

The final experiment was to understand the behavior of the device when the fluid inside it changes from one substance to another. In the first trial, the device was initially filled with the Sodium chloride solution of 20% concentration. The fluid inside the micropump was then changed gradually to distilled water. In the second trial, the reverse process was carried out, i.e., the device that was previously filled with distilled water was injected with a sodium chloride solution of 20% concentration. Due to the slight difference in base level data, the taken data were divided by the value measured at the beginning of the experiment. The results for such transients are presented in Fig. 10 with the corresponding areas around the lines showing the 95% confidence interval. It took around 100 data steps for the data to stabilize.

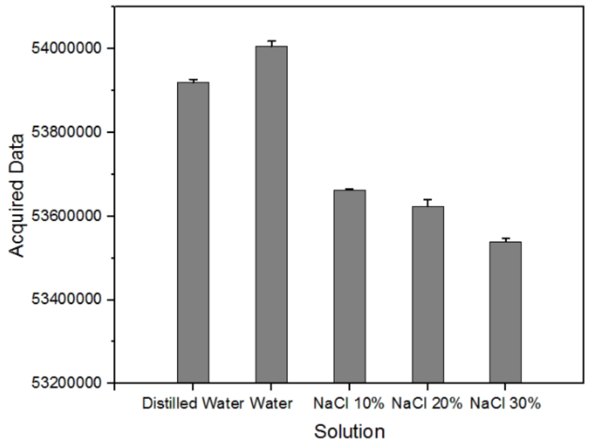

Fig. 9. The acquired data from the capacitive senor for different liquid

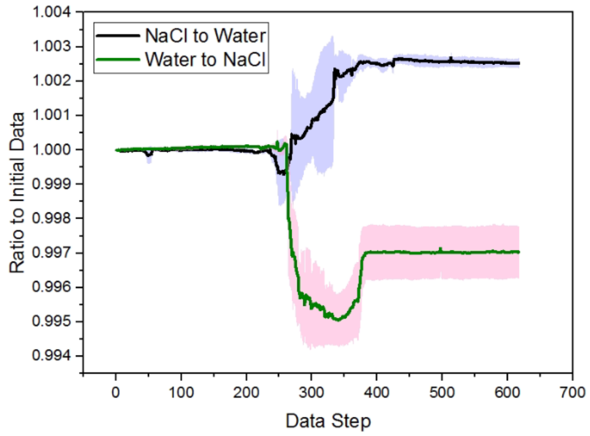

Fig. 10. Data acquired from the transient from sodium chloride 20% solution to distilled water and vice versa.

VI. Conclusion

Simulation results confirmed the mixing ability of the device. The mixing function was also demonstrated by the experiment with color-dyed water. The obtained data for water and chloride solution from the capacitive sensor were quite distinct. There is a recognized relationship between the concentration of NaCl and the received data. Thus, by measuring the capacitance between electrode plates embedded along the outlet channel, we can detect different liquids being mixed as well as the ratio or the concentration. This is expected to set the foundation to build a closed-loop pumping/mixing system.

Acknowledgment

This work was supported by the Vietnam Ministry of Science and Technology under Grant NĐT.101.TW/21.

References

[1] R. Garcia-Ramirez and S. Hosseini, "History of Bio-microelectromechanical Systems (BioMEMS)," *Lecture Notes in Bioengineering*, pp. 1–20, 2021, doi: 10.1007/978-981-15-6382-9_1.

[2] P. E. Guevara-Pantoja, R. J. Jiménez-Valdés, J. L. García-Cordero, and G. A. Caballero-Robledo, "Pressure-actuated monolithic acrylic microfluidic valves and pumps," *Lab on a Chip*, vol. 18, no. 4, pp. 662–669, Feb. 2018, doi: 10.1039/c7lc01337j.

[3] A. Pradeep, V. R. S., J. Stanley, B. G. Nair, and T. G. S. Babu, "Automated and programmable electromagnetically actuated valves for microfluidic applications," *Sensors and Actuators, A:*

Physical, vol. 283, pp. 79–86, Nov. 2018, doi: 10.1016/j.sna.2018.09.024.

[4] A. B. Bußmann, C. P. Durasiewicz, S. H. A. Kibler, and C. K. Wald, "Piezoelectric titanium based microfluidic pump and valves for implantable medical applications," *Sensors and Actuators, A: Physical*, vol. 323, p. 112649, Jun. 2021, doi: 10.1016/j.sna.2021.112649.

[5] J. C. Rife, M. I. Bell, J. S. Horwitz, M. N. Kabler, R. C. Y. Auyeung, and W. J. Kim, "Miniature valveless ultrasonic pumps and mixers," *Sensors and Actuators, A: Physical*, vol. 86, no. 1–2, pp. 135–140, Oct. 2000, doi: 10.1016/S0924-4247(00)00433-7.

[6] S. Rashidi, H. Bafekr, M. S. Valipour, and J. A. Esfahani, "A review on the application, simulation, and experiment of the electrokinetic mixers," *Chemical Engineering and Processing: Process Intensification*, vol. 126. Elsevier B.V., pp. 108–122, Apr. 01, 2018. doi: 10.1016/j.cep.2018.02.021.

[7] C. C. Cho, C. L. Chen, R. T. Tsai, and C. K. Chen, "A novel microfluidic mixer using aperiodic perturbation flows," *Chemical Engineering Science*, vol. 66, no. 23, pp. 6159–6167, Dec. 2011, doi: 10.1016/j.ces.2011.08.039.

[8] Y. Daghighi and D. Li, "Numerical study of a novel induced-charge electrokinetic micro-mixer," *Analytica Chimica Acta*, vol. 763, pp. 28–37, Feb. 2013, doi: 10.1016/j.aca.2012.12.010.

[9] L. le Van *et al.*, "Simulation and Experimental Study of a Synthetic Jet Valveless Pump," *IEEE/ASME Transactions on Mechatronics*, vol. 25, no. 3, pp. 1162–1170, Jun. 2020, doi: 10.1109/TMECH.2019.2960332.

[10] "7BB-20-6L0|Piezoelectric Diaphragms|Sound Components (Buzzer)|Murata Manufacturing Co., Ltd." https://www.murata.com/en-us/products/productdetail?partno=7BB-20-6L0 (accessed Sep. 29, 2021).

[11] "FDC2214 data sheet, product information and support | TI.com." https://www.ti.com/product/FDC2214 (accessed Sep. 29, 2021).

The 6th International Conference on
Engineering Mechanics and Automation (ICEMA 2021)
Hanoi, November 14, 2021

A Post-processing Approach Using Clustering for Vision-based Crack Detection Algorithms

Quang Manh Doan
Faculty of Engineering Mechanics and Automation
VNU University of Engineering and Technology
Hanoi, Vietnam
18020884@vnu.edu.vn

Van Duy Nguyen
Faculty of Engineering Mechanics and Automation
VNU University of Engineering and Technology
Hanoi, Vietnam
18020411@vnu.edu.vn

Cong Hieu Le
Faculty of Engineering Mechanics and Automation
VNU University of Engineering and Technology
Hanoi, Vietnam
18020508@vnu.edu.vn

Ngoc Khang Nguyen
Faculty of Engineering Mechanics and Automation
VNU University of Engineering and Technology
Hanoi, Vietnam
18020678@vnu.edu.vn

Tran Hiep Dinh*
Faculty of Engineering Mechanics and Automation
VNU University of Engineering and Technology
Hanoi, Vietnam
*corresponding author, tranhiep.dinh@vnu.edu.vn

Abstract*: With the advance of technology in recent years, infrastructure has been well developed, leading to an essential requirement in its monitoring and maintenance. Instead of using human labor, automatic systems such as mobile robots and unmanned aerial vehicles have been gradually employed to reduce workplace injuries and increase the efficiency of the process. Besides, vision-based methods have been developed to detect and recognize infrastructure degradation, such as surface cracks. Although the results of recent methods are promising, their dependency on the quality of the input image, which is impacted by some barriers such as lighting conditions or surface material, still remains. This study represents a new classification method to reduce noise and increases the quality of segmentations resulted from some recent crack detection techniques. With the employment of machine learning and image properties such as intensity, area, and shape, the proposed approach has improved the effectiveness of two recently analyzed techniques by almost 1%.

Keywords: crack detection, segmentation, noise cancellation, classification, clustering.

I. INTRODUCTION

Compared to traditional inspection techniques, computer vision-based approaches have recently attracted many researchers due to its advances in data collection, condition assessment, and risk management [1-2]. In general, techniques in this field can be classified into the following groups: (i) thresholding [3-5], (ii) Machine learning (ML) [6-8], and (iii) Deep Learning (DL) approaches [9-11]. These methods are based on the difference between the crack pixel and its background, or the features of crack images and their ground-truth that were extracted and learned from the ML and DL models.

Although the results obtained from ML and DL approaches are promising, it is dependent on the quality and size of the training dataset that is still a challenge of the field [12]. On the other hand, thresholding methods are based on the intensity difference between crack pixels and their surrounding, where an assumption of low intensity of the crack pixels are normally utilized. In [4], a recursive algorithm was proposed to continuously find a new threshold for dark regions in the histogram of the image until the intensity difference between these regions and the background is less than a given cutoff threshold. In [5], an automatic pavement crack detection approach was developed based on multi-scale images where parameters at each stage could be fine-tuned as per user's purposes. It is significant to see that the pixel intensity and region properties are essential in the aforementioned methods to improve the quality of crack detection results.

In this paper, a post-processing approach based on image properties is proposed for applications in crack detection. The approach is developed for noise cancellation of segmentations returned by thresholding-based crack detection techniques. The segmented regions are clustered into crack and noises using the Clustering by Fast Search and Find of Density Peaks (CFSFDP) algorithm [13] and ML. The best feature pair for the noise cancellation technique is evaluated and selected from four essential parameters: the area, the eccentricity, the brightness, and the contrast. Besides, two thresholding-based crack detection techniques are employed to verify the effectiveness of the proposed approach, namely the Multi-scale Fusion Crack Detection (MFCD) [5], and the Contrast-Based Autotuned Thresholding (CBAT) [14].

The contribution of this paper is two-fold: First, CFSFDP is adapted into the crack detection problem. Unlike the original CFSFDP where location information is utilized, image properties are proposed in this approach. Then, comprehensive experiments are conducted to select the best feature pair for the proposed technique where an accuracy improvement of almost 1% has been achieved. The rest of the paper is structured as follows: Section II gives a brief introduction about the MFCD, CBAT, and CFSFDP. The proposed noise cancellation (NC) technique is proposed in Section III. Experimental results, discussion, and conclusion will be presented respectively in Section IV and V.

II. RELATED WORK

A. *Multi-scale Fusion Crack Detection*

MFCD is a thresholding-based crack detection method that can extract crack pixels from input images without using any training data. The Gaussian method is first employed to create multiscale images and extracts features representing cracks at each scale. By tuning the input parameters, one can then find and fuse the crack candidates at different scales to get the result. However, MFCD is not computational effective due to its dependency on the image size, the number of scales, as well as the input threshold. Moreover, its final segmentations have not been optimized and still contain some non-crack regions that should be removed.

B. *Contrast-based Autotuned Thresholding.*

CBAT method is a variation of the Otsu algorithm [15] that calculates thresholds by recursively focusing on the darker side of the image histogram to separate the interested regions from the background. Each time a new threshold is identified, the interclass contrast between the background and foreground is updated. A pre-defined value is set to trigger the stop condition when the value is exceeded by the updated interclass contrast. Compared with the original Otsu and other variations, the quality of segmentation by CBAT has been much improved, especially on low-intensity images. However, CBAT is dependent on the stop condition and has not taken the region size into account. Hence, CBAT cannot identify the difference between crack and non-crack regions such as small round dark points, black-hole regions on the surface… which also appear in low-intensity levels.

C. *Clustering by Fast Search-and-Find of Density Peaks*

CFSFDP is a clustering algorithm that has been developed recently for data separation. First, the density peaks are calculated based on the local density (ρ_m) and the minimum distance (δ_m) to data points of higher density. A decision graph is then employed to assist a manual selection of cluster centers with high density. The local density (ρ_m) and the minimum distance (δ_m) of each data point are defined as follows:

$$\rho_m = \sum \chi(d_{mn} - d_c), \tag{1}$$

$$\delta_m = min\left(d_{mn}\right)\left(n : \rho_n > \rho_m\right), \tag{2}$$

where $\chi(x) = 1$ if $x < 1$ and $\chi(x) = 0$ otherwise, d_{mn} is the distance between the m-th point and other local data, d_c is a given threshold distance. This clustering technique can be directly applied in the crack detection problem if crack and non-crack regions are well separated in terms of locations. However, its effectiveness is much reduced if the location difference between those is minor. To overcome this challenge, we propose in this paper an implementation of CFSFDP using the image properties instead.

III. METHODOLOGY

Because both MFCD and CBAT are density-based crack detection algorithms, they can not have good segmentations with low-intensity images. Even though these algorithms are fine-tuned, in the final segmentation, there are many noise regions. The reason for this problem is those regions have the same pixel intensity as the crack regions. For dealing with this task, a noise cancellation approach base on other features is necessary. In this section, a brief introduction about image properties that will be used in the extended CFSFDP is presented. A comprehensive analysis is then conducted to find the best feature pair for the clustering algorithm.

A. *Area and Eccentricity*

Generally, cracks appear in an image from a point, a specific region on the surface, and randomly develop their branches in a variety of directions and shapes. Branches of crack normally appear in a long shape, narrow width, and could be connected together at intersections. Hence, the size of cracks is normally larger than that of non-crack regions. However, a large region is not always a crack, since potholes, sinkholes, or shadowed regions can also contain those characteristics. Although the size of regions is comparable to that of crack, their length-to-width ratio is small. With this in mind, the Area (A) and Eccentricity (E) are employed. Here, A is the ratio between the size of the foreground and background regions, E is the eccentricity of an ellipse that can be fitted to the segmented region, as can be seen in Figure 1. When E is close to 0, this region could be considered as circle-like regions or non-crack. When E is close to 1, the regions has a narrow width and line-like shape. Let N_i be the number of pixels in the i-th region of a segmentation, its properties A_i and E_i are given as:

$$A_i = \frac{N_i}{S}, \tag{3}$$

$$E_i = \sqrt{1 - \left(\frac{b_i}{a_i}\right)^2}, \tag{4}$$

where S is the size of the foreground, a_i and b_i are the length of the major and minor axis of the ellipse covering the foreground region.

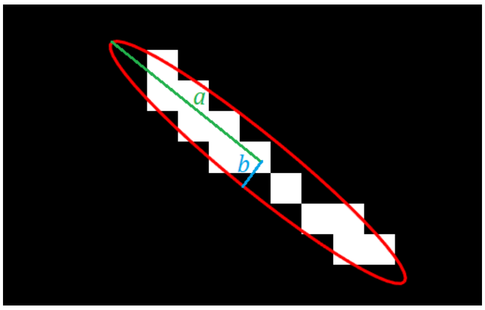

Figure 1: Eccentricity of ellipse.

B. *Brigtness and Contrast*

Besides the area and eccentricity, cracks are also featured by a high-intensity difference between the crack pixels and their surrounding [3,4]. However, these features are difficult to be detected in dark and low contrast images. This is also an obstacle for MFCD and CBAT to achieve high accuracy in these circumstances. To address this issue, two parameters representing the brightness (B_i) and the contrast (C_i) of each i-th region are utilized as follows:

$$B_i = \sum_{k=1}^{N} \frac{M_k}{N_i}, \tag{5}$$

$$C_i = \frac{max(R_i) - min(R_i)}{max(R_i) + min(R_i)}, \tag{6}$$

where M_k is the density of each pixel k, $max(R_i)$ and $min(R_i)$ are the maximum and the minimum intensities of the region.

C. Evaluation metric

In this article, the F-measure (F_1) [16] is used to evaluate the quality of MFCD and CBAT segmentations. F_1 is a similarity measure between a resulting segmentation and its ground-truth that is annotated by humans. This measure is calculated as the average of Precision (p) and Recall (r) with the same weight. The metric range is from 0 to 1 corresponding to an increase in segmentation quality and calculated as follows:

$$F_1 = \frac{2 \times p \times r}{p + r}. \tag{7}$$

The precision is the ratio between the crack pixels and that of the foreground area where the recall is the ratio between the detected crack and the actual ones. These metrics are calculated as

$$p = \frac{tp}{tp + fp}, \tag{8}$$

$$r = \frac{tp}{tp + fn}, \tag{9}$$

where *tp, fp, fn* are respectively the true positive, the false positive and the false negative.

D. Noise Cancellation with CFSFDP

As an intensity-based approach, MFCD and CBAT still return segmentation with noises when the difference between crack and background pixels is minimum. To deal with this problem, a noise cancellation approach is developed summarized as a flowchart in Figure 2. As discussed previously, it is possible to filter out those noises using the properties A, B, C, E, and the clustering algorithm CFSFDP. Instead of using the features of the original CFSFDP, the best two of the properties introduced in Eqs. (3)-(6) are employed. The properties are selected pairwisely and implemented in CFSFDP where crack and non-crack regions are labeled for training and testing. In this work, 156 segmentations of MFCD on two datasets: AigleRN [17] and CFD [18] are employed, resulting in 12562 labeled regions.

The data is then split into the train and test sets with the 80/20 ratio. Available classifiers and their variants in Python 3.8 are utilized to train the models. Let us denote the combination of A and B implemented in CFSFDP as DPAB, the remaining combinations are respectively denoted as DPAC, DPAE, DPBC, DPBE, and DPCE. The best classifier for DPBC is the ensemble Bagging Tree while that of the remaining combinations is the Gradient Boosting Tree. The selected classifiers are then employed on the test set to choose the best features pair for the proposed automatic noise cancellation. The performance of the classifiers on the test set is shown in Table I. Since DPAE outperforms other combinations on the test set, this combination is selected for the approach. Figure 3 presents an example of the noise cancellation process in a segmentation using MFCD.

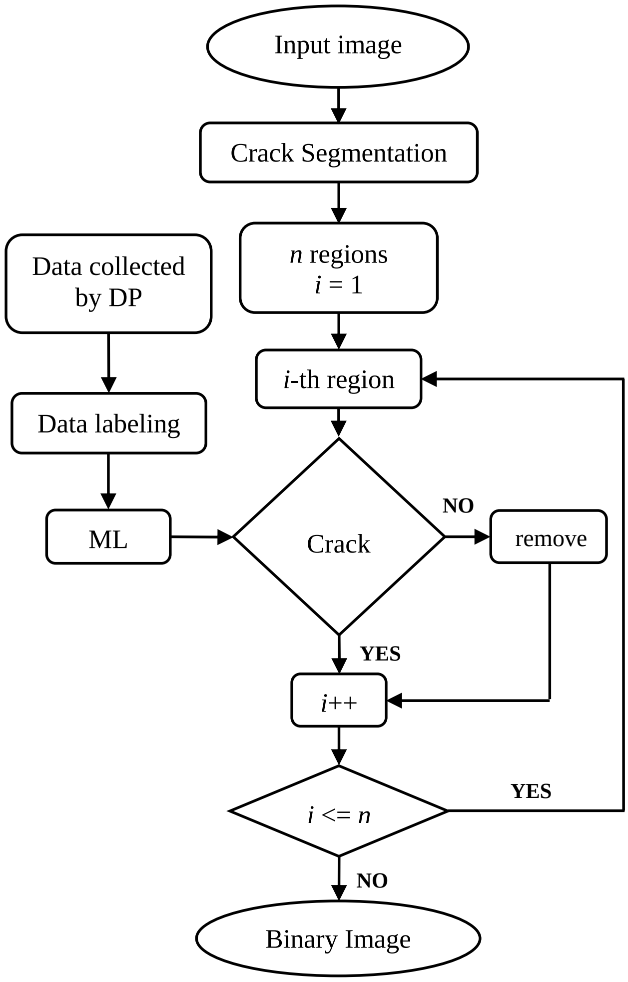

Figure 2: Noise cancellation flowchart.

TABLE I: Comparison between feature pairs

Combinations	MFCD	MFCD+NC	Gain
DPAB	0.7922	0.7981	0.0059
DPAC	0.7922	0.7991	0.0069
DPAE	0.7922	**0.8002**	**0.0080**
DPBC	0.7922	0.7975	0.0053
DPBE	0.7922	0.7970	0.0048
DPCE	0.7922	0.7962	0.0040

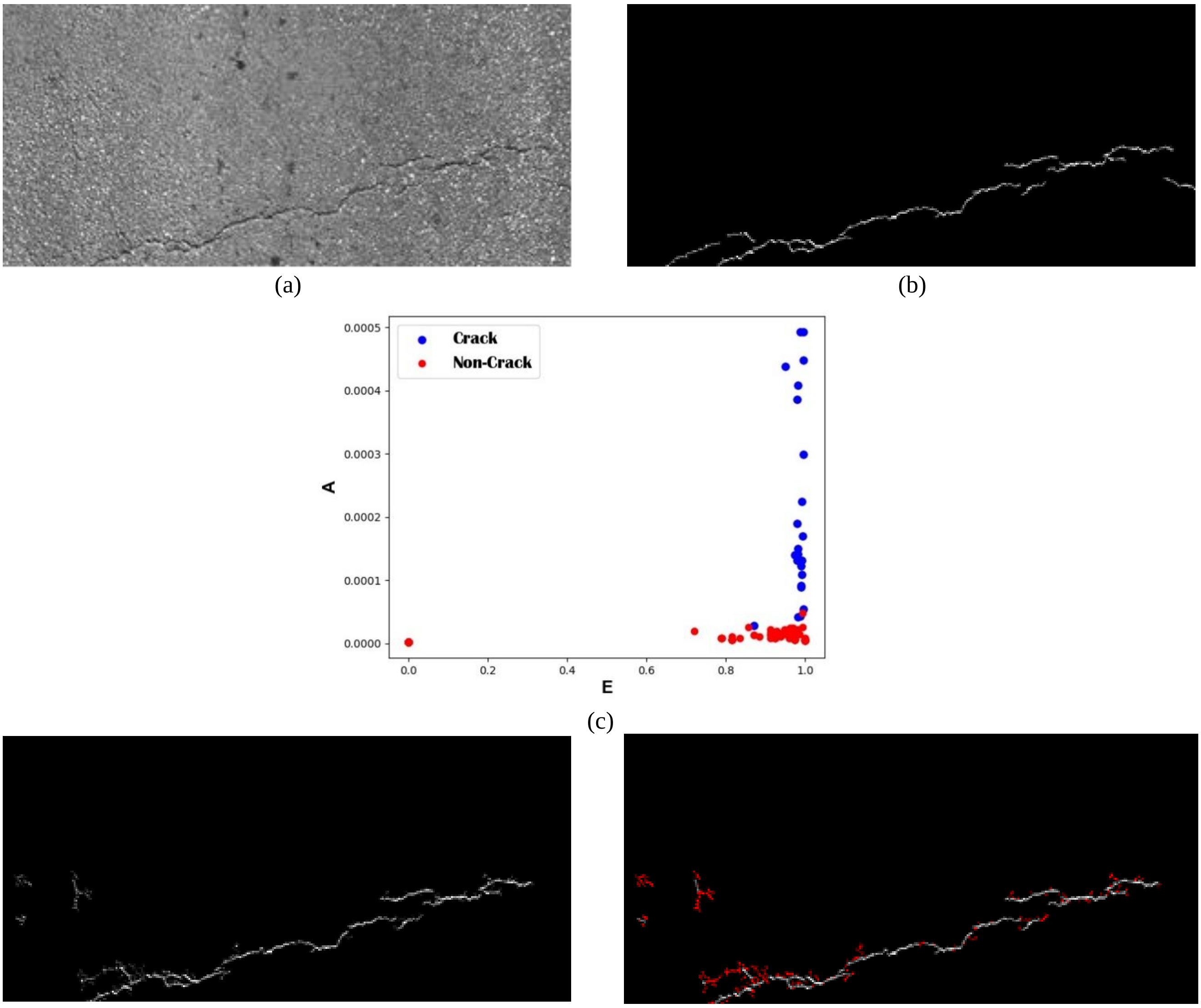

Figure 3: Demonstration of the noise cancellation process on MFCD:(a) Input image, (b) Ground-Truth, (c) Decision Graph, (d) Result of MFCD, (e) Noise detected (in red).

IV. Results

A. Noise Cancellation Results on MFCD

Figure 4 shows the performance of MFCD under the impact of the proposed noise cancellation DPAE, denoted as MFCD+DPAE. Notably, the segmentation results of MFCD+DPAE are better than that of the initial MFCD, where unwanted regions (represented in red) are removed. The quantitative results reported in Table II have verified that with the proposed NC, the performance of MFCD can be improved significantly. On all four sample images, the improvement of the evaluation metric F_1 is about 1% when using DPAE, especially over 3% on Image 4. Besides, the average F_1 in the test set is also improved. Since there is not much noise in some results of MFCD, the overall improvement is 0.8%.

B. Noise Cancellation Results on CBAT

Some results of DPAE on CBAT (CBAT + DPAE) are shown in Figure 5. Unlike the MFCD, CBAT segmentations are noisier and hence the difference between CBAT and CBAT+DPAE is more significant. It can be seen in the examples that most noises are removed after using DPAE. This is verified quantitatively in Table III, where an improvement of at least 2% is observed. Especially, a significant improvement of 11.98% is noted in Image 8. The impact of DPAE on CBAT is clearer than that on MFCD. The average result of CBAT+DPAE on 156 images shows a boost of 0.93% in F_1 score.

TABLE II: Quantitative results of MFCD+DPAE

Name	MFCD	MFCD+DPAE
Image 1	0.8653	**0.8783**
Image 2	0.8708	**0.8817**
Image 3	0.9168	**0.9372**
Image 4	0.9034	**0.9346**
Average result on the test set	0.7922	**0.8002**

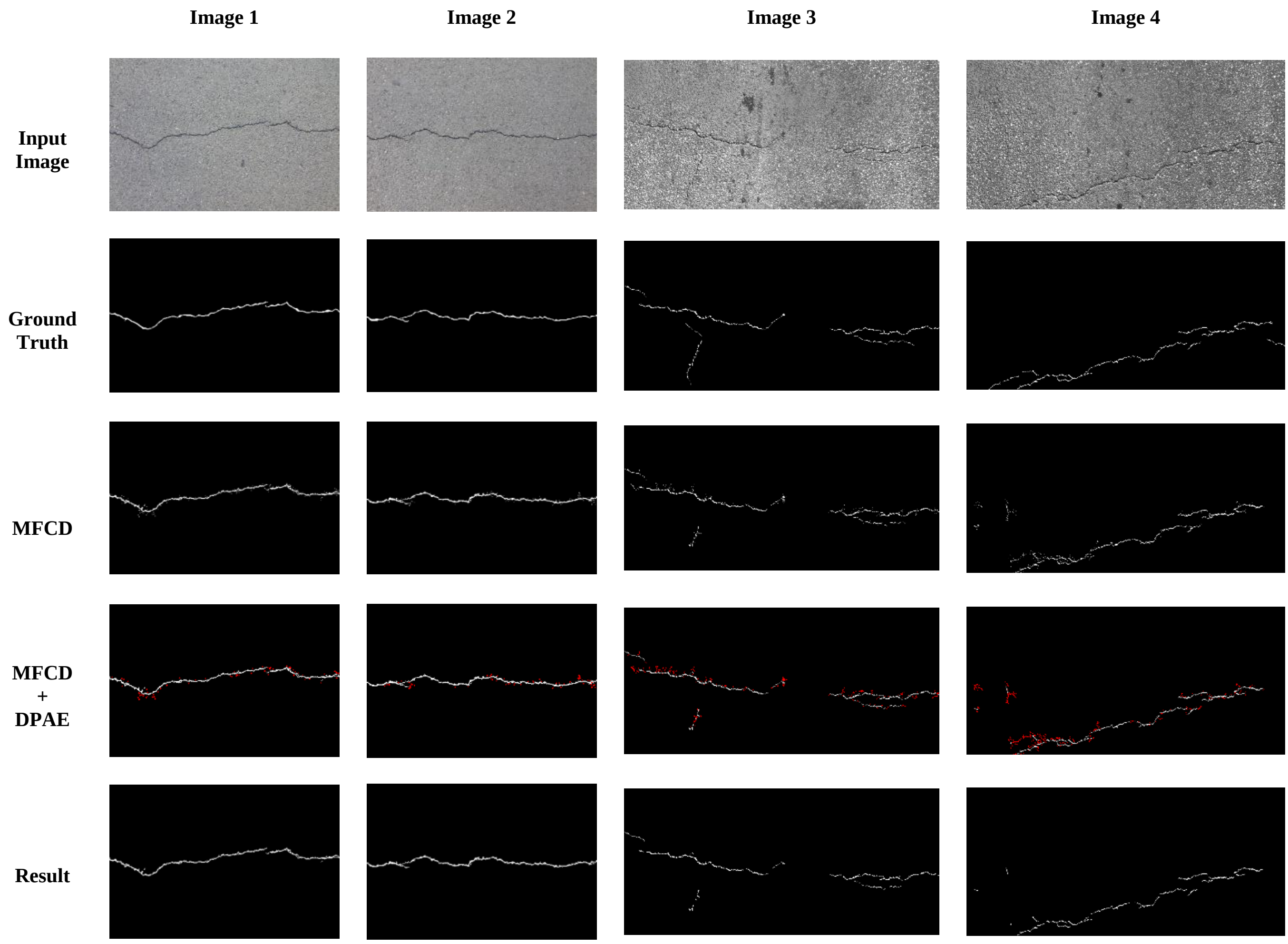

Figure 4: Noise cancellation on MFCD images.

TABLE III: Quantitative results of CBAT+DPAE

Name	CBAT	CBAT+DPAE
Image 5	0.7971	**0.8614**
Image 6	0.8440	**0.8713**
Image 7	0.7731	**0.8595**
Image 8	0.7557	**0.8755**
Average of 156 images	0.6890	**0.6983**

V. DISCUSSION

Experimental results have shown the significant impact of DPAE on both MFCD and CBAT. The improvement in terms of F_1 score on some segmentations of MFCD is up to 3%, although the accuracy of the MFCD alone is already around 90%. The average improvement of DPAE on segmentations of MFCD on the test set is approximately 0.8% since some segmentations in the test set do not contain noise. The effect of DPAE is more notable on crack detection algorithms that return more noises as CBAT. The overall improvement of CBAT compared to the one without noise cancellation is 0.93%.

VI. CONCLUSION

This paper proposed a noise cancellation technique based on clustering and image properties such as size, eccentricity, brightness, and contrast. A classification approach using CFSFDP and the Gradient Boosting Tree is then developed where training samples are extracted from two reputable image datasets: AigleRN and CFD. Experimental results have verified the impact of the proposed approach on two recent effective crack detection techniques, MFCD and CBAT. Although an improvement in accuracy of almost 1% has been achieved, the performance can be further enhanced by taking into account another shape-based feature and extend the dimension of the utilized clustering algorithm, which will be our future work.

ACKNOWLEDGEMENT

This work has been supported by VNU University of Engineering and Technology under project number CN20.38.

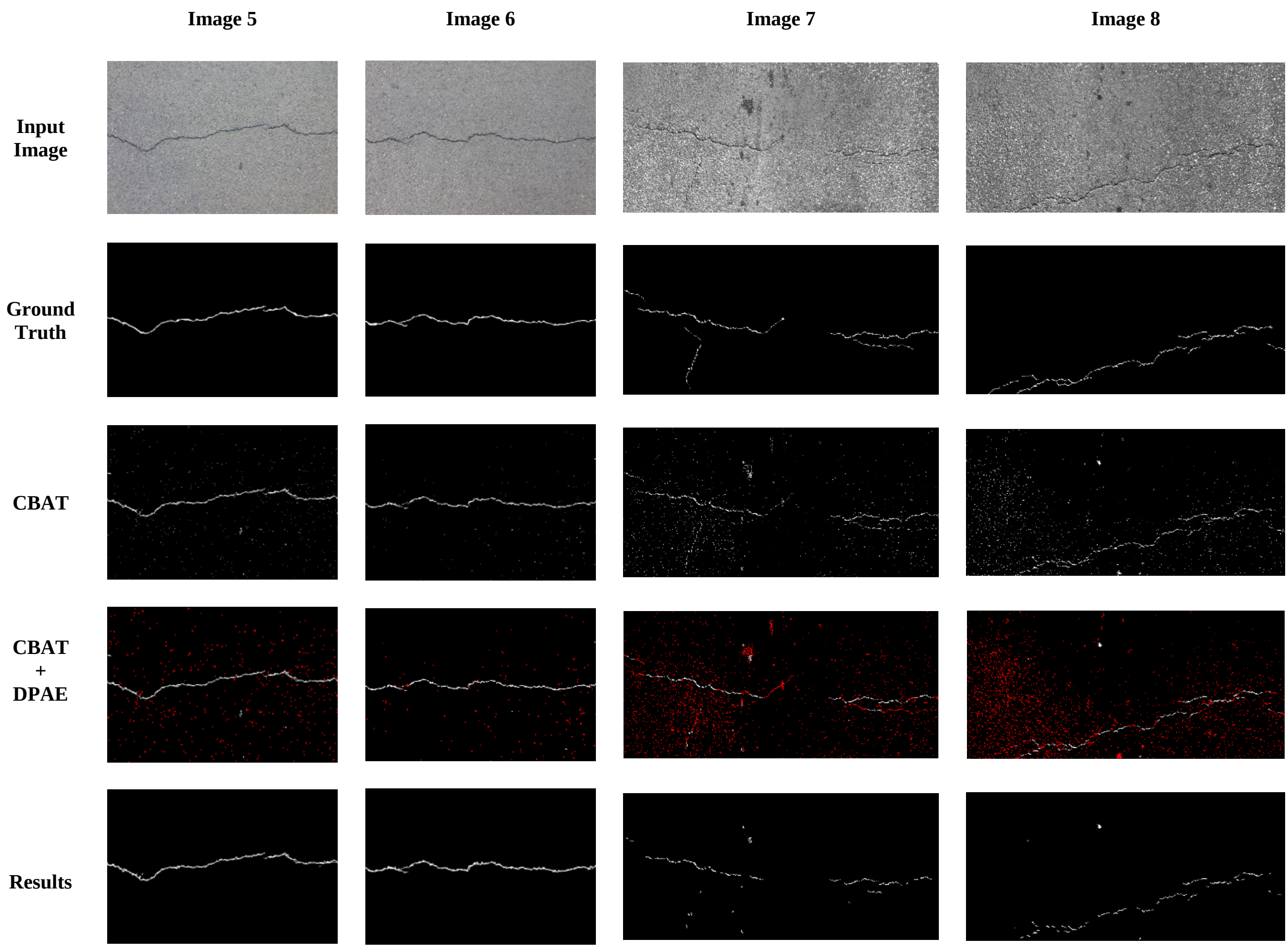

Figure 5: Result of noise cancellation on CBAT images

VII. REFERENCES

[1] H. M. La, T. H Dinh, N. H. Pham, Q. P. Ha, A. Q. Pham, "Automated robotic monitoring and inspection of steel structures and bridges", *Robotica 37*, no. 5, pp. 947-967, 2019.

[2] HF. Wang, L. Zhai, H. Huang, LM. Guan, KN. Mu, GP. Wang, "Measurement for cracks at the bottom of bridges based on tethered creeping unmanned aerial vehicle", *Automation in Construction 119*, 2020.

[3] X. T. Tran, T. H. Dinh, V. H. Le, Q. Zhu, Q. Ha, "Defect detection based on singular value decomposition and histogram thresholding", *In Proceedings of the 2020 IEEE/ASME International Conference on Advanced Intelligent Mechatronics (AIM)*, pp. 1149-1154, 2020.

[4] V. T. Hoang, M. D. Phung, T. H. Dinh, Q. P. Ha, "System Architecture for Real-Time Surface Inspection Using Multiple UAVs", *IEEE Systems Journal*, vol. 14, no. 2, pp. 2925-2936, 2020.

[5] H. Li, D. Song, Y. Liu, B. Li, "Automatic Pavement Crack Detection by Multi-Scale Image Fusion", *IEEE Transactions on Intelligent Transportation Systems*, vol. 20, no. 6, pp. 2025-2036, 2019.

[6] D. Ai, G. Jiang, L. S. Kei, C. Li, "Automatic pixel-level pavement crack detection using information of multi-scale neighborhoods", *IEEE Access*, vol. 6, pp. 24452-24463, 2018.

[7] Y. Shi, L. Cui, Z. Qi, F. Meng, Z. Chen, "Automatic road crack detection using random structured forests", *IEEE Transactions on Intelligent Transportation Systems*, vol. 17, no. 12, pp. 3434-3445, 2016.

[8] L. Zhang, G. Zhou, Y. Han, H. Lin, Y. Wu, "Application of internet of things technology and convolutional neural network model in bridge crack detectio", *IEEE Access*, vol. 6, pp. 39442-39451, 2018.

[9] C. V. Dung, L. D. Anh, "Autonomous concrete crack detection using deep fully convolutional neural network", *Automation in Construction*, vol. 99, pp. 52-58, 2019.

[10] W. Wang, C. Su, "Convolutional neural network-based pavement crack segmentation using pyramid attention network", *IEEE Access*, vol. 8, pp. 206548-206558, 2020.

[11] Q. Zou, Z. Zhang, Q. Li, X. Qi, Q. Wang, S. Wang, "Deepcrack: Learning hierarchical convolutional features for crack detection", *IEEE Transactions on Image Processing*, vol. 28, no. 3, pp. 1498-1512, 2018.

[12] W. Fang, L. Ding, P. E. Love, H. Luo, H. Li, F. Pe~na-Mora, B. Zhong, C. Zhou, "Computer vision applications in construction safety assurance", *Automation in Construction*, vol. 110, p. 103013, 2020.

[13] Rodriguez, Alex, Alessandro Laio, "Clustering by fast search and find of density peaks", *Science*, vol. 344, no. 6191, pp. 1492-1496, 2014.

[14] Q. Zhu, T. H. Dinh, M. D. Phung, Q. P. Ha, "Hierarchical Convolutional Neural Network With Feature Preservation and Autotuned Thresholding for Crack Detection", *IEEE Access*, vol. 9, pp. 60201-60214, 2021.

[15] N. Otsu, "A Threshold Selection Method from Gray-Level Histograms", *IEEE Transactions on Systems, Man, and Cybernetics*, vol. 9, no. 1, pp. 62-66, 1979.

[16] I. Pillai, G. Fumera, F. Roli, "Designing multi-label classifiers that maximize f measures: State of the art", *Pattern Recognition*, vol. 61, pp. 394-404, 2017.

[17] R. Amhaz, S. Chambon, J. Idier, and V. Baltazart, "Automatic crack detection on two-dimensional pavement images: an algorithm based on minimal path selection", *IEEE Transactions on Intelligent Transportation Systems*, vol. 17, no. 10, pp.2718-2729, Oct. 2016.

[18] Y. Shi, L. Cui, Z. Qi, F. Meng,and Z. Chen, "Automatic road crack detection using random structured forests", *IEEE Transactions on Intelligent Transportation Systems*, vol. 17, no. 12, pp.3434-3445, Dec. 2016.

The 6th International Conference on
Engineering Mechanics and Automation (ICEMA 2021)
Hanoi, November 14, 2021

A proposed design of vacuum gripper system integration for one specific robotic arm

Tran Van Viet
Mechatronics Department - Institute of Mechanics – VAST
264 Doi Can, Hanoi, Vietnam
viettran3354@gmail.com

Do Tran Thang
Mechatronics Department - Institute of Mechanics - VAST

Nguyen Van Khuong
Viettel High - Technology Industries Corporation

***Abstract*: Robotic arms have been widely used in many applications such as production lines, research and development, the military, medicine, space exploration, and so on. Ordinarily, conventional robotic arms consist of an arm and a gripper (a kind of tool). Today, there are plenty of robotic grippers developed with high flexibility, stability, and accuracy. This paper approaches a type of vacuum grippers used commonly thanks to its simplicity but flexibility enough, that works based on Bernoulli's principle - a high-pressured flow sucks the air in enclosed space between the clamp plate and a given object creating a tight grasp. The research issues of the paper will help to understand deeply vacuum gripper systems including both their advantages, disadvantages, and applicability. In the beginning, the paper focuses on the fundamentals of robotic grippers used for manipulating objects, calculation on the bearing load in some cases, and then designing a specific prototype integrated with one robotic arm for simulation and control purposes. Finally, some results will be shown for illustration and discussion. (*Abstract*)**

Key Words*: *Robot arms, vacuum grippers, robotic grippers, industrial robots *(key words)*

I. INTRONDUCTION AND SCOPE

Every gripper is a hand attached to robotic arms for manipulating objects in contact directly. Currently, there are many types of grippers given to many choices such as 2-finger grippers, 3-finger grippers, electromagnetic grippers, soft grippers, etc. To develop applications for robotic arms, the paper will show overviews of robotic grippers, especially vacuum grippers employed widespread in practical. This type of grippers follows the Venturi-principle which will generate a high-pressured dynamic flow in pipelines, this pulls the gaseous particles from a 3rd port into the outlet stream aimed to create the vacuum for application targets. The long-term objective here is to study related problems of vacuum grippers to step by step master technology processes then manufacture this type for real applications. In the scope, the paper will propose a prototyping design for a specific gripping system integrated into the SM6 robotic arm in practice. So that the SM6 robotic arm integrated an extra tool (a vacuum gripper) has capabilities to operate pick-and-place tasks with various objects owned different physical features.

The SM6 robot arm is the main outcome of the national project "Mastering the art of technological processes for designing and prototyping a 6 dofs robotic arm" executed by Mechatronics Department of the Institute of Mechanics belong to Vietnam Academy of Science and Technology. The SM6 robot arm can be able to do many tasks like traditional manipulators and even the same to cobots in near future.

This paper will present a topic related to designing a vacuum pick-and-place system integrated with the SM6 robotic arm to manipulate objects such as carton boxes up to a maximum weight of 3kg. This application is commonly operated in product packaging lines.

Previous articles on vacuum grippers are more referred including:

A K Jaiswal [1, 2] designed a vacuum gripping and positioning tool for robots, studying the applicability and advantages of this clamping system. A. Tiwari [3] studied the physics of suction cups, developing a theory of the contact between the suction cups and random rough surfaces. Robert Schaffrath [4] introduced a new concept of vacuum clamping machines without a central compressed air supply. Felix Gabriel [5] and colleagues modeled an energy-saving designed vacuum gripper in the handling and placing of objects. And many other researchers have raised issues related to this field which will be listed under the References section.

II. AN OVERVIEW OF VACUUM HANDLING SYSTEMS

A. Components of vacuum gripper systems

Vacuum tongs are mainly used to lift objects with smooth surfaces for both wood, metal, plastic materials, and glass panels. And it is not suitable for Rough, flawed, and soft surfaces. Here is an overview diagram of a basic vacuum clamping system in Figure 1 as below:

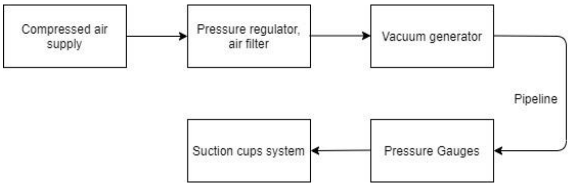

Fig. 1. Parts that make up the vacuum clamp

A typical gripping system will include the following parts: the suction cup is pressed against the surface of the product to form an enclosed space, the air pipe is used to connect the vacuum generator and the suction cup to help the system functioning properly, a Venturi vacuum generator, a pressure regulator – filter and a supply of compressed air for the application. There are also some additional parts such as accessories for suction cups, couplings, frames/racks, etc.

B. Design processes for Vacuum grippers

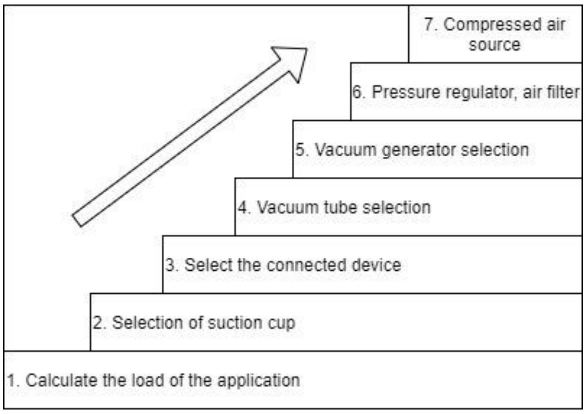

Fig. 2. Vacuum gripper design process

A step-by-step design process for vacuum clamps is described as shown in Figure 2.

III. A VACUUM SYSTEM DESIGN FOR SM6 ROBOT ARM

A. Calculation of loads

The load of the application is the mass of the object being lifted concerning the acceleration and the factor of safety applied.

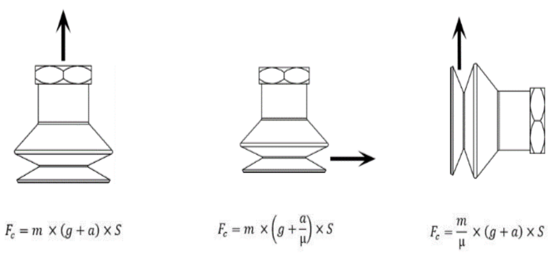

(a) (b) (c)

Fig. 3. Three cases of moving the object to be lifted

With the given application: the arm SM6 can lift a product with a mass of 3kg, the maximum acceleration of the arm is 1m/s^2.

Calculate the 3 main types of load applications as shown in the following figure (note, the arrow represents the movement of the lifting system).

Here:

- F_c is the payload (N)
- m is the mass of the load (kg)
- g is gravity acceleration (9.81 m/s^2)
- a is robot's acceleration (m/s^2)
- S is the factor of safety (this factor is usually 1.5 or 2, 4 recommended for special cases).
- μ is the coefficient of friction between the suction cup and the workpiece (0.1 for oil surfaces; 0.2 or 0.3 for wet surfaces; 0.5 for wood, metal, glass; 0.6 for rough surfaces).

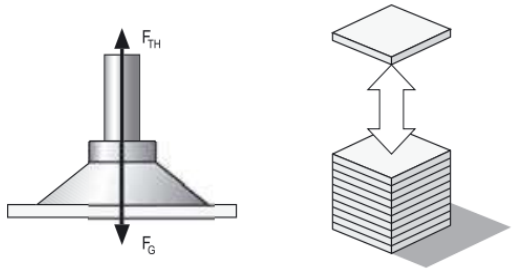

Fig. 4. Application of suction cups to lift and drop products

In the case of (a) in Figure 3: The suction cup and workpiece are horizontal, the robot moves up and down.

$$F_c = m \times (g + a) \times S \tag{1}$$

Applied cases: $F_c = 3 \times (9.8 + 5) \times 2 = 88.8$ (N).

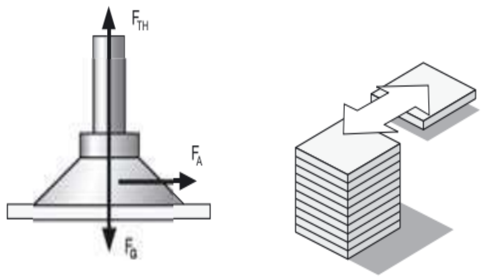

Fig. 5. Application of suction cups to lift and move products horizontally

In the case of (b): The suction cup and workpiece are horizontal, the robot moves horizontally.

$$F_c = m \times (g + a / \mu) \times S \tag{2}$$

Applied cases:

$F_c = 3 \times (9.8 + 5 / 0.5) \times 2 = 118.8$ (N).

In the case of (c): The suction cup and workpiece are vertical, the robot moves up and down.

$$F_c = \frac{m}{\mu} \times (g + a) \times S \tag{3}$$

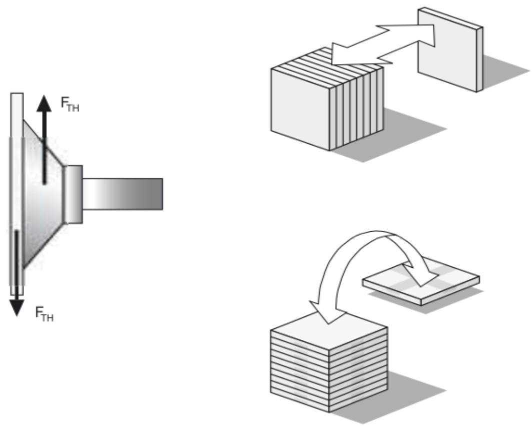

Fig. 6. Application of suction cups to lift, move and rotate products

Applied cases:

$$F_c = \frac{3}{0.5} \times (9.8 + 5) \times 4 = 355.2 \text{ (N)}.$$

B. Selection of suction cups

The design of a suction cup system will depend primarily on two basic factors:

- Weight (or load) of the object to be lifted: Increase safety, reliability, and speed by using multiple suction cups in each position.
- Surface material to be lifted: Materials to be handled in pick and place applications can be grouped into two categories (non-porous and porous).

The figure below shows the extent to which a vacuum is generated when handling two basic materials: porous and non-porous.

The application for handling carton boxes is a porous material, the generated vacuum will be about -55kPa.

The holding force of the suction cup is calculated as follows:

$$F_P = \frac{A \times P \times N}{1000} \quad (4)$$

Here:

- A is the contact area of a suction cup with the product surface (mm^2).
- P is the system vacuum pressure (kPa)
- N is the number of suction cups used.

The condition required to prevent objects from falling is $F_P \geq F_c$.

With the application is given in this article is stacking carton boxes on pallets, it will be necessary to move objects in two cases of load (a) and load (b). The payload in case (c) can be ignored for the sake of the application part of the job.

Applied cases: $F_P = F_c \Leftrightarrow \dfrac{A \times P \times N}{1000} = 118.8$

$$\Leftrightarrow A \times N \times 0.055 = 118.8 .$$

So that the required contact area of the suction cup for the application is A x N = 2160mm^2.

In addition, based on the material to be processed, the workpiece temperature, and many other factors to choose the right suction cup material and shape.

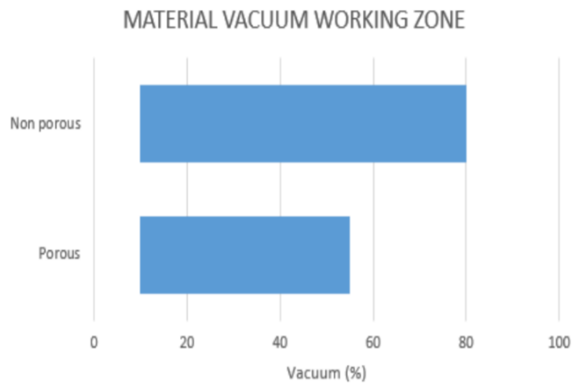

Fig. 7. Vacuum pressure generated by material types

Select the number of suction cups and the size of the suction cups according to the following table:

TABLE 1: SUCTION CUP SELECTION TABLE

Number of suction cups	1	2
Suction cup radius	26 mm	18.5 mm

As the result to select a suction cup with a radius of 26mm.

C. Selection of connecting devices

Connection devices can be accessories of suction cups, pipe joints with components, etc.

When handling objects with uneven surfaces using 2 or more suction cups, the suction cup attachment needs to be spring-loaded for elasticity. The purpose of the spring is to compensate for the different heights of the product, make sure all the suction cups are in contact with the object, and avoid hitting the product hard due to the elasticity.

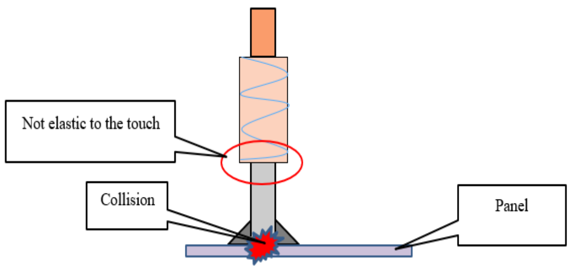

Fig. 8. Suction cup accessories

Pipe joints are susceptible to system gas leaks. Use as few couplings as possible and ensure tight seals do not cause air leaks in these components, resulting in reduced system efficiency.

D. Pipe selection

The size of the vacuum tube must match the suction cup used, high elastic flexible material.

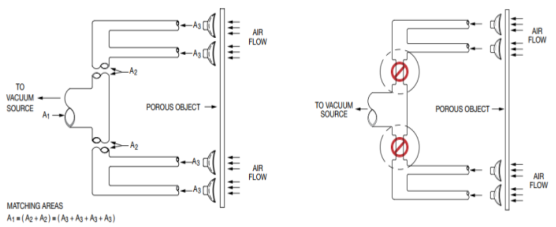

Fig. 9. Design principles of vacuum tubes

The gas pipeline needs to be uniform from start to finish: the pipe area of each branch must match the area of the next branch, and the main trunk must be sized to handle the maximum flow.

E. Selection of vacuum generators

The vacuum generator works on the Venturi principle, the main parameter to choose the vacuum generator is the suction flow of the device. Calculate the suction flow based on the suction cup diameter according to Table 2 and the following formula:

$$V = n \times V_S \tag{5}$$

Here:

- V (l/min) is the required suction flow of the system
- n is the number of suction cups used
- V_S (l/min) is the suction flow of 1 single suction cup.

TABLE 2: SUCTION CUP DIAMETER AND CORRESPONDING SUCTION FLOW REQUIREMENTS

Suction cup diameter	Suction flow requirements Vs	
Under 20mm	0.17(m^3/h)	2.83(l/min)
From 20-40mm	0.35(m^3/h)	5.83(l/min)
From 40-60mm	0.5(m^3/h)	8.3(l/min)
From 60-90mm	0.75(m^3/h)	12.7(l/min)
From 90-120mm	1(m^3/h)	16.6(l/min)

Applied cases: The system uses a suction cup with a diameter of 52mm.

$\Rightarrow V = 1 \times 8.3 = 8.3$ (l/min)

Then decide on a vacuum generator with suction flow parameters: 8.3(l/min).

F. Selection of regulators

The pressure regulator is usually integrated with the air filter, which is installed between the compressed air supply and the vacuum generator. This unit keeps a stable vacuum pressure level to feed the vacuum generator and filter dirt, debris, steam, etc. from the compressed air source to the vacuum generator.

Pressure regulators increase equipment life, lower maintenance costs, and higher flow capacity. Based on the effective pressure of the vacuum generator to select and set the appropriate pressure regulator parameters.

Fig. 10. Pressure regulators and air filters

G. Compressed air supply

Compressed air supplies usually use compressed air pumps. Based on the operating pressure range of the vacuum generator to choose the right vacuum pump to meet the required compressed air supply. The gas from the compressed air supply can go directly to the vacuum generator, but for the pressure to work stably and to ensure the safety of the equipment, it is recommended to install an additional pressure regulator and air filter.

It is necessary to ensure safety when operating the compressed air system, which can lead to unsafe fire and explosion. Carefully read the precautions when using the compressed air pump.

IV. TESTING AND ASSESSMENT

A. Paradigm

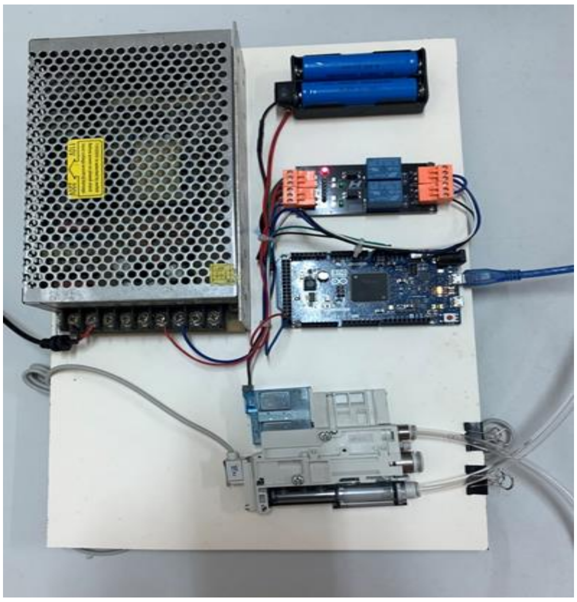

Fig. 11. The hardware system

Build a test model with the parameters described above to evaluate the system's reliability before integrating it into the SM6 robotic arm. The test model is controlled via Arduino and controlled on the computer by Matlab GUI software.

Fig. 12. The control software

B. Testing

Conduct a test run of two types of tasks that are typical for two commonly treated materials, porous and non-porous. For each type of task, the most important thing is to determine the level of vacuum pressure created in the system, calculate the relevant values for comparison and evaluation.

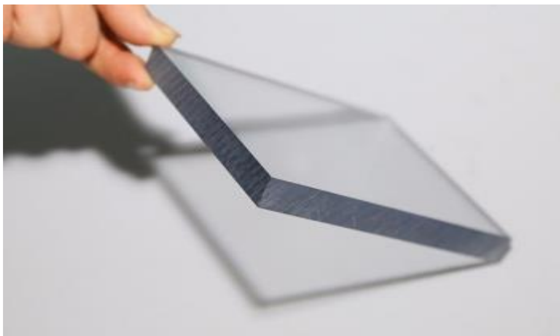

Fig. 13. A solid polycarbonate sheet

In the case of system testing with non-porous materials (plastic surface materials, glass surfaces), the output vacuum pressure level ranges from -80 to -90kPa.

Based on the obtained graph: Stage 1 is when the suction valve is turned on but the suction system has not picked up the object, the vacuum pressure creates about -20kPa because the system is open. Once the object is picked up, the pressure is about -90kPa (close to the ideal vacuum -101kPa). After turning off the suction valve, the pressure returns to 0.

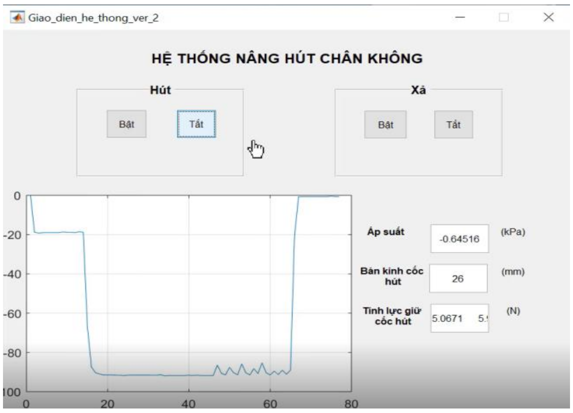

Fig. 14. Test results with Polycarbonate sheets

When handling materials with non-porous surfaces such as plastic surfaces, glass surfaces, etc., the vacuum pressure level is very good (about -90kPa).

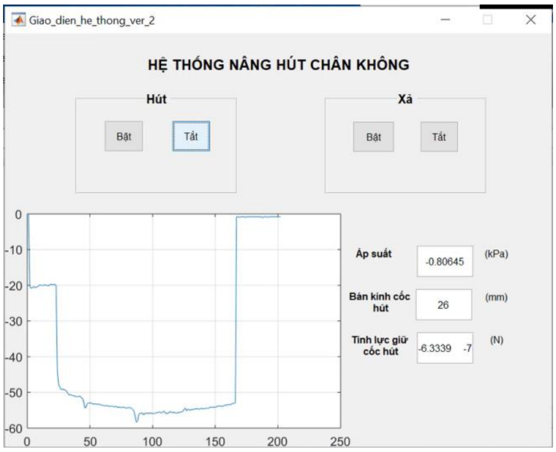

Fig. 15. Testing results with carton boxes

In the case of testing the system with a porous material such as a carton box, the degree of vacuum generated is in the range of -50 to -60kPa.

Stage 1 when the suction valve is turned on but the suction cup has not been in contact with the object, the vacuum pressure level in the system is -20kPa. After the suction cup picks up the object, the vacuum pressure level created for the porous material is in the range of -50 to -60kPa. Turn off the suction valve and the pressure level is 0.

When handling porous materials, the vacuum level produces about -50 to -60kPa due to gas leakage through the material but still meets the demand for product suction.

As such, the system generates a reliable vacuum level for use in the robotic arm.

V. THE PROPOSED INTERGRATING SOLUTION

A. Integrated vacuum grippers with SM6 control system

The SM6 uses an ACS Motion Control 8-axis controller called SpiiPlusEC Motion Controller to control the six joints of the arm via an EtherCAT line.

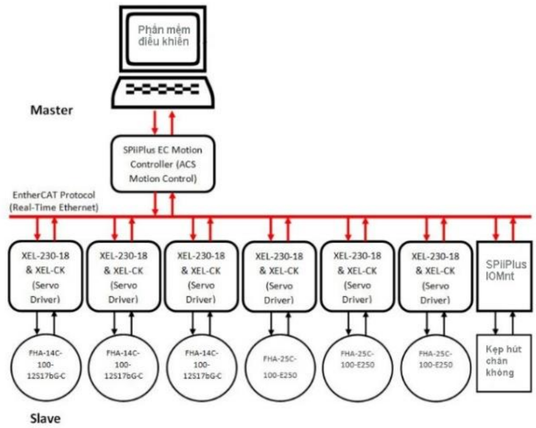

Fig. 16. The control system of SM6

For the SM6 controller to control the vacuum generator, it is necessary to use an intermediate device that can communicate with the controller through one of the communication methods that the controller supports such as RS232, RS485, EtherCAT [6].

The optimal control method for the system, control via EtherCat communication. The overview will be 1 control master, 7 execution slaves including 6 servos actuators for arm joints, and 1 I/O module for vacuum gripper units.

B. Integration with SM6 software.

Like other robotic arms, SM6 also has its software program called SM robot (Small Manipulator) to link between the user and the robot's controller.

SM robot software is built to perform three main tasks:

- Design motion trajectory for the robot.
- Simulation of robot kinematics and dynamics.
- Control and monitor the operation of the robot.

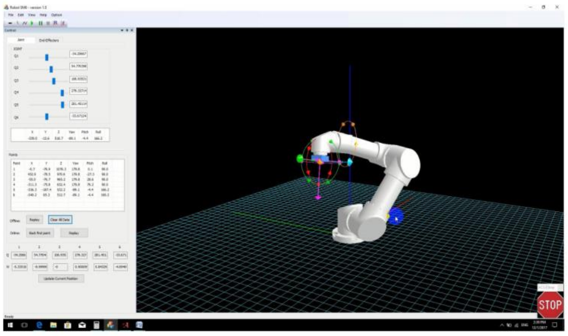

Fig. 17. SM6 robot control software

SM robot has not built the grip control function. Therefore, to control the vacuum clamping system, we need to build an additional module to help the controller (ACS SpiiPlusEC) control via I/O signals. Two supply valves and vacuum discharge valves are equivalent to 2 output signal pins.

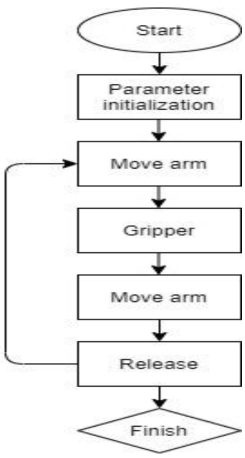

Fig. 18. SM6 with gripper control

VI. CONCLUSION

In this paper, vacuum clampers in industrial robot applications have been discussed from an overview to a step-by-step design of a particular clamping system. The objective of the paper is to describe a very detailed step-by-step gripper design process and then integrate it onto the SM6 robotic arm for a specific application. Compared to the human hand, the vacuum gripper system is very limited when handling a variety of materials, but it will bring high performance to factories. Vacuum gripping is effective when handling materials with smooth, smooth surfaces and limits air escape through the surface.

The article has high practical application significance and there will be many directions for development such as: mastering the technology of vacuum generation by Venturi principle to design desired performance vacuum generators, designing dedicated control for vacuum gripper so that it can be integrated into different types of arms, developing advanced features of vacuum clamp such as object lifted detection, workpiece drop detection, automatic break when enough pressure.

ACKNOWLEDGMENTS

This work was supported by the Vietnam Academy of Science and Technology (VAST) for developing robotic technology in microbiological fertilizer production lines.

REFERENCES

[1]. A K Jaiswal and B Kumar. “Design constraints of vacuum gripper of robots – as a pick and place operating tool,” ISSN: 2250 – 141X Vol.6 Issue 4, October 2016.

[2]. A K Jaiswal and B Kumar. “Vaccum gripper – an important material handling tool,” ISSN: 2250 – 141X Vol.7 Issue 1, February 2017.

[3]. A. Tiwari and B.N.J. Persson. “Physics of suction cups,” Preprint – May 2019.

[4]. Robert Schaffrath et al. “Vacuum gripper without central compressed air supply,” Procedia CIRP 97 (2021) 76 – 80.

[5]. Felix Gabriel et al. “Modeling of vacuum grippers for the design of energy efficient vacuum- based handling processes,” Production Engineering (2020) 14:545 – 554.

[6]. Mechatronics Department, Institute of Mechanics-VAST. “Complete and masters the technology of designing and manufacturing industrial robots with 6 degrees of freedom and applying products to industrial production lines,” National projects (2018).

Fabrication and Investigation of Flexible Strain Sensor for Sign Language Recognition System

Chi Tran Nhu
Faculty of Electronics and Telecomunications
VNU – University of Engineering and Technology
Hanoi, Vietnam
trannhuchi@vnu.edu.vn

Phu Nguyen Dang
Faculty of Electronics and Telecomunications
VNU – University of Engineering and Technology
Hanoi, Vietnam
phund@vnu.edu.vn

Van Nguyen Thi Thanh
Faculty of Electronics and Telecomunications
VNU – University of Engineering and Technology
Hanoi, Vietnam
vanntt@vnu.edu.vn

Ha Tran Thi Thuy
Faculty of Electronics
Posts and Telecommunications Institute of Technology
Hanoi, Vietnam
hatt@ptit.edu.vn

Van Dau Thanh
School of Engineering and Built Environment
Griffith University
Queensland QLD 4222, Australia
v.dau@griffith.edu.au

Tung Bui Thanh
Faculty of Electronics and Telecomunications
VNU – University of Engineering and Technology
Hanoi, Vietnam
tungbt@vnu.edu.vn

***Abstract*: In this study, an ultra-stretchable and highly sensitive strain sensor is successfully fabricated by 3D printing technology with a mixture of aqueous sodium chloride and silicone rubber. This strain sensor has dimensions of 50x10x10 mm, with a fluidic channel (6 mm) inside. The physical and mechanical properties of sensor were characterized by gauge factor measurement. Experimental results show that the resistance of the sensor changes when an external force deforms the ionic liquid shell; exhibiting impressive stretchability with wide range strain (100%), good bending properties and high sensitivity with a stable gauge factor of 2.1. Besides, the sensor also is investigated with a vertical pressing force. Initially, the resistance of the sensor increase slowly and it then jump rapidly to the saturation value at the force of 40 N. For application of sensor, the proposed sensor is applied to recognize the sign language through attaching five strain sensors on the fingers. The obtained result shows the sensor can detect the movement of the fingers and convert 10 letters of sign language into the voice with high accuracy, about 98%. On the other hand, the result also demonstrates the proposed sensor has high potential in healthcare, human motion monitoring and electronic skin.**

Keywords: strain sensor, gauge factor, 3D printing technology, sign language

I. INTRODUCTION

Strain sensor, the resistive or capacitive properties of which change as the strain or curvature applied to them are varied. The change in these electrical properties basically occurs due to the change in the device geometry in response to the applied mechanical stimulus. These sensors are used widely to measure mechanical deformation of structures [1], [2]. A strain sensor is characterized by a gauge factor or the sensitivity to strain. As the most commonly used strain sensor, metallic foil gauges have a gauge factor of approximately 2. Meanwhile, strain sensors based on semiconductor give much higher sensitivity. For example, single crystalline silicon demonstrates intrinsic gauge factors as high as 200 [3]–[5]. However, as an intrinsically stiff and brittle material, silicon is just suitable for small deformation measurement, i.e., strain less than 0.1%.

Recent studies have focused on the development of strain sensors for large deformation measurement for replacing the traditional strain sensors in various applications such as medical applications and soft robotics [6]. These sensors are developed with different fabrication strategies including but not limited to lithography [7], [8], 3D printing [9], [10], laser engraving [11]–[13], and mould based techniques [14]–[17]. Besides, various conductive agents are used such as eutectic Gallium-Indium (eGaIn) [10], [11], [14]–[21], carbon [7], [8], [13], [22]–[27], ionic fluids [12], [28]–[34] and optical fibers [35]. Also, several base substrates with varying viscosity and softness properties have been employed in the design of these sensors; polydimethylsiloxane (PDMS), soft silicone rubbers and hydrogels are among the most commonly used materials in these studies. However, emerging among them, the sensors that the ionic fluids combine with with elastomer (PDMS, Silicone), to make the sensor more elastic and suitable for soft applications are a trend now. Because they are low cost, easy to use and environmentally friendly.

In this paper, we introduce a low-cost, high-sensibility and ultra-stretchable strain sensor based on the ionic liquid of glycerin and sodium chloride (NaCl). Besides, a compact conditioning circuit is also designed for evaluating the strain sensing performance of the sensor. Based on the proposed sensor, a wearable application of the sensor has been demonstrated by using the sensor for detecting the motion of fingers.

II. PRINCIPLE OF FLUIDIC STRAIN SENSOR

In this study, we use a silicone rubber shell fill with a mixture of glycerin and sodium chloride. Glycerin is used in this mixture because it can protect electrodes from being frustrated by ionic liquid and increase the viscosity of the liquid. Silicone glue is applied at the interface between the electrodes minimize leakage of the mixture to the outside.

The proposed sensor is a type of resistive form. At rest state, the sensor has the length (l) and diameter (d). The resistance of the sensor can be measured by the following equation:

$$R = \rho \frac{l}{\frac{\pi d^2}{4}} \tag{1}$$

When the tube is stretched, the length of the sensor increases to $(l + \Delta l)$ while the section area is decreased $(d - \Delta d)$, as shown in the Fig.1a. The resistance of the sensor is changed to:

$$R = \rho \frac{l + \Delta l}{\frac{\pi (d - \Delta d)^2}{4}} \tag{2}$$

As can be seen from the formula (2), the resistance of the sensor rise when the silicon tube is stretched. As we know, when sodium chloride is dissolved in water, they will be turned into cations (Na^+) and anions (Cl^-), which are all electrical carriers. In normal condition, these ions move randomly in the electrolyte solution, but when we apply a DC (direct current) voltage to the liquid, it will change the rule of carrier's motion and make the measurement unstable. Positive electrode will attract anions while negative one will attract cations. This motion creates a current inside ionic liquid. That is the reason why we can use them as conductive material. Therefore, an alternating current source is used to improve the accuracy of measurement.

From the analyzed principle, we design the structure of the sensor. There is a conductive channel wrapped by two layer of silicone (eco-flex) in order to obtain the sandwiched channel structure. The electrodes are put at two ends of the channel to cover the holes and to connect to an external measurement circuit, as shown in the Fig. 1b.

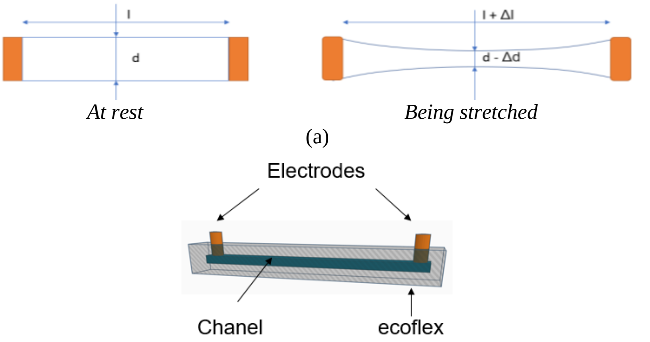

Fig. 1. Proposal of fluidic strain sensor. (a) Principle of the fluidic strain sensor, showing the geometry of the sensor at rest and when being stretched. (b) The structure of the sensor.

III. EXPERIMENTS

A. Sensor Fabrication

The proposed strain sensor is fabricated using a substrate as base material. The substrate is Smooth-On's EcoFlex 0010, which is an extremely soft, low-viscosity two component, addition cured room temperature vulcanizing silicone rubber. For the first part of the sensor, EcoFlex is mixed 1A:1B by weight, and poured into a 3D printed (Objet 500, 3D Printing Systems) mould (A) with the channel pattern and a total height of 50 mm. The mould is put in a vacuum chamber and degassed for 5 minutes in order to remove any air bubbles trapped inside the mixture. Before the sensor part can be demoulded, it is left to cure at high temperature (80 degree) for 2 hours, in LVO 2030 vacuum drying oven. For the second part of the sensor, a thin layer (2 mm) of EcoFlex is also fabricated similarly. However, it is only left to cure at room temperature for 15 minutes instead of putting the oven. Then the first layer is carefully placed onto the thin layer with the patterned surface facing down, preventing the channel from being filled by the semi-cured silicone, and the sensor is left to cure in the oven at 80 degree. After 2 hours, the sensor is taken out of the oven and demoulded, as shown in the figure 2.

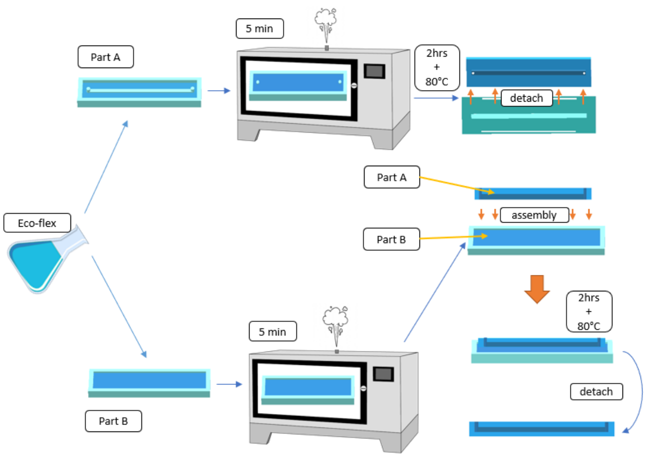

Fig. 2. The process of the strain sensor fabrication

The last step of sensor fabrication is filling the channel with a conductive liquid, namely a mixture of sodium chloride, water and glycerin. The channel is filled using a syringe fitted with a 25G needle. Gold-coated electrodes are inserted at two ends of the tube to make good contact with the liquid. Silicone glue is applied to the interface be-tween the electrode and the contact point for leaking prevention purpose as shown in the figure 3.

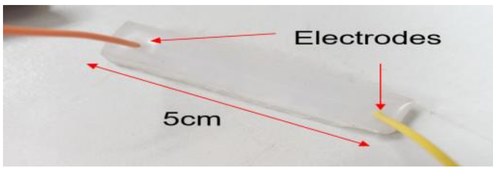

Fig. 3. A fabricated prototype of ionic liquid resistance strain sensor.

B. Experimental measurement of strain sensor

Resistance change can be measured by applying a current source to the resistor and measure the voltage drop. As mentioned above, with this ionic liquid resistive sensor, using the DC causes electrolysis at the two electrodes that can destroy the sensor. Furthermore, the parasitic capacitance between the electrode and the conducting liquid makes the measurement unstable [5]. Therefore, an AC source is utilized instead of the DC current source in this study to improve the accuracy of the measurement. The resistance of the sensor is measured by 4-point resistance measurement method using Howland current source as presented in Fig. 4. We can calculate the resistance of the sensor by using equation $R_s = \frac{V_s}{i_s}$, where the output signal amplitude (V_s) is determined by a conditioning circuit including an instrumentation amplifier and a peak detection circuit. The current value i_s through the sensor is determined by the reference resistor R_{ref} in the Howland current source as depicted $i_s = \frac{V_i}{R_{ref}}$. The current i_s depends only on R_{ref} and does not depend on the change of the resistance of the sensor when the sensor is stretched.

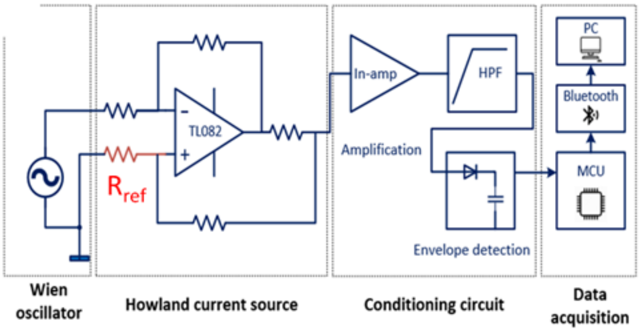

Fig. 4. Block diagram for strain gauge measurement

The current source is set to 2.0 μA and Wien circuit generated a sinusoidal oscillator with a frequency of 1 kHz. Input and output signals are observed through an oscilloscope, a liquid crystal display in the board monitor the resistance and voltage of the sensor. Arduino development KIT is used to display results in LCD and transfer measured values to a data acquisition computer.

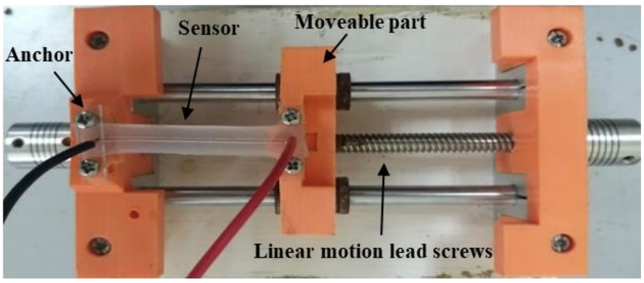

Fig. 5. Tensile strain generating platform

A tensile strain generating platform is designed and fabricated using 3D printing technology (Objet 500 printer from Stratasys) to apply strain to the sensor. It stretches the sensor easily and conveniently (Fig. 5). By fixing one end and pull another end by controlling the screw rod parallel to the sensor. A ruler is used to indicate the exact length of the sensor when being stretched. Signals from two electrodes are taken to the measurement circuit board to determine the resistance of the sensor. The sensors were fabricated in three different mixtures, namely 1%, 2% and 3% of NaCl. In addition, the sensor is also experimented with a force being applied to the sensor vertically. Experiment setup is established as shown in the figure 7a, with a mixture of 2% NaCl. The force is applied in the middle of the sensor with the contact area being 8*10 mm, a scale that put under the sensor as an applied force measuring device. Their properties are experimentally characterized and presented in the next session.

IV. Results and Discussions

In this study, we use Gauge factor as a fundamental parameter of the strain sensor. The Gauge factor is the relationship between can be defined as:

$$GF = \frac{\Delta R / R_0}{\varepsilon} \tag{3}$$

where ε is the applied strain, is the representative parameter to access sensitivity. The strain gauge of this kind of sensor was evaluated at different conductivities of the liquid. Experiment results are presented in Fig. 6 showing the change of sensor resistance due to the longitudinal strain of three different mixing ratios (1%, 2%, and 3% of NaCl). All the measurements are conducted at room temperature of around 25^oC. As can be seen, the proposed sensor can be stretched up to 100% and the resistance of the sensors increased linearly with the applied strain. The Gauge factor of the sensor is quite stable in the range from 2.01 to 2.4. This obtained result is same as previous studies [12], [33]. Furthermore, the results also show the resistance of the sensor increase gradually with the applied force being less than 40N, while it rises quickly when the force is bigger. The resistance of the sensor reach its limit point as the applied force is around 42N and this value still remain unchanged whether the force increase significantly, as shown in the Fig. 7b. This result can be explained that the length of the sensor rise and the diameter of a part of the sensor area where it is applied by the force decrease dramatically lead to the resistance of the sensor increase. When the applied force is over the limit value, the channel will be block and the ions can not move between two electrodes. Therefore, the resistance of the sensor is infinity.

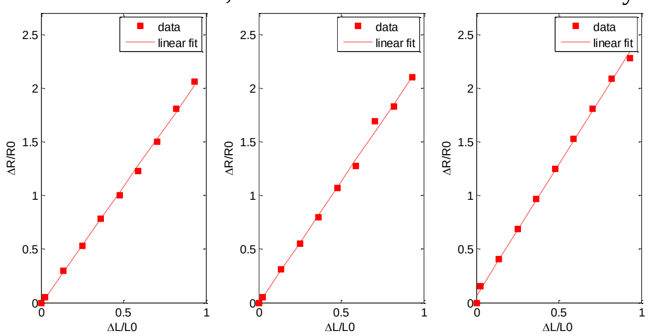

(a) (b) (c)

Fig. 6. Experimental results show the change of resistance due to strain of each sodium chloride ratio in ionic liquid mixture 1% NaCl (a), 2% NaCl (b), 3% NaCl (c).

Besides, the hysteresis of the sensor is also investigated with the force applying vertically. The time is recorded when the finger start moving from the sensor. The sensor back to the original state which there is no force applying to. The results show that the hysteresis is inversely proportional with the magnitude of the applied force. It is around 14.2 ms and 25.2 ms with the strong and light applied forces, respectively.

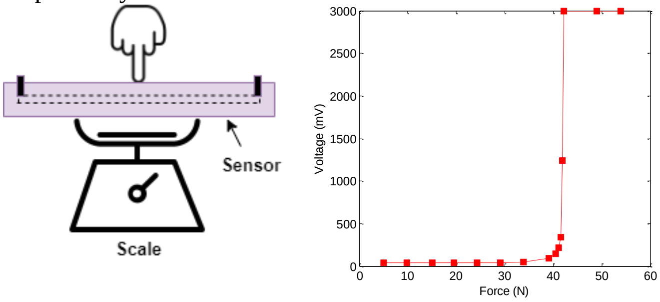

(a) (b)

Fig. 7. The property of the strain sensor when being pressed. (a) Experiment setup and (b) The obtained signal of sensor with the vertical applied force.

Furthermore, the proposed sensor design was applied in a finger motion detection experiment. Five sensors were attached on a human hand for finger movement detection (Fig. 8). For collecting information from five sensors, an analogue-switching IC was integrated in the measurement circuit for applying AC source to the sensors as well as sharing the signal conditioning circuit. The amplitude of the signal reflects the bending of the fingers marked in the figure. By combining the signal obtained from the sensors, the movement of the fingers can be realized. There is an on-board micro-controller (Atmega 328) for data collection and processing. After the data is analyzed and decoded into the language, it will be transferred to a speaker and display on a LCD screen. Besides, these data also are transmitted to the computer and smartphone through the HC05 Bluetooth module.

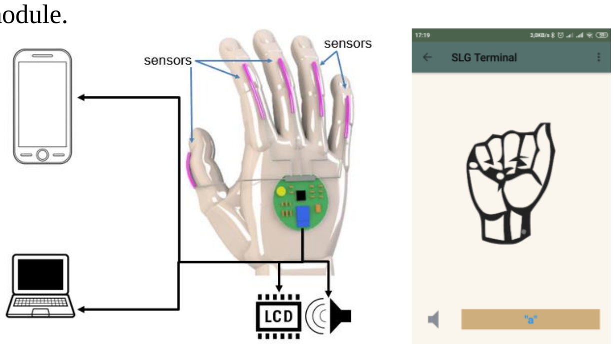

(a) (b)

Fig. 8. Proposed strain sensors are applied to recognize sign lanuguge. (a) The block digaram of sytem. (b) An application on the smartphone

On the computer and smartphone, we developed an application which can connect to the system through the Bluetooth communication (Fig. 8b). As can be seen, the application plays the voice through the speaker being available on the device. On the other hand, the letter also is displayed in a textbox and a hand shape respresenting sign language. These help people can hear and see the letter which a mute person want to communicate. With each letter, the resistance change of sensors is investigated repeatedly about 10 times to obtain the average value and limited range. The sensors are attached in order from thumb to little finger. From the obtained data, an algorithm is built to convert the digital signal into the voice. Firstly, the system is initialized to enable the communication and other function blocks. Then the system get the data from five sensors and save them to a temporary memory before being pass through the average filter. After that, the obtained data is decoded into the letters. The waiting time (1 second) make sure that the system is not confused with a quick movement of the hand. Finally, the data that is processed will be transferred to the executable block, including the speaker, smartphone and computer as show in the Fig. 8b. To evaluate the accuracy of the system, we conducted to experiment repeatedly about 15 times with each the letter. The result shows the average accuracy rate is 98%, as shown in the table I.

TABLE I. EXPERIMENT RESULTS WITH 10 DISTINGUISHED LETTERS

No.	Letter	Correct	Error	Accuracy (%)
1	A	13	2	86.67
2	B	15	0	100.00
3	C	14	1	93.33
4	D	15	0	100.00
5	E	15	0	100.00
6	F	15	0	100.00
7	V	15	0	100.00
8	W	15	0	100.00
9	Y	15	0	100.00
10	l	15	0	100.00
Total		**147/150**	**3**	**98.00**

V. CONCLUSIONS

A highly stretchable, low-cost, and hysteresis-free strain sensor was achieved by combining the ionic liquid of Water/NaCl/Glycerin with silicone shell, which is shaped by 3D printing technology. Furthermore, a measured system was also designed and fabricated to investigate the sensor. Several tests were performed in order to characterize the sensor. The results showed that the proposed sensor has a stable gauge factor of 2.1. The resistance of the sensor did not increase linearly with vertical applied force. The magnitude of vertical applied force effect to the hysteresis of the sensor.

Moreover, an application in sign language translation was developed based on the proposed sensor by attaching some sensor on the fingers. The result showed the sensors could detect 10 letter with high accuracy (98%). With obtained results, the proposed sensors showed outstanding durability, low latency, and ultra-stretchability. These excellent performance capabilities make the proposed sensor applicable for precise and quantitative strain sensing in various wearable electronic applications, such as human motion detection, personal health monitoring.

REFERENCES

[1] V. T. Dau, T. Yamada, D. Viet Dao, B. Thanh Tung, K. Hata, and S. Sugiyama, "Integrated CNTs thin film for MEMS mechanical sensors," Microelectronics J., vol. 41, no. 12, pp. 860–864, Dec. 2010, doi: 10.1016/J.MEJO.2010.07.012.

[2] B. T. Tung, H. M. Nguyen, D. V. Dao, S. Rogge, H. W. M. Salemink, and S. Sugiyama, "Strain sensitive effect in a triangular lattice photonic crystal hole-modified nanocavity," IEEE Sens. J., vol. 11, no. 11, pp. 2657–2663, 2011, doi: 10.1109/JSEN.2011.2157122.

[3] T. T. Bui, D. V. Dao, T. Toriyama, and S. Sugiyama, "Evaluation of the piezoresistive effect in single crystalline silicon nanowires," Proc. IEEE Sensors, pp. 41–44, 2009, doi: 10.1109/ICSENS.2009.5398124.

[4] K. Nakamura, D. V. Dao, B. T. Tung, T. Toriyama, and S. Sugiyama, "Piezoresistive effect in silicon nanowires - A comprehensive analysis based on first-principles calculations," 20th Anniv. MHS 2009 Micro-Nano Glob. COE - 2009 Int. Symp. Micro-NanoMechatronics Hum. Sci., pp. 38–43, 2009, doi: 10.1109/MHS.2009.5352099.

[5] S. Yang and N. Lu, "Gauge Factor and Stretchability of Silicon-on-Polymer Strain Gauges," Sensors 2013, Vol. 13, Pages 8577-8594, vol. 13, no. 7, pp. 8577–8594, Jul. 2013, doi: 10.3390/S130708577.

[6] S. Russo, T. Ranzani, H. Liu, S. Nefti-Meziani, K. Althoefer, and A. Menciassi, "Soft and stretchable sensor using biocompatible electrodes and liquid for medical applications," Soft Robot., vol. 2, no. 4, pp. 146–154, 2015, doi: 10.1089/soro.2015.0011.

[7] X. Z. Niu, S. L. Peng, L. Y. Liu, W. J. Wen, and P. Sheng, "Characterizing and Patterning of PDMS-Based Conducting Composites," Adv. Mater., vol. 19, no. 18, pp. 2682–2686, Sep. 2007, doi: 10.1002/ADMA.200602515.

[8] N. Lu, C. Lu, S. Yang, and J. Rogers, "Highly Sensitive Skin-Mountable Strain Gauges Based Entirely on Elastomers," Adv. Funct. Mater., vol. 22, no. 19, pp. 4044–4050, Oct. 2012, doi: 10.1002/ADFM.201200498.

[9] J. T. Muth et al., "Embedded 3D Printing of Strain Sensors within Highly Stretchable Elastomers," Adv. Mater., vol. 26, no. 36, pp. 6307–6312, Sep. 2014, doi: 10.1002/ADMA.201400334.

[10] A. Frutiger et al., "Capacitive soft strain sensors via multicore-shell fiber printing," Adv. Mater., vol. 27, no. 15, pp. 2440–2446, 2015, doi: 10.1002/adma.201500072.

[11] R. K. Kramer, C. Majidi, R. Sahai, and R. J. Wood, "Soft curvature sensors for joint angle proprioception," pp. 1919–1926, Dec. 2011, doi: 10.1109/IROS.2011.6094701.

[12] J. B. Chossat, Y. L. Park, R. J. Wood, and V. Duchaine, "A soft strain sensor based on ionic and metal liquids," IEEE Sens. J., vol. 13, no. 9, pp. 3405–3414, 2013, doi: 10.1109/JSEN.2013.2263797.

[13] O. A. Araromi, S. Rosset, and H. R. Shea, "High-Resolution, Large-Area Fabrication of Compliant Electrodes via Laser Ablation for Robust, Stretchable Dielectric Elastomer Actuators and Sensors," ACS Appl. Mater. Interfaces, vol. 7, no. 32, pp. 18046–18053, Aug. 2015, doi: 10.1021/ACSAMI.5B04975.

[14] Y. L. Park, C. Majidi, R. Kramer, P. Brard, and R. J. Wood, "Hyperelastic pressure sensing with a liquid-embedded elastomer," J. Micromechanics Microengineering, vol. 20, no. 12, 2010, doi: 10.1088/0960-1317/20/12/125029.

[15] P. M et al., "Highly stretchable electric circuits from a composite material of silver nanoparticles and elastomeric fibres," Nat. Nanotechnol., vol. 7, no. 12, pp. 803–809, 2012, doi: 10.1038/NNANO.2012.206.

[16] Y. Menguc et al., "Soft wearable motion sensing suit for lower limb biomechanics measurements," Proc. - IEEE Int. Conf. Robot. Autom., pp. 5309–5316, 2013, doi: 10.1109/ICRA.2013.6631337.

[17] Y. L. Park, B. R. Chen, and R. J. Wood, "Design and fabrication of soft artificial skin using embedded microchannels and liquid conductors," IEEE Sens. J., vol. 12, no. 8, pp. 2711–2718, 2012, doi: 10.1109/JSEN.2012.2200790.

[18] M. D. Dickey, R. C. Chiechi, R. J. Larsen, E. A. Weiss, D. A. Weitz, and G. M. Whitesides, "Eutectic Gallium-Indium (EGaIn): A Liquid Metal Alloy for the Formation of Stable Structures in Microchannels at Room Temperature," Adv. Funct. Mater., vol. 18, no. 7, pp. 1097–1104, Apr. 2008, doi: 10.1002/ADFM.200701216.

[19] Y.-L. Park, B. Chen, and R. J. Wood, "Soft artificial skin with multi-modal sensing capability using embedded liquid conductors," pp. 81–84, Jan. 2013, doi: 10.1109/ICSENS.2011.6127228.

[20] S. Zhu et al., "Ultrastretchable Fibers with Metallic Conductivity Using a Liquid Metal Alloy Core," Adv. Funct. Mater., vol. 23, no. 18, pp. 2308–2314, May 2013, doi: 10.1002/ADFM.201202405.

[21] C. Majidi, R. Kramer, and R. J. Wood, "A non-differential elastomer curvature sensor for softer-than-skin electronics," Smart Mater. Struct., vol. 20, no. 10, 2011, doi: 10.1088/0964-1726/20/10/105017.

[22] K.-Y. Chun et al., "Highly conductive, printable and stretchable composite films of carbon nanotubes and silver," Nat. Nanotechnol. 2010 512, vol. 5, no. 12, pp. 853–857, Nov. 2010, doi: 10.1038/nnano.2010.232.

[23] T. Yamada et al., "A stretchable carbon nanotube strain sensor for human-motion detection," Nat. Nanotechnol., vol. 6, no. 5, pp. 296–301, 2011, doi: 10.1038/nnano.2011.36.

[24] D. J. Lipomi et al., "Skin-like pressure and strain sensors based on transparent elastic films of carbon nanotubes," Nat. Nanotechnol. 2011 612, vol. 6, no. 12, pp. 788–792, Oct. 2011, doi: 10.1038/nnano.2011.184.

[25] M. A. Lacasse, V. Duchaine, and C. Gosselin, "Characterization of the electrical resistance of carbon-black-filled silicone: Application to a flexible and stretchable robot skin," Proc. - IEEE Int. Conf. Robot. Autom., pp. 4842–4848, 2010, doi: 10.1109/ROBOT.2010.5509283.

[26] A. Firouzeh and J. Paik, "Robogami: A Fully Integrated Low-Profile Robotic Origami," J. Mech. Robot., vol. 7, no. 2, pp. 1–8, May 2015, doi: 10.1115/1.4029491.

[27] S. Kumbay Yildiz, R. Mutlu, and G. Alici, "Fabrication and characterisation of highly stretchable elastomeric strain sensors for prosthetic hand applications," Sensors Actuators, A Phys., vol. 247, pp. 514–521, 2016, doi: 10.1016/j.sna.2016.06.037.

[28] Y. N. Cheung, Y. Zhu, C. H. Cheng, C. Chao, and W. W. F. Leung, "A novel fluidic strain sensor for large strain measurement," Sensors Actuators, A Phys., vol. 147, no. 2, pp. 401–408, 2008, doi: 10.1016/j.sna.2008.05.013.

[29] K. Noda, E. Iwase, K. Matsumoto, and I. Shimoyama, "Stretchable liquid tactile sensor for robot-joints," Proc. - IEEE Int. Conf. Robot. Autom., pp. 4212–4217, 2010, doi: 10.1109/ROBOT.2010.5509301.

[30] C.-Y. Wu, W.-H. Liao, and Y.-C. Tung, "Integrated ionic liquid-based electrofluidic circuits for pressure sensing within polydimethylsiloxane microfluidic systems," Lab Chip, vol. 11, no. 10, pp. 1740–1746, May 2011, doi: 10.1039/C0LC00620C.

[31] P. Manandhar, P. D. Calvert, and J. R. Buck, "Elastomeric ionic hydrogel sensor for large strains," IEEE Sens. J., vol. 12, no. 6, pp. 2052–2061, 2012, doi: 10.1109/JSEN.2011.2181993.

[32] [32] J.-Y. Sun, C. Keplinger, G. M. Whitesides, and Z. Suo, "Ionic skin," Adv. Mater., vol. 26, no. 45, pp. 7608–7614, Dec. 2014, doi: 10.1002/ADMA.201403441.

[33] C. T. Nhu et al., "Experimental Characterization of an Ionically Conductive Fluid Based High Flexibility Strain Sensor," Lect. Notes Networks Syst., vol. 63, pp. 318–323, Dec. 2018, doi: 10.1007/978-3-030-04792-4_42.

[34] C. T. Nhu, A. Nguyen Ngoc, V. T. Dau, C. Le Van, T. C. Duc, and T. T. Bui, "Wearable Fluidic Strain Sensor for Human Motion Sensing," Proc. IEEE Sensors, vol. 2020-October, Oct. 2020, doi: 10.1109/SENSORS47125.2020.9278685.

[35] T. A. Hampshire and H. Adeli, "Monitoring the behavior of steel structures using distributed optical fiber sensors," J. Constr. Steel Res., vol. 53, no. 3, pp. 267–281, Mar. 2000, doi: 10.1016/S0143-974X(99)00043-7.

A Study of Wall Cleaning Robot with Zigzag Motion Trajectory

Van-Tinh Nguyen
School of Mechanical Engineering
Hanoi University of Science and Technology
Hanoi, Vietnam.
tinh.nguyenvan@hust.edu.vn

Kim-Thuan Nguyen
Viettel Post Joint Stock Corporation
Hanoi, Vietnam.

Ngoc-Kien Nguyen
School of Mechanical Engineering
Hanoi University of Science and Technology
Hanoi, Vietnam.

***Abstract*: This paper presents a mechanical design and motion-control system of a Wall-Climbing Robot (WCR) which can move on the flat and curve surface for cleaning purposes. One of the most challenges with this type of robot that the researchers confront is how to keep the robot moving steadily on various types of surfaces with the most optimal approach. In this study, a new mechanical design of the Wall-Climbing robot using the Vacuum Principle and Wireless Control technology were proposed. This version of the robot enhances the ability of its movement on the various types of surfaces and optimizes control system. In detail, the Minimum Required Adhesion Force (FMRA) is calculated to be balanced with gravity and its torque. Moreover, a Wireless Control System (WCS) is designed to drive the Robot remotely. The optimal control trajectory and velocities are given based on theory calculations and comparisons.**

Keywords: Wall-Climbing Robot, Cleaning Robot, Vacuum principle, Wireless control.

I. INTRODUCTION

Cleaning skyscraper's wall manually is a high laboring intensity, low efficiency and high-risk job for workers. Therefore, a light-weight, compact, highly efficient, remotely controllable WCR would be an ideal solution for this issue. However, there is a challenging question for this type of Robot is: How to keep a weighted Robot stably moving of the wall? And which is the most optimal approach for Silo cleaning? To answer the first question, there are two functional objects that need to be defined: adhesion mechanism and locomotion. In addition, an efficient trajectory strategy and an optimum controlling velocity have to be applied for WCR for answering the second question.

Adhesion mechanism is to generate a force perpendicular to the wall so that the magnitude and torque it generates both outweigh gravity and its torque respectively. There are different types of adhesion mechanisms like pneumatic mechanism [1,2,3] (using suction cups and less flexible) and magnetic mechanism [4] (requiring many components and a large amount of power).

To meet the locomotion requirements, there are many types of mechanisms which have been applied. For instance, Avishai Sintov et al. [5] introduced a robot with claws, this robot has four legs with four-degrees-of freedom for each. It is able to climb on vertical and rough terrain, keep in position for a long period. Nishi A. and Miyagi H. [6] have developed three types of robots based on the wall-climbing mechanisms of insects. Kim, H. et al. [7] proposed a new concept of a wall-climbing robot able to climb a vertical plane by adopting a series chain on two tracked wheels. T. White et al. presented a climbing robot with locomotion based on arms and grippers [8]. Although, the many researches have been shown up, these mechanisms are likely to be inappropriate for the case of Silo's wall. Thus, changing the direction during the locomotion of the robot has still established one of the challenging problems in this field. This paper introduced a wall-climbing robot for cleaning Silo using vacuum principle where a high-speed RC brushless – Ducted Fan Motor (RC-DFM) was used to generate a sufficiently large vacuum pressure. This force could be able to balance with gravity and the torque of gravity, it means this mechanism could keep the Robot on the wall. Besides, this design enhances the ability of changing direction in motion of the robot.

Because this WCR needed to be lightweight, compact, and at low cost, the wheeling mechanism with four wheels had been used as a locomotion mechanism. Four DC motors had been assembled with four wheels to create movements for Robot, which was controlled by a designed WCS based on Arduino and its integrated modules. Control signals are sent from a control application, programmed, running on an Android phone, making it easy for users to install and use to control the Robot's movement actions.

Sweeping every accessible area on the Silo's Wall to clean is the main task of WCR. Hence, defining an efficient coverage path planning is of paramount importance for WCR. Several coverage path planning approaches are proposed [9,10]. These methods in [9,10] are not efficient for Silo's wall simply because they are for the dynamic environment and reduce the enemy stability of the adhesion force as well as make it difficult to control. This study illustrated an up-down zigzag path strategy as the shortest, most stable, and easiest controlling way. Furthermore, the robot's optimal speed is also calculated by using the Lagrange method and being based on the robot's direction of change and the time it takes to complete.

This paper is organized as the following: The next section addresses adhesion and locomotion mechanisms. An optimal approach for Silo cleaning is defined in the third section, while the fourth and fifth section describes the process of designing WCS. Afterwards, experimental results are presented in the sixth section, followed by the paper conclusions and future prospects.

II. ADHESION AND LOCOMOTION MECHANISM

A. *Adhesion mechanism*

One of the essential functions of the WCR is the adhesion mechanism, as the robot can stick properly and stably on the wall without any malfunction with the aid of the adhesion mechanism. To obtain this balance condition, an RC-DFM, which was able to operate at super high speed (speed max at 36500 rpm), was used to generate the sufficiently large Vacuum pressure. This pressure was exerting an adhesion force F_h, which was needed to be greater than the gravity, the FMRA. Assume that the wheels are absolutely stiff, adhesion mechanism is described in Figure 1.

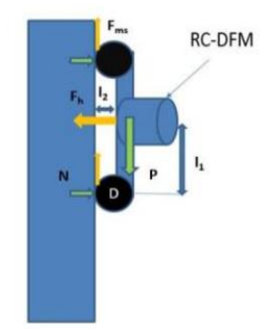

Fig. 1. Force analysis for calculating F_h.

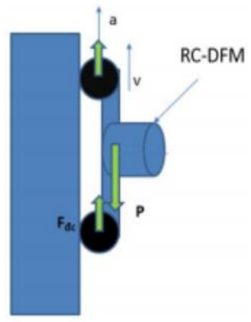

Fig. 2. Force analysis for calculating F_{dc}.

The adhesion force was calculated by:

$$F_h = 4.\,N \text{ (N)} \tag{1}$$

Where N is the force of the wall acting on the wheels inferred from following formula:

$$F_{ms} = 4.\mu.N \text{ (N)} \tag{2}$$

Where μ is the friction coefficient, Fms is the total friction force at 4 wheels which needs to be greater than gravity P:

$$F_{ms} > P = m.\,g \text{ (N)} \tag{3}$$

In which, m is weight of Robot, g is gravity acceleration. From (1), (2), (3), F_h can be deduced by the following inequality:

$$F_h > \frac{m.g}{\mu} \text{ (N)} \tag{4}$$

Moreover, to ensure anti-roll, the torque of F_h must be greater than the torque of gravity at the center of rotation D:

$$M_{F_h} = F_h.l_1 > M_P = P.l_2 = m.g.l_2$$

So then:

$$F_h > \frac{m.g.l_2}{l_1} \text{ (N)} \tag{5}$$

From (4) - (5), the volume, the size of the WCR and the RC-DFM type are selected most appropriate and optimal.

B. *Locomotion Mechanism*

The selection of Locomotion Mechanism for WCR was dependent upon the tasks that WCR required to perform. In this case, WCR needed to move flexibly in 2D plot coordinates similar to the Silo field surface without affecting on adhesion force and without failure. Therefore, the wheeled locomotion mechanism was used because of its better stability and ease of system adaptation as depicted in Figure 2. The driving force of each wheel F_{dc}, with the assumption of ignoring rolling friction, was calculated using the following formula:

$$F_{dc} > m.(a+g) \text{ (N)} \tag{6}$$

In which, $a = 0.2$ m/s^2 is maximum acceleration of required input. From this, the DC motor has been selected to ensure flexible movement and lightweight.

III. SURFACE CLEANING APPROACH

A. *Coverage path strategy*

An efficient coverage path strategy as shown in Figure 3 was defined to meet two fundamental rules, the easiest way for controlling, and the most stable pressure is maintained. Both of these rules are affected by changing the direction of the robot, i.e., when the robot changing its direction, it will lead to variation in the speed control of the wheels, which will be clarified in the next section, as well as pressure change for a certain period of time, ahead mentioned in Section 2. Therefore, the up-down zigzag path planning was used to reduce the maximum number of robot direction changes during the entire working process. The number of robot direction turns is calculated using the following formula:

$$N = \frac{2.\pi.R}{d} - 1 \tag{7}$$

Where d is the width of the robot's path.

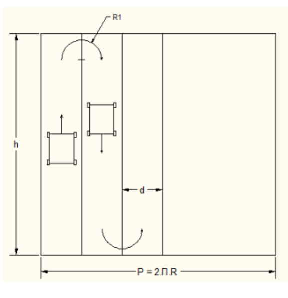

Fig. 3. Up – Down Zigzag path planning.

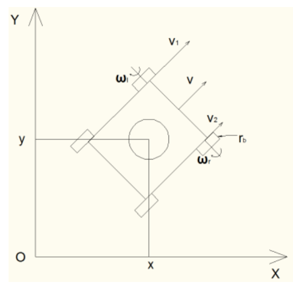

Fig. 4. Velocity analysin in Descartes coordinate.

B. *Controlling speed calculation*

The long velocity of the robot is dependent on the angular velocity of the left and right wheels with the hypothesis that two wheels on each have the same speed as depicted in Figure 4. Using the Lagrange method, robot velocity was calculated by the following formula:

$$v = \frac{v_1 + v_2}{2} = \frac{r_b.(\dot{w}_1 + \dot{w}_r)}{2} \tag{8}$$

Where v_1, v_2, w_1, w_2 are respectively the long and angular speeds of the left and right wheels. v_1, v_2 were calculated based on the working time condition, which requires the robot to finish cleaning as fast as possible within a minimum amount of time.

IV. MODEL AND MATERIALS

The 3D model of the robot is designed in CAD environment as shown in Figure 5, based on the conditions mentioned in sections A and B with the optimal calculated dimensions. The frame of WRC had been made of aluminum plates because this type of material was assuring solidity, low cost, and lightweight. Moreover, aluminum was also easy to deform facilitating for making WCR parts.

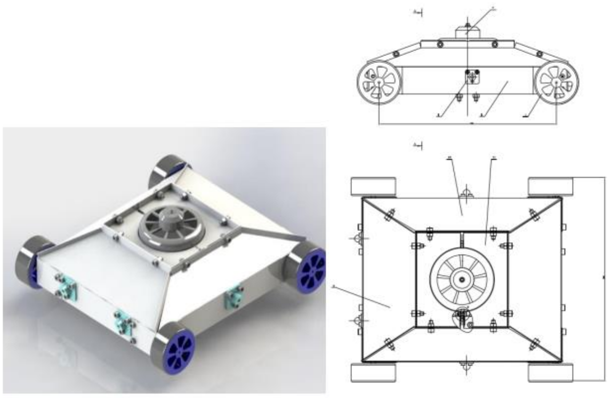

Fig. 5. 3D and 2D model of WCR.

V. WIRELESS CONTROL SYSTEM

The control system of the robot was designed according to the mentioned mechanical structures with two main components: maintaining the adhesion force (Sub-control system 1) and controlling the WCR's movement direction (Sub-control system 2)

A. *Sub-control system 1*

As can be seen in Figure 6 that RC-DFM was driven by an available Electric Speed Controller (ESC), which received control signals from a panel named CH3, and powered by DC power. When this device operating at high speed, ESC would be extremely hot (over 110 degrees), therefore it needed to be cooled by a liquid cooling mechanism. This cooling mechanism was basically a cycle of cooling liquid that was inserted into the aluminum heat-sink plate and expelled the hot heat.

B. *Sub-control system 2*

Figure 7 described the sub-control system 2. This was the main control component and also the soul of the Robot, ensuring its flexible movement and performing its cleaning function. The Arduino board was used to receive direction control signals from the phone app via a Bluetooth module called HC-06, a kind of wireless control technology. A firmware program was loaded into the Arduino via USB, a system program, helped the Arduino communicate with the modules connected directly to it. From there, control pulses would be sent to L298 Driver, which changed the power supply and current to the DC motors changing its rotation speed or direction of rotation. The electromagnetic valve was also provided with control pulses to open or close the air gates to perform the cleaning function.

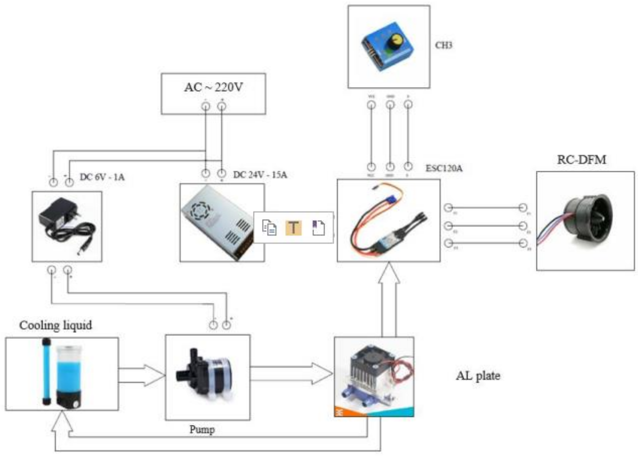

Fig. 6. Sub – control system 1.

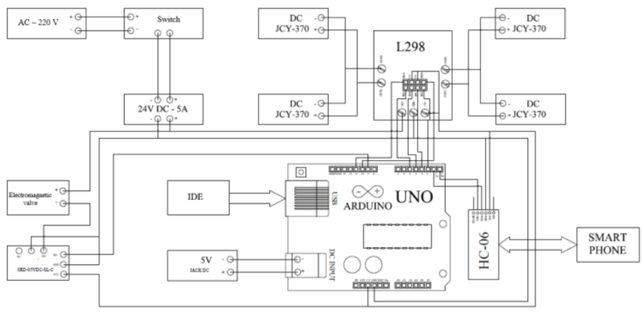

Fig. 7. Sub – control system 2.

VI. EXPERIMENTAL RESULTS

The actual prototype model of WCR was tested experimentally on the wall as shown in Figure 8, 9, 10 and Table I. Thanks to the use of high-capacity motors, incorporating the position changing mechanism of the RCDFM in the Z direction, had created a large pressure difference. Therefore, the adhesion force was always maintained at a large and meeting both initial conditions for the adhesion mechanism. As the result, WCR was kept firmly on the wall during the operation time without failure of falling. Moreover, the robot was wirelessly controlled for flexible and stable movement thanks to a frame made of aluminum metal and the locomotion mechanism of a wheel structure. Aside from that, an efficient approach for WCR was defined with the up-down zigzag path planning and an optimum velocity of robot made it fast and effective. However, because the surface of Silo had many rough spots due to strains, one of the 4 wheels at a time slipped or did not completely contact with the surface of the wall. This problem was solved by using the omnidirectional wheel instead.

Experimental results are show in Table II. From the measured data, it is clear that the Adhesion Forces are always greater than the highest required force Fh =m.g/μ = 61.3 N, even in moving toward the perimeter - the most intricate activity. Meanwhile, the average speeds are good for ensuring finishing the working path within the given time and the numbers of ΔZ are small enough for the maximum transfer speed limit of the Z-Shift mechanism. As a result, the WCR was moving stably to meet its target of cleaning the Silo's Wall.

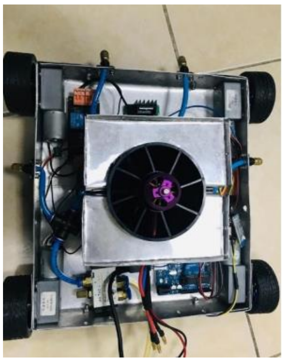

Fig. 8. WCR prototype.

Fig. 9. Control cabinet

Fig. 10. WCR on the wall.

TABLE I. CONFIGURATION OF WCS

Objects	Definition/ Value	Unit
Overall Weight	5	kg
Dimensions	450 x 400 x 180	mm
Speed max	0.5	m/s
Acceleration max	0.2	m/s^2
Air gate number	4	Gates
Power Supply	24	Volts
Coverage path type	Up-down zigzag	------
Completion time/ silo	5.4	hours

TABLE II. EXPERIMENTAL RESULTS

Activities	Average Adhesion Force (F_h)	Avaverage Speed (v)	$\Delta Z = \lvert Z_2 - Z_1 \rvert$
Moving upward	82.1 N	0.235 m/s	0.5 mm
Moving down	81.9 N	0.450 m/s	0.7 mm
Turning	79.7 N	0.126 m/s	1.7 mm
Moving toward perimeter	74.3 N	0.315 m/s	1.4 mm

VII. CONCLUSIONS

This research had successfully developed a new design of Wall Climbing Robot with high function performance. Thanks to the application of the vacuum principle and wireless control technology, the robot had been optimally designed with many positive points: stable and flexible on the wall movement, high solidity, lightweight, and low cost. Besides cleaning Silo's wall, WCR can be used for a wide range of purposes including high-rise-glassy building cleaning and inspection with added cameras, in the future.

REFERENCES

[1] Yu Yoshida and Shugen Ma. Design of a Wall-Climbing Robot with Passive Suction Cups. IEEE Int. Conf. Robot. Biomimetics, pp. 1513-1518 (2010).

[2] Li. Jun. Wall climbing robot based on negative pressure-thrust suction method. IEEE Int. Conf. Mechatronics Autom, pp. 604-609 (2008).

[3] C. Hillenbrand, D. Schmidt and K. Berns. CROMSCI: development of a climbing robot with negative pressure adhesion for inspections. Ind. Robot An Int. J., vol. 35, no. 3, pp. 228-237 (2008).

[4] L. P. Kalra, J. Gu and M. Meng. A Wall Climbing Robot for Oil Tank Inspection. IEEE International Conference on Robotics and Biomimetics, Kunming, pp. 1523-1528 (2006). doi: 10.1109/ ROBIO.2006.340155.

[5] Avishai Sintov, Tomer Avramovich, Amir Shapiro. Design and motion planning of an autonomous climbing robot with claws. Robotics and Autonomous System 59, pp. 1008–1019 (2011).

[6] Nishi A., Miyagi H. Propeller type wall-climbing robot for inspection use. Automation and Robotics in Construction X, pp. 189-196 (1993).

[7] Kim, H., Kim, D., Yang, H. et al. Development of a wall-climbing robot using a tracked wheel mechanism. J Mech Sci Technol 22, 1490–1498 (2008). https://doi.org/10.1007/s12206-008- 0413-x.

[8] T. White, N. Hewer, N. Luk and J. Hazel. The design and operational performance of a climbing robot used for weld inspection in hazardous environments. Proceedings 1998 IEEE International Conference on Control Applications, vol. 1, pp. 451-455, September (1998).

[9] A. Xu, C. Viriyasuthee, I. Rekleitis, Efficient complete coverage of a known arbitrary environment with applications to aerial operations, Auton. Robots 36 (4) (2014) 365–381.

[10] S.-h. LIU, J. Xia, X.-m. SUN, Y. Zhang, An efficient complete coverage path planning in known environments, J. Northeast Norm. Univ. 4 (2011) 008. (Natural Science Edition).

The 6th International Conference on Engineering Mechanics and Automation (ICEMA 2021)
Hanoi, November 14, 2021

Adjusting Material Amount of Proportional Technique for Bilinear Topology Optimization

Van-Tinh Nguyen
School of Mechanical Engineering
Hanoi University of Science and Technology
Hanoi, Vietnam.
tinh.nguyenvan@hust.edu.vn

***Abstract*—Topology optimization is a process which distributes material into necessary position of design area under the action of external force. The main purpose of this process is to decrease the mass of structure but still ensures its strength. In this field, proportional topology optimization (PTO) is a popular non-sensitivity technique. This method updates material density through the relationship between maximum stress at each iteration and allowable stress of material. Besides, the target of material amount is added or removed by certain ratio of total number of elements. It makes the optimization process take a long time to reach the convergence. This paper supposes that the ratio of moving material at each iteration has significant effect on the convergence of the optimization process. Thus, this paper proposes adaptive moving material using Sigmoid function for proportional technique. A cantilever with nonlinear characteristic material is used to verify the effectiveness of this approach.**

Keywords*— *Topology optimization, bilinear material, cantilever, material amount, convergence speed.

I. INTRODUCTION

Topology optimization methods allow designers to figure out the best structural layout under many requirements of load and constraint. In general, structural optimization is divided into three classes: size, shape, and topology optimization. Size optimization is to obtain the best sections while optimizing the shape is to find the best node positions of the predefined nodes of the structure. Both of them are based on the predefined design layout. Topology optimization redistribute material of a given design space until achieving the optimal layout through many iterations. Presently, the result of topology optimization is often used for the preliminary concept of design process and thus becomes an important part to construct the structure.

Firstly, literature review on topology optimization with linear material, some of "statue of art" are described in [1]-[4]. In recent years, the upgraded methods of topology have been developed as the following: Guo et al. applied moving morphable components for doing topology optimization, this solution was efficient to enhance computational cost associated with topology optimization substantially [5]. Continuously, Zhang et al. have developed the approach to preserve the smoothness of optimal design by using B-spline curves for the boundaries of moving morphable components or moving morphable voids [6]. Most recently, Hao Deng and Albert C. To applied deep learning to describe density distribution of material. This method assures the smoothness of the boundary and overcome the checkerboard problem in optimal layout [7].

For linear topology optimization, deformation of material is small under the action of external force and it is applied in many practical design problems. However, in many situations, nonlinear analysis also needs to be considered including energy absorption structures or crashworthiness design. For instance, Lei Li et al. presented the density-based framework to enhance the ability of energy absorption of optimal structure [8]. X Huang et al. introduced two sensitivity numbers to adjust principal design parameters by applying an adjoint method [9]. Newly, Suphanut Kongwat and Hiroshi Hasegawa applied the novel weight filtering method to prevent stress of element from fluctuation problem under cyclic load [10]. Besides, a class of nature-inspired evolutionary algorithm has been also adopted to topology optimization [11]-[14].

In topology optimization, proportional method is a non-sensitivity approach, where density of element is updated by using the ratio between the stress of this element and the stress summation of all the elements in the design space at the current generation. The target of the total density is added or removed depending on the relationship between the maximum stress and allowable stress. This moving material is set from 0.001 to 0.002 of the total number of elements. Fixing the moving material during optimization process results in high cost of computation, it takes a long time to reach the convergence. Thus, this paper proposes an adaptive volume factor for adding or removing material. This factor is generated by Sigmoid function. The moving material is set to be high at the beginning and gradually reduce through each iteration. The reduction of moving material at later iteration enhances the ability of exploitation and improve convergence speed. The result is validated on a benchmark model: cantilever with nonlinear material.

To this end, the rest of this paper is organized into eight sections. Section 2 depicted cantilever model with nonlinear material. Section 3 describes methodology for topology optimization. Proportional technique is in Section 4. Section 5 addresses numerical example and discussion. Finally, Section 6 includes some brief conclusions.

II. Optimization Problem

A. Cantilever model

In this paper, a numerical example described in Fig. 1 is considered. The design area is applied by a force of 2 kN in the downward direction at the middle corner and it is discretized to 100x50 elements. The structure is assigned with the bilinear elastoplastic material properties which are input as 285 MPa of yield stress, allowable stress is 600 MPa, Young's modulus of 207 GPa, and tangent modulus is 13,921 MPa, 0.3 for Poisson's ratio, and 10^{-9} for Young's modulus assigned to void regions E_{min}. The property of bilinear elastoplastic material is depicted in Fig. 2.

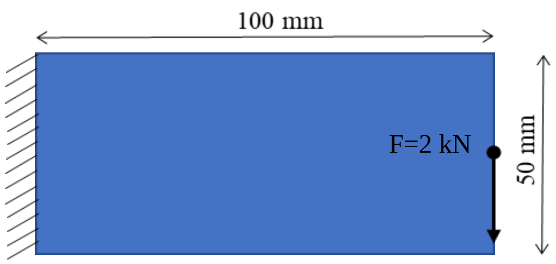

Figure 1. Cantilever model.

B. Optimization procedure

As This research adopted the compliance as objective function, where the target is to minimize the compliance while the maximum stress value is less than the allowable stress. The optimization problem is described as follows:

$$\text{Max C} = \sum \text{E.u}_i \quad (1)$$

Subject to

$$\sigma_{max} \leq \sigma_{allow} \quad (2)$$

Where E is Young's modulus, u_i is internal energy density of element i^{th}, σ_{max} is the maximum stress, and σ_{allow} is the stress limit.

III. Solid Isotropic Material with Penalization Method

Solid Isotropic Material with Penalization method (SIMP) is the most popular method for topology optimization [15]. The density distribution of material within a design domain is assigned a binary value:

- $x_e = 1$ where material is required (black);
- $x_e = 0$ where material is removed (white);

To avoid on-off nature of the problem, it causes matrix of stiffness singular, density of element varies continuously from x_{min} to 1, x_{min} is the minimum allowable relative density value for empty elements that are greater than zero. Since the material relative density can vary continuously, the material Young's modulus at each element can also vary continuously and is computed by the power law:

$$E_e = E_{min} + x_e^p.(E_o - E_{min}) \quad (3)$$

Where:

E_{min} is the elastic modulus of void element, E_o is the elastic modulus of solid element. Penalty value (p) for modified SIMP approach penal is set to 3.

IV. Density Filtering

The PTO method incorporates a density filtering. In the work of Bruns [16], a simple cone density filtering is introduced as the following:

$$\zeta_i = \frac{\sum_{j=1}^{n} w_{ij} d_j}{\sum_{j=1}^{n} w_{ij}} \quad (4)$$

$$w_{ij} = \max(0, r_{min} - r_{ij}) \quad (5)$$

Where ζ_i is filtered density of element i; d_i is non-filtered density of element i; w_{ij} is the filtering weight of elements i and j, r_{min} is the prescribed filtering radius, r_{ij} is the distance between elements i and j.

V. Proposed Proportional Optimization Algorithm

In the PTO for the SIMP method, the update function is used to renew the density of the design variable through each iteration. The proportional technique is a non-sensitivity method [17] which builds an equation based on a ratio of stress and uses this parameter to update the density value as in Eq. 6.

$$\rho_i^{new} = \rho_i^{prev} + xRem.\,(\frac{\sigma_i^q}{\sum_{i=1}^{N} \sigma_i^q}).\,\zeta_i \quad (6)$$

Where ρ_i^{new} is the new elemental density for the next iteration, and ρ_i^{prev} is the elemental density from the previous iteration; for the first proportional loop, we assume that the density value of the previous iteration is zero, σ_i is the elemental stress, and $xRem$ is the remaining material amount. $xRem$ is defined as follows:

- This paper proposes an adjusting strategy to replace the fixed volume ratio of the total target density in the traditional topology optimization method by adopting an adaptive parameter, r_{adap} as described in Eq. 7.

  $$r_{adap} = \frac{1}{1+e^{-10/iter}} \quad (7)$$

  Where r_{adap} is the adaptive volume ratio, and $iter$ is the current iteration. The gait of r_{adap} chart depends on the current iteration is shown in Fig. 2. In the beginning of the iteration, this value is set to be high to obtain a high speed and must be small for proper exploitation. As a result, we believe that it will steadily provide an optimal layout and reduce the calculation cost.

- The target material amount is calculated by Eq. 8.

  $$xTar = \sum_{i=1}^{n} x_i \pm 0.01*radap*(\text{total number of elements}) \quad (8)$$

  Where

  $$\begin{cases} + \,; if\ \sigma_{max} \leq \sigma_{allow} \\ - \ if\ \sigma_{max} \geq \sigma_{allow} \end{cases} \quad (9)$$

- The new density amount is revised through each loop by comparing it to the target material amount as in Eq. 10.

$$xRem_{new} = xTar - \sum_{i=1}^{n} \rho_i^{new} \quad (10)$$

- If $xRem_{new}$ is less than 0.001, the updating process is terminated. Otherwise, $xRem_{new}$ is set to $xRem$, and the updating process is repeated.

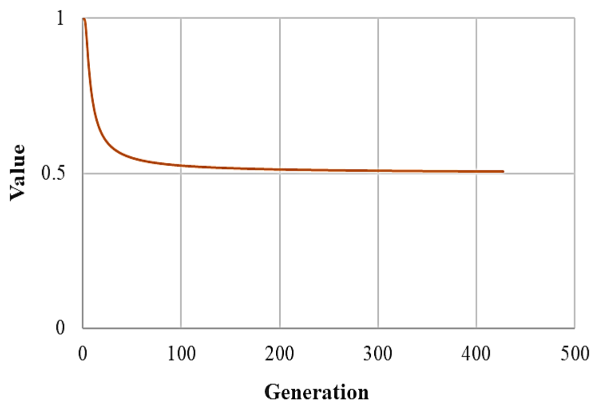

Figure 2: Adaptive parameter at each iteration.

Pseudocode of algorithm is described as below:

1. Building a cantilever model, assign the first density element to all elements.
2. While termination condition is not reached.

   Implementing FE analysis.

   Compliance calculation.

   Checking stop criteria, break if satisfied.

   Running proportional optimization algorithm.

   Generating adaptive volume factor at current iteration by Eq. 7.

   Calculating TA.

   Setting RA = TA.

   While remaining material amount (RA) is not small enough

   Applying filtering weight and calculating new density value by Eq. 6.

   Calculating new amount of material (CA).

   Updating RA = TA - CA.

   The process is repeated.

Where TA is the target material amount, RA is the remaining material amount, CA is the current material amount.

VI. Numerical Examples

The comparison of two proportional methods for topology optimization is shown in Fig. 3. For the old approach, the optimal layout is obtained when the maximum stress is 439.93 MPa. As can be seen in Fig. 3, it reached the convergence at 263 iterations while the proposed method obtained the optimal layout at 88 iterations with the maximum stress of 445.33 MPa. Thus, the convergence speed is improved 66.54%. Both methods kept 28% of initial material amount. The optimal layout and the stress distribution of the proposed method are shown in Fig. 4. As can be seen that the optimal layouts are distinct, and it is possible to sketch out the real structure for the purpose of manufacture.

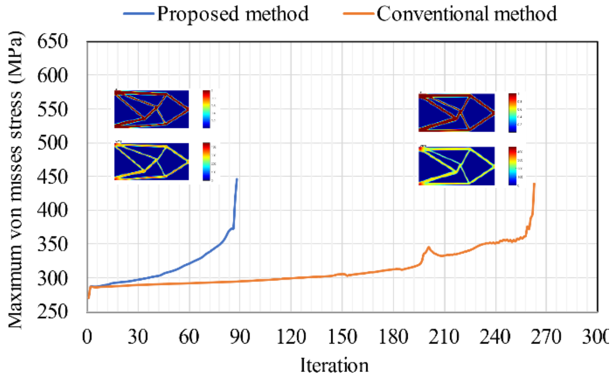

Figure 3: Maximum stress of two numerical simulation.

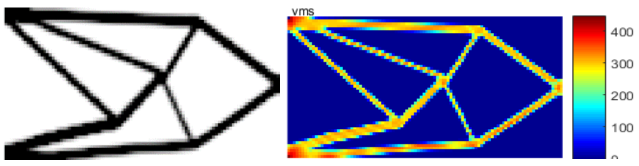

(a) (b)

Figure 4: Optimal layout for verification model (a) the optimal layout (b) the stress distribution for optimal layout.

VII. Conclusions

This research proposes a target material amount adjusting strategy for proportional method. The optimization procedure is implemented based on MATLAB and the numerical analysis is performed by LS-DYNA. The target of element density amount is adapted to enhance convergence speed of optimization process. The target material amount combined stress is to calculate the new element density. The fully stress design criterion and the filtering technique are applied in this paper. Then, the optimal layout is obtained when the difference between maximum stress and allowable stress is small enough or the compliance is constant. A cantilever model was used to verify the proposed method.

References

[1] M. P. Bendsøe and N. Kikuchi (1988) "Generating optimal topologies in structural design using a homogenization method," Computer methods in applied mechanics and engineering, vol. 71, no. 2, pp. 197-224.

[2] M. P. Bendsøe and O. Sigmund (1999) "Material interpolation schemes in topology optimization," Archive of applied mechanics, vol. 69, no. 9-10, pp. 635-654.

[3] Y. M. Xie and G. P. Steven (1993) "A simple evolutionary procedure for structural optimization," Computers & structures, vol. 49, no. 5, pp. 885-896.

[4] Y. M. Xie and G. P. Steven (1997) "Basic evolutionary structural optimization," in Evolutionary Structural Optimization: Springer, pp. 12-29.

[5] X. Guo, W. Zhang, and W. Zhong (2014) "Doing topology optimization explicitly and geometrically—a new moving morphable components based framework," Journal of Applied Mechanics, vol. 81, no. 8, p. 081009.

[6] W. Zhang, W. Yang, J. Zhou, D. Li, and X. Guo (2017) "Structural topology optimization through explicit boundary evolution," Journal of Applied Mechanics, vol. 84, no. 1, p. 011011.

[7] Deng, H., To, A.C. (2020) "Topology optimization based on deep representation learning (DRL) for compliance and stress-constrained design. Comput Mech 66, 449–469.

[8] Li, L., Zhang, G., and Khandelwal, K. (2017) "Topology optimization of energy absorbing structures with maximum damage constraint. Int. J. Numer. Meth. Engng, 112: 737– 775. doi: 10.1002/nme.5531.

[9] X Huang, Y M Xie, and G. Lu (2007) "Topology optimization of energy-absorbing structures, International Journal of Crashworthiness, 12:6, 663-675, DOI: 10.1080/13588260701497862.

[10] Kongwat, S., Hasegawa, H. (2020). "New weight filtering factor of nonlinear design for topology optimization under cyclic loading based on proportional technique. Journal of Mechanical Science and Technology 34 (4) (2020) 1635~1644. http://doi.org/10.1007 /s12206-020-0326-x.

[11] Hajela P., Lee E., Lin CY. (1993) "Genetic Algorithms in Structural Topology Optimization. In: Bendsøe M.P., Soares C.A.M. (eds) Topology Design of Structures. NATO ASI Series (Series E: Applied Sciences), vol 227. Springer, Dordrecht. https://doi.org/10.1007/978-94-011-1804-0_10.

[12] S.Y. Wang, K. Tai (2005) "Structural topology design optimization using Genetic Algorithms with a bit-array representation, Computer Methods in Applied Mechanics and Engineering, Volume 194, Issues 36–38, pp. 3749-3770.

[13] J. Y. Park and S. Y. Han (2013) "Swarm intelligence topology optimization based on artificial bee colony algorithm, Int. J. Precis. Eng, Man., 14 (1), pp. 115–121.

[14] Y.-S. Eom and S.-Y. Han (2014) "A new topology optimization scheme for nonlinear structures, Journal of Mechanical Science and Technology, 28 (7), pp. 2779-2786.

[15] Bendsøe, M.P. (1989) "Optimal shape design as a material distribution problem. Structural Optimization 1, 193–202. https://doi.org/10.1007/BF01650949.

[16] Bruns TE, Tortorelli DA. (2001) "Topology optimization of non-linear elastic structures and compliant mechanisms. Computer Methods in Applied Mechanics and Engineering. 190(26):3443–59.

[17] Biyikli E, To AC. (2015) "Proportional Topology Optimization: A New Non-Sensitivity Method for Solving Stress Constrained and Minimum Compliance Problems and Its Implementation in MATLAB. PLoS ONE 10(12): e0145041. doi:10.1371/ journal.pone.0145041.

The 6th International Conference on Engineering Mechanics and Automation (ICEMA 2021) Hanoi, November 14, 2021

Design and implement a UAV for low-altitude data collection in precision agriculture

Minh-Trung Vu
VNU University of Engineering and Technology
Hanoi, Vietnam
trung.vu.024@gmail.com

Truong-Son Nguyen
VNU University of Engineering and Technology
Hanoi, Vietnam
truongsonlifezero@gmail.com

Minh-Trien pham
VNU University of Engineering and Technology
Hanoi, Vietnam
trienpm@gmail.com

Cong-Hoang Quach [1]
VNU University of Engineering and Technology
Hanoi, Vietnam
quachconghoang89@gmail.com

***Abstract*: In recent years, along with the development of precision agriculture, Unmanned Aerial Vehicles (UAVs) in crop data collection is becoming more popular because of the advantages of collecting data in a large area. However, many crops and special growing conditions require low-flying UAVs to collect data such as orchards. This challenge with the safety control algorithm of the UAVs. The research aims to develop UAVs capable of autopilot and sampling at low altitudes. The safety control problem of UAV is solved by the Visual Inertial Odometry (VIO) algorithm using a stereo camera synchronized with an inertial measurement unit (IMU). Besides that, the UAV is equipped with a high-resolution RBG camera for data sampling. The system has been tested under various conditions of low-ceiling performance with altitude hold and obstacle avoidance requirements, and the collected data is satisfactory for use.**

Keywords: UAV, precision agriculture, Visual Inertial Odometry, low-ceiling

I. INTRODUCTION

In the last few years, the total volume of investments in the agricultural sector has increased by 80%. These investments aim to achieve productivity growth of at least 70% by 2050to meet the advanced needs of 9 billion people. At the same time, the agricultural sector has to address severe challenges such as environmental pollution, the limited availability of arable lands, and the decrease in the number of farmers. Farms must be extended and constantly innovate to improve and maintain productivity to meet the demands. The integration of Unmanned Aerial Vehicles (UAVs) with IoT (Internet of Things) devices, such as embedded sensors and communication elements, for agriculture operations is growing at a significantly faster pace than expected [1], [2]. These IoT devices greatly enhance management operations, including field mapping [3], [4], plant-stress detection [5], [6], biomass estimation [7], [8], weed management [7],[9], inventory counting [10], etc.

The most common application of unmanned aerial vehicles (UAVs) is to observe agricultural fields for soil conditions, crop growth, weed infestation, insects, plant diseases, and crop water requirements. It provides prescription data to guide the operation of precision implements. Realizing the decisions calls for variable-rate technology to implement tactical actions in seeding, fertilizer/chemical application and irrigation instead of only mapping the field one year for improvements in a subsequent year. Typically, UAVs always use high-range flyers combine with high-resolution cameras for the survey mission [11]. However, many crops and special growing conditions require low-flying UAVs to collect data, such as orchards. The other type of application is using drones for water crops or pesticide spraying. This application can help reduce herbicide use by 52% in Brazilian soybean field, but it cannot work automatically with the auto fly mission on complex farmland at low altitude. In a low-altitude fly range, UAVs will face numerous risks in a low-altitude flying range, including GPS dampening, obstacles, and so on. Therefore, achieving autonomous recognition of obstacles and real-time avoidance is one of the inevitable trends in the intelligent development of agriculture drones.

Obstacle detection, collision avoidance, path planning, localization, and control systems are the key parts required by an unmanned vehicle to be fully autonomous and able to navigate without being explicitly controlled [12]. In a challenging dynamic agricultural environment, tasks may become increasingly difficult for UAVs due to on-board payload limitations (e.g., sensors, batteries), power constraints, reduced visibility due to bad weather (e.g., rain, dust), and complications in remote monitoring. The robotics

[1] Corresponding Author: quachconghoang89@gmai.com (Cong-Hoang Quach)

community is working hard to address these challenges and bring technological levels suitable for demanding environments to ensure the success and safe navigation of unmanned vehicles[13][14]. Therefore, the UAV's controller needs an individual positioning system.

There has been a lot of research in recent times on visual and visual-inertial odometry for UAVs with a variety of proposed algorithms [15]. A monocular camera is an ideal sensor for this task because of its small size, cheap and straightforward hardware setting. But there are many problems in the system based on pure vision, so it is difficult to apply and practice [16]. Besides that, cameras and inertial measurement units have complementary properties. By combining and utilizing their measurement data, robustness and accurate positioning can be solved. The camera provides rich image information; the data is not easy to drift, contained in the IMU gyroscope, and the accelerometer can accurately provide short-term estimates. Visual and inertial navigation is becoming more and more popular among researchers, especially in UAV [17] .

At present, there are also very excellent visual-inertial navigation research results, such as Hong Kong University of Cience and Technology VINS [18], based on the ORB-SLAM2 improved IMU+ORB-SLAM2 system [19]. There are some problems in the monocular inertial navigation system. Because the monocular camera can not measure depth information, the monocular system cannot recover the measurement scale information. Due to the lack of direct distance measurement, it will be difficult to directly integrate the monocular visual structure with the inertial measurement. To solve these problems, many systems of stereo-base inertial odometry have been proposed [20]. The stereo camera can now obtain the depth information of the object so that the camera data can be better integrated with the IMU data and the system initialization is simpler.

Furthermore, the stereo vision algorithm is excellent for extracting information about the relative position of 3D objects and obstacle avoidance in autonomous systems. For example, the article, 3D path-planning and stereo-based obstacle avoidance for rotorcraft, demonstrates the complexity of working with stereo vision to build a 3D occupancy map. The experiments highlighted the need to keep the stereo cameras pointed along the velocity vector to avoid collisions.

In this paper, we design a fully autonomous drone for agriculture, developed and implemented. This design integrated both the stereo camera and an embedded computer for state estimation and obstacle avoidance. This article is divided as follows: Section II inquires about the platform and hardware system for the primary purpose. Section III defines the VIO and obstacle avoidance algorithm. Section IV introduces the results and discussion. Finally, Section V is the conclusion.

II. HARDWARE SYSTEM

The specifications for the design were listed in table 1 below, and these determine the choice of the suitable component.

TABLE 1.THE SPECIFICATIONS FOR THE DRONE DESIGN

Parameter	Value
Lifting thrust	10N
Weight	5Kg
Battery	4S 5200mAh
Range of radio frequency coverage	1Km
Frequency of control signals	2.4GHz

A. Hex-copter Body

The frame of the hex-copter was made of very light carbon fiber. Many other materials, such as aluminium and wood, were considered. But their weight dramatically affects the performance of the aircraft, especially the flight time. The body is divided into three parts: body frame, landing gear, and embedded computer connection path. The body frame enclosed all the needed components. The width of the structure was 450mm, and the height was 400mm.

Before choosing a motor for the design, the total weight needs to be estimated first. It was determined by function:

$$Thrust=(weight*2)/6 \quad (1)$$

Where: weight is the estimated weight of the loaded vehicle, which is obtained by adding the individual weights of all components in the aircraft. (For 2:1 thrust / weight ratio).

B. Embeded computer and camera

The Jetson Nano was integrated as a companion computer because of its inherent processing power. It serves as the main control system, which changes flight mode via the MAVLink protocol. An embedded computer connected to the stereo camera processes images to create depth and visual odometry images to replace GPS data in positioning. Because of the sampling rate and image quality, we use the Zed2 camera.

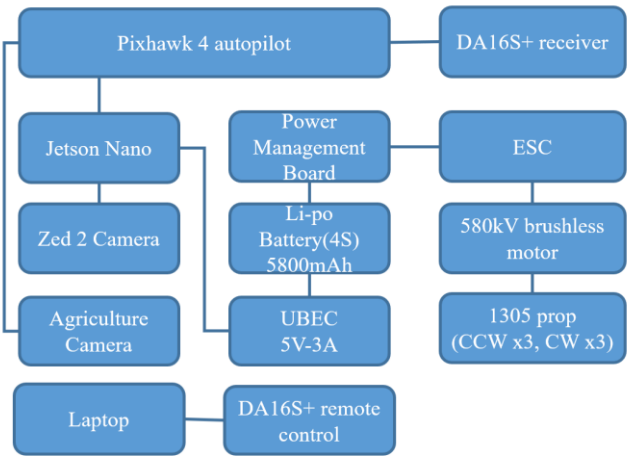

Figure 1.System connection

III. ALGORITHM

A. Visual-Inertial Odometry

In this paper, we use a VIO system called VINS-Fusion. This is an extended version of VINS-Mono [19]. VINS-Fusion is an optimization-based multi-sensor state estimator, which archives accurate self-localization for autonomous applications (UAVs, cars, AR/VR). It supports multiple visual-inertial sensor types (mono camera with IMU, stereo camera with IMU, and only stereo camera systems). The outstanding advantages of VINS-Fusion are:

- Multiple sensors support
- Online spatial calibration (transform between the camera and IMU)
- Online temporal calibration (time offset between the camera and IMU) [18]
- Visual loop closure

In this system, we use the stereo camera with IMU. The overview of the system is described in Fig. xxx. In the first block, measurement preprocessing, features are extracted and tracked, and IMU measurements between two consecutive stereo frames are pre-integrated. The initialization procedure provides all necessary values: pose, velocity, gyroscope bias, and three-dimensional feature location. This information will be used for bootstrapping the subsequent nonlinear optimization based on VIO. After a successful parameter initialization, the VIO with re-localization modules will start. This module tightly fuses pre-integrated IMU measurements, feature observations, and redetected features from the loop closure. Finally, the pose graph module performs global optimization to eliminate drift and achieve reuse proposal. Besides, camera-rate pose and IMU-rate pose are used in the online temporal calibration process.

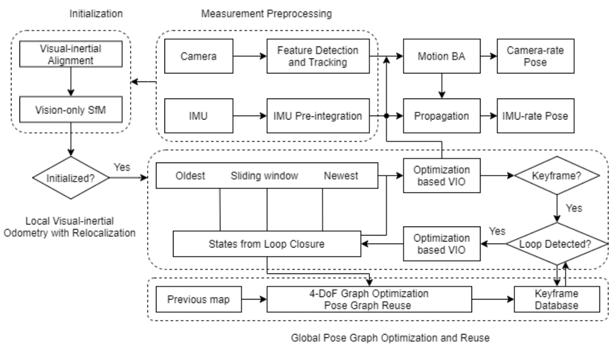

Figure 2. System overview

B. *Obstacle avoidance algorithm*

Obstacle avoidance is a two-step problem: Obstacle detection and path planning. There exist different algorithms, approaches, and solutions to path planning. The stereo vision camera helps to detect an object in front of the drone, and the computer will choose between 4 different flight modes, defined as follows:

- Go to the goal (GTG): Only used when no obstacle is detected. The quadcopter goes in a straight line toward its intended destination (waypoint to waypoint).
- Avoid obstacle (AO): This is a safe mode. Suppose the block gets too close to the drone. It will fly in the opposite direction of the aiming vector from the center of the UAV to the nearest sensed point.
- Avoid obstacle and go-to-goal (AO+GTG): This mode is used when an avoidable obstacle is sensed. It uses the result of a weighted sum vector between GTG and AO to decide where the flight direction will be.
- Follow wall (FW): Special mode in which the perceived obstacle is between the UAV and its target and the GTG + AO mode is not enough to evade said obstacle. The UAV follows the estimated contour of the obstacle until it is circumvented and then switches mode depending on the information available.

Algorithm 1 shows how a mode is chosen considering the available information and vectors. The transitions between modes are illustrated in the Finite State machine displayed in Fig3. Furthermore, the vectors mentioned in the description are represented in Fig4.

The algorithm is defined by information obtained from stereo vision. The closest distance measured by depth image was generated from the stereo camera. It is from smallest to highest and the angles at which each of the lengths was measured. Once a flight mode is chosen, the companion computer will send a flight control command to the flight controller in velocity vector format.

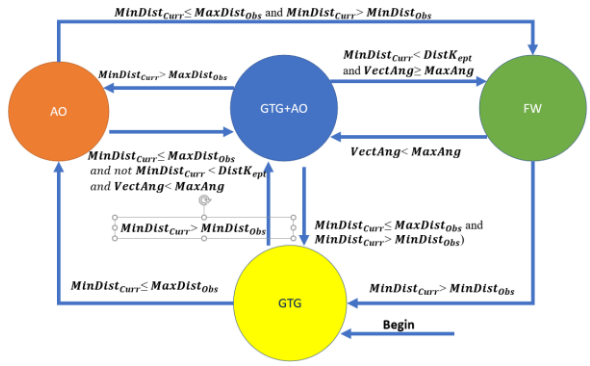

Figure 3.Mode transitions specified in Algorithm 1 represented by a Finite State Machine. The algorithm begins in the GTG mode and should end in the same mode.

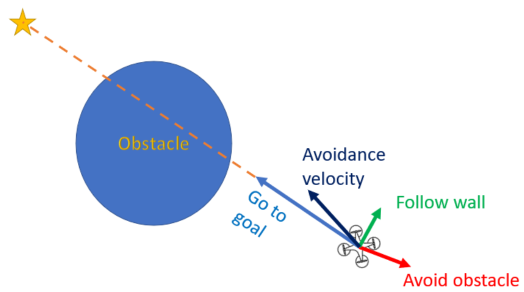

Figure 4.Vectors used in the obstacle avoidance algorithm to choose the current mode and flight trajectory.

Algorithm 1 Decision Making

Input: Current Mode *CM*, Go To Goal Vector $\boldsymbol{GTGV_{etc}}$, Avoid Obstacle Vector $\boldsymbol{AOV_{etc}}$, Current Minimum Distance to Closest Detected Obstacle $\boldsymbol{MinDist_{Curr}}$

Output: Current Mode *CM*

Initialization :

1: Define maximum perceivable distance to obstacle $\boldsymbol{MaxDist_{Obs}}$

2: Define minimum permissible distance to obstacle$\boldsymbol{MinDist_{Obs}}$**3:** Define distance to keep from estimated wall

$\boldsymbol{DistK_{ept}}$

4: Define maximum angle admissible between $\boldsymbol{GTBV_{ect}}$

and $\boldsymbol{AOV_{ect}}$, $\boldsymbol{MaxAng}$

Main Loop :

$\boldsymbol{VectAng} \leftarrow$ angleBetweenVectors($\boldsymbol{GTBV_{ect}}$, $\boldsymbol{AOV_{ect}}$)
if (*CM* = *GTG*) **then**
  if ($\boldsymbol{MinDist_{Curr}} \leq \boldsymbol{MinDist_{Obs}}$ **and** $\boldsymbol{MinDist_{Curr}} > \boldsymbol{MinDist_{Obs}}$) **then**
    CM ← *GTG+AO*
  else if ($\boldsymbol{MinDist_{Curr}} \leq \boldsymbol{MinDist_{Obs}}$) **then**
    CM ← *AO*
  end if
else if *(CM = GTG+AO)* **then**
  if ($\boldsymbol{MinDist_{Curr}} > \boldsymbol{MaxDist_{Obs}}$) **then**
    CM ← *GTG*
  else if ($\boldsymbol{MinDist_{Curr}} \leq \boldsymbol{MinDist_{Obs}}$) **then**
    CM ← *AO*
  else if ($\boldsymbol{MinDist_{Curr}} < \boldsymbol{DistK_{ept}}$ **and** $\boldsymbol{VectAng} \geq \boldsymbol{MaxAng}$) **then**
    CM ← *FW*
  end if
else if *(CM = AO)* **then**
  if ($\boldsymbol{MinDist_{Curr}} > \boldsymbol{MinDist_{Obs}}$) **then**
    if ($\boldsymbol{MinDist_{Curr}} < \boldsymbol{DistK_{ept}}$ **and** $\boldsymbol{VectAng} \geq \boldsymbol{MaxAng}$) **then**
      CM ← *FW*
    else
      CM ← *GTG+AO*
    end if
  end if
else if *(CM = FW)* **then**
  if ($\boldsymbol{VectAng} < \boldsymbol{MaxAng}$) **then**
    CM ← *GTG+AO*
  else if ($\boldsymbol{MinDist_{Curr}} > \boldsymbol{MaxDist_{Obs}}$) **then**
    CM ← *GTG*
  end if
end if

IV. EXPERIMENTS AND RESULT

In this section, we present our experiments with the system. The first part is to evaluate VINS-Fusion with the VIODE dataset [21], then to verify the obstacle avoidance algorithm. All these experiments were conducted in the AirSim simulation environment.

VIODE (VIO dataset in Dynamic Environments) is a benchmark for assessing the performance of VO/VIO algorithms in dynamic scenes. The environments are simulated using AirSim [22], a photorealistic simulator geared towards developing perception and control algorithms. VIODE's unique advantage over existing datasets lies in the systematic introduction of dynamic objects in increasing numbers and different environments. VIODE uses the same UAV trajectory to generate data series with growing moving objects in each scenario. Thus, with VIODE, we can isolate the influence of scene dynamics on the robustness of vision-based localization algorithms.

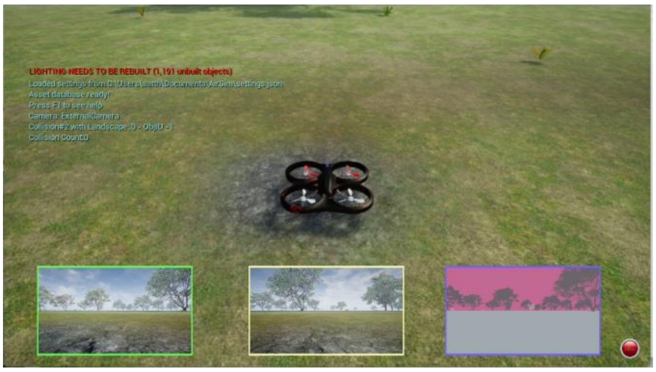

Figure 5. Simulation environment.

Firstly, for the VO/VIO algorithms, our experimental simulated a quadcopter with a front stereo camera with a 720x480 resolution and 90° FOV. The simulation environment was built on UE4 software and the drone, camera, was set up by Airsim open-source. This is a grass field with trees and rocks (Figure.1). For the pre-processing, we calibrate the camera first to find the project matrix for the VIO algorithm input. The result of VIO was shown below:

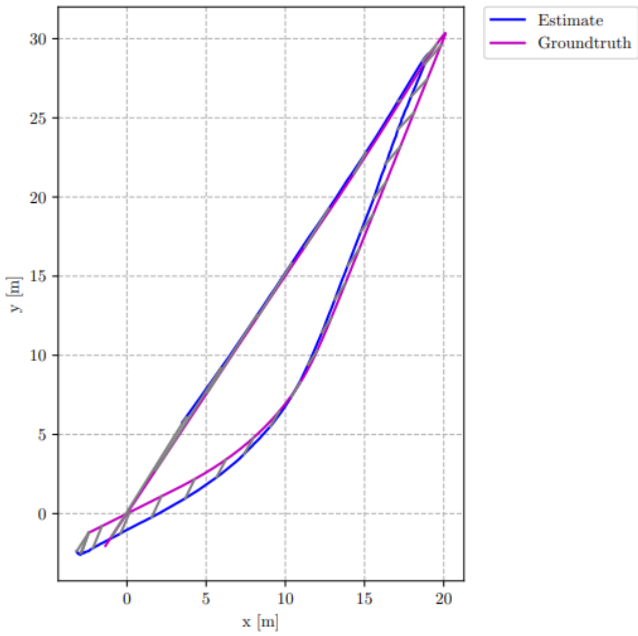

Figure 6. Trajectory simulation

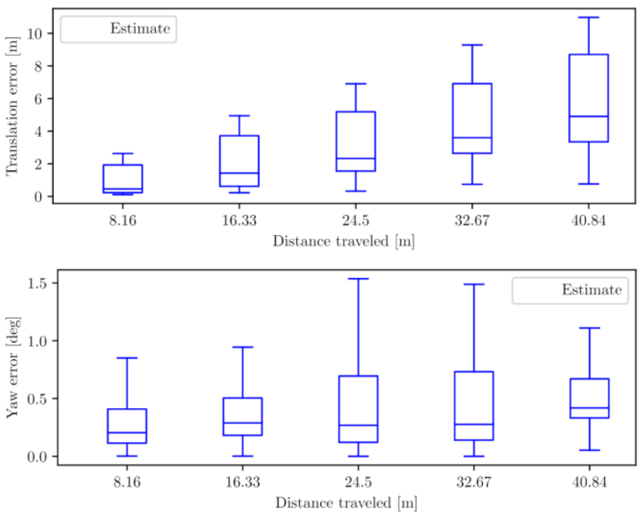

Figure 7. Translation error and Yaw error depend on distance.

Figure.2 shows the trajectory of the drone in the simulation with a velocity of 5m/s. In the first straight trip, the translation error is insignificant (Figure.3). During the next move, the system error was too big due to the drone's rotation and the environment did not have enough markers.

Because of the errors in the VIO algorithm, applying the obstacle avoidance algorithm, we reduced the flight speed to 2m/s and got the results as shown in Figure 8.

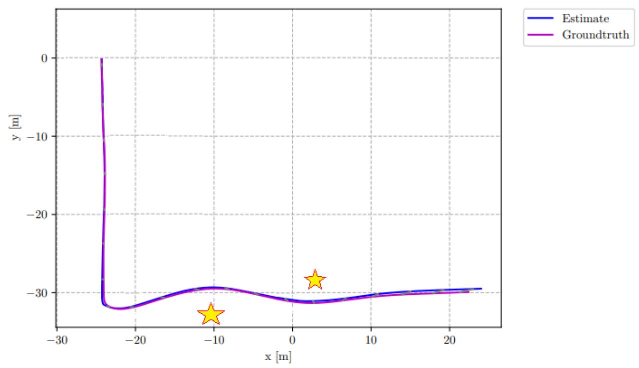

Figure 8. Trajectory in Obstacle avoidance

To investigate how the speed affects the algorithm, we tested the system many times with the camera sampling rate of 25 fps and the 50m distance results are shown below.

TABLE 2. TRANSLATION ERROR DEPEND ON DISTANCE VELOCITY

Velocity	Translation error
5 m/s	7,4%
4 m/s	5,2%
3 m/s	3,6%
2 m/s	1,4%

V. Conclusion

In conclusion, this device could potentially detect and avoid most obstacles. However, this implement only uses a front stereo camera; obstacles below, behind, and above drones may not be possible. Therefore, the drone cannot run in a more complex scenario and at high speed in the current state. Regardless, more tests will be undertaken to assess the current system's limitations and identify possible avenues for improvement. Furthermore, since most of the exposed behaviors rely on practical insights and geometrical calculations, a thorough mathematical proof of the algorithm has not been developed; therefore, future work will focus on deriving it. The VIO system error is insignificant, so it can replace GPS, but after a long time running, the cumulative error needs to be correct. In the future, we will improve the solution as well as the accumulated errors.

Acknowledgement

Quach Cong Hoang was funded by Vingroup Joint Stock Company and supported by the Domestic PhD Scholarship Program of Vingroup Innovation Foundation (VINIF), Vingroup Big Data Institute (VINBIGDATA), code VINIF.2020.TS.23.

References

[1] D. C. Tsouros, S. Bibi, and P. G. Sarigiannidis, “A review on UAV-based applications for precision agriculture,” *Inf.*, vol. 10, no. 11, 2019, doi: 10.3390/info10110349.

[2] U. R. Mogili and B. B. V. L. Deepak, “Review on Application of Drone Systems in Precision Agriculture,” *Procedia Comput. Sci.*, vol. 133, pp. 502–509, 2018, doi: 10.1016/j.procs.2018.07.063.

[3] S. Marino and A. Alvino, “Detection of Spatial and Temporal Variability of Vegetation Indices,” *Agronomy*, vol. 9, no. 226, p. 13, 2019.

[4] P. Surový, N. Almeida Ribeiro, and D. Panagiotidis, “Estimation of positions and heights from UAV-sensed imagery in tree plantations in agrosilvopastoral systems,” *Int. J. Remote Sens.*, vol. 39, no. 14, pp. 4786–4800, 2018, doi: 10.1080/01431161.2018.1434329.

[5] C. Cilia *et al.*, “Nitrogen status assessment for variable rate fertilization in maize through hyperspectral imagery,” *Remote Sens.*, vol. 6, no. 7, pp. 6549–6565, 2014, doi: 10.3390/rs6076549.

[6] M. Zaman-Allah *et al.*, “Unmanned aerial platform-based multi-spectral imaging for field phenotyping of maize,” *Plant Methods*, vol. 11, no. 1, pp. 1–10, 2015, doi: 10.1186/s13007-015-0078-2.

[7] A. Chang, J. Jung, M. M. Maeda, and J. Landivar, “Crop height monitoring with digital imagery from Unmanned Aerial System (UAS),” *Comput. Electron. Agric.*, vol. 141, pp. 232–237, 2017, doi: 10.1016/j.compag.2017.07.008.

[8] E. Honkavaara *et al.*, “Hyperspectral Reflectance Signatures and Point Clouds for Precision Agriculture by Light Weight UAV Imaging System,” *ISPRS Ann. Photogramm. Remote Sens. Spat. Inf. Sci.*, vol. 1, no. September, pp. 353–358, 2012, doi: 10.5194/isprsannals-I-7-353-2012.

[9] M. Pflanz, H. Nordmeyer, and M. Schirrmann, “Weed mapping with UAS imagery and a bag of visualwords based image classifier,” *Remote Sens.*, vol. 10, no. 10, pp. 1–17, 2018, doi: 10.3390/rs10101530.

[10] M. Rahnemoonfar and C. Sheppard, “Deep count: Fruit counting based on deep simulated learning,” *Sensors (Switzerland)*, vol. 17, no. 4, pp. 1–12, 2017, doi: 10.3390/s17040905.

[11] Y. Huang, S. J. Thomson, H. J. Brand, and K. N. Reddy, “Development and evaluation of low-altitude remote sensing systems for crop production management,” *Int. J. Agric. Biol. Eng.*, vol. 9, no. 4, pp. 1–11, 2016, doi: 10.3965/j.ijabe.20160904.2010.

[12] A. Foka, “Real-Time Hierarchical POMDPs for Autonomous Robot Navigation 2 Partially Observable Markov Decision Processes (POMDPs),” no. July, 2005.

[13] J. N. Yasin, S. A. S. Mohamed, M. H. Haghbayan, J. Heikkonen, H. Tenhunen, and J. Plosila, “Unmanned Aerial Vehicles (UAVs): Collision Avoidance Systems and Approaches,” *IEEE Access*, vol. 8, pp. 105139–105155, 2020, doi: 10.1109/ACCESS.2020.3000064.

[14] S. S. Esfahlani, “Mixed reality and remote sensing application of unmanned aerial vehicle in fire and smoke detection,” *J. Ind. Inf. Integr.*, vol. 15, no. June 2018, pp. 42–49, 2019, doi: 10.1016/j.jii.2019.04.006.

[15] R. Munguía, S. Urzua, Y. Bolea, and A. Grau, “Vision-based SLAM system for unmanned aerial vehicles,” *Sensors (Switzerland)*, vol. 16, no. 3, pp. 1–23, 2016, doi: 10.3390/s16030372.

[16] Y. Li and S. B. Lang, “A Stereo-Based Visual-Inertial Odometry for SLAM,” *Proc. - 2019 Chinese Autom. Congr. CAC 2019*, pp. 594–598, 2019, doi: 10.1109/CAC48633.2019.8997432.

[17] D. Scaramuzza and Z. Zhang, “Odometry of,” pp. 1–9, 2020.

[18] T. Qin and S. Shen, “[Best Student Paper Award] Online Temporal Calibration for Monocular Visual-Inertial Systems,” *Iros*, pp. 3662–3669, 2018.

[19] T. Qin, P. Li, and S. Shen, “VINS-Mono: A Robust and Versatile Monocular Visual-Inertial State Estimator,” *IEEE Trans. Robot.*, vol. 34, no. 4, pp. 1004–1020, 2018, doi: 10.1109/TRO.2018.2853729.

[20] C. Chen, H. Zhu, M. Li, and S. You, “A review of visual-inertial simultaneous localization and mapping from filtering-based and optimization-based perspectives,” *Robotics*, vol. 7, no. 3, 2018, doi: 10.3390/robotics7030045.

[21] K. Minoda, F. Schilling, V. Wuest, D. Floreano, and T. Yairi, “VIODE: A Simulated Dataset to Address the Challenges of Visual-Inertial Odometry in Dynamic Environments,” *IEEE Robot. Autom. Lett.*, vol. 6, no. 2, pp. 1343–1350, 2021, doi: 10.1109/LRA.2021.3058073.

[22] S. Shah, D. Dey, C. Lovett, and A. Kapoor, “AirSim: High-Fidelity Visual and Physical Simulation for Autonomous Vehicles,” 2017.

Design of PD Controller for Flexible Manipulators by Particle Swarm Optimization

Nguyen Quang Hoang
Department of Applied Mechanics
Hanoi University of Science and Technology
No. 1 Dai Co Viet Road, Hanoi
hoang.nguyenquang@hust.edu.vn

Than Van Ngoc
College of Electromechanical and Civil Engineering
Vietnam National University of Forestry
Xuan Mai Town, Chuong My District, Hanoi
thanvanngoc@gmail.com

***Abstract* — The robotic manipulators consisting of flexible links are widely used in industries such as construction, mining, medical, aerospace, and automation. With lightweight and slender links, flexible manipulators have some advantages compared to rigid ones such as material and energy saving. However, control of flexible manipulators has some challenges due to the flexibility of the link. This paper presents the dynamic modeling and control of a flexible manipulator of two links with translation and rotational joints. The finite element method and Lagrange equation are used to build the dynamic model. An optimal PD controller based on the Particle Swarm Optimization algorithm is designed to bring the endpoint to the desired position. The numerical simulations are carried to illustrate the proposed algorithm.**

Keywords* — *Flexible manipulator, Modeling, Finite element method, PD controller, PSO.

I. INTRODUCTION

Flexible manipulators have many advantages such as lighter weight and slimmer having lower material and energy costs than traditional robots with high rigidity and large size. However, flexible manipulators are time-varying nonlinear MIMO systems and which become more deformable and more difficult to control precisely. Therefore, for the problem of inverse kinematics and robot control the vibrate properties of the links cannot be ignored. This type of elastic manipulator is commonly used in fields such as space exploration, manufacturing automation, construction, and mining, where small-volume manipulators and large workspaces are required.

The study of flexible manipulators has attracted the attention of scientists in the last three decades. There have been many studies on the dynamics and control of manipulators with elastic links. These works are summarized in review articles such as: [1-6]. In general, the works focus on modeling and control design for elastic manipulators. Of these, five main methods are used to model flexible link manipulator, including: 1. Lumped Parameter Method (LPM) [7], 2. Finite Difference Method (FDM), 3. Assumed Mode Method (AMM) [8, 9,10], 4. Finite Element Method (FEM) [11, 12], 5. Rigid Finite Element Method (RFEM) [13]. Besides modeling, the rules controlling the position and trajectory of the links are also interested in research. Many control laws from linear, nonlinear, stable, adaptive, fuzzy logic, using neural networks, etc. have been established and applied to elastic manipulators [8, 9, 13, 14, 15, 16]. In addition, dark search algorithms like Particle Swarm Optimization (PSO) [18, 19] and Genetic Algorithms (GA) [20]..., which are the algorithm is very efficient in finding the optimal solution advantage of the problem [21, 22, 23].

In this paper, the finite element method and Lagrange 2 equation are used to build a dynamic model for a planar robot manipulator consisting of two translation and rotary joints with flexible links. Based on the received motion differential equation, an optimal PD controller based on the Particle Swarm Optimization algorithm is designed. The optimal criteria used in this paper is sum of square error in position and velocity. The layout of the paper consists of 5 parts: part 1 introduces, part 2 presents the application of the FEM method to building differential equations of motion for a two-stage planar manipulator system, part 3 presents PD control law and PSO algorithm, part 4 presents the numerical simulation results and finally the conclusion.

II. DYNAMIC MODEL OF FLEXIBLE MANIPULATOR

A. *Dynamic modeling*

The differential equation of motion of the flexible manipulator is established by the FEM method and the Lagrange 2 equation has the following matrix form:

$$\mathbf{M}(\mathbf{q})\ddot{\mathbf{q}} + \mathbf{C}(\mathbf{q},\dot{\mathbf{q}})\dot{\mathbf{q}} + \mathbf{D}\dot{\mathbf{q}} + \mathbf{K}\mathbf{q} + \mathbf{G}(\mathbf{q}) = \mathbf{B}\boldsymbol{\tau} \quad (1)$$

Where, $\mathbf{q} = [\mathbf{q}_r^T, \mathbf{q}_f^T]^T$ is the generalized coordinate vector of rigid motion and the small flexible deformation around its straight state, $\mathbf{M}(\mathbf{q})$ is generalized mass matrix, $\mathbf{K}$ is the generalized stiffness matrix, $\mathbf{D}$ is viscosity coefficient matrix, $\mathbf{C}(\mathbf{q},\dot{\mathbf{q}})$ is the Coriolis matrix, $\mathbf{G}$(q) is the generalized force matrix of gravity, and $\mathbf{B}$ is the constant matrix corresponding to the excitation force/torque $\boldsymbol{\tau}$. Details on the construction of this equation can be found in the documents [1, 24, 25].

B. *Equations of motion*

Consider the two-link flexible link manipulators with translational joint and rotational joint moving in the horizontal plane is shown as Figure 1.

The coordinate system $O_0x_0y_0$ is fixed frame at O_0. The relative coordinate systems $O_1x_1y_1$, Ax_2y_2 are attached to the translation link at O_1 and rotational link at A, respectively. B is the end-effector point.

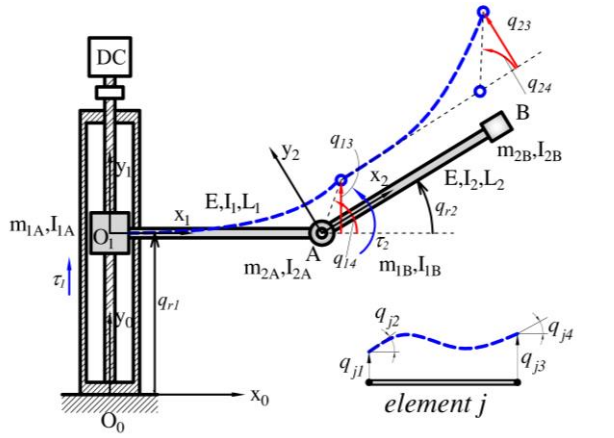

Fig. 1. The configuration diagram of two-link flexible manipulators

The parameters of the two flexible links include *link 1-O_1A:* the mass and moment of inertia of the weight at both ends of the link are m_{1A}, m_{2A} (kg), I_{1A}, I_{2A} (kg.m^2) respectively; the mass and moment of inertia of link are m_1 (kg), I_1 (kg.m^2) respectively; link 1 with length L_1 (m). *Link 2 - AB:* the mass and moment of inertia of the weight at both ends of the link are m_{1B}, m_{2B} (kg), I_{1B}, I_{2B} (kg.m^2) respectively; the mass and moment of inertia of the link are m_2 (kg), I_2 (kg.m^2) respectively; link 2 with length L_2 (m). m_e is the mass of the beam element and along with other parameters are shown details in Table 2.

Through some results in [26], it can see that when taking the number of elements of a stage as 1, 2, 3 or 4, the results are not much different, but the computational volume increases significantly, so in this paper we use the number of elements for per link is one ($n_{ej} = 1$).

The generalized coordinates for the links are:

$$\mathbf{q}_1 = [q_{r1}, q_{13}, q_{14}]^T \,;\; \mathbf{q}_2 = [y_A, \theta_2, q_{23}, q_{24}]^T \qquad (2)$$

in there: $y_A = q_{r1} + q_{13}$, , $\theta_2 = q_{r2}+q_{14}$. And the generalized coordinates vectors for the entire flexible manipulator are as follows:

$$\mathbf{q} = [q_{r1}, q_{r2}, q_{13}, q_{14}, q_{23}, q_{24}]^T \qquad (3)$$

Where the translational joint variable q_{r1} is driven by τ_1 force. The rotational joint variable q_{r2} is driven by τ_2 torque. The variables q_{13}, q_{14}, q_{23}, q_{24} are the elastic deformation bending and rotation angle at the endpoints of link 1 and link 2, respectively. Using Maple software calculate the mass and stiffness matrices for each link of the manipulator as follows:

$$\mathbf{M}_1 = \begin{bmatrix} m_{1A} + m_1 + m_{2A} & \frac{1}{2}m_1 + m_{2A} & -\frac{1}{12}m_1 L_1 \\ & \frac{13}{35}m_1 + m_{2A} & -\frac{11}{210}m_1 L_1 \\ sym & & \frac{1}{105}m_1 L_1^2 + I_{2A} \end{bmatrix},$$

$$\mathbf{K}_1 = \frac{EI_1}{L_1^3}\begin{bmatrix} 0 & 0 & 0 \\ 0 & 12 & -6L_1 \\ 0 & -6L_1 & 4L_1^2 \end{bmatrix} \qquad (4)$$

The mass matrix $\mathbf{M}_2$ and the stiffness matrix $\mathbf{K}_2$ of size 4x4 are symmetric matrices with the upper half-triangle elements as follows:

$$\mathbf{M}_2 = \begin{bmatrix} m_{1B} + m_2 + m_{2B} & (\frac{1}{2}m_2 + m_{2B})L_2\cos(q_{r2}+q_{14}) & (\frac{1}{2}m_2 + m_{2B})\cos(q_{r2}+q_{14}) & -\frac{1}{12}m_2 L_2\cos(q_{r2}+q_{14}) \\ & I_{1B} + \frac{1}{3}m_2 L_2^2 + m_{2B}L_2^2 + I_{2B} & \frac{7}{20}m_2 L_2 + m_{2B}L_2 & -\frac{1}{20}m_2 L_2^3 + I_{2B} \\ & & \frac{13}{35}m_2 + m_{2B} & -\frac{11}{210}m_2 L_2 \\ sym & & & \frac{1}{105}m_2 L_2^2 + I_{2B} \end{bmatrix}$$

$$\mathbf{K}_2 = \frac{EI_2}{L_2^3}\begin{bmatrix} 0 & 0 & 0 & 0 \\ & 0 & 0 & 0 \\ & & 12 & -6L_2 \\ sym & & & 4L_2^3 \end{bmatrix} \qquad (5)$$

Concatenating the mass and stiffness matrices of the links together, we get the mass matrix $\mathbf{M(q)}$ and the stiffness matrix $\mathbf{K}$ of the whole system of size 6x6 symmetric with the elements:

$$\mathbf{M(q)} = \begin{bmatrix} M_{11} & M_{12} & M_{13} & M_{14} & M_{15} & M_{16} \\ & M_{22} & M_{23} & M_{24} & M_{25} & M_{26} \\ & & M_{33} & M_{34} & M_{35} & M_{36} \\ & & & M_{44} & M_{45} & M_{46} \\ & & & & M_{55} & M_{56} \\ sym & & & & & M_{66} \end{bmatrix} \qquad (6)$$

Where, the elements of the matrix have the following values:

$$M_{11} = m_{1A} + m_1 + m_{2A} + m_{1B} + m_2 + m_{2B}$$
$$M_{12} = 1/2\,(m_2 + 2m_{2B})L_2\cos(q_{r2} + q_{14})$$
$$M_{13} = 1/2\,m_1 + m_{2A} + m_{1B} + m_2 + m_{2B}$$
$$M_{14} = (1/2\,m_2 + m_{2B})\,L_2\cos(q_{r2} + q_{14}) - 1/12\,m_1 L_1$$
$$M_{15} = 1/2\,(m_2 + 2m_{2B})\cos(q_{r2} + q_{14})$$
$$M_{16} = -1/12\,m_2 L_2\cos(q_{r2} + q_{14})$$
$$M_{22} = I_{1B} + (1/3\,m_2 + m_{2B})\,L_2^2 + I_{2B}$$
$$M_{23} = 1/2\,(m_2 + 2m_{2B})L_2\cos(q_{r2} + q_{14})\,;$$
$$M_{24} = I_{1B} + (1/3\,m_2 + m_{2B})\,L_2^2 + I_{2B}$$
$$M_{25} = (7/20\,m_2 + m_{2B})\,L_2\,;\; M_{26} = -1/20\,m_2 L_2^2 + I_{2B}$$
$$M_{33} = 13/35\,m_1 + m_{2A} + m_{1B} + m_2 + m_{2B}$$
$$M_{34} = (1/2\,m_2 + m_{2B})\,L_2\cos(q_{r2} + q_{14}) - 11/210\,m_1 L_1$$
$$M_{35} = 1/2\,(m_2 + 2m_{2B})\cos(q_{r2} + q_{14})$$
$$M_{36} = -1/12\,m_2 L_2\cos(q_{r2} + q_{14})$$
$$M_{44} = 1/105\,m_1 L_1^2 + 1/3\,m_2 L_2^2 + m_{2B}L_2^2 + I_{2A} + I_{1B} + I_{2B}$$
$$M_{45} = 7/20\,m_2 L_2 + m_{2B}L_2\,;\; M_{46} = -1/20\,m_2 L_2^2 + I_{2B}$$
$$M_{55} = 13/35\,m_2 + m_{2B}\,; M_{56} = -11/210\,m_2 L_2$$
$$M_{66} = 1/105\,m_2 L_2^2 + I_{2B}\,.$$

The overall stiffness matrix has the form:

$$\mathbf{K} = \begin{bmatrix} 0 & 0 & 0 & 0 & 0 & 0 \\ & 0 & 0 & 0 & 0 & 0 \\ & & 12EI_1/L_1^3 & -6EI_1/L_1^2 & 0 & 0 \\ & & & 4EI_1/L_1 & 0 & 0 \\ & & & & 12EI_2/L_2^3 & -6EI_2/L_2^2 \\ sym & & & & & 4EI_2/L_2 \end{bmatrix} \qquad (7)$$

The Coriolis matrix $\mathbf{C}(\mathbf{q},\dot{\mathbf{q}})$ is determined from the mass matrix $\mathbf{M}(\mathbf{q})$ according to the Christoffel formula [26] or using the Kronecker product [27]. The matrices **B** and **D** have the following form:

$$\mathbf{B}=\begin{bmatrix}1&0&0&0&0&0\\0&1&0&0&0&0\end{bmatrix}^T,\ \mathbf{D}=diag[d_1\quad d_2\quad 0\quad 0\quad 0\quad 0]\tag{8}$$

The generalized force vector $\mathbf{G}(\mathbf{q})$ is obtained from the expression of potential energy due to gravity, $\mathbf{G}(\mathbf{q}) = 0$ when the flexible manipulator moves in the horizontal plane.

III. DESIGN PD CONTROLLER WITH PSO

A. Overview of the PD controller

The PD controller has a simple structure, easy to use, so it is widely used in controlling objects according to the feedback principle.

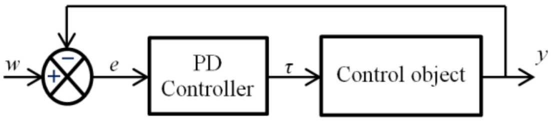

Fig. 2. Feedback control with PD controller

In this paper, the task of the flexible manipulator control problem is to give the law of driving force/moment acting on the joints to make the endpoint of the manipulator reach the desired position with high accuracy and least vibration. To build a PD controller for an elastic robot, we will choose two parameters Kp, Kd suitable for the controller to converge to the desired value. Specifically, the control function applied to the manipulator has the following form:

$$u(t)=K_p e(t)+K_d\dot{e}(t)\tag{9}$$

Where, $e(t)=q_r^{ref}-q_r^{real}(t)$ is the error between the received wanted signal q_r^{ref} and the feedback signal of system $q_r^{real}(t)$. $\dot{e}(t)=\frac{d}{dt}e(t)=-\frac{d}{dt}q_r^{real}(t)$. K_p, K_d which are the parameters of the PD controller and also matrices of the same size as the number of joints of the flexible manipulator. This paper presents the PSO algorithm to determine the optimal parameters K_p, K_d of the PD controller.

B. Particle swarm optimization algorithm

The PSO algorithm [18, 19] is a set-based optimization method, in which the system is initialized with a set of random elements and the algorithm finds the optimal by updating generations proposed by Eberhart and Kennedy. This algorithm simulates the behavior of a flock of birds or the collective intelligence of a group of social insects with limited individual capabilities. In the PSO algorithm, each i-th individual of the swarm is characterized by two parameters, the current position, and velocity of each individual, which are represented by the following two vectors:

$$X_i=(x_1,x_2,...,x_i)\,;\ V_i=(v_1,v_2,...,v_i)\tag{10}$$

The suitability of each individual will be evaluated by the objective function *J*. This function is defined as the sum of the squares of control errors $\mathbf{e}(t)$ and its derivative $\dot{\mathbf{e}}(t)$ in the control process as follows:

$$J=\sum_{j=1}^{k}\mathbf{e}^T(j)\mathbf{e}(j)+\sum_{j=1}^{k}\dot{\mathbf{e}}^T(j)\dot{\mathbf{e}}(j)\tag{11}$$

A particle is always searching in his own search space to replace his old position with a better new one. At each iteration, the two best values of velocity and position determined by the experience of the particle as well as the experience of the whole swarm are updated following Equations (12) and (13).

$$V_i^{k+1}=wV_i^k+c_1.rand_1(Pbest_i^k-x_i^k)+c_2.rand_2(Gbest_i^k-x_i^k)\tag{12}$$

$$X_i^{k+1}=X_i^k+V_i^{k+1}\tag{13}$$

where $V_i^k, X_i^k, V_i^{k+1}, X_i^{k+1}$ are the velocity vector and the position vector of the i-th particle at the k and k+1 iterations in the search space, respectively. $Pbest_i^k$ is the previous optimal index of each individual. $Gbest_i^k$ is the most optimal index between individuals in a population. *k* is the number of iterations. c_1 and c_2 are learning factors. $rand_1$, $rand_2$ are two random numbers between (0, 1).
w is the inertial weight, which is set by the following equation:

$$w=w_{\max}-\frac{w_{\max}-w_{\min}}{MaxIter}.iter\tag{14}$$

where *MaxIter* represents the maximum number of iterations, and *iter* it is the number of current iteration or generations.
The diagram of the PSO algorithm is described in Figure 3.

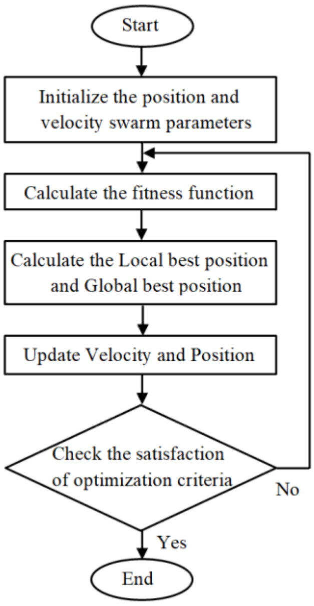

Fig. 3. Flowchart of PSO algorithm

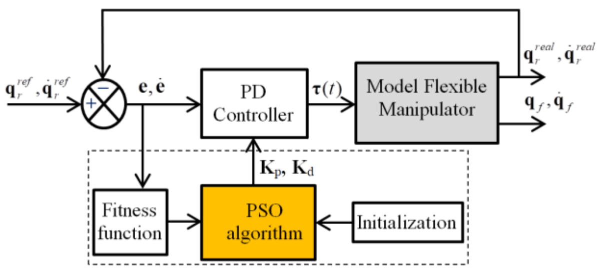

Fig. 4. PSO-based PD control block diagram

IV. NUMERICAL EXPERIMENTS

In this section, implement PSO algorithm (Figure 3) on the mfile part of Matlab [28], and build a closed-loop control system with PD controller for the flexible manipulator (Figure 4) on Simulink. The parameters for the model of the flexible robot arm and initialization parameters of the PSO algorithm considered is characterized by the following data;

TABLE I. PARAMETERS OF DYNAMIC MODEL

General Specifications	Link 1	Link 2
$\rho = 7830$ (kg/m^3)	$L_1 = 0.6$ (m);	$L_2 = 0.4$ (m);
$b = 0.02$ (m)	$n_{1e} = 1$	$n_{2e} = 1$
$h = 0.005$ (m)	$m_1 = \rho A L_1$ (kg)	$m_2 = \rho A L_2$ (kg)
$A = b.h$ (m^2)	$m_{1e} = m_1/N_1$ (kg)	$m_{2e} = m_2/N_2$ (kg)
$E = 2.1\text{x}10^{11}$ (N/m^2)	$m_{1A} = 0.05m_1$ (kg)	$m_{1B} = 0.05m_2$ (kg)
Coefficient of drag at	$m_{2A} = 0.05m_1$ (kg)	$m_{2B} = 0.05m_2$ (kg)
two joints:	$I_{1A} = 0.001$ (m^4)	$I_{1B} = 0.001$ (m^4)
$d_1 = 0.1$; $d_2 = 0.1$	$I_{2A} = 0.001$ (m^4)	$I_{2B} = 0.001$ (m^4)
	$L_{1e} = L_1/N_1$ (m)	$L_{2e} = L_2/N_2$ (m)
	$I_1 = bh^3/12$ (m^4)	$I_2 = bh^3/12$ (m^4)

TABLE II. DEFINE THE PSO'S PARAMETERS

Property	Symbol and Value
Number of practicles in a swarm	noP = 30
Max Iterations	MaxIter = 30
Acceleration constants	$c_1 = 2$, $c_2 = 2$
Number of optimization variables	Nvar = 2
Max and min inertia factor	*Wmax* = 0.9, *Wmin*=0.4
Lower bound of variables	Lb = [0 0]
Upper bound of variables	Ub = [500 500]

In this simulation, the endpoint E is required to move from the initial position with $\mathbf{q}_r^{ref\,0} = \begin{bmatrix} 0 & 0 \end{bmatrix}^T$ to the final position defined by $\mathbf{q}_r^{ref} = \begin{bmatrix} 0.8 & \pi/3 \end{bmatrix}^T$. The simulation time is $T = 5$s.

Run the program according to the algorithm set out to perform the population evolution and after 30 iterations we get the following results:

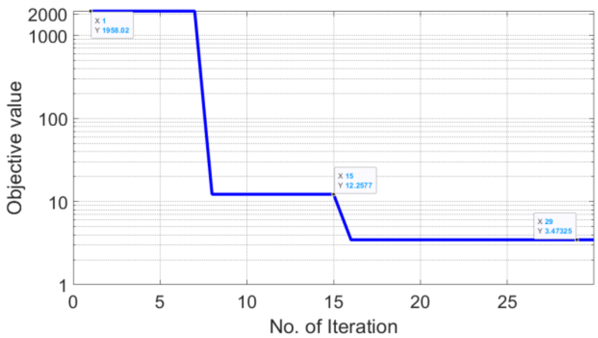

Fig. 5. Evolution of the objective function with iterations for the PD controller

Performing the maximum number of iterations, the optimal parameters of the PD controller K_p, K_d are selected when the objective function (11) reaches the minimum value as follows:

$$K_p = 137.0303*\text{diag}([1, 1]),\ \ K_d = 18.6387*\text{diag}([1, 1]).$$

After finding the optimal values of the PD controller and proceed to simulate the system's response on Simulink. The simulation results are shown in the figures from Figure 6. to Figure 12.

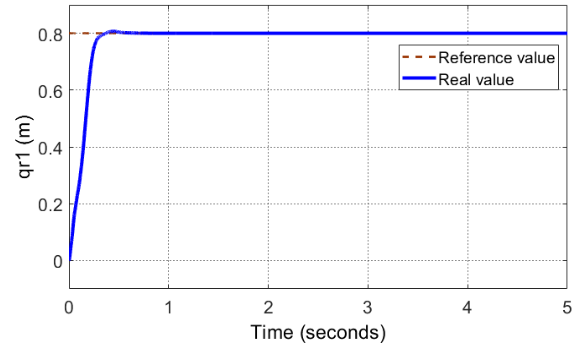

Fig. 6. Values of translational joint

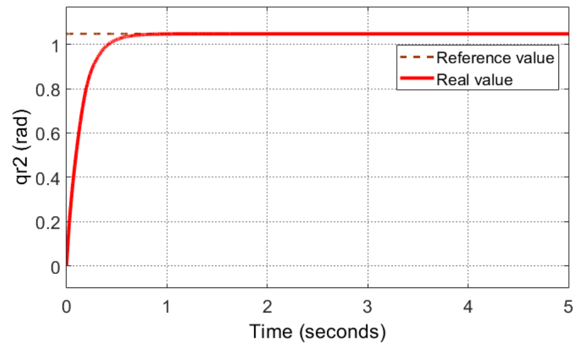

Fig. 7. Values of rotational joint

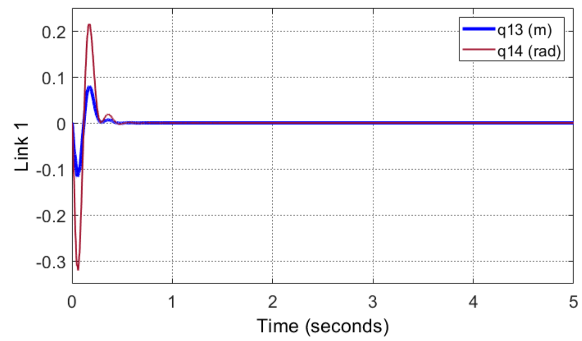

Fig. 8. Value of elastic displacement at the end of link 1

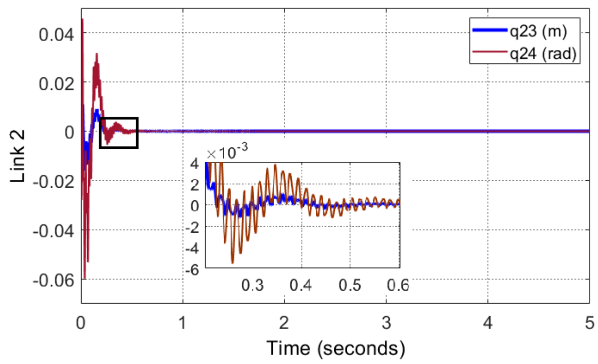

Fig. 9. Value of elastic displacement at the end of link 2

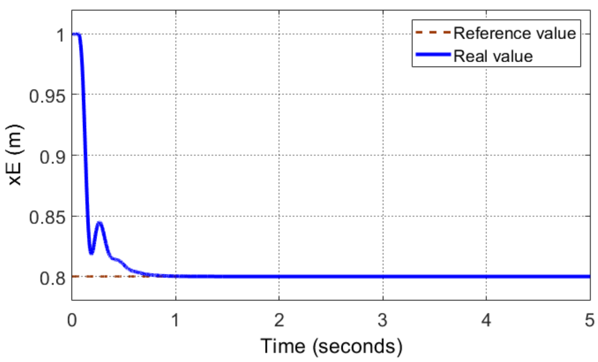

Fig. 10. Value of the endpoint in the x-axis direction

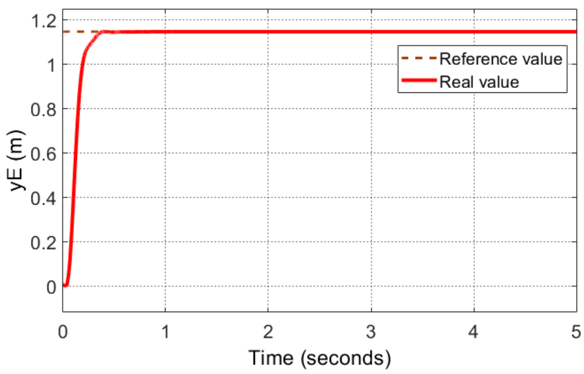

Fig. 11. Value of the endpoint in the y-axis direction

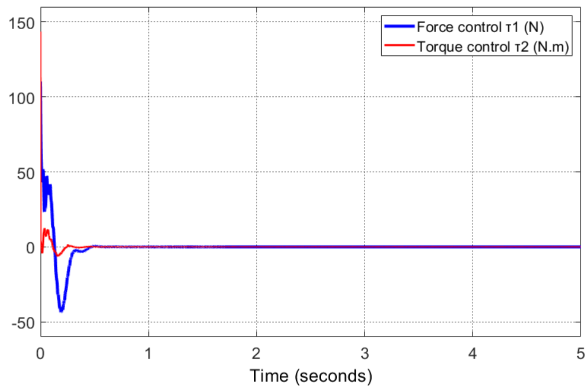

Fig. 12. Values of driving forces and torque at joints

Figures 6 and 7 show that the movement of the joints is relatively smooth and reaches quickly the set position after about 0.7 s, while the elastic oscillations reduce to zero (Fig. 7, 8). The endpoint approaches the desired position after a time of 0.7 s (Fig. 9, 10). From these results, it can be seen that the PD controller with parameters Kp, Kd optimized by PSO brings the endpoint to the desired position in a short time, while vibration response reduces quickly to zero.

V. Conclusion

This paper presents the dynamic model of a two-joint translational and rotary (T-R) planar manipulator with flexible links. The differential equation of motion of an elastic manipulator of general form is established. From these motion differential equations, the response of the system is simulated by Matlab/Simulink with a PD controller controlling the position of the manipulator in the joint space. The PSO optimization algorithm is presented and successfully applied to find the optimal parameters of the PD controller K_p, K_d. The simulation results show that the PSO-based PD controller can meet the requirement. However, the issue of tracking control in the operational space will be studied in a future work.

References

[1] Ahmed A. Shabana (1997): "Flexible Multibody Dynamics: Review of Past and Recent Developments". Multibody System Dynamics 1: 189–222.

[2] Santosha Kumar Dwivedy and Peter Eberhard (2006): "Dynamic analysis of flexible manipulators, a literature review". Mechanism and Machine Theory 41 749–777.

[3] K. Lochan, B.K. Roy, B. Subudhi (2016): "A review on two-link flexible manipulators". Annual Reviews in Control, Volume 42, Pages 346-367.

[4] Yanqing Gao, Fei-Yue Wang, Zhi-Quan Zhao (2012): "Flexible Manipulators: Modeling, Analysis and Optimum Design", Academic Press.

[5] R. E. Valembois, P. Fisette, and J. C. Samin (1997): "Comparison of Various Techniques for Modelling Flexible Beams in Multibody Dynamics". Nonlinear Dynamics 12: 367–397.

[6] [6-13]. Tamer M Wasfy and Ahmed K Noor (2003): "Computational strategies for flexible multibody systems". Appl Mech Rev vol 56, no 6, pp.533-613.

[7] Sang-Myeong Kim (2015): "Lumped Element Modeling of a Flexible Manipulator System". IEEE/ASME Transactions on Mechatronics, VOL. 20, NO. 2, 967-974.

[8] Benosman M., Le Vey G. (2002) "Joint trajectory tracking for planar multi-link flexible manipulator". IEEE Int. Conference on Robotics and Automation, Washington D.C., pp. 2461–2466.

[9] Yang H., Krishnan H., Ang Jr. M. (1997): "A simple rest-to-rest control command for a flexible link robot". IEEE Int. Conference on Robotics and Automation, Albuquerque. New Mexico, pp. 3312–3317.

[10] Benosman M., Le Vey G., Lanari L., De Luca A. (2001): "Rest-to-Rest Motion for Planar Multi-Link Flexible Manipulator Through Backward Recursion". Journal of Dynamic Systems, Measurement, and Control, 126(1), pp. 115-123.

[11] Javier García de Jalón, Eduardo Bayo (1994): "Kinematic and Dynamic Simulation of Multibody Systems, The Real-Time Challenge". Springer-Verlag NewYork, Inc.

[12] Usoro, P.B., Nadira, R., and Mahil, S.S. (1986). "A Finite Element/Lagrange Approach to Modeling Lightweight Flexible Manipulators". ASME Journal of Dynamic Systems, Measurement, and Control. 108: 198-205.

[13] Yuangang Tang, Fuchun Sun, Zengqi Sun (2006): "Neural network control of flexible-link manipulators using sliding mode". Neurocomputing 70, 288–295.

[14] Zhi-Cheng Qiu (2012) "Adaptive nonlinear vibration control of a Cartesian flexible manipulator driven by a ballscrew mechanism". Mechanical Systems and Signal Processing, 30, pp. 248–266.

[15] Dadfarnia, M., Jalili N., Xian B., Dawson D. M. (2004): "Lyapunov-Based Vibration Control of Translational Euler-Bernoulli Beams Using the Stabilizing Effect of Beam Damping Mechanisms". Journal of Vibration and Control, 10, pp. 933–961.

[16] Lammerts, I. M. M. (1993). "Adaptive computed reference computed torque control of flexible manipulators". Eindhoven: Technische Universiteit Eindhoven, DOI: 10.6100/IR402510..

[17] Yuangang Tang, Fuchun Sun, Zengqi Sun (2006): "Neural network control of flexible-link manipulators using sliding mode". Neurocomputing 70, 288–295.

[18] Yatim. H. M and I. Z. Mat Darus, "Swarm Optimization of an Active Vibration Controller for Flexible, Control and Signal Processing", ISBN: 978-1-61804-173-9 (2010).

[19] Kennedy. J and R. Eberhart, "Particle Swarm Optimization", Proceedings of IEEE International Conference on Neural Networks, Perth, (1995) 1942.

[20] Tokhi. M. O, A. K. M. Azad, "Flexible robot manipulators (modeling, simulation and control)", The Institution of Engineering and Technology, London, United Kingdom, ISBN: 978-0-86341-448-0 (2008).

[21] MD ZAIN, B. A., & Tokhi, M. O. (2008). Genetic algorithm optimization of pid controller for a flexible manipulator. In Advances In Mobile Robotics (pp. 431-438).

[22] Annisa, J., Darus, I. M., Tokhi, M. O., & Mohamaddan, S. (2018, August). Implementation of PID based controller tuned by evolutionary algorithm for double link flexible robotic manipulator. In 2018 International Conference on Computational Approach in Smart Systems Design and Applications (ICASSDA) (pp. 1-5). IEEE.

[23] Hizarci, H., & İkizoğlu, S. (2019, October). Position control of flexible manipulator using PSO-tuned PID Controller. In 2019 Innovations in Intelligent Systems and Applications Conference (ASYU) (pp. 1-5). IEEE.

[24] Seifried, R. (2014): "Dynamics of Underactuated Multibody Systems - Modeling, Control and Optimal Design". Solid Mechanics and Its Applications, Vol. 205, Springer.

[25] Ahmed A. Shabana: "Dynamics of Multibody Systems". Cambridge University Press 2005.

[26] L. Sciavicco and B. Siciliano(2012). "Modelling and control of robot manipulators". Springer Science & Business Media, 2012.

[27] Nguyen Van Khang (2011). Mechanics Research Communications 38, 294-29.

[28] R. K. Arora, "Optimization Algorithms and Applications". CRC Press, Inc, 2015.

The 6th International Conference on
Engineering Mechanics and Automation (ICEMA 2021)
Hanoi, November 14 2021

Design of UAV system and workflow for weed image segmentation by using deep learning in Precision Agriculture

Duc-Anh Dao
VNU University of Engineering and Technology
Hanoi, Vietnam
daoducanhc@gmail.com

Truong-Son Nguyen
VNU University of Engineering and Technology
Hanoi, Vietnam
truongsonlifezero@gmail.com

Cong-Hoang Quach
VNU University of Engineering and Technology
Hanoi, Vietnam
quachconghoang89@gmail.com

Duc-Thang Nguyen
VNU University of Engineering and Technology
Hanoi, Vietnam
thang.tom.3@gmail.com

Minh-Trien Pham*
VNU University of Engineering and Technology
Hanoi, Vietnam
trienpm@vnu.edu.vn

***Abstract*— Collecting and analyzing weed data is crucial, but it is a real challenge to cover a large area of fields or farms while minimizing the loss of plant and weed information. In this regard, Unmanned Aerial Vehicles (UAVs) provide excellent survey capabilities to obtain images of the entire agricultural field with a very high spatial resolution and at a low cost. This paper addresses the practical problem of the weed segmentation task using a multispectral camera mounted on a UAV. We propose the method to find the ideal workflow and system parameters for UAVs to maximize field crop coverage while providing data for reliable and accurate weed segmentation. Around the segmentation task, we examine several Convolutional Neural Networks (CNNs) architectures with different states (fine-tune) to find the most effective one. Besides that, our experiment using Near-infrared (NIR) and Normalized Difference Vegetation Index (NDVI) -the foremost spectroscopies - as an indicator of the vegetation density, health, and greenness. We implemented and evaluated our system on two farms, sugar beet and papaya, to conclude based on each stage of crop growth.**

***Keywords*— UAV, weed segmentation, deep learning, spectroscopy**

I. INTRODUCTION

Precision agriculture (PA) can be defined as the science of improving crop yields and assisting management decisions using high technology sensors and analysis tools [1]. PA spatially surveying critical health indicators of crop and applying treatment, e.g., herbicides, pesticides, and fertilizers, only to relevant areas. Because of that, weed treatment is a critical step in PA as it directly associates with crop health and yield. To overcome the above problem, in PA practices, Site-Specific Weed Management (SSWM) is used [2] SSWM focused on the divide the field into management zones that each one receives customized management. Therefore, it is necessary to generate an accurate weed cover map for precise herbicide spraying. Hence, we need to collect high-resolution data image data of the whole field. These images are usually captured by two traditional platforms, satellite, and manned aircraft. However, these conventional platforms present problems related to temporal and spatial resolution, and the successful use of these platforms is dependent on weather conditions [3].

In recent years, along with the development of science and technology, Unmanned Aerial Vehicles (UAVs) are considered a suitable replacement for image acquisition. The use of UAVs to monitor crops offers excellent possibilities to acquire field data in an easy, fast, and cost-effective way compared to previous methods. UAVs can fly at low altitudes and take ultra-high spatial resolution imagery (i.e., a few centimeters), allowing observing small individual plants and patches that are not possible with satellites or piloted aircraft [4]. This significantly improves the performance of the monitoring systems, especially in monitor and detect weeds systems. UAVs can serve as an excellent platform to obtain fast and detailed information on arable land when equipped with various sensors. From an orthomosaic map, producers can make beneficial decisions in terms of money and time, monitor the health of plants, get records quickly and accurately on damage or identify potential problems in the field. Moreover, this information is also essential data that enables new technologies such as machine learning, deep learning, etc., to improve productivity in precision agriculture.

Section II presents some common type of UAVs used in the agriculture robotics domain and cover related works using CNN models with multispectral images. Section III describes our proposed method on an available public dataset and details of our deep learning model. Section IV concludes two parts: i) the result of the public dataset, and ii) the procedure for acquiring, calibrating, and evaluating experimental datasets under real conditions. At last, section V concludes the paper.

II. RELATED WORK

In PA, UAVs are inexpensive and easy to use compared to satellites and manned-aircrafts, though limited by insufficient engine power, short flight duration, difficulty in maintaining

[1] * Corresponding Author: trienpm@vnu.edu.vn (Minh-Trien Pham)

flight altitude, and aircraft stability [5], [6]. In general, the payload capacity of the UAVs is about 20-30% of its total weight [7], which significantly governs the type of operation that can be performed with the system. Three major UAVs type can be used for precision weed management: fixed-wing, rotary-wing, and blimps. But the ability to hover in the air and agile manoeuvring makes rotary-wing well-suit to agriculture field inspections. This ability makes rotary-wing UAVs take ultra-high-resolution images and map small individual plants and patches [8]. Although fixed-wing UAVs can flight with high speed [9] and greater payload capacities than the rotary-wing platform, leading to images with coarse-spatial resolution and poor image overlap. Besides fixed-wing and rotary-wing, blimps are also used for obtaining aerial imagery [10]. Blimps are simple UAV platforms where the lift is provided by helium. However, they are not stable under high-speed conditions [11], and the development of highly sophisticated aerial systems (i.e., fixed- and rotary-wing UAVs) are maneuvered easily and attached with in-built sensors/cameras. Because of that, the use of blimps has declined in agricultural applications.

Moreover, one of the most critical parameters in a UAV flight is the altitude above ground level (AGL). It defines the pixel size on the captured images, flight duration and coverage area. It is crucial to determine the spatial quality required for orthomosaics to obtain the ideal pixel size in the images. According to Hengl [12], detecting the smallest object in an image generally requires at least four pixels. When choosing altitude AGL, the spatial resolution must be good enough while covering as many surfaces as possible. Low altitude AGL UAV flights can produce high-resolution images but are limited in the coverage area, thereby increasing flight duration. Therefore, the operation of UAVs is broken down into several flights due to battery life, causing a change in light condition, the unstable appearance of shade, etc.

Several works have been directed using RGB beside multispectral imagery of farming fields to face the substantial similarity in weeds and crops for weed detection technology. [13] using Excess Green Vegetation Index (ExG) [14] and the Otsu's thresholding [15] to remove background (soil, residues). After that, the authors applying a double Hough transform [16] to identify the maincrop lines. To specify crops and weeds, they applied the region-based segmentation method forming a blob coloring analysis. The crop will be any region with at least one pixel belonging to the detected lines; the remaining area means weed. Lambert et al. [17] apply the green normalized differential vegetation index (GNDVI) to classify. The reason for their choice is that high biomass crops such as wheat cause saturation of chlorophyll levels in the red wavelength, resulting in poor performance when using the normalized differential vegetation index (NDVI) [18].

Image segmentation aims to learn information in a given image at a pixel level, an essential but challenging task. In recent years, convolutional neural networks (CNN) have risen as a potent tool for computer vision tasks. The creation of the AlexNet network in 2012 had shown that a large, deep CNN could achieve record-breaking results on a challenging dataset using supervised training [19]. For example, in [20] and [21], authors apply AlexNet for weed detection in different crop fields: soybean, beet, spinach, and bean. Mortensen et al. [22] using a modified version of VGG-16 on the segmentation task of mixed crops from oil radish plots with barley, grass, weed, stump, and soil. However, these methods have a poor performance with low-resolution images because of the sequential max-pooling and down-sampling layers. To solve this issue, U-Net [23] has the mechanic that contracted features will reconstruct the image to input resolution. This paper uses a model based on this U-Net architecture (detail in Section III-C1).

III. METHODS

A. System overview

The main target of the proposed UAV system is to identify plants and weeds in UAV imagery, thereby providing a tool for precisely monitoring real fields. In the following, we will discuss general steps in the preliminary analysis and preparation of the data collection process.

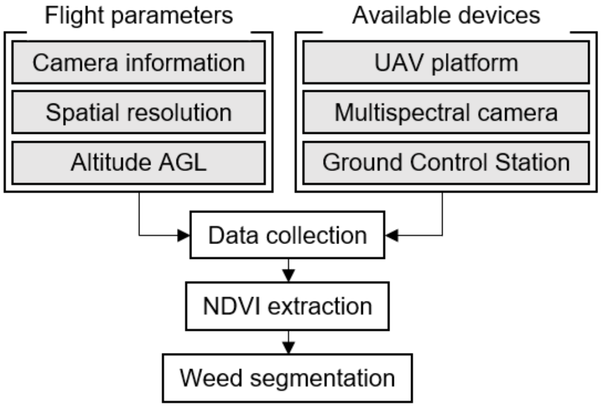

Fig. 1. General overview of the UAVs system used in the image collection process

First of all, it is essential to guarantee safety and accuracy before flying. Devices such as UAVs, computers, and controllers must be checked to see if it is working correctly to avoid system breakdowns and failures due to malfunctions. After that, several parameters need to be calibrated to ensure the UAV is in good condition and ready for take-off. Typically, inertial measurement unit (IMU), compass, and camera are the things that need calibration. The IMU, including the accelerometer, needs to be calibrated first to establish the standard altitude of the UAV and minimize errors due to inaccurate sensor measurements. Then there is the compass, making sure to avoid potential sources that could affect the magnetometer. For cameras, it is necessary to determine the lens parameters and the types of multispectral cameras before flying. In our case, UAV needs a 2-band multispectral camera (red channel at 660nm and near-infrared (NIR) at 790nm) as the minimum required to extract NDVI imagery, a central element in the soil separation task.

In our UAV system, the pilot can serve as Ground Control Point (GCP) to control and send UAV commands from the ground. The UAV sends the real-time images streaming to GCP while in the air; it moves between pre-scheduled waypoints while taking pictures on the ground. Figure 1 illustrates the overview UAVs system using in the image collection process.

B. Dataset and Data Augmentation

This paper uses the crop/weed dataset from a controlled field experiment [24] containing pixel-level annotations of sugar beet and weed images. A multispectral camera Sequoia mounted on a DJI Mavic – commercial MAV, recording datasets at 1 Hz and 2-meter height. A total of 149 images were captured in 3 separate field patches: crop-only, weed-only, and mixed. Each training/test image consisted of the red channel, NIR, and NDVI imagery.

The role of the NDVI spectrum is crucial in the soil segmentation task. The following examples will clarify the importance of NDVI imagery compared to the red channel or NIR in this task. In NIR, we hardly indicate the difference between soil and plant/weed. The red channel image can easily identify the contrast, but it depends on the light conditions when collecting data, causing instability and consistency during training. On the other hand, NDVI imagery is based on how plants reflect certain electromagnetic spectrum ranges, making non-plant materials like soil easily separated. Although the primary contribution of NDVI is used as an indicator of vegetation density, health, and greenness, it has shown excellent results in the ground segmentation task.

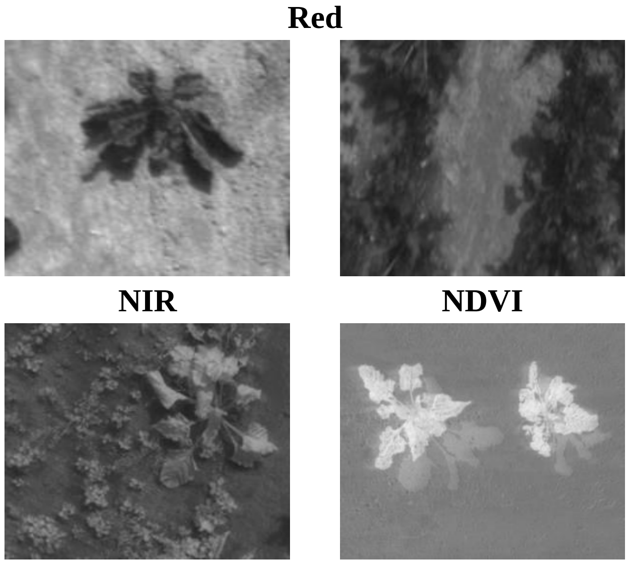

Fig. 2. Red in good light condition (top-left) and bad light condition (top-right). Bottom-left is NIR, and the bottom-right is NDI.

Next, we need to focus on the most crucial task: the distinction between weed and plant. As mentioned before, the training dataset is divided into crop-only and weed-only. The plant has broad leaves, thin twigs, while weed is small in size and distributed in clusters. It makes the recognition is more straightforward in the training process with an individual object. In that case, traditional computer vision or machine learning techniques like the random forest or support vector machine can get the task done. However, while plants often overlap with weeds in practical matters, pixel-by-pixel classification becomes difficult. To address this issue, we decide to use a more advanced solution: a deep learning model due to its robust feature learning and end-to-end training.

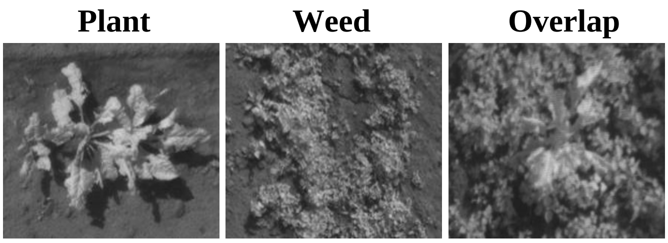

Fig. 3. Individual object: plant (left), weed (middle) and overlapping objects (right).

In our opinion, this dataset has two problems: (i) the quantity is not sufficiently large, and (ii) it impedes the training phase when separating the whole field to crop or weed-only part. To understand these problems, we need to emphasize that deep learning is a powerful tool that can successfully solve many issues related to computer vision. However, one of the significant limitations of this method is the need for large datasets to obtain excellent performance and generalization. Small data can exacerbate specific issues, like overfitting, measurement error, and especially in our case, sampling bias—the weed-only image up to 65% of the entire training set. Therefore, we propose a data augmentation strategy that enriches and removes the bias in this dataset.

TABLE I. NUMBER OF IMAGES AFTER APPLYING DATA AUGMENTATION

Subset	Original dataset	Augmented dataset
Training	125	3564
Testing	24	24
Total	149	3588

The purpose of this strategy is to combine crop-only and weed-only image pairs into one. First, morphological transformations (dilation and erosion) are applied to the crop-only images to remove noise and join separate parts. Then we find external contours, followed by drawing a rectangle mask for each of them. Finally, we use the alpha blending technique (alpha=1) to overlay the crop over the weed image. Figure 4 illustrates the augmentation strategy, and each class is labeled as follows {background, crop, weed} = {black, green, red}. The number of images generated after using data augmentation is shown in Table I.

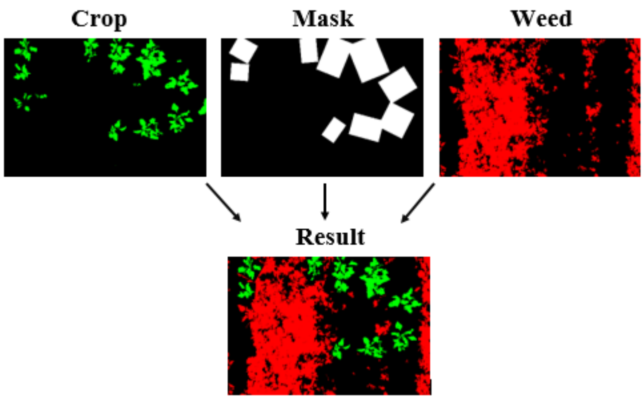

Fig. 4. Example of data augmentation.

C. *Modified U-Net Architecture with residual unit*

1) U-Net

U-Net is a deep learning model proposed for the image segmentation task. Its architecture creates a route for information propagation, thus using low-level details while retaining high-level information. It has the contraction (encoder) and expansion (decoder) paths, creating the unique U-shape. Each encoder layer comprises two convolution layers with Rectified Linear Units (ReLU) activation functions followed by max-pooling operation. Stack of that layers will learn features of increasing complexity levels while simultaneously performing downsampling. On the other hand, the decoder up-sample also appends feature maps of the corresponding encoder to combine global information with precise localization. The network's output has the same width and height as the original image, with a depth indicating each label's activation. For our segmentation mission, there are three classes: crop, weed, and soil.

2) Hybrid with the residual unit

Training neural networks with many deep layers would improve the model performance. However, that depth usually causes the vanish gradient problem makes it unable to propagate useful gradient information throughout the model. To address the degradation problem, He et al. [25] introducing a deep residual learning framework. Instead of letting layers learn the underlying mapping H(x) where x is the input of the first layer, the network will fit F(x) = H(x)-x which gives H(x) = F(x) + x. Although both methods could approximate the desired functions, the ease of training with residual functions is much better. With all that said, the model we use in this paper combines the strengths of both U-Net and the residual unit (ResBlock), and we call it the ResUNet model.

IV. EXPERIMENTAL RESULTS

A. Dataset Result

For quantitative evaluation, we use the F1 score (3) as the harmonic mean of the recall and precision, which gives an overall result on the network's positive labels.

$$F1 = 2.\frac{Precision\,.Recall}{Precision + Recall} \quad (3)$$

Where *precision* measures how accurate the neural network was at positive observations, and *recall* measures how effectively the neural network identified the target.

TABLE II. Performance comparision of 6 models

Resolution	**F1 Score (%)**					
	CNN	DeepLabV3	HSCNN	UNet	SegNet	ResUNet
256 x 256	64.29	58.01	66.36	66.16	69.11	**73.87**
512 x 512	66.76	68.91	77.15	77.78	75.23	**80.56**

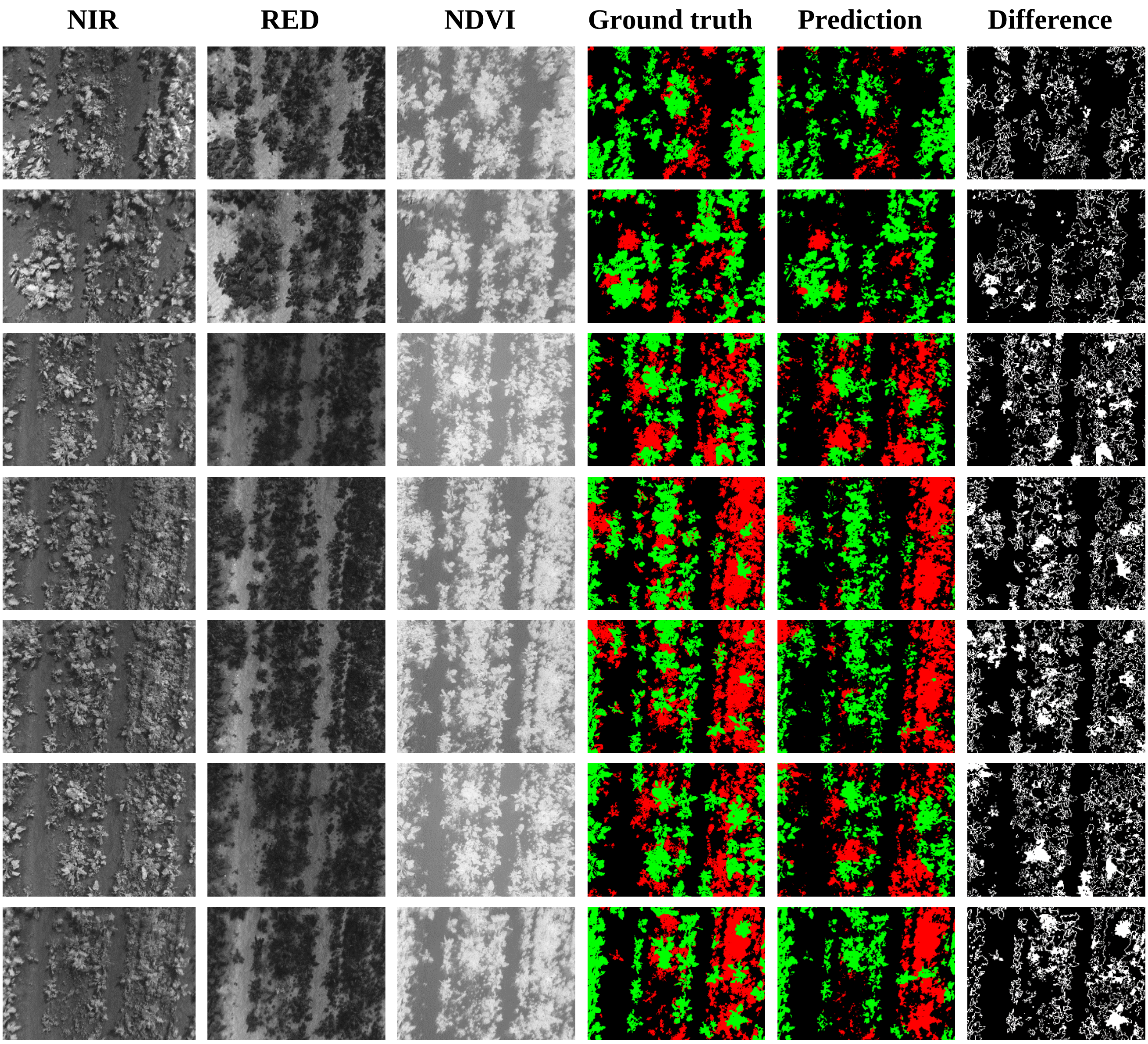

Fig. 5. Result of some examples (row-wise). The first three columns are the input of the model. The fourth and fifth columns are showing ground truth and the prediction. The last column is the difference between ground truth and prediction mask.

* Corresponding Author: trienpm@vnu.edu.vn (Minh-Trien Pham)

Table II shows the results of the proposed method. We chose to experiment with multiple resolutions because we wanted to simulate the altitude of the UAV when collecting data: lower resolutions taken at high altitudes would cover a wider field, thereby reducing sampling time. However, in return, it will lose detailed features of crops and weeds, directly affecting the final result of models.

In Sections II and III-C, we have presented the strengths and limitations of the models. The experimental results in Table II have demonstrated that CNNs are not suitable for complex tasks like segmentation. In contrast, ResUNet has shown its superiority when increasing accuracy by 3-4% compared to the second-best model. However, the numbers cannot summarize the entire results. We need to have specific illustrations to analyze this result more closely.

For visual examination, we present some examples of input data and the difference between ground truth and model probability (Fig. 5). The 3-channel input image is represented by the first three columns of spectral types: NIR, RED, and NDVI. The following two columns are the ground-truth annotation image and our probability output; each class is labeled as follows {background, crop, weed} = {black, green, red}. Finally, the last column gives a detailed look at the mistakes we encountered. The difference between ground truth and prediction images is shown in white pixels; the fewer white pixels an image has, the more accurate it is. It can be seen that misclassification areas of weed and crop appear with a low number. That case mainly occurs when dense areas of these two types overlap. This shows that our model needs improvement in some parameters, but overall the classification results are satisfactory. Besides that, there is significant misclassification in boundary areas occurring in both crops and weeds. In our opinion, the proposed spatial resolution and sampling frequency in the data acquisition process are not suitable. The poor spatial resolution makes the data not detailed enough to feed the segmentation model. High sampling frequency causes motion-blur phenomenon, which appears many times in this dataset. These factors induce the degradation of image quality, causing poor performance of the predictive model.

Besides illustrable errors, we are still investigating other factors that affect classification performance. We suspect it is due to i) shadow noises appears in most of the input images, ii) the absence of green and blue channels in the dataset. Shadows can reduce or lose all information in remote sensor images. That missing information content can render remote estimation of biophysical parameters inaccurate and prevents image interpretation [26]. Besides that, some papers using just RGB images from UAV [27], [28] can get great results, which led us to consider the underappreciated role of green and blue images in this dataset. However, since the scope of this paper can hardly reach such content, we would like this issue to future work and will be studied carefully.

B. Experiment

After verifying the model with the available datasets, we conducted experiments to verify the model under real conditions. In this experiment, the UAV was installed with a camera capable of capturing spectral images and flying at different altitudes. This data will then be calibrated before being fed into the deep learning model. And finally, the results of the model and analyze the results to make judgments about system parameters with data and model.

1) System Setting

To collect the data, we used a MapIR Survey3W multispectral camera mounted on the DJI Mavic 2 Enterprise, as shown below.

(a) (b)

Fig. 6. System components: (a) Mavic 2 Enterprise and MapIR Survey3W. (b) MapIR Survey3W

MapIR Survey3W is a low-cost multispectral camera. Its 12MP sensor and sharp non-fisheye lens (with -1% extreme low distortion glass lens allow it to capture aerial media efficiently. It has an 87° HFOV (19mm) f/2.8 aperture. In this experiment, we collect data for 3 wavelength bands, Near-Infrared 850nm, Red 660nm, and Green 550nm, at different heights of 3 meters, 5 meters, and 8 meters.

2) Data calibration

As we all know, our sun emits a large spectrum of light reflected by objects on the Earth's surface. A camera can be used to capture this reflected light in the wavelengths that the camera's sensor is sensitive to. We supply sensors based on silicon sensitivity in the Visible and Near-Infrared spectrum from about 400-1200nm. Using band-pass filters that only allow a narrow range of light to reach the sensor, we can capture the amount of reflectance of objects to that band of light. So, therefore, the image we obtain is always dependent on the ambient light conditions. In each different flight, the resulting image will have various reflection quality and to solve that problem, we use a calibration board as shown below.

Fig. 7. Calibrated Reflectance Panel (CRP)

To determine the transfer function, first convert the raw pixels of the panel image to units of radiance. Then calculate the average value of radiance for the pixels located inside the panel area of the image. The transfer function of radiance to reflectance for the i-th band is:

$$F_i = \frac{\rho_i}{avg(L_i)} \quad (4)$$

Where F_i is the reflectance calibration factor for band i, ρ_i is the average reflectance of the CRP for the i-th band (from the calibration data of the panel provided) is the average value of the radiance for the pixels inside the panel for band i. After performing the correction, we will proceed to calculate the NDVI by:

$$NDVI = \frac{NIR - RED}{NIR + RED} \quad (5)$$

Here are a few experimental images:

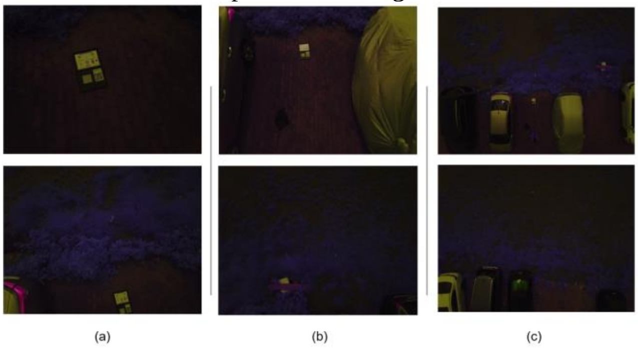

Fig. 8. Images of CRP and data samples at different heights: (a) 3 meter, (b) 5 meter and (c) 8 meter

Here are data after calibration:

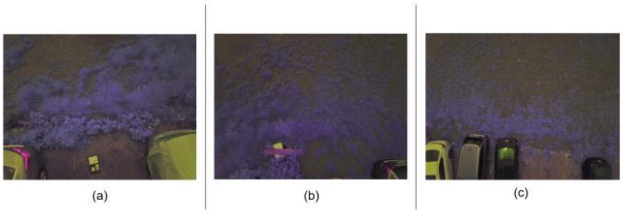

Fig. 9. Data after calibration at different heights: (a) 3 meter, (b) 5 meter and (c) 8 meter

3) Result

Experiments were conducted on papaya fields. There are a small number of immature papaya plants along with two kinds of weeds: *common chickweed* (Stellaria media) and *crabgrass* (Digitaria) (Fig. 10). We took 110 images at three different altitudes with a resolution of 4000 x 3000 pixels. The supervised dataset was annotated manually by science experts. This process took up about 45 minutes/image on average. After training the ResUNet model, we obtain F1-score: 0.82, 0.64, 0.61 at altitudes of 3, 5, and 8 meters, respectively.

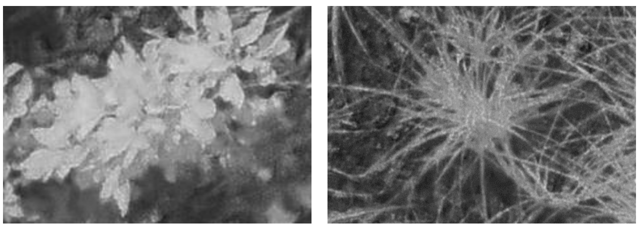

Fig. 10. Chickweed (left) and crabgrass (right)

The weed that appears much in this data set is chickweed. The morphological features of this weed are very similar to immature papaya. The difference is the size of weed leaves is smaller, and they grow denser than papaya. We find this is a challenging dataset with such slight differences and can only be completed when the image is sufficiently detailed. Our experiments show that only images taken at 3 meters (among the three experimental heights, 3, 5, and 8 meters) can detect plants (Fig. 11). It is entirely reasonable because a ground resolution of 0.2 mm/px (3 meters height and a resolution of 4000 x 3000 pixels) makes the images highly detailed and eligible to distinguish immature papaya plants from chickweed.

Ground truth **Prediction** **Difference**

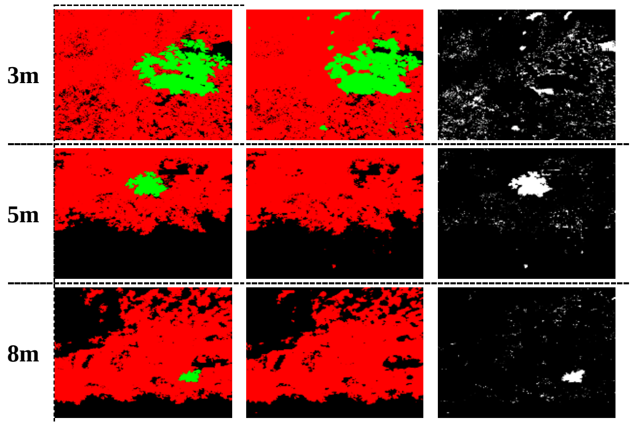

Fig. 11. The difference between ground truth and the model's prediction at different heights: 3, 5, and 8 meters (row-wise).

Though, that does not mean all data at an altitude of 5 or 8 meters is ineffective in practice. As we mentioned earlier, this dataset was challenging, and the crops were out of season at the time of data collection. That leads to many areas of dense weeds and overlapping between those areas and plants. Therefore, the images at 5 or 8 meters are not eligible for the segmentation task in this particular circumstance. However, in many practical cases, plant and weed classification is often implemented early to prevent the spread of weeds (early site-specific weed management (ESSWM)). In that cases, early-stage weeds sparsely grow, and overlapping objects appear with lower frequency. That makes the segmentation task more straightforward and suitable for high-altitude images as they can cover large fields, improving classification productivity while maintaining accuracy.

V. Conclusions

UAVs used in weed segmentation applications must distinguish crops from weeds to make interventions at the right time. This paper uses multispectral imagery to focus on papaya (our dataset) and sugar beet crops (public dataset). We trained six different models and evaluated them by using F1-score as a metric. Then, an assessment was performed by visually comparing ground truth with probability outputs. The proposed approach achieved an acceptable performance of 0.82 and 0.81 F1-score for papaya and sugar beet fields, respectively.

Our experiment has solved the practical problem of using UAV images for weed segmentation by deep learning. We have proposed a good workflow, and the UAV parameters were calculated and adjusted thoughtfully. From that, we produced acceptable results even on difficult classification conditions. Our UAV system at three different heights achieves remarkable results in weed detection and can fix the misclassification in boundary areas (section IV-A). More specifically, when plants and weeds have similar morphological/color features and high weeds density, the dataset should be captured at 3 meters height to preserve the details. In cases like ESSWM, 5 or 8 meters may be appropriate to optimize crop area management while ensuring classification quality.

We will further study the factors affecting the final classification results and make a clearer statement about the high-altitude UAV systems in different crop growth stages. To address this, we required more training data on large-scale, multiple weed varieties over longer periods of time to develop a weed detector with more efficient strategies. We are planning to build an extensive dataset to support future work in the agriculture robotics domain.

ACKNOWLEDGMENT

Quach Cong Hoang was funded by Vingroup Joint Stock Company and supported by the Domestic Ph.D. Scholarship Programme of Vingroup Innovation Foundation (VINIF), Vingroup Big Data Institute (VINBIGDATA), code VinIF 2020. TS.23.

REFERENCES

[1] P. Singh *et al.*, "Hyperspectral remote sensing in precision agriculture: present status, challenges, and future trends," in *Hyperspectral Remote Sensing*, Elsevier, 2020, pp. 121–146.

[2] D. C. Tsouros, S. Bibi, and P. G. Sarigiannidis, "A review on UAV-based applications for precision agriculture," *Inf.*, vol. 10, no. 11, 2019.

[3] F.-J. Mesas-Carrascosa *et al.*, "Assessing Optimal Flight Parameters for Generating Accurate Multispectral Orthomosaicks by UAV to Support Site-Specific Crop Management," *Remote Sens. 2015, Vol. 7, Pages 12793-12814*, vol. 7, no. 10, pp. 12793–12814, Sep. 2015.

[4] J. Torres-Sánchez, J. M. Peña-Barragán, D. Gómez-Candón, A. I. De Castro, and F. López-Granados, "Imagery from unmanned aerial vehicles for early site specific weed management," *Wageningen Acad. Publ.*, pp. 193–199, 2013.

[5] P. J. Hardin and T. J. Hardin, "Small-scale remotely piloted vehicles in environmental research," *Geogr. Compass*, vol. 4, no. 9, pp. 1297–1311, 2010.

[6] A. S. Laliberte, A. Rango, and J. Herrick, "Unmanned aerial vehicles for rangeland mapping and monitoring: A comparison of two systems," *Am. Soc. Photogramm. Remote Sens. - ASPRS Annu. Conf. 2007 Identifying Geospatial Solut.*, vol. 1, pp. 379–388, 2007.

[7] S. Nebiker, A. Annen, M. Scherrer, and D. Oesch, "A light-weight multispectral sensor for micro UAV—Opportunities for very high resolution airborne remote sensing," *Int. Arch. Photogramm. Remote Sens. Spat. Inf. Sci.*, vol. 37, no. Vi, pp. 1193–1200, 2008.

[8] H. Xiang and L. Tian, "Development of a low-cost agricultural remote sensing system based on an autonomous unmanned aerial vehicle (UAV)," *Biosyst. Eng.*, vol. 108, no. 2, pp. 174–190, Feb. 2011, doi: 10.1016/J.BIOSYSTEMSENG.2010.11.010.

[9] A. Frank, J. S. McGrew, M. Valenti, D. Levine, and J. P. How, "Hover, transition, and level flight control design for a single-propeller indoor airplane," *AIAA Guid. Navig. Control Conf.*, vol. 1, pp. 100–117, 2007, doi: 10.2514/6.2007-6318.

[10] D. Vericat, J. Brasington, J. Wheaton, and M. Cowie, "Accuracy assessment of aerial photographs acquired using lighter-than-air blimps: LOW-cost tools for mapping river corridors," *River Res. Appl.*, vol. 25, no. 8, pp. 985–1000, Oct. 2009, doi: 10.1002/RRA.1198.

[11] J. Everaerts, "The use of unmanned aerial vehicles (UAVs) for remote sensing and mapping," *Int. Arch. Photogramm. Remote Sens. Spat. Inf. Sci.*, vol. 37, no. March, pp. 1187–1192, 2008.

[12] T. Hengl, "Finding the right pixel size," *Comput. Geosci.*, vol. 32, no. 9, pp. 1283–1298, 2006.

[13] C. Gée, J. Bossu, G. Jones, and F. Truchetet, "Crop/weed discrimination in perspective agronomic images," *Comput. Electron. Agric.*, vol. 60, no. 1, pp. 49–59, Jan. 2008.

[14] D. M. Woebbecke, G. E. Meyer, K. Von Bargen, and D. A. Mortensen, "Color indices for weed identification under various soil, residue, and lighting conditions," *Trans. Am. Soc. Agric. Eng.*, vol. 38, no. 1, pp. 259–269, 1995.

[15] N. Otsu *et al.*, "A Tlreshold Selection Method from Gray-Level Histograms," *IEEE Trans. Syst. Man. Cybern.*, vol. C, no. 1, pp. 62–66, 1979.

[16] P.V.C. Hough, "Method and means for recognizing complex patterns," *U.S. Patent 30696541962*. Dec. 18, 1962.

[17] J. P. Lambert, D. Z. Childs, and R. P. Freckleton, "Testing the ability of unmanned aerial systems and machine learning to map weeds at subfield scales: a test with the weed Alopecurus myosuroides (Huds)," *Pest Manag. Sci.*, vol. 75, no. 8, pp. 2283–2294, Aug. 2019.

[18] A. A. Gitelson, Y. J. Kaufman, and M. N. Merzlyak, "Use of a green channel in remote sensing of global vegetation from EOS-MODIS," *Remote Sens. Environ.*, vol. 58, no. 3, pp. 289–298, Dec. 1996.

[19] KrizhevskyAlex, SutskeverIlya, and H. E., "ImageNet classification with deep convolutional neural networks," *Commun. ACM*, vol. 60, no. 6, pp. 84–90, May 2017.

[20] A. dos Santos Ferreira, D. Matte Freitas, G. Gonçalves da Silva, H. Pistori, and M. Theophilo Folhes, "Weed detection in soybean crops using ConvNets," *Comput. Electron. Agric.*, vol. 143, no. February, pp. 314–324, 2017.

[21] M. D. Bah, E. Dericquebourg, A. Hafiane, and R. Canals, *Deep learning based classification system for identifying weeds using high-resolution UAV imagery*, vol. 857. Springer International Publishing, 2019.

[22] A. K. Mortensen, M. Dyrmann, H. Karstoft, R. N. Jørgensen, and R. Gislum, "Semantic segmentation of mixed crops using deep convolutional neural network.," *CIGR-AgEng Conf. 26-29 June 2016, Aarhus, Denmark. Abstr. Full Pap.*, pp. 1–6, 2016.

[23] O. Ronneberger, P. Fischer, and T. Brox, "U-Net: Convolutional Networks for Biomedical Image Segmentation," *Med. Image Comput. Comput. Interv.*, vol. 9351, pp. 234–241, May 2015.

[24] I. Sa *et al.*, "WeedNet: Dense Semantic Weed Classification Using Multispectral Images and MAV for Smart Farming," *IEEE Robot. Autom. Lett.*, vol. 3, no. 1, pp. 588–595, Jan. 2018.

[25] K. He, X. Zhang, S. Ren, and J. Sun, "Deep Residual Learning for Image Recognition," *Proc. IEEE Comput. Soc. Conf. Comput. Vis. Pattern Recognit.*, vol. 2016-Decem, pp. 770–778, Dec. 2015.

[26] P. M. Dare, "Shadow analysis in high-resolution satellite imagery of urban areas," *Photogramm. Eng. Remote Sensing*, vol. 71, no. 2, pp. 169–177, 2005.

[27] H. Huang *et al.*, "Accurate Weed Mapping and Prescription Map Generation Based on Fully Convolutional Networks Using UAV Imagery," *Sensors*, vol. 18, no. 10, p. 3299, Oct. 2018, doi: 10.3390/S18103299.

[28] M. D. Bah, A. Hafiane, and R. Canals, "Deep Learning with Unsupervised Data Labeling for Weed Detection in Line Crops in UAV Images," *Remote Sens.*, vol. 10, no. 11, p. 1690, Oct. 2018, doi: 10.3390/RS10111690.

Design, Simulation, Fabircation and Characterization of a Pneumatic Soft Gripper

Duc Tien Nguyen
VNU University of Engineering and Technology
Vietnam National University - Hanoi
Ha Noi, Viet Nam
tiennd@vnu.edu.vn

Thanh Tung Bui
VNU University of Engineering and Technology
Vietnam National University - Hanoi
Ha Noi, Viet Nam
tungbt@vnu.edu.vn

Van Nguyen Thi Thanh
VNU University of Engineering and Technology
Vietnam National University - Hanoi
Ha Noi, Viet Nam
vanntt@vnu.edu.vn

***Abstract*: Studies on improvement of the end-effector of robot arms have been widely implemented. End-effectors made by hard robot technology from rigid materials face with several problems when utilising to grasp and hold complete-shaped or fragile objects. Recently, soft robot technology which dealing with constructing robots from highly compliant materials has been developed to improve the performance of the gripper. In this paper, we present the design and implementation of a soft pneumatic gripper for using in robot arm. The gripper consists of four pneumatic soft finger-liked actuators, which can fold in a designated direction by inflation of air from an external compressor. The soft actuator is composed of silicone (Ecoflex 00-30) with a chamber-based structure, which is fabricated using a 3D printed mold. By using finite element analysis (FEA) to adjusting the length and wall thickness in the air chamber, the proposed actuator can act like a finger instead of fully curled like an octopus' tentacle. We conduct a series of experiments to evaluate the performance of the pneumatic actuator as well as the constructed gripper. Specifically, the relation between bending angle and pressure are analysed from the results of the experiments and compared with simulation results to understand the entire operation mechanism of the gripper. Besides, we demonstrate the grasping of objects with diverse shapes and materials, from hard to fragile objects as glass cups, eggs, round fruits, and objects with many surfaces. The obtained results show that the prototype of proposed pneumatic gripper can grasp and hold of objects less than 80mm in diameter and 200g in weight, indicating the feasibility of using the gripper as an end-effector for robot arm in pick-and-place operations.**

Keywords: Soft robot, Slow pneumatic net, Soft gripper, Grasping

I. INTRODUCTION

In production lines that work with fruit, glassware, ceramics, these products always need attention because of their soft characteristics, many shapes and sizes, and they are easily broken if the grip force is greater than the limit of the object. There have been many models used to classify & pack these products, but most of them still have human supervision to ensure safety. But the limitation encountered is that the operating speed of the production line will be constrained to match the ability of human supervision. To reduce operating costs and improve working speed, automated product sorting systems are in high demand in these jobs.

Typical products mentioned include fruit, glass cups, ceramic cups. The common characteristics of these products are that they are easily damaged when the grasp force exceeds the tolerance, the surface is curved, slippery, difficult to hold. With fruit, the shape and mass of each fruit is not uniform. For the glass cup, the ceramic cup thickness is different, and the structure is easy to break when grasping to tight, dropped. Rigid grippers and vacuum cups have been widely used in the food industry, but rigid grippers can damage food ingredients and vacuum cups need flat or spherical surfaces to allow suction. The new grip mechanism that provides a gentle grip has the potential to take this task.

In recent years, pneumatic soft robotic grippers have attracted great attention from researchers because of their flexibility and adaptability. There are ribbed, cylindrical, and pleated designs. Before that, these ideas have been widely used to control soft robots, such as the soft planar grip controller [1], the soft gripper for biological sampling on deep reefs[2], and the soft gripper to identify the object[3]. According to [4], the main disadvantage of the pleated design is the complicated fabrication process because it has to go through many steps with precise manipulation. Recently the popularity of 3D printing technology makes mold making easier and several clamp designs have been proposed. MacCurdy[5]. presented a printable hydraulic two-finger clamp. Yap [6] presented a set of heavy duty flexible clamps fabricated using a common 3D printer and FDM (Fused Deposition Modeling) technology. This clamp holds promise for handling heavy loads and it can lift loads up to 5 kg with a maximum weight-to-weight ratio of 1805%. However, the authors concluded that this gripper is not suitable for applications requiring low pressure and thin force due to NinjaFlex's relatively stiff material properties.

The proposed model is an automatic robot whose job is to move to the work area, use the camera to take pictures and classify objects into the corresponding trays. To solve that problem, Figure. 1 shows the components included in the model: movable robot body, robotic arm with soft gripper, camera, working area for robot, objects with various shapes and surfaces. In this model, the goal to be achieved is the robot through the camera to observe and predict the object's shape, color, and dimensions such as length and width. The robot then relies on this information to decide about estimating the grip force provided to the soft gripper to successfully pick up the object, placing the object in the appropriate position in the tray. Because of the promising possibilities of flexibility in gripping, we expect to be able to apply the soft gripper in two typical cases: objects of the same type with different sizes; objects of roughly the same size but different materials and surfaces. This article will present the process of manufacturing a soft gripper and test its operability with the two cases mentioned above.

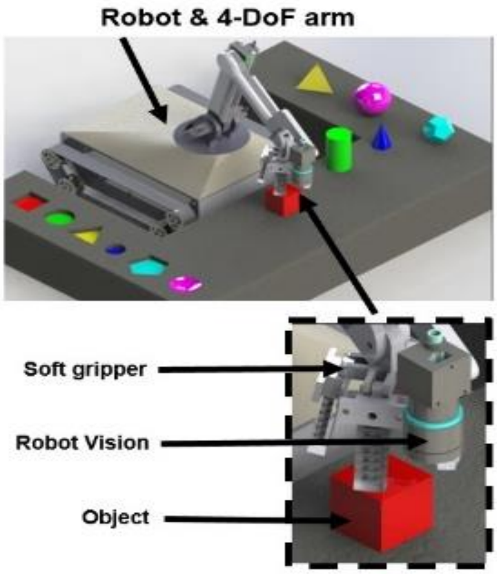

Fig. 1. Conceptual model of a robotic system using a soft gripper in pick-and-place operations to classify and sort objects

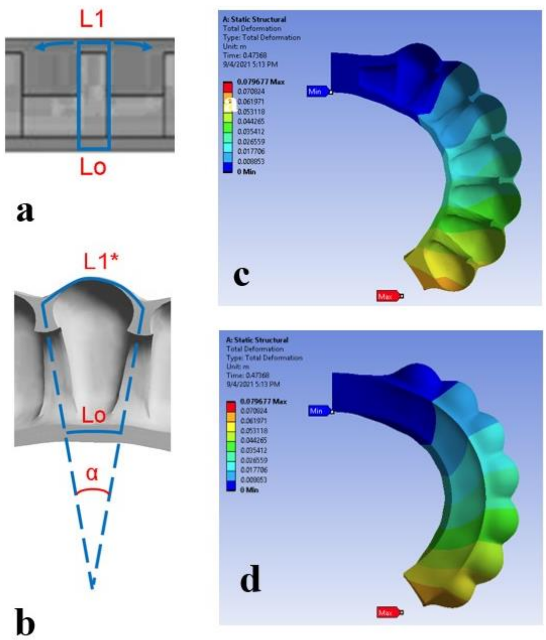

Fig. 2. Soft actuator simulation results. (a) and (b) shows the deformation of an air chamber before (a) and after (b) injection of air in the chamber. (c) and (d) show the deformation of a 7-chamber soft actuators. (c) cross-section view, (d) front view.

II. DESIGN & FABRICATE

A. Design & Simulation

The concept and design process are referenced from structural models of slow pneumatic net actuator (SPn) structure for simulation to predict displacement, bending angle, number of air cavities, upper and inner thickness between air chambers. In Fig. 2(a), is a cross-section of an air chamber of the soft actuator in the initial state, not supplied with air. L_0 and L_1 are equal (if the effect of gravity is ignored) are the length of the air chamber of the in-extensible layer and the extensible layer, respectively. When supplied with air as shown in Fig. 2b, L_1 will expand and reach a length of L_1* while L_0 will slight change or remains due to the bottom layer and material constricting. When the air chamber expands, it will create two concentric circles, the angle of the arc called α is the opening angle of the air chamber. Based on simulation and measuring the opening angle of single air chamber α is 15 *degrees* with the set pressure of 20 *KPa*, the top wall thickness is 1 mm, then design is a soft actuator with 7 air chambers. This number of air chambers is suitable for picking objects with a pick with 4 soft actuators arranged in a plus shape because the folding angle only needs to be less than or equal to 90 *degrees*. The simulation results are shown in Fig. 2b, c. The design and length, width and height are shown in Fig. 3 and Table I.

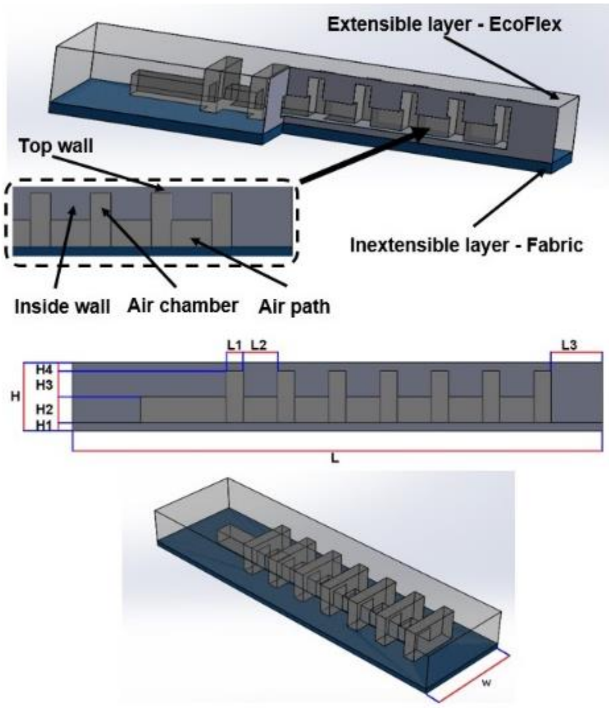

Fig. 3. Design of the proposed pneumatic actuator. (a) Structor of the actuator, (b) Cross section view showing the dimensions

The design of each actuator mechanism is based on the idea of the sPn (Slow Pneumatic-net) model [7]. A complete soft gripper consists of 4 actuator with the same shape, structure and size. With each actuator of the soft gripper, it will be base on human finger, includes 7 air chambers. The sPn design for air chambers fabricated with elastomeric materials. The air chambers are embedded in elastomeric structures that can be inflated with low pressures—less than 50 *KPa*. These chambers are interconnected and with a single supply of air path, they inflate like balloons and fold in the designed direction. Fig. 3 illustrates a schematic of a sPn, each consisting of an extensible top layer and an inextensible layer reinforced with non-stretch fabric. The extensible layer of the sPn actuator is interconnected.

To connect each actuator together, a rigid connector and a grip base have been designed and fabricated. The connector consists of two parts: the top half and the bottom half. The grip base has a 4-port with plus shape.

The assembly steps are showed in Fig. 4(a). First, the soft gripper (1) is inserted into the lower half of the connector (3). Then, the top half of the connector (2) is inserted (3) and held in place by screws. These three parts are combined into a Soft actuator and will be installed in the Grip base (4). The angle of Soft actuator with Grip base can be from 0 to 80 degrees and can be controlled at point C. Our Soft Gripper consists of 4 Soft actuators arranged in a plus sign. Fig. 4(b) presence the complete gripper after being assembling.

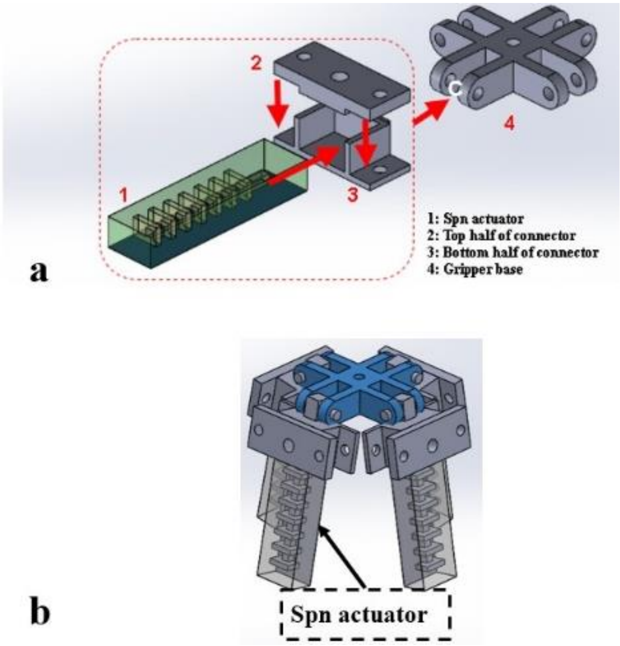

Fig. 4. Design of the soft gripper. (a) Steps to form the soft gripper using the pneumatic actuator and support parts, (b) The soft gripper after being assembled

B. Fabrication & Assemble

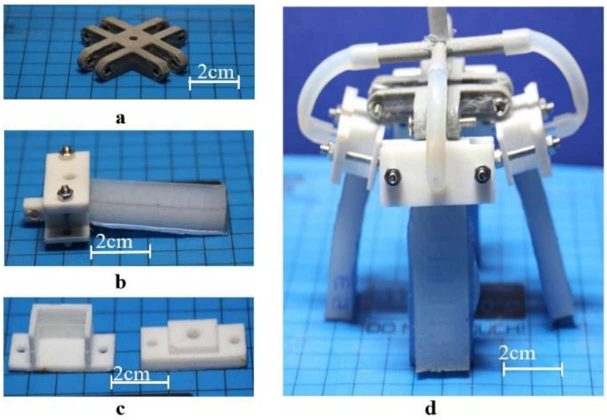

Fig. 5. 3D printed parts and fabricated pneumatic gripper. (a) gripper base, (b) soft actuator, (c) top aand bottom parts of the connector and (d) the assembled grippers.

Mold for 3 parts of the gripper has been fabricated by Cube Corexy 3D printer with the size of 400mmx400mmx300mm. With this proposed design, there is no need to add supporting details so there is no need for post-print processing. The printing material is undoped PLA plastic with a melting point of 190 degrees. We do not use doped resins because it is not possible to determine whether the added materials affect the solidification of the EcoFlex. The 3D printed parts are shown in Fig. 5(a-c).

TABLE I. DESIGN PARAMETERS OF A SOFT GRIPPER

Symbol	*Value (mm)*	*Meaning*
H	8	Soft actuator height
H_1	1	Inextensible layer thickness
H_2	3	Air path height
H_3	3	Air chamber height
H_4	1	Top wall thickness
L	62	Soft actuator length
L_1	2	Air chamber length
L_2	4	Inside wall length
L_3	6	Soft actuator tip length
W	17	Soft actuator tip width

After having the mold, based on the evaluations [8], [9] , we made it with EcoFlex 00-30 material in a 1:1 ratio. After waiting for 4 hours to cure all parts, the actuator is carefully removed from the mold. After that it is carefully remove excess material, especially in the contact areas of the sections to ensure that air does not leak out. Finally, the extensible layer attached with the inextensible layer (covered with eco-flex) to ensure that compressed air cannot escape and increase friction when picking up objects. Fig. 5(d) show a prototype of the gripper with design parameters are shown in Table I.

III. EXPERIMENT METHOD

In experiments, the equipment used included an air pump with a maximum pressure of 80 *KPa*, electronic valve, throttle valve to adjust the air flow rate to the soft gripper, a sensor convert compressed air pressure to analog signal, and multimeter to display the value from the pressure sensor. The experiment carried out included testing the properties of bending angle, holding weight of the gripper under different air pressures on several specimens.

A. No-load test - one actuator

In the experiments, the applied pressure increases from 0 *KPa* until the pressure caused the actuator to deform less or folding angle reaches 90 degrees. The tip displacement of the soft actuator is shown in Fig. 6(a) by taking an image and processing it on the ImageJ tool based on Java platform.

B. Load test – Gripper test

The load test is carried out by picking up objects of different mass and diameter. Air will be applied to the gripper to hold the object without falling out, then reduce the pressure until the object slides down. The moment the object slides down determines the minimum pressure required for each object. The test materials include: glass, porcelain, aluminum.

4 soft actuators with top wall thickness of 1mm were used for this experiment.

IV. RESULTS AND DISCUSSIONS

A. No-load test - one actuator

Fig. 6(a) presents the images of the soft actuator bending under the application of pressures in experiment simulation. Figs. 6(b-d) show the correlation between simulation and actual tip displacement. We have simulated and surveyed based on 3 sizes of top wall thickness of 0.5mm, 1mm, 1.5mm respectively. It can be seen that although the bending strain is equivalent, the response of the air chambers in reality is little bit different due to the imperfection of the manufacturing process. In addition, the pressure shown in these graphs is also the maximum pressure we evaluate with each top wall thickness to be able to operate without damage.

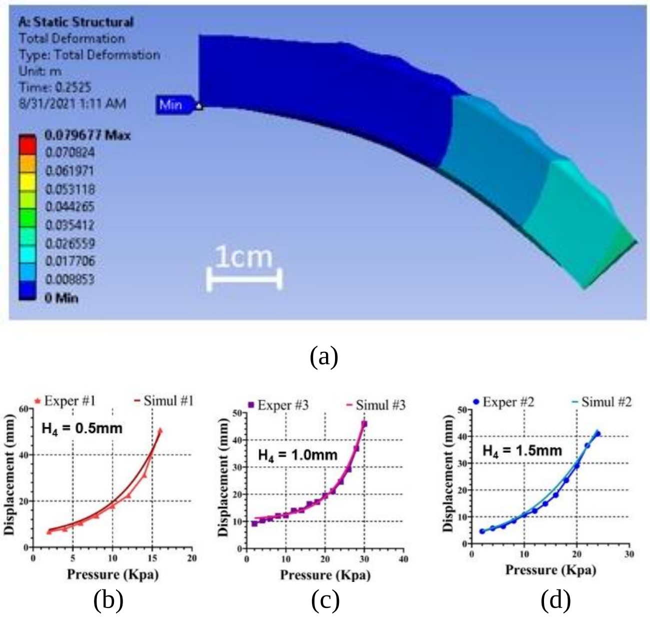

Fig. 6. Displacement of the tip of actuator at different applied pressures. (a) simulation result, (b, c, d) comparasion between simulations and experiments for the case of top wall thickness of 0.5mm, 1mm and 5 mm, respectively.

B. Results of load test

By picking up objects of increasing diameter and weight, we tested the load capacity of the gripper. Objects with diameters of 56mm, 64mm, 65mm and 72mm were used and gradually increase the mass until the pressure applied to the gripper reaches the limit and cannot be lifted. This test shows that the gripper described here can maintain grasp on platforms up to 72mm in diameter and under loads up to 120g. In the future the grip mass can be improved by designs with higher pressure limits or inextensible layers in place of other materials with better friction.

In Fig. 7 summarizes the results and shows the correlation between the mass and the minimum pressure required for each material. Tested materials include 304 stainless iron with a diameter of 72mm, porcelain with a diameter of 64mm, and aluminum with a diameter of 56mm and 65mm.

Fig. 8 shows the results of picking and holding of objects different in shapes and materials. Fig.8 (a-e) show the successful case while Fig. 8(f) is a failure due to the diameter of the object is over the working range of the gripper.

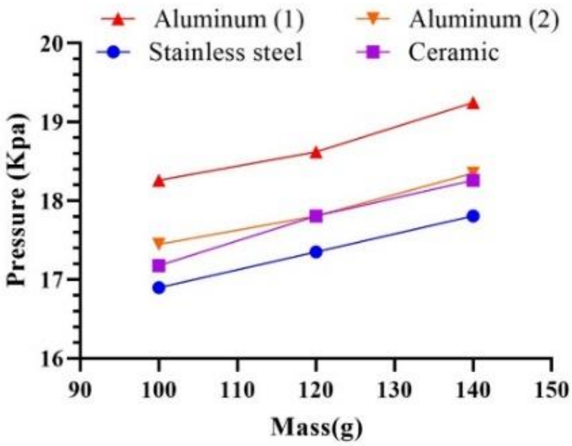

Fig. 7. The correlation between the mass and the minimum pressure required for each material

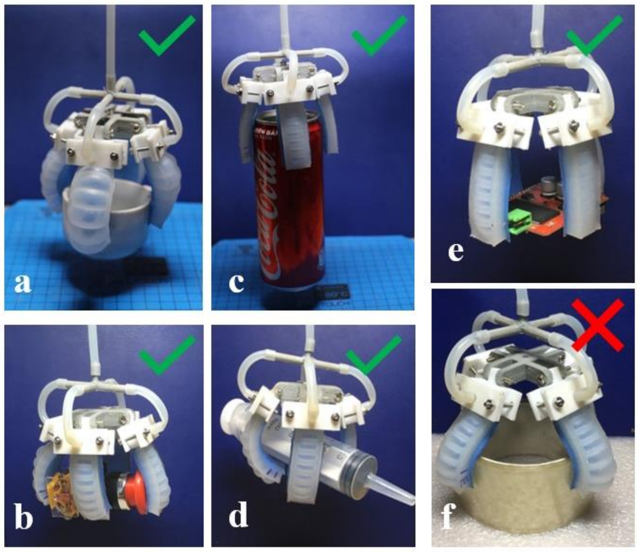

Fig. 8. Grasping test: **a** Creamic cup, **b** Stop button, **c** Aluminum can, **d** Syringe 60cc, **e** PCB 70x50mm, **f** tape (fail)

From the diagram it can be seen that between objects of different materials, the diameter of the grasp force is different. The surface of the objects with the gripper has different friction, so even with the same diameter of the same size (here, porcelain and aluminum), the grasp force to hold the object is different. This shows that the material that makes up the object will affect the minimum grabbing force required to keep the object from falling. Besides, with the same material but with different diameter, the object with the smaller diameter will need more force. This is explained by the fact that the griper will have to bend more for small diameter objects and vice versa for large diameter objects. Following that, increasing the pressure to fold more means that the contact area will be reduced.

V. Conclusions

This work has developed a soft gripper assembled constructed from four pneumatic soft finger-liked actuators, for grasping and holding of objects and surfaces which are difficult handle by solid grasp. Simulations was carried out to optimized the design. A prototype of the designed gripper was fabricated for experimental evaluation. The response of the pneumatic actuator, the reliability and durability of the gripper are under investigation. The initial results show that the proposed soft gripper can be used in robot end-effector for pick-and-place operations.

ACKNOWLEDGMENT

This work has been supported by VNU University of Engineering and Technology under project number CN20.44. The author would like to thank Mr. Minh Tran Cong, Mr. Viet Nguyen Tien, and Mr. Hung Nghiem Ngoc for their support in experiments.

REFERENCES

[1] R. K. Katzschmann, A. D. Marchese, and D. Rus, "Autonomous object manipulation using a soft planar grasping manipulator," *Soft Robotics*, vol. 2, no. 4, pp. 155–164, Dec. 2015, doi: 10.1089/soro.2015.0013.

[2] K. C. Galloway *et al.*, "Soft Robotic Grippers for Biological Sampling on Deep Reefs," *Soft Robotics*, vol. 3, no. 1, pp. 23–33, Mar. 2016, doi: 10.1089/soro.2015.0019.

[3] W. Burgard, Institute of Electrical and Electronics Engineers, Nihon Robotto Gakkai, IEEE/RSJ International Conference on Intelligent Robots and Systems 2015.09.28-10.02 Hamburg, and IROS 2015.09.28-10.02 Hamburg, *2015 IEEE/RSJ International Conference on Intelligent Robots and Systems (IROS) Sept. 28, 2015 - Oct. 2, 2015, Hamburg, Germany*.

[4] A. D. Marchese, R. K. Katzschmann, and D. Rus, "A recipe for soft fluidic elastomer robots," *Soft Robotics*, vol. 2, no. 1, pp. 7–25, Mar. 2015, doi: 10.1089/soro.2014.0022.

[5] IEEE Robotics and Automation Society and Institute of Electrical and Electronics Engineers, *2016 IEEE International Conference on Robotics and Automation : Stockholm, Sweden, May 16th 21st*.

[6] H. K. Yap, H. Y. Ng, and C. H. Yeow, "High-Force Soft Printable Pneumatics for Soft Robotic Applications," *Soft Robotics*, vol. 3, no. 3, pp. 144–158, Sep. 2016, doi: 10.1089/soro.2016.0030.

[7] B. Mosadegh *et al.*, "Pneumatic networks for soft robotics that actuate rapidly," *Advanced Functional Materials*, vol. 24, no. 15, pp. 2163–2170, Apr. 2014, doi: 10.1002/adfm.201303288.

[8] J. C. Case, E. L. White, and R. K. Kramer, "Soft material characterization for robotic applications," *Soft Robotics*, vol. 2, no. 2, pp. 80–87, Jun. 2015, doi: 10.1089/soro.2015.0002.

[9] H. K. Yap, J. C. H. Goh, and R. C. H. Yeow, "Design and characterization of soft actuator for hand rehabilitation application," in *IFMBE Proceedings*, 2015, vol. 45, pp. 367–370. doi: 10.1007/978-3-319-11128-5_92.

The 6th International Conference on
Engineering Mechanics and Automation (ICEMA 2021)
Hanoi, November 14, 2021

Development of a gripper for a fruit harvesting machine

Tran Thanh Tung
Faculty of Engineering Mechanics and Automation
University of Engineering and Technology, Vietnam National University Hanoi
Hanoi, Vietnam
tranthanhtung@vnu.edu.vn

***Abstract*: The paper proposes the conceptual design of a gripper be used with a harvesting machine. After reviewing some of the challenges posed by the robotic harvesting of tree fruit, the design objectives for the system are specified. The mechanical design and kinematic assessment of the system were also reviewed. The proposed gripper was able to perform an adaptive gripping that adapts to variable fruit geometries. Then an experimental gripper was built and tested in the lab. Finally, the experimental results and simulation calculations are processed, discussed, and analyzed to evaluate the reasonableness of the product**

Keywords: harvesting machine, gripper, mechanical design, prototype

I. INTRODUCTION

In agriculture, the process of harvesting products is the most time-consuming and labor-intensive process. Previous studies have shown that fruit harvesting time accounts for 40-80% of total working time and 30-60% of total agricultural production costs [1-3] For example, in Washington State, apple harvesting is, and pears require up to 30,000 workers with an estimated cost of $1100 to $2100 per year [4], [5]. Many researchers have proposed an automatic machine system to harvest large quantities of fresh fruit to reduce harvesting costs and reduce dependence on labor.

Automated machines are another way researchers have attempted to harvest fruits. The automatic fruit machines used in agricultural production have been researched and developed for nearly two decades [6-11]. However, the commercially successful use of machine system for the individual harvesting of specialty crops meet many obstacles. Some of the crucial factors limiting the efficiency of robotic specialty crop harvesting technologies include variable outdoor conditions, complex plant structures, variations in product shape and size, the delicacy of the products, and smaller economies of scale [12-14]. Due to rising labor costs and the increasing difficulty of employability in agricultural production sectors, the absence of mechanical harvesting is an important issue receiving much attention around the world. New mechanical harvesting technologies are required to support for the long-term sustainability of the world tree fruit industry, an economic sector that provided $24 Billion (USD) of production output in 2011 [15].

The gripper is the most critical part of the harvester when handling agricultural products because it is the part of the system that comes into direct contact with the produce. Since fruits are often irregular in shape and have poor mechanical properties, grippers must be adequately designed to pick them up. Besides increasing labor productivity, the most important thing of the gripper is not to damage the fruit when harvesting. A gripper can damage the fruit when excessive force is applied or improper picking technique is used.[16-18]

Many different design techniques have been explored for gripper designs. For example, Bulanon and Kataoka [19] designed a clamping machine that removes the fruit by lifting and rotating to cut the stalk from the branch. Although this method minimizes damage to the fruit, the system has a limited workspace when it has to approach the apple horizontally. Baeten et al. [20] developed a new gripper consisting of a flexible silicone funnel and vacuum suction. The average harvest time was about nine seconds in the experiments, but trunk pulling occurred on about 30% of harvested apple trees. It is also essential to pick apples logically so that nearby apples are not picked on the same branch. Zhao et al. [21] propose a circuit breaker using multiple sensors that show very impressive success rates in practical tests. To minimize the chance of stems being pulled, harvesting systems often require more complex control requirements, resulting in higher costs. Choi and Koc [22] present a set of clamps with interchangeable rubber pockets on the clamping surface. An example is a gripper by Davis et al. [23] to perform cucumber slicing with a stream of high-pressure air. The clamp design can be implemented very simply and with the nature of non-contact between the tool and the fruit.

This paper presents the development of a gripper that can grasp common fruits commonly grown in Vietnam. This gripper has a suitable mode of operation for carefully gripping and loosening horticultural products. The focus of this paper is on the conceptual design for an under-activated, fruits picking end-effector. The first section of the report reviews some of the unique challenges posed by robotic fruits harvesting and presents the design goals for this system. Then, after describing the mechanical design of the robotic manipulator, the end-effector's conceptual design and kinematic analysis are presented. The sequence of movements that the overall system will use for order picking is also proposed. Finally, the framework to complete the system's analysis, design, optimization, and testing is outlined.

II. DESIGN OBJECTIVES REQUIREMENTS

Typically, the harvesting of fruit products is an automatic machine, as shown in Figure 1. The most critical part affecting the machine's efficiency is the clamp, as it is the part that comes into direct contact with the fruit picking. Therefore, to make an effective gripper for automatic harvesters, mmechanical properties of fruits need to be examined and analyzed

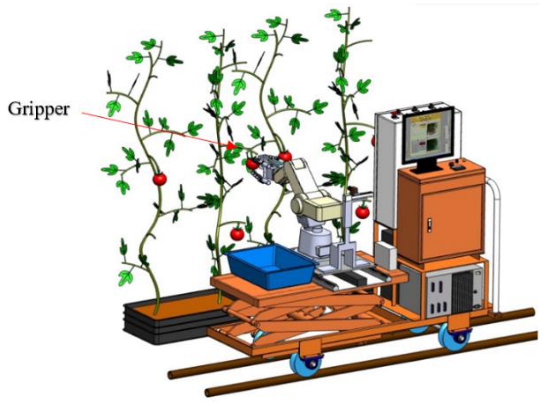

Figure 1. Automated harvesting machine [24]

This article deals with popular agricultural products in Vietnam such as apples, tomatoes, pears, and plums. Since 1961, the Organization for Economic Co-operation and Development (OECD) has issued reports on commercialized fruit products in the world along with their common sizes [25]. The relevant information is summarized in Table 1.

TABLE 1. SIZE OF SOME COMMON FRUITS IN AGRICULTURE [25]

Product	Min size (mm)	Max size (mm)
Oranges	50	120
Apples	45	110
Apricots	25	65
Clementine	30	60
Tomatoes	35	100
Lemons	40	90
Peaches	55	100
Oranges	50	120

Table 1 shows that the average size of most harvested fruits is usually between 40 and 100 mm. Weight varies by type, but it is generally between 50 and 500 g. The shape of these products is almost spherical, with some exceptions such as carrots or tomatoes. The mechanical properties of common fruits such as apples, cucumbers, peach, and tomatoes have been summarized in several research projects [26] [27] [28]. The data are described in Table 2. In general, tomatoes have the worst mechanical properties among fruits, so it is often used as a reference fruit for the design of the gripper..

TABLE 2. SIZES OF FRUITS AS FROM STANDARDS IN [26], [27], [28]

Product	Young's Modulus [MPa]	Young's Modulus deviation [MPa]	Poisson's Ratio [-]
Tomato – Ripe	2.32	-	0.74
Pear	5.80	0.50	0.25
Tomato – Unripe	4.07	-	0.55
Apple	12.89	2.43	0.32

The basic functional requirements of a fruit harvester are to reach the fruit, then separate the fruit produced from the tree. In addition to being efficient, productive, and economically viable, it is important that the system does not damage the picked fruit, damage adjacent fruit, and damage the tree branches. For example, grippers can damage fruit by applying too much force during picking or using improper picking techniques.

Typically a gripper consists of two or more rigid fingers and a mechanism for moving them to grasp an object, as shown in Figure 2. A gripper typically has a construction of one to three degrees of freedom. Controlling the force of the clamp is essential to avoid damage to the product. The low flexibility of a gripper is its main drawback as rigid fingers cannot wrap around an object or adapt to it however has the advantage of being easier to control

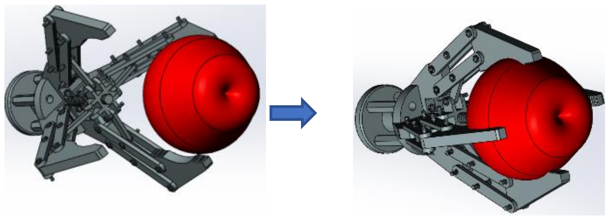

Figure 2. Gripper grasping fruit

III. GRIPPER DESIGN

The proposed solution is a four-finger gripper based on the handwheel slider mechanism, as shown in Figure 3. Fingers connected to the body rotate through sliders. The four-finger sliders are attached to the same frame, and their movement is controlled by an actuator consisting of a rotating disc and a lead screw. Even if soft fingers can be used, an alternative of using hard fingers such as the mechanism suggested above may be preferred as it is relatively easy to analyze, fabricate and test to grasp the product right way

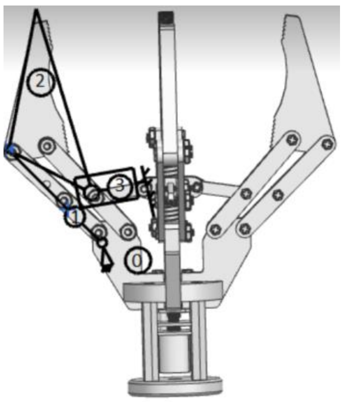

Figure 3. Kinematic scheme of the proposed gripper solution

The grasping index (G.I.) in [30] is used as the design criterion of the clamp, the GI index is used to evaluate the performance of the clamping mechanism. The GI is defined by

$$G.I. = \frac{F\ sin\,\zeta}{P} \qquad (1)$$

In which P is the force exerted by the actuator, F is the grasping force and ζ represents the configuration angle of the mechanism when grasping. The G.I. performance index can be further simplified by assuming ζ= 0 [31]

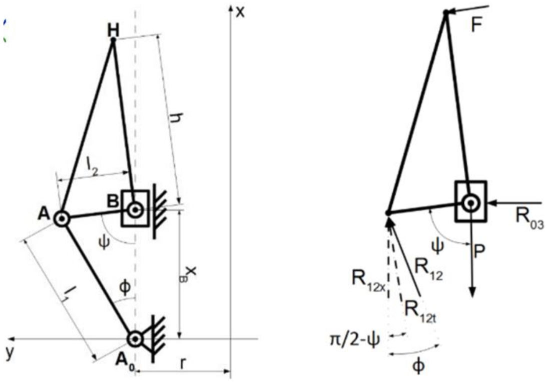

Figure 4. Kinematic diagram with design parameters

The following equations can be used regarding the gripper design parameters shown in Figure 4 to describe the kinematics of the gripper as

$$l_2\, sin\,\psi = l_1\, sin\,\phi \qquad (2)$$

$$cos\,\phi = \frac{x_B{}^2 + l_1{}^2 - l_2{}^2}{2x_B l_1} \qquad (3)$$

Where l1 and l2 are respectively the length of the first and second links of the mechanism, respectively and the position of the slider x_B describes the configuration of the mechanism.

In addition, the effectiveness of a gripper can be assessed by a static gripper balancing mechanism. Referring to Figure 3c, the static equilibrium equation for moments around point B and for forces in the X direction can be written as

$$F_h - R_{12t} l_2 = 0 \qquad (4)$$

$$R_{12x} - P = 0 \qquad (5)$$

In which forces R_{12x} and R_{12t} are components of reaction R_{12} on link AA_0, respectively. The reactions R_{12x} and R_{12t} can be calculated using the formula.

$$R_{12t} = R_{12}\, cos(\phi + \psi - \frac{\pi}{2}) \qquad (6)$$

$$R_{12x} = R_{12}\, cos\,\phi \qquad (7)$$

And then

$$P = \frac{Fh\, cos\,\phi}{l_2\, cos(\phi + \psi - \frac{\pi}{2})} \qquad (8)$$

Then, using Eq.. (2) and (8) into Eq. (1), the Grasping Index for the proposed gripper can be expressed as

$$G.I. = \frac{l_1}{h} tg\phi\, cos(\phi + \psi - \frac{\pi}{2}) \qquad (9)$$

As shown in Eq. (9), The G.I index of the gripper depends on the ratio of the lengths of the links and the height of the mechanism. The GI increases as link's length increases and height decreases. However, according to design standards, the minimum height of the gripper must be greater than half of the maximum diameter of the gripper. Another direct dependency of G.I. is on l_1. According to formula (9), the GI index directly depends on the l1 size. Therefore, the structure can be optimally designed in two different ways [14], namely:

- ❖ Maximizing the Mean Grasping Index, that can be expressed as

$$max\ G.I._{mean}\ subject\ to\ l_{i,min} < l_i < l_{i,max}\ for\ i = 1,2$$

- ❖ Minimizing Grasping Index deviation, by using as problem formulation

$$min \frac{G.I._{max} - G.I._{min}}{G.I._{mean}}\ subject\ to\ l_{i,min} < l_i < l_{i,max}\ for\ i = 1,2$$

Each gripper's geometry is limited between the minimum and maximum dimensions for the respective fruits, as shown in Table 5. Too small a gripper will cause fabrication and assembly to become problematic. Oversized gripper will cause waste of materials. To obtain the optimal value of the design parameters of the gripper, their dimensions were customized and G.I. evaluated for each possible combination of alternatives. Then, for each alternative, the mean G.I. and G.I. deviation is evaluated for all configurations. Using analytical calculation on Solidwork software, some optimization results are shown in Table 6.

Although the first option has a higher GI value, it has a higher error than the second option. The chosen design option is a mechanism with l_1 equal to 42.00 mm and l_2 equal to 45, 00 mm. The working stroke of the slider for this design variant is 15.00 mm, with x_B ranging from 31.00 to 46.00 mm. The distance from the top of the finger to the axis of symmetry, as shown in Figure 4, is equal to the mean radius of the fruit to be picked and can be expressed as

$$r_H = r + h\, sin(\frac{\pi}{2} - \psi) \qquad (10)$$

TABLE 5. DESIGN PARAMETERS SIZE

Parameter	Min (mm)	Max(mm)
l_1	25	50
l_2	15	50
r	30	42

TABLE 6. RESULTS OF GRIPPER OPTIMAZATION

l_1 (mm)	l_2 (mm)	GI_{mean}	Deviation
25.00	30.00	0.306214	0.14553
40.00	45.00	0.286543	0.030112

Using Solidworks software to analyze and calculate the clamp with the designed structure, r_H ranges from 7 mm to 60 mm. As a result, the clamp can grip any product in the diameter size range from 14 to 120 mm. The force P is calculated from the equation. 8 using force F, based on the geometry and configuration of the clamping mechanism. Once the gripper configuration has been determined from its kinematic equation, the force F can be calculated using the principles of mechanical balance. The following hypotheses relate to the fact that both the finger and the product are considered absolutes. The coefficient of friction between the grabbing finger and the fruit μ is 0.5. Each finger is loaded in the same direction (as axial symmetry) as the load Q. Hence, from Figure 4, the balance of forces on the Z-axis can be written as

$$3\mu F \sin\psi - 3F\cos\psi - Q = 0 \tag{11}$$

$$F = \frac{Q}{3(\mu \sin\psi - \cos\psi)} \tag{12}$$

By replacing Eq. 14 with Eq. 4, the maximum impact force Pmax can be easily calculated. Typically, the weight of fruits harvested in Vietnam is from 0.5 to 2N [9]. Assuming a product weight of 6.0 N with a design factor of safety of 2.5. A commercially available standard screw-nut shaft was selected for the design [15] and subsequently fabricated a prototype. Spindle and nut have trapezoidal thread, according to DIN103. Torque required to rotate the lead screw is given by [16] as

$$T = \frac{Pd_m}{2}\left(\frac{l+\pi\mu_s d_m}{\pi d_m+\mu_s l}\right) \tag{13}$$

Where l is the length of the screw, d_m its diameter, and μs the coefficient of friction for the contact between the screw and the nut. The static and dynamic friction coefficients between the lead screw and the nut are 0.33 and 0.15, respectively [15]. Therefore, the torque required to generate rotation is calculated as T = 0.3 Nm.

IV. Result and Discussion

A prototype has been fabricated by using metal cutting to verify the feasibility of the construction. The designed gripper was created with Solidwork software, as shown in Figure 4. The material that was used in Steel. The prototype is shown in Figure 5.

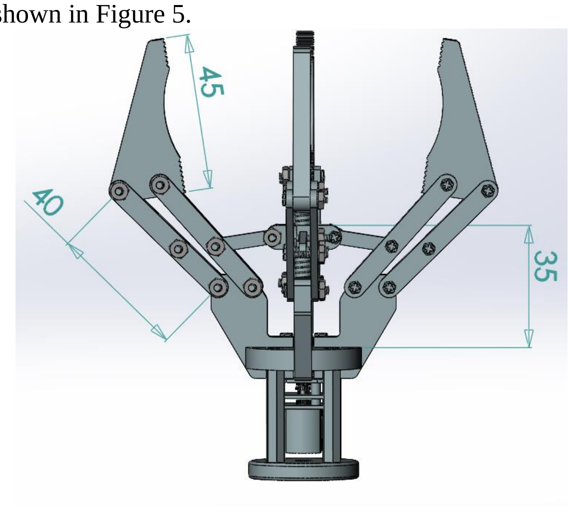

Figure 4. CAD design of the gripper

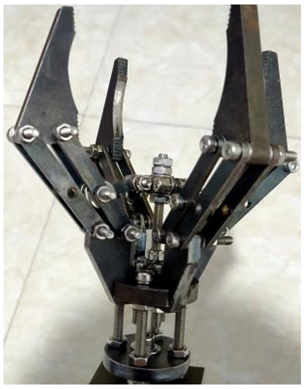

Figure 5 The Gripper propotype

Figure 6. Test configuration for static grasping force

Several tests have been carried out in the laboratory, with handles holding two of the most common fruits in Vietnam, tomatoes, and lemons, as shown in Figure 6. For each fruit, grip and hand movements were tested. Picking was repeated many times. The grasping tests were performed the same as the actual picking motion in the harvest, as it was observed in the simulation tests that for the maximum test velocity (2 m/s), the grip force F = 3.2N and contact time t = 4s as shown in Figure 7. The results show that the clamping machine does not damage the picked fruit

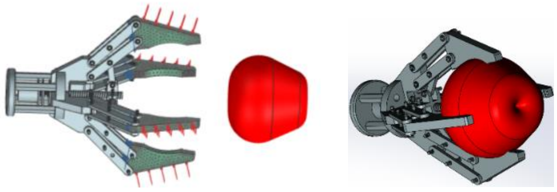

Figure 7. Simulation test

Then, similar to the manual picking sequence, the manipulator rotates the fruit 90^o degrees and exerts a downward force to remove the fruit from the tree. If the product is correctly recognized by the vision system, the gripping is usually successful. Moreover, it is challenging to design a universal clamp that works effectively for a variety of fruits. In this study, lemon and tomato are the preferred products for the design of the gripper. The results of planned experimental tests to determine the dynamic forces that occur during manual fruit harvesting will be used to develop a control scheme that ensures that applied forces will not damage the harvested fruit. After completing fabrication, the gripper will be optimized in preparation for full-scale laboratory and field tests with the complete system.

V. Conclusion

In this paper, a prototype gripper used in fruit harvesting machines has been designed and manufactured based on the requirements and characteristics of agricultural products. The kinematic calculations and optimal design for the clamp have been processed in detail on the basis of mathematics with the help of Solidworks design software. The clamps proposed in the study can pick up popular fruit products in Vietnam without damaging them, contributing to increased productivity and economic efficiency.

ACKNOWLEDGMENT

This work has been supported/partly supported by VNU University of Engineering and Technology under project number CN21.11

REFERENCES

[1] Giyasettin Cicek. Determination of harvesting costs and cost analysis for different olive harvesting methods. Journal of Food, Agriculture & Environment Vol.9 (3&4): 201-204. 2011.

[2] Peilin Li, Sang-heon Lee, Hung-Yao Hsu. Review on fruit harvesting method for potential use of automatic fruit harvesting system. Procedia Engineering 23 (2011) 351 – 366

[3] Demircan, V., Ekinci, K., Keener, H. M., Akbolat, D. and Ekinci, C.2006. Energy and economic analysis of sweet cherry production in Turkey: A case study from Isparta Province. Energy Conversion and Management 47:1761-1769.

[4] Galinato, S., & Gallardo, R. K. (2011). 2010 Estimated Cost of Producing Pears in North Central Washington (FS031E).

[5] Gallardo, R. K., Taylor, M., & Hinman, H. (2010). 2009 Cost Esimates of Establishing and Producing Gala Apples in Washington (FS005E).

[6] Sanders K F, Orange Harvesting Systems Review, Biosystems Engineering, vol.90, no.2, 2005, pp.115-125

[7] Coppock G E ; Hedden S L, Design and development of a tree-shaker harvest system for citrus fruit, Transaction of the ASAE, vol.11, no.3, 1968, pp.339-342

[8] Tillett N D, Robotic Manipulators in Horticulture: A Review, J.agric. Engng Res., vol.55, 1993, pp.89-105

[9] Ceres R, et al., Design and implementation of an aided fruit-harvesting robot(Agribot), Industrial Robot, vol.25, no.5, 1998, pp.337-346.

[10] Zhao, D., Lu, J., Ji, W., Zhang, Y., & Chen, Y. (2011). Design and Control of an Apple Harvesting Robot. Biosystems Engineering, 110, 112-122.

[11] Jun Li, Manoj Karkee, Qin Zhang, Kehui Xiao, Tao Feng, Characterizing apple picking patterns for robotic harvesting, Computers and Electronics in Agriculture, Volume 127,
2016, Pages 633-640.

[12] Arima, S., N. Hayashi, and M. Monta. 2004. Strawberry harvesting robot on table-top culture. ASAE Paper No. 043089.

[13] Bulanon, D. M., T. Kataoka, H. Okamoto and S. I. Hata. 2005. Feedback control of manipulator using machine vision for robotic apple harvesting. ASAE Paper No. 053114.

[14] Chiu, Y. C., S. Chen, and J. F. Lin. 2012. Development of an autonomous picking robot system for greenhouse grown tomatoes. In The 6th Intl. Symp. on Machinery and Mechatronics for Agr.and Biosystems Eng.

[15] Pollack, S., & Perez, A. (2013). Fruit and Tree Nut Yearbook. Economic Research Service, United States Department of Agriculture (USDA).

[16] Ahmadi, E., Ghassemzadeh, H.R., Sadeghi, M., Moghaddam, M., Neshat, S.Z., 2010. The effect of impact and fruit properties on the bruising of peach. J. Food Eng. 97, 110–117.

[17] Idah, P., Yisa, M., 2007. An assessment of impact damage to fresh tomato fruits. AU J. Technol. 10, 271–275.

[18] Kitthawee, U., Pathaveerat, S., Srirungruang, T., Slaughter, D., 2011. Mechanical bruising of young coconut. Biosyst. Eng. 109, 211–219

[19] Bulanon, D. M., & Kataoka, T. (2010). Fruit Detection System and an End Effector for Robotic Harvesting of Fuji Apples. Agricultural Engineering International: CIGR Journal, 12(1), 203-210.

[20] Baeten, J., Donne, K., Boedrij, S., Beckers, W., & Claesen, E. (2008). Autonomous Fruit Picking Machine: A Robotic Apple Harvester. Field and Service Robotics, 42, 531-539.

[21] Zhao, D., Lu, J., Ji, W., Zhang, Y., & Chen, Y. (2011). Design and Control of an Apple Harvesting Robot. Biosystems Engineering, 110, 112-122

[22] Choi, H., Koc, M., 2006. Design and feasibility tests of a flexible gripper based on inflatable rubber pockets. International Journal of Machine Tools & Manufacture 46, 1350–1361.

[23] Davis, S., Gray, J.O., Caldwell, D.G., 2008. A Non-Contact End Effector based on the Bernoulli Principle for handling of Sliced Tomatoes. Journal of Robotics and Computer Integrated Manufacturing 24 (2), 249–257

[24] Y. C. Chiu, P. Y. Yang, S. Chen. Development Of The End-Effector Of A Picking Robot For Greenhouse-Grown Tomatoes. Applied Engineering in Agriculture Vol. 29(6): 1001-1009, 2013

[25] OECD (2016). Fruit and Vegetables standards. http://www.oecd.org/tad/code/. Accessed 10 Feb 2016.

[26] Williams, S. H., Wright, B. W., Truong, V. D., Daubert, C. R., & Vinyard, C. J. (2005). Mechanical properties of foods used in experimental studies of primate masticatory function. American Journal of Primatology, 67(3), 329-346.

[27] Gładyszewska, B., & Ciupak, A. (2009). Changes in the mechanical properties of the greenhouse tomato fruit skins during storage. PUBLISHER UWM OLSZTYN 2009, 1.

[28] Babarinsa, F. A., & Ige, M. T. (2014). Young's Modulus for Packaged Roma Tomatoes under Compressive Loading. International Journal Of Scientific & Engineering Research, 3(10), 314-320.

[29] Joseph Davidson1* and Changki Mo. Conceptual Design Of An End-Effector For An Apple Harvesting Robot. Proceedings of the 6th Automation Technology for Off-road Equipment Conference (ATOE), 15-19 September 2014, Beijing, China

[30] Ceccarelli, M. (2013). Fundamentals of mechanics of robotic manipulation (Vol. 27). Springer Science & Business Media.

RUSSO, Matteo, CECCARELLI, Marco, CORVES, Burkhard, HÜSING, Mathias, LORENZ, Michael, CAFOLLA, Daniele and CARBONE, Giuseppe (2016). Design and test of a gripper prototype for horticulture products. Robotics and Computer- Integrated Manufacturing, 44, 266-275.

**The 6th International Conference on Engineering Mechanics and Automation (ICEMA 2021)
Hanoi, November 14, 2021**

Development of a Low-delivery-rate Syringe Infusion Pump towards Remote Monitoring of Biomedical Applications using Accessible IoT Technology

Hang Tran Thanh
University of Engineering and Technology
Vietnam National University, Hanoi
Hanoi, Vietnam
hangtt.uet@vnu.edu.vn

Duong Nguyen Dinh
University of Engineering and Technology
Vietnam National University, Hanoi
Hanoi, Vietnam
duongndrb@gmail.com

Vinh Nguyen Phuc
University of Engineering and Technology
Vietnam National University, Hanoi
Hanoi, Vietnam
vinhuet01@gmail.com

Hoang Tong Tran
University of Engineering and Technology
Vietnam National University, Hanoi
Hanoi, Vietnam
hoangtongtran1999@gmail.com

An Nguyen Ngoc
University of Engineering and Technology
Vietnam National University, Hanoi
Hanoi, Vietnam
ngocan@vnu.edu.vn

Loc Do Quang*
University of Science
Vietnam National University, Hanoi
Hanoi, Vietnam
locdq@hus.edu.vn

***Abstract*: Intravenous administration of drugs and fluids is a widespread technique in modern medical treatments. Administering medicines or fluids directly into a patient's bloodstream results in predictable and quick absorption of the drug or fluid supplied, which may be critical in the treatment of some acute illnesses that need fast action by pharmaceuticals or fluids. Syringe pumps are extremely important for delivering a precise amount of a chemical at certain times. Advances in wireless technology and the Internet of things (IoT) make it possible to utilize medical equipment wirelessly over great distances for remote monitoring. In this study, a framework for a low-cost medical syringe pump with variable and low delivery rates based on the accessible IoT technology for the administration of tiny amounts is proposed to improve health care field.**

Keywords: automatic syringe injection pump, continuous and low dose drug treatment, monitoring system, wireless device

I. INTRODUCTION

In traditional treatments, medicine injection is a popular way of administering a drug in order to get the desired effects fast and directly. Subcutaneous injection is one of the several medication injection procedures. It is injected into the fatty layer of subcutaneous tissue right beneath the skin. Because there are few blood arteries in subcutaneous tissue, the injected medicine diffuses very slowly and at a sustained absorption rate. As a result, it is extremely successful in administering vaccinations, growth hormones, and insulin, which need continuous delivery at a low dosage rate. Subcutaneous tissue injections are preferable for various pain drugs, such as morphine and hydromorphone, as well as allergy treatments. These medications are given as a one-time injection using a syringe or long-term injection through a pump placed on the skin's surface. However, the discomfort and agony associated with frequent medication injections may cause patients to miss or, in the worst-case scenario, discontinue clinical treatment [1]. This may be especially significant for individuals who have a chronic condition that requires life-long maintained care, such as diabetic patients who require insulin delivery. In order to avoid the negative consequences of repeated subcutaneous injections, a syringe pump is highly recommended when high accuracy and low flow are required, such as in pediatric situations or intensive treatments involving the application of tiny quantities of high concentration drugs over lengthy periods. For example, an automated epinephrine infusion is used to treat severe allergic responses quickly [2]. Insulin is supplied at a low dosage rate by syringe and insulin pump to distribute the substance over a long period [3]–[6]. The slow injection pace is analogous to how insulin is progressively released from the pancreas. Moreover, the syringe pump is genuinely utilized for in-vivo diagnosis, treatment, and research [7]–[10] which is adopted worldwide for both medical and scientific purposes. The precision of performance or the effectiveness of flow-rate control is critical for the utilization of droplet microfluidic systems [11]–[13]. Variations in manual liquid medicine administration systems may arise when being operated by a nurse or hospital staff. Hence, there have been researches on the development of syringe pumps with numerous variants [14]–[16] as well as commercial devices on the market. However, most commercial devices are currently expensive, and it is not permissible to meddle with the program to add functionality for research purposes. As a result, investigations on syringe pumps with upgrading features are favored.

Furthermore, with the expansion of communication technology, particularly the Internet of things (IoT), there is a possibility for syringe pumps to be connected with IoT [17], [18]. The Internet of Things (IoT) is the interconnection of physical items incorporated with electrical equipment, software, sensors, actuators, and network connections that allow data to be collected and sent across systems[7], [19]. Thus, a smart syringe pump may be created by adding smart communication and cloud servers to monitor for analysis and convenient remote observation. This approach reduces dangers while also saving time by developing software that collects, communicates, and analyzes data streams. In this paper, a Low-delivery-rate Syringe Infusion Pump using accessible IoT technology is suggested. This gadget will also have remote monitoring to guarantee that it operates smoothly at the patient's bedside. The method is simple, risk-free, and saves time for doctors, patients, and nurses.

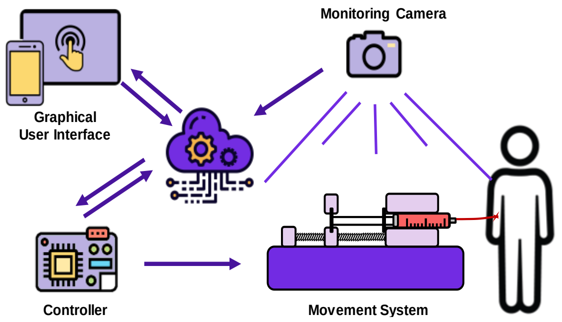

Fig. 1. The proposed system for towards Remote Monitoring of Biomedical Applications using Accessible IoT Technology

II. SYRINGE PUMP SYSTEM DESIGN

The general architectural elements required for remote monitoring IoT systems of biomedical applications consist of three main parts, including device part, Internet-connected smart gateway, and cloud support. In this study, we employed a three-channel low-delivery-rate syringe infusion pump for the device part to investigate how proposed IoT approaches could be undertaken for remote monitoring by the users. Construction and design of IoT syringe pump devices were accomplished in three stages. The first stage is about the mechanical design of the machine. Figure 2 demonstrates the concept of the mechanical component and planned machine construction. A picture of the open-up perspective of the syringe pump mechanism is shown for more clarity.

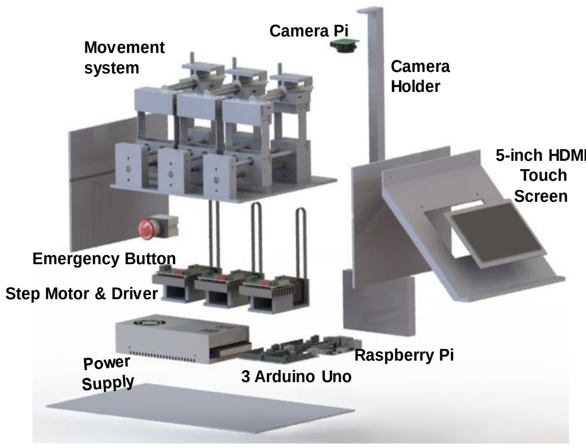

Fig. 2. The design of a low-delivery-rate syringe infusion pump

This study provides and implements experimental flow controls, safety measurements, and wireless control of the proposed system via the Internet. The suggested gadget eliminates the hazards, and the consuming time is reduced in operation by remotely regulating and monitoring. The monitoring video is broadcast to mobile phone applications in a loop, allowing people to see the functioning operation process. In the event of an error occurs, an emergency button on the right side of the syringe pump allows the system to be stopped promptly and without causing any harm.

An Android phone, a touch screen, a communication unit, a controller system, and a mechanic assembly handle syringes from the multi-channel syringe pump system. Fig. 3 illustrates how all components interact by displaying a block schematic of the proposed design for operating the syringe pump. The Control block is represented by the biggest block system, which is made up of three Raspberry Pi 3 Model B+, three Arduino Uno, three TB6560 motor drivers, and three NANOTEC ST4018L1804 KGR01 step motors that are controlled via smartphone or touch screen display by determining the step motor control parameters based on user inputs. The Power Supply block, which consists of a 24 V power supply that powers the entire system and is connected to a buck that switches from 24 V to 5 V to power the Raspberry Pi individually. The Raspberry Pi is attached to the camera block, which is used to monitor the system. The black wires are signal lines that link how the various blocks function together. By employing the assessable IoT technology, the proposed platform allows users to directly communicate with the devices and provide an interface to collect and display data gathered from IoT devices.

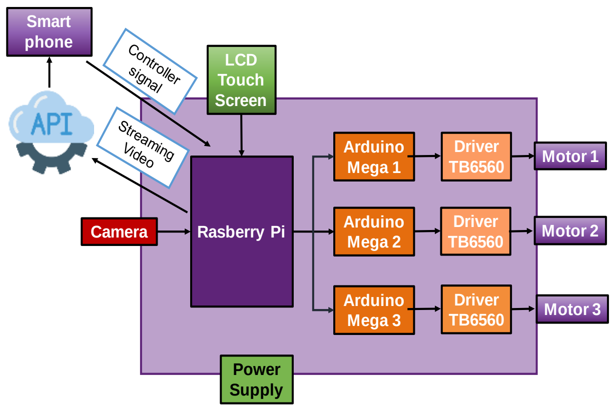

Fig. 3. The proposed device's block diagram

III. RESULTS AND DISCUSSION

A. Experimental system setup

Based on the platform of assessable IoT technologies that have been integrated with our proposed syringe pump device, a prototype of the IoT syringe pump device was designed and manufactured to provide a low-cost IoT approach towards remotely monitoring biomedical devices' operation. The materials used in the mechanical assembly of the syringe pump are depicted in Fig. 4. Only a few blocks of the machine's actuator, engine, and control system were visible from the exterior. Aluminum blocks were used to hold the syringe and the plunger, which was pushed by the actuator. A polished and anodized aluminum plate was used as the base for the whole system to provide sufficient stability to the sliding mechanism. A mild steel guide was used to make a screw for the planned lead-screw mechanism. The guide diameter was 6 mm, and the screw pitch was 2 mm. The brass nut in the moving mechanism is made of copper alloyed with zinc metal, which is easily molded, stamped, and deep drawn and has high strength, forming, and drawing characteristics. The display interface makes use of a 7-inch capacitive touchscreen Raspberry Pi display. Because of its durability, low cost, and great aesthetics, the system used black double-layer mica material. For monitoring reasons, a camera module (Raspberry V2 IMX219 8 MP) was mounted to the camera holder on the left side of the suggested gadget. On the right side, there was an emergency stop button to instantly halt the equipment when the workflow demanded it and an electric line to deliver power to the proposed gadget.

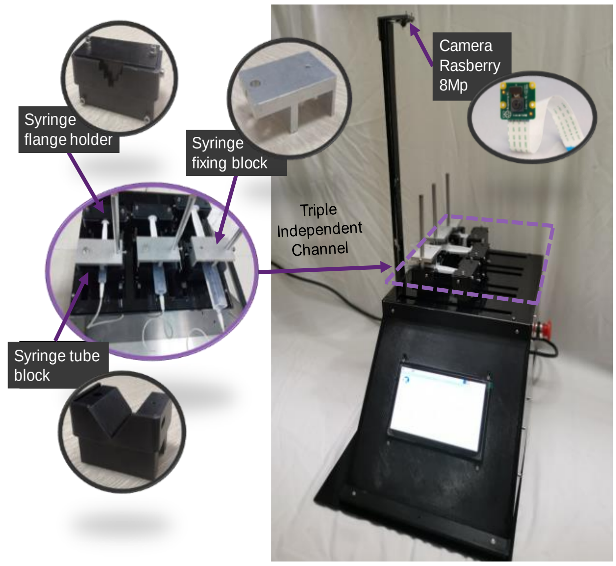

Fig. 4. Experimental setup of the proposed syringe pump system

B. Software design

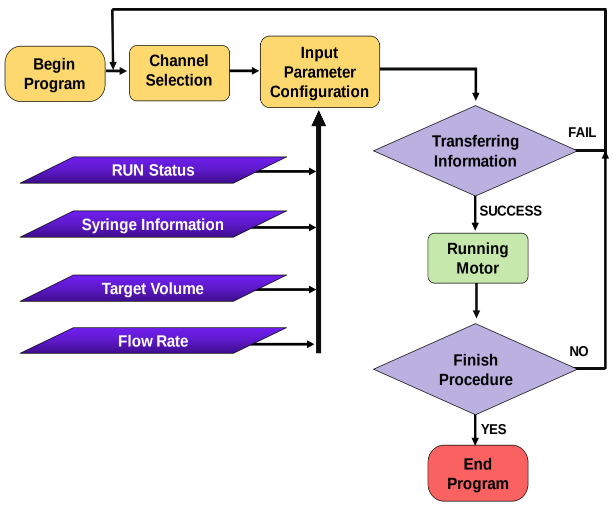

Fig. 5. The graphical user interface of the Syringe Pump system's control logic

To build the user interface for our proposed system, a specific graphical user interface is created to collect inputs from a touch screen display and a smartphone. The algorithm's primary goal was to satisfy the user's needs. For each syringe, the user enters a name (for example, "50 ml syringe"), volume, and flow rate. The program predicts the number of steps the motor must execute (depending on the motor's steps per revolution, gear ratio, and lead screw threads per millimeter) and distributes the time to dispense across these steps using several factors. A Raspberry Pi was employed to control the syringe pump system. The flow chart in Figure 5 shows how the Raspberry Pi connects with the stepper motors through driver boards. The software that operates with the syringe pump was written in Python, a programming language with a simple, versatile, and intelligible syntax. The code is one-of-a-kind, adaptable, and stored for future usage in order to add extra functionality for research reasons.

The sequence stages are clearly depicted as follows:

• Begin the application by powering up the machine. Set up all of the necessary conditions for operation.

• The pump is divided into three channels. Choose a one-channel pump to utilize. Check to see if the pump already has a syringe attached.

• Using the touch screen display, configure pump information. The user can provide optional settings to all pump channels in parallel based on their needs. The operating state of each pumping cycle, the kind of syringe, the user's intended goal volume, and the flow rate are factors. After setting the parameters on the touch screen to transmit the parameters to the Arduino. If the parameters set are satisfied, the user continues to press the button to execute the transferring procedure. If the flow rate is preposterous, leading to the uploading process failing, the system goes back to step 2 and repeat.

• If the motor starts, the user must wait for the pump to complete its cycle according to the pre-set parameters.

• Once the pump has finished transferring the amount of fluid desired by the user, the pump's activity is ended following the user's decision.

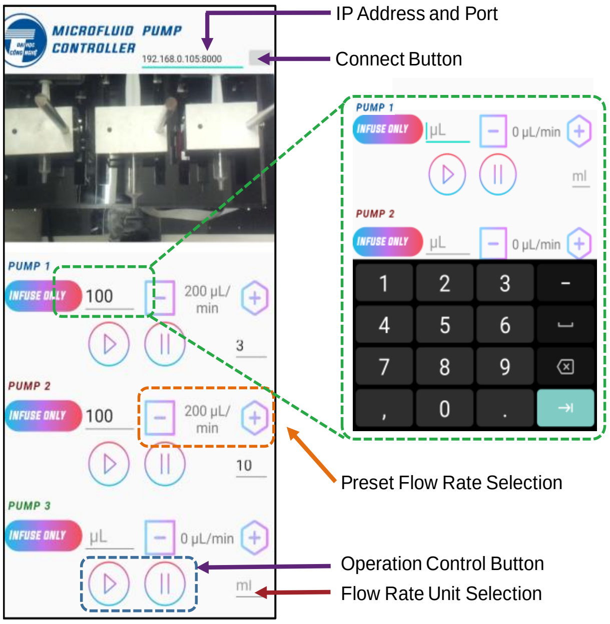

Fig. 6. Android user interface design application of the low-delivery-rate syringe infusion pump

From the IoT technologies embedded in our proposed hardware, the prototype of the proposed IoT syringe pump device was experimentally implemented to investigate the performance of our approach. In use, the device may hold a variety of syringes (Vinahankook) with capacities ranging from 1 ml to 50 ml. Users can also define a fixed goal volume ranging from 100 μl to 1000 μl using the interface. Furthermore, the user may choose from a range of flow rates ranging from 10 μl/min to 100 μl/min.

Aside from direct control on the touch screen, the syringe system was also wirelessly controllable. Integration with IoT makes a gadget smarter by saving time and decreasing risk. The proposed platform provides the integration protocols that can directly interface with the main control unit. The Raspberry Pi received information from the smartphone application’s user input via the Firebase Realtime Database. The data was sent from the client and synced in real-time with immediate updates on the cloud. Simultaneously, the Raspberry Pi identified and downloaded the new specifications. The information input could be entered using the keyboard or the plus and minus buttons to fill in. The smartphone application’s graphical user interface is described in Fig. 6.

Besides passing the information supplied by the user to the system, the Raspberry Pi was also configured to perform an additional function of live-streaming the video feed to monitor the microfluidic delivery system. The camera script immediately runs in the background when the users turn on the machine. The live stream area is where the real-time transmission image from the pump is displayed. Since that’s where the image is displayed, the image viewing process should not be interrupted or distracted by any factors. Therefore, the live stream display area has been placed on top of the application so that even when the user is manipulating the control area, the fingers will not block the image, avoiding inconvenience to the user experience. The block displays images using the built-in WebView engine in Android Studio. WebView is a system component provided by Chrome that allows Android applications to display content on the web. The video stream is sent to the HTML web that the Raspberry Pi relies on to generate. Users access the transmission line to watch by entering the IP address of the pump and the corresponding Port in the area, then click the button next to it, and the live stream signal will appear in the WebView area.

Live stream from the camera over the web using Raspberry Pi is relatively complicated. Currently, there is still no video standard that is universally supported by all web browsers on all platforms. Furthermore, the HTTP protocol was originally designed as a one-time protocol for delivering web pages. Since its invention, various features have been added to cater to the growing use cases (download files, resume, stream, etc.). However, the reality is that there is no universal solution for doing a live stream from Raspberry Pi at the moment. In order to resolve this problem, a proposed solution is to use a much simpler format: MJPEG, also known as Motion – JPEG. Motion - JPEG is a video compression format in which each frame or interlaced field of a digital video sequence is individually compressed as a JPEG image. Script used for live streaming, using Python’s built-in HTTP server module to create a simple live stream server. The program’s operation will be as follows: The program takes information from the Raspberry Pi, creates an HTML web to display one frame with a resolution of 640 pixels × 480 pixels. Then the program will recheck the stream status, get the video results from the Pi in MJPEG format, and then put that result on the newly created HTML. The user enters the IP address of the Raspberry Pi, followed by a ":" and the port address that the program sets. After entering, the user will see the real-time transmission from the camera.

Practical requirements that a control application needs to be convenient for users to use were resolved and fully integrated with our proposed syringe micropump system. All the control system's functions of the pump were already considered and embedded into the control software. Furthermore, the added ability to remotely monitor the device is a feature that no other micropump on the market has. The application interface is designed to provide an easy-to-use, user-friendly feeling by using minimalist buttons accompanied by gradient tones that bring depth to the overall application. The process of back-end operation of the application when controlling the micropump system using the Firebase Realtime Database platform and the program that helps the Raspberry Pi read that data to be transmitted to the Arduino has been discussed and explained in detail. And finally, the process of building and integrating the ability to remotely monitor the system using a camera connected to the Raspberry Pi has been thoroughly analyzed. A camera holder was used to catch the syringe pump for video recording. The quantity of injected liquid volume and process risks were determined by capturing video recordings of the syringe pump while the device was in operation. In our experimental implementations, our devices connect to the router with a data transfer rate of 20 Mbps and are already connected with five other devices, resulting in a time delay of about 1 second on average.

C. Syringe Pump Performance

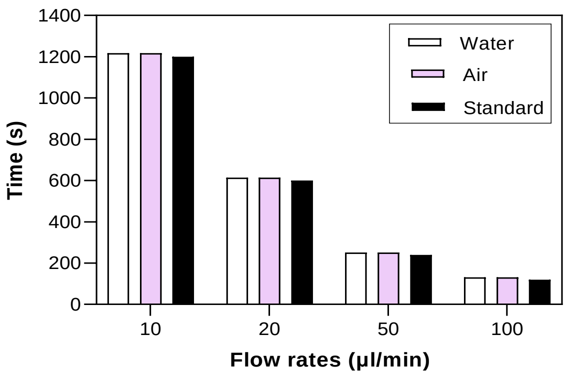

Fig. 7. Comparison of the theoretical calculation with two types of material inside syringe at various flow rates

Fig. 7 demonstrates the insignificant difference between the standard theoretical calculation and the experimental performance. In this experiment, the performance of the proposed device was examined by injecting water and air at the different flow rates, then validated by comparison with the theoretical calculation. Furthermore, there is no significant difference between the transferred times of the water and the air contained in the barrel. In the experimental examinations, the syringe pump system was set to both simultaneously pumps 200 µl water and 200 µl air with different flow rates, including 10 µl/min, 20 µl/min, 50 µl/min, and 100 µl/min.

Table I summarizes the more detailed performance of the experiment in Fig. 7. The error is defined as the percentage change in flow rate from the desired flow rate.

TABLE I. THE ACCURACY OF SYRINGE PUMP USING 1 ML SYRINGE WITH THE VARIOUS FLOW RATE

Machine's Flow Rate (µl/min)	Syringes' status	The measured time (s)	The standard calculated time (s)	Relative error (%)
10	Contain Water	1,217	1,200	1.43%
	Contain Air	1,217		
20	Contain Water	613	600	2.30%
	Contain Air	613		
50	Contain Water	251	240	4.76%
	Contain Air	251		
100	Contain Water	130	120	9.10%
	Contain Air	130		

The experimental data were recorded, which includes syringe size (ml), machine's flow rate (µl/min), syringe's status, the measured time (second), calculated time (second), and the relative error (percent). The accuracy is indicated through relative error using the equation (1):

$$RE = \frac{(CT - MT)}{CT} 100\% \qquad (1)$$

Where *CT*, *MT*, *RE* stand for the calculated time (second), means the measured time (second), and means the relative error (percent), respectively.

A high-performance, low-cost syringe pump device and a functional prototype were built and examined. By utilizing the simple mechanical approach, the design, experimental implementation, and validation of the proposed flexible and programmable low-delivery-rate syringe pump were conducted and analyzed. The relative error ranges from 1.43% to 9.1% of the desired flow rate, according to Table I. The syringe pump mechanism described here might be useful for low-resource environments as high precision, low-cost liquid delivery system.

D. Discussion

Under ambient conditions in the laboratory, our device achieves the performance of many single-use infusion therapy devices [20]. In addition, for microfluidic mixing research, the flow rate of fluidics in microfluidic devices is required very low to avoid puncturing the microfluidic channel but still achieve high efficiency in mixing. The performance of our proposed device is acceptable. Other significant sources of error may be related to the internal friction in the syringe backpressure. These elements have a more significant relative impact on low flow rates. Moreover, many factors can contribute to this error, including mechanical backlash in the lead screw mechanism, a calibration error, and a power supply error. These errors can be investigated to minimize and reduce in future research. The proposed machine attempts to give the user convenience and reduce most harm in the operation process. The graphical user interface was adopted for our proposed device with several advantages of improving performance, affordability, wireless controllability, and adjustability of parameters.

IV. CONCLUSION

In conclusion, we suggest a low-cost innovative syringe infusion pump for the biomedical industry's continuous and constant flow delivery. The proposed syringe pump is intended for stationary use at the patient's bedside. The gadget maintains a constant flow. There are provisions for safety, such as the monitoring element of the system, which assists the user in avoiding hazards throughout the operating process. It can be controlled at various flow rates thanks to a microcontroller and user-friendly Android phone software. Flow rates ranging from 10 ul/min to 100 ul/min can be consistently achieved with the current technology. The flow rate characterization assesses the accuracy and example range of volume flow rates with various syringe statuses. A lead screw mechanism with a narrower pitch and stepper motors with smaller step sizes were utilized and integrated into our proposed device to achieve a lower flow rate. This proposed technique used in this study will help create a new generation of IoT-accessible syringe infusion pumps.

ACKNOWLEDGMENT

This work has been supported by VNU University of Engineering and Technology under project number CN20.43.

REFERENCES

[1] T. Heise et al., “Impact of injection speed and volume on perceived pain during subcutaneous injections into the abdomen and thigh: a single-centre, randomized controlled trial,” Diabetes, Obes. Metab., Oct. 2014, vol. 16, no. 10, pp. 971–976.

[2] P. Ewan et al., “BSACI guideline: prescribing an adrenaline auto-injector,” Clin. Exp. Allergy, Oct. 2016, vol. 46, no. 10, pp. 1258–1280.

[3] J. Yuan et al., “Can the upper inner side of the thigh become a new option for insulin injection?,” Curr. Med. Res. Opin., Jul. 2016, vol. 32, no. 7, pp. 1319–1324.

[4] C. Patte et al., “Effect of Infusion Rate and Indwelling Time on Tissue Resistance Pressure in Small-Volume Subcutaneous Infusion like in Continuous Subcutaneous Insulin Infusion,” Diabetes Technol. Ther., Apr. 2013, vol. 15, no. 4, pp. 289–294.

[5] J. Weissberg-Benchell, J. Antisdel-Lomaglio, and R. Seshadri, “Insulin Pump Therapy: A meta-analysis,” Diabetes Care, Apr. 2003, vol. 26, no. 4, pp. 1079–1087.

[6] B. W. Bode, H. T. Sabbah, T. M. Gross, L. P. Fredrickson, and P. C. Davidson, “Diabetes management in the new millennium using insulin pump therapy,” Diabetes. Metab. Res. Rev., Jan. 2002, vol. 18, no. S1, pp. S14–S20.

[7] S. Dubey, A. Gambhir, S. K. Jain, A. V. Jha, A. Jain, and S. Sharma, “IoT application for the design of digital drug administration interface,” in 2017 International Conference on Information, Communication, Instrumentation and Control (ICICIC), 2017, pp. 1–5.

[8] H. T. Thanh, L. Do Quang, B.-A. Hoang, T. T. Bui, T. C. Duc, and C.-P. Jen, “A Serpentine Microchannel with Added Cavities Platform for Magnetic Separation of Lung Adenocarcinoma Cells Utilizing Aptamer-Conjugated Magnetic Bead Approach,” in 2021 21st International Conference on Solid-State Sensors, Actuators and Microsystems (Transducers), 2021, pp. 992–995.

[9] H. Vu-Dinh et al., “Immunomagnetic separation in a novel cavity-added serpentine microchannel structure for the selective isolation of lung adenocarcinoma cells,” Biomed. Microdevices, Dec. 2021, vol. 23, no. 4, p. 51.

[10] L. Do Quang et al., “Biological Living Cell in-Flow Detection Based on Microfluidic Chip and Compact Signal Processing Circuit,” IEEE Trans. Biomed. Circuits Syst., Dec. 2020, vol. 14, no. 6, pp. 1371–1380.

[11] K.-K. Liu, R.-G. Wu, Y.-J. Chuang, H. S. Khoo, S.-H. Huang, and F.-G. Tseng, "Microfluidic Systems for Biosensing," Sensors, Jul. 2010, vol. 10, no. 7, pp. 6623–6661.

[12] L. P. Xuan et al., "Development of a microfluidic flow-focusing droplet generating device utilising rapid prototyping technique," Int. J. Nanotechnol., 2020, vol. 17, no. 7/8/9/10, p. 708.

[13] L. Do Quang, H. T. Thanh, T. V. Quoc, C. N. Nhu, and H. N. Thu, "Development of A Flow Focusing Droplet Generation Microfluidic System Based On Rapid Prototyping Technique," The 7th International Workshop on Nanotechnology and Application - IWNA 2019, no. November. pp. 327–331, 2019.

[14] M. S. Cubberley and W. A. Hess, "An inexpensive programmable dual-syringe pump for the chemistry laboratory," J. Chem. Educ., 2017, vol. 94, no. 1, pp. 72–74.

[15] X. Zhang, K. Xia, and A. Ji, "A portable plug-and-play syringe pump using passive valves for microfluidic applications," Sensors Actuators, B Chem., 2020, vol. 304, no. July 2019, p. 127331.

[16] A. Supriyanto, R. Anggriani, S. W. Suciyati, A. Surtono, Junaidi, and S. Hadi, "A Control System on the Syringe Pump Based on Arduino for Electrospinning Application," J. Phys. Sci., 2021, vol. 32, no. 1, pp. 1–12.

[17] A. Juarez et al., "AutoSyP: A Low-Cost, Low-Power Syringe Pump for Use in Low-Resource Settings," Am. J. Trop. Med. Hyg., Oct. 2016, vol. 95, no. 4, pp. 964–969.

[18] I. Saidi, L. El, A. Ounip, and M. Benrejeb, "Design of an Electrical Syringe Pump Using a Linear Tubular Step Actuator," Int. J. Sci. Tech. Autom. Control Comput. Eng. IJ-STA, 2010, vol. 4, no. 2, pp. 1388–1401.

[19] I. Mahmoud, H. Rehaoulia, and M. Ayadi, "Design and modelling of a linear switched reluctance actuator for biomedical applications," Int. J. Phys. Sci., 2011, vol. 6, no. 22, pp. 5171–5180.

[20] C. C. P. Eagle and D. F. Capes, "Use of a New Syringe Pump (Springfusor ®) for Muscle Relaxant Infusion," Anaesth. Intensive Care, Aug. 1993, vol. 21, no. 4, pp. 444–446.

The 6th International Conference on Engineering Mechanics and Automation (ICEMA 2021)
Hanoi, November 14, 2021

Dynamic stability control and calculating inverse dynamics of a single-link flexible manipulator

Nguyen Van Khang
Hanoi University of Science and Technology
Hanoi, Vietnam
khang.nguyenvan2@hust.edu.vn

Dinh Cong Dat
Hanoi University of Mining and Geology
Hanoi, Vietnam
datdc171@gmail.com

Nguyen Van Quyen
Hanoi University of Science and Technology
Hanoi, Vietnam
quyen.nguyenvan@hust.edu.vn

***Abstract*: When a robot manipulator operates at high speeds, the elastic vibration of its links is inevitable. To study this vibration phenomenon, the present paper deals with problem of modelling, the dynamic stability control and calculating inverse dynamics of a single-link flexible manipulator. An algorithm to study dynamic stability and calculating inverse dynamics of flexible manipulators is proposed. The proposed algorithm is demonstrated and verified by the model of a flexible single-link manipulatort.**

Keywords: Flexible manipulator, linearization, Taguchi method, dynamic stability, periodic system.

I. INTRODUCTION

Recently, flexible robots have been used in space technology, nuclear reactors, medical engineering, and many other fields. Flexibility, small volume, high speed, and low power consumption are advantages over rigid robots. However, the elastic displacements created by flexible links are the main cause of questions about position accuracy, structure stability and vibration. Some scientists have done research to solve those problems. However, the research results obtained are still relatively few and need to be studied further.

Bayo et al. [1] and Asada et al. [2] have proposed two different algorithms for calculating the torques required to move the end effector of flexible manipulators. A brief description about the development of stabile and vibration analysis of flexible manipulators has been depicted here. Some studies on the dynamic stability control of elastic manipulators have been presented in [3-12]. Motion control problems of flexible robots are divided into two classes: regulation and tracking control [13]. The regulation is the control problem around the desired equilibrium configuration of the robot. By the regulation $\mathbf{q}_d$ is constant, thus $\dot{\mathbf{q}}_d = \ddot{\mathbf{q}}_d = \mathbf{0}$. If the equilibrium configuration of the rigid robot is chosen as the fundamental motion, the equation for the error dynamics in first order approximation has the following form $\dot{\mathbf{x}} = \mathbf{A}\mathbf{x} + \mathbf{f}(t)$, where $\mathbf{A}$ is a constant matrix. The task of dynamic stability control is to determine the eigenvalues of the matrix **A** of flexible manipulators [3, 4, 5, 6]. In [7] Kumar and Pratiher investigated the nonlinear phenomena of dynamic responses under 3:1 internal resonance in the two-link flexible manipulator. The tracking control in the joint space consists of a given time-varying trajectory $\mathbf{q}_d(t)$ and its successive derivatives $\dot{\mathbf{q}}_d(t)$ and $\ddot{\mathbf{q}}_d(t)$ which respectively describe the desired velocity and acceleration. In this case, **A** is no longer a constant matrix, but a time-varying matrix. Several schemes for performing these objectives do exist. Note that homogeneous linear differential equations or nonlinear autonomous differential equations can be only solved numerically. Therefore, the problem of dynamic stability control for the elastic manipulators in this case is usually only calculated by a numerical simulation method [8-12].

In this study, the linearization problem of the non-linear equations governing the motion of flexible manipulators in the vicinity of the periodic fundamental motion is addressed. A procedure based-Taguchi method [14–17] is proposed for design of the control parameters of a controller PD for the system of a single-link flexible manipulator that is described by a linear differential system with time-periodic coefficients. Then the calculation of actuator torques of the flexible manipulators is presented.

II. DYNAMICS OF A SINGLE-LINK FLEXIBLE MANIPULATOR

A. Equations of motion using the floating frame of reference approach

Using the floating frame of reference approach [18], the motion equations for a single-link flexible manipulator shown in Fig. 1 are derived. As shown in the figure, a single-link flexible manipulator OE of length *l* with a rotor located at the hut and a payload at the free end. The end of the link is attached to the O point (including the motor) revolving around O-axis, and mass m_E is attached at E. The link is considered as a homogeneous beam with area A.

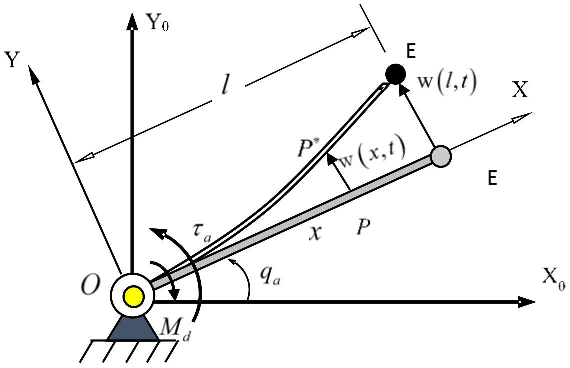

Fig. 1. Single-link flexible manipulator

To describe the kinematics, the position of point P on the flexible beam is given as

$$\begin{aligned} x_P &= x\cos q_a - w(x,t)\sin q_a \\ y_P &= x\sin q_a + w(x,t)\cos q_a \end{aligned} \tag{1}$$

Differentiation of Eq. (1) yields

$$v_P^2 = \dot{x}_P^2 + \dot{y}_P^2 = (w^2 + x^2)(\dot{q}_a)^2 + \dot{w}^2 + 2x\dot{w}\dot{q}_a \tag{2}$$

It follows that $v_E^2 = (w_E^2 + l^2)(\dot{q}_a)^2 + \dot{w}_E{}^2 + 2l\dot{w}_E\dot{q}_a$ (3)

The Euler-Bernoulli beam theory and Ritz-Galerkin method are applied to study the transverse vibration of the flexible link with assuming that the deformation in the longitudinal direction is negligibly small. Let the transverse deformation of the beam be written as

$$w(x,t) = \sum_{i=1}^{N} X_i(x)q_{ei}(t), w_E = \sum_{i=1}^{N} X_i(l)q_{ei}(t) \tag{4}$$

Where $q_{ei}(t)$ are unknown generalized coordinates of transverse deformation, $X_i(x)$ are a set of mode shapes of transverse deformation of a clamped - free beam and N is the number of modes used to describe the defection of the flexible link. The mode shapes are given as [19]

$$\begin{aligned} X_i(x) &= \cos(\beta_i x) - \cosh(\beta_i x) \\ &+ \frac{\cos\beta_i l + \cosh\beta_i l}{\sin\beta_i l + \sinh\beta_i l} - \sin(\beta_i x) + \sinh(\beta_i x) \end{aligned} \tag{5}$$

The kinetic energy of the flexible manipulator is given by

$$\begin{aligned} T &= T_1 + T_E + T_{OE} \\ &= \frac{1}{2}J_1(\dot{q}_a)^2 + \frac{1}{2}m_E v_E^2 + \frac{1}{2}\int_0^l \rho A v_P^2 dx \end{aligned} \tag{6}$$

where J_1 is the mass moment of inertia of link 1 (including the motor) with respect to the point O, m_E is the mass at point E, ρA is the mass per unit length of the beam.

Substituting Eqs. (1), (2), (3) and (5) into Eq. (6), we obtain the kinetic energy of system

$$\begin{aligned} T &= (\frac{1}{2}J_1 + \frac{1}{2}m_E l^2 + \frac{1}{6}\rho A l^3)(\dot{q}_a)^2 \\ &+ \frac{1}{2}m_E[w_E^2(\dot{q}_a)^2 + \dot{w}_E{}^2 + 2l\dot{w}_E\dot{q}_a] + \frac{1}{2}\rho A\int_0^l \dot{w}^2 dx \\ &+ \frac{1}{2}\rho A(\dot{q}_a)^2\int_0^l w^2 dx + \frac{1}{2}\rho A\dot{q}_a\int_0^l x\dot{w}dx \end{aligned} \tag{7}$$

The strain energy of the beam OE according to Reddy [20] is given by

$$\Pi_e = \frac{1}{2}EI\int_0^l \left(\frac{\partial^2 w}{\partial x^2}\right)^2 dx \tag{8}$$

where E and I is the modulus of elasticity, area moment of inertia of the beam, respectively.

Substitution of Eqs. (1), (4) and (5) into Eq. (8) yields

$$\begin{aligned} \Pi &= m_E g[l\sin q_a + \sum_{i=1}^{N} X_i(l)q_{ei}(t)\cos q_a] + \frac{m_{OE}gl\sin q_a}{2} \\ &+ \mu g\cos q_a\sum_{i=1}^{N} C_i q_{ei} + \frac{1}{2}EI\sum_{i=1}^{N}\sum_{j=1}^{N} k_{ij}^* q_{ei}q_{ej} \end{aligned} \tag{9}$$

where $C_i = \int_0^l X_i dx$; $k_{ij}^* = \int_0^l X_i'' X_j'' dx$ (10)

Lagrange equations have the following form [21]

$$\frac{d}{dt}\left(\frac{\partial T}{\partial \dot{q}_j}\right) - \frac{\partial T}{\partial q_j} = -\frac{\partial \Pi}{\partial q_j} + Q_j^* \; (j = \overline{1,n}) \tag{11}$$

where q_j are the generalized coordinates which include rigid body coordinete q_a as well elastic modal q_{ei}, and Q_j^* are generalized forces. In this paper $Q_j^* = \tau_{aj} + M_{dj}$, in which M_{dj} is damping force which has the following form

$$M_d = \alpha\dot{q}_a \tag{12}$$

By substituting Eqs. (7), (9) and (12) into Eq. (11), we obtain the equations of motion of the system as

$$\begin{aligned} &[J_1 + m_E l^2 + \frac{1}{3}\rho A l^3 + \rho A\sum_{i=1}^{N}\sum_{j=1}^{N} m_{ij}q_{ei}q_{ej} \\ &+ m_E\sum_{i=1}^{N}\sum_{j=1}^{N} X_i(l)X_j(l)q_{ei}q_{ej}]\ddot{q}_a \\ &+ [2m_E\sum_{i=1}^{N}\sum_{j=1}^{N} X_i(l)X_j(l) + 2\rho A\sum_{i=1}^{N}\sum_{j=1}^{N} m_{ij}]\dot{q}_a\dot{q}_{ei}q_{ej} \\ &+ [\rho A\sum_{i=1}^{N} D_i + m_E l\sum_{i=1}^{N} X_i(l)]\ddot{q}_{ei} \\ &= -m_E g[l\cos q_a - \sum_{i=1}^{N} X_i(l)q_{ei}\sin q_a] - \frac{m_{OE}gl\cos q_a}{2} \\ &+ \mu g\sin q_a\sum_{i=1}^{N} C_i q_{ei} + \tau - M_d \end{aligned} \tag{13}$$

$$\begin{aligned} &[m_E l X_i(l) + \rho A D_i]\ddot{q}_a + [m_E X_i(l)\sum_{j=1}^{N} X_j(l) \\ &+ \rho A\sum_{j=1}^{N} m_{ij}]\ddot{q}_{ej} + EI\sum_{j=1}^{N} k_{ij}^* q_{ej} \\ &- [m_E X_i(l)\sum_{j=1}^{N} X_j(l)q_{ej} + \rho A\sum_{j=1}^{N} m_{ij}q_{ej}]\dot{q}_a^2 \\ &= -m_E g X_i(l)\cos q_a - \mu g C_i\cos q_a \quad (i = \overline{1,N}) \end{aligned} \tag{14}$$

Where $D_i = \int_0^l xX_i dx$; $m_{ij} = \int_0^l X_i X_j dx$ (15)

If we choose N = 1 and use of symbols $q_{e1} = q_e$, the differential equations of the single-link flexible manipulator have the following form

$$[J_1+m_El^2+\frac{1}{3}\rho Al^3+(\rho Am_{11}q_e^2+m_EX_1^2(l)q_e^2)]\ddot{q}_a$$
$$+[\rho AD_1+m_ElX_1(l)]\ddot{q}_e+[2m_EX_1^2(l)+2\rho Am_{11}]\dot{q}_a\dot{q}_eq_e \tag{16}$$
$$+\frac{m_{OE}glcos q_a}{2}-\mu g\sin q_aC_1q_e$$
$$=-m_Eg[l\cos q_a-X_1(l)q_e\sin q_a]+\tau-M_d$$

$$m_EX_1^2(l)\ddot{q}_e+m_ElX_1(l)\ddot{q}_a+\rho AD_1\ddot{q}_a+\rho Am_{11}\ddot{q}_e$$
$$-m_E\dot{q}_a^2X_1^2(l)q_e-\rho A\dot{q}_a^2m_{11}q_e+EIk_{11}^{*}q_e \tag{17}$$
$$=-m_EgX_1(l)\cos q_a-\mu g\cos q_aC_1$$

B. Linearization of the motion equations about the fundamental motion

We consider now the problem of linearizing motion equations of the single-link flexible manipulator in Fig. 1 as a demonstration example.

1) The fundamental motion

The fundamental motion of the considered manipulator is the virtual rigid link motion of link OE [2]. In this rigid-link motion, the position of the point *E* on the link is given as

$$x_E^R=l\cos q_a^R(t),\quad y_E^R=l\sin q_a^R(t) \tag{18}$$

The mass moment of inertia of the virtual rigid link with respect to point O takes the form

$$J_O=\frac{1}{3}\rho Al^3+m_El^2+J_1 \tag{19}$$

Using the momentum theorem, it follows that

$$\tau_a^R(t)=M_d^R+(\frac{1}{3}\rho Al^3+m_El^2+J_1)\ddot{q}_a^R(t)$$
$$+gl(\frac{1}{2}m_{OE}+m_E)\cos q_a^R(t) \tag{20}$$

Assuming that the motion rule of the drive has the following form

$$q_a^R(t)=\frac{\pi}{2}+\frac{\pi}{2}\sin(\Omega t) \tag{21}$$

By differentiating Eq. (20) and then substituting the obtained result into Eq. (19) we have

$$\tau_a^R(t)=\alpha\frac{\pi\Omega}{2}\cos(\Omega t)$$
$$-\frac{\pi\Omega^2}{2}(\frac{1}{3}\rho Al^3+m_El^2+J_1)\sin(\Omega t) \tag{22}$$
$$+gl(\frac{1}{2}m_{OE}+m_E)\cos(\frac{\pi}{2}+\frac{\pi}{2}\sin(\Omega t))$$

From Eq. (20) the position of point *E* on the link is given as

$$x_E^R=l\cos q_a^R(t)=l\cos(\frac{\pi}{2}+\frac{\pi}{2}\sin(\Omega t))$$
$$y_E^R=l\sin q_a^R(t)=l\sin(\frac{\pi}{2}+\frac{\pi}{2}\sin(\Omega t)) \tag{23}$$

The fundamental motion of the manipulator is described by $\mathbf{q}^R(t)$ and $\boldsymbol{\tau}^R(t)$, where $\mathbf{q}^R(t)$ is the generalized coordinate of the manipulator

$$\mathbf{q}^R(t)=\begin{bmatrix}q_a^R(t) & q_e^R(t)\end{bmatrix}^T=\begin{bmatrix}q_a^R(t) & 0\end{bmatrix}^T \tag{24}$$

and $\boldsymbol{\tau}^R(t)$ is the torque

$$\boldsymbol{\tau}^R\ t\ =\begin{bmatrix}\tau_a^R & \tau_e^R\end{bmatrix}^T=\begin{bmatrix}\tau_a^R & 0\end{bmatrix}^T \tag{25}$$

In Eqs. (24) and (25) $q_e^R(t)$ denotes the elastic generalized coordinate and $\tau_e^R(t)$ the elastic torque of the virtual rigid link.

2) Linearization of the motion equations

The differential equations of the manipulator according to Eqs. (16) and (17) can be expressed in the following matrix form

$$\mathbf{M}(\mathbf{q})\ddot{\mathbf{q}}+\mathbf{C}(\mathbf{q},\dot{\mathbf{q}})\dot{\mathbf{q}}+\mathbf{g}(\mathbf{q})=\boldsymbol{\tau}(t) \tag{26}$$

where $\mathbf{q}$, $\dot{\mathbf{q}}$ and $\ddot{\mathbf{q}}$ are vectors of generalized coordinates, generalized velocity and acceleration, respectively

$$\mathbf{q}=\begin{bmatrix}q_a,q_e\end{bmatrix}^T,\boldsymbol{\tau}(t)=\begin{bmatrix}\tau_a(t),\tau_e(t)\end{bmatrix}^T=\begin{bmatrix}\tau_a(t),0\end{bmatrix}^T \tag{27}$$

Let Δq_a and Δq_e are the difference between the real motion $\mathbf{q}(t)$ and the fundamental motion $\mathbf{q}^R(t)$, it follows that

$$q_a(t)=q_a^R(t)+\Delta q_a(t)=q_a^R(t)+y_1(t) \tag{28}$$

$$q_e(t)=q_e^R(t)+\Delta q_e(t)=y_2(t) \tag{29}$$

where y_1 and y_2 are called the additional motion or the perturbed motion. Similarly, we have

$$\boldsymbol{\tau}(t)=\begin{bmatrix}\tau_a(t),\tau_e(t)\end{bmatrix}^T=\begin{bmatrix}\tau_a(t),0\end{bmatrix}^T \tag{30}$$

By substituting Eqs. (28), (29) into Eq. (24) and using Taylor series expansion around the fundamental motion, then neglecting nonlinear terms, we obtain a system of linear differential equations with time-varying coefficients for the manipulator as follows [22]

$$\mathbf{M}_L(t)\ddot{\mathbf{y}}+\mathbf{C}_L(t)\dot{\mathbf{y}}+\mathbf{K}_L(t)\mathbf{y}=\mathbf{h}_L(t) \tag{31}$$

Matrices $\mathbf{M}_L(t)$, $\mathbf{C}_L(t)$, $\mathbf{K}_L(t)$ and vector $\mathbf{h}_L(t)$ in Eq. (31) have the following forms

$$\mathbf{M}_L(t)=\left[\begin{array}{c:c}J_1+m_El^2 & \rho AD_1\\ +\frac{1}{3}m_{OE}l^2 & +m_ElX_1(l)\\ \hdashline m_ElX_1 & m_EX_1^2(l)\\ +\rho AD_1 & +\rho Am_{11}\end{array}\right] \tag{32}$$

$$\mathbf{C}_L(t)=\begin{bmatrix}\alpha & 0\\ 0 & 0\end{bmatrix} \tag{33}$$

$$\mathbf{K}_L(t)=\begin{bmatrix}k_{11} & k_{12}\\ k_{21} & k_{22}\end{bmatrix} \tag{34}$$

where

$$k_{11}=-l\sin q_a^R(t)m_Eg-\frac{m_{OE}gl\sin q_a^R(t)}{2},$$
$$k_{12}=k_{21}=-m_EgX_1(l)\sin q_a^R(t)-\mu g\sin q_a^R(t)C_1,$$
$$k_{22}=-m_E[\dot{q}_a^R(t)]^2X_1^2(l)-\rho A[\dot{q}_a^R(t)]^2m_{11}+EIk_{11}^{*}.$$

and $$\mathbf{h}_L(t)=\begin{bmatrix}0\\ -m_EgX_1(l)\cos q_a^R(t)-\mu g\cos q_a^R(t)C_1\\ -m_ElX_1\ddot{q}_a^R(t)-\rho AD_1\ddot{q}_a^R(t)\end{bmatrix} \tag{35}$$

where fundamental motion $q_a^R(t)$ is given by Eq. (21) and constants $C_1, D_1, X_1, m_{11}, k_{11}^{*}$ are determined by Eqs. (5), (10) and (15). It should be noted that matrices

$\mathbf{M}_L(t)$, $\mathbf{C}_L(t)$, $\mathbf{K}_L(t)$ and vector $\mathbf{h}_L(t)$ in this example are time-periodic with least period *T*. For numerical simulation, the calculating parameters of the considered manipulator are listed in Tab. I.

TABLE I. PARAMETERS OF THE MANIPULATOR

Parameters of the model	Variable and unit	Value
Length of link	$l\ m$	0.9
Sectional area of beam	$A(m^2)$	$4\cdot 10^{-4}$
Density of beam	$\rho\left(\frac{kg}{m^3}\right)$	2710
Inertial moment of sectional area of beam	$I(m^4)=\frac{bh^3}{12}$	$1.33333\cdot 10^{-8}$
Modulus	$E\left(\frac{N}{m^2}\right)$	7.11×10^{10}
Mass moment of inertia of link 1 (including the motor)	$J_1\ kg.m^2$	5.86×10^{-5}
Mass of payload	$m_E\ kg$	0.1
Drag coefficient	$\alpha\left(\frac{N.m.s}{rad}\right)$	0.01

It follows from the parameters in Tab. 1 that

$$C_1=-0.7046317896,\ D_1=-0.4607100845,$$
$$m_{11}=0.8998501520,\ k_{11}^*=16.95515100,\ X_1=-2\,.$$

III. DYNAMIC STABILITY CONTROL OF A FLEXIBLE MANIPULATOR USING THE FLOQUET THEORY

In the steady of a flexible manipulator, the matrices $\mathbf{M}_L(t)$, $\mathbf{C}_L(t)$, $\mathbf{K}_L(t)$ and vector $\mathbf{h}_L(t)$ of the linear differential equations (31) are time-periodic with the least period $T=2\pi/\Omega$. For calculation of dynamic stability condition, we shall consider a system of homogeneous linear differential equations

$$\mathbf{M}_L(t)\ddot{\mathbf{y}}+\mathbf{C}_L(t)\dot{\mathbf{y}}+\mathbf{K}_L(t)\mathbf{y}=0 \tag{36}$$

According to Floquet theory [23], the characteristic equation of Eq. (36) is independent of the chosen fundamental set of solutions. From characteristic equation of Eq. (36) we can calculate the Floquet multipliers $\rho_k(k=1,...,n)$. If $\left|\rho_k\right|<1$, the trivial solution $\mathbf{y}=0$ of Eq. (36) will be asymptotically stable. Conversely, the solution $\mathbf{y}=0$ of Eq. (36) becommes unstable if at least one Floquet multiplier has modulus being larger than 1. In this case we need to design the controller for stabilization the motion of flexible manipulator.

A. The PD controller

It should be noted that the PD controller applied on the input link can be selected according to the formula

$$\Delta\tau_a=-k_{d1}(\dot{q}_{\mathbf{a}}-\dot{q}_{\mathbf{a}}^R)-k_{p1}(q_{\mathbf{a}}-q_{\mathbf{a}}^R)=-k_{d1}\dot{y}_1-k_{p1}y_1 \tag{37}$$

The linearized equation according to Eq. (31) now takes the form

$$\mathbf{M}_L(t)\ddot{\mathbf{y}}+\mathbf{C}_L(t)\dot{\mathbf{y}}+\mathbf{K}_L(t)\mathbf{y}=\mathbf{h}_L(t)-\mathbf{K}_D\dot{\mathbf{y}}-\mathbf{K}_P\mathbf{y} \tag{38}$$

Where $\mathbf{K}_D$ and $\mathbf{K}_P$ are diagonal matrices with positive elements as

$$\mathbf{K}_D=\begin{bmatrix}k_{d_1} & 0\\ 0 & 0\end{bmatrix};\ \mathbf{K}_P=\begin{bmatrix}k_{p_1} & 0\\ 0 & 0\end{bmatrix} \tag{39}$$

It follows from Eqs. (38) that

$$\mathbf{M}_L(t)\ddot{\mathbf{y}}+[\mathbf{C}_L(t)+\mathbf{K}_D]\dot{\mathbf{y}}+[\mathbf{K}_L(t)+\mathbf{K}_P]\mathbf{y}=\mathbf{h}_L(t) \tag{40}$$

Eq. (40) can then be written in the form

$$\mathbf{M}_L^1(t)\ddot{\mathbf{y}}+\mathbf{C}_L^1(t)\dot{\mathbf{y}}+\mathbf{K}_L^1(t)\mathbf{y}=\mathbf{h}_L^1(t) \tag{41}$$

$$\text{Where}\ \begin{array}{l}\mathbf{M}_L^1(t)=\mathbf{M}_L(t),\mathbf{K}_L^1(t)=\mathbf{K}_L(t)+\mathbf{K}_P\\ \mathbf{C}_L^1(t)=\mathbf{C}_L(t)+\mathbf{K}_D,\mathbf{h}_L^1(t)=\mathbf{h}_L(t)\end{array} \tag{42}$$

Eq. (41) can then be expressed in the compact form as

$$\dot{\mathbf{x}}=\mathbf{P}\ t\ \mathbf{x}+\mathbf{f}(t) \tag{43}$$

where we use the state variable **x:**

$$\mathbf{x}=\left[\mathbf{y}^T,\dot{\mathbf{y}}^T\right]^T,\dot{\mathbf{x}}=\left[\dot{\mathbf{y}}^T,\ddot{\mathbf{y}}^T\right]^T \tag{44}$$

and the matrix of coefficients **P**(*t*), vector **f**(*t*) are defined by

$$\mathbf{P}(t)=\begin{bmatrix}\mathbf{0} & \mathbf{E}\\ -\mathbf{M}_L^{-1}\mathbf{K}_L^{(1)} & -\mathbf{M}_L^{-1}\mathbf{C}_L^{(1)}\end{bmatrix},\mathbf{f}\ t\ =\begin{bmatrix}\mathbf{0}\\ \mathbf{M}_L^{-1}\mathbf{h}_L^{(1)}\end{bmatrix} \tag{45}$$

To study the dynamic stability conditions of the manipulators, the properties of the homogeneous linear differential system corresponding to Eq. (43) is now considered

$$\dot{\mathbf{x}}=\mathbf{P}\ t\ \mathbf{x} \tag{46}$$

where $\mathbf{P}\ t$ is a matrix of periodic elements with period *T*. Based on the stable criteria according to the Floquet multipliers [23], the gain values of the PD controller in Eq. (37) are chosen so that all Floquet multipliers of Eq. (46) have negative real parts and the transient oscillation time is as short as possible.

B. A procedure for determination of gain values according to Floquet multipliers using the Taguchi method

Taguchi developed the orthogonal array method to study the systems in more convenient and rapid way, whose performance is affected by different factors when the system study become more complicated with increase in the number of factors [14-17]. This method can be used to select best results by optimization of parameters with a minimum number of test runs. We note that Taguchi method has the following advantages: It is not necessary to use the derivative of the target function to calculate optimal parameters, and the method allows the determination of multiple stable parameters for the linear differential systems with time-periodic coefficients of complex structures.

In this section we present a procedure for determining the control parameters of the flexible manipulator shown in Fig. 1. This section presents an algorithm based on the Taguchi method to optimally design the gain values of the PD controller. It should be noted that the gain values of the PD controller in this paper are called the control parameters.

Step 1: Selection of control parameters and initial levels of control parameters

The gain values of the PD controller are chosen as components of the vector of control parameters which has the following form

$$\mathbf{x} = \begin{bmatrix} x_1 & x_2 \end{bmatrix}^T = \begin{bmatrix} k_{p1} & k_{d1} \end{bmatrix}^T \tag{47}$$

The initial three levels of each control parameter are chosen at random as shown in Tab. II.

TABLE II. CONTROL PARAMETERS AND INITIAL LEVELS OF EACH CONTROL PARAMETER

Levels	Control parameters	
	kp1	***kd1***
1	1	0.5
2	5	7
3	25	26

Step 2: Calculation of Floquet multipliers and selection of target function

The Floquet multipliers of Eq. (46) are calculated to the algorithms in [24] and can be arranged in a vector as follows

$$\rho = [\rho_1 \quad \rho_2 \quad \rho_3 \quad \rho_4]^T \tag{48}$$

Step 3: Selection of orthogonal array and calculation of signal-to noise ratio (SNR)

Three levels of each control parameter are applied, necessitating the use of an L9 orthogonal array [16, 17]. Coding stage 1, stage 2, stage 3 of the control parameters are the symbols 1, 2, 3. The signal-to noise ratio (SNR) of control parameter $\mathbf{x}$ is evaluated using the following formula [16, 17]

$$\eta_j = (\mathrm{SNR})_j = -10\log_{10}\left(\left|\rho_{\max}\right|_j - \rho_d\right)^2, \quad j = \overline{1,9} \tag{49}$$

where $\left|\rho_{\max}\right|_j$ is the biggest modulus of Floquet multipliers in the j^{th} experiment, and ρ_d is desired value of the target function. The desired value of the target function is usually chosen empirically. In this example we choose $\rho_d = 0.3$. The obtained results are shown in Tab. III.

TABLE III. EXPERIMENTAL DESIGN USING L9 ORTHOGONAL ARRAY

Trial (j)	Control parameters			Results
	kp1	***kd1***	$\lvert\rho\rvert_{\max}$	SNR
1	1	1	4.0561	-11.4948
2	1	2	1.2233	0.6930
3	1	3	1.0570	2.4184
4	2	1	0.4767	15.0542
5	2	2	0.6879	8.2258
6	2	3	0.9062	4.3473
7	3	1	0.4802	14.8872
8	3	2	0.0181	10.9991
9	3	3	0.4158	18.7229

Step 4: Analysis of signal-to-noise ratio (SNR)

Using the values of SNR of control parameters in the Tab. 3, we can calculate the mean value of the SNR of control parameters corresponding to the levels 1, 2, 3

$$SNR(k_{p1}^1) = [SNR(1) + SNR(2) + SNR(3)]/3 = -2.79447$$

$$SNR(k_{p1}^2) = [SNR(4) + SNR(5) + SNR(6)]/3 = 9.2091$$

$$SNR(k_{p1}^3) = [SNR(7) + SNR(8) + SNR(9)]/3 = 14.86973$$

$$SNR(k_{d1}^1) = [SNR(1) + SNR(4) + SNR(7)]/3 = 6.148867$$

$$SNR(k_{d1}^2) = [SNR(2) + SNR(5) + SNR(8)]/3 = 6.6393$$

$$SNR(k_{d1}^3) = [SNR(3) + SNR(6) + SNR(9)]/3 = 8.4962$$

In which $SNR(k_{p1}^1), SNR(k_{p1}^2), SNR(k_{p1}^3)$, $SNR(k_{d1}^1), SNR(k_{d1}^2), SNR(k_{d1}^3)$ are the mean square deviation of the control parameters $k_{p1}^1, k_{p1}^2, k_{p1}^3, k_{d1}^1, k_{d1}^2, k_{d1}^3$ at the levels 1, 2, 3, respectively. Then the SNR of the control parameters can be plotted to use for optimization of seat displacement as shown in Fig. 2

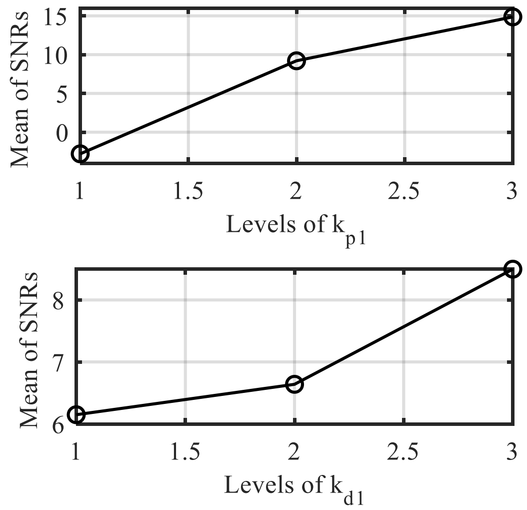

Fig. 2. Diagram of level distribution of mean signal-to-noise ratio of the control parameters

From Fig. 2, the optimal signal-to-noise ratio of the control parameters can be derived as follows

$$\begin{aligned} SNR\left(k_{p1}\right) &= 14.86973, \\ SNR\left(k_{d1}\right) &= 8.4962 \end{aligned} \tag{50}$$

Step 5: Selection of new levels for control parameters

From Eq. (50) it can be seen that the optimal SNR of the control parameters is different. This makes it easy to perform iterative calculation. Firstly, new levels for control parameters are selected. Based on the level distribution diagram of the parameter in Fig. 2, we choose the new levels of control parameters as follows: The optimal parameters are levels with the largest value of the parameters, namely, k_{p1} level 3, k_{d1} level 3. Therefore, we have the values of the new levels as follows:

If level 1 is optimal then the next levels are

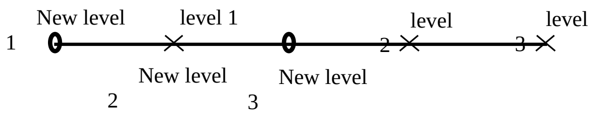

$$\begin{cases} \text{level 2\_new} = \text{level 1\_old} \\ \text{level 1\_new} = \text{level 1\_old} - \dfrac{\text{level 2\_old} - \text{level 1\_old}}{2} \\ \text{level 3\_new} = \text{level 1\_old} + \dfrac{\text{level 2\_old} - \text{level 1\_old}}{2} \end{cases}$$

If level 2 is optimal then the next levels are

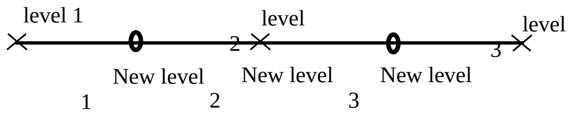

$$\begin{cases} \text{level 2\_new} = \text{level 2\_old} \\ \text{level 1\_new} = \text{level 2\_old} - \dfrac{\text{level 2\_old} - \text{level 1\_old}}{2} \\ \text{level 3\_new} = \text{level 2\_old} + \dfrac{\text{level 3\_old} - \text{level 2\_old}}{2} \end{cases}$$

If level 3 is optimal then the next levels are

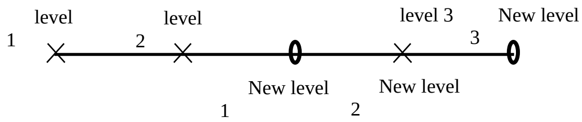

$$\begin{cases} \text{level 2\_new} = \text{level 3\_old} \\ \text{level 1\_new} = \text{level 3\_old} - \dfrac{\text{level 3\_old} - \text{level 2\_old}}{2} \\ \text{level 3\_new} = \text{level 3\_old} + \dfrac{\text{level 3\_old} - \text{level 2\_old}}{2} \end{cases}$$

According to the rule presented above, we have the new levels of control parameters in Tab. IV.

TABLE IV. CONTROL FACTORS AND NEW LEVELS OF CONTROL PARAMETERS

Levels	**Control parameters**	
	kp1	***kd1***
1	15	16.5
2	25	26
3	35	35

Then the analysis of signal-to-noise ratio is performed as the step 2.

Step 6: Check the convergence condition of the signal-to-noise ratio and determine the optimal control parameters

After 60 iterations, we obtain the optimal noise values of the control parameters with the results listed in Tab. V.

TABLE V. SNR VALUES OF THE CONTROL PARAMETERS AND ANOM AND ANOVA IN THE ROW OF THE SNR

Trial	**Calculation Results**			
	SNR (kp1)	***SNR (kd1)***	***Mean***	***Variance***
1	14.8697	8.4962	11.68295	10.15538
2	23.1742	20.9025	22.03835	1.290155
3	27.3572	28.9904	28.1738	0.666836
4	33.4549	34.104	33.77945	0.105333
5	44.2991	47.0856	45.69235	1.941146
…	…	…	…	…
56	274.9553	274.9553	274.9553	0
57	274.9553	274.9553	274.9553	0
58	274.9553	274.9553	274.9553	0
59	274.9553	274.9553	274.9553	0
60	274.9553	274.9553	274.9553	0

To determine the mean and variance of SNR we use the following formulas

$$Mean = \frac{SNR(k_{p1}) + SNR(k_{d1})}{2} \tag{51}$$

$$Variance = 0.5 \cdot \begin{pmatrix} \left[SNR(k_{p1}) \text{ - } Mean\right]^2 \\ +\left[SNR(k_{d1}) \text{ - } Mean\right]^2 \end{pmatrix} \tag{52}$$

According to the above analysis, we obtain the optimal parameters of after 60 iterations.

The optimal control parameters are given as follows:

$$k_{p1} = 37.1617, k_{d1} = 29.241 \tag{53}$$

Using these values, it is easy to find the optimal Floquet multipliers of Eq. (46): $\rho_1 = 0.3, \rho_2 = \rho_3 = \rho_4$ (54)

C. *Determine control parameters in a number of common speed ranges*

We choose the desired motion rule of the active links such as Eq. (21)

$$q_a(t) = \pi/2 + \pi/2 \sin(\Omega t) \tag{55}$$

Using the algorithm presented in paragraph 3.2, we can determine the control parameters corresponding to some popular speed ranges as follows table:

TABLE VI. CONTROL PARAMETERS IN SEVERAL SPEED RANGES

Ω	2π	4π	6π	8π
kp₁	37.1617	28.7617	22.2666	23.0147
kd₁	29.241	11.7501	6.7208	6.8628
Ω	10π	12π	14π	
kp₁	20.1903	15.0579	33.0861	
kd₁	5.4368	3.7542	4.4094	

IV. APPROXIMATE CALCULATION OF INVERSE DYNAMICS OF FLEXIBLE MANIPULATOR

In previous section, the stability analysis of the flexible manipulator has been studied. In this section an approximate method for calculation of inverse dynamics of flexible manipulator is proposed.

A. *Calculating periodic oscillation of a flexible manipulator*

The linearized differential equations of motion of the single - link flexible manipulator have the following form

$$\mathbf{M}_L^{(1)}(t)\ddot{\mathbf{y}} + \mathbf{C}_L^{(1)}(t)\dot{\mathbf{y}} + \mathbf{K}_L^{(1)}(t)\mathbf{y} = \mathbf{h}_L^{(1)}(t) \tag{56}$$

As known in the theory of linear differential equations [23] when the system of homogeneous linear differential equations is asymptotically stable, then the system of differential equations having the right side (56) has periodic solution. Using the algorithm proposed by Khang et al. in

[24], the periodic oscillation of the system of equations (56) can be calculated in the following form

$$\mathbf{y}^{*} = \begin{bmatrix} \mathbf{y}_1^{*} & \mathbf{y}_2^{*} \end{bmatrix} \tag{57}$$

When the parameters $\mathbf{K}_P$ and $\mathbf{K}_D$ are chosen so that the system of homogeneous linear differential equations is asymptotically stable is stable quickly, the solution of equation (56) has the form $\mathbf{y} \approx \mathbf{y}^{*}$. (58)

Using the control parameters in Table VI, some simulation results of solutions of Eq. (51) are shown in Figs 3-5.

Case 1: $\Omega = 2\pi$

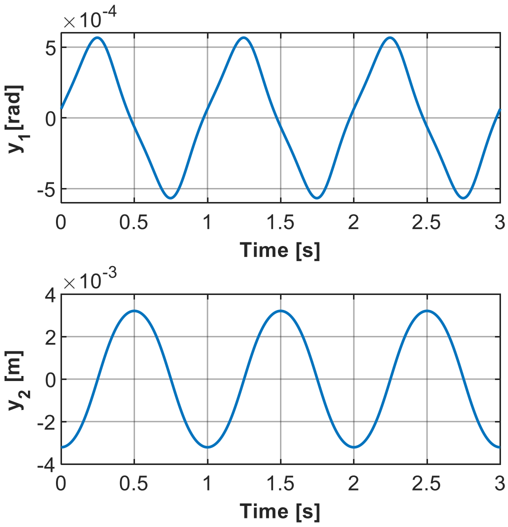

Fig. 3. Periodic vibrations of perturbed motions by $\Omega = 2\pi$

Case 2: $\Omega = 6\pi$

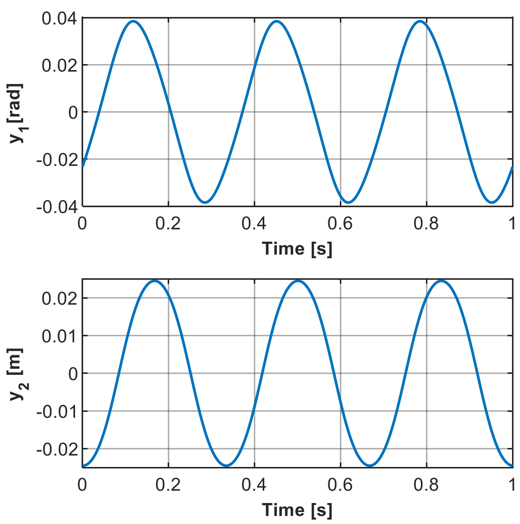

Fig. 4. Figure 4. Periodic vibrations of perturbed motions by $\Omega = 6\pi$

Case 3: $\Omega = 10\pi$

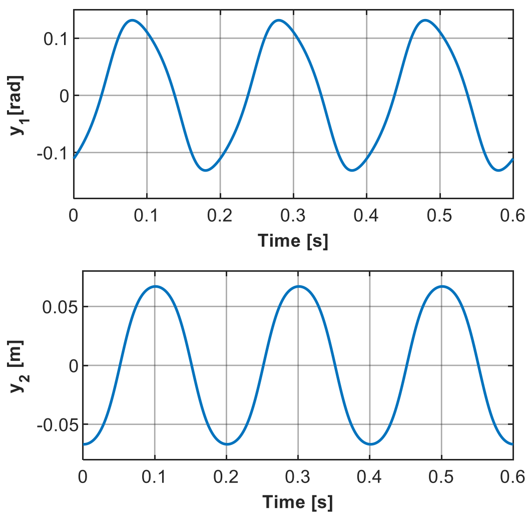

Fig. 5. Periodic vibrations of perturbed motions by $\Omega = 10\pi$

From perturbed motions $\mathbf{y}$, we call determine the generalized coordinats, velocities and accelerations of flexible manipulator

$$\begin{aligned} q_{ai}(t) &\approx q_{ai}^{R}(t) + y_i(t), \quad i = 1,\ldots,n \\ q_{ej}(t) &= y_{n+j}(j = 1,\ldots,m) \end{aligned} \tag{59}$$

B. Determining the motion of the operating point E

From the periodic oscillation calculated above, we can find the elastic displacement of the elastic beam *OE*

$$w(x,t) = X_1(x) y_2(t). \tag{60}$$

From Eq. (60) we have the elastic displacement from point E

$$w(l,t) = X_1(l) y_2(t). \tag{61}$$

Then the position of the point E is given as

$$x_E(t) = l\cos(q_a^R + y_1) - w(l,t)\sin(q_a^R + y_1) \tag{62}$$

$$y_E(t) = l\sin(q_a^R + y_1) + w(l,t)\cos(q_a^R + y_1) \tag{63}$$

From there the position error of the point E is determined by the following formula

$$d_e = \sqrt{(x_E - x_E^R)^2 + (y_E - y_E^R)^2} \tag{64}$$

Using the control parameters in Table VI, some simulation results of the position of point E are shown in Figs 6-8.

Case 1: $\Omega = 2\pi$

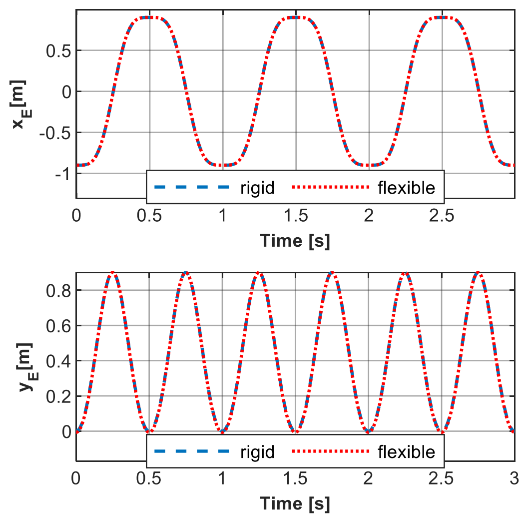

Fig. 6. Motion graph of operating point E by $\Omega = 2\pi$

Case 2: $\Omega = 6\pi$

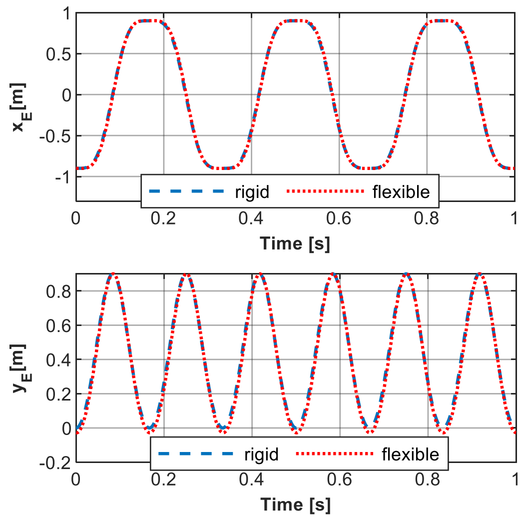

Fig. 7. Motion graph of operating point E by $\Omega = 6\pi$

Case 3: $\Omega = 10\pi$

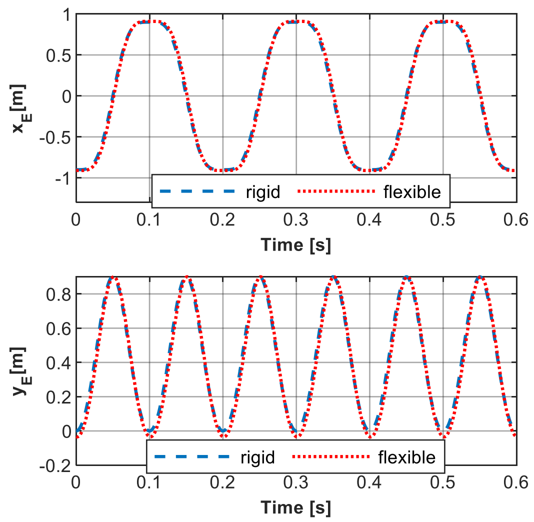

Fig. 8. Motion graph of operating point E by $\Omega = 10\pi$

C. Calculating inverse dynamics of flexible manipulator

By substituting Eqs. (60) - (63) into Eq. (16) it get the actuator torque of a single-link flexible manipulator

$$\begin{aligned}\tau = M_d &+ \left[\begin{matrix} J_1 + m_E l^2 + \frac{1}{3}\rho A l^3 \\ +(\rho A m_{11} q_e^2 + m_E X_1^2(l) q_e^2) \end{matrix}\right] \ddot{q}_a \\ &+ \left[\rho A D_1 + m_E l X_1(l)\right] \ddot{q}_e \\ &+ \left[\begin{matrix} [2m_E X_1^2(l) + 2\rho A m_{11}]\dot{q}_a \dot{q}_e q_e \\ + \frac{m_{OE} g l \cos q_a}{2} - \mu g \sin q_a C_1 q_e \\ + m_E g[l \cos q_a - X_1(l) q_e \sin q_a \end{matrix}\right]\end{aligned} \tag{65}$$

The actuator torque of rigid system $\tau_a^R(t)$ is given as Eq. (22)

Using the control parameters in Table VI, some calculation results of actuator torque are shown in Figs 9-10.

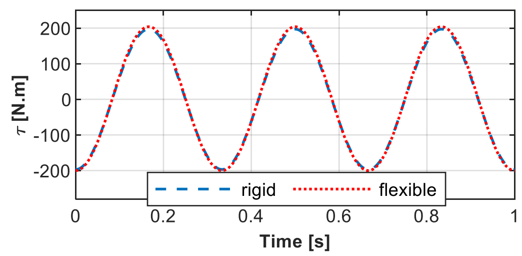

Fig. 9. Actuator torque by $\Omega = 6\pi$

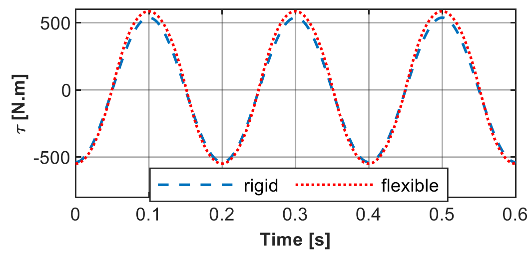

Fig. 10. Actuator torque by $\Omega = 10\pi$

V. Conclusions

In the present paper, the linearization problem of the equation of motion of flexible manipulators in the vicinity of a fundamental motion is addressed. Using the Floquet theory, the dynamic stability control of a single-link flexible manipulator has been investigated. Based on Taguchi method, the stability gain values of the controller PD at the independent joint of a single-link flexible manipulator were presented. An approach to calculate inverse dynamics of flexible manipulators has been presented.

Through numerical simulation, the efficiency and usefulness of the proposed algorithm were demonstrated as well. It is believed that the results of this study can be extended to flexible multi-link manipulators, and thus, can be of great importance for slewing space structures where the transported object is sensitive to vibrations.

ACKNOWLEDGMENTS

This paper was completed with the financial support of the Vietnam National Foundation for Science and Technology Development (NAFOSTED) under grant number 107.04-2020.28

CONFLICT OF INTEREST

The author(s) declared no potential conflicts of interest with respect to the research, authorship, and publication of this article.

REFERENCES

[1] E. Bayo, P. Papadopoulos, J. Stubbe, M.A. Serna, "Inverse dynamics and kinematics of multi-link elastic robots: An iterative frequency domain approach," The International Journal of Robotics Research, vol. 8, iss. 6, pp. 49-62, 1989.

[2] H. Asada , Z-D. Ma, and H. Tokumaru, "Inverse dynamics of flexible robot arms: Modeling and computation for trajectory control," ASME Journal of Dynamic Systems, Measurement, and Control, vol. 112, iss. 2, 177-185, 1990.

[3] B. C. Chiou, and M. Shahinpoor, "Dynamic stability analysis of a two-link force-controlled flexible manipulator," ASME Journal of Dynamic Systems, Measurement, and Control, vol. 112, iss. 4, pp. 661-666, 1990.

[4] N. Popplewell, and Daqing Chang, "Influence of an off-set payload on a flexible manipulator," Journal of sound and vibration, vol. 190, no. 4 , pp. 721-725, 1996.

[5] M. P. Coleman, "Vibration eigenfrequency analysis of a single-link flexible manipulator," Journal of sound and vibration, vol. 212, no. 1, pp. 109-120, 1998.

[6] Degao Li, Jean W. Zu, and Andrew A. Goldenberg, "Dynamic modeling and mode analysis of flexible-link, flexible-joint robots," Mechanism and machine Theory, vol. 33, no. 7, pp. 1031-1044, 1998.

[7] Pravesh Kumar and Barun Pratiher, "Modal characterization with nonlinear behaviors of a two-link flexible manipulator," Archive of Applied Mechanics, vol. 89, no. 7, pp. 1201-1220, 2019.

[8] Ahmet S. Yigit, "On the stability of PD control for a two-link rigid-flexible manipulator," ASME Journal of Dynamic Systems, Measurement, and Control, vol. 116, pp. 208-216, 1994.

[9] S. Choura, and A. S. Yigit, "Control of a two-link rigid–flexible manipulator with a moving payload mass," Journal of Sound and vibration, vol. 243, no. 5, pp. 883-897, 2001.

[10] Atef A. Ata, Waleed F. Fares, and Mohamed Y. Sa'adeh, "Dynamic analysis of a two-link flexible manipulator subject to different sets of conditions," Procedia Engineering, vol. 41, pp. 1253-1260, 2012.

[11] Wei Ding and Yunian Shen, "Analysis of transient deformation response for flexible robotic manipulator using assumed mode method," In 2017 2nd Asia-Pacific Conference on Intelligent Robot Systems (ACIRS) (pp. 331-335). IEEE.

[12] Xinxin Yang, Shuzhi Sam Ge, and Wei He, "Dynamic modelling and adaptive robust tracking control of a space robot with two-link flexible manipulators under unknown disturbances," International Journal of Control, vol. 91, no. 4, pp. 969-988, 2018.

[13] C. C. de Wit, B. Siciliano, G. Bastin (Eds.), Theory of robot control. Springer Science & Business Media, 2012.

[14] R. K. Roy, A primer on the Taguchi method. Society of Manufacturing Engineers, 2010.

[15] G. Taguchi, S. Chowdhury, Y. Wu, Taguchi's quality engineering handbook. John Wiley & Sons, New Jersey, 2005.

[16] R. A. Zambanini, The application of Taguchi's method of parameter design to the design of mechanical systems. Master Thesis, Lehigh University, 1992.

[17] N.V. Khang, , N.T.V. Huong, N.D.T. Dinh, V. D. Phuc, "Optimal control of vibration by multiple tuned liquid dampers using Taguchi method," Journal of Mechanical Science and Technology, vol. 33, iss. 4, pp. 1563-1572, 2019.

[18] A. A. Shabana, "Flexible multibody dynamics: review of past and recent developments," Multibody system dynamics, vol. 1, no. 2, pp. 189-222, 1997.

[19] D. J. Inman, Engineering vibration (Second Edition). Englewood Cliffs, NJ: Prentice Hall, 2001.

[20] J.N. Reddy, Energy principles and variational methods in applied mechanics. John Wiley & Sons, New Jersey, 2002.

[21] J.G. De Jalon and E. Bayo, Kinematic and dynamic simulation of multibody systems: the real-time challenge. Springer, 2012.

[22] N. V. Khang, N.P. Dien, H.M. Cuong, "Linearization and parametric vibration analysis of some applied problems in multibody systems," Multibody System Dynamics, vol. 22, no. 2, pp. 163-180, 2009.

[23] B. P. Demidovich, Lectures on the Mathematical Stability Theory (in Rusian). Nauka, Moscow, 1967.

[24] N.V.Khang and N.P. Dien, "Parametric vibration analysis of transmission mechanisms using numerical methods," In: Advances in Vibration Engineering and Structural Dynamics, pp. 301-331, 2012.

The 6th International Conference on
Engineering Mechanics and Automation (ICEMA 2021)
Hanoi, November 14, 2021

Fitting Models to Crack Coordinate Data Using Change Detection

Cong Hieu Le
Faculty of Engineering Mechanics and Automation
VNU University of Engineering and Technology
Hanoi, Vietnam
18020508@vnu.edu.vn

Tran Hiep Dinh*
Faculty of Engineering Mechanics and Automation
VNU University of Engineering and Technology
Hanoi, Vietnam
*Corresponding author, email: tranhiep.dinh@vnu.edu.vn

***Abstract*: This paper deals with the curve fitting problem and its application in crack detection. Due to the variety of real-world crack, modeling the propagation path is a challenging issue. To take this problem, a modeling method based on simulated crack and model fitting is proposed. First, a dataset of simulated crack is generated based on fracture mechanics and interfacing Abaqus and MATLAB. For each simulated crack, available regression models in Python are employed to approximate the development path. The resulting models are then utilized to approximate segments of real-world crack obtained from some reputable datasets. A similarity-based approach is proposed to predict the crack segments. Experimental results have shown a high correlation between the simulated crack and the real one.**

Keywords: crack detection, machine learning, change detection, image processing

I. Introduction

Vision-based crack detection has recently drawn great attention from research groups in automation and computer science [1-2]. Crack detection approaches, in general, can be divided into low-level feature based [3-4], machine learning-based [5-6], and deep learning-based [7-8] techniques. Although promising results have been achieved in all three groups, the data collection process is still a high risk, time consuming, and costly task. For deep learning-based approaches, this problem is even more critical, as the detection result is reliant on the quantity and quality of the training data.

To aid with this matter, simulated crack can be an important alternative, where a non-limited training samples can be generated and the development path of which is also similar to the real-world crack. However, there is a huge difference in terms of data points representing the simulated crack and the real-world ones. While the number of crack coordinates are dependent on the fracture mechanics theory, that of the real-world ones are based on the resolution of the digital camera in used. Here, we propose an approach to approximate real-world crack by dividing it into segments for fitting models of simulated crack. For a successful segmentation of crack from images, an accurate change detection algorithm is required to find turning points of the interested crack.

As discussed in [9], the goal of the change detection algorithm is to detect “significant” changes while rejecting “unimportant” ones. This process requires a detailed modeling of all types of changes (significant and non-critical) and can be categorized into simple differencing, significance and hypothesis tests, or predictive models. For instance, color and texture-based spatial information is employed in [10] to describe local information while preserving lighting variation, including shadows. This approach relies on a pixel level feedback scheme that automatically adjusts internal sensitivity for scale changes and updates. The approach is, however, sensitive to noise and can be impacted by the size of the input data due to its processing mechanism at pixel level.

This work studies the effectiveness of two change-detection-based methods for fitting models to crack coordinate data: one is developed based on the derivative of segment direction and another one is based on the similarity between the simulated and the actual data. The contributions of this paper are summarized as follows:

(i) an approach for fitting models to crack coordinate data using change detection, and

(ii) comprehensive experiments on 5 reputable datasets for performance evaluation of the participated methods.

The rest of the paper is structured as follows: Section III presents the utilized datasets, one is obtained from fracture mechanics-based simulation and the rest are crack images captured by digital cameras.

II. Datasets

In this section, one simulated and five real-world crack image datasets are introduced, the details of which are as follows:

- *SimulatedCrack*: the dataset consists of 797 crack paths on a concrete beam, generated via a developed interface between Abaqus and MATLAB. Simulations are processed in Abaqus, the inputs of which are continuously fed from MATLAB by automatically changing the simulation parameters. The crack paths are obtained in the form of the crack tip coordinates.
- *CrackTree260* [11]: the dataset contains 260 road crack images of size 512x512.
- *CRKWH100* [12]: the dataset consists of 100 road pavement images of size 512x512.
- *Stone331* [12]: the dataset contains 331 images of stone surface, where crack occurs via cutting the

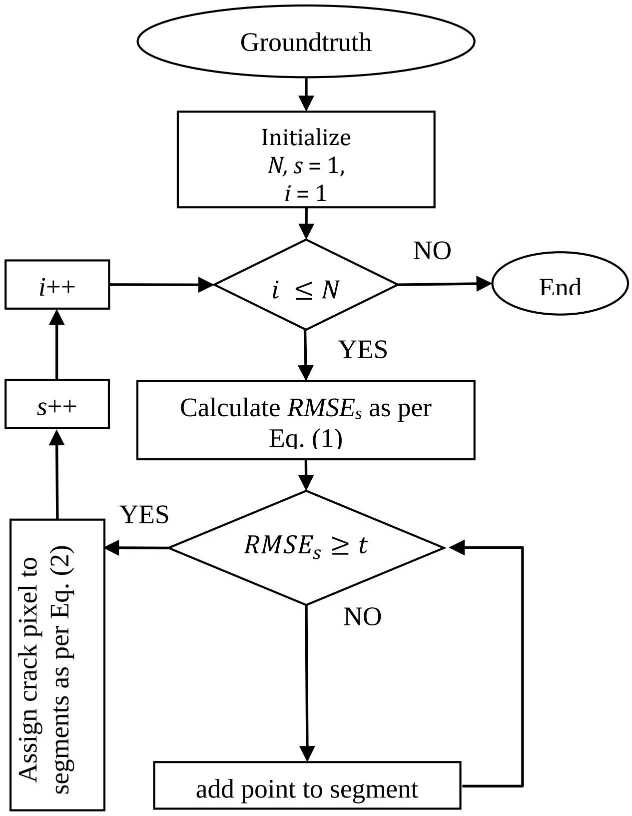

Figure 1. Flowchart of the proposed SA.

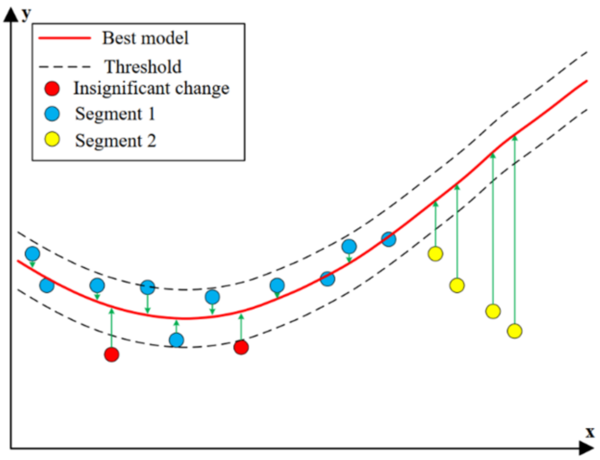

Figure 2. An example of insignificant changes

stone. The size of each image in the dataset is 512x512.

- *CFD* [13]: the dataset contains 118 images of size 480x320 reflecting urban road surface.
- *Crack500* [14]: the dataset contains 1896 images of pavement crack, the size of which is around 2000x1500.

Out of 5 real-world crack image datasets, CrackTree260, CRKWH100, and Stone331 are captured using an area-/line-array camera, while CFD and Crack500 are captured using a mobile phone camera. Existing regression models in Python 3.8.8 are employed to approximate the crack paths of the SimulatedCrack dataset. The result of the process is 25 Models x 797 Simulated Crack paths, denoted as MSC, which will be used for performance assessment of the analyzed change detection techniques.

III. Methodology

In this section, two approaches for change detection of crack path will be developed: a Similarity-based Approach (SA) and a Difference-based Approach (DA).

A. *Change Detection based on the Similarity between Real-World and Models of Simulated Crack*

For each groundtruth obtained from the real-world crack image dataset, the annotated crack is first thinned to one pixel width using skeletonization. Then, a segment of at least five consecutive crack pixels C_s is considered where the best fit model M_s of which is selected from the MSC. The similarity between C_s and M_s is calculated via the Root Mean Square Error (*RMSE*) between those two. Let L_s be the pixel number of the concerned segment C_s, the *RMSE* can be calculated as follow:

$$RMSE_s = \sqrt{\frac{\sum_{j=1}^{L_s}(y_j - \hat{y}_j)^2}{L_s}}, \tag{1}$$

where y_j and $\hat{y}_j$ are respectively the actual and predicted pixel of C_s and M_s. Once the *RMSE* has been calculated, another pixel p_i will be added to the segment where the error between the segment and the model obtained from the initial points are updated. The process is run recursively and ended when the error is larger than a pre-defined threshold. A new search is re-initialized with a new segment. The flowchart of the algorithm is illustrated in Fig. 1., where N_i and s are respectively the number of pixel of the annotated crack and the number of segment. The mechanism of assigning a pixel p_i is described as

$$p_i = \begin{cases} C_s, & RMSE_s < t \\ C_{s+1}, & RMSE_s \geq t. \end{cases} \tag{2}$$

Notably, when a point occurs at k and causes the change in RMSE as stated in Eq. (2), a further check is required to verify whether the change is significant [1]. A change is defined as insignificant when the *RMSE* between the new segment formed by k and its four adjacent neighbors and the best fit model of the previous segment does not exceed the pre-defined threshold t. In this case, k and the aforementioned data points are merged into the previous segment instead of a new one. An example of insignificant changes is illustrated in Fig. 2.

B. *Change Detection based on Difference*

In a comparison with the proposed SA presented in the previous section, a simple yet still widespread technique, the DA is presented. Let (x_i, y_i) be the coordinates of the i-th point of the annotated crack, the difference feature of this point is calculated as the vertical coordinate difference with its previous point as

$$\Delta_{y_i} = y_i - y_{i-1}. \tag{3}$$

To detect the change, the annotated crack is firsted rotated into the horizontal direction so that $x_i > x_{i-1}$. The difference features of two consecutive pixels are then analyzed and a

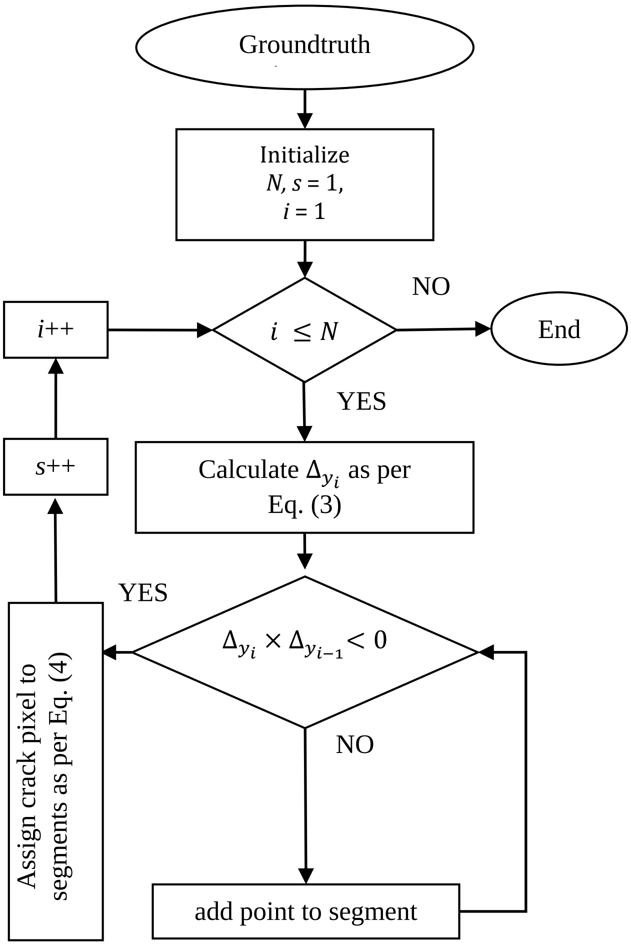

Figure 3. Flowchart of the DA approach.

change in sign of those features is also a change in direction of the annotated crack, i.e.

$$\Delta_{y_i} \times \Delta_{y_{i-1}} < 0. \tag{4}$$

The mechanisms of initializing segments and insignificant change are set identical to that of the SA approach. The condition for assigning data points to segments is as follows:

$$p_i = \begin{cases} C_s, & \Delta_{y_i} \times \Delta_{y_{i-1}} > 0 \\ C_{s+1}, & \Delta_{y_i} \times \Delta_{y_{i-1}} < 0 \end{cases} \tag{5}$$

The flowchart and an illustration of the SA algorithm are presented respectively in Fig. 3 and Fig. 4.

IV. Results

In this section, the performance of SA and DA is evaluated via analyzing the fitness of the SimulatedCrack models to the annotated crack obtained from real-world images. Beside the RMSE, the Coefficient of Determination R^2 í also employed and given as follows:

$$R^2 = 1 - \frac{\sum_{i=1}^{N}(y_i - \hat{y}_i)^2}{\sum_{i=1}^{N}(y_i - \bar{y}_i)^2}. \tag{6}$$

Table I reports the average RMSE, R^2, the number of models (NM), and processing time of the techniques SA and

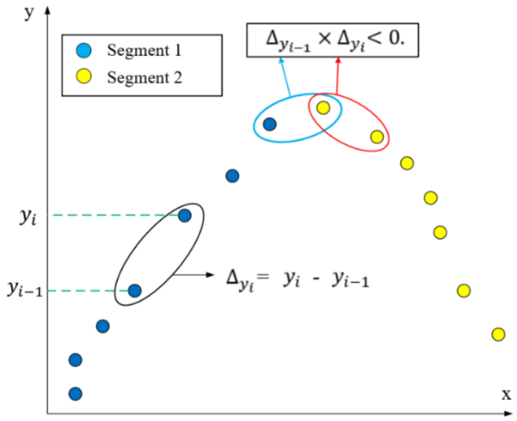

Figure 4. An illustration of the DA algorithm.

DA on the CrackTree260, CRKWH100, Stone331, CFD, and Crack500 datasets. Although both approaches perform well on all interested datasets, it is worth noting that SA performs better than DA in terms of error metrics RMSE, and R^2 since the mechanism of this fitting approach is designed to minimize the error while that of DA is not.

In terms of the average number of models required for each image, SA required less models to approximate a real-world crack than DA in the CrackTree260, CRKWH100, and Stone331 while DA performs better in this category in the remaining datasets. Generally speaking, the shape variations of cracks in the former 3 datasets are less complicated compared to that of the crack in the Crack500 and CFD datasets. Although a higher NM is required for SA in Crack500 and CFD, its fitting error and the coefficient determination is much better than that of DA. This can be verified in Fig. 5(a), where the correlation between the NM difference Δ_{NM} and the corresponding difference of *RMSE* and R^2 of two techniques on 5 image datasets is illustrated. For each dataset, those differences are calculated as

$$\Delta_{NM} = NM_{SA} - NM_{DA}, \tag{7}$$

$$\Delta_{RMSE} = RMSE_{SA} - RMSE_{DA}, \tag{8}$$

$$\Delta_{R^2} = R^2{}_{SA} - R^2{}_{DA}. \tag{9}$$

In another note, DA is more computational effective than SA, due to its straightforwardness implementation. In general, NM of SA is approximately 5% higher than that of DA and hence, DA processing time is about 16% faster than that of SA. The difference in NM reaches its highest in the CDF dataset, where the time difference is also at 46%. In this dataset, the difference in the fitting errors is also the maximum among 5 datasets. The correlation between Δ_{NM} and the difference in processing time is demonstrated in Figure 5(b).

Table II presents some fitting results of SA and DA on some sample images of 5 image datasets along with the number of models used in each image. Notably, on datasets with complicated crack structures (Crack500 and CFD), the fitness level of SA is much better than that of DA and also a higher number of models is required. On simpler datasets (CrackTree260, CRKWH100, and Stone331), the performance difference between two datasets is not

TABLE I. QUANTITATIVE RESULTS OF SA AND DA ON 5 IMAGE DATASETS

Datasets		RMSE↓	R^2↑	NM↓	Time(s)↓
CrackTree260	SA	0.002887	0.997670	**35-36**	**272.26**
	DA	**0.002337**	**0.997941**	41-42	289.17
CRKWH100	SA	**0.002430**	**0.997080**	**37-38**	311.27
	DA	0.003115	0.990629	38-39	**290.68**
Stone331	SA	**0.001879**	0.999404	**19-20**	162.53
	DA	0.001907	**0.999429**	22-23	**162.46**
CFD	SA	**0.002525**	**0.991711**	36-37	291.12
	DA	0.007070	0.962632	**22-23**	**157.25**
Crack500	SA	**0.005804**	**0.994894**	21-22	175.27
	DA	0.008898	0.982872	**19-20**	**132.01**

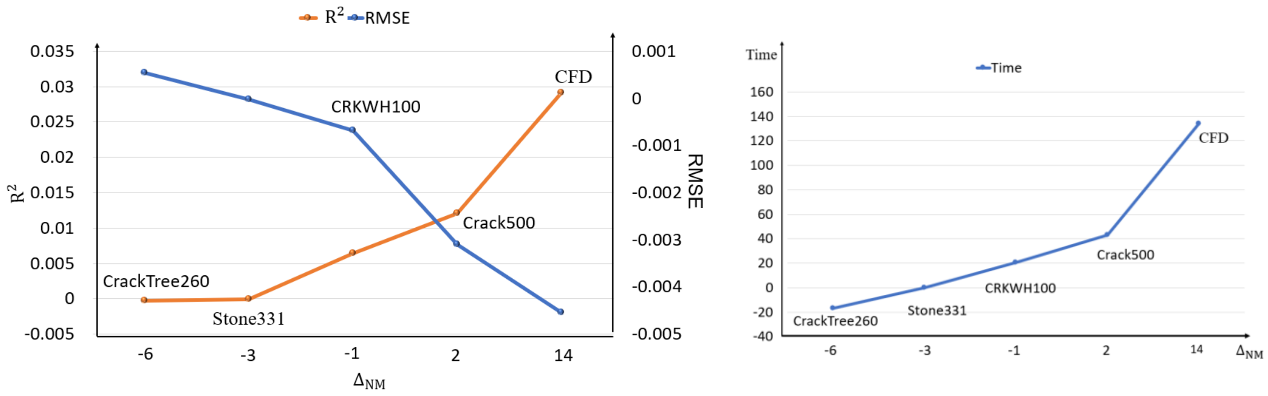

(a) (b)

Figure 5. Correlation between the difference in model number and (a) fitting errors, and (b) processing time.

significant, where DA event out-performs SA on some images.

V. CONCLUSION

In this paper, a change detection method for fitting models to crack coordinate data has been introduced. The method has been developed based on minimizing the fitting error between the models obtained from a simulated crack dataset and actual crack obtained from digital cameras. Comprehensive experiments have been conducted to evaluate the effectiveness of the proposed method. The outperformance of our approach against a difference-based technique has been verified, where SA returns the best fitting errors on four out of five reputable crack image datasets. The computational complexity of SA is still not optimal and will be improved in our future work.

ACKNOWLEDGEMENT

This work has been supported by VNU University of Engineering and Technology under project number CN20.38.

TABLE II. CORRELATION BETWEEN THE DIFFERENCE IN MODEL NUMBER AND (A) FITTING ERRORS AND (B) PROCESSING TIME.

Dataset	Groundtruth	SA	DA
CrackTree260		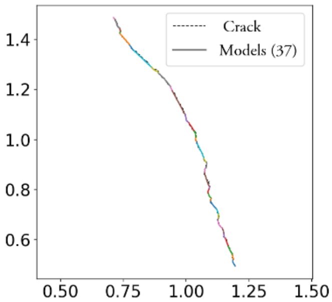	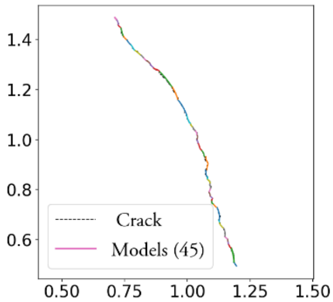
CRKWH100		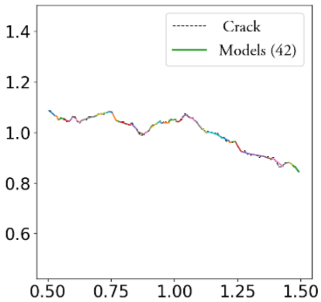	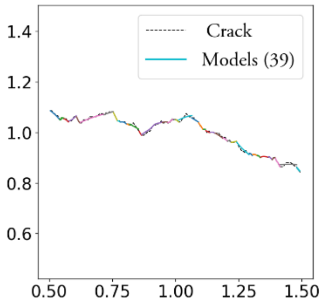
Stone331	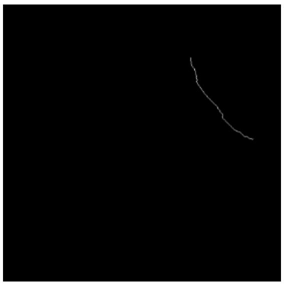	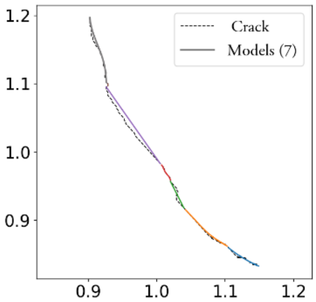	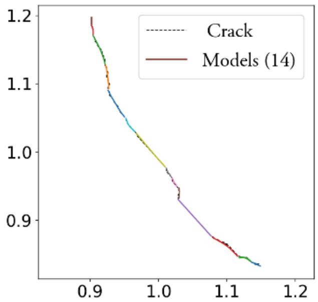
CFD	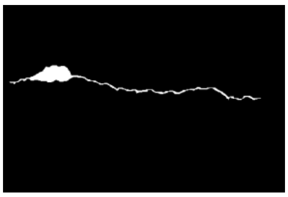	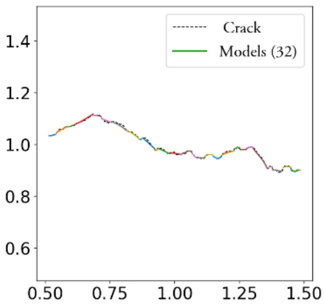	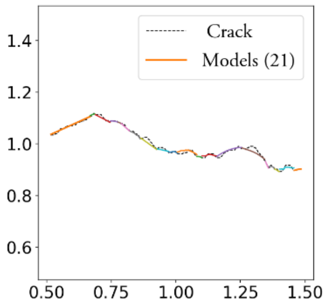
Crack500		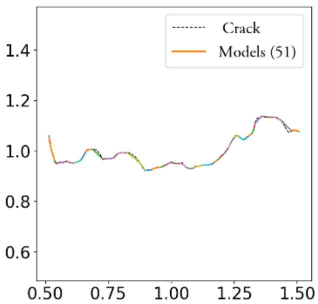	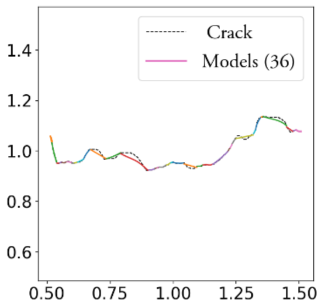

REFERENCES

[1] W. Cao, Q. Liu and Z. He, "Review of Pavement Defect Detection Methods," *IEEE Access*, vol. 8, pp. 14531-14544, 2020.

[2] J. -M. Guo, H. Markoni and J. -D. Lee, "BARNet: Boundary Aware Refinement Network for Crack Detection," *IEEE Transactions on Intelligent Transportation Systems*, pp. 1-16, doi: 10.1109/TITS.2021.3069135.

[3] H. Li, D. Song, Y. Liu and B. Li, "Automatic Pavement Crack Detection by Multi-Scale Image Fusion," *IEEE Transactions on Intelligent Transportation Systems*, vol. 20, no. 6, pp. 2025-2036, June 2019.

[4] T. H. Dinh, Q. P. Ha and H. M. La, "Computer vision-based method for concrete crack detection," in *Proceedings of the 14th International Conference on Control, Automation, Robotics and Vision (ICARCV)*, pp. 1-6, 2016.

[5] H. Oliveira and P. L. Correia, "Automatic Road Crack Detection and Characterization," *IEEE Transactions on Intelligent Transportation Systems*, vol. 14, no. 1, pp. 155-168, March 2013.

[6] Y. Shi, L. Cui, Z. Qi, F. Meng and Z. Chen, "Automatic Road Crack Detection Using Random Structured Forests," *IEEE Transactions on Intelligent Transportation Systems*, vol. 17, no. 12, pp. 3434-3445, Dec. 2016.

[7] Yang, X., Li, H., Yu, Y., Luo, X., Huang, T. and Yang, X., "Automatic pixel - level crack detection and measurement using fully convolutional network," *Computer - Aided Civil and Infrastructure Engineering*, vol. 33, no. 12, pp.1090-1109, 2018.

[8] Q. Zhu, T. H. Dinh, M. D. Phung and Q. P. Ha, "Hierarchical Convolutional Neural Network With Feature Preservation and Autotuned Thresholding for Crack Detection," *IEEE Access*, vol. 9, pp. 60201-60214, 2021.

[9] R. J. Radke, S. Andra, O. Al-Kofahi and B. Roysam, "Image change detection algorithms: a systematic survey," *IEEE Transactions on Image Processing*, vol. 14, no. 3, pp. 294-307, March 2005.

[10] P. St-Charles, G. Bilodeau and R. Bergevin, "SuBSENSE: A Universal Change Detection Method With Local Adaptive Sensitivity," *IEEE Transactions on Image Processing*, vol. 24, no. 1, pp. 359-373, Jan. 2015.

[11] Q. Zou, Y. Cao, Q. Li, Q. Mao, and S. Wang, "CrackTree: Automatic crack detection from pavement images," *Pattern Recognition Letter*, vol. 33, no. 3, pp. 227–238, 2012.

[12] Zou, Q., Zhang, Z., Li, Q., Qi, X., Wang, Q., & Wang, S., "Deepcrack: Learning hierarchical convolutional features for crack detection," *IEEE Transactions on Image Processing*, vol.28, no. 3, 1498-1512, 2018.

[13] Y. Shi, L. Cui, Z. Qi, F. Meng, and Z. Chen, "Automatic road crack detection using random structured forests," *IEEE Transactions on Intelligent Transportation Systems,* vol. 17, no. 12, pp. 3434–3445, Dec. 2016.

[14] F. Yang, L. Zhang, S. Yu, D. Prokhorov, X. Mei and H. Ling, "Feature Pyramid and Hierarchical Boosting Network for Pavement Crack Detection," *IEEE Transactions on Intelligent Transportation Systems*, vol. 21, no. 4, pp. 1525-1535, April 2020.

Improvement in Mixing Efficiency of Passive Micromixer with Integrated Grooves

Cuong Nguyen Nhu
Faculty of Electronics and Telecommunications (FET)
VNU University of Engineering and Technology
line 4: Hanoi, Vietnam
cuongnn241@vnu.edu.vn

Hang Nguyen Thu
Faculty of Electronics and Telecommunications (FET)
VNU University of Engineering and Technology
Hanoi, Vietnam
hangnt97@vnu.edu.vn

Thao Pham Ngoc
Faculty of Electronics and Telecommunications (FET)
VNU University of Engineering and Technology
Hanoi, Vietnam
thao.pham@vnu.edu.vn

Abstract*: Micro-scale fluidic devices have attracted increasing attention in numerous fields of chemical reactions, biomedical diagnostics, food safety control, environmental protection. Micromixer is an important part of a microfluidic system and considerably influences the efficiency and sensitivity of these devices. Here, our paper presents the improved designs of passive micromixers with the emphasis on the concave grooves that imposed on the serpentine channels to significantly induce molecular diffusion and chaotic mixing phenomena of fluid transport. Improved microfluidic passive mixer devices were designed, analyzed of simulation with and without using the grooves on U-folded channel, and then compared to the conventional Y structure. Simulation results demonstrate that the serpentine micromixer with obstacles increased the mixing performance by 2.35 times compared to the conventional Y-shaped mixers and 1.47 times compared to the ones without obstacles. The incorporation of grooves greatly enhances mixing in the flow path due to strong laminar perturbations. Also, according to the theoretical/numerical calculations, the effect of the geometry of the integrated obstacles and their arrangement pattern in the microchannel was studied extensively. The incorporation of numerous grooves in the microchannels resulted in enhanced performance of the micromixer in terms of reduction in mixing time. It was found, that the mixing efficiency of the passive micromixers can be improved to an excellent value by the positions and more densely distributed concave grooves. This achievement is a great step toward the next generation of high-efficiency passive micromixers at a lower cost in the future.

Keywords: passive mixer; serpentine channel; grooves; mixing simulation.

I. INTRODUCTION

In the past decade, microfluidic devices have played a significant role in the field of biomedical analysis, environment protection, food safety control, drug delivery, and so on [1–5]. These devices have received increasing attention due to their compact size, automatic operation, faster detection, less reagent, higher sensitivity, and in-field use. One of the most important components of micro-scale fluidic devices is micromixers, a considerable influence on the efficiency and sensitivity of the fluidic systems.

Due to the small dimensions and high surface-to-volume ratio, the micro-scale fluidic devices present unique and very different physical mechanisms in comparison to the macroscopic ones. Unlike the mixing effect in microfluidic devices is often achieved by the convection influences, the microfluidic ones rely on the external turbulences, and/ or novel microstructures at micro-scale dimensions to increase the transfer efficiency. In microchannels, the flow rates of fluids are very low, while the flows are basically in the laminar regime with the Reynold number lower than 1. It indicates that the mixing of fluid flows is significantly dependent on the diffusion mechanism at very low mixing efficiency. It is crucial to enhance the mixing efficiency to develop efficient micromixers, in particular, and micro-scale fluidic systems, in general. Therefore, the mixing efficiency can be considered as one of the most fundamental challenges and a key parameter for a micromixer. A wide variety of micromixers, different mixing principles have been extensively reported by many research groups.

Micromixers can be broadly classified into two types: active and passive. Active micro-mixers use actuators, improve mixing efficiency by stirring liquid flow using external forms of energy supply such as electrokinetic time-pulsed actuation [6–8], pressure perturbation [9], electrohydrodynamic (EHD) force [10]. This type of mixer is efficient; however, they suffer from complicated design and high fabrication costs. In contrast, passive micromixers do not have actuators or require external energy. The mixing is based on chaotic mixing phenomena and molecular diffusion of fluid transport. The advantages of these mixers are a simpler fabrication process, but, in spite of this, their mixing efficiency can approach that of the active mixers.

In the literature, the different mechanisms of mixing can be found due to the different structures of passive mixers as follows:

(i) flow lamination by using various geometries of micromixer such as T-mixer or Y-mixer or zig-zag or multi-layer mixers [11–13];

(ii) chaotic mixing by using stretching or folding [14–15];

(iii) split and recombine concepts by using complex channel elements, such as multiple flow passages, 3D structures, and curved or non-straight channels [16].

Various micro-structures and optimized structural dimensions of the microchannels are often investigated to maximize the mixing performance of passive micromixers by decreasing the diffusion path, or manipulating the laminar flow within the channels, so the enhancement of chaotic advection can be realized. However, the extent of mixing is not deeply studied by theoretical/numerical calculations throughout the wide spectrum of studies on microfluidic mixing. Just a few studies specifically investigated the influence of geometrical size; position and density of novel shapes affect the mixing performance.

In the present work, serpentine mixers with and without concave grooves were studied, compared to the conventional Y micro-structure, and then their mixing performance was investigated by Finite Element Method (COMSOL Multiphysics). The different obstructions were simulated, optimized, and designed for real chip micromixers. In our study, various theoretical studies of influencing parameters will be specifically considered to form a solid basis for the real fabrication in the next steps. The design of such mixers employed twisted microchannel systems in order to increase the fluid transfers inside the pump while reducing the sizes and operation time. The grooves are intentionally added along the microchannel to increase the chaotic advection and facilitate the mixing process.

II. MIXING STRUCTURES

The serpentine micromixers are passive micromixers with 2 inputs and 1 output and are shown in Fig. 1. Both of these were designed to overcome the disadvantages of passive mixers and active mixers with their simple design, easy fabrication, and relatively high mixing efficiency. The channel has a depth of 50 µm and a width of 300 µm. The design employed the twist and turn structure with the radius of each twist being 525 µm as in Fig. 1 (a).

This meandering design helps lengthen the microchannel while maintaining the compact size of the device so that it is suitable for miniature devices. The serpentine mixer with added obstacles as in Fig. 1 (b) was created by introducing the bulkheads into the microchannel as in Fig. 1 (c). These bulkheads have a width of 40 µm and a length of 140 µm. These obstacles were expected to increase the mixing efficiency of mixers by adding more chaos to the system.

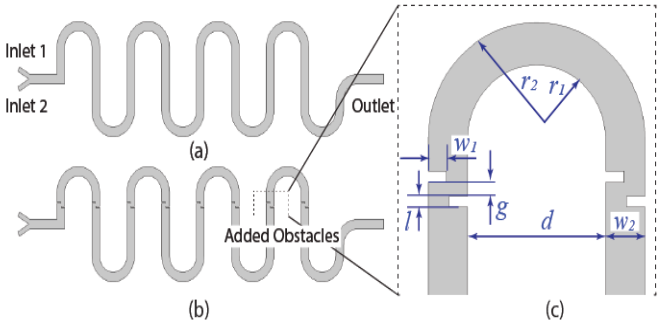

Fig. 1. Design of two serpentine micromixers (a) without; (b) with grooves; (c) zoom in to U-folded channel of (b)

TABLE I. PARAMETERS OF SERPENTINE MIXERS

Parameters	Symbols	Value
Folding length	d	1050 μm
Groove's width	w_1	80 μm
Channel's width	w_2	300 μm
Groove's length	l	140 μm
Gap between grooves	g	100 μm
Inner channel's radius	r_1	525 μm
Outer channel's radius	r_2	825 μm

III. SIMULATION

In order to investigate the characteristics of the flow inside the microchannels as well as to compare the performance enhancement of the proposed structure, simulation studies were performed. We used COMSOL Multiphysics as our tool for finite element analysis, solver. The simulation was a one-way coupling. Each inlet was fed with a fluid flow with the velocity of 3×10-4 m/s, while the outlet was defined by setting the pressure to be 0 Pa. Wall condition was set to non-slip. The concentration at inlet 1 was set at 1 mol/m3, while the figure for inlet 2 was set to 0 in order to assume that the fluid at inlet 1 and inlet 2 was different. The other physical properties used in the simulation are shown in Tab. I.

TABLE II. PHYSICAL PROPERTIES IN SIMULATION MODELS

Properties	Value	Unit
Fluid density	998	kg/m^3
Dynamic viscosity	1×10^{-3}	Pa·s
Diffusivity	0.8×10^{-12}	m^2/s
Velocity	3×10^{-4}	m/s

The uncompressed flow is governed by the Navier-Stokes equation along with the continuity equation [17]:

$$\rho\left(\frac{\partial u}{\partial t} + u\cdot\nabla u\right) = -\nabla p + \nabla\cdot\mu\nabla u \quad (1)$$

$$\nabla\cdot u = 0 \quad (2)$$

where v is the local velocity (m/s) and ρ is the pressure (Pa), µ is the liquid viscosity (Pa·s).

The description of diffusion is governed by Fick's laws, in which the molar flux caused by diffusion is proportional to the concentration gradient and the rate of change of concentration is in proportion to the second derivative of concentration of space.

$$N_i = -D_i\nabla c_i \quad (3)$$

$$\frac{\partial c_i}{\partial t} = D_i\nabla^2 c_i \quad (4)$$

Where N_i, D_i and c_i is the molar flux (mol m^{-2} s^{-1}), diffusion coefficient (m^2 s^{-1}), and the concentration (mol m^{-3}) respectively.

IV. PERFORMANCE IMPROVEMENT VERIFICATION

In order to prove the performance enhancement of the serpentine structure, we also conducted the simulation with the conventional Y-shaped mixer. The concentration profiles of both the conventional Y-shaped and the two types of serpentine mixers are shown in Fig. 2.

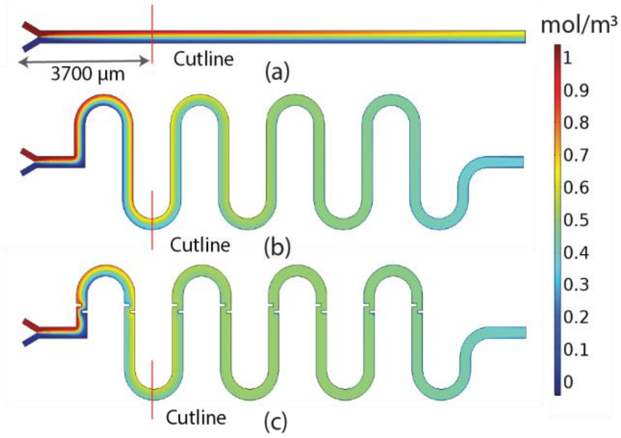

Fig. 2. Concentration profiles of (a) conventional Y-shaped mixer; serpentine mixers (b) without and (c) with grooves

Qualitatively, the performance of the serpentine mixer was improved compared to the conventional Y-shaped mixer. As for the mixer that does not include obstacles, the mixing capability depends solely on the diffusion of the two liquids and thus, is subject to the contact time between the two-liquid flows. Due to the twisted shape, the length of the channel is considerably increased compared to the conventional Y-shaped structure. This resulted in more time for two liquid flows to come into contact and for the diffusion to take place. At the outlet of the Y-shaped mixers, the liquid was not homogenous and was basically two co-flow streams. Meanwhile, those at the serpentine mixer and serpentine mixer with baffles were quite uniform. Acceptable mixing concentration was achieved at the third turn of the channel. At the same time, the same mixing concentration was produced right at the second turn in the mixer with integrated obstacles. For quantitative evaluation, the concentration values were extracted at the second turn. In addition, we also chose the standard deviation (std) of the data along the cutline as a metric to evaluate the performance. The standard deviation demonstrates how uniform the values on the cutline are. The larger standard deviation is tantamount to a more uneven mixing while smaller amounts mean that the mixing process is carried out better. Concentration values along the cutline were taken, and the standard deviation was derived by [18]:

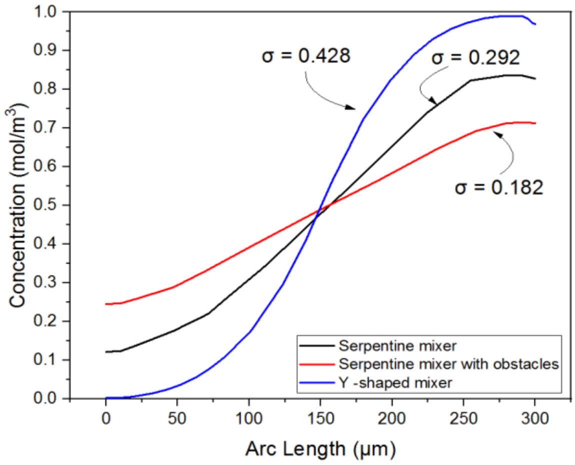

Fig 3. Concentration and std of the values at the cutline

$$\sigma = \sqrt{\frac{1}{N}\sum_{i=1}^{N}(c_i - \mu)^2} \quad (5)$$

in which, σ is the standard deviation, N is the number of concentration values taken along the cutline, c_i is the individual concentration values, and $\mu = \frac{1}{N}\sum_{i=1}^{N} c_i$ is the mean of all the concentration values.

Therefore, if the fluids are better mixed, a small standard deviation is achieved. For the Y-shaped mixer, the mixing performance was quite poor according to the extracted data. The concentration varied from 0 to 1 with a deviation of 0.428 as in Fig. 3. At the cutline, the flows were not mixed well and were still separated flows. For the serpentine mixer, the range of the concentration values was much narrower, ranging from 0.1 to 0.8 mol/m^3 with a standard deviation of 0.292. Thus, it can be implied that the performance was enhanced by 1.47 times by adopting the twisted structure. At the same time, for the mixer with the integrated obstacles, the minimum value of the concentration was approximately 0.25 and the maximum value of the concentration was 0.71, which were even narrower compared to the previous mixers the S-shaped mixer. The calculated standard deviation was 0.182. It can, therefore, be concluded that the serpentine mixer with obstacles has a mixing performance of 2.35 times higher than the conventional Y-shaped mixer and 1.47 times higher than the one without obstacles.

V. IMPACT OF THE GEOMETRY ON THE MIXING EFFICIENCY

Impact of channel width in serpentine channels

We study the influence of the width in serpentine channels on the performance of the mixers. The geometries of input terminals and lengths for all microchannels investigated were fixed to the same values. The width of the microchannel now varied from 200 µm to 700 µm to investigate the impact of channel width. When the width of the channel was 700 µm, the mixing performance was

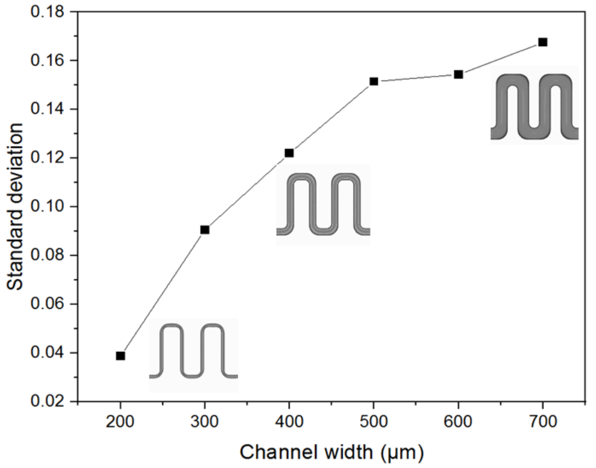

Fig. 4. Dependence of the mixing performance and channel width in serpentine microchannels

lowest (the standard deviation was the highest) as in Fig. 4. However, it should be noted that due to the limitation of the fabrication process, smaller channel width than 100 µm might not be feasible for simple methods, such as rapid prototyping by using the 3D printer.

Impact of the length of the grooves

In the original design, with 300 µm of the channel's width, each obstacle was 140 µm long, 80 µm wide. When fluid flow flows through the channel, one stream will collide and be blocked by the baffles while the other one can pass through. This creates a chaotic mixing inside the channel. The blocked stream will have to change its direction in order to continue to flow. As in Fig. 5**Error! Reference source not found.**, the blocked stream will turn 90 degrees and merge with the unblocked one. This is where the mixing progressed is accelerated. Streams will merge into one another alternatively, increasing the mixing performance of the structures. The length of the obstacles was investigated

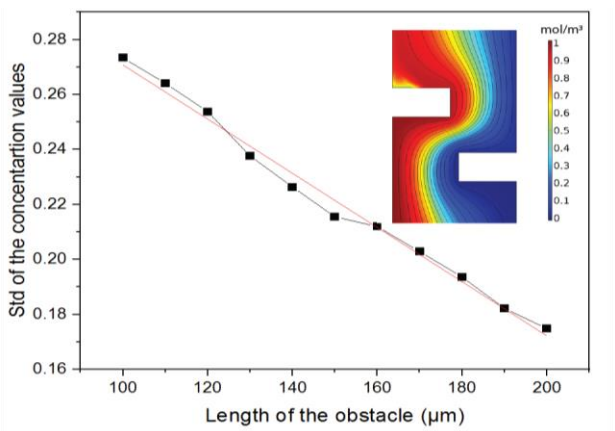

Fig. 5. Relationship between the grooves' length and the mixing performance

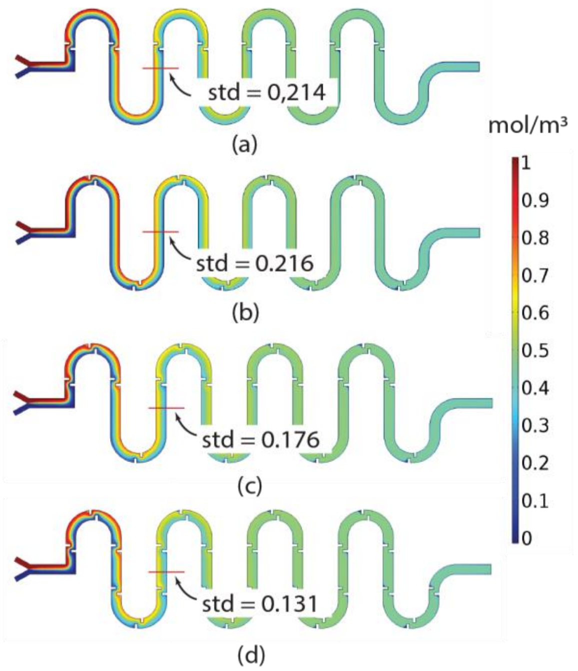

Fig. 6. Influence of (a;b) groove 's positions and (c; d) densities of grooves on mixing efficiencies

from 100 µm to 200 µm and the standard deviation values at the cutline are shown in Fig. 5. It can be seen that the standard deviation of the concentration values at the cutline decreased as the length of the obstacles increased. When the obstacles were 200 µm long, the standard deviation was the lowest, at 0.17. Therefore, it can be concluded that the performance is improved by increasing the length of the integrated grooves.

Impact of the position of the obstacles

To investigate further the influence of these added grooves, we conduct a simulation with different placements of the grooves. To be more specific, we considered four cases of placing grooves:

(1) two grooves were placed horizontally as in Fig. 6(a).

(2) two grooves were placed vertically as in Fig. 6(b).

(3) combined case (1) and case (2) as in Fig. 6(c).

(4) five grooves were placed uniformly as in Fig. 6(d).

The simulation results are shown in Fig. 6. We can see that the first two cases of placement (case 1 and case 2) produce evenly mixed results, with the mixing performance being slightly better with the grooves in case 2. In case 3, the performance was increased. The standard deviation of such a case was 0.176. As the number of grooves continued to increase, the performance was enhanced significantly. Case 4 resulted in the highest mixing performance among four investigated cases, with a considerable improvement of 63.4% in comparison with case 1 and case 2.

Impact of the ratio geometries between the groove's dimension and the width of the serpentine microchannel with densely distributed concave grooves.

In addition to the study on the position as well as the dense distribution of the integrated grooved, we also perform further studies on the impact of dimension ratio between the grooves and serpentine microchannel. From the

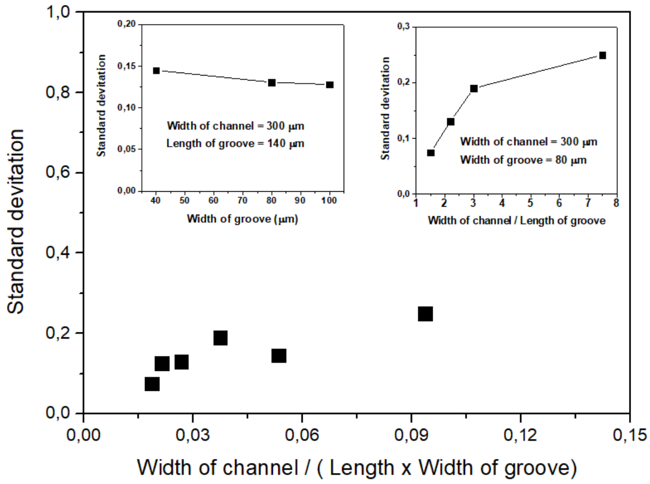

Fig. 7. Relationship between the ratio geometries between the groove's dimension and the width of serpentine microchannel

TABLE III. SIMULATED PARAMETERS OF MICROCHANNEL AND GROOVES

w_2 [µm]	l [µm]	w_1 [µm]	$(w_2/l)/w_1$	Standard deviation
300	40	80	0,09375	0,25
300	140	40	0,053571429	0,145
300	100	80	0,0375	0,19
300	140	80	0,026785714	0,131
300	140	100	0,021428571	0,128
300	200	80	0,01875	0,075

optimized configuration in Fig. 6(d), which found the highest performance among four cases, we performed a parametric study on the width/length of the grooves and the width of main channels. The simulated values of width and length of concave grooves were studied while the width of the channel was kept at 300 µm. The simulation results are shown in Figure 7, and all simulated parameters are indicated in Tab III. Similar to previous studies, the performance was also evaluated in terms of standard deviations of values at cutlines.

In the inserted Fig. 7, the simulation study shows that width of the width has a neglectable impact on the performance. Increasing the grooves' width from 40 µm to 100 µm only improve the performance by 13%. In contrast to the width, the grooves' length has a great influence on the mixing performance. In fact, a rather linear relationship between the standard deviation and the grooves' length was achieved.

Depending on these relationships, the influence of the ratio geometries between the groove's dimension and the width of the serpentine microchannel with densely distributed concave grooves on mixing efficiency relates to the proportion to

$$\frac{Width\ of\ microchannel}{(Length\ x\ Width)\ of\ groove}$$

At the same width of the microchannel, while the length of the groove contributes to the significant impact, the small effect of the width groove can be increased the mixing efficiency. Therefore, the performance of the mixer can be further improved by increasing the grooves' length. However, it should be noted that if grooves are too long, it could lead to channel clogged channels and difficulty in fabrication due to the high aspect ratio.

VI. CONCLUSION

The serpentine mixers with the integrated grooves have been thoroughly studied. The grooves created a chaotic mixing inside the channel by causing flow merging. Despite the more complexity in the fabrication process, the proposed mixers with grooves increased the mixing performance by 2.35 times compared to the conventional Y-shaped mixers and 1.47 times compared to the ones without grooves. The dependences of the mixing performance on the grooves' width, position, and channel width were also studied, and the relationships were found. In the future, we will fabricate the proposed micromixers and conduct experiments to validate the simulation results. With the obtained results, our mixers have the potential for lab-on-a-chip systems with outstanding advantages.

VII. ACKNOWLEDGMENT

This work was supported by the Vietnam Ministry of Science and Technology under Grant NĐT.101.TW/21.

VIII. REFERENCES

[1] F. Fontana, M. P. A. Ferreira, A. Correia, J. Hirvonen, and H. A. Santos, "Microfluidics as a cutting-edge technique for drug delivery applications," Journal of Drug Delivery Science and Technology, vol. 34. Editions de Sante, pp. 76–87, Aug. 01, 2016, doi: 10.1016/j.jddst.2016.01.010.

[2] J. Ahn, J. Ko, S. Lee, J. Yu, Y. T. Kim, and N. L. Jeon, "Microfluidics in nanoparticle drug delivery; From synthesis to pre-clinical screening," Advanced Drug Delivery Reviews, vol. 128. Elsevier B.V., pp. 29–53, Mar. 15, 2018, doi: 10.1016/j.addr.2018.04.001.

[3] S. T. Sanjay et al., "Recent advances of controlled drug delivery using microfluidic platforms," Advanced Drug Delivery Reviews, vol. 128. Elsevier B.V., pp. 3–28, Mar. 15, 2018, doi: 10.1016/j.addr.2017.09.013.

[4] C. Te Kung et al., "Microfluidic synthesis control technology and its application in drug delivery, bioimaging, biosensing, environmental analysis and cell analysis," Chemical Engineering Journal, vol. 399. Elsevier B.V., p. 125748, Nov. 01, 2020, doi: 10.1016/j.cej.2020.125748.

[5] K. Mao et al., "Paper-based microfluidics for rapid diagnostics and drug delivery," J. Control. Release, vol. 322, pp. 187–199, Jun. 2020, doi: 10.1016/j.jconrel.2020.03.010.

[6] J. C. Rife, M. I. Bell, J. S. Horwitz, M. N. Kabler, R. C. Y. Auyeung, and W. J. Kim, "Miniature valveless ultrasonic pumps and mixers," Sensors Actuators, A Phys., vol. 86, no. 1–2, pp. 135–140, Oct. 2000, doi: 10.1016/S0924-4247(00)00433-7.

[7] S. O. Catarino, L. R. Silva, P. M. Mendes, J. M. Miranda, S. Lanceros-Mendez, and G. Minas, "Piezoelectric actuators for acoustic mixing in microfluidic devices - Numerical prediction and experimental validation of heat and mass transport," Sensors Actuators, B Chem., vol. 205, pp. 206–214, Dec. 2014, doi: 10.1016/j.snb.2014.08.030.

[8] S. Rashidi, H. Bafekr, M. S. Valipour, and J. A. Esfahani, "A review on the application, simulation, and experiment of the electrokinetic mixers," Chemical Engineering and Processing: Process Intensification, vol. 126. Elsevier B.V., pp. 108–122, Apr. 01, 2018, doi: 10.1016/j.cep.2018.02.021.

[9] Y. Daghighi and D. Li, "Numerical study of a novel induced-charge electrokinetic micro-mixer," Anal. Chim. Acta, vol. 763, pp. 28–37, Feb. 2013, doi: 10.1016/j.aca.2012.12.010.

[10] F. Yang, W. Zhao, and G. Wang, "Electrokinetic mixing of two fluids with equivalent conductivity," Chinese J. Chem. Eng., May 2021, doi: 10.1016/j.cjche.2021.03.032.

[11] M.Okuducu, M. Aral, "Novel 3-D T-shaped passive micromixer design with helicodial flows", Processes, vol. 7, no. 9, p.637, 2019, doi: 10.3390/pr7090637.

[12] S. Hossain, M. Ansari, K. Kim, "Evaluation of the mixing performance of three passive micromixers". Chem. Eng. J., vol. 150, pp. 492–501, 2009, doi: 10.1016/j.cej.2009.02.033

[13] T. Terje, S. Maciej, A. Erik, G. Oliver, "A novel passive micromixer: lamination in a planar channel system", Microfluid. Nanofluid., vol. 8, no. 2, pp. 209–215, 2010, doi: 10.1007/s10404-009-0456-z.

[14] X. Yu, Y Lin, Z. Wang, S. Tu, Z. Wang, "Design and evaluation of an easily fabricated micromixer with three-dimensional periodic perturbation", Chem. Eng. J. vol. 171, pp. 291–300, 2011, doi: 10.1016/j.cej.2011.04.003.

[15] H. Cho, B. Kim, B. Kwak, S. Shin, S. Lee, K. Kim, H. Jung, "Optimization of microscale vortex generators in a microchannel using advanced response surface method", Int. J. Heat Mass Transf. vol. 54, pp. 118–125, 2011, doi: 10.1016/j.ijheatmasstransfer.2010.09.061.

[16] M. Juraeve, D. Kang, "Mixing performance of a cross-channel spit-and- recombine micro mixer combined with mixing cell", Micromachines, vol. 11, no. 7, p. 685, 2020, doi: doi.org/10.3390/mi11070685.

[17] "What Are the Navier-Stokes Equations?" https://www.comsol.com/multiphysics/navier-stokes-equations (accessed Jul. 02, 2021).

[18] "Standard Deviation." https://www.nlm.nih.gov/nichsr/stats_tutorial/section2/mod8_sd.html (accessed Jul. 02, 2021).

The 6th International Conference on Engineering Mechanics and Automation (ICEMA 2021) Hanoi, November 14, 2021

Model Predictive Control for Piezoelectric Actuated System with Hysteresis

Tran Vu Minh
Dept. of Manufacturing Technology
Hanoi University of Science and Technology
Hanoi, Viet Nam
minh.tranvu@hust.edu.vn

Abstract: **In this paper, a discrete second order linear model is used to describe the piezoelectric actuated stage. To suppressing the hysteresis phenomenal of the piezoelectric actuated stage, this paper proposes a tracking control with model predictive technique. The proposed controller is successful in mitigate the nonlinearity of piezoelectric actuator at low frequency. The experimental results verify the feasibility of the proposed method.**

Keywords: model predictive control, hysteresis, piezo electric actuator.

I. INTRODUCTION

Piezoelectric actuator (PEA) are applied in the high-precision devices and ultra-precision positioning field, such as optical equipment, scanning narrow tunneling microscope, and photoelectric imaging processing systems, because of their rapid response speed, strong actuated forces [1,2]. However, the accuracy of PEA is damaged due to the hysteresis phenomenon [3]. To solve this problem, various modeling methods have been proposed to detect the hysteresis of the piezoelectric actuated table, which mainly include the differential equation-based models and the operator-assisted models. So far, the Duhem model, Bouc-Wen model are the most common differential equations-based models [4]. For example, Lin et al. [6] conducted in-depth research on generalized Duhem models. In [7], the Bouc-Wen model was used to represent the hysteresis nonlinearity of the piezoelectric actuated stage and achieved the great results. The Preisach and Prandlt-Islinskii (PI) are two representative of hysteresis operator-assisted models. The Preisach model describes the hysteresis nonlinearity by the supper position of series of Preisach operators with the values of 0–1 [8–10]. The PI model used two basic operators of Play and Stop [11].

Based on the aforementioned hysteresis models, some control techniques have been developed, trying to eliminate the hysteresis effects and granting high-precision tracking control for the piezoelectric actuators, such as the a multivariable compensator for the hysteresis. The compensator is based on the combination of the inverse multiplicative structure with the model [12]. Liu et al. used a fusion of unknown direction hysteresis model with adaptive neural control techniques [13]. Li et al. utilize the so-called Preisach plane, the Preisach model is re-expressed into a control-oriented form, in which the input signal is explicitly expressed [14]. Nguyen et al. [15] use a discrete-time quasi-sliding-mode control with a new sliding variable to reduce the effects of the hysteresis nonlinearity. Shan et al. [16] proposed a robust output feedback controller to degrade the hysteresis nonlinearity. He et al. [17] presented adaptive law to estimate the input hysteresis which is formulated as a linear desired input and a “disturbance-like” term. Ge et al. [18] proposed a hybrid controller included of inverse Preisach model as feedforward compensation and PID control to enhance the tracking accuracy for a piezoelectric actuated system.

This paper adopts a discrete second order linear system to modeling the PEA. Parameters of the model are identified using least square method. Furthermore, the model predictive control method is employed on the linear model to control the PEA. Experiments on PEA are conducted to verify the effectiveness of proposed method.

This paper is organized as follows. In the Section 2, the PEA is modeled by a discrete second order linear systems. The design of the model predictive control law is presented in Section 3. Experimental setup and experimental results are shown in Section 4. Finally, the conclusion is in Section 5.

II. MODELLING THE PEA SYSTEM

This section proposes a PEA model derived by linear system modeling method [19]. Afterward, the parameters of the model are identified based on statistical method and assumes that objectives are black-boxes. The obtained model is simple and can be used as a nominal model of model-based control methods. It should be noted that nonlinearities of PEAs is neglected because this is only the linear system modelling method. In this identification, Auto-regressive exogenous (ARX) model is applied because ARX model is suitable for least square method and is usually used for system identification. The identified PEA discrete model G(z) has second-order denominator and first-order numerator polynomials, and is expressed as follows:

$$G(z) = \frac{X(z)}{Y(z)} = \frac{p_1 z^{-1} + p_2 z^{-2}}{1 + q_1 z^{-1} + q_2 z^{-2}} \tag{1}$$

where $Y(z)$ is z-transformation of PEA displacement; $X(z)$ is z-transformation of applied voltage; and p_1, p_2, q_1, q_2 are model parameters.

Equation (1) can be rewritten as

$$y(k) = p_1 x(k-1) + p_2 x(k-2) - q_1 y(k-1) - q_2 y(k-2) = \varepsilon^T \rho \quad (2)$$

where $\varepsilon(k)^T = [x(k-1), x(k-2), y(k-1), y(k-2)]$, $\rho = [p_1, p_2, -q_1, -q_2]^T$ is the parameter vector which is to be identified; Equation (2) is linear, so the vector of ρ can be readily identified by using the least squares method as follows.

Let N be the number of sampling cycles for input and output data. Define

$$A = \begin{bmatrix} \varepsilon(N)^T \\ \varepsilon(N-1)^T \\ \vdots \\ \varepsilon(1)^T \\ \varepsilon(0)^T \end{bmatrix} \text{ and } Y = \begin{bmatrix} y(N) \\ y(N-1) \\ \vdots \\ y(1) \\ y(0) \end{bmatrix}, \quad (3)$$

they give:

$$\rho = (A^T A)^{-1} A^T Y \quad (4)$$

The input $x(k) = 20 * (-0.06 * k * 0.0005 + 1.1)\, sin(2 * \pi * k * 0.0005 + 3 * \pi/2) + 1.1$ is applied to the PEA for identification, the sampling time period is chosen as 0.0005 s. Fig.1 shows the input signal and measured output signal.

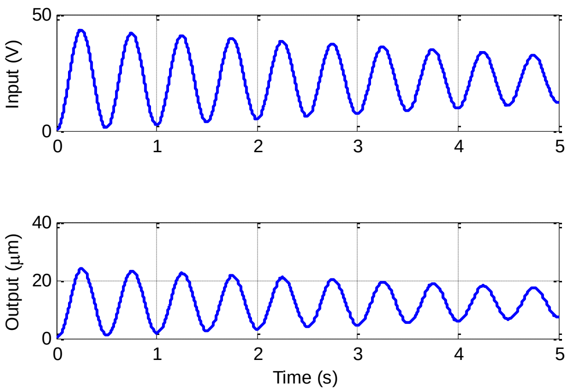

Fig. 1. Input and output signal for identification

First, by using least square method, the values of p_1, p_2, q_1, and q_2 are approximated. Afterwards, the identified parameters are validated by comparing the input-output relationship of the model and of the PEA. During this step, the parameters can be manually refined if required.

As the result, the identified parameters are shown in table 1.

TABLE I. IDENTIFICATION RESULTS OF LINEAR PEA MODEL USING LEAST SQUARE METHOD.

Parameters	p_1	p_2	q_1	q_2
Value	0.0262	0.0077	-0.9549	0.0167

III. MODEL PRIDICTIVE CONTROLLER DESIGN

Model predictive control (MPC) is an advanced method of process control [20]. Model predictive controllers rely on dynamic models of the process; most often are linear empirical models obtained by system identification. The main advantage of MPC is the fact that it allows the current time step to be optimized, while keeping future time steps in account. This is achieved by optimizing a finite time-horizon, and then only the current time step is implemented. Fig. 2 shows the basic structure of MPC.

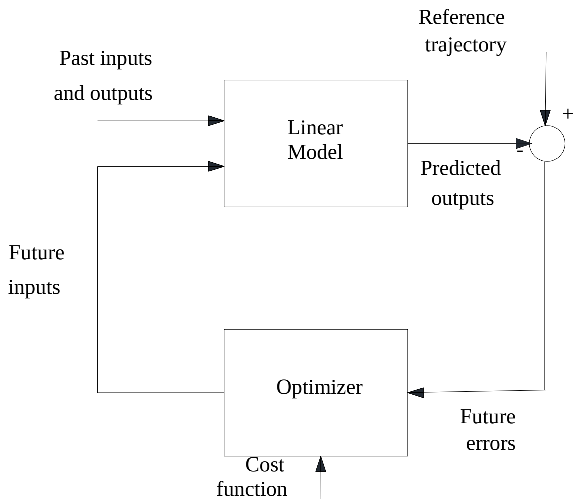

Fig. 2. Basic structure of MPC

Model Predictive Control (MPC) is a multivariable control algorithm that needs the following information:

(I1) Internal dynamic model of the process.

(I2) History of past inputs and outputs.

(I3) Optimization cost function P over the preceding prediction horizon, to calculate the optimum control inputs.

The optimization cost function is given by:

$$P = \sum_{i=1}^{N_p} \vartheta(i)\big(\hat{y}(k+i|k) - y_d(k+i|k)\big)^2 + \textstyle\sum_{i=1}^{N_s} \varphi(i)\big(\Delta\hat{x}(k+i|k)\big)^2 \quad (5)$$

where $\hat{y}(k|i)$ is the i[th] step predicted output from time k, $y_d(k|i)$ is the i[th] step reference signal from time k, $\Delta\hat{x}(k|i)$ is the difference between i[th] step predicted input from time k and control input at time k, N_s is the number of predicted steps; ϑ and φ are weighting coefficients.

The transfer function (1) is changed into state space as follow:

$$y(k) = -q_1 y(k-1) - q_2 y(k-2) + p_1 x(k-1) + p_2 x(k-2) \tag{6}$$

Denote $x_1(k+1) = x_2(k) = y(k)$, it gives

$$\begin{cases} x_1(k+1) = x_2(k) \\ x_2(k+1) = -a_1 x_2(k) - a_2 x_1(k) + b_1 u(k) + b_2 u(k-1) \end{cases} \tag{7}$$

Introduce new state $x(k) = x(k-1) + \Delta x(k)$, Equation (7) becomes

$$\begin{bmatrix} x_1(k+1) \\ x_2(k+1) \\ x(k) \end{bmatrix} = \begin{bmatrix} 0 & 1 & 0 \\ -a_2 & -a_1 & b_1+b_2 \\ 0 & 0 & 1 \end{bmatrix} \begin{bmatrix} x_1(k) \\ x_2(k) \\ x(k-1) \end{bmatrix} + \begin{bmatrix} 0 \\ b_1 \\ 0 \end{bmatrix} \Delta x(k)$$

$$y(k) = \begin{bmatrix} 0 & 1 & 0 \end{bmatrix} \begin{bmatrix} x_1(k) \\ x_2(k) \\ x(k-1) \end{bmatrix} \tag{8}$$

For simplicity denote $A = \begin{bmatrix} 0 & 1 & 0 \\ -a_2 & -a_1 & b_1+b_2 \\ 0 & 0 & 1 \end{bmatrix}$, $B = \begin{bmatrix} 0 \\ b_1 \\ 0 \end{bmatrix}$ and $C = \begin{bmatrix} 0 & 1 & 0 \end{bmatrix}$.

In this paper, 3 steps ahead are predicted. It means $N_s = 3$.

Now, the predictions along the horizon are given by

$$\begin{bmatrix} \hat{y}(k+1) \\ \hat{y}(k+2) \\ \hat{y}(k+3) \end{bmatrix} = \begin{bmatrix} CA\hat{x}(k) + CB\Delta x(k) \\ CA^2\hat{x}(k) + CAB\Delta x(k) + CB\Delta x(k+1) \\ CA^3\hat{x}(k) + CA^2B\Delta x(k) + CAB\Delta x(k+1) + CB\Delta x(k+2) \end{bmatrix}$$

$$= \begin{bmatrix} CA \\ CA^2 \\ CA^3 \end{bmatrix} \hat{x}(k) \begin{bmatrix} CB & 0 & 0 \\ CAB & CB & 0 \\ CA^2B & CAB & CB \end{bmatrix} \begin{bmatrix} \Delta x(k) \\ \Delta x(k+1) \\ \Delta x(k+2) \end{bmatrix} \tag{9}$$

Denote $D = \begin{bmatrix} CB & 0 & 0 \\ CAB & CB & 0 \\ CA^2B & CAB & CB \end{bmatrix}$; $E = \begin{bmatrix} CA \\ CA^2 \\ CA^3 \end{bmatrix}$,

the solution that provides the optimum input difference as:

$$\begin{bmatrix} \Delta x(k) \\ \Delta x(k+1) \\ \Delta x(k+2) \end{bmatrix} = (D^T D + \varphi I)^{-1} D^T \left(y_d - E\hat{x}(k)\right) \tag{10}$$

The matrices D and E can be easily calculated by q_1, q_2, p_1, p_2 from table 1, The weighting coefficients are chosen as $\vartheta(i) = 1$ and $\varphi = 0.1$.

IV. EXPERIMENTAL RESULTS

The PEA using for experiments is PFT-1110. The displacement is measured by the 2nm resolution noncontact capacitive displacement sensor (PS-1A Nanotex). Input/output data are handled by an interface board AIO-163202F-PE installed on PCI-Express bus. The control program is implemented on computer in C language

The experiment is conducted to verify the effectiveness of MPC controller with the sinusoid trajectory at three difference frequencies.

Fig. 3 shows the control input for the experiment at 1 Hz. The tracking result is shown in Fig. 4. The maximum output error is 3%.

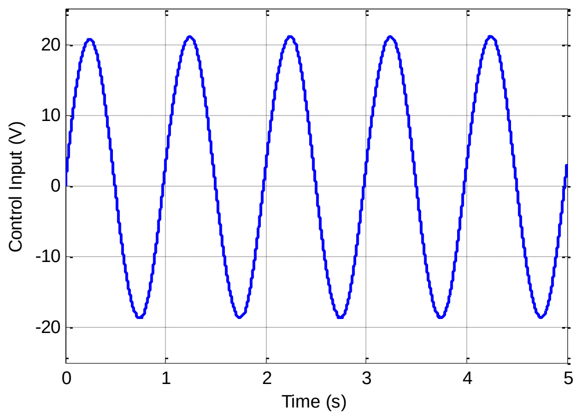

Fig. 3. Control input for in MPC (1 Hz) (3 predictive steps)

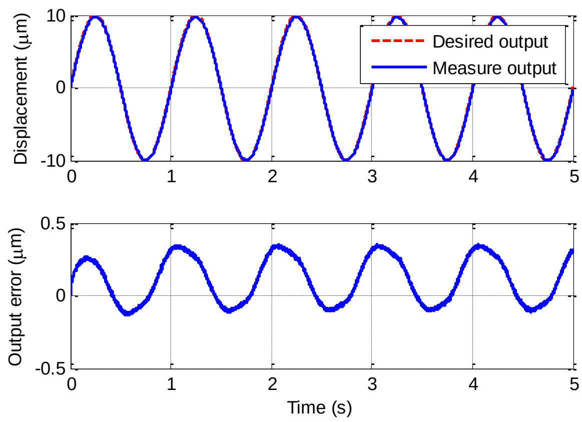

Fig. 4. Tracking result for MPC (1 Hz) (3 predictive steps)

Fig. 5 shows the control input for the experiment at 10 Hz. The tracking result is shown in Fig. 6. The maximum output error is 7%.

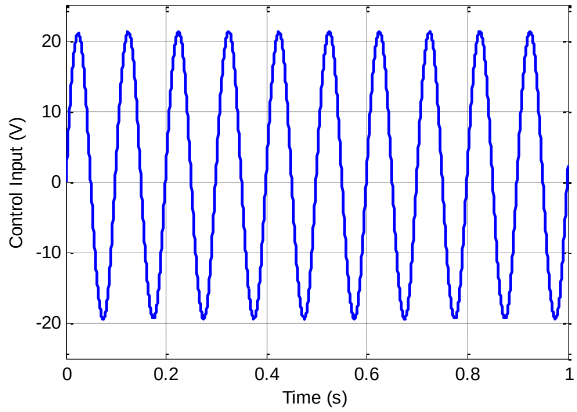

Fig. 5. Control input for MPC (10 Hz) (3 predictive steps)

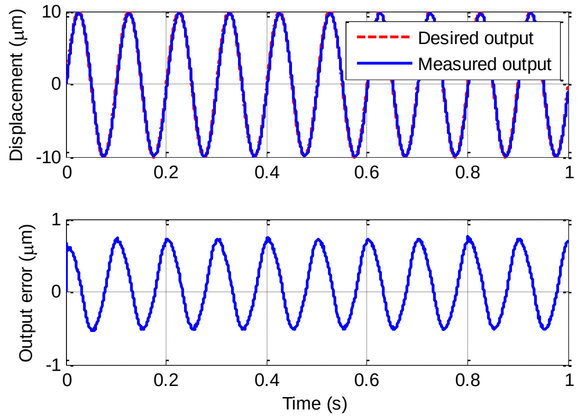

Fig. 6. Tracking result for MPC (10 Hz) (3 predictive steps)

Fig. 7 shows the control input for the experiment at 30 Hz. The tracking result is shown in Fig. 8. The tracking result is shown in Fig. 6. The maximum output error is 18%.

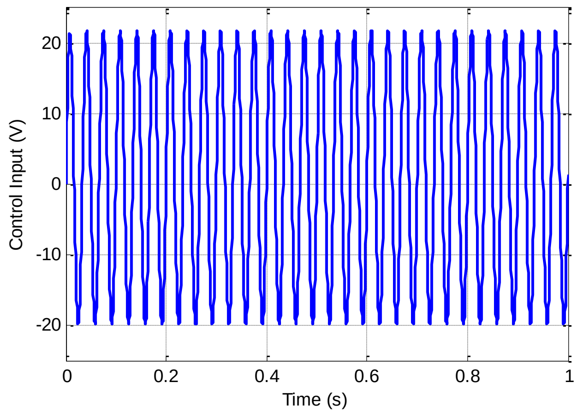

Fig. 7. Control input for MPC (30 Hz) (3 predictive steps)

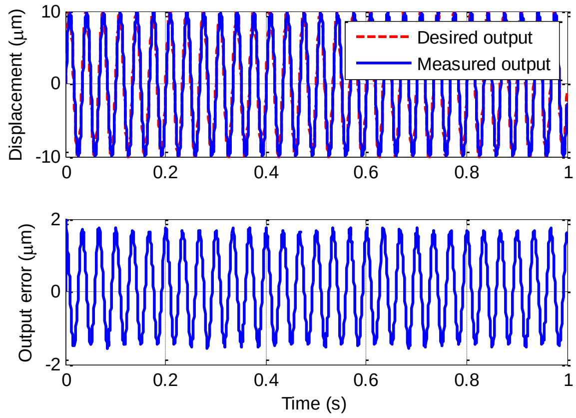

Fig. 8. Tracking result for MPC (30 Hz) (3 predictive steps)

V. CONCLUSION

This paper has discussed the model predictive control technique for piezoelectric actuators, where the model of PEA is regarded as linear model. The parameters of the model are identified using least square method. The proposed method shows its effectiveness in tracking performance. Moreover, it is simple and easy to be implemented. However, due to the strong nonlinearity hysteresis at high frequency, MPC couldn't provide accuracy.

REFERENCES

[1] Zawierta, M.; Fleming, A.; Putrino, G.; Yong, Y. Multimodal atomic force microscopy with optimized higher eigenmode sensitivity using on-chip piezoelectric actuation and sensing. Nanotechnology 2019, 8, 085503.

[2] Gu, G.Y.; Zhu, L.M.; Su, C.Y. Modeling and compensation of asymmetric hysteresis nonlinearity for piezoceramic actuators with a modified Prandtl-Ishlinskii model. IEEE Trans. Ind. Electron. 2014, 61, 1583–1595.

[3] Qin, Y.D.; Duan, H. Single-Neuron adaptive hysteresis compensation of piezoelectric actuator based on hebb learning rules. Micromachines 2020, 11, 84..

[4] Ding, B.X.; Li, Y.M. Hysteresis compensation and sliding mode control with perturbation estimation for piezoelectric actuators. Micromachines 2018, 9, 241.

[5] Ounissi, A.; Landry, M.; Kaddouri, A.; Abdessemed, R. PSO based parameter identification of Colman-Hodgdon hysteresis model of a piezoelectric actuator and PID feedback controller. Contemp. Eng. Sci. 2014, 7, 179–192.

[6] Lin, C.J.; Lin, P.T. Tracking control of a biaxial piezo-actuated positioning stage using generalized Duhem model. Comput. Math. Appl. 2012, 64, 766–787.

[7] Xu, R.; Zhang, X.Y.; Guo, H.Y.; Zhou, M.L. Sliding mode tracking control with perturbation estimation for hysteresis nonlinearity of piezo-actuated stages. IEEE Access 2018, 6, 30617–30629.

[8] Li, Z.; Su, C.Y.; Chai, T.Y. Compensation of hysteresis nonlinearity in magnetostrictive actuators with inverse multiplicative structure for Preisach model. IEEE Trans. Autom. Sci. Eng. 2014, 11, 613–619. [CrossRef] 9. Li, C.T.; Tan, Y.H. Adaptive output feedback control of systems preceded by the Preisach-type hysteresis. IEEE Trans. Syst. Man Cybern. B Cybern. 2005, 35, 130–135.

[9] Xiao, S.L.; Li, Y.M. Modeling and high dynamic compensating the rate-dependent hysteresis of piezoelectric actuators via a novel modified inverse Preisach model. IEEE Trans. Control Syst. Technol. 2013, 21, 1549–1557.

[10] Liu, S.N.; Su, C.Y.; Li, Z. Robust adaptive inverse control of a class of nonlinear systems with Prandtl-Ishlinskii hysteresis model. IEEE Trans. Autom. Control. 2014, 59, 2170–2175.

[11] Kuhnen, K. Modeling, identification and compensation of complex hysteretic nonlinearities: A modified Prandtl-Ishlinskii approach. Eur. J. Control 2003, 9, 407–418.

[12] D. Habineza, M. Rakotondrabe and Y. Le Gorrec, "Bouc–Wen Modeling and Feedforward Control of Multivariable Hysteresis in Piezoelectric Systems: Application to a 3-DoF Piezotube Scanner," in *IEEE Transactions on Control Systems Technology*, vol. 23, no. 5, pp. 1797-1806, Sept. 2015, doi: 10.1109/TCST.2014.2386779.

[13] Z. Liu, G. Lai, Y. Zhang, X. Chen and C. L. P. Chen, "Adaptive Neural Control for a Class of Nonlinear Time-Varying Delay Systems With Unknown Hysteresis," in *IEEE Transactions on Neural Networks and Learning Systems*, vol. 25, no. 12, pp. 2129-2140, Dec. 2014, doi: 10.1109/TNNLS.2014.2305717.

[14] Z. Li, X. Zhang, C. Su and T. Chai, "Nonlinear Control of Systems Preceded by Preisach Hysteresis Description: A Prescribed Adaptive Control Approach," in *IEEE Transactions on Control Systems Technology*, vol. 24, no. 2, pp. 451-460, March 2016, doi: 10.1109/TCST.2015.2441001.

[15] Nguyen, M.L.; Chen, X.K.; Yang, F. Discrete-time quasi-sliding-mode control with prescribed performance function and its application to piezo-actuated positioning systems. IEEE Tans. Ind. Electron. 2018, 65, 942–950.

[16] Shan, J.J.; Yang, L.; Li, Z. Output feedback integral control for nano-positioning using piezoelectric actuators. Smart Mater. Struct. 2015, 24, 045001.

[17] W. He and T. Meng, "Adaptive Control of a Flexible String System With Input Hysteresis," in *IEEE Transactions on Control Systems Technology*, vol. 26, no. 2, pp. 693-700, March 2018, doi: 10.1109/TCST.2017.2669158.

[18] Ge, P.; Jouaneh, M. Generalized Preisach model for hysteresis nonlinearity of piezoceramic actuators. Precis. Eng. 1977, 20, 99–111.

[19] Ljung, “System Identification,” Birkhäuser, Boston, USA, 1998.

[20] E. F. Camacho and C. Bordons, “Model Predictive Control,” Springer-Verlag, London, England, 2007.

Multi Mobile Robot System Application on Transportation in the Warehouse: an Introduction

Hanh Nguyen Thi Hong
Institute of Mechanics
Vietnam Academy of Science and Technology
Hanoi, Vietnam
nguyenhonghanh.imech@gmail.com

Hung Truong Xuan
Vietnam National Space Center
Vietnam Academy of Science and Technology
Hanoi, Vietnam
txhung@vnsc.org.vn

Phuong Phung Kim
Insitute of System Integration
Le Quy Don Technical University
Hanoi, Vietnam
phuongpk.isi@lqdtu.edu.vn

***Abstract*: Firstly introduced in the 1980s, multi mobile robot systems (MMRS) have been rapidly developed in research activities and practical usage. Based on a swarm of mobile robots with the ability to plan, coordinate tasks and organize operations, a MMRS has many advantages compared to a single robot, such as space coverage as well as operational efficiency. They can successfully handle complex tasks that a single mobile robot lacks the ability to perform. In this article, we introduce a specific application of MMRS in the items distribution system of the warehouse or the fulfillment center. For this use case, the "collective" feature of the MMRS is exceptionally well-suited to the requirements of warehouse management systems, being able to simultaneously handle multiple tasks with fast delivery speed, reduction of inventory time, flexible quick adaptation with the warehouse reconfiguration and the goods arrangement. This application is speedily growing with many applicable solutions and proposed models in recent years. State of art solutions were combinations of the mobile robot and the human staff, the mobile robots moving in 2D or 3D space carrying a package of goods or the whole storage pod. The number of robots can be hundreds to thousands to cover different area types: from mini-mart storage to huge fulfillment centers. The MMRS herein can be integrated with new technologies: cloud computing, IoT, artificial intelligence and high-end sensors, actuators, embedded computers to improve not only the functions of each robot but also the features of the whole system. We also surveyed this MMRS application in Vietnam in order to realize its prospects.**

Keywords: multi robot system, multi mobile robot system, mobile robot, distribution system of warehouse, fulfillment center

I. INTRODUCTION

The initial concept of multi-robot system (MRS) was formed in the late 1980s along with several works in the distributed robotic systems and the research objects are mobile robots. Since then, there are a lot of issues and topics are considered to look into, for example, biological inspirations; communication; architectures; task allocation and control; localization and mapping; exploration; object transport and manipulation; motion coordination and control; formation control; reconfigurable robots and multi-agent robots; multi-sensor fusion and so on [1], [2], [3]. Generally, MRS is a set of many robotic units that are integrated with advanced technology, embedded computers, smart sensors, and state-of-art communication networks. They can share tasks to achieve a common goal by exchanging information, coordination and cooperation during the operation. The robots may operate under the same environmental conditions and are capable of performing complex and difficult missions that are not accomplished by a single robotic unit. Moreover, MRS can achieve redundant ability and the robots may perform the assigned tasks in a reliable, fast and cost-saving way in terms of the total system.

Darmanin and Bugeja [4] indicate several major application areas of MRS: surveillance, search and rescue; foraging and flocking with swarm-based systems; formation and exploration; cooperative manipulation; team heterogeneity; adversarial environment. Rizk and et al. [5] surveys the application fields of heterogeneous MRS according to the task complexity and the levels of automation. Existing works mostly are exploration, mapping and navigation; surveillance and target tracking; search and retrieve or prosecute; formation control. Moreover, there are also logistics and transportation; service robotics in both public and private domains; exploration in hazardous environments; entertainment areas, etc. The application fields are not only on the ground but also in the water and space.

The advantages of MRS over a single robot are as follows:

- MRS has a better spatial distribution to cover a large area;

- MRS achieves gradually better performance, such as shorter completion time of a task, less energy consumption...;

- MRS provides a sustainable solution with fault tolerance, redundancy, reliability, flexibility, scalability;

- MRS offers lower costs by using low-cost robotic elements to complete jobs that require a high-cost, complex robot to perform.

Multi mobile robot system (MMRS) is a subset of MRS, which mainly consists of mobile robots. The MMRS can be classified into collective swarm systems and intentionally cooperative systems [6]. In the former, each unit can perform its own task and require a little knowledge of other members. Based on the homogeneous structure and configuration, the units of the collective swarm system can act as the redundant units when the others stop working. There are some features of the collective swarm systems, including the number of units in the system is very large (maybe up to thousands of units); scale can be changed easily, such as the coverage area or the number of active units; high redundancy because of the homogeneous configuration and structure, Fig. 1 displays the collective swarm systems in the Amazon fulfillment center. In the latter, each unit in the intentionally cooperative system has to acquire the information of the other members nearby and they work together based on their conditions, abilities and capacities to achieve the goal. The intentionally cooperative system can be extended to robotic elements with different configurations.

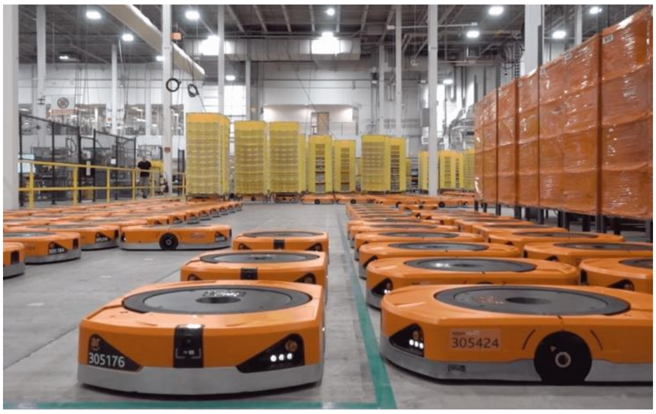

Fig. 1. MMRS in an Amazon fulfillment center

We aim to introduce about a specific application of MMRS which is goods transportation in warehouses in this paper. The rest of the article is organized into five sections as follows. In Section II, we present an overview of warehouses and their evoluton; how suitable MMRS is for warehouse operations. Subsequently, Section III introduces some dedicated case-studies based on their unique features and Section IV describes several key technology approaches that help MMRS to fit this application. Afterwards, we introduce some activities concerning MMRS in Vietnam in Section V and, finally, Section VI contains some conclusions.

II. WAREHOUSE OVERVIEW

A warehouse is a building where large quantities of goods are stored, especially before they are sent to shops to be sold and it can be used by factories, importers and exporters, distributors, transport companies, etc. Warehouses usually have a large floor area, located in industrial areas or suburbs of cities or residential areas. After introducing mass production and supply chain in the late 1920s, the warehouse has evolved to new forms to fulfill the advanced product distribution approaches. Two of those evolutions are distribution centers and fulfillment centers.

A distribution center is a type of warehouse used to store goods for distribution to wholesalers, retailers, or possibly directly to consumers and is the essential component of the supply chain nowadays. Distribution centers are the hubs to stock a large number of products and are sometimes acted as fulfillment centers. A fulfillment center is a type of warehouse specializing in packaging orders and can bring goods directly to the consumers. It is the last component of the supply chain.

TABLE I. WAREHOUSE COMPARISON

Traditional warehouse	***Distribution/Fulfillment Center***
Store the maximum amount of all goods at any time, anywhere:	Store the right amount of the right kind of goods in the right place and at the right time:
- Store goods only	- Besides storing goods, provide other value-added services such as mixing, fulfilling order, packaging, etc.
- Long storage time and slow delivery speed	- Short storage time and fast delivery speed
- An efficient storage place for goods	- Customer-oriented, be an efficient connection between suppliers and customers
- Simple operations	- Complex operations, often equipped with the latest technology for management, order processing, transportation, etc.

Distribution/fulfillment centers are continuously playing an important role in the development of human society to shape the flow of goods from the suppliers to the consumers through the supply chain. The major different things of those centers from traditional warehouses are mentioned in Table I. Normally, goods are stored temporarily in a short time and delivered to the retailers or directly to the consumers as soon as possible. Nowadays, there are many state-of-art technologies or high technology solutions to be applied in the distribution system of warehouses or other systems to cut operating costs and improve operational efficiency. They are two crucial factors to impact the evolution of these types of warehouses and MMRS is considered as one of the key solutions to transport goods in the warehouses.

MMRS can provide quick deployment in a short time, less than six months depending on the size of the warehouses. Besides, flexibility is another important feature because MMRS can reconfigure itself easily with a small amount of required time, enlarge or reduce the number of active units according to actual operation in the warehouse. The consequences of the quick deployment and the flexibility are lowering the initial investment costs as well as reducing the reinvestment costs in the future.

MMRS also has the ability to handle multiple tasks concurrently by distributing tasks to each unit and managing the operation of the system. In combination with a reasonable arrangement of goods in the warehouses, MMRS can help to reduce the transportation time and improve the performance of the distribution system of warehouses then. On the other hand, MMRS can be used to rearrange goods between areas in the warehouse to optimize the storage space.

III. MMRS IN WAREHOUSE 'S TRANSPORTATION

The usage of MMRS as service robots in logistic application has increased sharply in recent years. The statistical data from IFR shows the growth rate is about 40% in 2018-2020 period and will reach 259 thousand units in 2023, top 1 application of service robots [7]. We introduce some exciting MMRS solutions in this section, such as Chuck, Fabric's MMRS, Skypod and Kiva, as follow. All of them have several unique features to improve the goods transportation activities. Table II demonstrate the difference between all four solutions.

TABLE II. MMRS COMPARISON

	Chuck	**Fabric's robots**	**Kiva (Amazon Robotic)**	**Skypod**
payload (kg)	up to 90	less than 10	up to hundreds	up to 30
navigation method	optimal free way (SLAM-based)	optimal virtual guideline (reference marks)		optimal virtual guideline (SLAM-based)
collision avoidance	yes			

movement direction	2D (flat floor)			3D (flat/ inclined floors, climb up/down)
equipped bin/racks *1	yes	no		
associate *2	with pickers	with elevators	no	

*1: The mobile robots have already equipped the bins/racks during the operation.

*2: The mobile robots can work together with people or other units.

Chuck is a solution of collaborative mobile robotics to cooperate with humans when processing tasks in the warehouse, such as picking, counting, replenishment and sorting goods. The robot leads the coworker and notices the quantity of goods to be handled during the task. This solution is developed for the fulfillment centers by 6River Systems (6RS), a US-based start-up company founded in 2015 [33]. Chuck is integrated with cloud-based software that allows optimal performance, the working time as well as the walking distance, and provides real-time management and monitoring activity. Machine learning algorithm and artificial intelligence-based software are used for path planning and movement. The robot can move completely automatically along the corridors in the warehouse and it can deal successfully with any arising uncertainties, such as slow down during over-crowd situation and obstacle avoidance. The robot equips several modular rack configurations to be able to store different types of goods and can handle up to 90.7 kg. The initial investment cost of the Chuck system is about 250,000 USD for a group of 8 robots and the operating cost is about 50,000 USD per year [32].

A micro-fulfillment solution for online grocery or convenience retailers is developed by Fabric, an Israeli start-up company founded in 2015, and it is heavily based on specialized MMRS to transport goods in the storage [34]. The micro term aims to fulfillment centers, whose areas are less than 1000 m2 and install very dense storage racks. The reference marks are installed across the warehouse floor every few feet to provide the virtual guideline for the movement of the mobile robots. The robots are very small and move around in the warehouse to carry the storage baskets, which are picked by the lift robots, to the packing zone. The associates pick the order items and the baskets are returned to the storage racks by the robots then. Due to the dense storage racks, robots can move not only in the corridors between racks but also under the racks. Fabric offers this solution to allow retailers to develop online services with the stores located inside or nearby the town or residential areas, thus shortening the delivery time. The storage can be converted from the underground space or the basement of the building.

The Skypod system developed by Exotec, a startup founded in 2015 in France, is to process the orders in very large fulfillment centers. The robots are designed to be able to not only move on flat or small inclined floors but also climb up and down the storage racks by using the special guides mounted along with the racks [35]. This movement approach is to maximize storage space, such as increasing the rack height as well as the density of racks. When moving on the warehouse floor, the robot uses the virtual map navigation method (SLAM) to locate its positions and detect the obstacles or the other robots. The management software arranges virtual paths for the robots across the floor to manage the operation smoothly and adjusts its scale according to the order-processing requirement through real-time reconfiguration in the software. The maximum carrying capacity of the robot is about 30 kg, including the weight of the bin.

Kiva Systems, a US-based startup founded in 2003, has developed a concept of the distribution system using a very large number of mobile robots (hundreds to thousands of units). The robots bring the goods to the desired location to process the order instead of workers moving and picking the goods in the storage. This idea is to save the daily walking time and reduce the number of workers in the warehouse. Kiva Systems was acquired by Amazon and deployed in the Amazon fulfillment centers. Amazon had deployed more than 200,000 robots in 26 fulfillment centers, out of its 175 centers worldwide, together with hundreds of thousands of human workers by the end of 2019. Those systems allow Amazon to deploy the Amazon Prime service to meet customers' fast delivery requirements. These new technologies increase the company store up to 40 percent more inventory and also help the pickers' jobs easier. The robots raise the average picker's productivity by around three or four times [36]. The success of Kiva affects the implementation of mobile robots in distribution facilities, a multi-billion dollar market, leading to the appearance of many startups in this field around the world. It indicates that robotics and automation can not only create new markets but also revolutionize established ones as well, here is logistic and goods distribution services [8].

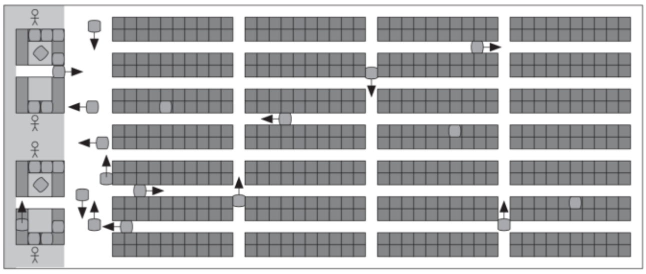

Fig. 2. Typical layout of Kiva installation in fulfillment center

The Kiva solution consists of two main units: storage racks, inventory pods, and mobile robots, drive units. The reference marks are installed as a grid across the warehouse floor to provide the virtual guideline for the movement of the mobile robot. The mobile robots have small compact structures to fit under the inventory pods. They also integrate lifting mechanisms that allow them to lift storage racks off the ground and transport them to the stations around the warehouse perimeter. They only bring the correct racks to the stations where a worker picks the desired products to fulfill the orders. After finishing the picking process, the robot delivers the rack to an empty location in the warehouse and waits for a new transport request. Fig. 2 shows a typical layout of a Kiva installation in a warehouse/distribution center [9]. This process can be taken simultaneously by many mobile robots to fulfill the orders continuously in real-time. The Kiva system architecture allows to create operational flexibility, reduce the number of the stations as well as the robots according to the demands of the warehouse operation.

IV. Technological Approaches

As discussed in Section II, MMRS fits the warehouses for goods transportation. There are some technological approaches implemented in MMRS to take important roles so that those systems can provide quick deployment, flexibility;

reduce the transportation time; improve the performance through multi-tasking capability. In our point of view, these technological approaches are path planning, task allocation, localization and navigation. Later, we present them in detail with some insight discussions, especially path planning and task allocation.

A. Path Planning

Path planning aims for movement from initial positions to reach goal positions with collision-free motions. Each robot must deal with not only static obstacles, if any, but also dynamic ones, which are other robots or human. A good path planning approach is expected to achieve several optimal goals, such as time, energy, system performance, etc. According to [10], the path planning approaches are classified into several groups: heuristic, artificial potential field (APF), artificial intelligence types, behavior decomposition, cased-based learning, and rolling windows. Considering the coverage path planning (CPP) of multi-robots [11], the path planning approaches are classified into grid-based search, geometric, reward based, near best view, random incremental planners.

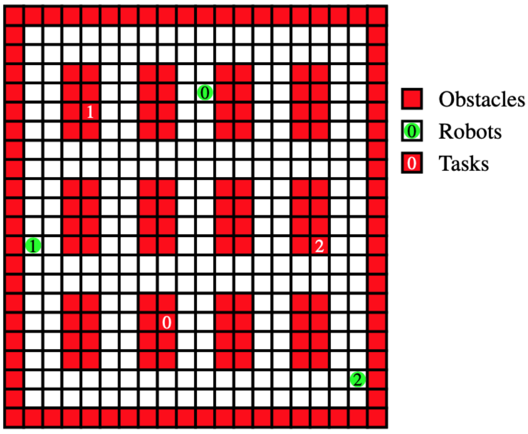

Fig. 3. Warehouse layout in [18]

In 1985, Artificial Potential Field (APF) was firstly introduced to handle obstacle avoidance by using a differentiable real-valued function, called a potential function, that guides the motion of the robot [12]. The function typically consists of two elements: attractive element and repulsive element. The former pulls the robot towards the goal, and the latter pushes the robot away from the obstacles. Based on the gradient of the potential function points in the direction that locally maximally increases, the robot can set a necessary path to move towards the goal. Since then, there are many variations of the APF to be proposed to solve the collision-free path planning. Some of them try to have a new addition in the repulsive element, for instance, a regulative factor based on the shortest distance between the robot and the target [13], a constant gain determined by experience [14], all repulsive force generated by other nearby robots [15]; or in the attractive element, such as a minimum threshold value [16]. Modifications of the potential function are also introduced, for example, a random factor [14], a rotating potential field [17], two additional elements: excitation and relaxation [18]. Fig. 3 displays the warehouse layout in which the path planning is implemented. All the modifications aim to improve the performance of the APF method to mostly avoid the collision, avoid local minimum, and suppress oscillation.

Besides APF, artificial intelligence and population-based approaches are used frequently to solve the path planning problem. The former is mainly reinforcement or deep reinforcement learning. The first introduction of the latter was particle swarm optimization (PSO) for the optimization of continuous nonlinear functions [19]. It is a simulation of a simplified social model of bird flocking, fish schooling. Each agent (particle) moves around the space evaluating the positions and remembers its own best position. Meanwhile, other agents also knew the globally best position that one member of the flock had just found. They adjust movement to converge on that position. Some recent improved PSO is proposed to compute an optimal collision free path for each robot: the IPSO [20] with two evolutionary operators (EOPs), multi-crossover inherited from the genetic algorithm, and bee colony operator; the multi-objective particle swarm optimization (MOPSO) [21] with the probabilistic window to combine the current information obtained through the robot sensors and experiences of the previous robots by assigning a probability to the reachable positions; the cooperatively coevolving particle swarm optimization (CCPSO2) [22] to solve the multi-robot persistent coverage and cooperative coverage. Together with PSO, there are several recent proposed evolutionary methods to adopt to path planning, such as artificial bee colony (ABC) for neighborhood search planner [23], combined invasive weed optimization (IWO) technique along with a firefly optimization algorithm [24], ant colony optimization (ACO) for obtaining the optimal path, which contributes to minimizing the energy/time consumption [25], a hybridization of kidney-inspired (KA) and sine–cosine algorithm (SCA) for path planning [26], a genetic algorithm (GA), using four operations: selection, mutation, evolutionary reversal, and slide [27].

B. Task Allocation

According to [6], an MMRS mission is defined as a set of orders (tasks) that must be fulfilled completely in the warehouse. Each incoming order can be further broken down into a list of items as independent subtasks or hierarchical subtask trees or roles-based by automated planners or designers. After that, the task assignment or task allocation (MRTA) is implemented based on several factors, such as the number of robots needed to complete an order, the number of items that one robot can complete in a desired amount of time, the relation between the order/item and the time window in which the task is distributed to the robot, etc. So, the classification of task allocation is described as follow:

- Single-robot tasks or subtasks (SR), to be performed by only one robot at a time,
- Multi-robot tasks or subtasks (MR), to be performed by more than one robot at the same time,
- Instantaneous assignment of tasks or subtasks (IA), to be assigned at once,
- Time-extended assignment of tasks or subtasks (TA), to be assigned in the future.

When the intelligent warehouse receives simultaneous multiple customer demands, the MMRS can be considered as multi-task robots facing dynamic multiple customer demands. Normally, in order to execute task allocation effectively, the warehouse can be simplified as following assumptions [28]:

(1) Each unit is equipped with the necessary sensors for detecting the environment.

(2) Each unit can only run in four directions i.e. up, down, left and right.

(3) The units and tasks are identical to each other.

(4) Units are independent when performing tasks.

(5) The maximum completion time and total completion time of a unit are measured by its movements (the shortest distance between the start and end points).

(6) The runtime between the packaging station and the racks is fixed.

(7) Units are executing tasks without considering collision. The proposed approaches are based on the PSO to solve multi-order task scheduling and path planning for MMRS.

Several proposed methods were introduced recently. Task allocation can be solved together with path planning by using the algorithm based on PSO [28]. The nearest-neighbor based Clustering And Routing (nCAR) algorithm is presented in [29] to allow picking more than one object on a single run to improve the SR task. Therefore, the overall travel time of the robot is reduced. The combination of Monte Carlo Tree Search (MCTS) methods and the decentralized planner is introduced to warrant the scalability, flexibility and robustness of the MRTA for MMRS, especially when the number of robots is very large [30].

TABLE III. NAVIGATION TYPE COMPARISON

	Tapes	Spot/ Inertial	Laser/ Target	SLAM
route type	fixed route	fixed route	free route	free route
localization	fixed mark	fixed mark/ software	fixed mark/ software	software
speed	limited	high	high	high
installation	time consuming	time consuming	quick	quick
modifica-tion	time consuming	time consuming	easy	easy
accuracy	very good	very good	good	quite good
cost	low	low to medium	high	high

C. *Localization and Navigation*

The first navigation/guidance solution was proposed in 1953 by Arthur "Mac" Barrett, using a guidewire system. After one year, the first self-driving tractor was built and was able to move around guided by a guidewire. The navigation technology has also changed rapidly since then and became more and more mature. When navigating, the mobile robot can locate itself and obstacles as well as other robots. The navigation methods can be divided into two broad groups [31]: fixed route guidance methods and free route guidance methods. The former are mature technologies: electromagnetic wire, optical or magnetic tape, and fixed spots. The latter are an inertial guide, ultrasonic guide, laser, vision, and GPS which are based on advanced technologies and have very excellent prospects. Navigation selection is very crucial for the implementation of an MMRS. Mobile robot navigation consists of several methods to improve accuracy, stability, and flexibility. Spot/inertial navigation normally is the combination of spot method, inertial guide, and vision; SLAM usually consists of ultrasonic guide, laser, and vision. When operating in the outdoor environment, GPS is equipped to enhance navigation. Table III presents the difference between several well-known navigation types that can be implemented in warehouses. Fig. 4 displays four navigation types: tapes on the right bottom, spot/inertial on the left bottom, laser/target on the left top, SLAM on the right top.

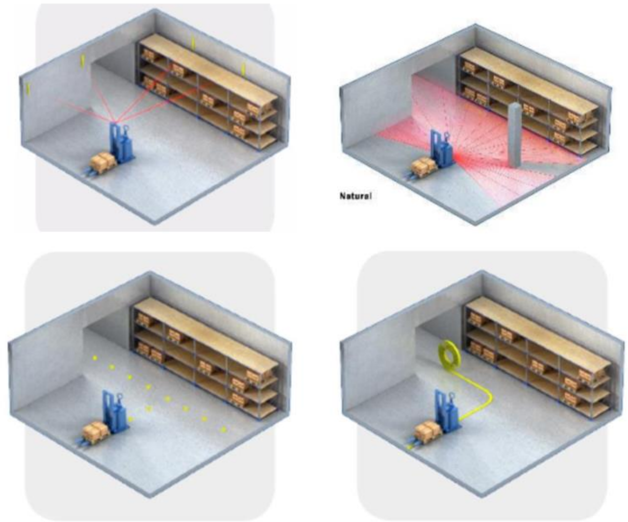

Fig. 4. Four navigation types [37]

V. MMRS APPLICATIONS IN VIETNAM

Robots and mobile robots are fascinating research areas in Vietnam. According to the database of National Agency for Science and Technology Information, the research activities have mostly focused on the solutions of the single mobile robot [38]. Their applications are household appliances, goods transportation, healthcare, and agriculture. A few projects of MMRS have just been announced in recent years, the Vibot system of Le Quy Don University as well as the Green Phoenix project of the Phenikaa Corporation. They intend to develop a multi-mobile robots system for transportation in the isolated infectious diseases areas in hospitals or medical facilities.

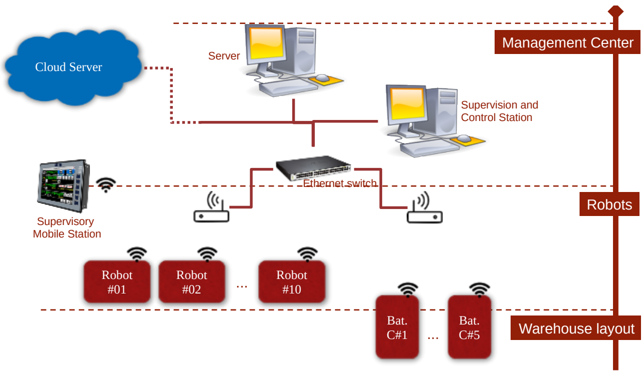

Fig. 5. System architecture of ImeBots

ImeBots is another MMRS project, which is under-development by Institute of Mechanics, Vietnam Academy of Science and Technology. The system architecture of ImeBots is displayed in Fig. 5 which has ten units (mobile robots) and one Management Center. All units can communicate with each other and the Center by using an ad-hoc wireless network. The Server aims to collect and store operation data only. It works independently from the other stations, the Supervision & Control Station (SCS) and the Supervision Mobile Station (SMS). The SCS performs the monitoring and global control functions of the entire system, including operations of all robots. Besides, the SMS performs the monitoring functions only and it can be moveable along with the operator.

The concept of ImeBots is to handle the goods transportation during order fulfillment in the warehouse with the objective function is time-consuming reduction and some boundary conditions: shorten travel distance, energy-saving etc. All units can move unlimited around the warehouse, even below the storage racks. They carry the required racks along corridors to the picking stations which are located on the right as displayed in Fig. 6. After the pickers finish their goods-picking, the mobile robots return the racks to original positions and start to process the next delivery task. Task allocation and path planning are critical to ImeBots so that each order can divide successfully into tasks and each task can assign to each unit. In principle, each robot can have its free will to handle local control by itself within the boundary of global control. All units execute optimally their own tasks in parallel based on path planning algorithms together with the virtual guideline with reference marks. They also share their positions and operation states to other units and the SCS, SMS through an ad-hoc communication network. Then, all units can update their own map during the navigation. Considering the ImeBots concept, the movable storage racks should be arranged in rows and also created corridors to allow robot access, as displayed in Fig. 6. The robot identifies the required rack using computer vision, carries it by lifting and moves along the corridors.

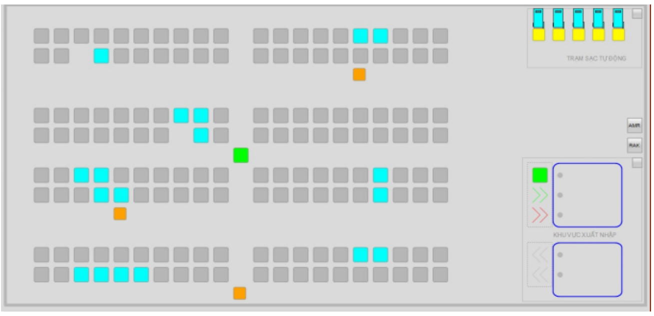

Fig. 6. Warehouse layout

VI. CONCLUSIONS

MMRS has the features and capabilities to be extraordinarily well-suited to the requirements of order fulfillment process in the warehouse. They are able to simultaneously handle multiple tasks with fast delivery speed, reduction of inventory time, flexible quick adaptation with the warehouse reconfiguration and the goods arrangement. Although this application is quickly growing around all over the world, but being very limited in Vietnam. Therefore, we can expect the development of a similar system in the future, along with the exceptionally rapid development of e-Commerce in Vietnam.

ACKNOWLEDGMENT

This research was supported by the Program "Supporting Research, Development and Technology Application of Industry 4.0" (KC-4.0/19-25) of the Ministry of Science and Technology in Vietnam through the funding of the Project "Research and Development for a Multi Mobile Robots System that Integrates some Key Technologies of the 4th Industrial Revolution (Industry 4.0), Application in logistics", no. KC-4.0-34/19-25.

REFERENCES

[1] T. Arai, E. Pagello, and L. E. Parker, “Guest editorial advances in multirobot systems,” IEEE Trans. Robot. Autom., vol. 18, no. 5, pp. 655–661, 2002, doi: 10.1109/TRA.2002.806024.

[2] A. Gautam and S. Mohan, “A review of research in multi-robot systems,” in 2012 IEEE 7th International Conference on Industrial and Information Systems (ICIIS), 2012, pp. 1–5, doi: 10.1109/ICIInfS.2012.6304778.

[3] Y. Cai and S. X. Yang, “A Survey on multi-robot systems,” in World Automation Congress 2012, 2012, pp. 1–6.

[4] R. N. Darmanin and M. K. Bugeja, “A review on multi-robot systems categorised by application domain,” in 2017 25th Mediterranean Conference on Control and Automation (MED), 2017, pp. 701–706, doi: 10.1109/MED.2017.7984200.

[5] Y. Rizk, M. Awad, and E. W. Tunstel, “Cooperative Heterogeneous Multi-Robot Systems: A Survey,” ACM Comput. Surv., vol. 52, no. 2, Apr. 2019, doi: 10.1145/3303848.

[6] L. E. Parker, D. Rus, and G. S. Sukhatme, “Multiple Mobile Robot Systems,” in Springer Handbook of Robotics, B. Siciliano and O. Khatib, Eds. Cham: Springer International Publishing, 2016, pp. 1335–1384.

[7] "IFR Press Conference", World Robotics 2020 Report, 2020.

[8] R. D’Andrea, “Guest Editorial: A Revolution in the Warehouse: A Retrospective on Kiva Systems and the Grand Challenges Ahead,” IEEE Trans. Autom. Sci. Eng., vol. 9, no. 4, pp. 638–639, 2012, doi: 10.1109/TASE.2012.2214676.

[9] P. R. Wurman, R. D’Andrea, and M. Mountz, “Coordinating Hundreds of Cooperative, Autonomous Vehicles in Warehouses,” AI Mag., vol. 29, no. 1, p. 9, 2008, doi: 10.1609/aimag.v29i1.2082.

[10] H. Zhang, W. Lin, and A. Chen, “Path Planning for the Mobile Robot: A Review,” Symmetry (Basel)., vol. 10, no. 10, p. 450, Oct. 2018, doi: 10.3390/sym10100450.

[11] R. Almadhoun, T. Taha, L. Seneviratne, and Y. Zweiri, “A survey on multi-robot coverage path planning for model reconstruction and mapping,” SN Appl. Sci., vol. 1, no. 8, p. 847, 2019, doi: 10.1007/s42452-019-0872-y.

[12] O. Khatib, “Real-time obstacle avoidance for manipulators and mobile robots,” in Proceedings. 1985 IEEE International Conference on Robotics and Automation, Mar. 1985, vol. 2, pp. 500–505, doi: 10.1109/ROBOT.1985.1087247.

[13] S. M. H. Rostami, A. K. Sangaiah, J. Wang, and X. Liu, “Obstacle avoidance of mobile robots using modified artificial potential field algorithm,” EURASIP J. Wirel. Commun. Netw., vol. 2019, no. 1, p. 70, 2019, doi: 10.1186/s13638-019-1396-2.

[14] Z. Wu, W. Su, and J. Li, “Multi-robot path planning based on improved artificial potential field and B-spline curve optimization,” in 2019 Chinese Control Conference (CCC), Jul. 2019, pp. 4691–4696, doi: 10.23919/ChiCC.2019.8865232.

[15] F. Matoui, B. Boussaid, B. Metoui, and M. N. Abdelkrim, “Contribution to the path planning of a multi-robot system: centralized architecture,” Intell. Serv. Robot., vol. 13, no. 1, pp. 147–158, 2020, doi: 10.1007/s11370-019-00302-w.

[16] T. Zhao, H. Li, and S. Dian, “Multi-robot path planning based on improved artificial potential field and fuzzy inference system,” J. Intell. Fuzzy Syst., vol. 39, pp. 7621–7637, 2020, doi: 10.3233/JIFS-200869.

[17] Z. Pan, D. Li, K. Yang, and H. Deng, “Multi-Robot Obstacle Avoidance Based on the Improved Artificial Potential Field and PID Adaptive Tracking Control Algorithm,” Robotica, vol. 37, no. 11, pp. 1883–1903, 2019, doi: 10.1017/S026357471900033X.

[18] K. F. E. Tsang, Y. Ni, C. F. R. Wong, and L. Shi, “A Novel Warehouse Multi-Robot Automation System with Semi-Complete and Computationally Efficient Path Planning and Adaptive Genetic Task Allocation Algorithms,” in 2018 15th International Conference on Control, Automation, Robotics and Vision (ICARCV), Nov. 2018, pp. 1671–1676, doi: 10.1109/ICARCV.2018.8581092.

[19] J. Kennedy and R. Eberhart, “Particle swarm optimization,” in Proceedings of ICNN’95 - International Conference on Neural Networks, Nov. 1995, vol. 4, pp. 1942–1948 vol.4, doi: 10.1109/ICNN.1995.488968.

[20] P. K. Das and P. K. Jena, “Multi-robot path planning using improved particle swarm optimization algorithm through novel evolutionary operators,” Appl. Soft Comput., vol. 92, p. 106312, 2020, doi: https://doi.org/10.1016/j.asoc.2020.106312.

[21] S. Thabit and A. Mohades, “Multi-Robot Path Planning Based on Multi-Objective Particle Swarm Optimization,” IEEE Access, vol. 7, pp. 2138–2147, 2019, doi: 10.1109/ACCESS.2018.2886245.

[22] G. Sun, R. Zhou, B. Di, Z. Dong, and Y. Wang, “A Novel Cooperative Path Planning for Multi-robot Persistent Coverage with Obstacles and Coverage Period Constraints,” Sensors, vol. 19, no. 9, p. 1994, Apr. 2019, doi: 10.3390/s19091994.

[23] A. Q. Faridi, S. Sharma, A. Shukla, R. Tiwari, and J. Dhar, “Multi-robot multi-target dynamic path planning using artificial bee colony and evolutionary programming in unknown environment,” Intell. Serv. Robot., vol. 11, no. 2, pp. 171–186, 2018, doi: 10.1007/s11370-017-0244-7.

[24] M. R. Panda, S. Dutta, and S. Pradhan, “Hybridizing Invasive Weed Optimization with Firefly Algorithm for Multi-Robot Motion Planning,” Arab. J. Sci. Eng., vol. 43, no. 8, pp. 4029–4039, 2018, doi: 10.1007/s13369-017-2794-6.

[25] C. Gao, Y. Kou, Z. Li, A. Xu, Y. Li, and Y. Chang, “Optimal Multirobot Coverage Path Planning: Ideal-Shaped Spanning Tree,” Math. Probl. Eng., vol. 2018, p. 3436429, 2018, doi: 10.1155/2018/3436429.

[26] P. K. Das, “Hybridization of Kidney-Inspired and Sine–Cosine Algorithm for Multi-robot Path Planning,” Arab. J. Sci. Eng., vol. 45, no. 4, pp. 2883–2900, 2020, doi: 10.1007/s13369-019-04193-y.

[27] R. Sun, C. Tang, J. Zheng, Y. Zhou, and S. Yu, “Multi-robot Path Planning for Complete Coverage with Genetic Algorithms,” in Intelligent Robotics and Applications, 2019, pp. 349–361.

[28] Z. Li, A. V. Barenji, J. Jiang, R. Y. Zhong, and G. Xu, “A mechanism for scheduling multi robot intelligent warehouse system face with dynamic demand,” J. Intell. Manuf., vol. 31, no. 2, pp. 469–480, 2020, doi: 10.1007/s10845-018-1459-y.

[29] C. Sarkar, H. S. Paul, and A. Pal, “A Scalable Multi-Robot Task Allocation Algorithm,” in 2018 IEEE International Conference on Robotics and Automation (ICRA), 2018, pp. 5022–5027, doi: 10.1109/ICRA.2018.8460886.

[30] D. Claes, F. Oliehoek, H. Baier, and K. Tuyls, “Decentralised Online Planning for Multi-Robot Warehouse Commissioning,” in Proceedings of the 16th Conference on Autonomous Agents and MultiAgent Systems, 2017, pp. 492–500.

[31] E. Olcay, F. Schuhmann, and B. Lohmann, “Collective navigation of a multi-robot system in an unknown environment,” Rob. Auton. Syst., vol. 132, p. 103604, 2020, doi: https://doi.org/10.1016/j.robot.2020.103604.

[32] C. Reiser, "6 River Systems Demonstrates Collaborative Robotics Solution", Logistics Viewpoints, ARC Advisory Group, 2018, <https://logisticsviewpoints.com>

[33] 6 River Systems website, <https://www.6river.com>

[34] Fabric website, <https://www.getfabric.com>

[35] Exotec website, <https://www.exotec.com>

[36] J. Del Rey, "How robots are transforming Amazon warehouse jobs - for better and worse", Vox News, Vox Media, 2019, <https://www.vox.com>

[37] C. Russell. AGV Navigation: Pros and Cons. ModexShow 2018.

[38] Web Portal, National Agency for Science and Technology Information, 05/2021, <https://db0.vista.gov.vn/>

Research and Fabrication of a Carbon Fiber Parabolic Reflector Antenna for Satellite Ground Station at S-band

Linh Phuong Ta
Vietnam National Space Center – Vietnam Academy of Science and Technology
Hanoi, Vietnam
tplinh@vnsc.org.vn

Hung Xuan Truong
Vietnam National Space Center – Vietnam Academy of Science and Technology
Hanoi, Vietnam
txhung@vnsc.org.vn

Duong Nam Bui
Vietnam National Space Center – Vietnam Academy of Science and Technology
Hanoi, Vietnam
bnduong@vnsc.org.vn

Huy Xuan Le
Vietnam National Space Center – Vietnam Academy of Science and Technology
Hanoi, Vietnam
lxhuy@vnsc.org.vn

Phuong Viet Vu
Vietnam National Space Center – Vietnam Academy of Science and Technology
Hanoi, Vietnam
vvphuong@vnsc.org.vn

Minh Duc Nguyen
Vietnam National Space Center – Vietnam Academy of Science and Technology
Hanoi, Vietnam
ndminh@vnsc.org.vn

***Abstract*: The applications of carbon fiber material are growing strongly in recent days and it obtains a lot of interest in research and development in satellite technology. Its significant advantages over conventional metal materials (such as steel, aluminum, copper…) are lightness, higher durability and the flexibility in constructing complex structures. In this paper, the possibility of using Carbon Fiber Reinforced Polymer (CFRP) is studied for the design and manufacture of a commonly used satellite ground station antenna topology - the parabolic reflector. The proposed antenna system consists of the reflector and an axial-mode helical radiating element working as the feed antenna, which allows transmitting and receiving circular polarization waves for satellite communication. The feed antenna and the simplified model of the CFRP reflector are constructed and simulated by electromagnetic simulation software for analyzing the electromagnetic properties in 3D wave propagation environment. Furthermore, to evaluate the effects of the CFRP material to the electrical properties of the antenna, an experimental sample has been created and its directional conductivity values are measured using the four-probe method. In order to mimic the isotropic conductivity of the metal material, the four laminae topology of CFRP is designed, in which, the directions of the carbon fibers in each laminate are 0°, 45°, 90° and 135°, respectively. The laminae have been bonded together by epoxy resin, then being molded to form the parabolic reflector. The simulation and measurement results of the important antenna parameters such as input reflection coefficient (S_{11}) and impedance matching, gain, radiation pattern and axial ratio are presented. The results showed an identical match between simulation and measurement to prove the availability of Carbon Fiber Parabolic Reflector of the antenna. The chosen operation frequency range lies within S-band, which is the frequency band suitable for telecommunicate between ground station and satellite.**

Keywords: component, formatting, style, styling, insert

I. INTRODUCTION

The carbon fiber composite (CFC) is a well-known improved material that can be considered as a candidate for replacing the conventional materials, such as aluminum or other conductors, in the modern material industry. The significant advantages of this material are light weight, high stiffness, high corrosion resistance, relatively good electrical and thermal conductivity. Among the CFC materials, carbon fiber reinforced polymer (CFRP) has an increasing number of applications in the aerospace field, especially in satellite technology such as spacecraft building, satellite's solar panels and payload support structures, space and small ground station antennas, etc. The CFRP material is a combination of carbon fibers (acts as the reinforcement) and a polymer matrix (typically resin), in which the fibers are embedded. This material is commonly built as laminates and its high tensile strength is only available in the fiber direction [1]. Furthermore, unlike metal or aluminum, the electromagnetic properties of CFRP reveal a high anisotropic manner, in which, for example, the conductivity along the fiber direction is generally several order of magnitudes higher than that through the transverse or through-thickness directions. The carbon fiber laminates can be in various topologies such as unidirectional fibers, or woven fabrics with different weaving patterns of two (bi-direction) or more than two directions. In the latter category, the conductivity is more uniform (more likely to the isotropic conductivity of conventional metal), however, the trade-off is the decrease of tensile strength. In the past, most of the CFRP applications focused on electromagnetic shielding properties, but in recent times, the possibility of applying this material to antenna design is gaining more attention. For examples, ASELSAN [2] manufactures antenna pedestal and reflector antenna from carbon fiber for shipborne satellite communication terminal. AISat, a small satellite developed by DLR, uses carbon fiber helical antenna for AIS receiving [3]. NEA Scout, a 6U Cubesat demonstrated an X-band, medium gain patch antenna array which is mounted on a carbon fiber deployable wing near the solar cells in the same panel [4]. Furthermore, along with the growing applications in patch and microstrip antennas, carbon fiber material can also be used in manufacturing reflection ground for popular antennas such as monopole, dipole (also presented in [1]), or radio-frequency identification (RFID) antenna [5]. Moreover, large deployable reflectors with membranes using carbon fiber reinforced silicone (CFRS) have been introduced in [6], and a parabolic offset-feed reflector antenna using CFRP is designed for W-band millimeter-wave radar systems in [7]. A 1/4-scaled sample of a self-deploying reflector antenna has been introduced in [8], the results are detailed in term of dynamic deployment analysis, but the information of the antenna expected gain and radiation pattern is not clear. The carbon composite also has potential applications when using as reflective mirrors at future satellite frequency bands such as Q-band or W-band, as demonstrated in [9].

In this paper, the design of a CFRP parabolic reflector antenna in S-band is introduced. The feed antenna is a conventional axial-mode helical which can provides right hand circular polarization (RHCP) as well as an adequate gain. The proposed antenna can be applied in S-band satellite communication in small or mobile ground stations that need lightweight terminals, or further develop to a deployable antenna configuration for satellite communication terminals of satellites belong to the nano, micro or cubesat classes.

II. Design and Fabrication of the CFRP Material

A. Carbon Fiber Configuration Selection

Amongst carbon composite materials, the CFRP is the most suitable material in constructing lightweight structures because of its much higher Young's modulus per material density in comparison to that of metals [10]. However, its conductivity is much lower than that of metals and the highly anisotropic behaviour of this electric property will prevent CFRP from being a good material for antenna reflector, unless it is configured properly. In order to overcome this problem, the experimental CFRP material used in this paper is 2x2 carbon fiber twill weave pattern, and each bi-directional carbon fiber ply is oriented and stacked based on the configuration presented in [11]:

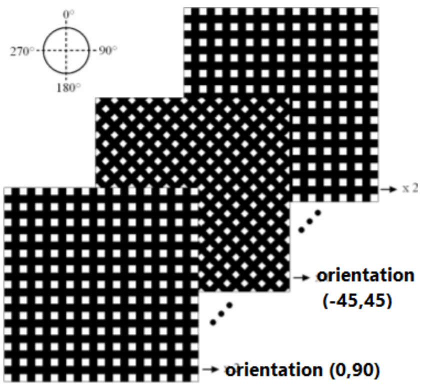

Fig. 1. *Illustration of the laminae forms by stacking plies of carbon fiber (redrawn from [11])*

As can be seen in Fig. 1, the bidirectional carbon fiber plies are being stacked to form 4 fiber directions: (0°, 90°) and (-45°, 45°), thus the isotropic of the conductivity is significantly increased. Theoretically, about 9 or 10 plies can be stacked together, with more than 4 directions in order to create even more isotropic conductivity, but in this case, the fabrication will become very complex. Furthermore, the tensile strength of the carbon fiber laminae will reduce, as mentioned in the previous section. Consequently, we decided that the best compromise in our case is using 4 plies with 4 directions.

B. CFRP Manufacturing

The carbon fiber used in this research is T400H, provided by Torayca. The general properties of the carbon fiber are showed as follows: Filament diameter: 7 µm, tensile strength: 4410 Mpa, density: 1.8 g/cm^3, carbon content: 94%.

The properties of carbon ply are: Yarn type: 3K Carbon fiber, weight (nominal): 200 g/m^2, thickness: 0.2 mm, nominal construction: 5.5 yarns/cm (warp), 5.5 picks/cm (weft). The matrix used in the experimental material is common industrial epoxy resin.

There are various methods for manufacturing CFRP material, and the technologies are selected according to the requirements of the products. The commonly used methods and processes are manual fabrication, resin coating, resin injection, resin transfer moulding (which is a resin injection method), carbon fiber sheet moulding compound (which is a press method) [12], extrusion, pre-impregnated (prepregs), etc. Within the scope of this research, the resin mixed coating method is selected due to its advantages such as: Simple, low cost, easy to control the ratio of epoxy resin and reinforcement material (carbon fiber) in the mixture. However, this method is limited to processing and manufacturing CFRP products which have not high mechanical properties. The resin mixed coating method is illustrated in Fig.2.

In this method, the carbon fiber reinforced material is mixed with the epoxy resin in a specified ratio. A chopper gun is used to spray a mixture of epoxy resin onto the first carbon fiber ply, which is laid up from a mold. After that, the second ply is pressed on the wet epoxy resin layer. The process is iterated until the final fourth ply has been stacked up. The carbon fiber plies and mixed epoxy resin layers are then sandwiched together, and the deposited materials are left in a room with common atmospheric conditions and waited for curing. Consequently, the CFRP material has been created with the shape and size of the mould.

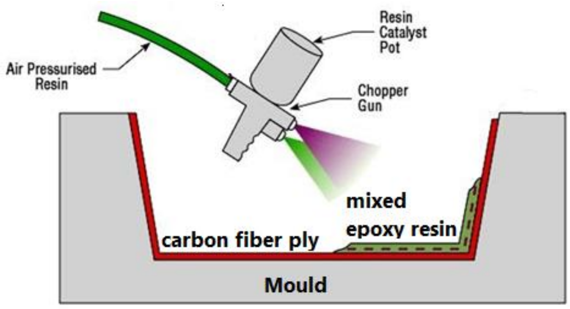

Fig. 2. *Illustration of the resin mixed coating method (redrawn from [13])*

The fabricated CFRP parabolic is shown in the following figure:

Fig. 3. *The CFRP parabolic reflector manufactured by resin mixed coating method*

There are some important parameters need to be carefully controlled in the curing process, such as type of epoxy resin, the product's thickness, environment temperature and the thermal conductivity of the mould material. The temperature change rate is another key parameter that decides the mechanical properties of the product. In detail, due to the difference between thermal expansion coefficients of the reinforced carbon fiber and the epoxy resin, a large, sudden temperature change during the curing process can leads to a deformation of the bonding between these two materials, or even leads to the breakage of the matrix and the de-lamination of carbon fiber in the plies.

III. Design of the Antenna System

A. *The Feed Antenna*

There are two commonly used antenna types for feeding: The horn antenna and the helical antenna. In this design, the latter is chosen because of its significant advantages: Provides natural circular polarization, which is suitable for satellite communications. In addition, the helical antenna has high efficiency, typically more than 90%. Furthermore, the ease of manufacturing and modification make it the most suitable antenna candidate for our experiment. The simulated helical antenna has the following parameters:

- Operation frequency: 2.1 GHz – 2.2 GHz.

- Antenna gain: better than 10 dBi.

- Antenna radiation mode: Axial (end-fire).

- Antenna polarization: Right hand circular polarization (RHCP).

The simulated feed antenna is demonstrated as follows:

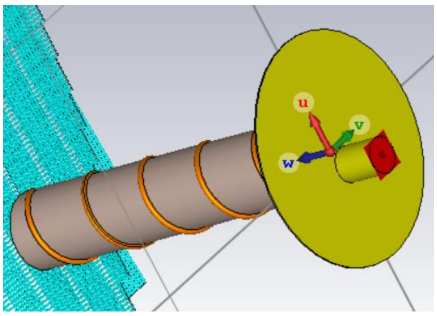

Fig. 4. *Simulation of the feed helical antenna*

The simulation results of the important antenna parameters such as input reflection coefficient (S_{11}), antenna gain and far-field radiation pattern will be illustrated in the below figures:

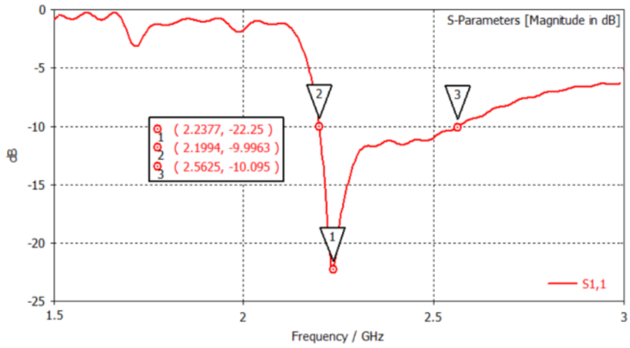

Fig. 5. *Simulation result of the input reflection coefficient (S_{11})*

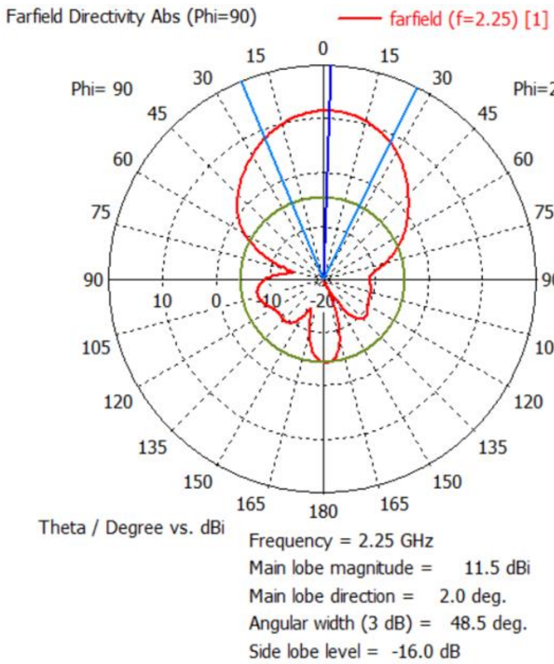

Fig. 6. *Simulation result of the 2D radiation pattern*

Fig. 5 and Fig. 6 show that the center operation frequency of the feed antenna is around 2.25 GHz, and the corresponding values of gain and S_{11} at the main radiation direction at this frequency are 11.2 dBi and -20 dB, respectively. The half-power beam width (HPBW) of the main lobe is 48.5° and the side lobe level is approximately -16 dB. These results are acceptable for a typical helical antenna that operates in end-fire radiation mode.

B. *The Parabolic Reflector*

The conventional parabolic reflector with prime focus feed is chosen. This configuration is the simplest form of a parabolic reflector antenna, in which, the reflector and the feed antenna are both positioned along the main axis of the parabola. This is the boresight direction of the parabolic reflector antenna.

The expected antenna parameters are listed as follows:

- Operation frequency: 2.1 GHz – 2.2 GHz.

- Antenna gain: better than 16 dBi.

- Impedance (10 dB) bandwidth: 60 MHz or better

- Antenna polarization: Left hand circular polarization (LHCP).

The inversion of the polarization sense is caused by the reflection of the antenna radiation wave from the parabolic surface. To reduce the meshes calculation time of the simulation, a simplified configuration of the parabolic reflector is used. The simulated parameters are: 65 cm (diameter), 4.5cm (depth of the parabola), 45 cm (focal length), 0.75 (f/D – ratio between focal length and diameter). The antenna's effective aperture is approximately 0.17 m^2. The simulation of the antenna system (including the reflector and the feed antenna) is shown in Fig. 7. The simulated carbon fiber properties are set to be the same as the T400H mentioned in the previous section.

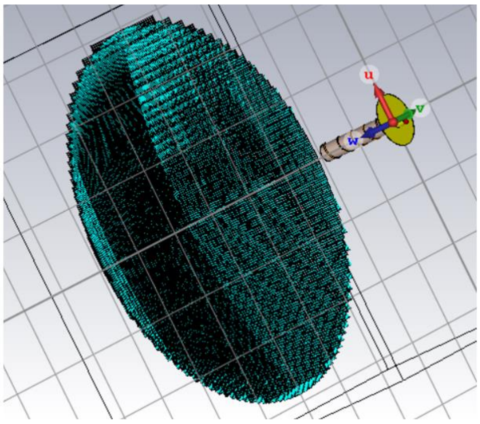

Fig. 7. *Simulation result of the parabolic reflector antenna*

The simulation results of S_{11}, antenna gain and far-field pattern are demonstrated below:

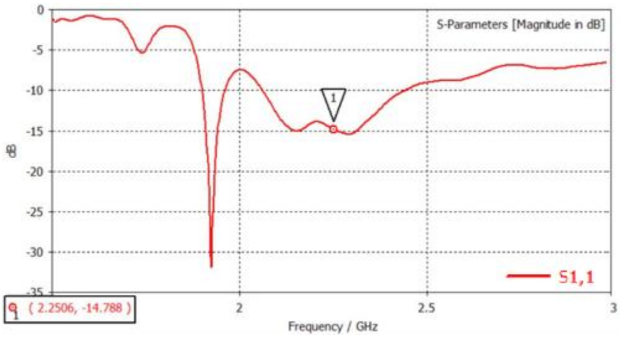

Fig. 8. *Simulation of the S_{11} of the antenna system*

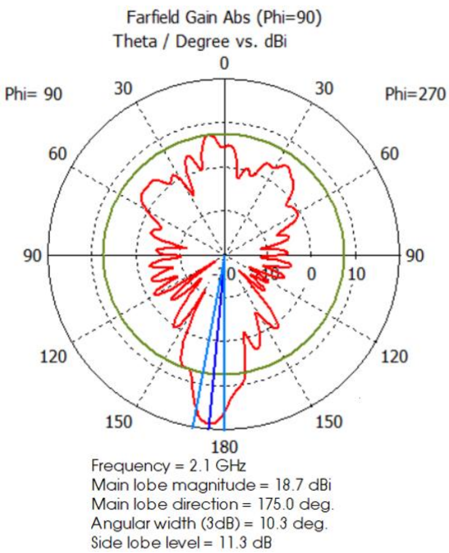

Fig. 9. *Simulation of the 2D radiation pattern of the antenna system*

From Fig. 8 and Fig. 9, it is clearly seen that the center operation frequency of the feed antenna is the same as that of the standalone feed antenna, and the operation bandwidth is more symmetrical from the center frequency. The gain and S_{11} at the boresight direction at 2.25 GHz are in turn 18 dBi and -15 dB. The half-power beam width (HPBW) of the main lobe is 10.3° and the side lobe level is about -12 dB. These results are acceptable for a small reflector antenna that operated in S-band.

IV. Testing and Verification of The Antenna System

A. *Measurement of The Conductivity of The CFRP*

To determine the material conductivity, a sample of our CFRP is created. The four-probe method is used. The measurement configuration is shown in the below figures:

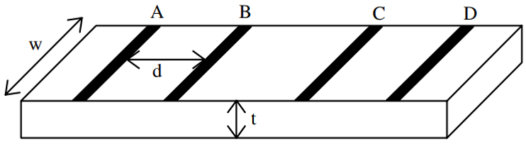

Fig. 10. *The four-probe test configuration used in this experiment [14]*

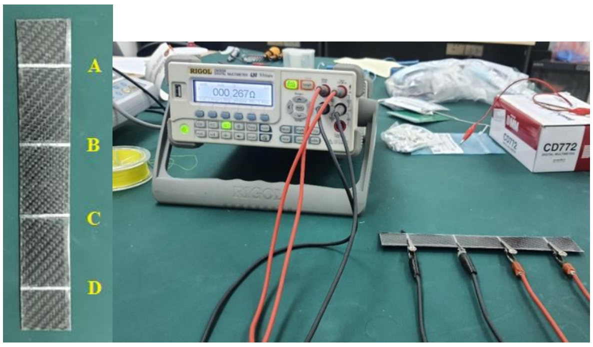

Fig. 11. *The CFRP specimen and the test setup*

As can be seen in Fig.10, the test configuration includes 4 electrodes, which are divided in 2 pairs. The inner pair is for voltage measurement and the outer pair is for current measurement. The two voltage electrodes (A and D) are placed on the same plane with the two current electrodes (B and C). The distance between the voltage contact and the current contact is *d*. This configuration leads to the easiness of mounting electrodes on the material surface while maintaining the accuracy of the measurement result. The longitudinal resistivity of the specimen will be calculated as:

$$R_L = \rho_L \frac{d}{w(t/2)} \tag{1}$$

Where, $\boldsymbol{R_L}$ is the resistance, $\boldsymbol{\rho_L}$ is the longitudinal resistivity and *w* is the width of the specimen. The longitudinal conductivity is then being reached by simply inverting the longitudinal resistivity value. The through-thickness resistance is negligible in compared with $\boldsymbol{R_L}$ in this case, as showed in [14].

The test setup is presented in Fig. 11, in which, the electrodes on the CFRP specimen are connected with the DM3058E Digital Multimeter through wires. The dimensions of the CFRP sample is *210 mm (length) x 30 mm (width) x 0.5 mm (thickness)*, and the distance d is 50mm. The measurement was carried out in our laboratory at room temperature. The measured resistance of the sample is 0.267 Ω, and according to (1), the longitudinal resistivity will be calculated and its value is $4.005*10^{-5}$ Ω.m, thus, the longitudinal conductivity (σ_{L}) is approximately $2.5*10^{4}$ S/m. The measured conductivity is nearly similar to the measured values of the CFRP samples such as IM600/133, T700/2510 [15].

B. *Measurement of The Feed Antenna*

The helical radiation element and the reflection ground are fabricated by copper, and the antenna supporting cylinder is created by 3D-printing PVC. The dielectric constant of the PVC does not affected to the antenna radiation pattern and gain. The antenna radiation pattern measurement is done by the Multi-purpose Near-field system, provided by NSI, in which, the near-field measured antenna pattern is calculated and after that, being converted to far-field by the Fourier transform The measured antenna pattern and S_{11} of the antenna is shown below:

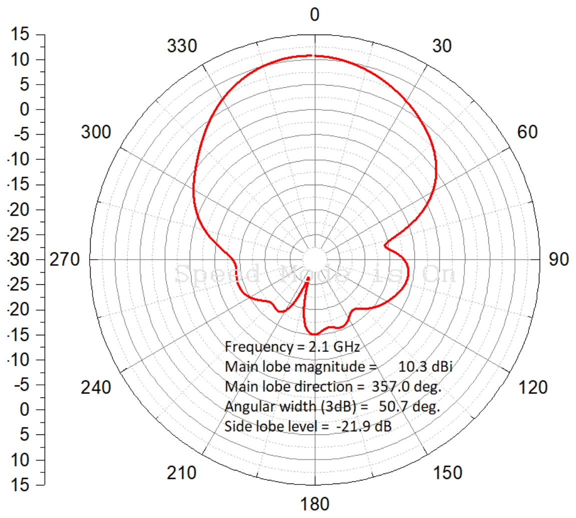

Fig. 12. *Measured 2D far-field radiation pattern of the feed antenna*

Fig. 13. *The measured S_{11} of the feed antenna*

From the above figures, we can see that there is a good agreement between the experimental and the simulated results (in Fig. 5 and Fig.6). However, the center operation frequency has been slightly decreased, it is around 2.1 GHz and the corresponding S_{11} is -20.5 dB.

C. *Measurement of The Parabolic Reflector Antenna*

The fabricated parabolic reflector antenna is shown in Fig. 14. It consists of the CFRP parabolic reflector and the feed antenna, which is connected to the reflector by a 25mm-diameter PVC pipe. The dielectric constant of this PVC pipe is the same with that of the feed antenna supporting cylinder, so the effect to the antenna performance is negligible. The total weight of the antenna system is 1.2kg, around one-third the weight of the steel K+ parabolic reflector which was used as the mould.

The CFRP reflector antenna is tested and verified in the EMC room of Military Institute of Science and Technology (MIST). The EMC room is a full anechoic chamber with the dimensions of 7m in length and 5m in width. Our antenna acted as the transmitting antenna, and the receiving antenna is a linear polarized Horn-Vivaldi antenna with known gain, which is rotated through azimuth and elevation angles in order to scan the antenna pattern. To reduce the detrimental effect to the antenna measurement performance, the whole antenna system is placed on styrofoam, as shown in Fig.15.

Fig. 14. *The CFRP parabolic reflector after manufactured*

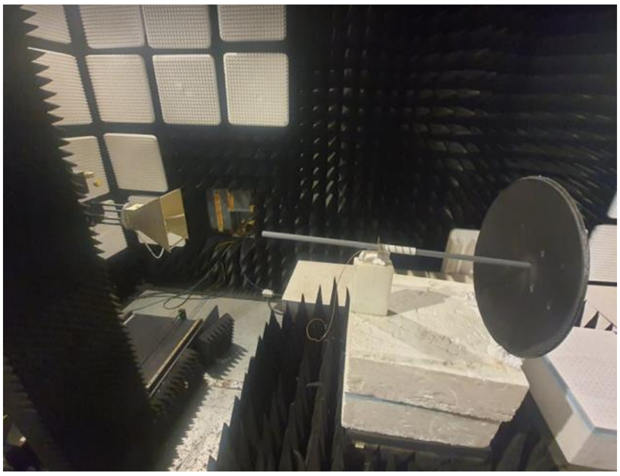

Fig. 15. *The antenna test configuration*

The measured S_{11} of the antenna is demonstrated in Fig.16. The operation region decreased about 70 MHz in comparison to the simulation result in Fig.8. However, S_{11} value at the center frequency is -30 dB, much better than that of the simulation.

Fig. 16. *The measured S_{11} of the CFRP parabolic reflector antenna*

The measured antenna radiation patterns by azimuth and elevation angle scanning are shown in the following figures:

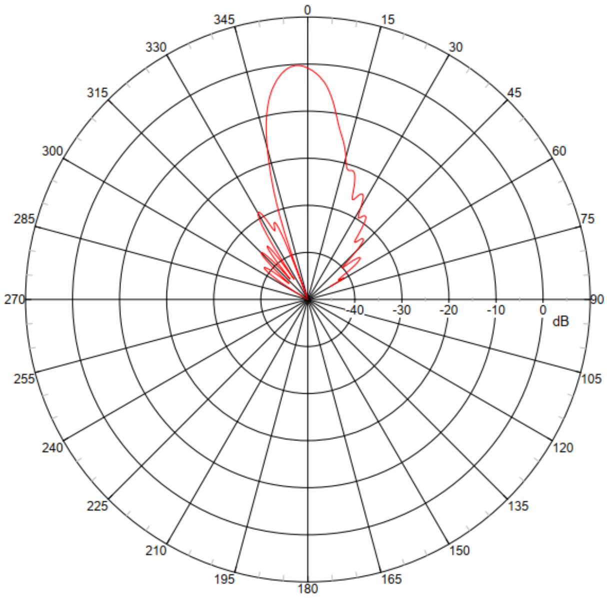

Fig. 17. *The azimuth scanning radiation pattern of the antenna*

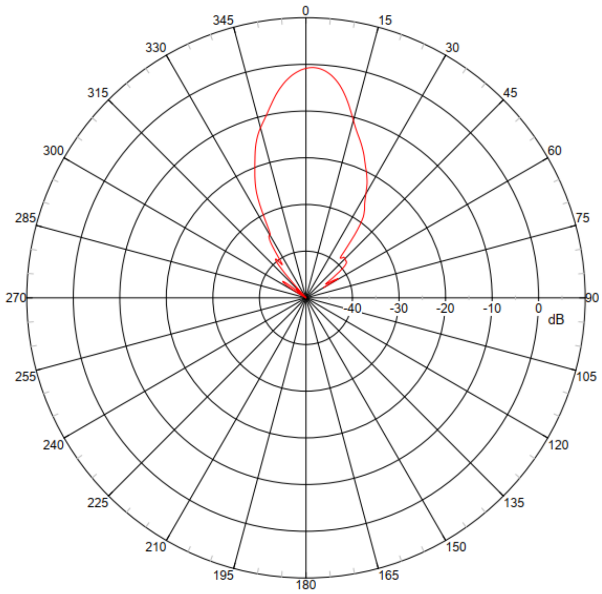

Fig. 18. *The elevation scanning radiation pattern of the antenna*

The results of the measurement is similar to the simulation beam pattern in Fig.9. The beamwidths of the two patterns are 12.18° and 14.56°, respectively. The directivity of the CFRP parabolic reflector antenna can be calculated by the following formula:

$$\boldsymbol{D} = 27000 / (\theta_H . \theta_V) \quad (2)$$

where θ_H is the azimuthal beamwidth and θ_V is the elevated beamwidth. The calculated value of D is 21 dBi. The antenna efficiency is about 50% (-3 dB) so we have the antenna gain is around 18 dBi at the frequency range of 2.05 GHz – 2.1 GHz, as predicted in the simulation.

V. Conclusion

The feasibility of applying carbon fiber reinforced polymer (CFRP) in fabrication of parabolic reflector antenna for S-band satellite communication is presented in this paper. The simulations and measurements are demonstrated, and a good agreement between these two sets of results has been achieved. Furthermore, a preliminary assessment of the CFRP's conductivity, an important electrical parameter which can affects to the antenna performance, has been implemented using the four-probe method, and it can be used as a reference for future works. The fabricated antenna showed good gain and input reflection coefficient at the operation frequency range of 2 GHz - 2.1 GHz. Furthermore, the antenna's weight is significantly reduced, so it can be applied to small and mobile satellite ground station.

Our future works are further increasing the antenna gain and efficiency, and take a more profound research about the effect of the CFRP's conductivity and epoxy matrix to the radiation performance of the antenna. Moreover, a deployable configuration of the CFRP reflector and other flexible shapes of the reflector element will be studied in order to mount on small satellites in the future.

Acknowledgment

This research is granted by Technology Development Program at VAST level through the national projects titled ”Development of Shock test kit for nano and micro satellites - UDPTCN 05/21-23”.

References

[1] G. Artner, R. Langwieser and C. Mecklenbräuker, “Carbon fiber reinforced polymer as antenna ground plane material up to 10 GHz”. 11th European Conference on Antennas and Propagation (EUCAP) pp. 3601-3605, March 2017.

[2] Online material, available at: https://www.aselsan.com.tr/en/capabilities/space-technologies/naval-platform-satellite-communication-system/acrosat-shipborne-satellite-communication-terminal

[3] T. Sproewitz, J. Block, A. Bäger, L. Hauer and M. Schuetze, "Deployment verification of large CFRP helical high-gain antenna for AIS signals," 2011 Aerospace Conference, Big Sky, MT, pp. 1-12, March 2011.

[4] N. Chahat et al, “Advanced CubeSat Antennas for Deep Space and Earth Science Missions: A review”. IEEE Antennas and Propagation Magazine, vol. 61, pp. 37 – 46, Sep 2019.

[5] A. Mehdipour, C. W. Trueman, A. R. Sebak and S. V. Hoa, "Carbon-fiber composite T-match folded bow-tie antenna for RFID applications," 2009 IEEE Antennas and Propagation Society International Symposium, Charleston, SC, pp. 1-4, July 2009.

[6] L. Datashvili and H. Baier, "Derivation of different types of antenna reflectors from the principle of highly flexible structures," The 8th European Conference on Antennas and Propagation (EuCAP 2014), pp. 4-8, April 2014.

[7] S. Futatsumori, K. Morioka, A. Kohmura, M. Shioji and N. Yonemoto, "Evaluation of fan beam carbon fiber reinforce plastics offset parabolic reflector antenna for W-band millimeter-wave radar systems," 2014 International Symposium on Antennas and Propagation Conference Proceedings, pp. 307-308, Dec 2014.

[8] O. Soykasap, S. Karakaya and E. Kaplan, "Self-deploying composite shell reflector antenna for Ku-band missions: 1.5 m diameter demonstrator," 2013 6th International Conference on Recent Advances in Space Technologies (RAST), pp. 631-636, Jun 2013.

[9] D. Henke, G. Lacy, P. Niranjanan and D. Chalmers, "Measurements of Composite Reflectors across Q-Band (33–50 GHz) and W-Band (75–115 GHz)," 2018 18th International Symposium on Antenna Technology and Applied Electromagnetics (ANTEM), pp. 1-3, Aug 2018.

[10] G. Artner, P. K. Gentner, J. Nicolics, C. F. Mecklenbräuker, "Carbon Fiber Reinforced Polymer with Shredded Fibers: Quasi-Isotropic Material Properties and Antenna Performance," International Journal of Antennas and Propagation. pp.1-11, Jan 2017.

[11] R. Assis and I. Bianchi, "Analysis of microstrip antennas on carbon fiber composite material," Journal of Microwaves, Optoelectronics and Electromagnetic Applications, vol.11, pp. 154-161, June 2012.

[12] Y. Kageyama, K. Akai, N. Nishino, K. Kageyama, "Selection of Molding Method for CFRP Automotive Body Parts - Resin Injection vs. Compression," Advances Production Management Systems: Innovative Production Management Towards Sustainable Growth Volume, vol.459, pp. 455–463, Aug 2015.

[13] Online material, available at:

https://www.gurit.com/-/media/Gurit/Datasheets/guide-to-composites.pdf

[14] D. Chung and S. Wang, "Discussion on paper 'The electrical resistance response of continuous carbon fibre composite laminates to mechanical strain' by N. Angelidis, C.Y. Wei and P.E. Irving, Composites: Part A 35, 1135-1147 (2004)," Composites Part A: Applied Science and Manufacturing, vol. 37, pp. 1490-1494, Sep 2006.

[15] Y. Wang, “Multiphysics Analysis of Lightning Strike Damage in Laminated Carbon/Glass Fiber Reinforced Polymer Matrix Composite Materials: A Review of Problem Formulation and Computational Modeling,” Composites Part A: Applied Science and Manufacturing, vol. 101, pp543-553, July 2017.

The 6th International Conference on Engineering Mechanics and Automation (ICEMA 2021)
Hanoi, November 14, 2021

Solution for robot cleaning the photovoltaic panels in Vietnam

*Duong Vu
Mechanical Engineering Faculty
Duy Tan University
Da Nang, Vietnam
duongvuaustralia@gmail.com

Anh Hoang Vo
Mechanical Engineering Faculty
Duy Tan University
Da Nang, Vietnam
vhanh83@gmail.com

Trung Duy Dao
Training center
Nat.Res.Inst. of Mech. Eng.
Hanoi, Vietnam
trungdd@narime.gov.vn

Quy Thu Le
KeyLab for Weld.&Surf.Tech.
Nat.Res.Inst. of Mech. Eng.
Hanoi, Vietnam
ORCID: 0000-0002-4351-4154

***Abstract*:** According to the Vietnam Renewable Energy Development Project to 2030 with an outlook to 2050, the strategic goal was set forth: the share of solar power in total electricity production shall account for 0.5% in 2020; 1.6% in 2025, and 3.3% in 2050. And accordingly, the total solar power production shall increase from a negligible level at present up to 12,000 MW in 2050. To reach this goal, huge capital investment to grow the solar energy capacity is needed. But from the other side, the continuous maximum effective energy extracted from the sun (namely the photovoltaic panel-PV, as the main component in the supply system) reduces the installation and production costs and makes it easier to meet the demanded peak electrical power. The accumulation of dust decreases the net output power and reduces the system efficiency significantly. Therefore, it is notably important to keep the solar panels clean from physical conditions such as dust, muddy rain, bird dropping, and other harmful substance on the surface of the PV. There are many types of solar panel cleaning systems based on the principle of operation. It is found that manual cleaning economically is not viable for solar photovoltaic panel (SPV) plants. It is costly as it requires professionally trained technicians. Utilizing robotic cleaning is the most recent trend in recent years. But the question remains for discussion is: with water or dry cleaning? The other aspect is the water supply for cleaning is required. The lifetime of the PV depends on the scratching effect on the surface of the PV. The size and configuration of the robot are also the problems concerning the allowable pressure on the surface of the PV to keep it from bending too far. From this analysis, this work aims to review all cleaning methods for solar panel and design a promotive, cost-effective robot for PV cleaning. This study presents a preliminary design and fabrication of a semi-automatic robot for cleaning the PV suitably in the local conditions of Vietnam.

Keywords: *Photovoltaic panel; Robot cleaning; Vietnam climate environment; Light intensity; Dust accumulation.*

I. ASK THE PROBLEM

The problem of using renewable energy, including solar energy, has been concerned by the Vietnamese government for many years [1]. There are many factors affecting the efficiency of electricity generation from solar panels such as light intensity, number of daylight hours, panel temperature, dust, and bird droppings [2].

Studies and surveys have shown that the accumulation of density and dust on the surface of solar panels significantly reduces their performance. For example, in Thailand, a country that is said to have similar climate and environmental conditions as Vietnam, environmental pollution, farming conditions, and practices have created a lot of dust and this dust will accumulate significantly on the surface of solar panels, reducing their electricity generation efficiency. Research results in Thailand show that the efficiency of solar panels is reduced by 1.6-3% if dust accumulates within 1 month and reaches 6-8% within 2 months. However, after cleaning the dust, the effective rate increased to 10% [3]. Not only that, the research results of an organization called SINTEF in Europe [4] were published and also show that the efficiency of solar panels is reduced due to the influence of dust layer thickness in intense conditions that irradiation from the sun varies (Fig. 1).

According to the report of this organization, in different geographical regions of the world, the effect of dust on solar panel performance is also very different, when standard sampling is solar panels placed at an angle of 24.6 ^{0}, cleaned daily for comparison. In Kuwait, the panel capacity is reduced by 17% due to sand accumulation on the surface after 6 days. Nevertheless, depending on the season in this area, spring-summer the decrease is observed higher than autumn-winter (20% in 6 months). The Middle East region is a worst-case scenario to evaluate the influence of dust caused by sandstorms, which can reduce solar panel capacity by 70-80%. Therefore if the panel is not cleaned regularly, even daily, it can be considered that the system is disabled. However, even in the UK where is considered the cleanest area in the world, the efficiency of the panels is reduced by 5-6% after a month of not cleaning the surface. In Central Europe, no need for a very short cleaning cycle, but due to human activities, it still needs cleaning weekly or every other week. The danger of dust accumulation causes a cell on the panel to become a resistor, causing a short circuit leading to complete system damage. On the other side, there are also other factors such as air humidity, temperature, wind speed and direction, regional traffic environment, air pollution level, farming environment, which also significantly affect the amount of this dust accumulated [5]. Besides, there are factors such as static charge, chemistry, biology in dust particles, then the shape, size, and specific gravity of dust particles also affect the ability to accumulated dust on the surface of solar panels [6]. However, the research results have shown that the dust accumulation density mainly depends on the tilt angle when installing solar panels [7], on rainfall, intensity of rain, duration of rain, and especially acidity (pH) in rainwater due to severe climate change [8, 9].

It is possible to summarize and evaluate the effects of dust accumulation on the surface of solar panels through the diagram below (Fig. 2).

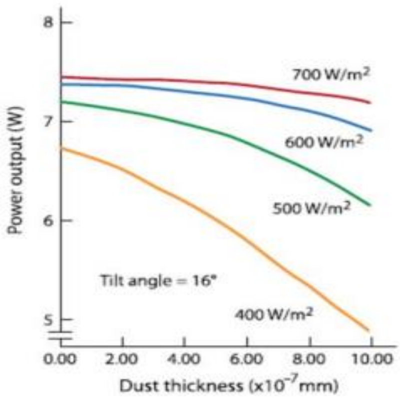

Fig. 1. The thickness of the dust layer reduces the light intensity on the panel surface

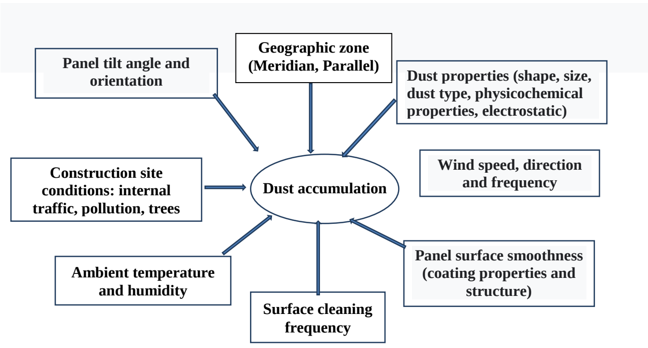

Fig. 2. Factors affecting the accumulation of dust on the surface of panels

From here, there is a group of methods to clean the surface of solar panels, and they all have their advantages and disadvantages, but depending on each specific condition of the environment, human resources, economic condition, the scale of investment, power generation capacity, to choose them accordingly.

II. SOLUTIONS FOR CLEANING THE SURFACE OF SOLAR PANELS

The battery surface cleaning methods include: manual, automatic and passive. The passive method is self-cleaning which base on a very hydrophobic or hydrophilic surface treatment solution. The manual method is only applied on a family scale, due to low productivity, but it has economic advantages of low cost. An automatic method is a group of solutions that will be discussed a lot due to its advantages in productivity when it was applied to large projects and solar power plants.

2.1. Manual method (Fig. 3)

The main disadvantages of this method are low productivity, difficult to mechanize and automate, not to mention lack of safety due to having to climb high and steep slopes. Manual cleaners also often use solvents, if not cleaned, they will remain on the surface of the panel, causing opaque glass. Another solution is to use a vacuum cleaner, but productivity does not increase significantly [9,10]. On a small scale, people still use manual methods with a productivity of 1 m^2/min [11]. Not to mention the excessive stress concentration allowed by people standing on the panels will cause damage, because the pressure on the panel surface should not exceed 5400 Pa with distributed load [12]. To clean larger solar cell systems, mechanized methods can be used, running fire trucks along the battery banks and pumping water under pressure.

Fig. 3. Cleaning solar panels

2.2. The "self-cleaning" method

This method can be with or without water. If water is used, an automatic sprinkler system is installed (Fig. 4). However, the efficiency of this method is not high because it loses too much water and does not cover most of the area of the panels [13, 14].

Fig. 4. Sprinkler system

Another self-cleaning solution is to cover the surface of the panel with a thin (transparent) pellucid film, which was made of a superhydrophilic or superhydrophobic material. The superhydrophobic membrane, when placed at an angle of about 30 degrees, does not absorb water, but flows down and drags dust particles [15, 16, 17]. It has been tested using Polydimethylsiloxane (PDMS) material to cover the surface of the panel, achieving an efficiency of up to 13.8% of the repetition frequency, when cleaning dust with carbon powder with an angle of 45^o. In general, this superhydrophobic material when covering the surface of solar panels achieves 90% dust-proof efficiency after flushing. The line of superhydrophilic materials is based on the photocatalytic effect of TiO2 compounds [17] to reduce the possibility of dust collection [17, 18, 19]. However, the basic disadvantage of this method is that there is an additional cost to spray those special layers on each solar panel and their adhesion will also degrade over time, under the influence of sunlight.

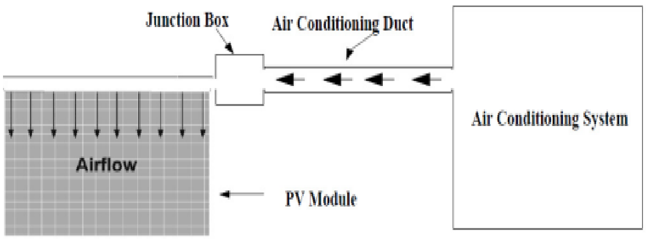

Fig. 5. Dust blower convection flow

The hydrophobic coating also depends on the angle of inclination of the plane of the panel, which will still accumulate dust, but not easily let the dust wash away [20,21]. In this group, there is also a cleaning type based on the principle of convection current (Fig. 5) from the air conditioner blowing on the surface of the solar panel to collect heat and at the same time, due to the strong airflow, it also reduces dust accumulation. This is a type of dust-free cleaning that does not use water, suitable for arid climates such as deserts in the United Arab Emirates. However, in terms of the economic efficiency and productivity of this method, it is controversial.

The electromotive force generated between the two parallel electrode layers is also used to push dust off the surface of the solar panel [22-25]. The effectiveness of this method depends on factors such as electrode size, voltage, frequency, surface inclination angle (Fig. 6). Proponents for the idea of using the method of "self-cleaning" the surface of solar panels have given quite convincing evidence when the statistics of research on solar power systems across Iran have been published [26].

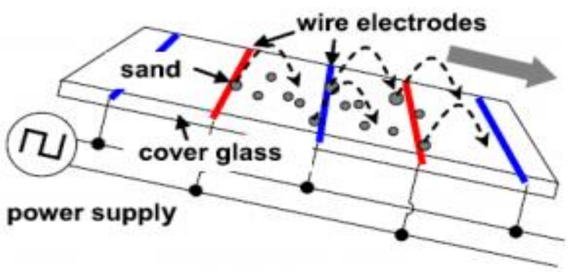

Fig. 6. Principle of electrostatic force, pushing dust

2.3 Methods of using robots

To use robots to clean the surface of solar panels is considered a promising direction, due to its ability to automate and increase productivity.

The Gekko robot series [27,28] has the advantages of high cleaning efficiency, safety and ease of use. In particular, the Gekko farm robot model [29] is very flexible to change the size to suit the width of the solar panel, very convenient to install, using the via radio wave joystick. The Solar Brush robot [30] has the very advantage of cost and environmental protection. Robot Hector [31] has the advantages of small and compact size and weight, moreover fully automatic and low cost. Robot Helotex [32] is based on the principle of using a PLC with a PIC microcontroller. They had been analyzed more closely on the advantages and disadvantages, comparing these types of robots in terms of installation costs, effectiveness in terms of surface cleaning according to published results [33] to find that there is no which solution is completely advantageous, depending on the specific use conditions to choose. The analysis results of solar panel surface cleaning solutions can be summarized in the following diagram (Fig. 7).

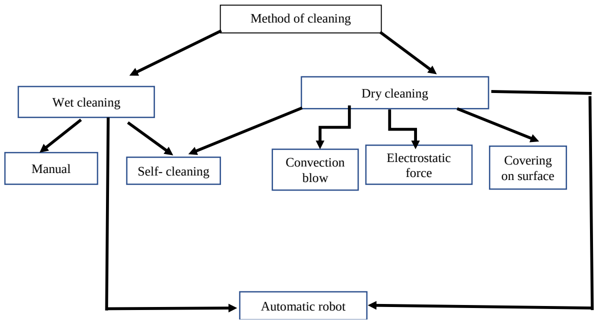

Fig. 7. Summary of cleaning methods

III. ROBOT DESIGN OPTION IN VIETNAM

According to published data [34] about the solar energy market of Vietnam, both domestic and foreign investors, the potential as well as the projects that have been and are being invested is very significant, of which the main source of solar power is from industrial-scale projects. Besides, due to people's living standards are raised, favorable geographical conditions in many regions stretching across the country, therefore households are also a source of both supply and consumption of this energy. Nevertheless, Vietnam's environmental conditions are certainly both due to the lack of good management of dust and smoke emissions, and cleanliness in the air as well as in Southeast Asian countries, while the water supply is better than desert regions like the Middle East. The level of exploitation and operation of semi-automatic and automatic systems of the robot type is completely consistent with technical knowledge and common practices. Some types of robots that have not been officially commercialized, which were manufactured by Vietnam, are listed in Table 1.

TABLE 1. SOME SOLAR CELL CLEANING ROBOTS MADE IN VIETNAM

Company name	Ssun - GP solar company	SolarCleanBot-CT.R1, Chi Thanh company	VPT-RB1200-S1-Vu Phong company	VTS - Vinh Tan Solar Power Plant
Price, VND	125,000,000	200,000,000	Not announced	Not announced
Parameter	1.2 m long, 2 rotating brushes Weighs 30 kg 2 lithium batteries weighing 4 kg Continuous working: 8 hours	Not announced	Not announced	Water consumption: 0.8 -1*l* water/battery panel Aluminum frame structure
Principle	Semi-automatic	Semi-automatic	Semi-	Semi-

			automatic	automatic
Scope of application	Private house, penthouse	Factory roof	Private house, mini farm factory	-

Based on the above analysis, it shows that the potential market for robot surface cleaning panels (solar panels) is quite large. However, until now, no product of this line has been officially registered as a product trademark and industrial-scale application in Vietnam. Besides, there are some providers of solar panel cleaning services, but they import equipment. The design and manufacture of a series of solar panel cleaning robots from Vietnam is set out to proactively supply and competitive prices. However, it makes sense to give an open design product on that basis to further upgrade to an automatic remote control.

A technological solution using a robot with water spray to clean the surface of solar panels is said to be suitable for the conditions of Vietnam. This robot would consist of software and hardware. Because the robot's operation characteristics are not complicated, the control software can use a control system including PLC and microcontroller. Where Arduino style board is based on Atmega 328 microcontroller, due to the reasonable price. The hardware will be based on a system of motors (DC) and position sensors, and the total source is the rechargeable battery. Table 2 presents the main characteristics of the research robot.

TABLE 2. MAIN FEATURES OF THE ROBOT

Feature	Request
General	Principle of cleaning: Water spray under pressure Level of control : Semi-automatic Dust resistance: Withstands dust, wind and sand Heat resistance: Up to 40 ^{0}C Water resistance: Spray water does not damage the structure Improved possibility: Open system Total weight: Not more than 50 kg Price: No more than 100 million VND Ability to disa: ssemble and operate: Simple, need 1-2 people Mass of brush part: Not more than 20 kg Dimensions of the robot body excluding the brush (length x width x height): 1200 mm x 1000 mm x 450 mm Rechargeable battery for 2 hours of continuous use: 42 V Remote control distance limit: 200 m
Environmental impact	Spray water consumption: Less than 0.5 liter/min Noise level: No more than 80 dB Total capacity: Under 400 W Water supply type for robot: Pump directly by tube The ability to recover and reuse water: There is a recall
Mechanical drive	Maximum tilt angle:35^0 Speed (productivity) of cleaning dust: Not less than 1 m^2/min Transition clearance between 2 panels:8-10 cm
Cleaning ability	Dust cleaning degree: Over 90 % Width of cleaning surface:2000 mm. max Brush diameter:250 mm Brush width:1100 mm
Maintenance	Battery removal time: No more than 3 minutes Brush life: Over 150 hours Uptime between maintenance intervals: About 500 hours

3.1 Detailed description of the control principle and structure

a) General block diagram

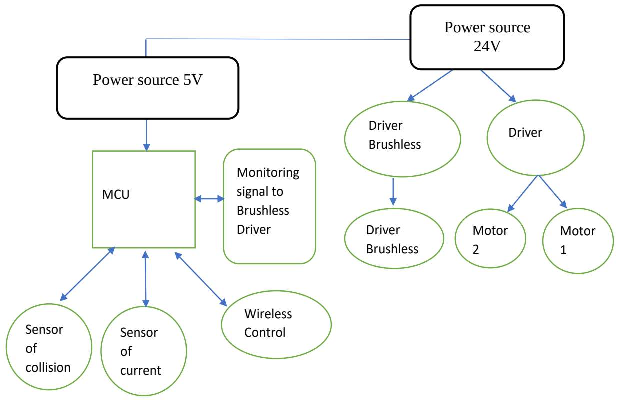

Fig. 8. Block diagram of the control circuit

Figure 8 is a block diagram of the control circuit. Basing on this diagram, the robot's operation process can be conceived as follows:

b) Block diagram details

- Source (Fig. 9). This is the part that provides power for the robot to work, the supply power includes:

+ 24 V source provides power for 4 motors which were installed to the wheels to help the robot move and is the main source of power on the Robot;

+ 12 V source that supply to the sensor and motor control attached to the robot's wheels;

+ 5 V source is the main power for the central circuit;

+ Besides, to ensure a stable source and control energy, the authors designed an additional power indicator and main power source protection circuit.

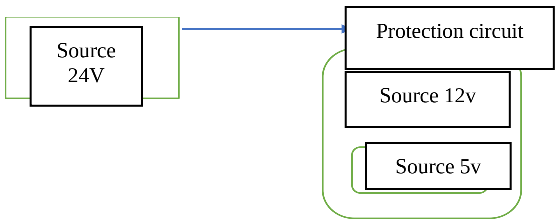

Fig. 9. Power supply

To reduce the weight of the robot when walking on the glass, we minimize the use of batteries on the body, and connect the power to an external source, specifically of the 220 VAC AC circuit to 24 VDC.

- Brushless Driver: Fig. 10.

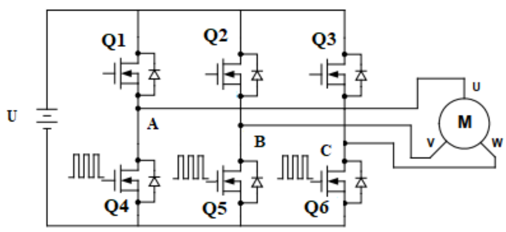

Fig. 10. Motor control

The principle of motor speed control is to use pulse width modulation (PWM). The controller determines the position of the rotor shaft and outputs a voltage to control the closing and opening of the semiconductor key or transistor switches (mosfets) that supply voltage to the motor. For simplicity, we only modulate the pulse width of the lower transistor switches (Q4, Q5, Q6), the upper transistor switches when stimulated will conduct completely (pulse width is 100%, see Fig.11).

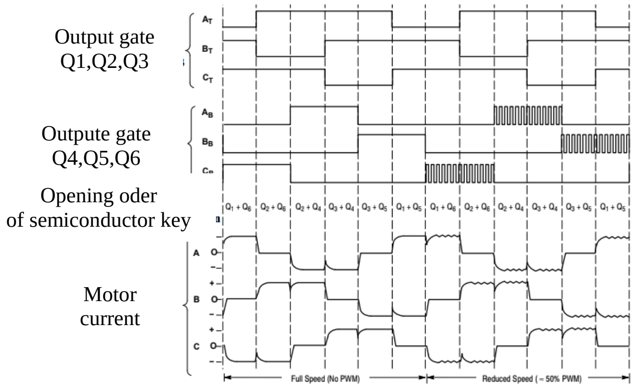

Fig.11. Pulse modulation

A brushless motor used for robot control high speed can be up to 10 rpm, suitable for glass surface cleaning tools.

- DC Driver (Fig. 12). The basic principle of DC motor speed control is that the H-bridge circuit including the Fets as the function of the key to unlock the control. Through pulse modulation (PWM) from the microcontroller, the speed and direction of the motor can be changed.

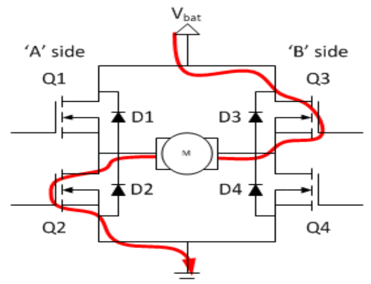

Fig.12. Principle of DC motor control

- Control board (Fig. 13)

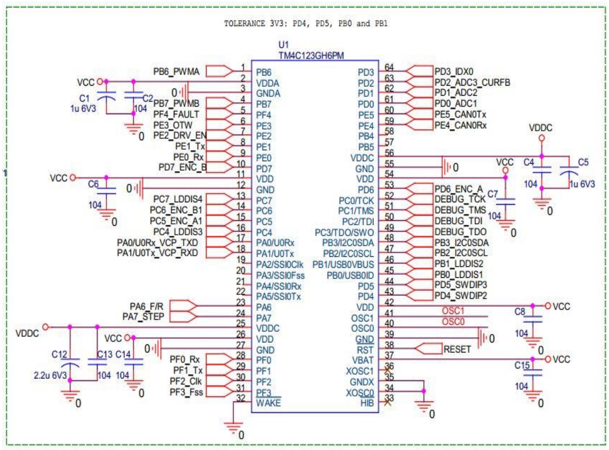

Fig.13. Control board

The central circuit was designed with the main microprocessor which is TM4C123GH6PM. This is the microcontroller that realizes the main tasks to communicate with the relevant peripherals used throughout the project. The circuit is designed with a full range of communication ports such as UART, COM, physical connection port to the peripheral ...., and can be expanded thanks to the pre-designed attached empty connection ports.

The main functions of the MCU:

+ Speed, brushless motor, and DC motor direction control;

+ Control on/off of the glass cleaning water pump;

+ Record current, warn of robot errors;

+ Receive wireless signal from the operator.

- Collision sensor:

The main function of the collision sensor is to prevent the robot from falling off the solar panel when moving and navigating. This type of sensor (OADK 25I7480/S14C) produces an analog signal, with a resolution of 0.3-4 mm, suitable for collision detection purposes. This sensor has a fast response time of < 32 ms (according to the manufacturer's specifications) to ensure that data is always collected and served for accurate and efficient control signal processing and output. The advantage of this type of sensor is that it is less affected by ambient light sources, ensuring stability when working in places where light sources often appear. The compact structure, effective operation with high resolution, and reasonable price are the reasons that helped the authors decide to choose this sensor.

- Wireless controller: The wireless PS2 controller can catch waves up to 10m, suitable for observing and controlling the robot at will. This PS2 wireless controller integrates the vibration mode that featured gamepad chassis in the existing market. The handle has a high sensitivity; the button is soft. This PS2 wireless controller has 2 flexible rotating levers to help players who applied the game extremely accurately.

3.2. Circuit principle diagram (Fig. 14)

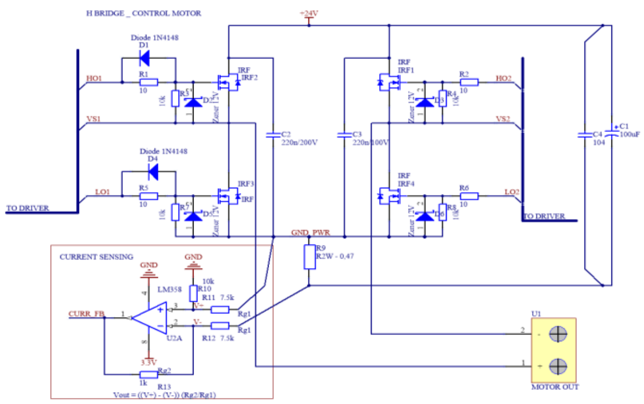

Fig.14. Principle diagram of H bridge circuit

a) DC motor control circuit

- H-bridge circuit controls the speed and direction of the motor with a load capacity of 500 W, peak current can be up to 40 A. Besides, Current Sensing protection circuit has the effect of interrupting the circuit, stopping the motor when overload current occurs.

- Driver for H-bridge (IC IR2184) control, Fig. 15.

- Driver source LM2576 is the source for driver chip.

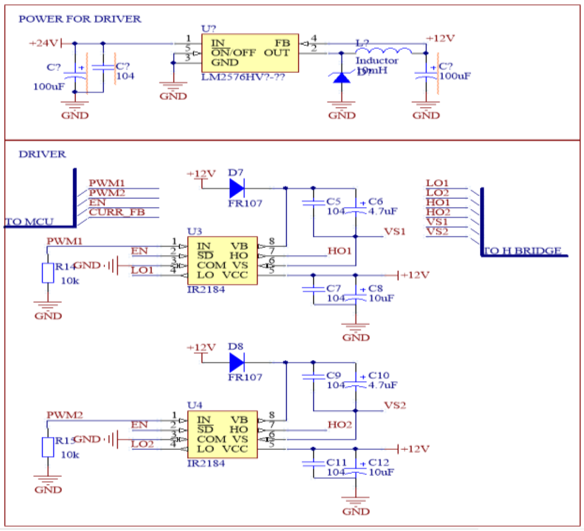

Fig. 15 Driver

b) Brushless driver control circuit (Fig. 16)

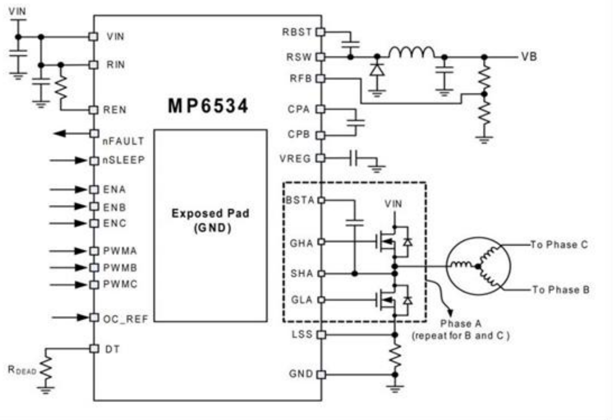

Fig. 16. MP6534 brushless motor driver controller

The MP6534 is a gate driver IC designed for brushless, 3-phase DC motor control applications. It is capable of driving three half-bridges, consisting of six MOSFET N-channels up to 55 V. The MP6534 includes a 500mA buck regulator to generate local power for a microcontroller or other circuit. The MP6534 has bootstrap capacitors to generate the voltage, supplying for the high-side MOSFET driver A inside small bootstrap circuit maintains a sufficient gate control voltage at a full duty cycle. Internal safety features include programmable overcurrent protection (OCP), adjustable dead time protection, undervoltage lockout (UVLO), and turn off the heat. MP6534 is available in a 40-contact QFN package (5 mm x 5 mm) with a heatsink plate.

c) Main circuit (Fig. 17)

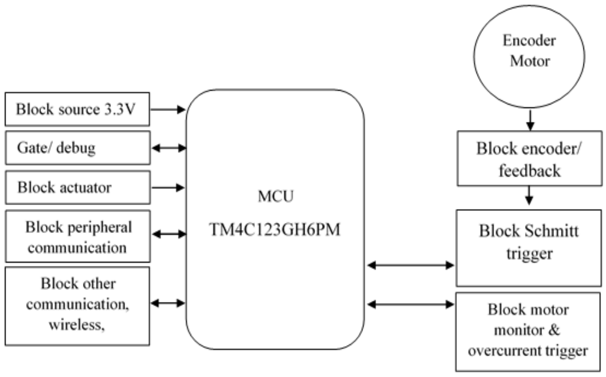

Fig. 17. General scheme

- Microcontroller TM4C123GH6PM: functions to control all activities of the robot (Fig. 18); power and external communication (Fig. 19).

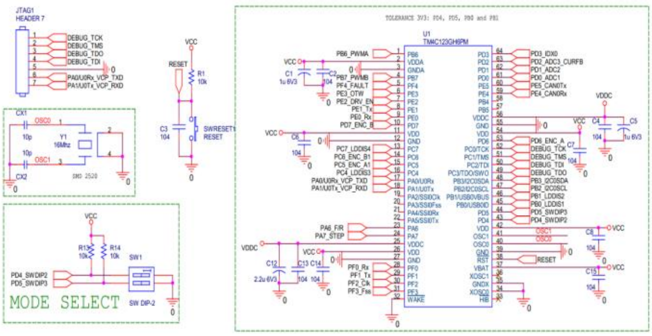

Fig. 18. Central microcontroller

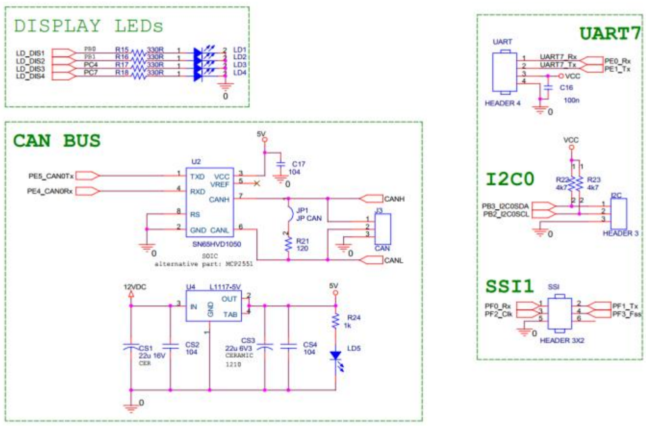

Fig. 19. Source and external communication

- Control Input & Feedback block: the engine's encoder reads the block, using PID algorithm to control motor speed more accurately and smoothly (Fig. 20);

- Schmitt trigger block: The block handles noise for the encoder when the engine is running, helping the signal from the encoder to be accurate, avoiding errors (Fig. 21); The trigger IC (SN74LVC1G14) block helps to recover the signal if an error occurs;

- Overcurrent control and handling block (to power stage): Overcurrent handling block, causing stuck on the motor and damage to the circuit;

- The remaining blocks are peripheral communication blocks for sensors, for driver control ...

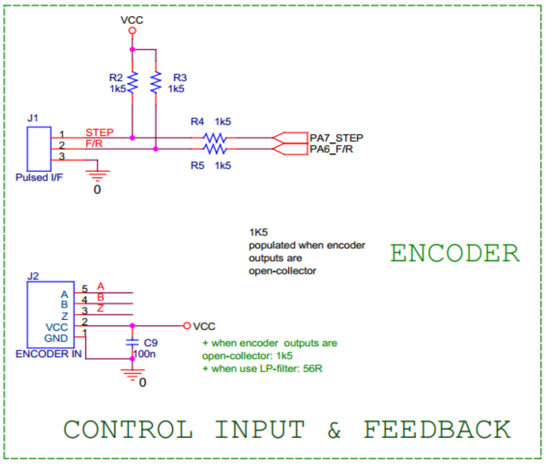

Fig. 20. Control & Feedback block

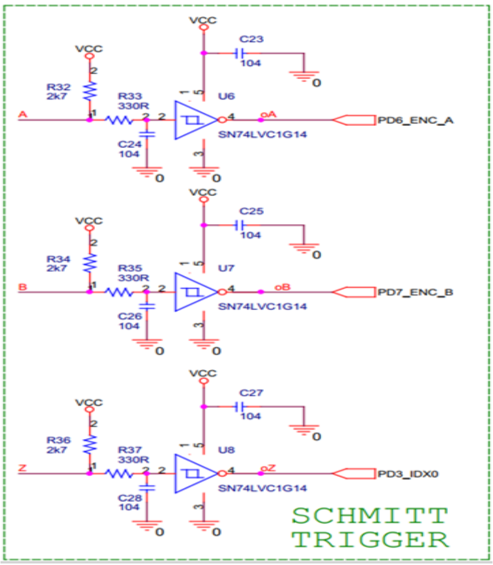

Fig. 21. Schmitt trigger block

3.3. Algorithm diagram

a) Fall detection algorithm: to prevent the robot from slipping off the solar panel (Fig. 22).

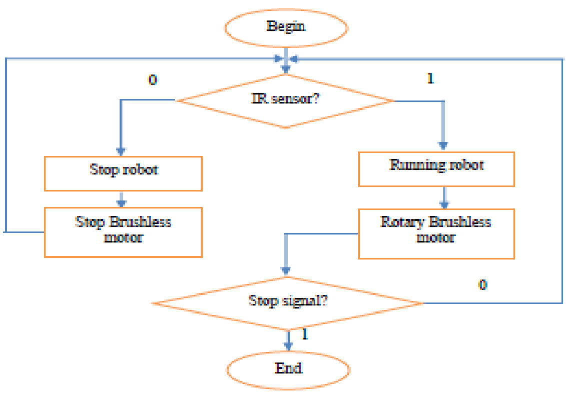

Fig. 22. Obstacle avoidance algorithm

The sensor placed under the robot body ramp will activate the brush when it moves alongside the panel. The robot will interrupt the signal to the cleaner when it moves over the panel border.

b) Robot control algorithm (Figs 23, 24). To control the robot in a zigzag pattern

Place the robot in the left corner of the panel (received sensors 1 and 2), when receiving the signal from the operator, the robot runs until sensor 1 does not receive it (out of upper limit), sensor 2 (left) is still receiving, robot facing left about 25 cm and perform the back and forth to the upper limit of the panel. Until sensor 2 (left) does not receive and sensor 1 (upper) does not, exit, complete the cleaning cycle (sensor 3, right -preventive).

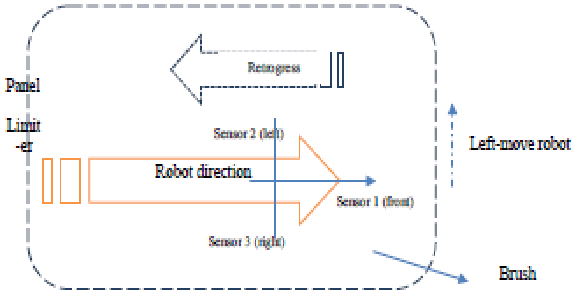

Fig. 23. Sensor installation on brush and direction of travel

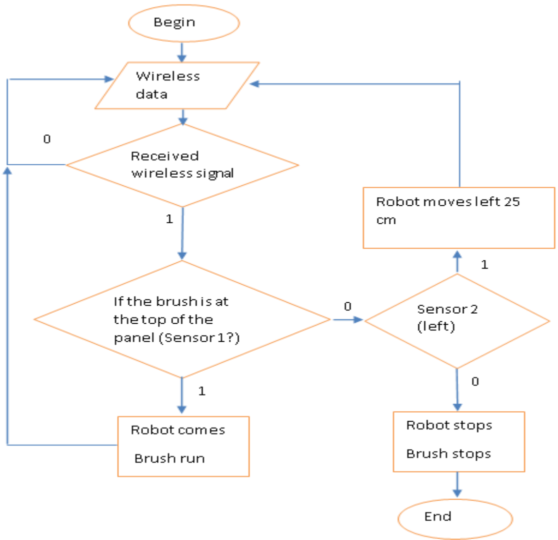

Fig. 24. Robot control algorithm

IV. CONCLUSION

1. The article summarizes the factors that cause dust and sand to accumulate on the surface of solar panels, minimizes the ability to illuminate and generate energy, and at the same time analyzes solutions to clean these panels, in terms of their main advantages/disadvantages.

2. Vietnam, a developing country, which has a great demand for energy sources in general, and renewable energy in particular, is not an exception to these trends.

3. In the first step, the general configuration and main design parameters have been outlined for a remote-controlled

robot, using water spray, with a brush motor and a robot body. The robot can move on the junction between two arrays of interconnected panels because it is fitted with soft chains.

4. In the next study, when there is a survey of the operating robot, the cleaning efficiency will be assessed, which related to the energy generation efficiency and the product cost as a composite criterion, that will be the basis launching to improve, upgrade and soon put the commercialization on the market.

V. REFERENCES

[1]. White Paper Vietnam Renewable Energy Industry, spire-white-paper-on-renewable-energy-in-vietnam.pdf.

[2]. K. Chailoet and E. Pengwang, "Assembly of modular robot for cleaning various length of solar panel, International Conference on Engineering," IOP Conf. Ser.: Mater. Sci. Eng. 639 (2019) 012014

[3]. N. Sakarapunthip, D. Chenvidhya, S. Chuangchote, K. Kirtikara, T. Chenvidhya, and W. Onreabroy, "Effects of dust accumulation and module cleaning on performance ratio of solar rooftop system and solar power plants," Jpn. J. Appl. Phys. 56 (2017) 08ME02

[4]. R. Ryningen, R. Kvande , Report – Cleaning of solar modules, SINTEF,(2016),28143.http://www.prodsp.hu/wp-content/uploads/2018/10/Cleaning-of-solar-modules-a-literature-review-SINTEF-ProDSP.pdf.

[5]. Talia R.S.Martz-Oberlander, "The Dirt on Solar Energy: A Study of Dutch solar panel efficiency losses from soiling",(2017), BSc_thesis_Martz-Oberlander_2017.pdf.

[6]. Arabatzis Ioannis, Todorova Nadia, Fasaki Ioanna, Tsesmeli Chrysovalanti, Peppas Antonis, Li Wen Xin, Zhao Zhiwei, "Photocatalytic, self-cleaning, antireflective coating for photovoltaic panels: Characterization and monitoring in real condition", Solar Energy,2018, Vol. 159, pp 251-259.

[7]. Lu, Hao&Zhao, Wenjun , "Effects of particle size and tilt angles on dust deposition characteristics of a grond- mounted solar photovotaic system", Applied Energy, Elsevier,vol.220(C), 2018,pp.514-526, DOI: 10.1016/j.apenergy.2018.03.095.

[8]. Tuan Nguyen Van,Ha Pham, Ly Thi Pham et al, "Effect of tropical climate on the reliability of electronic energy meter", The 3rd International Workshop on Corrosion Protection of Materials (CPM2018), 2018,Hanoi, Vietnam.

[9]. Quy Le Thu, Tuan Nguyen Van, Nguyen The Vinh et al , "Collection and treatment of climatic data for establishment of accelerated weathering test for electric meter", The 5th Asian Materialsn Data Symposium (AMDS2016), 2016, Hanoi, Vietnam.

[10]. Mallikarjun G.Hudedmani, Gita Joshi, Umayal R M, Ashwini Revanka , "A Comparative Study of Dust Cleaning Methods for the Solar PV Panels", Advanced Journal of Graduate Research, ISSN : 2456-7108, 2017, Vol1(1)PP. 24-29.

[11]. Rafi Zahedi, Parisa Ranjbaran, Gevork B.Gharehpetian, Fazel Mohammadi, Roya Ahmadiahangar,"Cleaning of Floating Photovoltaic Systems: A Critical Review on Approaches from Technical and Economic Perspectives",2021,Energy,14, http://doi.org/10.3390/en14072018.

[12]. Yixian Lee, Andrew A.O.Tay,"Stress Analysis of Silicon Wafer-Based Photovoltaic Modules Under IEC 61215 Mechanical Load Test", PV Asia Pacific Conference 2012, Energy Procedia 33 (2013) 265 – 271, www.sciencedirect.com.

[13]. Cazzaniga, R.; Cicu, M.; Rosa-Clot, M.; Rosa-Clot, P.; Tina, G.M.; Ventura, C., "Floating photovoltaic plants: Performance analysis and design solutions", Renew. Sustain. Energy Rev. 81,2018,pp 1730–1741.

[14]. Siecker, J.; Kusakana, K.; Numbi, B.P.,"A review of solar photovoltaic systems cooling technologies", Renew. Sustain. Energy Rev. 79,2017,pp. 192–203.

[15]. Gaofa He, Chuande Zhou, Zelun Li , "Review of Self-Cleaning Method for Solar Cell Array", International Workshop on Automobile, Power and Energy Engineering, Procedia Engineering 16 (2011) pp. 640 – 645.

[16]. Xu, Q.; Zhao, Q.; Zhu, X.; Cheng, L.; Bai, S.; Wang, Z.; Meng, L.; Qin, Y., "A new kind of transparent and self-cleaning film for solar cells", Nanoscale, Vol 8, 2016,pp.17747–17751.

[17]. Park, Y.B.; Im, H.; Im, M.; Choi, Y.K., "Self-cleaning effect of highly water-repellent microshell structures for solar cell applications", J. Mater. Chem.Vol 21,2011,pp. 633–636.

[18]. Zhong, H.; Hu, Y.; Wang, Y.; Yang, H., "TiO 2 /silane coupling agent composed of two layers structure: A super-hydrophilic self-cleaning coating applied in PV panels", Appl. Energy, 204,2017,pp. 932–938.

[19]. Alam, K.; Ali, S.; Saher, S.; Humayun, M., "Silica Nano-Particulate Coating Having Self-Cleaning and Antireflective Properties for PV Modules". In Proceedings of the IEEE 21st International Multi-Topic Conference (INMIC), Karachi, Pakistan, ;2018, pp. 1–5.

[20]. Son, J.; Kundu, S.; Verma, L.K.; Sakhuja, M.; Danner, A.J.; Bhatia, C.S.; Yang, H., (2012), "A practical superhydrophilic self cleaning and antireflective surface for outdoor photovoltaic applications", Sol. Energy Mater. Sol. Cells, 98, 46–51.

[21]. Sami Virtanen , "Self- Cleaning Technologies on solar module and their effect on performance", Bachelor's Thesis, JAMK University of Applied Sciences, 2017, 161420274.pdf.

[22]. Rafi Zahedi, Parisa Ranjbaran, Gevork B.Gharehpetian, Fazel Mohammadi, Roya Ahmadiahanga, "Cleaning of Floating Photovoltaic Systems: A Critical Review on Approaches from Technical and Economic Perspectives", 2021, Energies,14, http://doi.org/10.3390/en14072018.

[23]. Masuda, S.; Fujibayashi, K.; Ishida, K.; Inaba, H., "Confinement and transportation of charged aerosol clouds via electric curtain", Electr. Eng. Jpn., 92,1972,pp. 43–52.

[24]. Wu, G.; Inderbitzin, A.; Bening, C. , "Total cost of ownership of electric vehicles compared to conventional vehicles: A probabilistic analysis and projection across market segments", Energy Policy, 80,2015 pp. 196–214.

[25]. Mazumder, M.; Horenstein, M.N.; Stark, J.W.; Girouard, P.; Sumner, R.; Henderson, B.; Sadder, O.; Hidetaka, I.; Biris, A.S.; Sharma, R., "Characterization of electrodynamic screen performance for dust removal from solar panels and solar hydrogen generators", IEEE Trans. Ind. Appl., 49,2013,pp. 1793–1800.

[26]. Dipankar Dep, Nisarg L.Brahmbhatt (2017), "Review of yield increase of solar panels through soiling prevention, and a proposed water-free automated cleaning solution", Renewable and Sustainable Energy Reviews, http://dx.doi.org/10.1016/j.rser.2017.10.014.

[27]. Saeid Beygzadeh, Vahid Beygzadeh, Tohid Beygzadeh, " Thermodynamic and economic comparison of photovoltaic electricity generation with and without self - cleaning photovoltaic panels " ,Energy Equip.Sys./vol.7 /No.3/ 2019, pp.263-270.

[28]. http://www.serbot.ch/en/solar-panels-cleaning/gekko-solar-robot.

[29]. http://www.serbot.ch/en/solar-panels-cleaning/gekko-solar-farm-robot.

[30]. http://www.aerialpower.com/solarbrush.

[31]. Hardt, M., Martınez, D., González, A., Garrido, C., Aladren, S., Villa, J. R., & Saenz, J. HECTOR—Heliostat Cleaning Team-Oriented Robot. In Solar-PACES 2011 Conference, Granada, Spain, September 2011, (pp. 20-23).

[32]. http://www.greentechmedia.com/articles/read/sunpower-clean-up-solar-with-aquisition-of-greenbotics#gso6xruc.

[33]. Patil P.A, Bagi G.S, Wagh M.M., "A Review on Cleaning Mechnism of Solar Photovoltaic Panel", International Conference on Energy, Communication,Data Analys and Soft Computing (ICECDS-2017).

[34]. Vietnam Renewable Energy Report, British Chamber of Commerce Vietnam (2021).

The 6th International Conference on
Engineering Mechanics and Automation (ICEMA 2021)
Hanoi, November 14, 2021

Design and Integrate Control System for 3R2S2S typed Delta Robot

Hiep Dam Dinh
University of Engineering and Technology
Ha Noi, Viet Nam
damhiep99@gmail.com

Huy Khuat Duy
University of Engineering and Technology
Ha Noi, Viet Nam
zanghuy109@gmail.com

Linh Nguyen Ngoc
University of Engineering and Technology
Ha Noi, Viet Nam
nlnguyen@vnu.edu.vn

***Abstract*: In the paper, a mechanical design and an integrated control system has been studied in order to create a 3R2S2S typed delta robot can perform some desired tasks. Firstly, geometric structure of a 3R2S2S Delta robot was defined. Alike parallel robots, it includes two platforms, one fixed and joined to a moveable platform by three parallel chains. Next, the kinematic equations of robot are considered to solve the forward and inverse kinematic model. Mechanical design of robot was implemented with the support of Inventor software. The control system was integrated with the use of DMC 2163 driver card. A control algorithm was installed to provide some desired motion tasks. A complete model of 3R2S2S typed delta robot with control and monitoring software has been successfully developed. Validation of proposed robot system was done by simulation and experimental results.**

Keywords: delta parallel robot, 3R2S2S, DMC

I. Introduction

Delta robot, one of the most successful parallel mechanisms, has been widely applied in many sophisticated fields, such as microelectronics [1–3], medicine [4,5], intelligent logistics [6,7] and 3D printing [8,9]. It inherits not only all the virtues of the traditional parallel robot, but also possesses some unique features such as lighter weight, faster motion, higher efficiency and larger payload capacity, which are elaborated in [10,11].

Different from the conventional manipulator kinematic diagram, delta robot is constructed from series of parallel dynamic links, from the output stage (which directly performs technological operations) to the fixed price. Thanks to this geometric structure, the moving platform is always oriented and can only reciprocate in 3 XYZ axes and works in parallel with the fixed top platform. That is reason why it is called a parallel robot. The difference in the kinematic diagram also creates many different characteristics of the robot kinematics. Delta robot has 4 popular forms: 3-PRPaR, 3-RRPaR, 3-P2S2S and 3-R2S2S.

In this paper, it is presented approach to design a 3R2S2S typed delta robot with the use of Galil DMC 2163 card as the main control board, provides execution of desired motion tasks. The paper is organized as follows. In the next section, the kinematic structure of delta robot is explained and the forward and inversed kinematic problems have been solved. The third section is devoted to mechanical design and control system integration of 3R2S2S typed delta robot. In this section, mechanical design of robot is done by the support of Inventor software. Control system includes electronic parts, actuator part and human-machine interface (HMI) in computer. Validation of presented delta robot is confirmed by numerical simulation in Matlab/Simulink software as well as experimental results. Final conclusion and recommendations for the future work are given in the last section.

II. Kinematic consideration of delta robot [12]

Delta robot is capable of XYZ translational control of its moving platform within its workspace. In order to develop kinematic equations for robot, we define the points $B_i, A_i, P_i \quad i = 1,2,3$ are the hips, the knees and the ankles of three identical legs. The fixed base Cartesian reference frame is {B}, whose origin is located in the center of the base equilateral triangle. The moving platform Cartesian reference frame is {P}, whose origin is located in the center of the platform equilateral triangle. The joint variables are $\Theta = \{\theta_1 \quad \theta_2 \quad \theta_3\}^T$ and the Cartesian variables are $\{X \quad Y \quad Z\}^T$. The length of each active arm is L and the length of each passive arm is l. R is the distance from {O} to near fixed platform side, r is distance from {P} to a moving platform vertex.

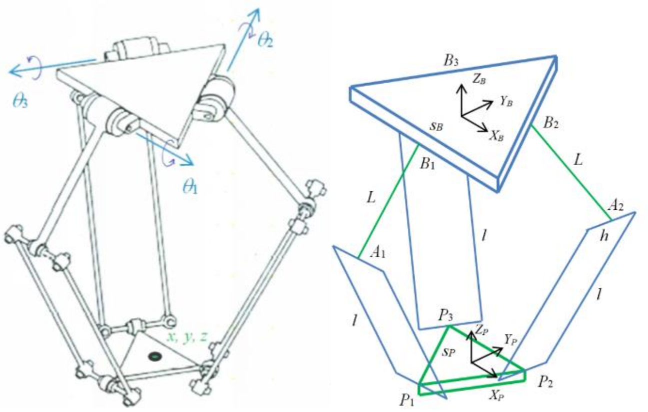

Fig. 1. Delta Parallel Robot Diagram

The fixed-base revolute joint points B_i are constant in the base frame {B} and the platform-fixed U-joint connection points P_i are constant in the base frame {P}:

$$B_1 = \begin{Bmatrix} 0 \\ -R \\ 0 \end{Bmatrix}; \quad B_2 = \begin{Bmatrix} \frac{\sqrt{3}}{2}R \\ \frac{1}{2}R \\ 0 \end{Bmatrix}; \quad B_3 = \begin{Bmatrix} -\frac{\sqrt{3}}{2}R \\ \frac{1}{2}R \\ 0 \end{Bmatrix}$$

$$P_1 = \begin{Bmatrix} 0 \\ -r \\ 0 \end{Bmatrix}; \quad P_2 = \begin{Bmatrix} \frac{\sqrt{3}}{2}r \\ \frac{1}{2}r \\ 0 \end{Bmatrix}; \quad P_3 = \begin{Bmatrix} -\frac{\sqrt{3}}{2}r \\ \frac{1}{2}r \\ 0 \end{Bmatrix}$$

The vectors $\{L_i\}$ are dependent on the joint variables $\Theta = \{\theta_1 \quad \theta_2 \quad \theta_3\}^T$:

$$L_1 = \begin{Bmatrix} 0 \\ -Lcos\theta_1 \\ -Lsin\theta_1 \end{Bmatrix}; L_2 = \begin{Bmatrix} \frac{\sqrt{3}}{2}Lcos\theta_2 \\ \frac{1}{2}Lcos\theta_2 \\ -Lsin\theta_2 \end{Bmatrix}; L_3 = \begin{Bmatrix} -\frac{\sqrt{3}}{2}Lcos\theta_3 \\ \frac{1}{2}Lcos\theta_3 \\ -Lsin\theta_3 \end{Bmatrix}$$

Substituting all above values into the vector-loop closure equations yields:

$$l_1 = \begin{Bmatrix} X \\ Y + Lcos\theta_1 + a \\ Z + Lsin\theta_1 \end{Bmatrix};$$

$$l_2 = \begin{Bmatrix} X - \frac{\sqrt{3}}{2}Lcos\theta_2 + b \\ Y - \frac{1}{2}Lcos\theta_2 + c \\ Z + Lsin\theta_2 \end{Bmatrix};$$

$$l_3 = \begin{Bmatrix} X + \frac{\sqrt{3}}{2}Lcos\theta_3 - b \\ Y - \frac{1}{2}Lcos\theta_3 + c \\ Z + Lsin\theta_3 \end{Bmatrix}$$

Where:
$$a = R - r$$
$$b = \frac{\sqrt{3}}{2}r - \frac{\sqrt{3}}{2}R$$
$$c = \frac{1}{2}r - \frac{1}{2}R$$

From the lengths of the forearm links on the coordinate axes, the three applicable constraints state that the passive arm lengths must have the correct, constant length l:

$$l = \sqrt{l_{ix}^2 + l_{iy}^2 + l_{iz}^2} \qquad i = 1, 2, 3.$$

Square both sides of the equation and set $K = X^2 + Y^2 + Z^2$ then the three constraints yield the kinematics equations for the Delta Robot:

$$\begin{cases} 2L(Y + a)cos\theta_1 + 2ZLsin\theta_1 + K + a^2 + L^2 + 2Ya = l^2 \\ -L\left(\sqrt{3}(X + b) + Y + c\right)cos\theta_2 + 2ZLsin\theta_2 + K + b^2 + c^2 \\ \qquad + L^2 + 2Xb + 2Yc = l^2 \\ L\left(\sqrt{3}(X - b) - Y - c\right)cos\theta_3 + 2ZLsin\theta_3 + K + b^2 + c^2 \\ \qquad + L^2 - 2Xb + 2Yc = l^2 \end{cases}$$

A. *Inverse kinematic model*

From the above three kinematic equations, we can summarize as follows:

$$E_i\, cos\theta_i + F_i\, sin\theta_i + G_i = 0 \qquad i = 1, 2, 3$$

With E_i, F_i, G_i are defined as follows:

$$E_1 = 2L(Y + a)$$
$$F_1 = 2ZL$$
$$G_1 = K + a^2 + L^2 + 2Ya - l^2$$
$$E_2 = -L\left(\sqrt{3}(X + b) + Y + c\right)$$
$$F_2 = 2ZL$$
$$G_2 = K + b^2 + c^2 + L^2 + 2(Xb + Yc) - l^2$$
$$E_3 = L\left(\sqrt{3}(X - b) - Y - c\right)$$
$$F_3 = 2ZL$$
$$G_3 = K + b^2 + c^2 + L^2 + 2(-Xb + Yc) - l^2$$

Set $t_i = \tan\frac{\theta_i}{2}$ then the kinematic equation becomes:

$$E_i\left(\frac{1 - t_i^2}{1 + t_i^2}\right) + F_i\left(\frac{2t_i}{1 + t_i^2}\right) + G_i = 0$$
$$\leftrightarrow (G_i - E_i)t_i^2 + (2F_i)t_i + (G_i + E_i) = 0$$

Solve the above quadratic equation we find t_{i1}, t_{i2}:

$$t_{i_1} = \frac{-F_i + \sqrt{E_i^2 + F_i^2 - G_i^2}}{G_i - E_i} \text{ and } t_{i_2} = \frac{-F_i - \sqrt{E_i^2 + F_i^2 - G_i^2}}{G_i - E_i}$$

We choose $t_i > 0$ and obtain the inverse kinematic model:

$$\theta_i = 2\,\text{atan}\left(\frac{-F_i - \sqrt{E_i^2 + F_i^2 - G_i^2}}{G_i - E_i}\right)$$

B. *Forward kinematic model*

From the connecting joint between the active arm and the passive arm A_i (with $i = 1, 2, 3$) we draw additional lines A_iA_{iv} parallel to the SP plane and directed to the origin and define three virtual sphere centers A_{iv}:

$$A_{1v} = \begin{Bmatrix} 0 \\ -R - Lcos\theta_1 + r \\ -Lsin\theta_1 \end{Bmatrix} A_{2v} = \begin{Bmatrix} \frac{\sqrt{3}}{2}(R + Lcos\theta_2 - r) \\ \frac{1}{2}(R + Lcos\theta_2 - r) \\ -Lsin\theta_2 \end{Bmatrix}$$

$$A_{3v} = \begin{Bmatrix} -\frac{\sqrt{3}}{2}(R + Lcos\theta_3 - r) \\ \frac{1}{2}(R + Lcos\theta_3 - r) \\ -Lsin\theta_2 \end{Bmatrix}$$

Then the forward kinematics solution is the intersection of three known spheres. Let the sphere be referred as a vector center point {C} and radius r_c, $(\{C\}, r_c)$. The coordinates of the point P to be found in the intersection of the three known spheres: $(A_{1v}, l), (A_{2v}, l), (A_{3v}, l)$.

$$\begin{cases} (x - x_1)^2 + (y - y_1)^2 + (z - z_1)^2 = l^2 \\ (x - x_2)^2 + (y - y_2)^2 + (z - z_2)^2 = l^2 \\ (x - x_3)^2 + (y - y_3)^2 + (z - z_3)^2 = l^2 \end{cases}$$

We also have all Z sphere-center heights are the same, $z_1 = z_2 = z_3 = z_n$.

Solving the above system of equations, we find the coordinates of the point P.

III. MECHANICAL DESIGN, HARDWARE COMPONENTS AND CONTROL SYSTEM

The entire Delta Robot control system includes an mechanical design of 3R2S2S type delta robot, electronics hardware consisting of a control board (motherboard) DMC - 2163, a 24VDC power supply, an amplifier AMP 20540, an encoder motor, and computer that contains control software (Fig. 2).

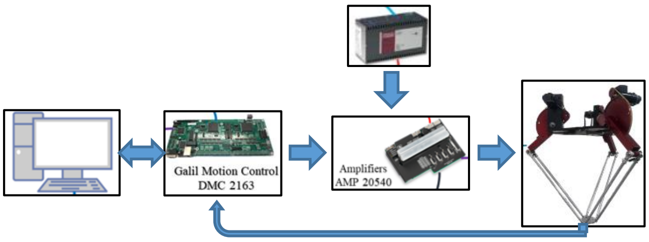

Fig. 2. Overview diagram of the whole system

A. *Mechanical Design*

Mechanical design of robot is carried out with the support of Inventor software. They include some main parts such as a fixed platform, three active arms (each consists of a semicircle fixed join with a rod), three passive arms which are parallelogram mechanisms, a moving platform and a robot stand. All main mechanical parts are made from aluminum to ensure both sustainability as well as decreasing the weight.

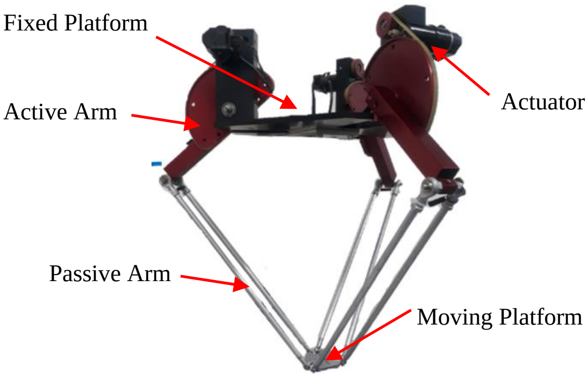

Fig. 3. The 3R2S2S typed Delta robot

As shown in Fig. 3, Delta robot is composed of three identical arms in parallel between the top fixed base and the bottom moving end-effector platform. The two platform designs are presented in Fig. 4. Each arm consists of two parts: active and passive. The active arm of robot is constructed from a rod fitted with a semicircular plate (Fig. 5). The top revolute joint is fixed with the active arm and actuated via base-fixed rotational actuators through belt. Thanks to this configuration, the torque transfers to the active arm is increased. The passive arm is parallelogram 4-bar mechanisms of the three lower links ensure the translation-only motion (Fig. 6).

TABLE I. PARAMETERS OF 3R2S2S DELTA ROBOT

Notation	Descriptions	Value	Unit
R	The distance from {O} to near fixed platform side	75	mm
r	r is distance from {P} to a moving platform vertex	22.95	mm
L	Length of active arm	160	mm
l	Length of passive arm.	400	mm
θ_i	Revolute joint angle between L and plane SB		deg

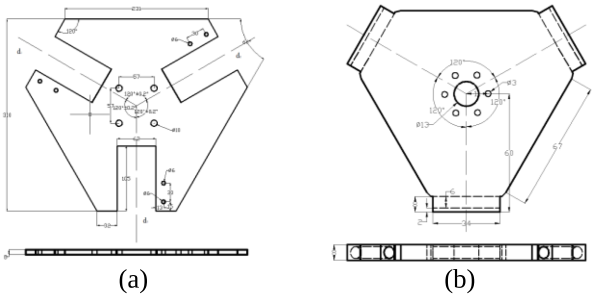

Fig. 4. Fixed platform (a) and moving platform (b)

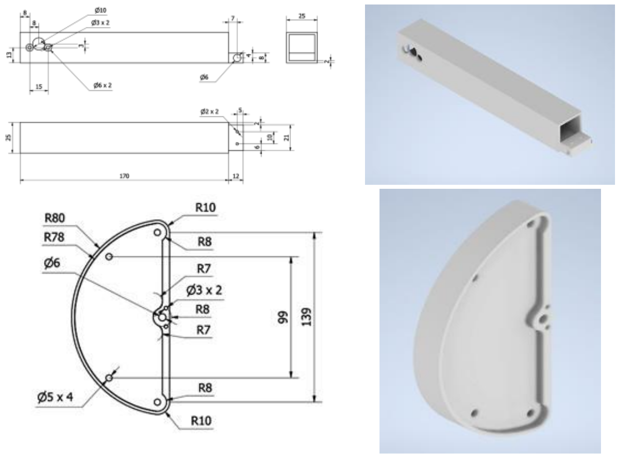

Fig. 5. Active arm

Fig. 6. Passive Arm

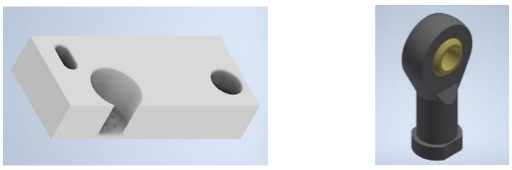

Fig. 7. Other parts

B. *Hardware Setup*

The hardware setup includes a computer, a Galil Motion Controller DMC-2163, a 24VDC power supply, an amplifier AMP-20540 and three DC motor with attached encoder (Fig. 2). Computer play a role as human-machine-interface allow user to setup parameter to system. The DMC 2163 controller board receives data from the computer and instant position of robot to calculate the control signal for actuator (three DC motors) and transmit to the amplifier.

1) *Galil Motion Control (DMC-2163)[13][14]*

The DMC-21x2/21x3 can be used for applications involving jogging, point-to-point positioning, vector positioning, electronic gearing, multiple move sequences, and contouring. The controller eliminates jerk by programmable acceleration and deceleration with profile smoothing. For smooth following of complex contours, the DMC-21x2/21x3 provides continuous vector feed of an infinite number of linear and arc segments. The controller also features electronic gearing with multiple master axes as well as gantry mode operation.

Each DMC-21x2/21x3 provides two communication channels: RS-232 (up to 19.2K Baud) and 10BaseT Ethernet. For synchronization with outside events, the DMC-21x2/21x3 provides uncommitted I/O, including 8 digital inputs and 8 digital outputs. Further I/O is available if the auxiliary encoders are not being used (2 inputs/each axis). Dedicated TTL inputs are provided for forward and reverse limits, abort, home, and definable input interrupts.

2) Power supply and Amplifier components

The AMP-20540 (four-axis) are multi-axis brush/brushless amplifiers that are capable of handling 500 watts of continuous power per axis. The AMP-20540 Brushless drive modules are connected to a DMC-21x3 controller via the 96 pin DIN connector. The standard amplifier accepts DC supply voltages from 18-60 VDC. The AMP-205x0 family provides for the addition of 8 analog input to the DMC-21x3. The analog inputs accept +/- 10 V input and have a resolution of 12 bits.

TABLE II. SPECIFICATIONS OF AMP - 20540

Parameters	Specification
Supply Voltage	18-60 VDC (Up to 80V optional)
Continuous Current	7 Amps
Peak Current	10 Amps
Nominal Amplifier Gain	0.4, 0.7, and 1.0 A/V
Switching Frequency	60 kHz (up to 140 kHz)
Minimum Load Inductance	0.5 mH
Brushless Motor Commutation angle	120° (60° option available)

3) Motor and encoder

Three integrated encoder DC motors are used to drive the active arms of the Delta robot (Fig. 8). The parameters of this motor and the optical encoder are pointed out in TABLE III and TABLE IV.

Fig. 8. Maxon DC motor with encoder

TABLE III. PARAMETERS OF DC MOTOR

Parameters	Specification
Mass	340g
Size	Ø30 x 65 mm
Working voltage	15V
Engine rotation speed at no load	7200 rpm
Maximum torque	931 Nm
Working performance	85%
Maximum axial load	110N
Working temperature	−30°C to 100°C

TABLE IV. PARAMETERS OF ENCODER

Parameters	Specification
Operating temperature	$-40\ to\ 100^oC$
Supply voltage (Vcc)	$-0.5\ to\ 7V$
Output voltage	$-0.5\ to\ Vcc$
Output current	$-1\ to\ 5mA$
Number of pulses in one round	1000 pulses

C. Control System

The control system includes the control algorithm and the human-machine-interface (HMI) which are coded in the Visual Studio software environment. The software framework is part of the robotic assembly cell. Parameters of system are set up by user through HMI.

For the positioning task, each coordinate of the input position is calculated, given the reference and measured position of the robot. The input values for the task space are then converted to joint space using inverse kinematics. These values are sent to DMC controller. DMC controller using PID algorithm to calculate the control signal for each motor to create torque applied to each active arm of the robot (Fig. 9).

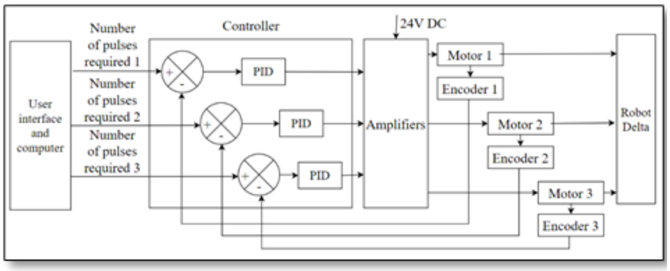

Fig. 9. The structure of control system

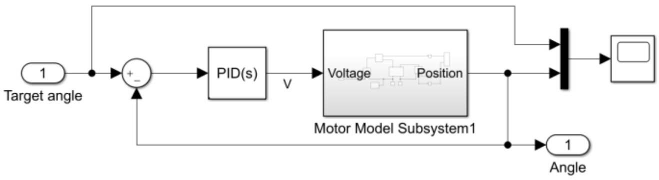

Fig. 10. Position control of DC motor

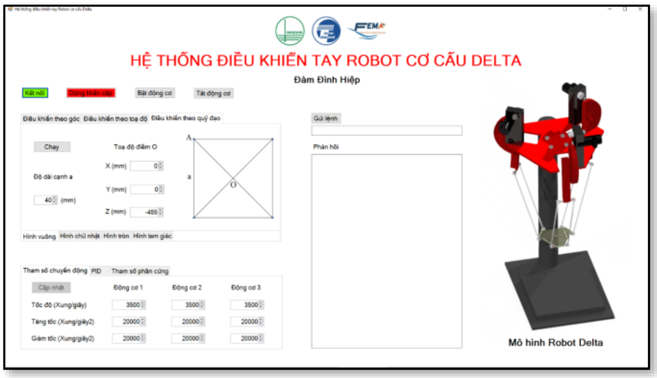

Fig. 11. Control and monitoring interface

IV. SIMULATION AND EXPERIMENTS

A. Simulation set up and results

The whole system is shown in Fig. 12. The two trajectory generator blocks are built to create the rectangular obit and circular orbit. Plan the trajectory of an end effector so that the end actuator travels in a rectangular or around a fixed center at a certain speed and acceleration. The kinematic parameters of the end effector are transformed into the angular motion parameters of the active arm by the inverse kinematics model. PID position control will secure that each DC motor will move the arm to the right angle (Fig. 14).

The CAD model of 3R2S2S delta robot which was built under Inventor software environment in previous section will be used to import into Matlab via the Simmechanics toolbox. We obtain the Simmechanics model of robot with the connection between each robot arm (Fig. 15).

In order to check the motion performance of the robot, the driving force and the sensor are added into the SimMechanics model. The driving force is generated by a DC motor. Sensor will detect the motion parameters of the active arm, through the forward kinematics model to calculate the end effector motion parameters (Fig. 17).

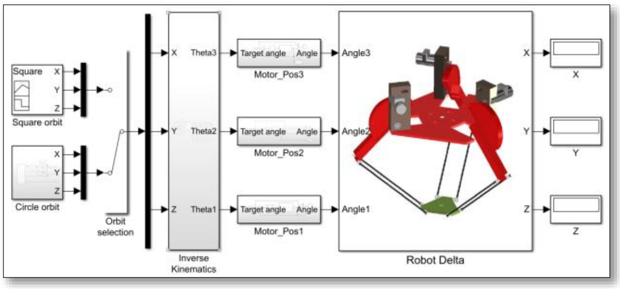

Fig. 12. 3R2S2S Delta Robot control system

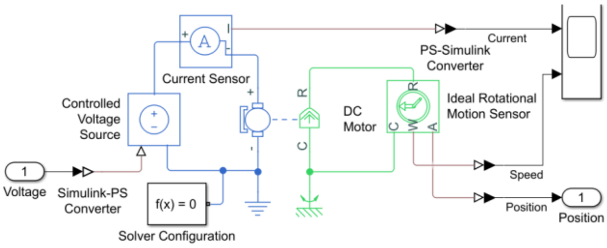

Fig. 13. DC motor block

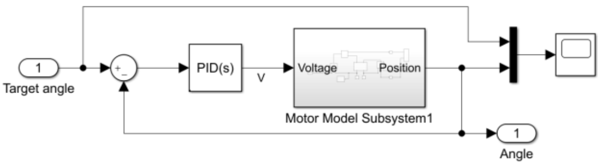

Fig. 14. Position control of DC motor block

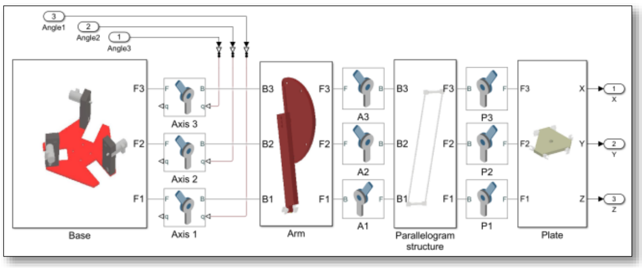

Fig. 15. 3R2S2S Delta Robot Model block

We will test the operation of the system in two cases: a 60mm square trajectory and 20mm diameter circular trajectory. The simulation results from the first case are shown in Fig. 16 and Fig. 17.

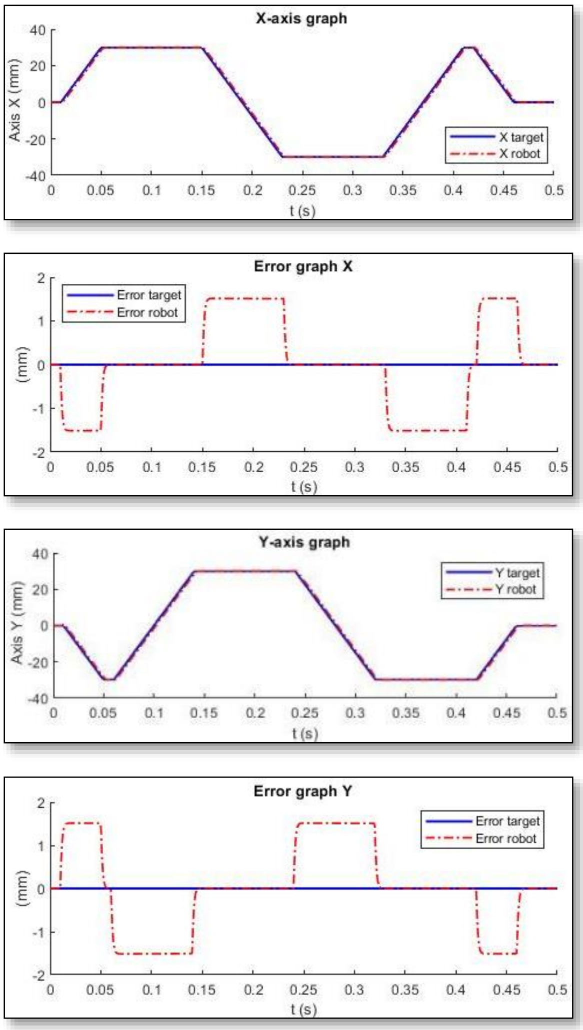

Fig. 16. X and Y axis motion trajectory and error

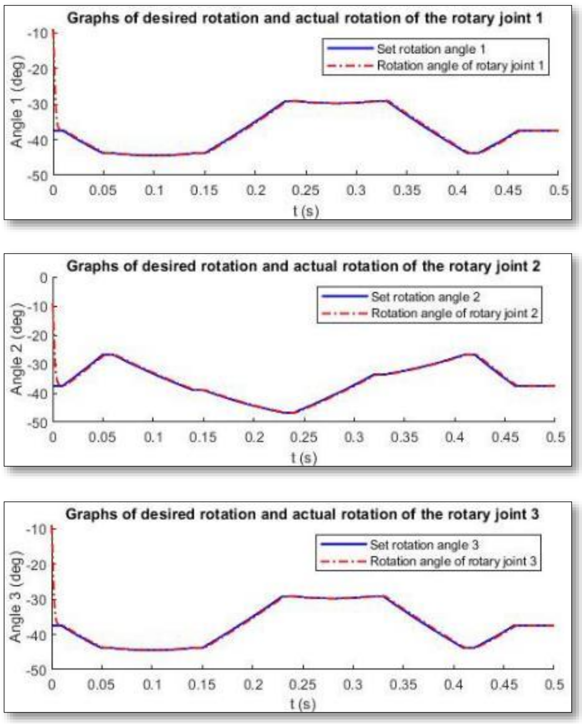

Fig. 17. The rotation angle of each active arm

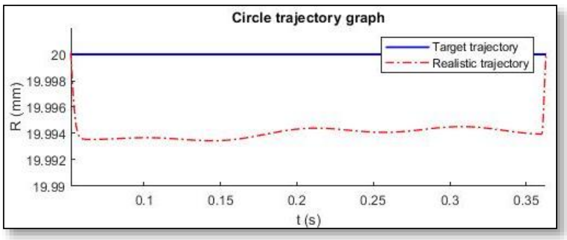

Fig. 18. The radius of trajectory

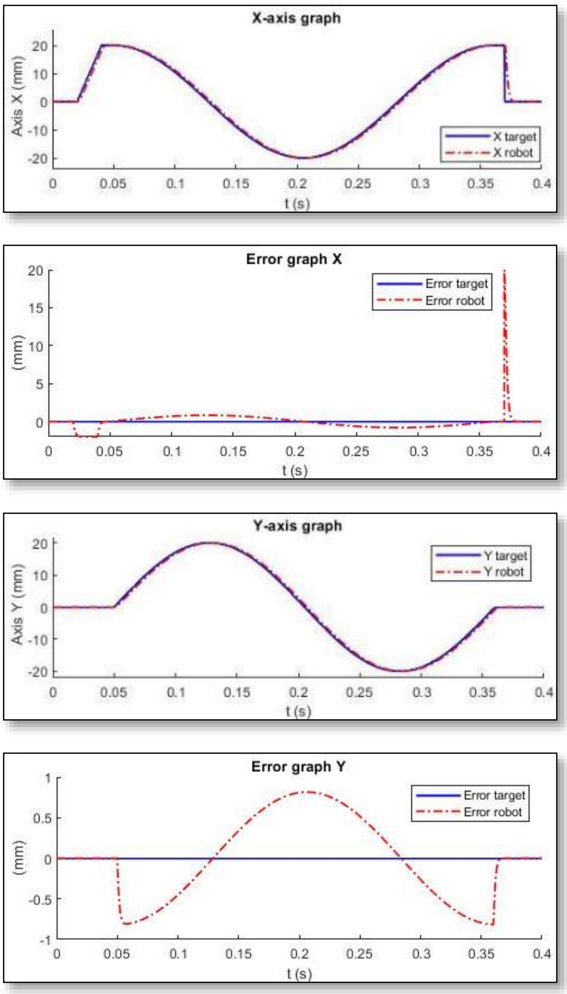

Fig. 19. X and Y axis motion trajectory and error

In the second simulation test, the circular trajectory generator is used. The specified coordinates is the center and 20mm radius of motion

Through simulation experiments, we can verify the motion of 3R2S2S Delta robot kinematics model and continue testing with the real system in the next part.

B. *Experimental Results*

The performance of Delta robot continues verifying with the real mechanical model and control system. To evaluate the performance of the developed Delta robot, a measurement set-up is built. Some tests are carried out to ensure the operation of the robot system:

- The angle of an active arm is considered in Fig. 21.
- The position of center point of moving platform is verify in Fig. 22
- Trajectory motion (Fig. 23 and Fig. 24).

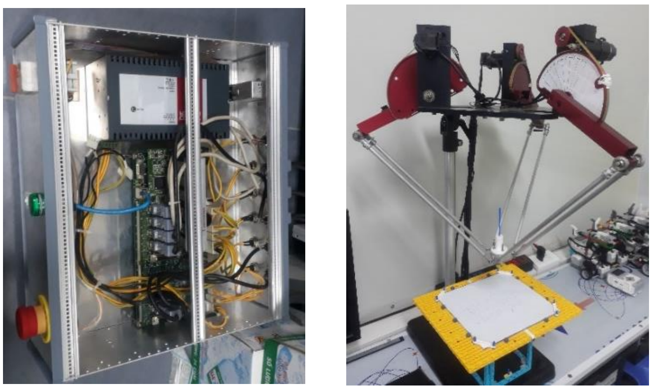

Fig. 20. Experimental system

(a) (b)

Fig. 21. Joint angle of active arm

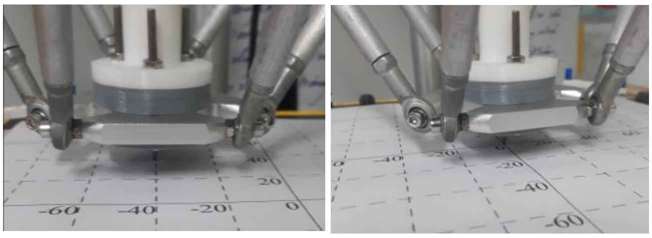

(a) (b)

Fig. 22. Point to point motion test

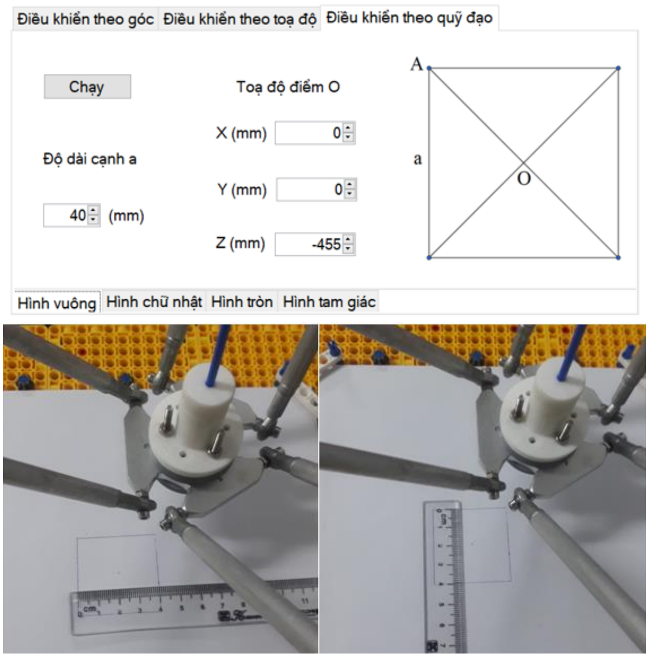

Fig. 23. Experiment result with 60mm rectangular trajectory

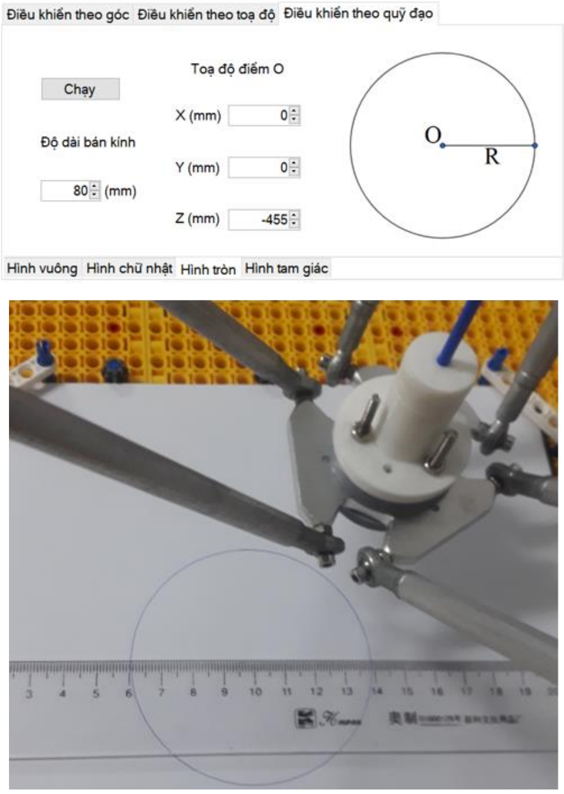

Fig. 24. Experiment result with 20mm diameter circular trajectory

V. CONCLUSION

This work demonstrates a design of a 3R2S2S typed delta robot with DMC 2163 controller board for performing multifunctional operations. The design of the proposed Delta robot includes the three-axis rotation of the wrist, a pointer and a six-axis robotic arm. The robot system's implementation involves the construction of mechanical design, integrating electronics components and control system. The simulations and experiments were carried out to verify the operation of robot system. The results obtained reveal that the developed Delta robot completes the tasks effectively.

In the future work, we will investigate of different methods of the path planning as well as improving and comparison of different control strategies. We also consider the parallel-link robot system.

ACKNOWLEDEMENT

This work has been supported by VNU University of Engineering and Technology under CN 20.40 project.

REFERENCES

[1] Borchert, G.; Battistelli, M.; Runge, G.; Raatz, A. Analysis of the mass distribution of a functionally extended delta robot. Robot. Comput.-Integr. Manuf. 2015, 31, 111–120.

[2] Correa, J.E.; Toombs, J.; Toombs, N.; Ferreira, P.M. Laminated micro-machine: design and fabrication of a flexure-based delta robot. J. Manuf. Process. 2016, 31, 370–375

[3] Coronado, E.; Maya, M.; Cardenas, A.; Guarneros, O.; Piovesan, D. Vision-based control of a delta parallel robot via linear camera-space manipulation. J. Intell. Robot. Syst. 2017, 85, 93–106.

[4] Bekelis, K.; Radwan, T.A.; Desai, A.; Roberts, D.W. Frameless robotically targeted stereotactic brain biopsy: feasibility, diagnostic yield, and safety. J. Neurosurg. 2012, 116, 1002–1006.

[5] Lin, Y.; Wang, X.; Wu, F.; Chen, X.; Wang, C.; Shen, G. Development and validation of a surgical training simulator with haptic feedback for learning bone-sawing skill. J. Biomed. Inform. 2014, 48, 122–129.

[6] Yang, X.; Feng, Z.; Liu, C.; Ren, X. A geometric method for kinematics of Delta robot and its path tracking control. In Proceedings of the International Conference on Control, Automation and Systems, Gyeonggi-do, Korea, 22–25 October 2014.

[7] Kelaiaia, R. Improving the pose accuracy of the Delta robot in machining operations. Int. J. Adv. Manuf. Technol. 2017, 91, 2205–2215.

[8] Morocho, D.; Anita, S.; Celi, R.; Loza, D.; Mariela, P. Study, design and construction of a 3D printer implemented through a delta robot. In Proceedings of the CHILEAN Conference on Electronics Engineering, Information and Communication Technologies, Santiago De Chile, Chile, 28–30 October 2015

[9] He, K.; Yang, Z.; Bai, Y.; Long, J.; Li, C. Intelligent fault diagnosis of delta 3D printers using attitude sensors based on support vector machines. Sensors 2018, 18, 1298.

[10] Bengoa, P.; Zubizarreta, A.; Cabanes, I.; Mancisidor, A.; Pinto, C.; Mata, S. Virtual sensor for kinematic estimation of flexible links in parallel robots. Sensors 2017, 17, 1934

[11] Shang, D.; Li, Y.; Liu, Y.; Cui, S. Research on the motion error analysis and compensation strategy of the Delta robot. Mathematics 2019, 7, 411.

[12] Robert L. Williams II, Ph.D, *The Delta Parallel Robot: Kinematics Solutions*, Mechanical Engineering, Ohio University, October 2016.

[13] Galil Motion Control, Inc, *DMC-21x3 AMPLIFIERS & ACCESSORIES*, User manual/command reference, Galil Motion Control, Inc.

[14] Galil Motion Control, Inc, *DMC-21x2/21x3, USER MANUAL*, Galil Motion Control, Inc.

[15] Galil Motion Control, Inc, *DMCWin32 Galil Windows API Tool Kit*, USER MANUAL, Galil Motion Control, Inc.

[16] Galil Motion Control, Inc, *COMMAND REFERENCE*, Optima/Econo DMC-2xxx Series, Galil Motion Control, Inc.

[17] https://docs.microsoft.com/vi-vn/visualstudio/get-started/visual-studio-ide?view=vs-2019

[18] https://devblogs.microsoft.com/cppblog/c99-library-support-in-visual-studio-2013/

[19] https://www.microsoft.com/en-us/research/project/f-at-microsoft-research/?from=http%3A%2F%2Fresearch.microsoft.com%2Fen-us%2Fum%2Fcambridge%2Fprojects%2Ffsharp%2F

[20] https://docs.microsoft.com/en-us/dotnet/desktop/winforms/overview/?view=netdesktop-5.0

[21] https://docs.microsoft.com/en-us/archive/msdn-magazine/2006/vs-2005-guided-tour/pure-c-hello-c-cli

[22] https://www.galil.com/sw/pub/all/doc/gclib/html/index.html

[23] https://octopart.com/tis+300-124-tracopower-5399280

[24] https://html.alldatasheet.com/html-pdf/88955/HP/HEDS-5540-A11/27/1/HEDS-5540-A11.html

[25] https://www.maxongroup.com/maxon/view/product/273752

[26] https://plctech.com.vn/winform-la-gi/

The 6th International Conference on
Engineering Mechanics and Automation (ICEMA 2021)
Hanoi, November 14, 2021

Analysis and design of a photovoltaic water pumping system

Cuong Hung Tran
Faculty of Engineering Mechanics and Automation
University of Engineering and Technology
Ha Noi, Viet Nam
tchung@vnu.edu.vn

Ngoc Linh Nguyen
Faculty of Engineering Mechanics and Automation
University of Engineering and Technology
Ha Noi, Viet Nam
nlnguyen@vnu.edu.vn

***Abstract*: Solar energy is considered to be one of the most promising renewable energies in the world. Water pumping systems using solar photovoltaic energy have been used increasingly widely in recent decades as one of the most popular solar energy applications. This paper aims to analyze and design a simple standalone photovoltaic (PV) water pumping system used for agriculture applications. Initially, solar pumping systems with direct couplings with the pump were utilized; however, their limited performance caused the system to not operate at the maximum output of the PV generator. In the last decade, these systems have been improving their performance due to the addition of the maximum power point tracker (MPPT) and control systems.**

Keywords: Photovoltaic pumping system, MPPT controller, Perturb and Observe (P&O)

I. INTRODUCTION

More than half a million Vietnamese do not have access to electricity, mainly in mountainous regions or on islands. In addition, our country has great potential for renewable energy sources such as solar, wind, hydroelectric, biomass. For supplying electrical power, these sources of energy represent a promising economic and environmental solution [1]. Solar energy is one of the best sources of electricity for villages since it is abundantly available and relatively simple to maintain structures. Water pumping systems using solar photovoltaic energy have been used increasingly widely in recent decades in rural areas of many developing countries as one of the most popular applications of solar energy [2]. Various studies have found that the performance and economic sustainability of solar photovoltaic water-pumping systems (PVWPS) are cost-effective and reliable for irrigation purposes [3] [4]. The advantages of these systems are low maintenance, no pollution, easy installation, reliability, the possibility of unattended operation, and the capability to be matched to demand [5].

Generally, a PVWPS can be categorized into a grid-connected and off-grid system. Off-grid systems are further subdivided into battery-driven and direct-driven systems. Direct coupling systems without battery storage are the most commonly used. Since the energy produced from solar PV is direct current (DC) in nature, the conversion losses are minimal when the DC pumping system is in operation.

The main variables that influence the performance of PVWPS are total dynamic head, the quantity of fluid extracted, variation of solar radiation level, PV and motor pump technology. A detailed analysis of the individual system and its components is given in the following sections.

A maximum power point tracking system (MPPT) ensures that the PV module will always operate at the maximum power under any weather condition. Many MPPT techniques in the literature can be used to change the system operating point [6] [7]. In this work, the Perturbation and Observation (P&O) method is used to track the Maximum Power Point. It is the most widely applied method in the PV industry because of its simplicity, robustness, and ease of implementation. However, it also presents drawbacks such as slow response slow response speed, oscillation around the MPP in steady-state.

This paper is structured as follows. Following the introduction, Section 2 presents the modeling of components PV pumping systems. Section 3 describes the MPPT algorithm in this work. The simulation results and discussion are illustrated in Section 4. Finally, the conclusion is given in Section 5.

II. MODELING OF COMPONENTS PV PUMPING SYSTEMS

In this study, the system is composed of four main parts: a PV array, a DC-DC Boost converter controlled by MPPT algorithm, a motor-pump, and a storage tank. A simple schematic of the pumping system is shown in **Fig. 1** . In this study, a PVWPS has been designed specifically for tomato greenhouses.

A. Storage tank

In this work, the water storage tank plays the role of batteries. It is sized to meet the load demand. A maximum daily amount of water should be calculated to determine the capacity of a tank.

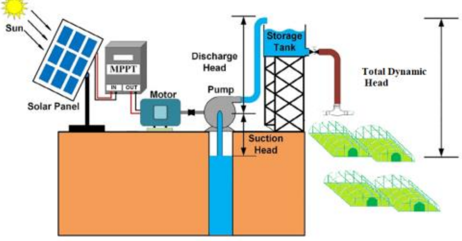

Fig. 1. Components of PV pumping systems **[8]**

B. Motor-pump

There are two basic types of motors: alternating current (AC) and direct current (DC), where each category has its own types and applications [5]. **Fig. 2** shows the type of motors used in photovoltaic water pumping systems. DC motors are generally more efficient than AC motors. Moreover, they do not require an inverter since PV arrays generate DC power. However, DC motors may need periodic replacement after 2000-4000 hours due to the mechanical moving parts.

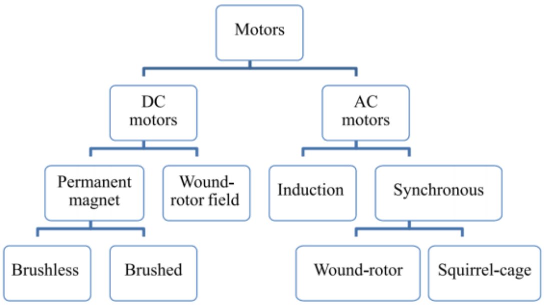

Fig. 2. Motor classifications chart **[5]**

Pumps can be classified into rotodynamic (centrifugal) and volumetric (positive displacement). The centrifugal pump is the most widely used; it has relatively high efficiency, is simple, requires low maintenance and is able to pump a high volume of water. Moreover, centrifugal pumps can be connected directly with PV modules.

C. Total Dynamic Head (TDH)

TDH is one of the essential parameters in designing a pumping system. It is the total equivalent height that fluid is to be pumped, taking into account friction losses in the pipe:

$$TDH = \text{Static Height} + \text{Static Lift} + \text{Friction Loss} \quad (1)$$

Where:

- Static Height is the maximum height reached by the pipe after the pump
- Static Lift is the height the water will rise before arriving at the pump.

Hydraulic power required to supply a water flow rate (Q) at a certain TDH is given by [2]:

$$P_H(W) = Q.TDH.\rho.g \quad (2)$$

Where Q is water flow rate (m^3/h); ρ is the water density; g is the acceleration due to gravity (9.81 m/s^2).

The electric power required for the motor-pump is give by:

$$P_{E\_req}(W) = \frac{P_{H\_req}(W)}{\eta_P.\eta_m} \quad (3)$$

Where η_P : efficiency of the pump, η_m : efficiency of the motor

The approximate value of the rated power of the photovoltaic panel can be calculated as [2]:

$$P_{PV\_produce}(W) = \frac{P_{E\_req}(W) \times G_{ref}}{G_{Glob} \times F_Q} \quad (4)$$

Where:

- $P_{PV\_produce}$ is the peak power of the PV array under Standard Test Conditions (STC)
- G_{ref} is the incident solar radiance at STC
- G_{Glob} is the global solar radiance on a horizontal surface
- F_Q is the quality factor of the system

D. PV array model

In the literature, several models for the PV cell are used. The most commonly used is the one-diode equivalent circuit [9]. In this model, a photovoltaic cell is modeled as a current source. The photocurrent depends on the irradiation and the cell temperature. The PV module equivalent circuit is shown in **Fig. 3**

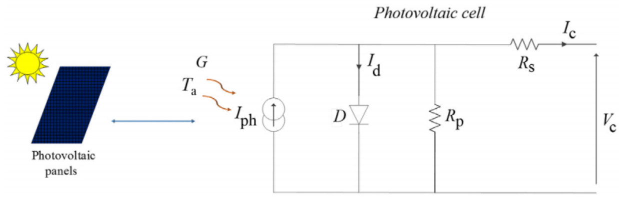

Fig. 3. Photovoltaic cell model

The characteristic equation is:

$$I_c = I_{ph} - I_0\left(\exp\frac{e(V_c + R_s I_c)}{nkT_c} - 1\right) - \frac{V_c + R_s I_c}{R_{sh}} \quad (5)$$

Where I_0 is the saturation current; e is the charge of an electron; k is Boltzmann's gas constant; n is the idealizing factor of the diode, R_s represents the losses due to the contacts as well as the connection, R_{sh} represents the leakage currents in the diode. MATLAB/Simulink has been used to develop a dynamic model for a PV module based on equation **(5)**.

III. MPPT CONTROLLER

The PV systems operation depends strongly on temperature, irradiation, and load characteristics. When a direct connection is carried out between the source and the load, the output of the PV module is not optimal. It is necessary to add an adaptation device To overcome this problem. As the load operating voltage is greater than the PVG's at the MPP, a DC-DC converter is chosen to be a Boost converter.

A maximum power point tracking system (MPPT) is a technique applied to PV systems to extract the maximum power generated by the PV array at different weather conditions. The MPPT algorithms can be classified into conventional algorithms (normally effective in case of not having any shading objectives) and algorithms that are based on stochastic and AI techniques [5] [10] [11].

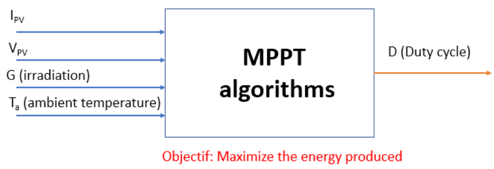

Fig. 4. General schematic diagram of MPPT algorithms

A. DC-DC Boost converter

The connection of a PV generator to a load requires an adaptation. The architecture of the DC-DC Boost converter is presented in **Fig. 5**.

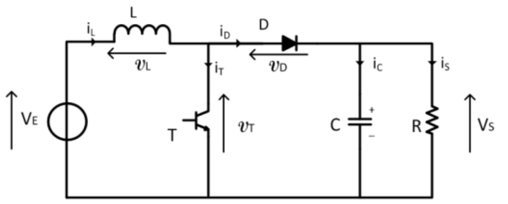

Fig. 5. Schematic diagram of a Boost converter

Fig. 6 shows the shape of the switch control signal T and α is the duty cycle:

$$\alpha=\frac{T_{ON}}{T_d}$$

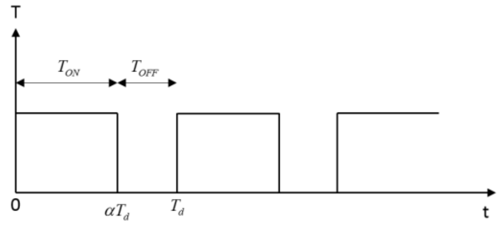

Fig. 6. Switch of control signal

Depending on the switch and diode state, there are two operating states (configurations) [12]:

- State 1: When the switch is closed, the diode is open.
- State 2: When the switch is open, the diode is closed.

Depending on the evolution of the current in the inductance, there are two modes of conduction:

- Continuous Conduction Mode (MCC): The current in the inductor does not cancel out over a switching period. It is, therefore, continuous.
- Discontinuous Conduction Mode (MCD): The current in the inductor goes to zero before the end of a switching period. The current in the inductor is discontinuous.

We are interested in the mode of continuous conduction in this study.

State 1:

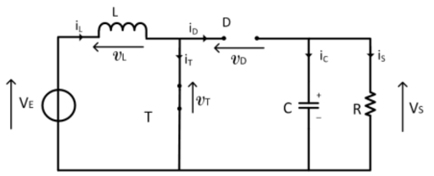

Fig. 7. Boost converter Operation at Switch ON

The voltage across the inductor is:

$$v_L=V_E=L\frac{di_L}{dt}>0 \tag{6}$$

So:

$$i_L=\frac{V_E}{L}t+I_{L_{MIN}} \tag{7}$$

Where $I_{L_{MIN}}$ is the minimum value of the current in the inductance.

State 2:

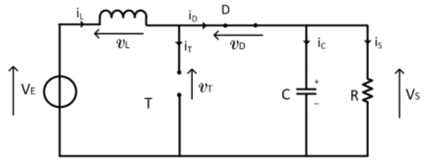

Fig. 8. Boost converter Operation at Switch OFF

The voltage across the inductor is:

$$v_L=V_E-V_S=L\frac{di_L}{dt}<0 \tag{8}$$

So:

$$i_L=\frac{V_E-V_S}{L}(t-\alpha T_d)+I_{L_{MAX}} \tag{9}$$

Where $I_{L_{MAX}}$ is the maximum value of the current in the inductance.

By definition, the average voltage of an inductor is 0 so:

$$\langle v_L\rangle=\frac{1}{T_d}\int_0^{T_d} v_L dt=\frac{1}{T_d}\left(\int_0^{\alpha T_d} V_E dt+\int_{\alpha T_d}^{T_d}(V_E-V_S)dt\right)=0 \tag{10}$$

$$\langle v_L\rangle=\alpha V_E+(V_E-V_S)(1-\alpha)=0 \tag{11}$$

Finally, we get the following relation:

$$V_S=\frac{V_E}{1-\alpha} \tag{12}$$

B. P&O method

In this study, the P&O method is applied to implement the MPPT algorithm. The P&O method uses the PV current and voltage measurements and compares their previous and present values. In fact, it consists in perturbing the panel voltage and comparing the PV power value obtained with its previous value. The increase in the PV power generates an increase of the perturbation voltage.

In this method, the step-size is a very important factor. A larger step-size leads to a faster response but more oscillations around its MPPT point. On the other hand, a smaller step-size improves efficiency but slows convergence [13].

The oscillations that P&O can generate are considered the main drawback of this method. However, P&O method is the most widely applied method in the PV industry because of its simplicity, robustness, and ease of implementation.

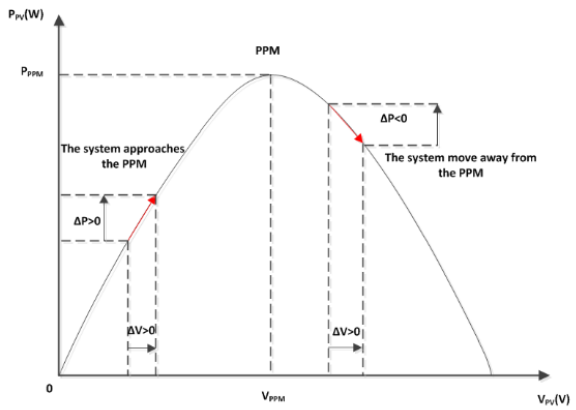

Fig. 9. Principle of P&O method

The flow chart in **Fig. 10** illustrates the P&O method.

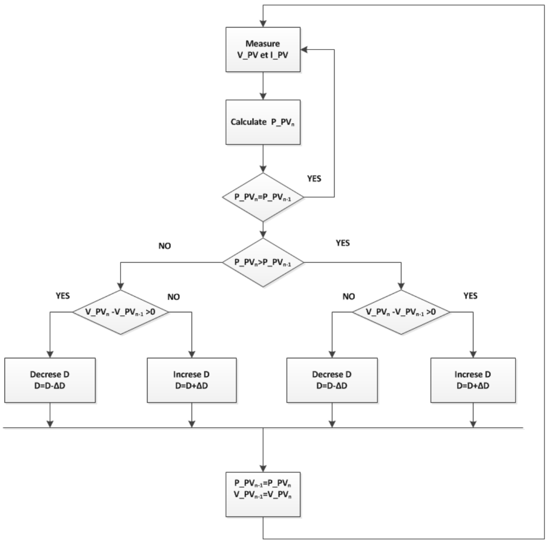

Fig. 10. Flowchart of the P&O algorithm

IV. SIMULATION, RESULTS & DISCUSSION

A. Simscape

Simscape is a Matlab tool that uses a physical modeling approach for creating System models. As opposed to the Simulink blocks that represent mathematical operations or operate on signals, Simscape blocks represent physical components directly. With Simscape blocks, a system model is built in the same way as a physical system is assembled [14].

The Simulink model is essentially a representation of the actual mathematical equations that govern the behavior of the system. One of the biggest challenge in building a representative system model is user-knowledge of the system. Someone who knows a system well enough including all the mathematical equations may find it easy to replicate the equations in a tool such as Simulink. However, someone who is encountering a system the first time may find it quite difficult to transition from a physical world to the level of abstraction necessary for a mathematical model. Simscape automatically constructs, from the model, equations that characterize the system behavior, which are in turn integrated with the rest of the Simulink model.

In this work, Sim-Electronics and Sim-Hydraulics block sets were used to implement the whole system in Matlab/Simulink environment.

B. Parameters

- *Storage tank*

The maximum amount of water required by one square meter of tomatoes per day is 15 l/m^2/day. We suppose the area is 1000 m^2 (around 2800-3200 tomatoes), hence the daily water requirement is 15 m^3/day. With evaporation and storage losses taken into account, the tank's capacity is around 16 m^3.

- *Total Dynamic Head (TDH)*

Static Height = 03 (m)
Static Lift = 05 (m)
Friction Loss = 0.15 (m)
So TDH = 8.15 (m)

C. Simulation

Results simulations were achieved by using Sim-Electronics and Sim-Hydraulics blocks in Matlab/Simulink. Two systems are presented in this section: Direct connection and MPPT connection. In the direct connection, the PV generator is directly connected to the Moto-pump (**Fig. 11**), while in the MPPT connection a MPPT controller is placed between the source and the Moto-pump (**Fig. 12**).

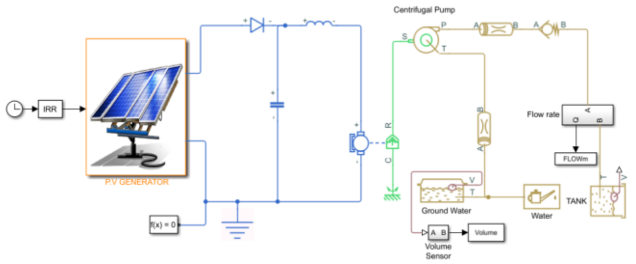

Fig. 11. Pumping system with direct connection of the PVG

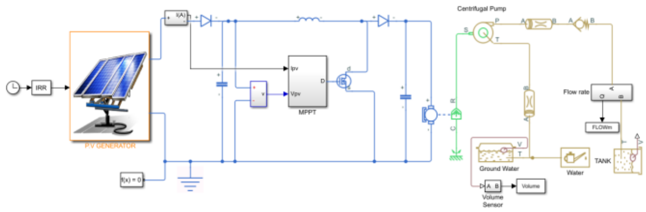

Fig. 12. Pumping system with MPPT connection of the PVG

a) Simulation under Standard Test Conditions (STC)

The results are obtained during one minute under STC: 1000 W/m^2 irradiance and 25°C temperature. **Fig. 13** shows the PV power under STC in two cases. Compared to direct connection, the system with MPPT connection shows greater power. **Fig. 14** shows the speed of a DC motor. This speed can be seen as the image of the PV generator voltage. **Fig. 15** shows the progress of the tank volume. Regarding the slope of each curve, the tank volume can reach 15,45 m^3 at STC in five hours (number of peak sun hours par day) in case of MPPT connection while in the other case, the tank will be filled with 14,45 m^3 in five hours.

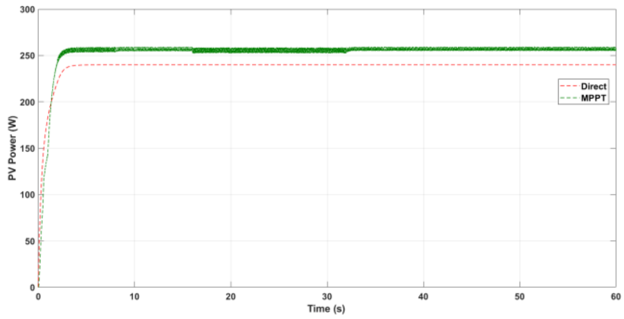

Fig. 13. PV Power under STC

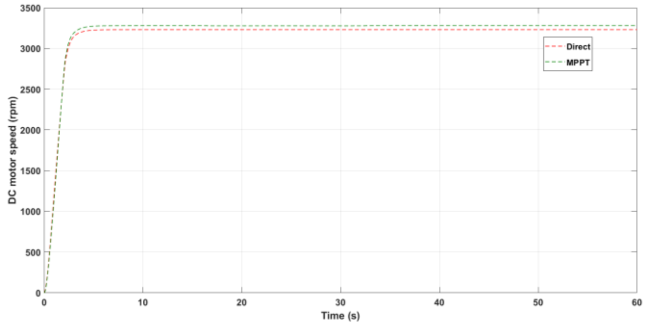

Fig. 14. DC motor speed under STC

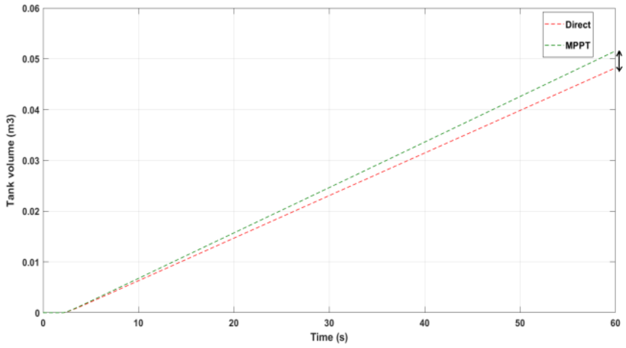

Fig. 15. Variation of the storage tank volume under STC

b) Simulation under variable conditions

The system is also tested in varying climatic conditions (variable irradiance) within 60 seconds in **Fig. 16**.

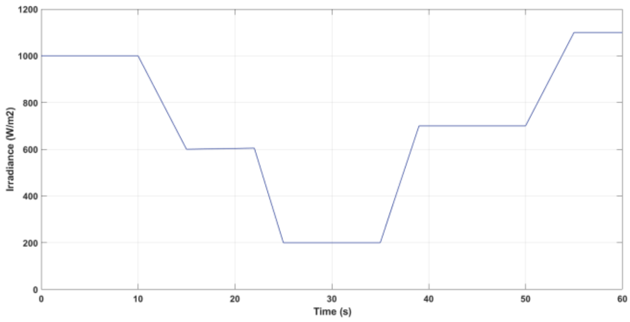

Fig. 16. Variation of irradiance

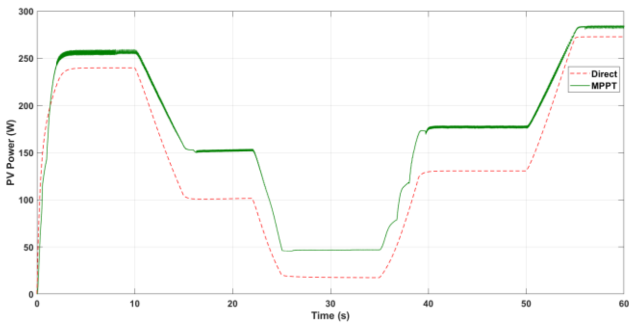

Fig. 17. PV Power under variation of irradiance

Fig. 17 show that the power of the PVG is directly proportional to the irradiance and is shaped like the irradiance curve. It can be observed that MPPT connection produces more power than direct connection. The results demonstrate that MPPT controller has a good response time regarding the irradiance variation. The speed of the DC motor is shown in **Fig. 18**.

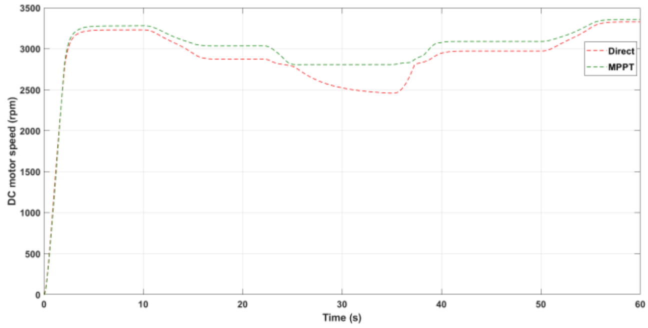

Fig. 18. DC motor speed variation of irradiance

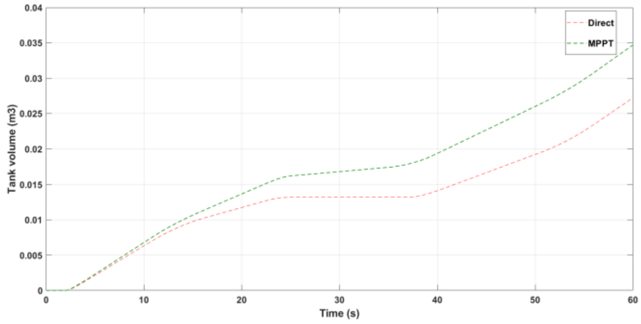

Fig. 19. Progress of the tank volume under variable conditions

Fig. 19 shows the progress of the tank volume. The results of simulation show that compared to direct connection, MPPT has a distinct advantage. It can be seen that in only one minute, the difference reaches 0.0076 m^3. If we assumed this will happen regularly during five hours, the difference would reach 3.8 m^3, which represents a very important amount of water.

V. CONCLUSION

In this study, we present a simple but efficient photovoltaic water pumping system. We estimated the daily energy captured by greenhouses, calculated the amount of water needed, sized the pump, and PV array in this study. Results simulations were achieved by using Matlab/Simulink/Simscape. Based on the amount of water gained each day (3.8 m3), a MPPT connection system can supply an additional (1387 m3) of water each year. The results obtained demonstrate the pumping system's good performance with MPPT algorithm.

ACKNOWLEDGMENT

This work has been supported/partly supported by VNU University of Engineering and Technology under project number CN20.39.

REFERENCES

[1] X.-L. Dang, "Contribution à l'étude des systèmes Photovoltaïque/Stockage distribués. Impact de leur intégration à un réseau fragile.," Ecole Doctorale Sciences Pratiques de Cachan., 2014.

[2] R. J. Chilundo, U. S. Mahanjane, and D. Neves, "Design and Performance of Photovoltaic Water Pumping Systems: Comprehensive Review towards a Renewable Strategy for

Mozambique," *JPEE*, vol. 06, no. 07, pp. 32–63, 2018, doi: 10.4236/jpee.2018.67003.

[3] L. Qoaider and D. Steinbrecht, "Photovoltaic systems: A cost competitive option to supply energy to off-grid agricultural communities in arid regions," *Applied Energy*, vol. 87, no. 2, pp. 427–435, Feb. 2010, doi: 10.1016/j.apenergy.2009.06.012.

[4] S. Rehman and A. Z. Sahin, "Performance Comparison of Diesel and Solar Photovoltaic Power Systems for Water Pumping in Saudi Arabia," *International Journal of Green Energy*, vol. 12, no. 7, pp. 702–713, Jul. 2015, doi: 10.1080/15435075.2014.884498.

[5] D. H. M. Tamer Khatib, "Photovoltaic Water Pumping Systems: Concept, Design, and Methods of Optimization," Elsevier, 2021, pp. i–ii. doi: 10.1016/B978-0-12-821231-8.09989-3.

[6] M. A. Abo-Sennah, M. A. El-Dabah, and A. E.-B. Mansour, "Maximum power point tracking techniques for photovoltaic systems: a comparative study," *IJECE*, vol. 11, no. 1, p. 57, Feb. 2021, doi: 10.11591/ijece.v11i1.pp57-73.

[7] M. Mao, L. Cui, Q. Zhang, K. Guo, L. Zhou, and H. Huang, "Classification and summarization of solar photovoltaic MPPT techniques: A review based on traditional and intelligent control strategies," *Energy Reports*, vol. 6, pp. 1312–1327, Nov. 2020, doi: 10.1016/j.egyr.2020.05.013.

[8] K. Muralidhar and N. Rajasekar, "A review of various components of solar water- pumping system: Configuration, characteristics, and performance," *Int Trans Electr Energ Syst*, vol. 31, no. 9, Sep. 2021, doi: 10.1002/2050-7038.13002.

[9] D. H. Muhsen, T. Khatib, and F. Nagi, "A review of photovoltaic water pumping system designing methods, control strategies and field performance," *Renewable and Sustainable Energy Reviews*, vol. 68, pp. 70–86, Feb. 2017, doi: 10.1016/j.rser.2016.09.129.

[10] N. A. Kamarzaman and C. W. Tan, "A comprehensive review of maximum power point tracking algorithms for photovoltaic systems," *Renewable and Sustainable Energy Reviews*, vol. 37, pp. 585–598, Sep. 2014, doi: 10.1016/j.rser.2014.05.045.

[11] J. P. Ram, T. S. Babu, and N. Rajasekar, "A comprehensive review on solar PV maximum power point tracking techniques," *Renewable and Sustainable Energy Reviews*, vol. 67, pp. 826–847, Jan. 2017, doi: 10.1016/j.rser.2016.09.076.

[12] S. Bacha, I. Munteanu, and A. I. Bratcu, *Power Electronic Converters Modeling and Control*. London: Springer London, 2014. doi: 10.1007/978-1-4471-5478-5.

[13] C. H. Tran, F. Nollet, N. Essounbouli, and A. Hamzaoui, "Modeling and Simulation of Stand Alone Photovoltaic System using Three Level Boost Converter," in *2017 International Renewable and Sustainable Energy Conference (IRSEC)*, Tangier, Dec. 2017, pp. 1–6. doi: 10.1109/IRSEC.2017.8477246.

[14] S. Das, "Modeling and Simulation of Mechatronic Systems using Simscape," *Synthesis Lectures on Mechanical Engineering*, vol. 5, no. 1, pp. 1–171, Mar. 2020, doi: 10.2200/S00972ED1V01Y201912MEC024.

Fruit Picking Robotic Arm for Agricultural Applications

Pham Manh Thang*
Faculty of Mechanics and Automation
VNU University of Engineering and Technology
Hanoi, Vietnam
thangpm@vnu.edu.vn

Bui Thanh Lam
Faculty of Mechanical Engineering
Hanoi University of Industry (HaUI)
Hanoi, Vietnam
lambt@haui.edu.vn

Hoang Van Manh
Faculty of Mechanics and Automation
VNU University of Engineering and Technology
Hanoi, Vietnam
manhv87@vnu.edu.vn

Ngo Anh Tuan
Faculty of Mechanics and Automation
VNU University of Engineering and Technology
Hanoi, Vietnam
natuan@vnu.edu.vn

Dang Anh Viet
Faculty of Electronics and Telecommunications (FET)
VNU University of Engineering and Technology
Hanoi, Vietnam
vietda@vnu.edu.vn

Kim, Jong-Wook
Department of Electronic Engineering
Dong-A University
Busan, Korea
kjwook@dau.ac.kr

Abstract: **Robotic arms are popular and highly applicable robots in many fields nowadays. Following the development trend, they are increasingly improved to become an important technology in production. In this work, a 4-degree-of-freedom robotic arm is studied and designed for application of fruit picking in agriculture. The position of the robot is controlled by coordinates sent from the image processing system through an inverse kinematic model. The robot can operate stably in flexible working positions. The control system consists of an Arduino Mega microcontroller and a servo motor. Through experiments, the average errors of the position in the x, y, z directions are 5.5%, 3.21%, and 9.84%, respectively. The average travel time to the set coordinates is 7.8 seconds. The results after various test cases show that the robot performs well with the accuracy and response time satisfying the specifications in the design.**

Keywords: Robotic Arm, Fruit picking, Position control, Kinematics.

I. Introduction

The world is witnessing a huge development in technology, most notably the industrial revolution 4.0. Along with it is the presence of robotic arms that appear widely in different fields. They have a wide range of applications from factories [1-3], schools [4], medical services [5], mapping [6], to industrial applications [7]. Their abilities are advantageous: high quality, accuracy, efficiency and economy, able to work in hazardous environments, in demanding jobs with precision. Robots can also be reprogrammed to be able to perform a number of different tasks. With a lot of potential benefits, it confirms that robotic technology plays an essential role in the industrial revolution 4.0 [8-10].

Robots with four degrees of freedom have been studied in many scientific articles and have high applicability [11-15]. S. Krut et al. [11] proposed an optimal design for a parallel 4-degree-of-freedom robot to perform pick-and-place actions at high speed and high acceleration. The design achieved good dynamic equilibrium and eliminated singularities during working. Du MengMeng et al. [12] studied the kinematics and parameterization model of the 4-DOF Scara robotic arm. The structure of the robot was developed to reduce inertia, smooth motion, and minimize torque for agricultural applications.

In agriculture, the application of self-harvesting and caring robots for fruit trees is gradually becoming popular all over the world. Typically, the orange picking robot (Hannan & Burks, 2004) is designed to automatically harvest fruit trees, and the Kondo Et strawberry picking robot is developed in laboratories. In Vietnamese agriculture, one of the countries with the strength of agricultural products, the application of robotic arms in farms is extremely necessary.

In this project, we used a robot with four degrees of freedom combined with an image processing system to automatically pick fruits. The robot includes 2 reciprocating joints and 2 rotating joints to ensure flexible operation to working positions. The picking element is designed to be firm and suitable for many types of fruit. The setpoint coordinates are sent to the microcontroller by the image processing system. The Arduino Mega microcontroller is used to process the signal from the image processing system and give control commands to the servo motor, based on the inverse kinematics calculation of the robot. Experimental results show that the robot has good performance, small error, and low latency. The robot has high applicability in the purpose of picking fruit according to the specified coordinates.

II. System design

A. Mechanical design

The system is a five degree of freedom robotic arm. Link 1,2,3,4 have lengths of 70 cm, 80 cm, 30 cm, and 10 cm, respectively. The joints of the robot work with rotation angles of (J1, 00), (J2, 00), (J3, 1800), and (J4, 1800). Each axis has a maximum operating angle, so the workspace must be determined for future testing. The maximum grip weight is 11.76 N and the maximum line speed is 100 mm/s. Fig. 1 shows the structure of the fruit picking robot. The end-effector is fixed for positioning, picking, and grasping. This design offers a simple and compact mechanical construction that not only provides sufficient DOF for pick and place tasks, but also facilitates highly efficient motion control.

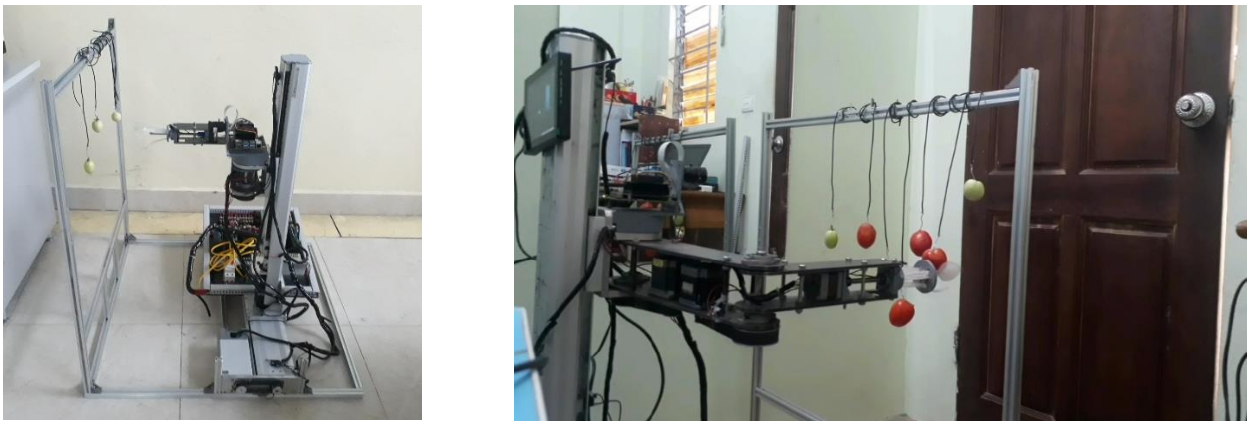

Fig. 1. The robotic arm realization

The control signals of the transducer are transmitted from the computer or controlled by a pre-programmed microcontroller. The end effector consists of three fingers as shown in Fig. 2. The nail is opened and closed by a moving device for opening and gripping. Each finger is attached with a soft coating material to reduce damage to fruit and vegetable during gripping. In addition, the end effector is equipped with a limit switch to detect the opening and closing range.

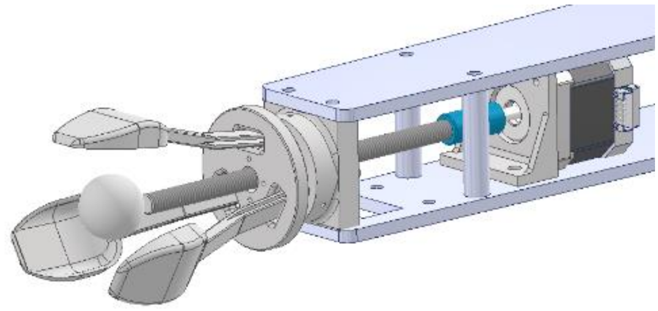

Fig. 2. The end effector

B. *Image processing unit*

The NVIDIA Jetson Nano Deverloper Kit is a small but very powerful computer that allows you to run multiple neural networks simultaneously for applications such as image classification, object detection, segmentation, and speech processing, all in a single platform that is easy to use and consumes less than 5 watts. The Jetson Nano also delivers 472 GFLOPS to run modern AI algorithms quickly, with a 64-bit ARM quad-core CPU, an onboard 128-core NVIDIA GPU, as well as 4GB of LPDDR4 memory. It is possible to run multiple neural networks and process several high-resolution sensors simultaneously.

Fig. 3. NVIDIA Jetson Nano Developer Kit B01

The 12.3MP IMX477 camera is suitable for industrial use and other applications such as security or that require a higher level of image fidelity. This camera offers up to 12.3MP resolution, which is nearly 50% larger area per pixel compared to Raspberry Pi Camera 8MP, thus providing better visual effects.

Fig. 4. Camera IMX477 12.3MP

C. *Controller*

Movements of the links are driven by a NEMA 23 Teknic ClearPath Servo motor that operates at a maximum speed of 4000 RPM and a maximum torque of 2 Nm. Joint 1 (horizontal) is driven through a worm gearbox with a ratio of 20:1 and a holding torque of 10.17 N m. Vertical movement (y-axis) uses a gear box with a gear ratio of 10:1. These two joints are linked by a *L*-shaped aluminum plate, so that the rotation axis of the two gearboxes is perpendicular to each other. The two swivel joints use a belt drive with a 1:2 gear ratio. The velocity of the rotary joints (i.e., servomotors) can be adjusted through frequency pulses varied from 0 to 500 kHz. The pulse signals are generated by the Arduino Uno microcontroller. The communication between the Arduino and the servo motor is established based on the transmission ports in the UART environment.

III. POSITION CONTROL

For fruit picking systems, the operator needs to approach different locations with high precision and flexibility. To achieve this goal, a motion control approach is presented in this section by fully exploiting the mechanical structure of the 4-DOF system developed from the inverse kinematics equation.

A. Inverse kinematics

The kinematic description of the 4-DOF controller is illustrated in Fig. 5. Let $[x, y, z]$ T ∈ R3 be the position of the end effector. According to the kinetic diagram shown in Fig. 5 and the Denavit – Hartenberg kinetic equations [37], the forward kinematics function can be obtained:

$$\begin{cases} x_e = l_2 + l_3.\mathrm{C}\,q_3 + l_4.\mathrm{C}\,q_3\,.\mathrm{C}\,q_4 - l_4.\mathrm{S}\,q_3.Sq_4 \\ y_e = -q_2 \\ z_e = q_1 + l_3.\mathrm{S}\,q_3 + l_4.\mathrm{C}\,q_3\,.\mathrm{S}\,q_4 - l_4.\mathrm{C}\,q_4.Sq_3 \end{cases} \quad (1)$$

Where:

- di – distance between xi and xi+1
- θi – rotating angle around zi-axis so that xi is parallel to xi+ai – distance between zi and zi+1
- αi – rotating angle around xi-axis so that zi is parallel to zi+1

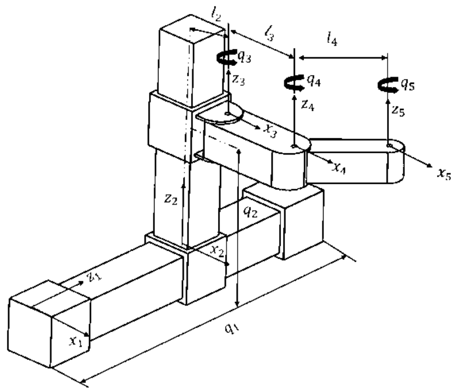

Fig. 5. Coordinating systems on each joint

Inverse kinematics is a calculation to find angular variables (joints) of the robot in determining the position and orientation of the end effector [6]. The Pythagorean theorem and the trigonometry rules can help solve the inverse kinematics problem by looking at two sides, especially the top and side projection of the system. Displacement q2 is a vertical axis of rotation that can easily be determined. Fig. 6 is the top projection used to find the rotation of q3, q4 and displacement of q1.

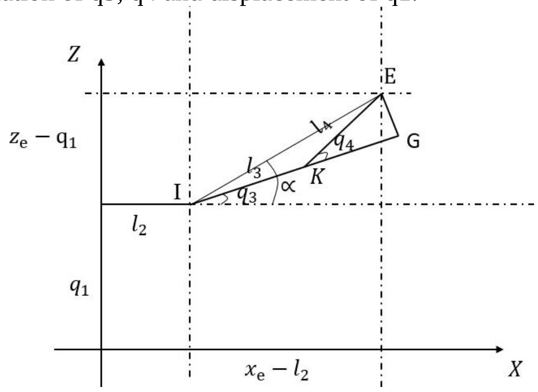

Fig. 6. Top projection

The values of the angular variables and the link lengths are listed in Table 1. From Fig. 5, we have:

$$\begin{cases} q_2 = -y_e \\ q_4 = arc\cos\left(\dfrac{(z_e - q_1)^2 + (x_e - l_2)^2 - l_3{}^2 - l_4{}^2}{2l_3l_4}\right) \\ q_3 = arc\sin\dfrac{z_e - q_1}{\sqrt{(z_e - q_1)^2 + (x_e - l_2)^2}} - arc\sin\dfrac{\sqrt{l_4{}^2 - l_4{}^2\dfrac{((z_e - q_1)^2 + (x_e - l_2)^2 - l_3{}^2 - l_4{}^2)^2}{4(l_3l_4)^2}}}{\sqrt{(z_e - q_1)^2 + (x_e - l_2)^2}} \\ q_1 = z_e - l_3\sin q_3 - l_4\sin(q_3 + q_4) \end{cases} \quad (2)$$

TABLE I. SYSTEM PARAMETERS

Variables	Values
d1	0.89 m
d2	0.78 m
d3	0.3 m
d4	0.33 m
q1	(0 m, 0.8 m)
q2	(0 m, 0.7 m)
q3	(0^0, 180^0)
q4	(-90^0, 90^0)

The inverse kinematics characteristics to compute the joint parameters [q1, q2, q3, q4] T from the position of the end effector $[x, y, z]$ T. In general, gradient-based optimization solvers [38, 39] can be used to compute the inverse kinematics of a controller. However, since the 3-DOF controller has a simple structure and is easy to exploit, its inverse kinetics can be determined by the analytic expression in (2), which can avoid the repetitive and complex optimal procedure, thus helps save time and minimizes errors.

IV. EXPERIMENT AND RESULTS

A. Workspace

The workspace is the total volume that the end effector can be achieved. The workspace size depends on the extent of the x, y, and z axis coordinates. The test is carried out by comparing the reference trajectory and the measured position of the link after being moved based on the inverse kinematics calculation. Fig. 8(a) shows the results of x-axis coordinates, the end effector can reach a maximum length of 74 cm from the position of the base and has a good response from 40 to 65 cm. The nearest point that the robot can reach is 36 cm, despite some significant errors. The points from 0 to 36 cm are unknown positions for the end effector. The end-effector cannot touch the object at those ranges because the link is too long while the object is too close to the robotic arm. Unknown state also occurs for points further than 74 cm as the length of the link is too short to reach to that point. The same pattern occurs for the z-axis coordinates, as shown in Fig. 8(c). The z-axis travel range is limited from 0 cm to 70 cm. Experiments also showed that the height (y-axis) that the robotic arm can achieve is from 20 cm to 80 cm, as shown in Fig. 8(b). The distance from 0-20 cm is where the motor and reducer are located, so the robot is limited by this height. A height of 30 to 65 cm is the most optimal distance where the end-effector can precisely reach. In addition, the average errors of the position of the end effector at the x, y, and z coordinates are 3.7%, 8.89% and 9.84%, respectively. Errors are acceptable in a range between 40 cm to 65 cm for x and y coordinates, and between 25 and 65 cm for the z coordinate.

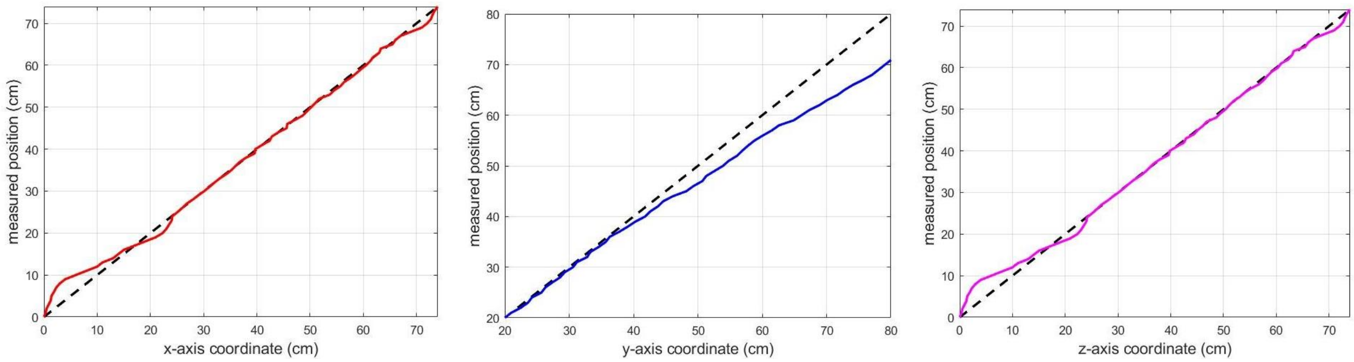

(a) (b) (c)

Fig. 8. Responses in x, y, z-axis

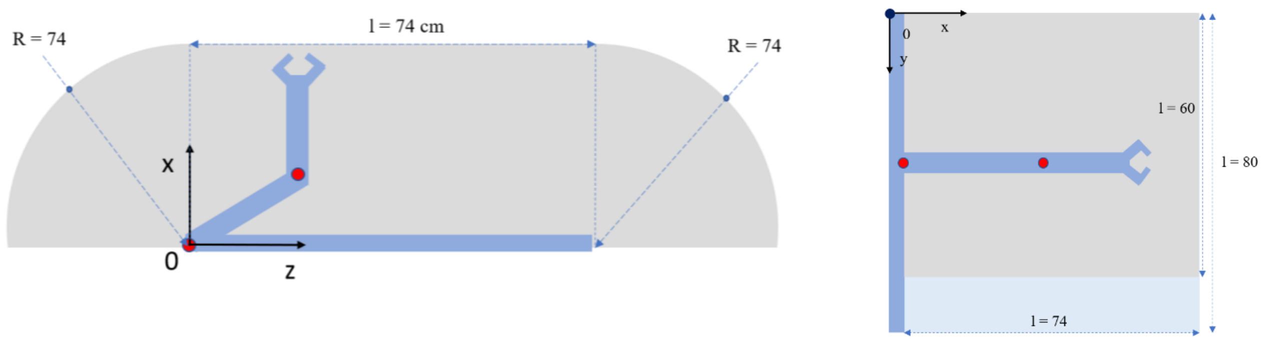

(a) (b)

Fig. 9. Front and top projection of the workspace

Based on the inverse kinematics calculation of the x, y and z coordinates, the workspace of the robotic arm can be clearly defined. Figures 9(a) and 9(b) illustrate the robotic arm workspace in front and top projections. The results show that the robotic arm cannot select or place an object outside the workspace. The closer the object's position is to the edge of the workspace, the more inaccurate the robotic arm gets.

B. Tomatoes picking

In this part, a series of robot operations are presented to pick up tomatoes from the coordinates sent by the image processor. Various coordinates are given to evaluate the accuracy and efficiency of the robotic arm. Initially the arm is in the default position. The position (33, 20, 30) in (x, y, z) is chosen as the origin. The end effector will go to the coordinates where the object is placed. After the end effector reaches the desired coordinates, the gripper picks up the object and returns it to the storage area. After picking up an object, the robot will continue to receive next coordinates. The robot arm will work automatically until no more objects are detected. We can see that the robot has completed the work at different coordinate axes in Fig. 8.

Fig. 10. Tomatoes picking test

V. CONCLUSIONS

This study has presented the system design and motion control of a 4-degree-of-freedom robotic arm for fruit picking in agriculture. The system is composed of an image processing unit, a 4-DOF robot controller and the end effector responsible for carrying out fruit picking. Through experimental evaluation, the system has achieved precise and agile movement that can be applied in practice at a reasonable price. Using the inverse kinematics equation has improved the robot's ability to pick and drop fruit. With the industrial revolution 4.0 taking place rapidly, accompanied by the growing agriculture in Vietnam, this system has an enormous application potential and a great basis for development. For future development, more research on optimizing the workspace for better performance in path tracking and improving the precision of object classification task should be conducted.

ACKNOWLEDGMENTS

This work has been supported by Vietnam National University, Hanoi (VNU), under project No. QG.20.80. The authors would like to thank VNU and all the other partners of the project.

REFERENCES

[1] Byambasuren, Bat-Erdene, et al. "Application of image processing and industrial robot arm for quality assurance process of production." 2020 IEEE Region 10 Symposium (TENSYMP). IEEE, 2020. Byambasuren, Bat-Erdene, et al. "Application of image processing and industrial robot arm for quality assurance process of production." 2020 IEEE Region 10 Symposium (TENSYMP). IEEE, 2020.

[2] Buhl, Jens F., et al. "A dual-arm collaborative robot system for the smart factories of the future." Procedia manufacturing 38 (2019): 333-340.

[3] My, Chu A., et al. "Novel robot arm design and implementation for hot forging press automation." International Journal of Production Research 57.14 (2019): 4579-4593.

[4] Weber, Moritz, Katrin Pitz, and Reiner Anderl. "Using a Six-Axis Articulated Robot Arm for Teaching Mechanical Engineering Students Software Development." ASME International Mechanical Engineering Congress and Exposition. Vol. 58400. American Society of Mechanical Engineers, 2017.

[5] Sandoval, J., et al. "Collaborative framework for robot-assisted minimally invasive surgery using a 7-DoF anthropomorphic robot." Robotics and Autonomous Systems 106 (2018): 95-106.

[6] Wang, Yiming, et al. "Autonomous 3-D reconstruction, mapping, and exploration of indoor environments with a robotic arm." IEEE Robotics and Automation Letters 4.4 (2019): 3340-3347.

[7] Oyekan, John, et al. "Applying a 6 DoF Robotic Arm and Digital Twin to Automate Fan-Blade Reconditioning for Aerospace Maintenance, Repair, and Overhaul." Sensors 20.16 (2020): 4637.

[8] Goel, Ruchi, and Pooja Gupta. "Robotics and industry 4.0." A Roadmap to Industry 4.0: Smart Production, Sharp Business and Sustainable Development. Springer, Cham, 2020. 157-169.

[9] Poór, Peter, Tomáš Broum, and Josef Basl. "Role of collaborative robots in industry 4.0 with target on education in industrial engineering." 2019 4th International Conference on Control, Robotics and Cybernetics (CRC). IEEE, 2019.

[10] TQ Vinh, PM Thang, PM Duong. "Mạng thông tin điều khiển trong hệ thống tự động hóa tòa nhà", VNU Journal of Science: Natural Sciences and Technology, 2010.

[11] N Van Thang, PM Thang, TD Tan. "The performance improvement of a low-cost INS/GPS integration system using the street return algorithm", Vietnam Journal of Mechanics, Special Issue, 2012.

[12] Iizuka, Michiko, and Yoko Ikeda. "Regulation and innovation under the 4th industrial revolution: The case of a healthcare robot, HAL by Cyberdyne." Technovation 108 (2021): 102335.

[13] Pierrot, Francois, et al. "Optimal design of a 4-DOF parallel manipulator: From academia to industry." IEEE Transactions on Robotics 25.2 (2009): 213-224.

[14] Roshanianfard, Ali, Du Mengmeng, and Samira Nematzadeh. "A 4-DOF SCARA robotic arm for various farm applications: Designing, kinematic modelling, and parameterization." Acta Technologica Agriculturae 24.2 (2021): 61-66.

[15] Roshanianfard, Ali, Du Mengmeng, and Samira Nematzadeh. "A 4-DOF SCARA robotic arm for various farm applications: Designing, kinematic modelling, and parameterization." Acta Technologica Agriculturae 24.2 (2021): 61-66.

[16] Rahul, K., Hifjur Raheman, and Vikas Paradkar. "Design of a 4 DOF parallel robot arm and the firmware implementation on embedded system to transplant pot seedlings." Artificial Intelligence in Agriculture 4 (2020): 172-183.

[17] Muladi, Muladi, Siti Sendari, and Ilham Ari Elbaith Zaini. "Colour-based PBEJCT Sorting in a Wide Range and Dense Target Points using Arm Robot." 2nd International Conference on Vocational Education and Training (ICOVET 2018). Atlantis Press, 2019.

The 6th International Conference on
Engineering Mechanics and Automation (ICEMA 2021)
Hanoi, November 14, 2021

Image processing algorithms for an agricultural harvesting robot in natural lighting conditions

Bui Thanh Lam
Faculty of Mechanical Engineering
Hanoi University of Industry (HaUI)
Hanoi, Vietnam
lambt@haui.edu.vn

Hoang Van Manh*
Faculty of Mechanics and Automation
VNU University of Engineering and Technology
Hanoi, Vietnam
manhhv87@vnu.edu.vn

Pham Manh Thang
Faculty of Mechanics and Automation
VNU University of Engineering and Technology
Hanoi, Vietnam
thangpm@vnu.edu.vn

Ngo Anh Tuan
Faculty of Mechanics and Automation
VNU University of Engineering and Technology
Hanoi, Vietnam
natuan@vnu.edu.vn

Dang Anh Viet
Faculty of Electronics and Telecommunications (FET)
VNU University of Engineering and Technology
Hanoi, Vietnam
vietda@vnu.edu.vn

Pham Manh Tuan
Faculty of Mechanics and Automation
VNU University of Engineering and Technology
Hanoi, Vietnam
phamtuan@vnu.edu.vn

Abstract: **The process of automation and modernization is having a strong impact on the agricultural sector recently. In this process, robots play an important role as they are the key driving smart and automotive agriculture. In order for a robotic system to work efficiently, vision processing module is crucial. This study presents an automatic classification and detection system of fruit objects to be harvested for a fruit picking robot. The method is based on the object analysis algorithm by color and image segmentation. The color features are extracted in the HSV color space and then used as input to the OpenCV library-based processing algorithm which will automatically calculate the values for the classification threshold. Different fruits were used to evaluate the automatic sorting method. The resulting objects extracted by this method are presented in binary images. Various experimental results show that the automatic system can extract mature fruit from complex agricultural background and the extraction accuracy is more than 95%. This method is very effective for computer vision systems to detect and select fruits. Along with this is the strong applicability in practice.**

Keywords: Machine vision, OpenCV library, Harvesting robot, Image processing.

I. INTRODUCTION

Since the 1990s, with the development of computer and information technology, artificial intelligence, machine vision and other new technologies in agricultural machinery are becoming more and more popular. Robots composed of agronomic technology, mechanical technology, electronic technology and artificial intelligence technology is one of the new research focuses in the field of agricultural machines [1-4]. Research on agricultural robots has been launched since the 1980s [4-9]. For example, Japan has developed a robot used to spray pesticides. In the early 1990s, Korea began to research the technology of coupling automation, but the results only partially realized mechanical operations with a lower degree of automation and speed. In European countries with developed agriculture such as Italy and France, grafting is a fairly common job. Because these countries do not have their own grafting robots, part of the grafting works is still manual, while others use grafting robots from Japan. At present, many harvesting robots have been developed, such as tomato picking robot, cucumber picking robot, etc.

Fruit is an essential product in human life and the automation in agriculture to harvest fruit is more and more demanded. Therefore, robot picking of ripe fruit is becoming the focus of recent studies. Ripe and unripe fruits have different color characteristics. Fruits are usually green before ripening, then they turn yellow, red or orange as the result of their pigments when ripe. The ripening period of the fruit is also divided into many different stages: the semi-ripe period (the top of the fruit is red-orange extending to the abdomen, the color is about 50%), the ripening period (the color of the fruit is characteristic full bloom, but the base is still green) and the final ripening period (full color and solid color). Fruit picking robot mainly handles at the stage when fruits needing to be harvested, which is the period of ripening. For the task of analyzing a large number of fruits, image-based classification is an accurate and optimal method. The images of fruits are recognized through the computer's vision sensors. They are usually displayed in many different color spaces such as HSV, RGB, OHTA, etc. Image processing algorithms will take these images as the input, then output and classify the fruits. Color-based object selection is also widely used in automated robotics industries. There are many rapid object extraction methods used for modern robots studied [9-1].

X. Wei et al. described the implementation of an antinational system for a humanoid robot based entirely on variant vision in space [4]. They use a histogram built in the HSV color space, but the conversion relationship of the HSV from the RGB color space is non-linear. An adaptive color-based robotic vision system using the proposed pixel classification method was used to overcome the non-linear problem [5,6]. For robotic systems, vision sensors are ideal due to their low cost, wide availability, high data content and information speed. Object extraction method is an important part of machine vision [7]. In addition, it is essential to process the information in the minimum time. Therefore, it is important that the image processing algorithms be fast and accurate, which is also the goal of every research. In this paper, we propose a fruit object extraction system based on HSV color space and OpenCV library. HSV is a color space that helps images to be displayed visually and processed easily. Instead of plotting small vectors on an image, in HSV the vectors are mapped to H, S, and V values. This makes it easy to select the desired range of values. This system is operated in practice with complex environment, so OpenCV-Python is a useful open-source image processing library to use. MATLAB is also a well-known programming language for image processing, but it can be said that computer vision applications developed using OpenCV-Python are easier, less complicated. The vision sensor used is an IMX camera, the computer used is a jetson nano module. The frames after being acquired must undergo some preprocessing operations such as converting the color space. The main advantage of using Python-OpenCV is that it can simplify all preprocessor operations. There are several predefined libraries available in OpenCV to perform these operations. These libraries will provide all the functionality. We use a series of algorithms to process the input image from the camera, convert the color space, get the object profile, and calculate it to give the actual coordinates to the robot's microcontroller. Finally, the actual images of fruits are tested to check the performance of the system.

II. THEORY AND SOFTWARE LIBRARY

A. Calibration solution for camera

The process of converting images from zero to image space often gives non-preferred results because they are not maximized and is often distorted.

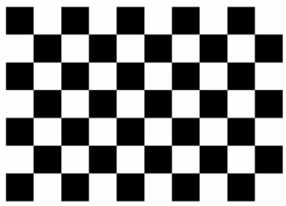

Fig. 1. Camera calibration checkerboard

When the camera is placed parallel and centered and has a standard position to ensure parameters of focus, the epipolar curves of distorted image will be corrected to become straight lines. The technique used to do this is called camera calibration. Camera calibration is done by taking checkerboard patterns at different angles to calculate the camera's internal parameters. Based on these parameters, it is possible to correct the distortion of the image by a suitable algorithm. The checker box shown in Fig. 1 is used to evaluate the curvature of the image obtained from the camera. Image distortion can be in the form of a convex or concave sphere as shown in Fig. 2.

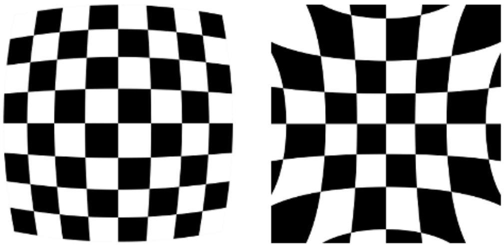

Fig. 2. Image distortion

Radial distortion occurs when light rays bend closer to the edges of the lens than to its optical center. The smaller the lens, the greater the distortion. The radial distortion coefficient models this type of strain. Distorted points are represented as (x_D, y_D).

$$\begin{aligned} x_D &= x(1 + k_1 r^2 + k_2 r^4 + k_3 r^6) \\ y_D &= y(1 + k_1 r^2 + k_2 r^4 + k_3 r^6) \end{aligned} \quad (1)$$

Where:

- x, y: Pixel coordinates are not distorted.
- k_1, k_2, k_3 : Radial distortion coefficient of the glazing system.
- $r^2 = x^2 + y^2$

B. Algorithm to convert jetson camera coordinates to real coordinates

The problem of determining real coordinates from image coordinates can be address using OpenCV.

Equation (2) show the relation of 2D coordinates on image with real 3D coordinates:

$$\begin{bmatrix} u \\ v \\ 1 \end{bmatrix} = \begin{bmatrix} f_x & 0 & c_x \\ 0 & f_y & c_y \\ 0 & 0 & 1 \end{bmatrix} \begin{bmatrix} r_{11} & r_{12} & r_{13} & t_1 \\ r_{21} & r_{22} & r_{23} & t_2 \\ r_{31} & r_{32} & r_{33} & t_3 \end{bmatrix} \begin{bmatrix} X \\ Y \\ Z \\ 1 \end{bmatrix} \quad (2)$$

Where:

- X, Y, Z: The actual coordinates of the object need to be determined.
- u, v : Coordinates of the projection point in pixels.
- A: Internal matrix of camera parameters.
- c_x, c_y : Coordinates of the reference point, always in the center of the image.
- f_x, f_y: Focal length

To simplify the calculation, the coordinates are converted to the following:

$$\begin{bmatrix} x \\ y \\ z \end{bmatrix} = R \begin{bmatrix} X \\ Y \\ Z \end{bmatrix} + t \quad (3)$$

Finally, the coefficient of real coordinates X, Y, Z in space is given as:

$$\left(s \begin{bmatrix} u \\ v \\ 1 \end{bmatrix} A^{-1} - t \right) R^{-1} = \begin{bmatrix} X \\ Y \\ Z \end{bmatrix} \quad (4)$$

In the case of using a 2D camera, it is not possible to calculate the depth of the object in which we can reduce and assign the approximate coefficient of one coordinate in advance. Fig. 3 shows the actual coordinates after calculation.

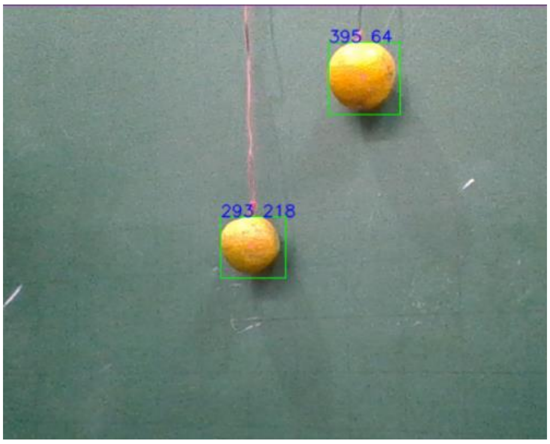

(a) Screen coordinates

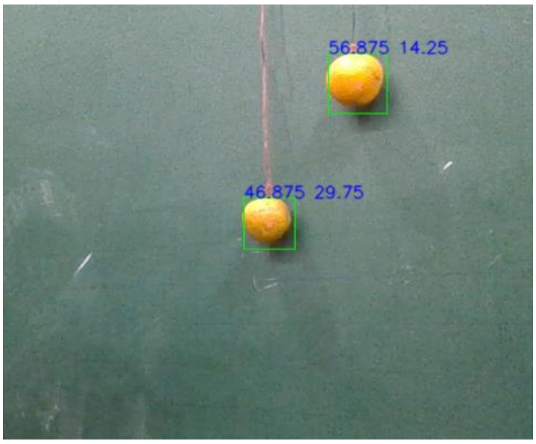

(b) Actual coordinates

Fig. 3. Coordinates in screen and actual coordinates after transformation

C. RGB to HSV color conversion algorithm

The RGB color space can be seen in Fig. 4(b). Colors that are often combined between red (R), green (G) and blue (B) are referred to the three primary colors [8]. This is also the most common color space. Each element can take a value from 0 to 255. Where (0,0,0) represents black and (255,255,255) represents white. From the three primary colors, different types of color spaces can be calculated using linear or non-linear transformations. Choosing the best color space is still one of the difficulties in color image segmentation. Here, we study the selection of HSV color space to process the classification of ripe fruits. The HSV color space is represented by three values of H (Hue), S (Saturation), and V (Value) as shown in Fig. 4(a).

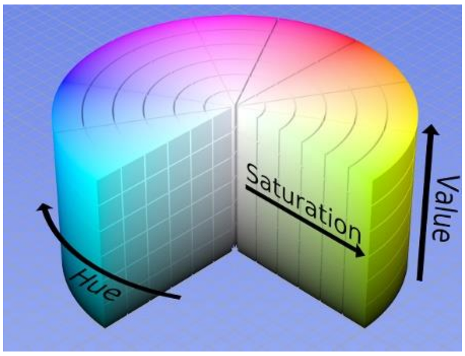

(a) HSV color space

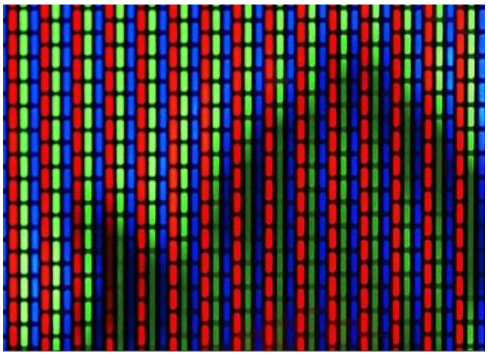

(b) RGB color space

Fig. 4. HSV and RGB color spaces

The R, G, B values are divided by 255 to change the range from 0 – 255 to 0 – 1 as shown in equation (5).

$$\begin{aligned} R' &= \frac{R}{255} \\ G' &= \frac{G}{255} \\ B' &= \frac{B}{255} \\ C\,max &= max(R', G', B') \\ C\,min &= min(R', G', B') \\ \Delta &= C\,max - Cmin \end{aligned} \tag{5}$$

With $\Delta = 0$, $C\,max = R'$, $C\,max = G'$, $C\,max = B'$, the formula for the relation between coefficients R, G, B when converted to color system H, S, V is:

$$\begin{aligned} H &= \begin{cases} 0° \\ 60° \times (\frac{G'-B'}{\Delta} + 6) \\ 60° \times (\frac{B'-R'}{\Delta} + 2) \\ 60° \times (\frac{R'-G'}{\Delta} + 4) \end{cases} \\ S &= \begin{cases} 0 & C\,max = 0 \\ \dfrac{\Delta}{Cmax} & C\,max \neq 0 \\ \quad V = Cmax \end{cases} \end{aligned} \tag{6}$$

From the conversion formula, we get the image of the object captured by the camera in Fig. 5(a) and the conversion result shown in Fig. 5(b).

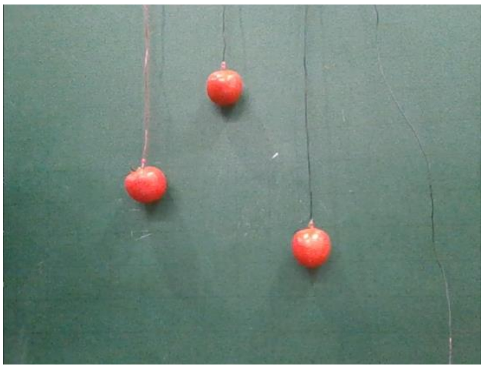

(a) RGB color space

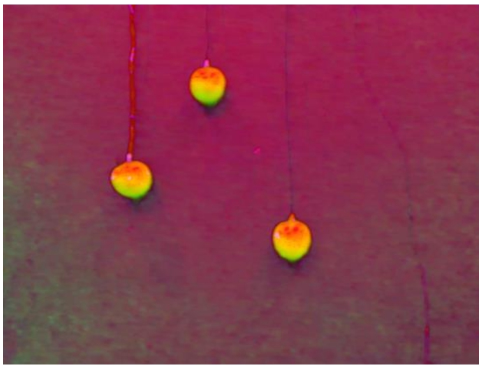

(b) HSV color space

Fig. 5. Image of objects in RGB and HSV color space

D. *Image processing based on OpenCV library*

Profile-based object extraction can track objects of any color. Besides, it is possible to track both static and dynamic objects. In the case of still images, we must load the image into the program and then use the predefined OpenCV functions to track the object. In the case of video, we can track both live video and recorded video. Live video can be also controlled using Python OpenCV code. The function that performs the direct image acquisition function is:

cam = cv2.VideoCapture (0)

This function is a predefined function in the OpenCV library to get the frames directly from the camera. This simply creates an object for the camera and using this object we can control video recording and other web cam related functions. VideoCapture() can have parameters like 0,1,2, etc., which represent the camera connected to the computer system. 0 is the default camera system, 1 can be the first external camera connected to the system, and so on. When the system starts to receive the video, it decomposes the video into picture frames. All image processing will take place on these frames. Each frame will be processed separately. Image representation is the first step of object tracking. When the object is present in the frame, it is represented. The image needs to be distinguished from the background. The color of the object is the main criterion for identifying the object. Using certain thresholding functions, each color object can be represented separately in the background. When the image is represented in the HSV color space, each value will have an upper amplitude band and a lower amplitude band. The upper and lower band ranges of some primary colors are shown in Table 1. After setting the ranges of values, the filtered object can be seen in Fig. 6(a).

TABLE I: VALUE RANGES OF PRIMARY COLORS

Color	Lower range	Upper range
Red	[160,170,50]	[179,250,220]
Green	[53,74,160]	[90,147,255]
Yellow	[110,50,150]	[130,260,255]

Whenever objects are detected in the frame, a square outline is drawn for the object. That contour will represent the object's boundaries. The next step is to find the center of the object. Here, the object focus is considered based on the area inside the contour.

If the image moment inside the contour is set to M, then the coordinates of the center can be calculated as follows:

cx = int(M['m10']/M['m00'])

cy = int(M['m01']/M['m00'])

Contour properties of an object can be obtained by using the cv2.boundingRect(contour) function in the OpenCV library. The tracked subject is shown in fig. 6(b).

(a) The object after filtering

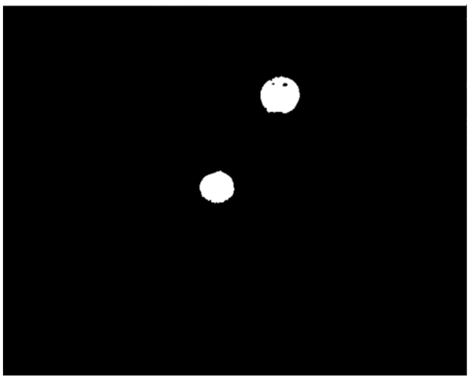

(b) The object to be determined

Fig. 6. Object image after filtering and identified object

III. SYSTEM DESIGN

We use NVIDIA Jetson Nano Developer Kit which shown in fig. 7. This is a small but powerful computer that allows users to run multiple neural networks in parallel for applications such as image classification, object detection, segmentation, and speech processing. All in the same platform which is easy to use and only consume power less than 5 watts. The Jetson Nano also delivers 472 GFLOPS to run modern AI algorithms quickly, with a 64-bit ARM quad-core CPU, an onboard 128-core NVIDIA GPU, as well as 4GB of LPDDR4 memory. It is possible to run multiple neural networks in parallel and process several high-resolution sensors simultaneously. Aside from that, the 12.3MP IMX477 Camera is suitable for industrial use and applications such as Security Cameras and other specialized optical devices that require a higher level of image fidelity. This camera offers up to 12.3MP resolution, which is nearly 50% larger area per pixel compared to Raspberry Pi Camera 8MP, thus providing better visual effects.

Fig. 7. Jetson nano and camera IMX

The system algorithm diagram is shown in Fig. 8. First, the IMX camera acquires images from the environment. The image is processed by the Jetson module, displayed in RGB as input to the image processing unit based on the OpenCV library. Then the conversion function performs the conversion from the coordinates on the image to the actual coordinates. Finally, the signal is passed to the robot for processing. Serial communication is based on UART communication.

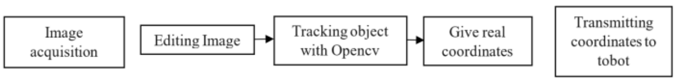

Fig. 8. System model

IV. EXPERIMENTAL RESULTS

Experiments were repeated many times to evaluate the efficiency of the system. There are in total twenty times that the experiment is given and compared with different cases. As mentioned, images in the HSV color system are represented by three color parameters. The user can edit the parameters in the color window. In addition, the min and max parameters are also changed to expand the color detection range. Fig. 9 is the available interface including 6 scales: LowH, HighH, LowS, HighS, LowV and HighV. These scales correspond to minimum and maximum values of hue, saturation, and exposure.

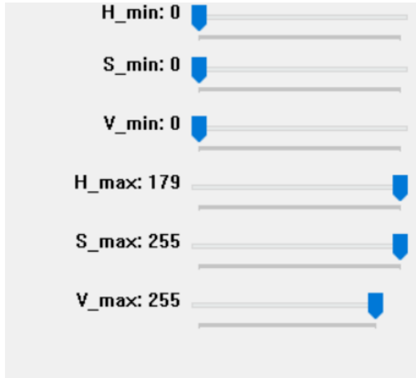

Fig. 9. Color adjustment trackbar

Some of the object classification results are shown in Fig. 10. Ripe tomatoes in fig. 10(a), strawberries in fig. 10(b) and apples in fig. 10(c) were selected as the subjects. They are processed and graded on each frame of the video. The coordinates of the object are determined and displayed on the screen with high accuracy (over 90%). The percentages of pick-ups are shown in Table 2.

TABLE II. PERFORMANCE ANALYSIS OF THE SYSTEM

Image	Total	Recognized	Extract rate (%)
Tomato	30	27	90
Lemon	30	28	93
Orange	30	30	100

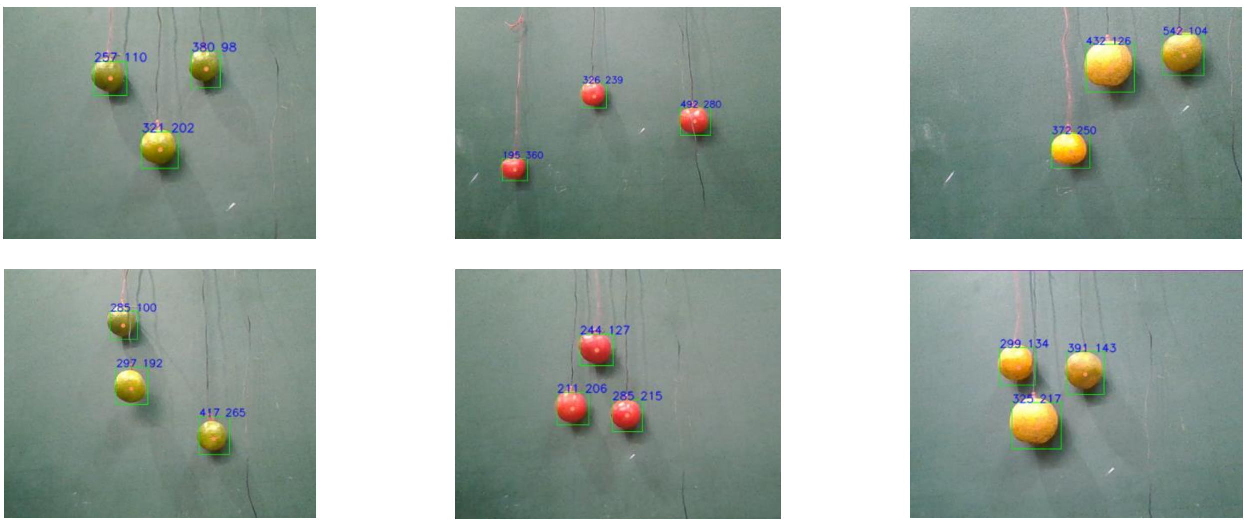

(a) Lemon (b) Tomato (c) Orange

Fig. 10. Extraction results of fruits

V. CONCLUSION

In this study, a real-time objective location image processing system applied in agriculture is presented. The number of experimental results indicates that the system can successfully recognize ripe fruits from complex environments. The extraction rate of more than 90% helps the fruit picking robot to reach the object accurately, results in completing the task of picking fruit efficiently. Therefore, this system shows a strong applicability in practice.

In the future, fruit yield will not be limited to fresh use. As the consumption of fruit products is increasing, there will appear special growing establishments that provide raw materials for the production of fruits, juices, canned fruit products, etc. In this future agricultural scheme, the development of fruit picking robot can effectively reduce the fruit-growing labors and will be helpful for promoting a larger fruit production area, and thus obtain more economic benefits.

ACKNOWLEDGMENTS

This work has been supported by Vietnam National University, Hanoi (VNU), under project No. QG.20.80. The authors would like to thank VNU and all the other partners of the project.

REFERENCES

[1] Pivoto, Dieisson, et al. "Scientific development of smart farming technologies and their application in Brazil." Information processing in agriculture 5.1 (2018)

[2] Virk, Ahmad Latif, et al. "Smart farming: an overview." Smart Village Technology (2020): 191-201.

[3] R Shamshiri, Redmond, et al. "Research and development in agricultural robotics: A perspective of digital farming." (2018).

[4] Metta, Giorgio. An attentional system for a humanoid robot exploiting space variant vision. Massachusetts inst of tech cambridge artificial intelligence lab, 2001.

[5] Browning, Brett, and Manuela Veloso. "Real-time, adaptive color-based robot vision." 2005 IEEE/RSJ International Conference on Intelligent Robots and Systems. IEEE, 2005.

[6] Bruce, James, Tucker Balch, and Manuela Veloso. "Fast and inexpensive color image segmentation for interactive robots." Proceedings. 2000 IEEE/RSJ International Conference on Intelligent Robots and Systems (IROS 2000)(Cat. No. 00CH37113). Vol. 3. IEEE, 2000.

[7] TQ Vinh, PM Thang, PM Duong. "Mạng thông tin điều khiển trong hệ thống tự động hóa tòa nhà", VNU Journal of Science: Natural Sciences and Technology, 2010.

[8] Lottes, Philipp, et al. "Effective vision‐based classification for separating sugar beets and weeds for precision farming." Journal of Field Robotics 34.6 (2017)

[9] Elina, Olga. "Development of Innovative Technologies in Russian Agro-Industry." 2019 International Conference on Engineering Technologies and Computer Science (EnT). IEEE, 2019.

[10] N Van Thang, PM Thang, TD Tan. "The performance improvement of a low-cost INS/GPS integration system using the street return algorithm", Vietnam Journal of Mechanics, Special Issue, 2012.

[11] Sheets, Kaitlin D. "The japanese impact on global drone policy and law: Why a laggard united states and other nations should look to japan in the context of drone usage." Ind. J. Global Legal Stud. 25 (2018)

[12] Wan, Shaohua, and Sotirios Goudos. "Faster R-CNN for multi-class fruit detection using a robotic vision system." Computer Networks 168 (2020)

[13] Fu, Longsheng, et al. "Application of consumer RGB-D cameras for fruit detection and localization in field: A critical review." Computers and Electronics in Agriculture 177 (2020).

[14] Fu, Longsheng, et al. "Faster R–CNN–based apple detection in dense-foliage fruiting-wall trees using RGB and depth features for robotic harvesting." Biosystems Engineering 197 (2020)

[15] Santos, Luís, et al. "Deep learning applications in agriculture: A short review." Iberian Robotics conference. Springer, Cham, 2019.

[16] Hespeler, Steven C., Hamidreza Nemati, and Ehsan Dehghan-Niri. "Non-destructive thermal imaging for object detection via advanced deep learning for robotic inspection and harvesting of chili peppers." Artificial Intelligence in Agriculture 5 (2021)

[17] T. S. Tran, V. M. Hoang, MT. Pham. A survey for wireless sensor network applications. The 4th International Conference on Engineering Mechanics and Automation (ICEMA-4), 2016.

[18] Zhao, Yuanshen, et al. "Detecting tomatoes in greenhouse scenes by combining AdaBoost classifier and colour analysis." Biosystems Engineering 148 (2016)

SESSION 2
FLUID MECHANICS

The 6th International Conference on Engineering Mechanics and Automation (ICEMA 2021)
Hanoi, November 14, 2021

A sensitivity method studying regional response to external sources of pollution and its application to 1D water pollution problem

Thu Ha Tran
Institute of Mechanics
(of Vietnam Academy of Science and Technology)
University of Engineering and Technology
(of Vietnam National University, Hanoi)
Ha Noi, Viet Nam
ttha@imech.vast.vn

Hong Son Hoang
Torus actions
Toulouse, France
sonhoang@torus-actions.fr

Hong Phong Nguyen
Institute of Mechanics
(of Vietnam Academy of Science and Technology)
University of Engineering and Technology
(of Vietnam National University, Hanoi)
Ha Noi, Viet Nam
hphongbk@gmail.com

***Abstract*: Prediction of current water pollution is a very important task for life safety of human and life species. To this end, it is imperative to be able to define uncertainty in the model prediction. That is the task of sensitivity analysis whose role is to identify what uncertainty in the model outputs is attributable to the model inputs (parameters in this case). Traditionally this is achieved by running the model for many different random samples of the parameter space to determine their impact on the model outputs. It provides information on how much of the output variance is controlled by each parameter of the inputs. In this paper, we follow the adjoint approach for computing sensitivity of the response function to changes in the input source. This approach allows us to compute the gradient of the response function with respect to the measurement values. One finds that the sensitivity is strongest in the pollution source area. That is one of few methods that is capable of finding the pollution source location for the situation when there is insufficient information on the initial system state and measurements. The method is applied to study the 1D Bugger equation of water pollution.**

Keywords: Output sensitivity, response function, source pollution, 1D Bugger equation of pollution.

I. Introduction

Study on pollution is a very important issue. For example, water pollution matters because it harms the environment on which people depend. Traditionally, people have inhabited places with ready access to fresh water. A large part of the world's population is directly dependent on access to natural freshwater sources. That is why water pollution should matter to a large number of the population. The ability to know in advance and with high accuracy the effect of pollutant emission changes from one (source) region onto another (response) region of interest would help decision makers to improve public health and the environment. Also, knowing exact locations of an emission source that could have an impact on the region considered during a given time period allows to avoid severe damage to people and property, negatively affecting socio-political economy ...To solve the pollutant water problem by simulating the initial condition, the measurement values and the observer areas play very important roles. However, in practice, it is difficult to assign good values to them. To overcome this difficulty, in this paper we develop a tool for computing the sensitivity in the form of the gradient of the response function (RF) with respect to measurement values. The method is based on estimating the gradient of the RF with respect to observations. The pollutant source area is identified by the high level of the gradient. The objective of this paper is to provide an efficient tool based on adjoint equation (AE) approach for computation of the sensitivity of the output (system response) with respect to input parameters (see Dimet et al., 2014; Shutyaev, 1995). It allows us to obtain the information on how the output is affected by each input parameter. In the next section, the statement of the problem is given. The AE approach is presented in detail in section 3 for the computation of the sensitivity of the response function to changes in source inputs. It is seen here that by running the AE backwards in time one can produce sensitivity of the response function to any source located in the domain of consideration.

II. Variational method based AE approach

2.1 Mathematical formulation of the problem

Suppose the flow under consideration contains a passive tracer issued from several sources for the time period $[0,T]$. Let the system of equations governing the flow and the associated system of tracer observations be given. What we are interested in is to know what contribution of a source S in producing this passive tracer. Let us assume that the one dimensional velocity field $U = U(x, t)$ evolves according to the Burgers equation given by :

$$\begin{cases} \frac{dU}{dt} + U\frac{\partial U}{\partial x} - \nu\frac{\partial^2 U}{\partial x^2} = f, x \in \Omega = [L_1, L_2], \mathrm{t} \in [0,\mathrm{T}]; \\ U(0) = U_0, \quad \mathrm{t} = 0, \text{initial condition}; \\ U = U_1, \quad \mathrm{x} = L_1, \text{boundary condition on } L_1; \\ \alpha U + \beta\frac{\partial U}{\partial x} = U_2, \mathrm{x} = L_2, \text{boundary condition on } L_2; \end{cases} \quad (2.1)$$

Where the flow coefficient ν(m^2/s) is supposed to be constant, *U=U(x,t)* is the unknown function belonging for any t to a Hilbert space $R_U = L_2(\Omega), \Omega = [L_1, L_2], U \in R_U$, f is a nonlinear operator mapping $\mathfrak{I}_U$ into $\mathfrak{I}_U$ with $\mathfrak{I}_U = L_2(0,T;R_U)$. The concentration of pollutant, considered as a passive tracer, in its turn, is described by

$$\begin{cases} \frac{dC}{dt} + U\frac{\partial C}{\partial x} - \eta\frac{\partial^2 C}{\partial x^2} = S, x \in \Omega = [L_1, L_2], \mathrm{t} \in [0,\mathrm{T}]; \\ C(0) = C_0, \quad \mathrm{t} = 0, \text{initial condition}; \\ C = C_1, \quad \mathrm{x} = L_1, \text{boundary condition on } L_1; \\ \gamma C + \lambda\frac{\partial C}{\partial x} = C_2, \mathrm{x} = L_2, \text{boundary condition on } L_2; \end{cases} \quad (2.2)$$

Here the concentration diffusion coefficient η(m^2/s) is supposed to be constant; *C=C(x,t)* is the pollutant concentration which is an element of the Hilbert $R_C = L_2(\Omega)$, $C_0 \in R_C$; S is the pollutant source. The problem we are interested in is to retrieve the fields U, C from the observations $U_{obs} \in R_U$ related to the system state U and from $C_{obs} \in R_C$ - observations for the concentration C of the pollutant..

2.1.1 *Estimation of the initial condition.*

To estimate the trajectory of system state over the period [0,T] based on observations, let us follow the variation method (VM). According to variation method [see (Dimet, 2014), (F.X.L.Dimet, 2002), (Tran, 2019)], the optimal trajectory of variation couple U(t) and C(t) $t \in [0,T]$ is proposed to find, among all possible trajectories, the one which minimizes, for example, the cost function J,

$$J(U_0, C_0) = \frac{1}{2}\int_0^T < V_{2U}(H_U U - U_{obs}), (H_U U - U_{obs}) >_{R_U} dt$$
$$+\frac{1}{2}\int_0^T < V_{2C}(H_C C - C_{obs}), (H_C C - C_{obs}) >_{R_C} dt$$
$$+\frac{1}{2}\,\|V_{1U}\,(U_0 - \bar{U})\|^2_{R_U} + \frac{1}{2}\,\|V_{1C}\,(C_0 - \bar{C})\|^2_{R_C}. \quad (2.3)$$

where $\|f\|^2_{\Omega} = \int_{L_1}^{L_2} f(x).f(x)dx$; $(U_0,C_0) \in R_U \times R_C$, $(\bar{U}, \bar{C}) \in R_U \times R_C$ are given (background state), $(U_{obs}, C_{obs}) \in R_{Uobs} \times R_{Cobs}$ are observational data), R_{Uobs}, R_{Cobs} are Hilbert spaces (observation spaces), $H_U: R_U \to R_{Uobs}$, $H_C: R_C \to R_{Cobs}$ are linear bounded operators, $V_{1U}: R_U \to R_U$, $V_{1C}: R_C \to R_C$; $V_{2U}: R_{Uobs} \to R_{Uobs}$, $V_{2C}: R_{Cobs} \to R_{Cobs}$ are chosen symmetric positive definite operators. H_U and H_C are the observation operators.

Consider the following data assimilation problem with the aim to identify the initial condition: for given S find $U_0 \in R_U = L_2(\Omega)$, $C_0 \in R_C = L_2(\Omega)$, $U \in R_U$ and $C \in R_C$ such that they satisfy (2.1)-(2.2), and on the set of solutions to (2.1)-(2.2), the functional $J(U_0,C_0)$ takes the minimum value.

The minimization problem (2.3), in principle, can be solved using the theory of optimal control but it is very difficult since we have to seek an optimal trajectory in the functional space. Simplicity can be made by reducing the space of control variables from the functional space to the space of the initial state. Namely, we will suppose that the trajectories U(t), C(t), t ∈ [0, T] are determined by the initial conditions U_0, C_0. This assumption reduces the initial minimization to the problem of finding the estimate U_0^* and C_0^* which minimizes the objective function J. To do that, we need to compute the gradient of J with respect to U_0 and C_0:

$$J(U_0^*, C_0^*) = \underset{U_0, C_0}{arg}\, J(U_0, C_0) \quad (2.4)$$

Then the corresponding optimal problem is written in the form:

$$\begin{cases} \frac{dU}{dt} + U\frac{\partial U}{\partial x} - \nu\frac{\partial^2 U}{\partial x^2} = f, x \in \Omega = [L_1, L_2], \mathrm{t} \in [0,\mathrm{T}]; \\ U(t=0) = U_0, \quad \text{initial condition}; \\ U = U_1, \quad \mathrm{x} = L_1, \text{boundary condition on } L_1; \\ \alpha U + \beta\frac{\partial U}{\partial x} = U_2, \mathrm{x} = L_2, \text{boundary condition on } L_2; \\ \frac{dC}{dt} + U\frac{\partial C}{\partial x} - \eta\frac{\partial^2 C}{\partial x^2} = S, x \in \Omega = [L_1, L_2], \mathrm{t} \in [0,\mathrm{T}]; \\ C(t=0) = C_0, \quad \text{initial condition}; \\ C = C_1, \quad \mathrm{x} = L_1, \text{boundary condition on } L_1; \\ \gamma C + \lambda\frac{\partial C}{\partial x} = C_2, \mathrm{x} = L_2, \text{boundary condition on } L_2 \\ \mathrm{J}(U_0, C_0) = \min_{U_0^* C_0^*} J(U_0^*, C_0^*). \end{cases} \quad (2.5)$$

By the similar method as done in (Dimet *et al.*, 2014), let P, Q (adjoint variables) be the solutions of the following AEs

$$\begin{cases} \frac{dP}{dt} + U\frac{\partial P}{\partial x} + \nu\frac{\partial^2 P}{\partial x^2} - Q\frac{\partial C}{\partial x} = H_U^* V_{2U}(H_U U - U_{obs}), \\ x \in \Omega = [L_1, L_2], \mathrm{t} \in [0,\mathrm{T}]; \\ P(t=T) = 0 \\ P = 0, \ \mathrm{x} = L_1 \\ \left(U + \frac{\nu\alpha}{\beta}\right)P + \nu\frac{\partial P}{\partial x} = 0, \mathrm{x} = L_2 \ if\ \beta \neq 0 \\ P = 0, \mathrm{x} = L_2 \ if\ \beta = 0 \end{cases} \quad (2.6)$$

$$\begin{cases} \frac{dQ}{dt} + \frac{\partial UQ}{\partial x} + \eta\frac{\partial^2 Q}{\partial x^2} = H_C^* V_{2C}(H_C C - C_{obs}), \\ x \in \Omega = [L_1, L_2], \mathrm{t} \in [0,\mathrm{T}]; \\ Q(t=T) = 0 \\ Q = 0, \ \mathrm{x} = L_1 \\ \left(U + \frac{\eta\gamma}{\lambda}\right)Q + \eta\frac{\partial Q}{\partial x} = 0, \mathrm{x} = L_2 \ if\ \lambda \neq 0 \\ Q = 0, \mathrm{x} = L_2 \ if\ \lambda = 0 \end{cases} \quad (2.7)$$

One can show that the gradient of the cost function satisfies the relationship: $\nabla J = \left(J'_{U_0}, J'_{C_0}\right)$

with $J'_{U_0} = V_{1U}^2(U_0 - \bar{U}) - P(0)$ (2.8)

$J'_{C_0} = V_{2U}^2(C_0 - \bar{C}) - Q(0)$ (2.9)

The optimal problem is solved by finding U_0, V_0 from the equations

$$V_{1U}^2(U_0 - \bar{U}) - P(0) = 0 \text{ and } V_{2U}^2(C_0 - \bar{C}) - Q(0) = 0 \quad (2.10)$$

2.1.2 *Sensitivity of the response function to C_{obs}.*

Let the response function be defined by:

$G_{\Omega} = C$ (2.11)

Introduce a direction c_{obs} in the space of C_{obs} and compute the Gateaux derivative of function G_Ω in the direction c_{obs} by the following formula:

$$\hat{G}_\Omega = \hat{C} \tag{2.12}$$

By definition, the sensitivity of the response function G_Ω with respect to the observation C_{obs} is the gradient of the response function G_Ω in the direction c_{obs}. Following the guidelines of the derivation of the gradient presented in section 2.1, let $\hat{U}, \hat{C}, \hat{P}, \hat{Q}$ be the Gateaux derivatives of U, C, P, Q in the direction c_{obs}. Using the equation optimality system (2.5)-(2.7) ([see (B.Daryoush, 2008)] we obtain the equations for $\hat{U}$, $\hat{C}$, $\hat{P}$, $\hat{Q}$.

$$\begin{cases} \frac{d\hat{U}}{dt} + \hat{U}\frac{\partial U}{\partial x} + U\frac{\partial \hat{U}}{\partial x} - \nu\frac{\partial^2 \hat{U}}{\partial x^2} = 0, \\ x \in \Omega = [L_1, L_2], \mathrm{t} \in [0, \mathrm{T}]; \\ \hat{U}(t=0) = \hat{U}_0, \quad \text{initial condition}; \\ \hat{U} = 0, \quad \mathrm{x} = L_1, \text{boundary condition on } L_1; \\ \alpha\hat{U} + \beta\frac{\partial \hat{U}}{\partial x} = 0, \mathrm{x} = L_2, \\ \text{boundary condition on } L_2 \end{cases} \tag{2.13}$$

$$\begin{cases} \frac{d\hat{C}}{dt} + \hat{U}\frac{\partial C}{\partial x} + U\frac{\partial \hat{C}}{\partial x} - \eta\frac{\partial^2 \hat{C}}{\partial x^2} = 0, \\ x \in \Omega = [L_1, L_2], \mathrm{t} \in [0, \mathrm{T}]; \\ \hat{C}(t=0) = \hat{C}_0, \quad \text{initial condition}; \\ \hat{C} = 0, \mathrm{x} = L_1, \text{boundary condition on } L_1; \\ \gamma\hat{C} + \lambda\frac{\partial \hat{C}}{\partial x} = 0, \quad \mathrm{x} = L_2, \\ \text{boundary condition on } L_2 \end{cases} \tag{2.14}$$

$$\begin{cases} \frac{d\hat{P}}{dt} + \hat{U}\frac{\partial P}{\partial x} + U\frac{\partial \hat{P}}{\partial x} + \nu\frac{\partial^2 \hat{P}}{\partial x^2} - \hat{Q}\frac{\partial C}{\partial x} - Q\frac{\partial \hat{C}}{\partial x} = \\ H_U^* V_{2U}\left(H_U\hat{U} - u_{obs}\right), x \in \Omega = [L_1, L_2], \mathrm{t} \in [0, \mathrm{T}]; \\ \hat{P}(T) = 0 \text{ condition when t = T} \\ \hat{P} = 0, \ \mathrm{x} = L_1 \\ \left(U + \frac{\nu\alpha}{\beta}\right)\hat{P} + \hat{U}P + \nu\frac{\partial \hat{P}}{\partial x} = 0, \mathrm{x} = L_2 \ if\ \beta \neq 0 \\ \hat{P} = 0, \mathrm{x} = L_2 \ if\ \beta = 0 \end{cases} \tag{2.15}$$

$$\begin{cases} \frac{d\hat{Q}}{dt} + \frac{\partial \hat{U}Q}{\partial x} + \frac{\partial U\hat{Q}}{\partial x} + \eta\frac{\partial^2 \hat{Q}}{\partial x^2} = H_C^* V_{2C}\left(H_C\hat{C} - c_{obs}\right), \\ x \in \Omega = [L_1, L_2], \mathrm{t} \in [0, \mathrm{T}]; \\ \hat{Q}(T) = 0 \text{ condition when t = T} \\ \hat{Q} = 0, \ \mathrm{x} = L_1 \\ \left(U + \frac{\eta\gamma}{\lambda}\right)\hat{Q} + \hat{U}Q + \eta\frac{\partial \hat{Q}}{\partial x} = 0, \mathrm{x} = L_2 \ if\ \lambda \neq 0 \\ \hat{Q} = 0, \mathrm{x} = L_2 \ if\ \lambda = 0 \end{cases} \tag{2.16}$$

Multiplying equation (2.13) by P^1 ,equation (2.14) by Φ (2.15) by $-\Psi$, equation (2.16) by $-\Lambda$, and then integrating it in t from 0 to T and over $\Omega = [L_1, L2]$ and adding them we have:

$$\int_0^T \langle \hat{P}, \frac{\partial \Psi}{dt} + \frac{\partial U\Psi}{\partial x} - \nu\frac{\partial^2 \Psi}{\partial x^2} \rangle_{L_2(\Omega)}\, dt + \int_0^T \langle \hat{Q}, \frac{\partial \Lambda}{dt} + U\frac{\partial \Lambda}{\partial x} - \eta\frac{\partial^2 \Lambda}{\partial x^2} + \frac{\partial C}{\partial x}\Psi \rangle_{L_2(\Omega)}\, dt + \int_0^T \langle \hat{C}, -\frac{\partial \Phi}{dt} - U\frac{\partial U\Phi}{\partial x} - \eta\frac{\partial^2 \Phi}{\partial x^2} - \frac{\partial Q\Psi}{\partial x} + H_C^* V_{2C} H_C \Lambda \rangle_{L_2(\Omega)}\, dt + \int_0^T \langle \hat{U}, -\frac{\partial P^1}{dt} - U\frac{\partial P^1}{\partial x} - \nu\frac{\partial^2 P^1}{\partial x^2} - \frac{\partial P}{\partial x}\Psi + H_U^* V_{2U} H_U \Psi + Q\frac{\partial \Lambda}{\partial x} + \Phi\frac{\partial C}{\partial x} \rangle_{L_2(\Omega)}\, dt + \int_0^T \nu\frac{\partial \hat{U}}{\partial x}P^1\Big|_{x=L_1} dt + \int_0^T \nu\frac{\partial \hat{P}}{\partial x}\Psi\Big|_{x=L_1} dt + \eta\int_0^T \frac{\partial \hat{Q}}{\partial x}\Lambda\Big|_{x=L_1} dt + \eta\int_0^T \frac{\partial \hat{C}}{\partial x}\Phi\Big|_{x=L_1} dt + \int_0^T \langle c_{obs}, V_{2C} H_C \Lambda \rangle_{L_2(\Omega)} dt + \langle \hat{P}(0), \Psi(0) \rangle_{L_2(\Omega)} + \langle \hat{Q}(0), \Lambda(0) \rangle_{L_2(\Omega)} + \langle \hat{C}(T), \Phi(T) \rangle_{L_2(\Omega)} - \langle \hat{C}(0), \Phi(0) \rangle_{L_2(\Omega)} + \langle \hat{U}(T), P^1(T) \rangle_{L_2(\Omega)} - \langle \hat{U}(0), P^1(0) \rangle_{L_2(\Omega)} + AA_2 + BB_2 \tag{2.17}$$

where:

$$AA_2 = \begin{cases} \left(\begin{array}{c} \int_0^T \hat{P} \cdot \left(\frac{\nu\alpha}{\beta}\Psi + \nu\frac{\partial \Psi}{\partial x}\right)\Big|_{x=L_2} dt + \\ \int_0^T \hat{U} \cdot \left(\frac{\nu\alpha}{\beta}P^1 + \nu\frac{\partial P^1}{\partial x} + UP^1 + P\Psi\right)\Big|_{x=L_2} dt \end{array} \right) & if\ \beta \neq 0 \\ \left(-\int_0^T \nu\frac{\partial \hat{P}}{\partial x} \cdot \Psi]_{x=L_2} dt - \int_0^T \nu\frac{\partial \hat{U}}{\partial x} \cdot P^1]_{x=L_2} dt \right) & if\ \beta = 0 \end{cases}$$

$$BB_2 = \begin{cases} \left(\begin{array}{c} \int_0^T \hat{Q} \cdot \left(\frac{\eta\gamma}{\lambda}\Lambda + \eta\frac{\partial \Lambda}{\partial x}\right)\Big|_{x=L_2} dt + \\ \int_0^T \hat{C} \cdot \left(\frac{\eta\gamma}{\lambda}\Phi + \eta\frac{\partial \Phi}{\partial x} + U\Phi + Q\Psi\right)\Big|_{x=L_2} dt \end{array} \right) & if\ \lambda \neq 0 \\ \left(-\int_0^T \eta\frac{\partial \hat{Q}}{\partial x} \cdot \Lambda|_{x=L_2} dt - \eta\frac{\partial \hat{C}}{\partial x} \cdot \Phi]_{x=L_2} dt \right) & if\ \lambda = 0 \end{cases}$$

If P^1 , Φ , Ψ and Λ are the solutions of the equations:

$$\begin{cases} -\frac{\partial P^1}{dt} - U\frac{\partial P^1}{\partial x} - \nu\frac{\partial^2 P^1}{\partial x^2} - \frac{\partial P}{\partial x}\Psi + \\ H_U^* V_{2U} H_U \Psi + Q\frac{\partial \Lambda}{\partial x} + \Phi\frac{\partial C}{\partial x} = 0 \\ P^1 = 0, \ \mathrm{x} = L_1 \\ \left(\frac{\nu\alpha}{\beta}P^1 + \nu\frac{\partial P^1}{\partial x} + UP^1 + P\Psi\right)\Big|_{x=L_2} = 0 \ if\ \beta \neq 0 \\ P^1 = 0, \ \mathrm{x} = L_2 \ if\ \beta = 0 \\ P^1(t=T) = 0 \end{cases} \tag{2.18}$$

$$\begin{cases} \frac{\partial \Phi}{dt} + \frac{\partial U\Phi}{\partial x} + \eta\frac{\partial^2 \Phi}{\partial x^2} + \frac{\partial Q\Psi}{\partial x} - H_C^* V_{2C} H_C \Lambda = 0 \\ \Phi = 0, \ \mathrm{x} = L_1 \\ \left(\frac{\eta\gamma}{\lambda}\Phi + \eta\frac{\partial \Phi}{\partial x} + U\Phi + Q\Psi\right)\Big|_{x=L_2} = 0 \ if\ \lambda \neq 0 \\ \Phi = 0, \ \mathrm{x} = L_2 \ if\ \lambda = 0 \\ \Phi(t=T) = 0 \end{cases} \tag{2.19}$$

$$\begin{cases} -\frac{\partial \Psi}{dt} - \frac{\partial U\Psi}{\partial x} + \nu\frac{\partial^2 \Psi}{\partial x^2} = 0 \\ \Psi = 0, \ \mathrm{x} = L_1 \\ \left(\frac{\nu\alpha}{\beta}\Psi + \nu\frac{\partial \Psi}{\partial x}\right)\Big|_{x=L_2} = 0 \ if\ \beta \neq 0 \\ \Psi = 0, \ \mathrm{x} = L_2 \ if\ \beta = 0 \\ \Psi(t=0) = v_1 \end{cases} \tag{2.20}$$

$$\begin{cases} \frac{\partial\Lambda}{dt}+U\frac{\partial\Lambda}{\partial x}-\eta\frac{\partial^2\Lambda}{\partial x^2}+\frac{\partial C}{\partial x}\Psi=0 \\ \Lambda=0,\ x=L_1 \\ \left.\left(\frac{\eta\gamma}{\lambda}\Lambda+\eta\frac{\partial\Lambda}{\partial x}\right)\right|_{x=L_2}=0\ if\ \lambda\neq 0 \\ \Lambda=0,\ x=L_2\ if\ \lambda=0 \\ \Lambda(t=0)=v_2 \end{cases} \quad (2.21)$$

where v_1 and v_2 are chosen so that $P^1(0,v_1,v_2)=V_{1U}^2\Psi(0)$ and $\Phi(0,v_1,v_2)=V_{1C}^2\Lambda(0)$ then the equation (2.17) becomes:

$$\int_0^T\langle\hat{C},1\rangle_{L_2(\Omega)}dt=\int_0^T\langle V_{2C}H_C\Lambda,c_{obs}\rangle_{L_2(\Omega)}dt \quad (2.22)$$

As from the equations (2.12) and (2.22),

$$\int_0^T\langle\frac{dG_\Omega}{dC_{obs}},c_{obs}\rangle_{L_2(\Omega)}dt=\int_0^T\langle V_{2C}H_C\Lambda,c_{obs}\rangle_{L_2(\Omega)}dt \quad (2.23)$$

It deduces from the equation (2.23) that the gradient of function G_Ω respected to C_{obs} in every time moment t is calculated by the formula: $\frac{dG_\Omega}{dC_{obs}}=V_{2C}H_C\Lambda$ (2.24)

We get a coupled system of four differential equations (2.18)-(2.21) of the first order with respect to time. The first two equations (2.18) and (2.19) have final conditions and the terms being the functions of the variables from the other last two equations (2.20)-(2.21) while the last two equations have the initial conditions being the functions of initial variables from the first two equations (2.18)-(2.19): that is a non-standard problem.

2.2 Solving the non-standard problem

To solve the non-standar problem (2.18)-(2.21) let us define the cost function:

$$\Im(v)=\frac{1}{2}\|V_{1U}^2v_1-P^1(0)\|_{L_2(\Omega)}^2+\frac{1}{2}\|V_{1C}^2v_2-\Phi(0)\|_{L_2(\Omega)}^2 \quad (2.25)$$

Let $v^*=(v_1^*,v_2^*)$ be the solution of the minimum problem (2.25). If at $v^*=(v_1^*,v_2^*)$ the equations:

$$V_{1U}^2v_1^*-P^1(0,v_1^*,v_2^*)=0,\ V_{1C}^2v_2^*-\Phi(0,v_1^*,v_2^*)=0 \quad (2.26)$$

are satisfied, then the minimum problem (2.25) will be solved.

As in the last section let us introduce $\hat{P}^1$, $\hat{\Phi}$, $\hat{\Lambda}$, $\hat{\Psi}$ and $\hat{\Im}(v)$ be the Gateaux derivatives with respect to v (in the direction $\hat{v}=(\hat{v}_1,\hat{v}_2)$) of the variables of the optimality problem (2.26) given by equations (2.18)-(2.21) and (2.25) [see (B.Daryoush, 2008)]. $\hat{P}^1$, $\hat{\Phi}$, $\hat{\Lambda}$, $\hat{\Psi}$ and $\hat{\Im}(v)$ are given by the following equation systems:

$$\begin{cases} -\frac{\partial\hat{P}^1}{dt}-U\frac{\partial\hat{P}^1}{\partial x}-\nu\frac{\partial^2\hat{P}^1}{\partial x^2}-\frac{\partial\hat{P}^1}{\partial x}\Psi-\frac{\partial P^1}{\partial x}\hat{\Psi} \\ +H_U^*V_{2U}H_U\hat{\Psi}+Q\frac{\partial\hat{\Lambda}}{\partial x}+\hat{\Phi}\frac{\partial C}{\partial x}=0 \\ \hat{P}^1=0,\ x=L_1 \\ \left.\left(\frac{\nu\alpha}{\beta}\hat{P}^1+\nu\frac{\partial\hat{P}^1}{\partial x}+U\hat{P}^1+P\hat{\Psi}\right)\right|_{x=L_2}=0\ if\ \beta\neq 0 \\ \hat{P}^1=0,\ x=L_2\ if\ \beta=0 \\ \hat{P}^1(t=T)=0 \end{cases} \quad (2.27)$$

$$\begin{cases} \frac{\partial\hat{\Phi}}{dt}+\frac{\partial U\hat{\Phi}}{\partial x}+\eta\frac{\partial^2\hat{\Phi}}{\partial x^2}+\frac{\partial Q\hat{\Psi}}{\partial x}-H_C^*V_{2C}H_C\hat{\Lambda}=0 \\ \hat{\Phi}=0,\ x=L_1 \\ \left.\left(\frac{\eta\gamma}{\lambda}\hat{\Phi}+\eta\frac{\partial\hat{\Phi}}{\partial x}+U\hat{\Phi}+Q\Psi\right)\right|_{x=L_2}=0\ if\ \lambda\neq 0 \\ \hat{\Phi}=0,\ x=L_2\ if\ \lambda=0 \\ \hat{\Phi}(t=T)=0 \end{cases} \quad (2.28)$$

$$\begin{cases} -\frac{\partial\hat{\Psi}}{dt}-\frac{\partial U\hat{\Psi}}{\partial x}+\nu\frac{\partial^2\hat{\Psi}}{\partial x^2}=0 \\ \hat{\Psi}=0,\ x=L_1 \\ \left.\left(\frac{\nu\alpha}{\beta}\hat{\Psi}+\nu\frac{\partial\hat{\Psi}}{\partial x}\right)\right|_{x=L_2}=0\ if\ \beta\neq 0 \\ \hat{\Psi}=0,\ x=L_2\ if\ \beta=0 \\ \hat{\Psi}(t=0)=\hat{v}_1 \end{cases} \quad (2.29)$$

$$\begin{cases} \frac{\partial\hat{\Lambda}}{dt}+U\frac{\partial\hat{\Lambda}}{\partial x}-\eta\frac{\partial^2\hat{\Lambda}}{\partial x^2}+\frac{\partial C}{\partial x}\hat{\Psi}=0 \\ \hat{\Lambda}=0,\ x=L_1 \\ \left.\left(\frac{\eta\gamma}{\lambda}\hat{\Lambda}+\eta\frac{\partial\hat{\Lambda}}{\partial x}\right)\right|_{x=L_2}=0\ if\ \lambda\neq 0 \\ \hat{\Lambda}=0,\ x=L_2\ if\ \lambda=0 \\ \hat{\Lambda}(t=0)=\hat{v}_2 \end{cases} \quad (2.30)$$

$$\hat{\Im}(v)=\langle V_{1U}^2v_1-P^1(0),V_{1U}^2\hat{v}_1-\hat{P}^1(0)\rangle_{L_2(\Omega)}+\langle V_{1C}^2v_2-\Phi(0),V_{1C}^2\hat{v}_2-\hat{\Phi}(0)\rangle_{L_2(\Omega)} \quad (2.31)$$

By the similar way in (Dimet et al., 2014) multiplying (2.27)–(2.30) by $-R_1$, Q_1, R_2, $-Q_2$ then integrating it in t and over $\Omega=]L_1,L_2[$ and adding them we have:

$$\begin{aligned} &\int_0^T\langle\hat{P}^1,\frac{\partial R_1}{dt}+\frac{\partial UR_1}{\partial x}-\nu\frac{\partial^2R_1}{\partial x^2}\rangle_{L_2(\Omega)}+\int_0^T\langle\hat{\Psi},\frac{\partial R_2}{dt}+U\frac{\partial R_2}{\partial x}+\nu\frac{\partial^2R_2}{\partial x^2}+\frac{\partial P}{\partial x}R_1-H_U^*V_{2U}H_UR_1-Q_2\frac{\partial C}{\partial x}-Q\frac{\partial Q_1}{\partial x}\rangle_{L_2(\Omega)}- \\ &\int_0^T\langle\hat{\Phi},\frac{\partial Q_1}{dt}+U\frac{\partial Q_1}{\partial x}-\eta\frac{\partial^2Q1}{\partial x^2}+\frac{\partial C}{\partial x}R_1\rangle_{L_2(\Omega)}+ \\ &\int_0^T\nu\frac{\partial\hat{P}^1}{\partial x}R_1\Big|_{x=L_1}dt-\int_0^T\nu\frac{\partial\hat{\Psi}}{\partial x}R_2\Big|_{x=L_1}dt+A+B+ \\ &\int_0^T\langle\hat{\Lambda},\frac{\partial Q_2}{dt}+\frac{\partial UQ_2}{\partial x}+\eta\frac{\partial^2Q_2}{\partial x^2}+\frac{\partial QR_1}{\partial x}-H_C^*V_{2C}H_CQ_1\rangle_{L_2(\Omega)}- \\ &\eta\int_0^T\frac{\partial\hat{\Lambda}}{\partial x}Q_2\Big|_{x=L_1}dt-\eta\int_0^T\frac{\partial\hat{\Phi}}{\partial x}Q_1\Big|_{x=L_1}dt- \\ &\langle\hat{\Lambda}(T),Q_2(T)\rangle_{L_2(\Omega)}+\langle\hat{v}_2,Q_2(0)\rangle_{L_2(\Omega)}- \\ &\langle\hat{\Psi}(T),R_2(T)\rangle_{L_2(\Omega)}+\langle\hat{v}_1,R_2(0)\rangle_{L_2(\Omega)}- \\ &\langle\hat{P}^1(0),R_1(0)\rangle_{L_2(\Omega)}-\langle\hat{\Phi}(0),Q_1(0)\rangle_{L_2(\Omega)} \end{aligned} \quad (2.32)$$

where:

$A=$

$$\begin{cases} \begin{pmatrix} -\int_0^T\hat{\Psi}.\left.\left(\frac{\nu\alpha}{\beta}R_2+\nu\frac{\partial R_2}{\partial x}+UR_2+PR_1\right)\right|_{x=L_2}dt \\ -\int_0^T\hat{P}^1.\left.\nu\left(\frac{\alpha}{\beta}R_1+\frac{\partial R_1}{\partial x}\right)\right|_{x=L_2}dt \end{pmatrix} if\ \beta\neq 0 \\ \left(+\int_0^T\nu\frac{\partial\hat{\Psi}}{\partial x}.R_2]_{x=L_2}dt+\int_0^T\nu\frac{\partial\hat{P}^1}{\partial x}.R_1|_{x=L_2}dt\right)\quad if\ \beta=0 \end{cases}$$

$$B = \begin{cases} \left(\begin{array}{c} -\int_0^T \widehat{\Phi}\,.\,\eta\left(\frac{\gamma}{\lambda}Q_1 + \frac{\partial Q_1}{\partial x}\right)\Big|_{x=L_2} dt - \\ \int_0^T \widehat{\Lambda}\,.\left(\frac{\eta\gamma}{\lambda}Q_2 + \eta\frac{\partial Q_2}{\partial x} + UQ_2 + QR_1\right)\Big|_{x=L_2} dt \end{array} \right) if\ \lambda \neq 0 \\ \left(\int_0^T \eta\frac{\partial\widehat{\Lambda}}{\partial x}.\,Q_2|_{x=L_2}dt + \eta\frac{\partial\widehat{\Phi}}{\partial x}.\,Q_1]_{x=L_2}dt\right)\ if\ \lambda = 0 \end{cases}$$

Let R_1, R_2 , Q_1 and Q_2 satisfy the following problems:

$$\begin{cases} \frac{\partial R_1}{dt} + \frac{\partial UR_1}{\partial x} - \nu\frac{\partial^2 R_1}{\partial x^2} = 0 \\ R_1 = 0,\ \ x = L_1 \\ \left(\frac{\alpha}{\beta}R_1 + \frac{\partial R_1}{\partial x}\right)\Big|_{x=L_2} = 0\ if\ \beta \neq 0 \\ R_1 = 0,\ \ x = L_2\ if\ \beta = 0 \\ R_1(t=0) = V_{1U}^2 v_1 - P^1((0, v_1, v_2)) \end{cases} \qquad (2.33)$$

$$\begin{cases} \frac{\partial R_2}{dt} + U\frac{\partial R_2}{\partial x} + \nu\frac{\partial^2 R_2}{\partial x^2} + \frac{\partial P}{\partial x}R_1 \\ -H_U^* V_{2U} H_U R_1 - Q_2\frac{\partial C}{\partial x} - Q\frac{\partial Q_1}{\partial x} = 0 \\ R_2 = 0,\ \ x = L_1 \\ \left(\frac{\nu\alpha}{\beta}R_2 + \nu\frac{\partial R_2}{\partial x} + PR_1 + UR_2\right)\Big|_{x=L_2} = 0\ if\ \beta \neq 0 \\ R_2 = 0,\ \ x = L_2\ if\ \beta = 0 \\ R_2(t=T) = 0 \end{cases} \qquad (2.34)$$

$$\begin{cases} \frac{\partial Q_1}{dt} + U\frac{\partial Q_1}{\partial x} - \eta\frac{\partial^2 Q1}{\partial x^2} + \frac{\partial C}{\partial x}R_1 = 0 \\ Q_1 = 0,\ \ x = L_1 \\ \left(\frac{\gamma}{\lambda}Q_1 + \frac{\partial Q_1}{\partial x}\right)\Big|_{x=L_2} = 0\ if\ \lambda \neq 0 \\ Q_1 = 0,\ \ x = L_2\ if\ \lambda = 0 \\ Q_1(t=0) = V_{1C}^2\Lambda(0) - \Phi(0, v_1, v_2) \end{cases} \qquad (2.35)$$

$$\begin{cases} \frac{\partial Q_2}{dt} + \frac{\partial UQ_2}{\partial x} + \eta\frac{\partial^2 Q_2}{\partial x^2} + \frac{\partial QR_1}{\partial x} - H_C^* V_{2C} H_C Q_1 = 0 \\ Q_2 = 0,\ \ x = L_1 \\ \left(\frac{\eta\gamma}{\lambda}Q_2 + \eta\frac{\partial Q_2}{\partial x} + UQ_2 + QR_1\right)\Big|_{x=L_2} = 0\ if\ \lambda \neq 0 \\ Q_2 = 0,\ \ x = L_2\ if\ \lambda = 0 \\ Q_2(t=T) = 0 \end{cases} \qquad (2.36)$$

Then the equation (2.32) becomes:

$$\langle \widehat{P}^1(0), (V_{1U}^2 v_1 - P^1((0, v_1, v_2)))\rangle_{L_2(\Omega)} + \langle \widehat{\Phi}(0), V_{1C}^2\Lambda(0) - \Phi(0, v_1, v_2)\rangle_{L_2(\Omega)} = \langle \hat{v}_1, R_2(0)\rangle_{L_2(\Omega)} + \langle \hat{v}_2, Q_2(0)\rangle_{L_2(\Omega)}$$

Putting the last equation to the equation (2.31) and using the symmetry positive properties of V_{1U}^2 and V_{1C}^2 we have:

$$\widehat{\mathfrak{I}}(v) = \nabla\mathfrak{I}\hat{v}$$

where $\nabla\mathfrak{I} = (\mathfrak{I}'_{v_1}, \mathfrak{I}'_{v_2}), \mathfrak{I}'_{v_1} = V_{1U}^2(V_{1U}^2 v_1 - P^1(0)) - R_2(0), \mathfrak{I}'_{v_2} = V_{1C}^2(V_{1C}^2 v_2 - \Phi(0)) - Q_2(0)$ (2.37)

We have obtained now the gradient of the cost function $\mathfrak{I}$(v) in the form (2.37).

III. Algorithm to calculate the gradient of the response function G_Ω

From the last 2 sections we have the following algorithm to calculate the gradient of the response function G_Ω:

- 1. Solve equations (2.18)-(2.21), (2.33)-(2.36);

- 2. Have $\nabla\mathfrak{I}$(v) by the formula (2.37);

- 3. Using the optimal method based on inverse BFGS update in [see (Bonnans, 2006), (Gilbert, 1989)] solve the optimal control problem finding the minimum of $\mathfrak{I}$(v) with the value $v^* = (v_1^*, v_2^*)$;

- 4. Put the obtained values v_1^*, v_2^* into the relations $\Psi(0) = v_1^*$, $\Lambda(0) = v_2^*$;

- 5. Solve again the problems (2.20), (2.21);

- 6. Have the value of the gradient of the response function $\frac{dG_\Omega}{dC_{obs}}$ in time moment t by the formula (2.24).

IV. Numerical experiment on one dimensional problem

In this section, we give numerical results of the sensitivity of a response region to foreign sources for one dimensional flow test. The physical space is the interval **Ω** = [0, 1] and the time domain is considered as the interval [0, 1]. We consider the problem of pollution by a single type that is produced by a source located all over the physical space. The pollutant evolves according to the one dimensional advection diffusion equation (2.2). The coeficcients ν=1(m^2/s), η=0.4(m^2/s), The picture of concentration is described by the left of figure 1. The evolution of the advection water pollution is defined in this example. The source points are x_1 = 0.3, x_2 = 0.4 The measurement areas are in the following cases: case 1: $x_{1,obs}^1 = 0.3m$; $x_{2,obs}^1 = 0.4m$; case 2: $x_{1,obs}^2 = 0.4m$; $x_{2,obs}^2 = 0.5m$;case 3: $x_{1,obs}^3 = 0.5m$; $x_{2,obs}^3 = 0.6m$;case 4: $x_{1,obs}^4 = 0.6m$; $x_{2,obs}^4 = 0.7m$;case 5: $x_{1,obs}^2 = 0.7m$; $x_{2,obs}^2 = 0.8m$;

In these different cases, the gradient of response function, defined by the formula (4.144), are displayed in the figures 1.b-1.f. From the figure 1 one sees that the value of sensitivity $\frac{dG_\Omega}{dC_{obs}}$ is stronger as the measurement is closer to the pollution source and becomes strongest when the measurement area is situated at the pollution source area.

V. Conclusion

In this paper, we have developed a sensitivity method to compute the sensitivity of the response function to the observation. The response function is constructed on the solution of the assimilation problem which is a function of the observation. The proposed method is based on using the adjoint equation approach. The simple numerical example presented here clearly shows the usefulness of the present approach which enables us to decide on where the location of the pollution source is. In this sense, the sensitivity study is proved to be an important tool to detect the location of the pollutant source.

ACKNOWLEDGEMENTS

The authors gratefully acknowledge the financial support from the VAST01.09/21-22 funds.

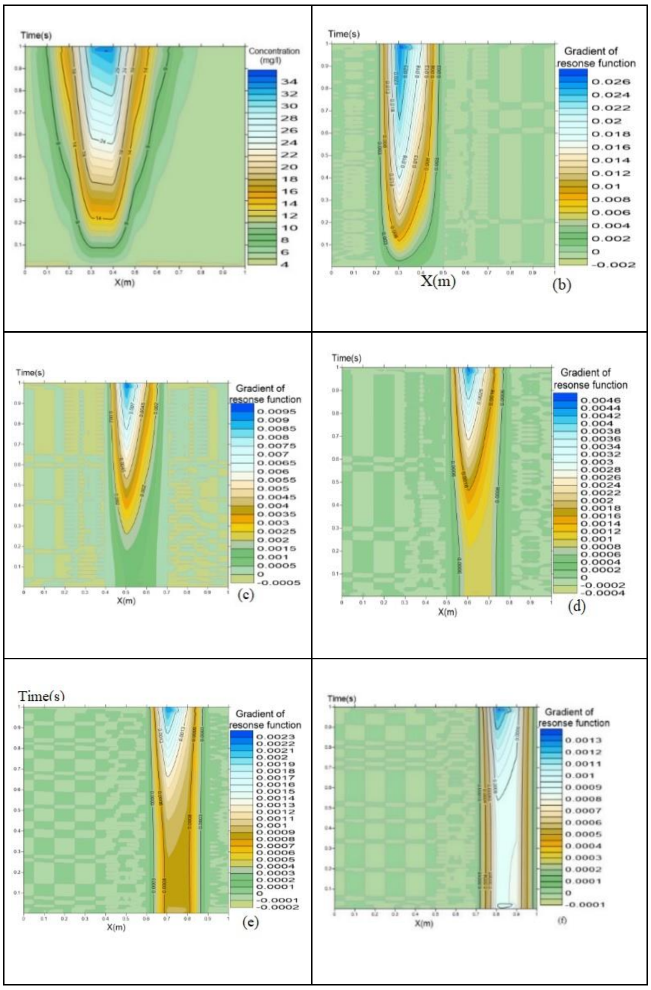

Fig. 1. Concentration field in the channel in the period time 1s (left side) ; The gradient of response function with respect to measurement values $\frac{dG_{\Omega}}{dC_{obs}}$ in the difference cases of measurement areas (b-f).

REFERENCES

[1] Bonnans, J. F., Gilbert, J. Ch., C. and Sagastizábal C. A. - Numerical optimization, theoretical and numerical aspects. Second edition. Springer, 2006.

[2] Daryoush B., Encyeh D. N. - Introduction of Frechet and Gateaux Derivative, Applied Mathematical Sciences 2 (20) (2008) 975 – 980.

[3] Gilbert, Lemarechal I. C. - Some numerical experiments with variable-storage quasi-Newton algorithm, Math program. 45 (3) (1989), 407-435.

[4] F.-X. Le Dimet, V. P. Shutyaev and T. H. Tran. "General sensitivity analysis in data assimilation". Russian Journal of Numerical Analysis and Mathematical Modelling V. 29, N.2, (2014), p. 107-127. doi:10.1515/rnam-2014-0009.

[5] Le Dimet F.X., Ngnepieba P., Shutyaev V. On error analysis in data assimilation problems. Russ. J. Numer. Anal. Math. Modelling, 2002,17, pp.71-97.

[6] V.P.Shutyaev,Some properties of the control operator in the problem of data assimilation and iterative algorithms.Russ. J.Numer.Analys.Math.Modelling10(1995),357–371.

[7] Tran Thu Ha, Nguyen Hong Phong, François-Xavier Le Dimet, Hong Son Hoang." Data assimilation and pollution forecasting in Burgers' equation with model error function". C. R. Mecanique. 347 (2019), p. 423-444

Application of GIS tool and hydrologic modelling for flow simulation of Cau river basin

Tran Thi Thanh Huyen
Institute of Mechanics, Vietnam Academy of Science and Technology
Hanoi, Vietnam
Email: ttthuyen@imech.vast.vn

Nguyen Chinh Kien
Institute of Mechanics, Vietnam Academy of Science and Technology
Hanoi, Vietnam

***Abstract*: The Cau river is one of the major basins in Thai Binh river system and located in the northeastern region of Vietnam. This area has a special geographical position, diversified and substantial water resources. It plays a very important role in social and economical development of provinces within its catchment, such as Bac Kan, Thai Nguyen, Bac Giang and Bac Ninh province. In the recent years, the climate change has caused the extreme weather patterns, like flood inundation, becoming more and more serious. As a result, the study of simulation and forecast of discharge of the Cau river basin is necessary to serve the planning and management the river system in sustainable development.**

This paper presents the research and application of hydrologic modeling combined with geographic information systems (GIS) to calculate and simulate the runoff in Cau river basin. The calibration and verification results showed the high reliability of this model, it would be very useful in flood controlling and mitigating for whole area.

Keywords: Cau river, GIS, hydrologic modelling, simulation, NSE index.

I. INTRODUCTION

A. *Study area*

Cau river basin is one of the major river basins in Vietnam, with a basin area of 6,030 km^2, with a length of over 288 km, with a special geographical position, diversity and richness in resources as well As for the development history, it has great socio-economic significance of the provinces located in its basin. But for a long time, floods as well as environmental degradation cause impacts on environmental aspects but also affect the sustainable development of the river basin. The density of hydrological monitoring stations in this basin is sparse, currently the only discharge station is Thai Nguyen (Fig. 1). Therefore, the study on simulation and forecast of flow in the river system of Cau river basin is necessary to serve the planning and management and ensure the sustainable development of the river basin.

In the condition that the survey and measurement data to serve the simulation and forecast of flows in the basins are incomplete, the application of GIS model has the most advantages because: (1) Toolkit GIS can support to edit and add documents easily; (2) Can be connected to the widely applied computational models today; (3) Satisfy the requirement of calculating flow characteristics for general management and river basin planning.

Geographic information systems (GIS) are currently the main source of data for hydrologic modelling, namely on topography, physical characteristics of streamlines and use and soil type. The use of digital elevation models (DEM) for automated delineation of watersheds and river networkshas increased considerably in recent years. There are GIS analysis tools that allow the processing of topographic data and the determination of several hydrological parameters. Advantages of usingthese automated approaches include reliability and reproducibility of the process, saving time and labour.

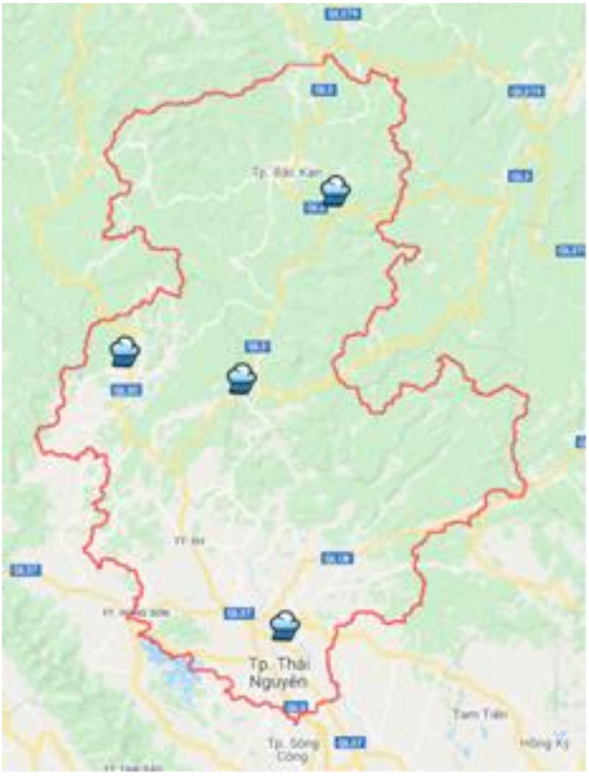

Fig. 1. The location of study area.

The GIS tools (Arc Hydro and HEC-GeoHMS within ArcGIS environment) are mainly applied in this research. The delineation of the stream network and sub-basins was done with the use of Arc Hydro tools, which were designed by ESRI in association with Center for Research in Water Resources from the University of Texas at Austin. Arc Hydro tools support the derivation of physical and hydrological data from DEMs in ArcGIS environment. HEC-GeoHMS was developed by USACE as a geospatial hydrology set of tools to work in ArcGIS environment and facilitate the transfer of data to HEC-HMS. It can display spatial information, basin characteristics, perform spatial analysis and built files that can be directly used by HEC-HMS.

The Hydrologic Engineering Center's – Hydrologic Modelling System (HEC-HMS) was developed by the Hydrologic Engineering Center, from the US Army Corps of Engineers (USACE). Over the past years, it has been used to develop hydrologic models for flood forecasting in many regions of the world. The models developed herein are event-based, implying that they are suitable for simulating rainfall-runoff processes of single events or floods.

B. Topographic Data

The Earth topography elevation data chosen in this paper is the digital elevation model (DEM) - the Advanced Land Observing Satellite (ALOS) World 3D-30m (AW3D30). ALOS World 3D (AW3D) global DEM data were produced using the data acquired by the Panchromatic Remote Sensing Instrument for Stereo Mapping (PRISM) operated on the ALOS (nicknamed "Daichi") from 2006 to 2011. The operator of the satellite - the Japan Aerospace Exploration Agency (JAXA) - produced the global DEM using approximately 3 million images.

We use the updated topographic data (verion 3.2) in 2021 with horizontal resolution of approximately 30 meters.

C. Hydrological Data

There are four rain stations in the study area used to simulate the flow: Thai Nguyen, Dinh Hoa, Cho Moi, Thac Rieng as shown in Table 1. The measured data in 2019 and 2020 are carried out (Fig. 2, Fig. 3)

TABLE 1. THE POSITION OF 4 HYDROLOGICAL STATIONS

Station	**Longitude**	**Latitude**
Thai Nguyen	105°49'60.00"E	22°28'60.00"N
Dinh Hoa	105°37'60.00"E	21°55'0.00"N
Cho Moi	105°46'43.21"E	21°53'7.23"N
Thac Rieng	105°49'60.00"E	22°28'60.00"N

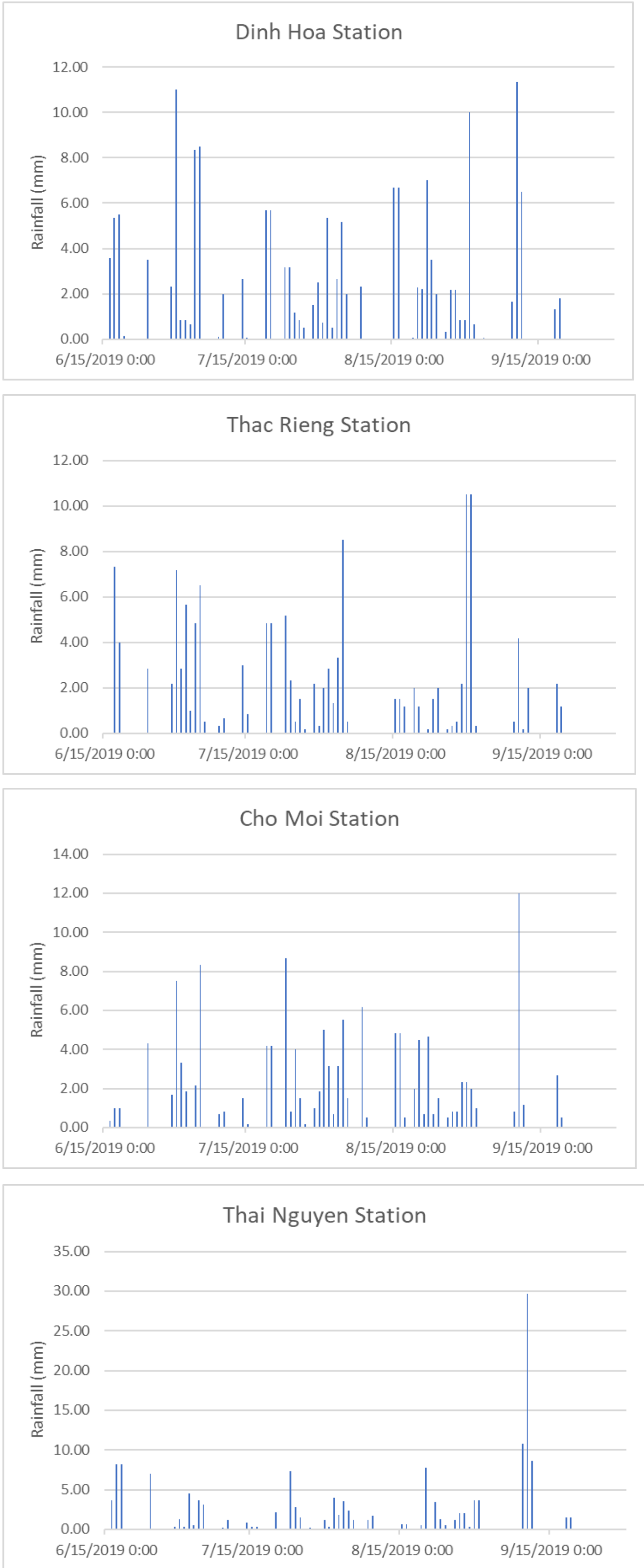

Fig. 2. Rainfall in observation (15/6/2019-30/9/2019).

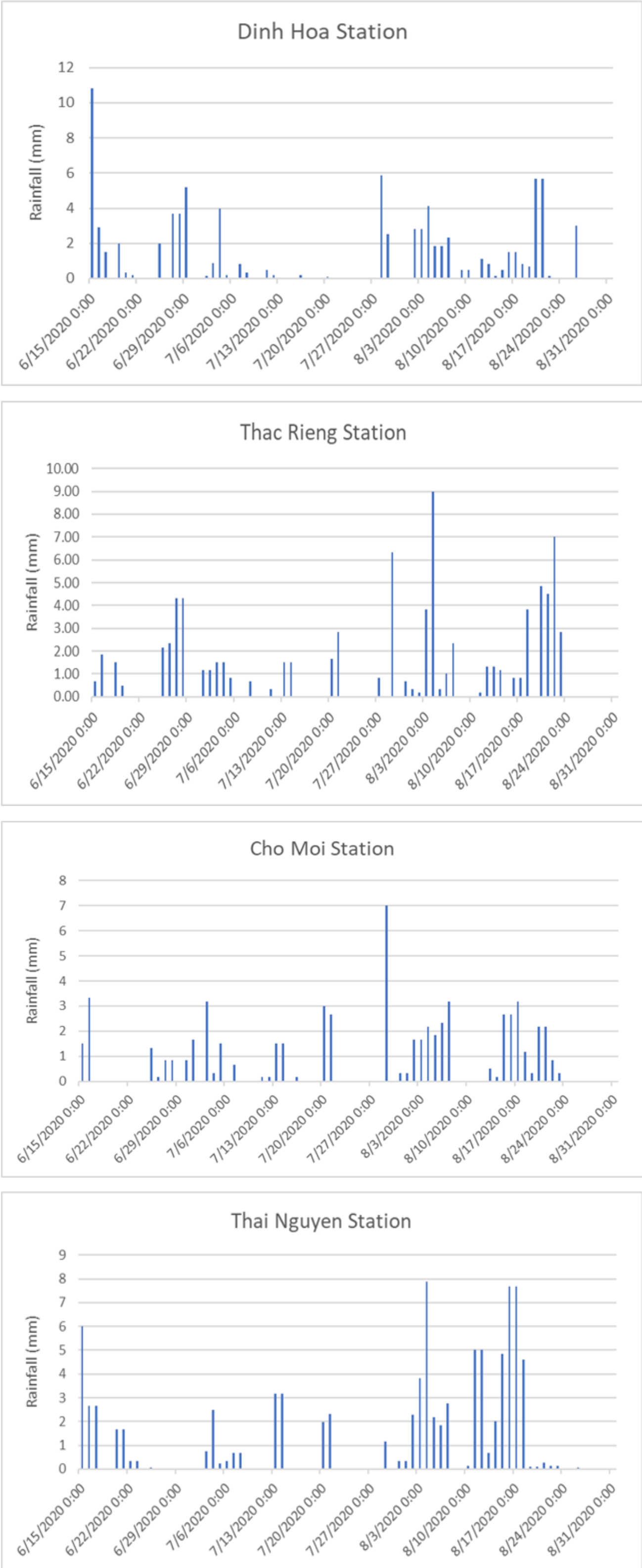

Fig. 3. Rainfall in observation (15/6/2020-31/8/2020).

II. METHODOLOGY

A. GIS (Geographic Information System) tool

This study applies GIS tools connected to the HEC-HMS calculation software to simulate the flow throughout the Cau river basin.

The advantage of HEC-HMS is that: the parameters of the model are included in the calculation through the GIS supporting tools from the input data which is a set of databases such as DEM topographical digitized maps, distribution of hydro-meteorological stations in the basin, map of current land use, map of land classification, river network system.

In which, the digitized topographic map DEM is used to simulate subbasins, river network system (Fig. 4). The Hydro-meteorological map for the division of rain zones (Thiesen method). The land use map and soil classification are used to serve the calculation of permeability coefficient (Curve Number method).

Based on the GIS and HEC-HMS, the characteristics of the subbasins, river network, flow direction, slope, watershed delineation, etc are included in the flow simulation through the HEC-HMS model (Fig. 5).

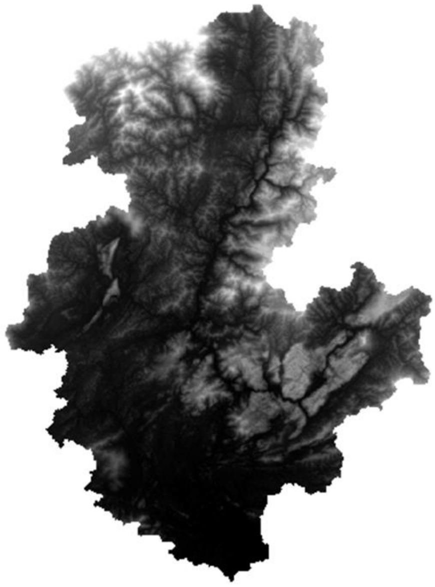

Fig. 4. Digital Elevation Model (DEM) of Cau river basin.

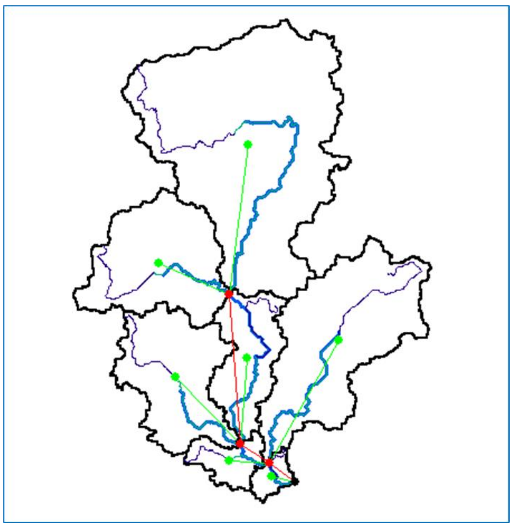

Fig. 5. Delineation of stream network and subbasins.

B. HEC-HMS hydrological model

The input data used for the calculation of the model includes the characteristics of the basin, the river network (on the basis of connection with the GIS tool) and the hydrometeorological data at the rain gauge stations. In the

HEC-HMS model, the most difficult parameters to determine include: determining the permeability loss method, the flow propagation mechanism, etc.

However, this study is applied GIS tools for preliminary determination. these parameters. Based on the superior features of the GIS tool, especially the ability to connect the flow calculation modules through the setting of parameters for each grid cell, the flow distribution map over time is determined.

This result, together with the meteorological parameters, are included in the HEC-HMS calculation model to adjust according to the monitoring data of the flow accordingly through the automatic verification function by the optimization program. parameterize. This set of optimal parameters is the basis for forecasting the flow rate according to different floods and at any locations on the river network in the basin.

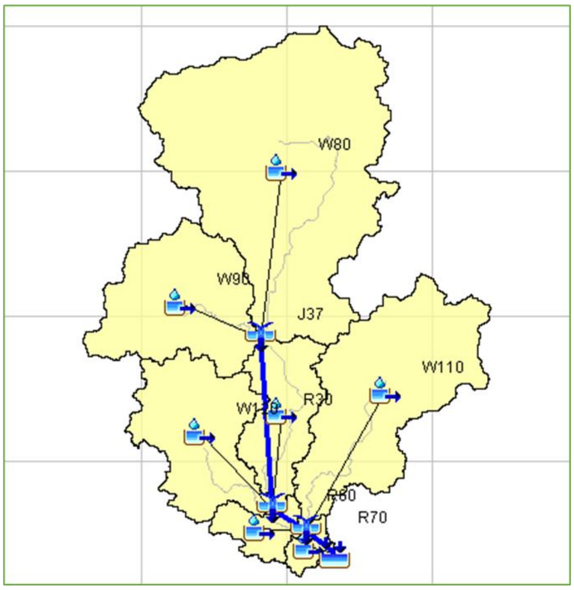

Fig. 6. Map in HEC-HMS.

HEC-HMS components include basin model meteorological models control specifications and input data, such as time-series data, gridded data, etc.

It offers different methods to simulate the several hydrologic processes and uses seven different types of elements to route water through the drainage area: Sub-basin, Reach, Reservoir, Junction, Diversion, Source and Sink

Loss function – SCS CN/Initial and loss method: In order to estimate the effective rainfall, the base flow should be separated from direct runoff. The effective rainfall volume is defined as approximately equal to the volume of direct runoff. Once the effective rainfall volume is determined, it should be distributed in time, using the selected loss method. Two of the most widely used methods were tested, namely, SCS-Curve Number (SCSCN) and the Initial and Constant Rate.

The strength of the model is because it includes cumulative rainfall, soil type, land use and antecedent soil moisture (Maidment, 1993). The effective rainfall is given by:

$$P_e = \frac{(P - I_a)^2}{P - I_a + S}$$

where P_e is the precipitation excess at time t, P is accumulated rainfall depth at time t, I_a is the initial abstraction (initial loss), often described as $I_a = 0.2S$ and $S = (25400 - 254CN)/CN$ is the potential maximum retention, which describes the ability of the watershed to abstract and retain storm precipitation. The curve number CN varies between 30 (soils with high infiltration rates) to 100 (water bodies/impermeable surfaces).

Transform function – SCS Unit Hydrograph: The unit hydrograph (UH) concept, introduced in the United States of America by Sherman in 1932, was a major step forward in hydrological analysis (Shaw, 1994). He defined it as the hydrograph of direct runoff resulting from unit depth (often 1 cm) of effective rainfall falling in a given duration, such as 1 hour or 1 day, generated uniformly in time and space over the catchment area. From the definition, the UH is always associated with a given duration. This duration depends on the excess rainfall duration used to derive it. From the assumptions of the method, the duration should be long enough for the entire catchment to respond, but it should not be too long, as the assumptions of the method become unrealistic.

The SCS UH is a (synthetic) dimensionless unit hydrograph, defined by one parameter, the time of rise or time of peak (T_p):

$$q_p = \frac{CA}{T_p}$$

where A is the area (km^2), C = 2.08, $T_p = t_r/2 + t_p$, with $t_p = 0.6T_c$. T_c is time of concentration and t_r the duration of the storm. In HEC-HMS, the UH is systematically defined based on the duration equivalent to the time step of the calculations. In the present case, as the calculations will have 1h time step, the software computes the 1h-UH, according to the specified lag time t_p.

III. MODEL VERIFICATION

In this report, several calculations using the measured data in 2019 and 2020 are carried out (Table 2). To evaluate the accuracy between calculated results and the observed data, index Nash-Sutcliffe Efficiency (NSE) is used.

TABLE 2. CALCULATION TIMES

Kind	Start	End
Calibration	09/09/2019	17/09/2019
Verification	02/08/2020	11/08/2020

A. Calibration result

With the collected data, the authors calculated and simulated the discharge into Cau river basin from September 9th to September 17th, 2019.

The results of calibration of the model with 7 subbasins (W80. W90, W100, W110, W120, W130, W140) are displayed in the following Table 3.

TABLE 3. PARAMETERS USED FOR MODEL CONSTRUCTION

Parameters		W80	W90	W100	W110
Subbasin **Loss method: SCS Curve Number**	Curve Number	3	5	18	9
Transform method: Method: Standard	Standard Lag (HR)	2	1.5	1.2	1
	Peaking Coefficient	0.23	0.25	0.14	0.3
Base flow method: Recession	Initial Discharge (m3/s)	28.5	30.2	29.4	27.9
Threshold Type: Threshold Discharge	Recession Constant	0.7	0.61	0.75	0.82
Routing method: Muskingum	Muskingum K (HR)	7	6	5	6
	Muskingum X	0.25	0.31	0.27	0.19
Parameters		W120	W130	W140	
Subbasin **Loss method: SCS Curve Number**	Curve Number	20	13	16	
Transform method: Method: Standard	Standard Lag (HR)	1	0.1	0.1	
	Peaking Coefficient	0.16	0.5	0.29	
Base flow method: Recession	Initial Discharge (m3/s)	28.6	31	28	
Threshold Type: Threshold Discharge	Recession Constant	0.65	0.49	0.77	
Routing method: Muskingum	Muskingum K (HR)	8	5	4	
	Muskingum X	0.25	0.33	0.26	

A relatively good agreement between the simulated and observed hydrographs (Fig. 7) is shown.

The value of NSE in calibrating model is about 0.85. So, it indicates the agreement of the simulated hydrograph to the observed.

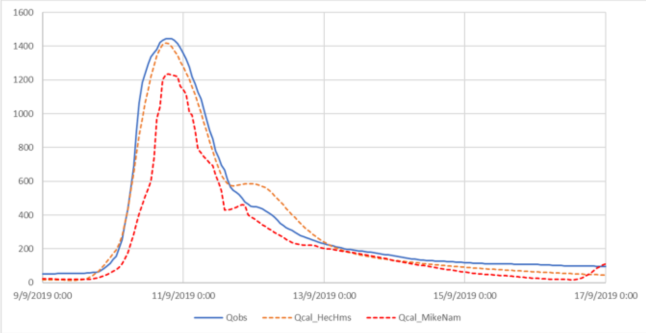

Fig. 7. Comparision in observed and simulated discharge of Cau river basin (09/09/2019 -17/09/2019) – Calibration result.

B. *Validation result*

Based on the reliability in the calibration result, we apply these parameters in Table 3 and verify the model with 2020 data from August 2nd to August 11th. The performance in Fig. 8 shows the value of NSE is approximately 0.8.

The good agreement of the model and observed direct runoff indicates that the preliminary estimation of the model parameters is relatively accurate. They can serve as initial parameters in the HEC-HMS model, and modified to improve the agreement with the observed hydrographs. This corresponds to the calibration process.

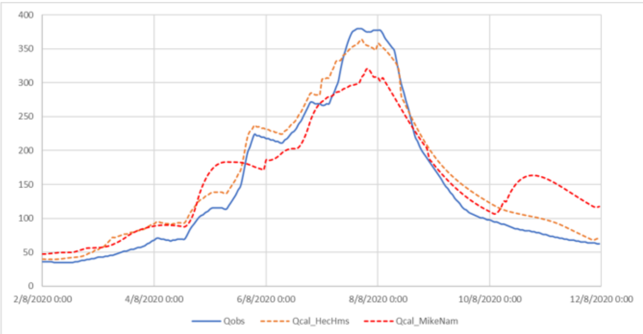

Fig. 8. Comparision in observed and simulated discharge of Cau river basin (02/08/2020 -11/08/2020) - Validation result.

Besides, to confirm the reliability of HEC-HMS model, we use another rainfall-runoff model (Mike-Nam) to simulate the flow in the study area with the value of NSE in calibration and validation is 0.65 and 0.63, respectively, (Fig.7 and Fig.8). So, the hydrological modelling HEC-HMS is suitable in this research.

IV. CONCLUSION

The model provides the same level of accuracy used by the authorities responsible for flood monitoring in the region. This powerful accuracy of the developed model suggests that HEC-HMS may be suitable for flood modelling and forecasting in catchments.

After setting up and putting the HEC-HMS model into calculations, the authors found that the application of the HEC-HMS model to forecast the flow into Cau river basin is completely feasible and has certain reliability. However, it is necessary to have a denser system of rain gauges in the Cau river basin to fully reflect the local rain in the model instead of a few rain stations representing the whole basin as at present.

This result is also the basis for establishing the HEC-HMS model for other basins in the Thai Binh river system.

REFERENCES

[1] ALOS Global Digital Surface Model "ALOS World 3D - 30m" (AW3D30). http://www.eorc.jaxa.jp/ALOS/en/aw3d30/.

[2] HEC HMS user manual.

[3] HEC GEOHMS user manual.

[4] Maidment, D.R. (1993). Hand book of hydrology. McGraw-Hill.

[5] Shaw, E. M. (1994). Hydrology in practice, VNR Int.

[6] US. Army Corps of Engineers (USACE). (2000). Hydrologic Modeling System: Technical Reference Manual. Davis, CA: U.S. Army Corps of Engineers, Hydrologic Engineering Center.

[7] U.S. Army Corps of Engineers (USACE). (2017). Hydrologic Modeling System: Applications Guide. Davis, CA: U.S. Army Corps of Engineers, Hydrologic Engineering Center.

Evaluation of salinity intrusion on Kone – Ha Thanh river system

Nguyen Tuan Anh
Institute of Mechanics, Vietnam Academy of Science and Technology
Hanoi, Vietnam
ntanhvc@gmail.com

Duong Thi Thanh Huong
Institute of Mechanics, Vietnam Academy of Science and Technology
Hanoi, Vietnam

Nguyen Chinh Kien
Institute of Mechanics, Vietnam Academy of Science and Technology
Hanoi, Vietnam

Nguyen Thi Hang
Institute of Mechanics, Vietnam Academy of Science and Technology
Hanoi, Vietnam

Abstract: **Kone - Ha Thanh River Basin is the largest river basin in Binh Dinh province, with its area of about 3640 km^2. This is an economic, cultural, social and political center of the whole province. In dry season, the amount water from upstream decreases, salt water from the sea go into the river, causing river water to be contaminated with salt which seriously affects people's lives, living and production. Therefore, the calculation of salinity intrusion scenarios on the river is essential to minimize the damages.**
In this study, a model of calculation combining hydrological, hydraulic and water quality was built, established, adjusted and tested for good results. Some scenarios are calculated, giving the characteristics of salinity intrusion on the Kone-Ha Thanh river system. This result helps to effectively use of irrigation dams on the Kone-Ha Thanh river system thereby minimizing the damage caused by salinity intrusion.

Keywords: Salnility intrusion, Kone – Ha Thanh River.

I. INTRODUCTION

A. Study area

The research area is 3640 km^2 mainly in Binh Dinh province. The total population is over one million people in 9 districts, 97 communes.

The most studies in this region use commercial models such as Mike to focus on flood calculation, there are also some salinity intrusion studies for the Kone-Ha Thanh region such as the project "Vietnam Disaster Management" funded by the World Bank but only in calculating the scenario of climate change and sea level rise, does not apply to the current and future states of the region. Therefore, in this report, we build and develop a set of hydrology and hydraulic models to calculate a number of salinity intrusion scenarios that correspond to the current state of the research area.

In recent years, drought happens more and more seriuosly leading to salinity instrusion farther into the river. To operates Dams on Kone-Ha Thanh province, especially Van Phong Dam, in mitigating the bad effects of salinity instrusion, it’s neccesary to calculate scenarios to research how far salt water comes into the river in diffirent situations. So, in this research the authors calculate 2 scenarios of salinity instrusion with the base scenario in dry season of the year 2021.

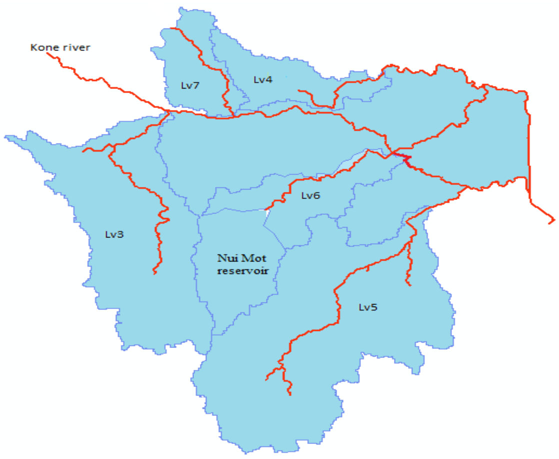

Fig 1: Research area.

B. Collected Data

1. *Data for Hydrology model*

For hydrology model, the authors have collected DEM 30 x 30m, Rainfall data in 2020 and 2021 in dry season as table 1.

TABLE 1: RAINFALL STATION

Station	Longitude	Latitude
Qui Nhon	109°13'24.08"E	13°45'59.82"N
An Nhon	109° 6'49.60"E	13°53'14.05"N
Binh Nghi	108°57'49.14"E	13°54'33.78"N

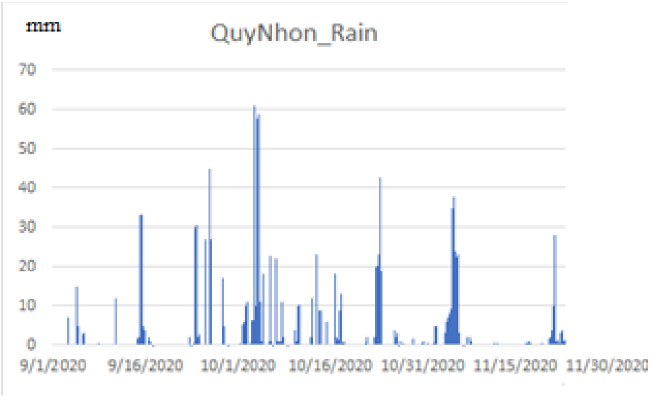

Fig 2: Rainfall data at Qui Nhon station in 2020.

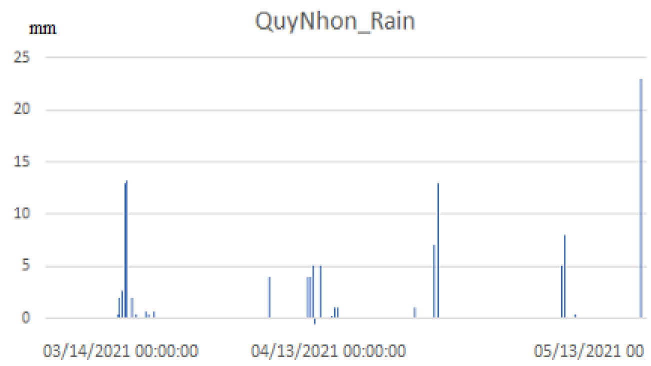

Fig 3: Rainfall data at Qui Nhon station in 2021.

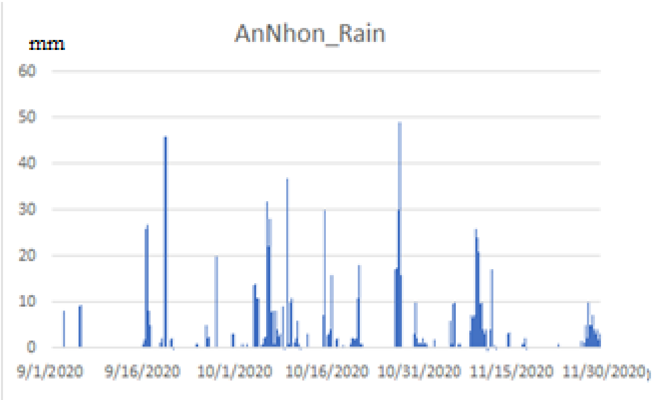

Fig 4: Rainfall data at An Nhon station in 2020.

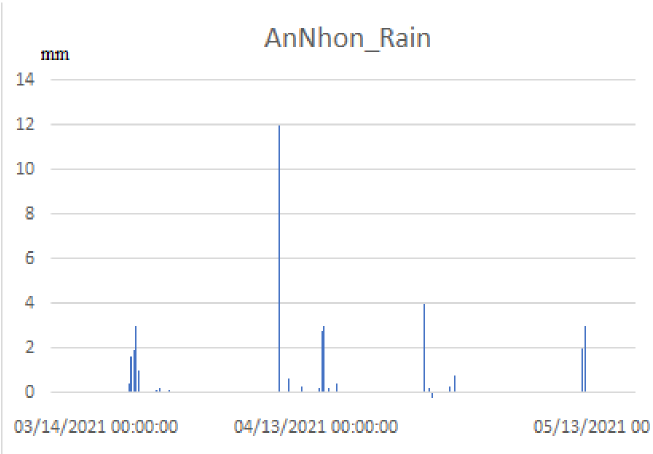

Fig5: Rainfall data at An Nhon station in 2021.

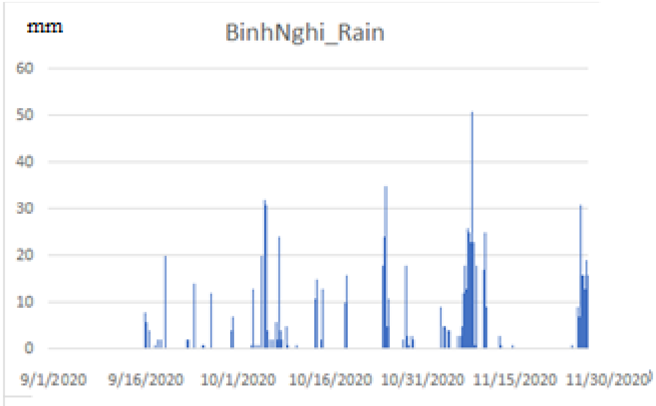

Fig 6: Rainfall data at Bình Nghi station in 2020.

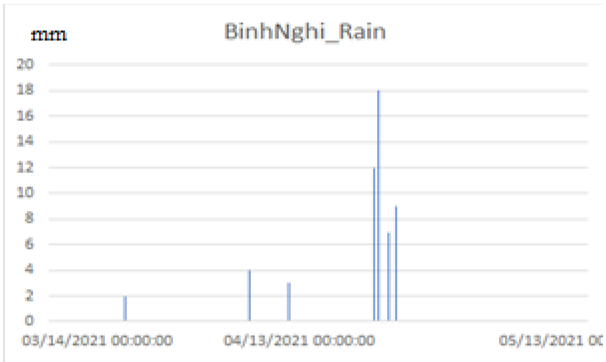

Fig 7: Rainfall data at Bình Nghi station in 2021.

2. *Data for Hydraulic model*

The authors have collected tide and salinity data at downstream boundaries in 2020 and 2021, 91 cross sections on Kone – Ha Thanh rivers, outlet discharges at Van Phong Dam. The input data for hydraulic model include:

Upstream boundary: Van Phong Dam on Kone river.

Lateral boundaries are calculated by hydrology model: Lv3, Lv4, Lv6 on Kone river, Lv5 on Dap Da river, Lv7 on Ha Thanh river.

Downstream boundaries: Water level and salinity at river estuaries of Ha Thanh, Say, Tan An, Go Cham, Dap Da river.

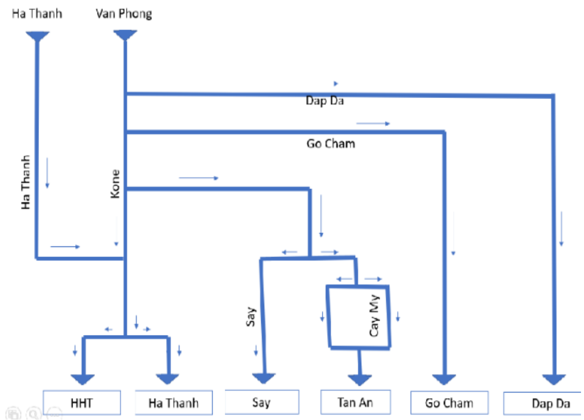

Fig 8: River network of Kone – Ha Thanh.

II. METHODOLOGY

This study combines hydrological, hydraulic and water quality to calculate salinity instrusion in Kone – Ha Thanh river system.

The advantage of this method is that: the result of hydrology model will be used for the input of hydraulic model. So from rainfall data the authors can calculate the water level and salnity instrusion on Kone – Ha Thanh river system.

A. Hydrology model

The Distribution Hydrology model simulates the process of forming the flow generated by rain in the basin based on the equation of mass conservation:

$$\frac{\partial V}{\partial t} + \boldsymbol{u}.\boldsymbol{grad}(V) = P_0 \qquad (1)$$

Where:

V: is the volume of liquid mass considered; U: is the velocity of the flow between grid cells; P0: is rainfall.

Because:

$$\boldsymbol{u}.\boldsymbol{grad}(V) = div(V.\boldsymbol{u}) - V.div(\boldsymbol{u})$$

With the uncompressed liquid we have $div(\boldsymbol{u}) = 0$, using equation Green-Ostrogradski

$$\iint_S div(m.\boldsymbol{u}).dS = \oint_\Gamma m.\boldsymbol{u}.\boldsymbol{n}.d\Gamma$$

From (1) we have :

$$\iint_S \frac{\partial V}{\partial t}.dS + \oint_\Gamma V.\boldsymbol{u}.\boldsymbol{n}.d\Gamma = \iint_S P_0 \qquad (2)$$

The velocity of the flow exchanged between cells is calculated according to the formula:

$$\|\boldsymbol{u}\| = \sqrt{S}.\frac{H^{2/3}}{K_m} \qquad (3)$$

Since the grid used to calculate is a square grid (DEM), it is recommended to replace the velocity expression into the analytical equation we obtain:

$$\Delta H + \sum_{j=1}^{4} \frac{H_j^{5/3}}{K_m}.\sqrt{S}.\frac{\Delta t}{\Delta x} = P_0.\Delta t \qquad (4)$$

Where:

S: slope; Km: Manning rough coefficient; Δx: grid cell width; Δt: Time step; j: Flow direction of grid cell (j =1 ÷ 8); Q: The water level of the grid cell; ΔH: The change in the water level of the grid cell from the time of t1 to t2 .

B. Hydraulic model

The Distribution Hydraulic model simulates discharges and water level on Kone – Ha Thanh river system and sality as well. The equation of Hydraulic model as follow:

$$B\frac{\partial H}{\partial t} + \frac{\partial Q}{\partial x} = q \qquad (5)$$

$$\frac{\partial Q}{\partial t} + \frac{\partial}{\partial x}\left[\beta\frac{Q^2}{A}\right] + gA + \left[\frac{\partial H}{\partial x} + S_f\right] = 0 \qquad (6)$$

where, x and t denote space and time; A is the area of wet cross-section; B - the width of cross-section; H - water level; Q - discharge; β – is momentum correction factor ($\beta \approx 1$); q is additional (or loss) discharge per unit length; S_f - friction slope (defined by the formula: $S_f = g|Q|Q/C^2R$ with R – hydraulic radius) and C – Chezy coefficient.

Advection - Dispersion equation:

$$\frac{\partial A_t S}{\partial t} + \frac{\partial QS}{\partial x} = \frac{\partial}{\partial x}\left(A_t D\frac{\partial S}{\partial x}\right) + G(S) \qquad (7)$$

where S is pollutant concentration; D – diffusion coefficient; G(S) – additional source.

Numerical solving techniques :

The hydrological model uses the finite volume on structure grids. The Preissman 4-points finite difference scheme is applied for 1D hydraulic equations (5) and (6), the up-wind scheme for the mass conservation equation (7).

III. CALIBRATION, VERIFICATION AND SCENARIOS CALCULATION

In this report, several calculations using the collected data in 2020 and 2021 are carried out to evaluate the saliny instrusion incase of changing oulet discharge of Van Phong Dam.

A. Calibration

By using collected rain data, the authors calculated 5 subbasins by hydrology model and got the results for the input of hydraulic model.

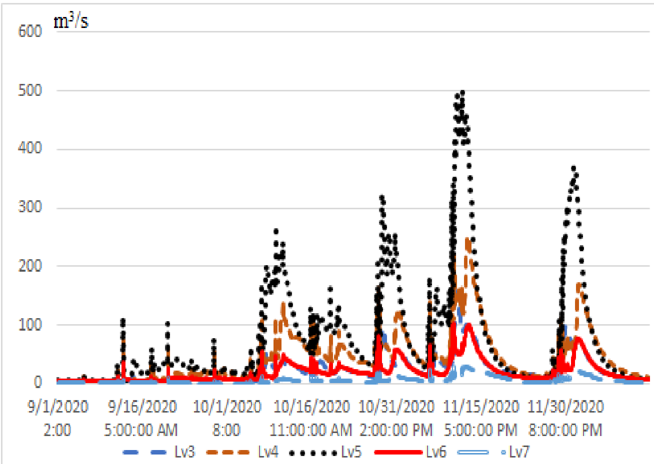

Fig 9: Outlet discharges of subbasins 2020.

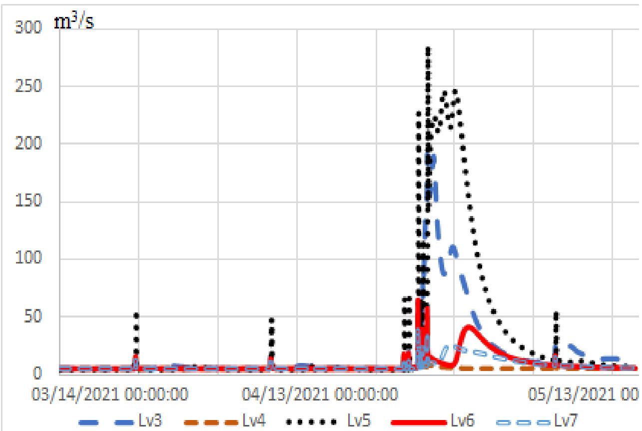

Fig 10: Outlet discharges of subbasins 2021.

After using 2020 data for hydraulic model calibration, the authors evaluate the accuracy between calculated results (Cal.) and the Observed data (Obs.), index Nash-Sutcliffe Efficiency (NSE) is used.

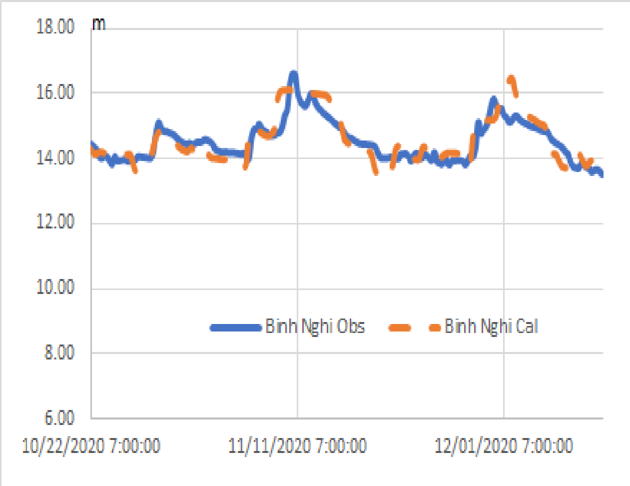

Fig 11: Calculated and observed water level at Binh Nghi station in 2020.

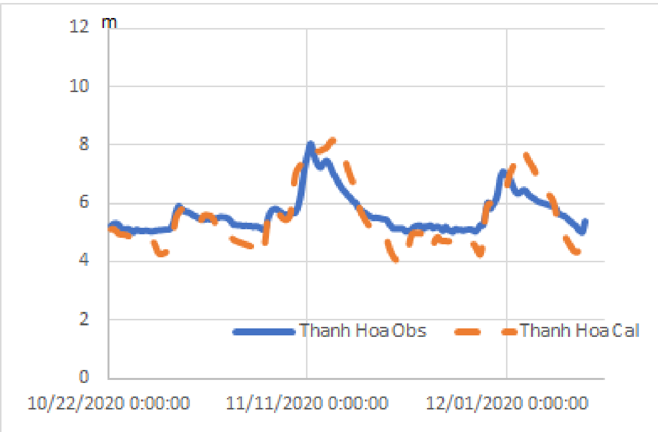

Fig 12: Calculated and observed water level at Thanh Hoa station in 2020.

TABLE 2: NSE INDEX AT BINH NGHI AND THANH HOA STATION IN 2020.

Station	Binh Nghi	Thanh Hoa
NSE	0.86	0.71

NSE > 0.75 is a very good result., according to Moriasi et. al. [3].

On the basic parameter of hydraulic model the authors calculate the salinity instrusion in 2020 on Kone – Ha Thanh river system. The results are shown in fig 13 and fig 14.

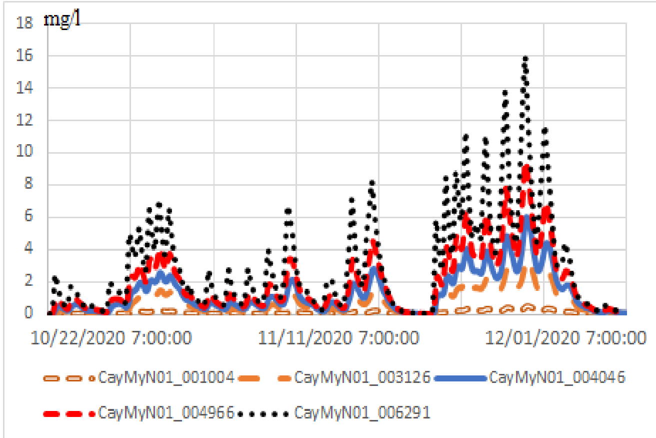

Fig 13: Salinity on Kone- Ha Thanh in 2020.

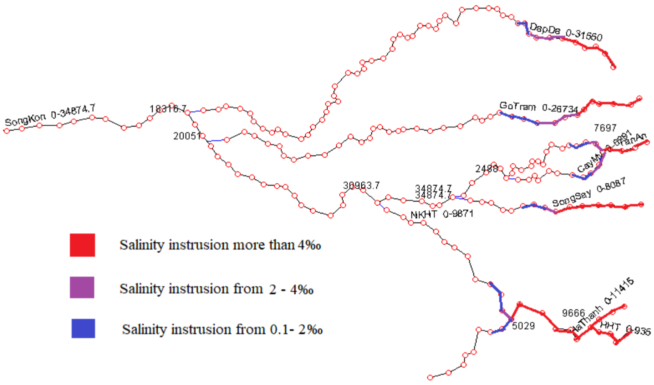

Fig 14: Salinity instrusion in 2020.

B. *Verification*

On the basis of the calibration parameters of hydraulic model, calculations using the observed data in 2021 are carried out. The result are in fig 15 and fig 16 that are good at NSE index.

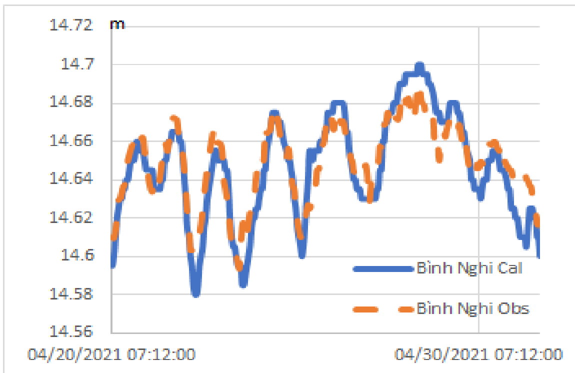

Fig 15: Calculated and observed water level at Binh Nghi station in 2021.

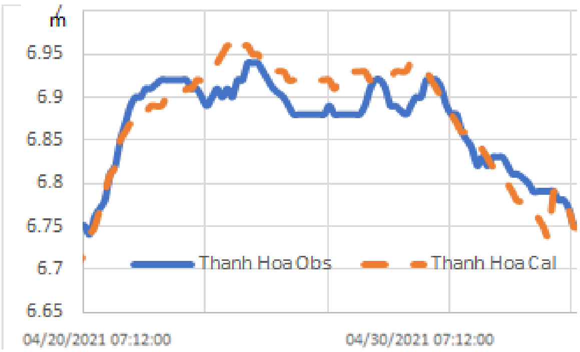

Fig 16: Calculated and measured water levels at Thanh Hoa station in 2021.

TABLE 3: NSE INDEX AT SOME STATIONS IN 2020.

Station	Binh Nghi	Thanh Hoa
NSE	0.74	0.7

NSE > 0.75 is a very good result., according to Moriasi et. al. [3].

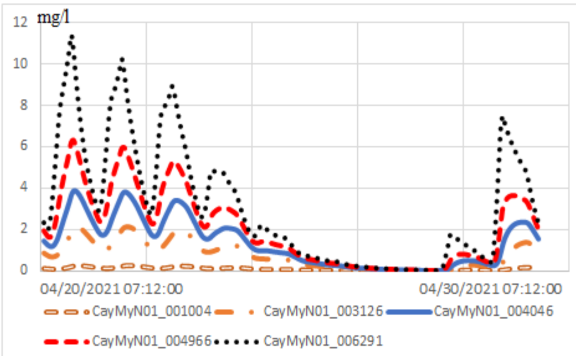

Fig 17: Salinity on Kone- Ha Thanh in 2021 at Cay My.

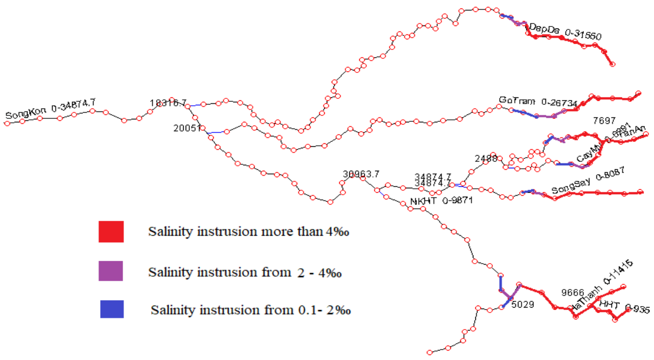

Fig 18: Salinity instrusion in 2021.

C. Scenarios calculation

To estimate effects of salinity intrusion in dry season through operating Van Phong Dam, we calculated two scenarios in comparison with the 2021 dry season. Scenario 1: increase the outlet discharge of Van Phong in 2021 by 100 m^3/s. Scenario 2: reduce the outlet discharge of Van Phong in 2021 by 100 m^3/s.

There are 5 river estuaries in the reseach area, the authors concentrated on saltility instrusion at Cay My estuary, near Phuoc An commune, to study the scenarios that have been proposed.

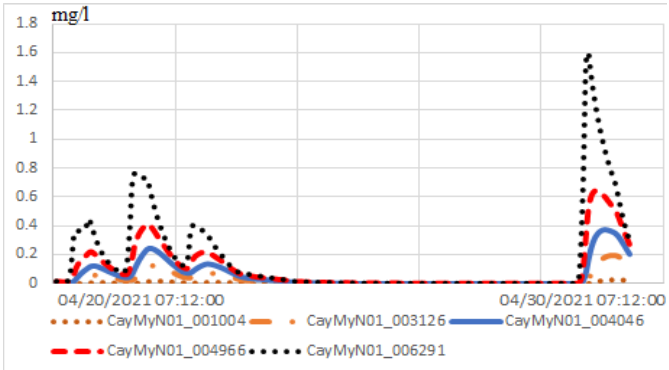

Fig 19: Salinity in scenario 1 at Cay My.

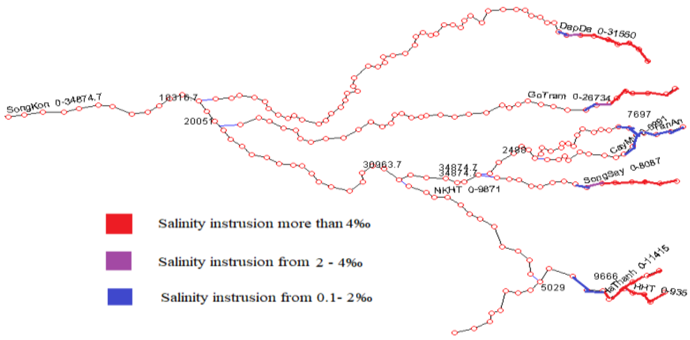

Fig 20: Salinity instrusion in scenario 1.

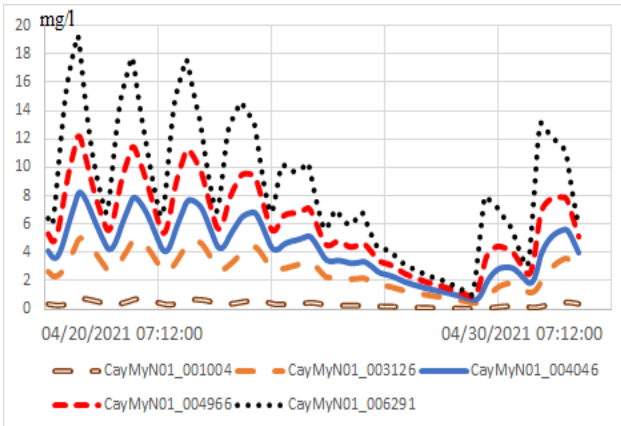

Fig 21: Salinity in scenario 2 at Cay My.

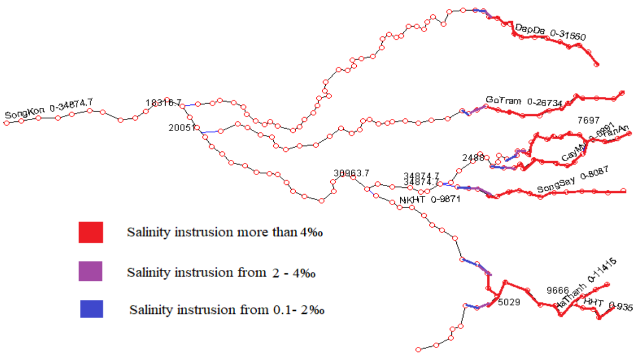

Fig 22: Salinity instrusion in scenario 2.

IV. CONCLUSION

The authors have built a set of hydrology and hydraulic models combined with a saltwater intrusion calculation module to calculate salinity intrusion scenarios during the dry season of 2020 and 2021. This models has been updated with the latest terrain, data to calibrate and verify the models with good results. Basing on set of parameters founded, the authors has built two scenarios that are suitable with reality, the 2021 dry season data, this is equivalent to the multi-year average in the dry season considers as base scenario.

TABLE 4: COMPARISON OF SALINITY INTRUSION

(more than 4mg/l) between scenarios at river estuaries.

Station	Salinity Instrusion(Km)		
	Scenario 1	2021	Scenario 2
Cay My	0.00	3.17	5.28
Dap Da	3.55	6.29	8.21
Go Tram	3.69	4.87	4.88
Ha Thanh	3.34	5.00	8.09
Song Say	3.00	4.03	8.21

The calculation results indicate that if the outlet discharge of Van Phong Dam is about 100 m3/s higher than íts outlet discharge in 2021 (scenario 1) will reduce the sality intrusion from 3-6 km. In case the flow of Van Phong dam decreases by 100 m3/s compared to the multi-year average (scenario 2), salinity intrusion will go 2-4 km farther into the river than in dry season 2021.

V. References

[1]. Báo cáo đánh giá rủi ro lưu vực sông Kone - Hà Thanh, dự án quản lý thiên tại Việt Nam (VN-Haz/WB5) 2017-2019.

[2]. Đề tài cấp Nhà nước KC-08-13 (2004), Báo cáo tổng kết đề tài: “Nghiên cứu cơ sở khoa học cho các giải pháp tổng thể dự báo phòng tránh lũ lụt ở đồng bằng sông Hồng”.

[3]. Moriasi, D.N.; Arnold, J.G.; Van Liew, M.W.; Binger, R.L.; Harmel, R.D.; Veith, T. “Model evaluation guidelines for systematic quantification of accuracy in watershed simulations”. Trans. ASABE 2007, 50, 885–900.

[4]. Nguyễn Chính Kiên, Nguyễn Thị Hằng. “Thử nghiệm một số phương pháp số giải bài toán ước tính thông số tối ưu cho mô hình thủy văn”, Hội nghị 45 năm thành lập Viện Hàn lâm Khoa học và Công nghệ Việt Nam.

[5]. Nguyen Chinh Kien, Dinh Van Manh and Hoang Van Lai (2014), Evaluation of salinity intrusion in the Southwest coastal zone of Vietnam, ICEMA3, HaNoi.

The 6th International Conference on Engineering Mechanics and Automation (ICEMA 2021)
Hanoi, November 14, 2021

Study on the influence of period and wave amplitude on the output power of linear generator by numerical methods

Huy Diep Do
Faculty of Engineering Mechanics and Automation
University of Engineering and Technology, Vietnam National University Hanoi
Hanoi, Viet Nam
diepdh@vnu.edu.vn

The Ba Dang
Faculty of Engineering Mechanics and Automation
University of Engineering and Technology, Vietnam National University Hanoi
Hanoi, Viet Nam
badt@vnu.edu.vn

***Abstract*: Wave energy conversion is a very important and interesting research field in Vietnam. In the early research work, an experimental permanent magnet linear generator was developed and researched. In this article, we used a method that combines Ansys numerical simulation with the MatlabSimulink program to study the power output of a linear generator using multiple dual Halbach magnet arrays. The results show that the simulation method helps to find the appropriate structure and design parameters to obtain the maximum system power output and efficiency. With the help of the MatlabSimulink program, we can study the influence of wave period and amplitude on power output, therefor we can choose suitable working conditions for the wave energy system.**

Keywords: wave energy conversion, linear generator, Halbach arrays, Matlab-simulink

I. INTRODUCTION

In the current global fight against climate and environmental changes, research into renewable energy resources to meet the rapidly growing energy demand plays a decisive role. Among the renewable energy sources, the ocean waves have the greatest power density, which can be many times higher than those of sun, wind and others (Czech and Bauer, 2012). In addition, Farrok et al. (2020) in a recent in-depth review indicated that ocean wave energy is readily available at any location in the ocean, either offshore or on the coast along the coastlines, with a total usable power of 1-10 TW, which is approximately 50 to 150 kW of power on one meter of wavefront and a resource of around 1,170 TWh / year could be harvested worldwide. As highlighted and discussed by these authors, great efforts have been made worldwide with different technological approaches on different scales, both in research and in production, in order to achieve high goals in the field of energy conversion of sea waves. These authors have also shown that while oceanic wave energy (OWE) stores a considerable amount of energy, its installed capacity so far is negligible compared to other RERs, and energy generation from OWE is still in its early stages and extensive research is required to find it out to make it fertile like wind and solar power plants. For a long time, at least since the first attempt by Pierre-Simon Girard in 1799 (Clment et al. (2002); Christine Miller (2004)). Indeed, the extraction of ocean wave energy has attracted quite a broad and especially recently rapidly growing interest around the world. This area has become one of the fastest growing research areas in the last few decades.

Among the previously developed and validated technologies for electrical energy generation from ocean wave energy that have been developed and validated so far, permanent magnet excited linear generators have proven to be advantageous and advantageous properties as directly driven wave energy transmission devices (Liu Z. (2020); Trapanese, M. (2017)). Various designs of permanent magnet linear generators, also with Halbach magnet arrays, have been intensively developed and investigated in recent years, among other things to increase performance and efficiency (Jun J., (2016); Rezaeealam, B. (2017)). It is believed that modeling tools can provide a powerful and reliable means of optimizing various structural, manufacturing, and operating parameters in order to achieve the best efficiency and performance of practical systems.

In Vietnam, research on wave energy conversion is still at a very early stage. Recently, Ba D.T. et al. (2015) designed, manufactured and tested an experimental linear generator system with a permanent magnet translator. The results have shown adequate performance of the system. However, the efficiency achieved was still quite low. It turned out that the magnet structure was not optimally designed and constructed, which led to inadequate magnetic field strength and flux distribution and thus to an undesirable high level of efficiency. In this study, we present a simulation-based study to obtain optimized parameters to improve the magnetic field strength and magnetic flux distribution of the linear generator using a six-sided dual Halbach permanent magnet array that follows the structure previously built in the VNUs project QG14.01 system to further improve the efficiency and performance of the system. Then the wave period and amplitude are changed to see the output power of the linear generator variation.

II. NUMERIACAL SIMULATION OF LINEAR GENERATOR

A. Magnetic field inside linear generator

The magnetic field distribution in the unit is numerically determined based on the Laplace and Poisson equations applied to the as constructed PM arrangement. In this section, a magnetic field analysis is conducted based on the geometric dimensions of the magnet configuration, from which appropriate dimensions of the magnet arrangement can be selected to optimize the magnetic flux density within the generator. Figure 1 shows the longitudinal section of the linear generator under this investigation. The generator space under study as shown in Figure1 is divided into two regions based on the magnetic field configuration in the arrangement of the permanent magnets. The air gap or the free space inside the inducting coil with the permeability μ_0 is referred to as Region 1. Region 2 represents the volume of the installed rare-earth magnets. The correlation between the magnetic field intensity $\boldsymbol{H}$ (in A/m) and the magnetic flux density $\boldsymbol{B}$ (in Tesla) is defined by the magnetic fields in Regions 1 and 2 as follows:

$$\boldsymbol{B}_1 = \mu_0 \boldsymbol{H}_1, \quad (1)$$

$$\boldsymbol{B}_2 = \mu_0 \mu_1 \boldsymbol{H}_2 + \mu_0 \boldsymbol{M}, \quad (2)$$

where μ_0 is the free space permeability with a value of 4.10^{-7} H/m, μ_1 is the relative permeability of the permanent magnets, $\boldsymbol{M} = \boldsymbol{B}_{rem}/\mu_0$ in A/m is the magnetization, and $\boldsymbol{B}_{rem}$ is the remanence.

The Gauss law for the magnetic flux states that $\nabla \cdot \boldsymbol{B}_i = 0$, where i = 1,2. With the magnetic vector potential $\boldsymbol{A}_i$, we obtain

$$\boldsymbol{B}_i = \nabla \times \boldsymbol{A}_i, \quad (3)$$

Therefore, the Gaussian equation can be written as

$$\nabla \times \boldsymbol{B}_i = -\nabla^2 \boldsymbol{A}_i, \quad (4)$$

For Region 1, the combination of Maxwell equation and (1) gives

$$\nabla \times \boldsymbol{B}_1 = \nabla \times \mu_0 \boldsymbol{H}_1 = \mu_0 \boldsymbol{J}, \quad (5)$$

Substituting (4) into (5) yields $\nabla^2 \boldsymbol{A}_1 = -\mu_0 \boldsymbol{J}$ where $\boldsymbol{J}$ (A/m^2) is current density in the field. In permanent magnet $\boldsymbol{J}$ = 0, therefore the Laplace equation for Region 1 is obtained as

$$\nabla^2 \boldsymbol{A}_1 = 0, \quad (6)$$

For Region 2, the combination of Maxwell equation and (2) gives

$$\nabla \times \boldsymbol{B}_2 = \mu_0 \mu_1 \boldsymbol{J} + \mu_0 \nabla \times \boldsymbol{M}, \quad (7)$$

Similarly, (4) and (7) yield the Poisson equation for Region 2

$$\nabla^2 \boldsymbol{A}_2 = -\mu_0 \nabla \times \boldsymbol{M}, \quad (8)$$

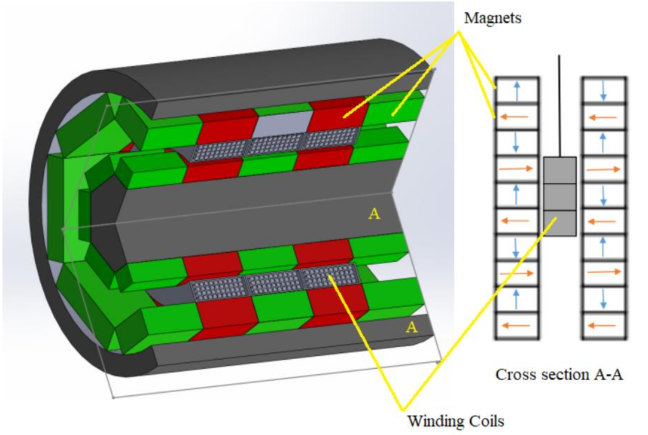

Fig. 1. Longitudinal section of the linear generator

Numerical calculation methods or analytical techniques are usually employed to solve Laplace and Poisson equations. The finite element method, however, can provide more detailed results than that of analytical calculations, especially in solving the field problems of the objects with complicated shapes. It is also known that simplified 2-D representation can also provide acceptable results in solving the problem for symmetrical objects with a simple shape.

In the previous works (Ba D.T., 2015), computational simulations were carried out by the finite element method (FEM) using the FlexPDE tool. The magnetic material used in the system was NdFe35 permanent magnets with the characteristics given in Table 1. In this work, the approach of 2-D representation for the six-sided dual Halbach permanent magnet array structure is applied with the same parameters of the magnet.

TABLE 1. SPECIFICATIONS OF THE MAGNETIC MATERIAL

Magnet's Specifications	Parameter
Relative permeability	1.0997785406
Magnetic coercivity (A/m^2)	-890000
Bulk conductivity (Siemens/m)	625000
Remanence Br (Tesla)	1.23

Two configurations of magnets in the generator were used to verify the simulation process. The first one is the magnet arrangement, shown in the recent work "Numerical Simulation and Experimental Analysis for a Linear Trigonal Double-Face Permanent Magnet Generator Used in Direct Driven Wave Energy Conversion," by Ba D.T., Anh N.D. and Ngoc P.V. in 2015 and the second is the dual Halbach-type magnet arrangement shown in Figure 2.

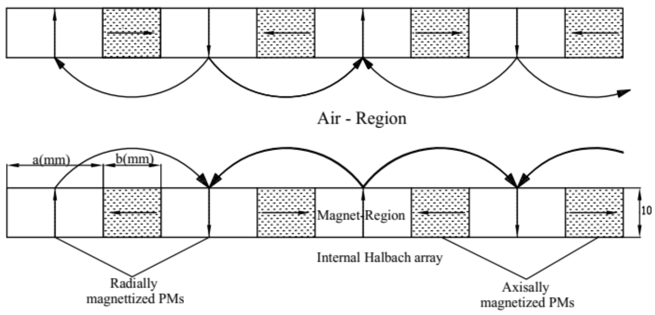

Fig. 2. Scheme of dual Halbach arrays magnets.

There was only one array of magnets which are along the Y – axis polarized with 7 mm space apart in configuration 1 and the dimensions of the used magnets were 25 mm long (along the X – axis) and 10 mm thick. The magnets in the configuration 2 are arranged in the dual Halbach array structure as shown in Fig. 2. As seen, in this configuration two types of permanent magnets are placed one after the other: the ones vertically polarized along the Y – direction are of the length a (in mm) and the ones horizontally polarized along the X – direction are of the length b (in mm), i.e. the latter magnets fill the free space of 7 mm between the magnets in the previous configuration 1. Further it is to note that the distance between the two sets of the magnets opposite to each other in the second configuration is 16 mm

Figure 3 shows the comparison of the magnetic field intensity calculation results for the two above described magnet configurations. It is clearly to see that by using the structure of Halbach arrays, the magnetic flux density inside the linear generator is increased. The blue-dot line shows the generator's magnetic flux density at the center line as reported in (Ba D.T., 2015), and the red line shows the generator's magnetic flux density when using the double Halbach array structure. The peak value of the magnetic field density at the center is found improved by about 10.8 percent, so an increase in the efficiency of the generator can be accordingly expected.

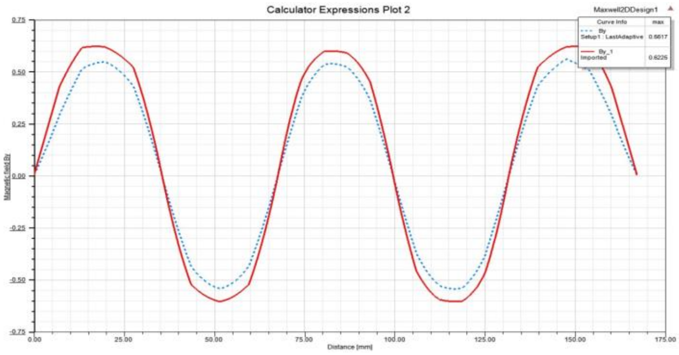

Fig. 3. Magnetic flux density at center of generator in two types

Figure 4 and Figure 5 in the following show the results of the simulation approach to obtain the overall magnetic field distribution in the tubular linear generator with the dual Halbach magnet array as described above. In these numerical computations, the following structure parameters of the Halbach magnet array were used: the Y – axially polarized magnets are 25 mm in length, X – axially polarized magnets are 7 mm in length. All the magnets in the arrangement were of the NdFe35 type providing Br = 1.23 Tesla and 10 mm in thickness.

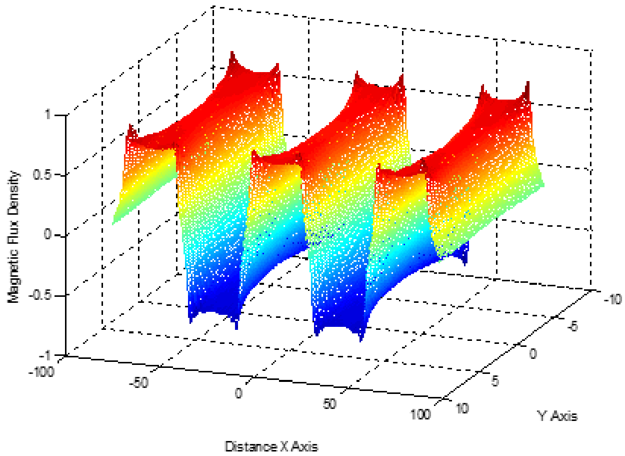

Fig. 4. Field intensity (By) contribution of Y – axially polarized magnets in the generator

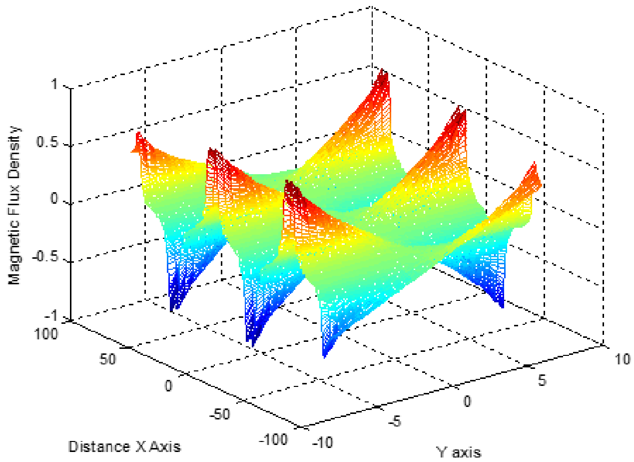

Fig. 5. Field intensity (Bx) contribution of X – axially polarized magnets in the generator

The overall magnetic flux density in the generator is established by the contributions from the different sets of permanent magnet blocks consisting of those polarized along the Y – axis and those polarized along the X – axis, arranged in the Halbach arrays. Based on the above shown considerations, the thickness of all individual magnets was first set at 10 mm for the calculations to obtain the total magnetic field flux density. The calculations were carried out first to find the maximal magnetic flux density in the dependence on the length a (in mm) of the magnet blocks polarized along the Y – axis (the vertical direction – varies from 10 mm to 40 mm) and the set length b (in mm) of the magnets polarized along the X – axis (the horizontal direction) and the results are shown in Figure 6 below for the case b = 10 mm.

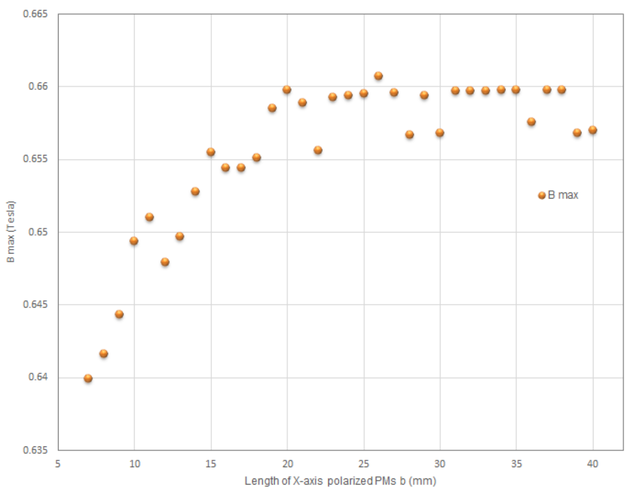

Fig. 6. Magnetic field intensity depending on the length a of the magnet blocks polarized along the Y – axis

As it is seen, the magnetic field intensity increases steadily with the increasing length of the magnet polarized in the Y – direction and asymptotically approaches a visible saturation at the lengths over 30 mm. Considering these results, for the next calculations to study the variation of the magnet field intensity with the length of the horizontally polarized (along X – axis) magnet blocks, the length polarized along the Y – axis was set at a = 32 mm. The results are depicted in Figure7. It is also clearly seen in the figure, the field intensity approaches the saturation when the values of b are increased to beyond 20 mm.

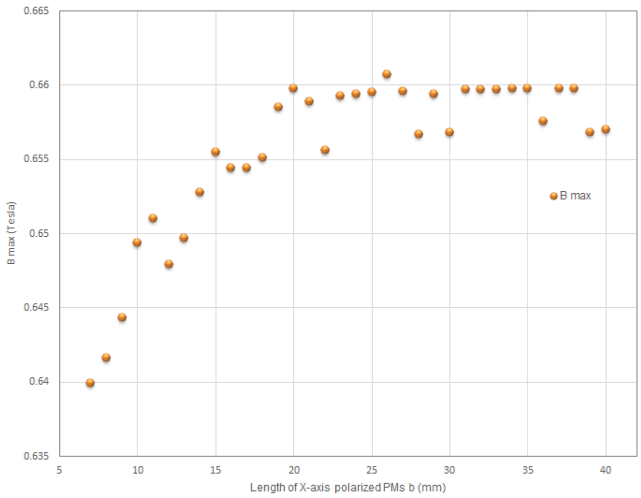

Fig. 7. Magnetic field intensity depending on the length b of the magnet blocks polarized along the X-axis

Based on these findings, for further considerations in this work the dimensions of the magnet blocks of the Halbach arrays are chosen as a = 32 mm for those polarized along the Y – axis and b = 25 mm for those polarized along the X – axis at the fixed thickness of 10 mm.

To calculate the magnetic flux density distribution in the as-designed generator the frequency of the magnetic flux density distribution is considered as symmetrical with the central axis onward along the X – direction and with the circulating period as well. Considering the field intensity distribution profile of the actual generator design shown in Figure3 above, a function as a numerical approximation is proposed in order to numerically calculate the magnetic field flux distribution and then the output power of the generator system. The magnetic field flux distribution along the X – axis of the as designed linear generator can be accounted for by the following expression:

$$\varphi_x(y) = \hat{\varphi} \sin\left(\frac{2\pi}{\lambda} x\right), \qquad (9)$$

In this equation, $\hat{\varphi}$ is the maximal average value of the intensified magnetic flux, which is counted from the center surface of the external magnet and λ is the longitudinal wavelength of the periodical fluctuation of the magnetic field strength determined by the construction of magnet arrays. As a result, the magnetic flux distribution can be interpreted as the combination of the sine and cosine functions in the equation (10) below

$$\varphi_x(y) = \hat{\varphi} \sin\left(\frac{2\pi}{\lambda} x\right) = \sum \{A_n \sin(n\omega x) + B_n \cos(n\omega x)\}, \qquad (10)$$

The comparison between the actual field intensity distribution in the generator and the calculated distribution by means of the approximation function is shown in Figure 8 below.

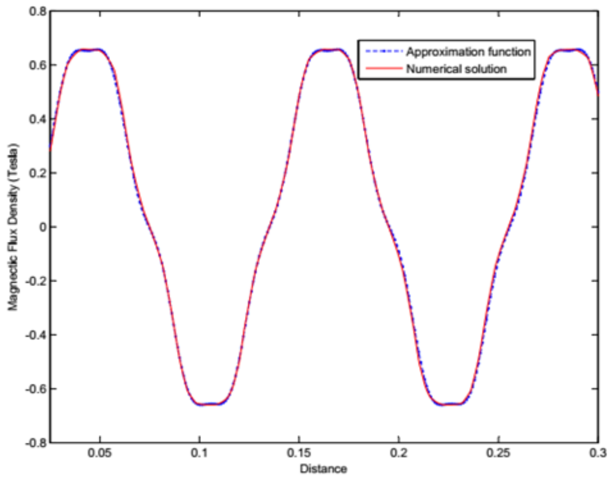

Fig. 8 Numerical solution and approximation function of magnetic field

The maximum value as well as the special distribution of the magnetic field strength is reproduced satisfactorily by the numerical approximation calculation with the as-described solution function. The further investigation of electromotive energy output of the generator will follow with this numerical profile of the magnetic field.

B. *Energy output of the linear generator*

In order to derive the electromotive force along with the linear generator's power output, a program called Matlab-simulink has been designed and carried out.

To this purpose the relative motion of the inductive coil is considered in relation to the first buoy. The magnets, however, are connected to the generator housing and the second buoy. With the parameters given above, the total displacement, i.e. the relative motion between these two components is calculated, using $x(t) = s_1(t) - s_2(t)$, where $s_1(t)$ is defined as the displacement of the very first buoy, while that of the second one is defined as $s_2(t)$. The solution of this motion problem is made easier by considering the displacement of the magnets along with the relative motion of the inductive coil as a periodic oscillation caused by the up–and–down movement of the wave by using the equation:

$$x(t) = s_1(t) - s_2(t) = d \cdot sin(\omega_m t),$$

where d is the wave oscillation amplitude, ω_m is the angular frequency that is also included to the collector buoy oscillation.

The distribution of the magnetic flux intensity coming from the magnet arrangement and also the alternator opposed to the oscillations of the inductive coil, therefore, are formulated as below:

$$\varphi_x = \hat{\varphi}\sin\left(\frac{2\pi}{\lambda}x(t)\right) = \sum_{n=1}^{\infty}\left(A_n \sin\left(nwx(t)\right) + B_n \cos\left(nwx(t)\right)\right), \tag{11}$$

The total amount of the magnetic field flux generated by the movement out of the field is given by: $\Phi_B = \int \varphi_x \dot{x} dt$. As a result, in a coil of N windings, as stated by the Faraday law, an electromotive force is generated, which is expressed as:

$$\varepsilon = -N\frac{d\Phi_B}{dt}, \tag{12}$$

For every chosen volume of the magnet array as well as the spatial period of the translator movement through that volume, the cross-section field of the inductance varies, and thus the adjustment of the wire diameter and the number of the windings affects the amount of voltage induced in the coils.

Considering the generator design, the cross-section of the inductive coil relative to the magnetic field distribution should be adjusted accordingly to the length of the magnet array as well as its repeating length (i.e. the spatial period of the magnetic field intensity) in order to ensure that one this spatial period corresponds to three phases of the induced electric voltage in the inductive coil. The diameter of the conductor wire to be used for winding the coil and the number of windings can be appropriately accounted from this consideration, using the following expression:

$$N = round(l/d_{dd}) \times round(p/d_{dd}),$$

where l is the length of the magnet array, p is the spatial period of the magnetic field intensity, d_{dd} denotes the diameter of the winding wire and N denotes the number of windings. The math *round* function returns the value of a number rounded to the nearest integer (see Figure 9).

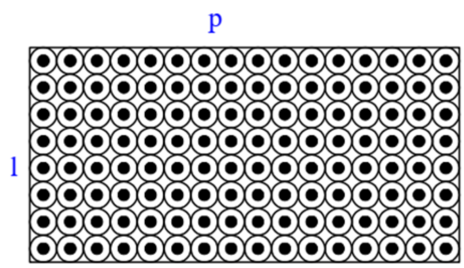

Fig. 9 Cross section of winding coil

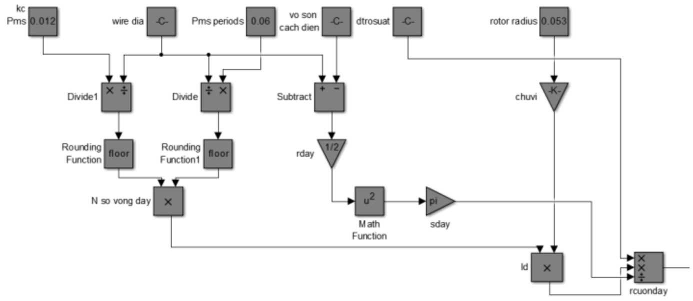

Fig. 10. Block diagram for the calculation of the number of windings and the resistance of an inductive coil

The expression $R = \rho\ \frac{l_d}{S_d}$ is applied to calculate the coil resistance (R), with ρ denoting the conductor material specific resistivity, l_d denoting the conductor wire length, and S_d denoting the wire cross-section (see Figure 10).

Thereupon, the inductance of the coil denoted with L (measured in Henry) is calculated using the expression:

$$L = \mu_o.\mu.N^2.S/l_{coil}$$

In this expression, the coil cross section is defined as S, μ_0 is the permeability coefficient of the air space, μ is the coil core permeability, N is the number of windings of the coil, and l_{coil} is the length of the coil (see Figure11)

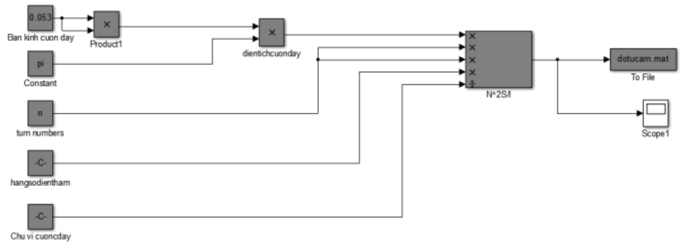

Fig. 11. Block diagram of the coil inductance

Following the Kirchhoff Law for the electric circuit, the equation accounting the electric current in the circuit arose in the inducting coil when the generator is connected to a normal external resistance has the following form. (Figure 12):

$$L\frac{dI_L(t)}{dt} = -\left(\frac{R_L + R_i}{L}\right)R_L I_L(t) + \frac{R_L e(t)}{L}, \tag{13}$$

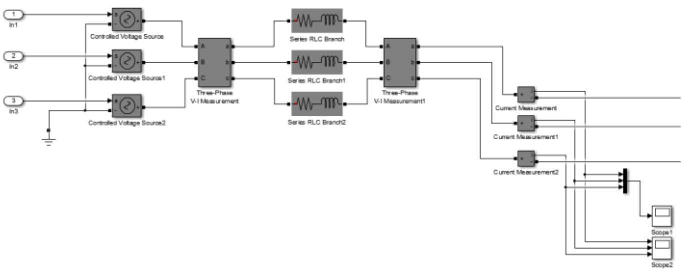

Fig. 12. Diagram generator with external circuit

The design parameters of the linear generator are given in the Table 2 below.

TABLE 2. DESIGN OF THE LINEAR GENERATOR

Specifications Of The Linear Generator	Parameters
Magnet sizes (mm)	10x32x50 10x25x50
Cross section of winding coil (mm)	14x38
Wire's diameter (mm)	0,7
The resistivity of conductor (10^{-7} Ω.m)	1,72
Rotor's radius (mm)	53
Coil numbers	3
Magnet sides	6
Relative permittivity (10^{-7} T.m/A)	4π

The relative motion of the translator is caused by the incident wave and is considered based on the parameters from both the inductive coil and the magnet array (see Table 3).

TABLE 3. INCIDENT WAVE PARAMETERS

Waves Characteristics	Parameter
Amplitude wave (m)	0.5
Wave period (s)	5

With the considerations and the generator design parameters as explained and given above, the simulation approach to study the performance of the generator was carried out using the Matlab-Simulink program. Results are shown in Figures. 13 (a,b,c) below. Figure13a presents the currents in the three individual coils, Figure 13b shows the total electromotive forces in the three corresponding coils, and Figure13c demonstrates the resulting power characteristics registered on the external loads

Fig. 13a. Currents sperately in 3 winding coils

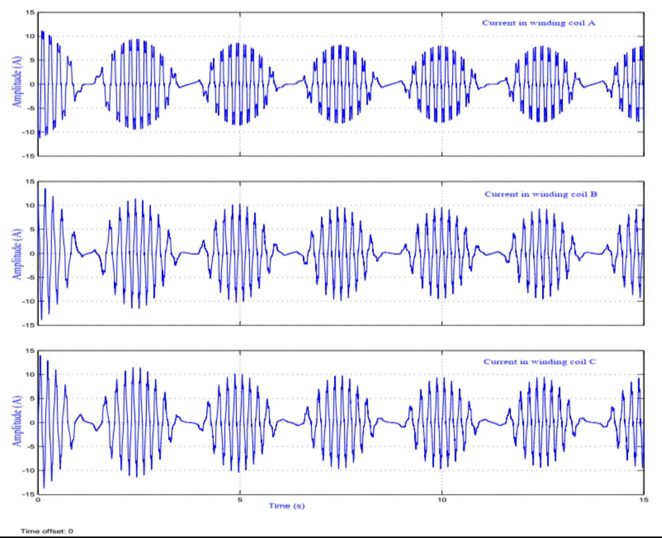

Fig. 13b. The total electromotive forces in winding coils

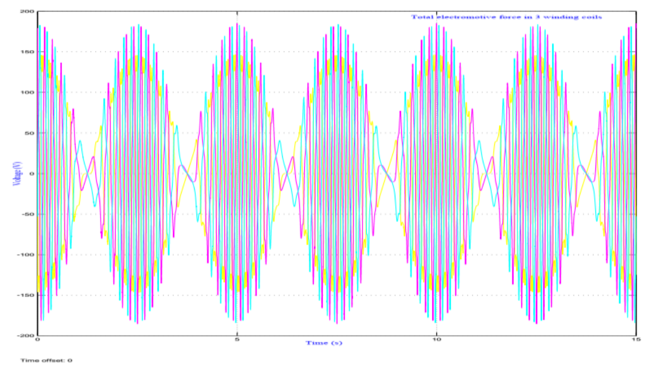

Fig. 13c. Power output characteristics of the generator

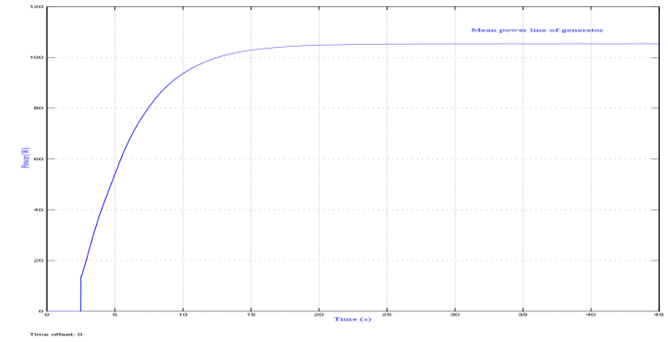

Fig. 13. Result of the simulation: a) Electric induced currents in the individual winding coils b) The total electromotive forces in winding coils c) The power characteristics of the as designed generator

When we take a deep look over Figure13, the estimated outcome has pointed out the streams within three coils through Fig.13a. Moreover, the total amount of electromotive forces within the three coils are also shown in Fig.13b. Finally, Fig.13c demonstrates the turnout power on outsider loads.

III. INFLUENCE OF WAVE PERIOD ON OUTPUT POWER

With the assumptions set out above, the problem is simplified with the oscillation of waves acting on the buoy according to the simple oscillation formula:

$$x(t) = s_1(t) - s_2(t) = d \cdot sin(\omega_m t),$$

As is known, the wave frequency ω_m is calculated through the wave period according to the relationship

$$\omega = 2\pi f = \frac{2\pi}{T}$$ where T is the wave period.

TABLE 4. GENERATOR POWER DEPENDS ON THE PERIOD OF WAVE OSCILLATION

Wave periods (s)	Power (W)
2.5	421.7
3	296.7
3.5	219.2
4	167.7
4.5	130
5	105.4
5.5	85
6	75
6.5	65
7	57
7.5	50
8	45

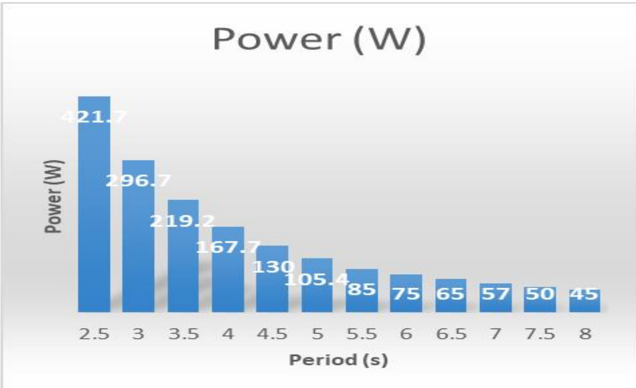

Fig. 14. Dependence of generator output power with wave period

From the table 4 and figure 14 results can be drawn the conclusion, with the sea-area with continuous wave, short period continuously, the generator output energy will be more obtained, with the sea area with larger wave period, the output power will be higher. the efficiency of the energy converter decreases.

IV. INFLUENCE OF WAVE AMPLITUDE ON OUTPUT POWER

Similar with the section about, the incident wave amplitude is varied with values to see how output power changing. Using formula $x(t) = s_1(t) - s_2(t) = d \cdot sin(\omega_m t)$, we have the results when the period is 5 second.

TABLE 5. GENERATOR POWER DEPENDS ON THE AMPLITUDE OF WAVE

Wave amplitudes (m)	Power (W)
0.2	17
0.3	37.9
0.4	67.5
0.5	105.4
0.6	151.8
0.7	206.6
0.8	270

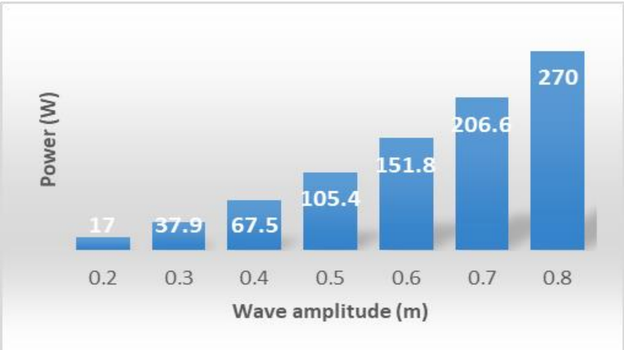

Fig. 15 Dependence of generator output power with wave amplitude

The results of Figure 15 show that, the stronger the amplitude of the waves, the higher the power received at the output of the generator. For waves with small oscillation amplitudes, the efficiency of the device will be lower.

V. CONCLUSION

We have applied Ansys Simulation in combination with Matlab-Simulink program to study in detail the parameters affecting the performance and output power of a permanent magnet linear generator for wave energy conversion. We have proposed a method using Hallbach magnet arrays to improve the output of ironless linear generator. By our simulation study using the program Matlab-simulink, it is shown that the flux density is greatly enhanced by the suitable structure of the Halbach array and thus, the maximum output power can also be optimized by induction coil construction. In addition, the simulation results also show that the wave energy converter operates highly efficiently in the sea areas with short wave period and less effective in the sea with long wave period. And for places with large waves and strong fluctuations, the device works more effectively.

REFERENCES

[1] Czech, B.; Bauer, P. (June 2012). "Wave Energy Converter Concepts: Design Challenges and Classification", *IEEE Industrial Electronics Magazine*, 6 (2): 4–16, doi:10.1109/MIE.2012.2193290

[2] Omar Farrok, Md Rabiul Islam and Wei Xu (2020), "Recent Progress in Electrical Generators for Oceanic Wave Energy Conversion: *IEEE Access*, vol. 8, pp. 138595-138615, 2020, doi: 10.1109/ACCESS.2020.3012662.

[3] Clément A. et al. (2002). "Wave energy in Europe: current status and perspectives". *Renewable and Sustainable Energy Reviews*. 6 (5): 405–431. doi:10.1016/S1364-0321(02)00009.

[4] Christine Miller (August 2004). "Wave and Tidal Energy Experiments in San Francisco and Santa Cruz". [online] https://www.outsidelands.org/wave-tidal.php (Accessed 27 April 2021).

[5] Liu Z., Zhang R., Xiao H. and Wang X. (2020) "Survey of the mechanisms of power take of (PTO) devices of wave energy converters". *Acta Mech. Sin.* 36, 644–658. https://doi.org/10.1007/s10409-020-00958-z

[6] Trapanese, M., Cipriani, G., Corpora, M. and Di Dio, V., (2017) "A general comparison between various types of linear generators for wave energy conversion," in *IEEE OCEANS 2017-Anchorage*, Anchorage, AK, USA, pp. 1–5.

[7] Jun J., Shin Y. and Kim J.H. (2016). "Linear electric generator with Halbach array to self-charge a smartphone". *Journal of Vibroengineering*, Vol. 18, Issue 1, 2016, p. 587-594.

[8] Rezaeealam, Behrooz. (2017). "Permanent Magnet Tubular Generator with Quasi-Halbach Array for Free-Piston Generator System". *International Journal of Power Electronics and Drive Systems* (IJPEDS). 8(4). 1663. Doi:10.11591/ijpeds.v8.i4.pp1663-1672.

[9] Ba, D.T., Anh, N. D. and Ngoc P. V., (2015) "Numerical Simulation and Experimental Analysis for a Linear Trigonal Double-Face Permanent Magnet Generator Used in Direct Driven Wave Energy Conversion," in *Procedia Chemistry* Volume 14, 2015, pp 130-137. ISSN: 1876 – 6169

Effect of the Mesh Types on the Prediction of Flow Aerodynamic around Airfoil

Tam Hoang Van
VNU - University of Engineering and Technology,
Vietnam National University (HaNoi)
144 XuanThuy, CauGiay, HaNoi, VietNam
17020415@vnu.edu.vn

Anh Dinh Le
School of Aerospace Engineering, VNU-University of Engineering and Technology,
Vietnam National University (Hanoi)
144 Xuanthuy, Caugiay, Hanoi, Vietnam
Corresponding author: anh.ld@vnu.edu.vn

***Abstract*: Recently, several mesh types have been developed for numerical application in industry such as the structured mesh, the triangle mesh, the Chimera mesh, and the polyhedral mesh. Each of the mesh types has its advantages in handling complex geometries, computation time, convergence property, and numerical accuracy. This study aims to investigate the effect of those mesh types on the accuracy of the numerical results. The flow aerodynamic around the NACA0012 hydrofoil is selected for validation. The numerical result is performed using the commercial software Ansys Fluent 2019R3 and is quantitatively compared with the experimental data for a wide attach angle. As the result, the discrepancy between the numerical and the experimental data of the lift, drag, and skin friction coefficients increases as the attack angle increases for all mesh types. The structured mesh produces the results that are closest to the experiment. The polyhedral mesh shows the fastest convergence but the results are not as accurate as in the structured mesh. On the other hand, neither numerical results nor computational time is insufficiently produced by using the triangular mesh.**

Keywords: structured mesh, triangle mesh, polyhedral mesh, chimera mesh, NACA0012, Fluent

I. INTRODUCTION

Nowadays, Computational Fluid Dynamics (CFD) becomes an effective tool in the design and analysis of many industrial applications such as aerospace engineering, chemical engineering, thermal engineering, turbo-machine, etc. Although having some advantages against the experiment, the numerical accuracy is highly influenced by many factors such as the numerical scheme, boundary condition, numerical model, and the mesh quality. Along with these factors, the quality of the mesh has a significant impact on the numerical behavior such as the simulation time, the convergent rate, and the accuracy, which are known to be influenced by the aspect ratio, the cell skewness, or the orthogonal property, etc.

Recently, several mesh types have been introduced to associate with the complex geometry and can be divided into four types of mesh: structured mesh, the triangle mesh, chimera mesh, and polyhedral mesh. Different types of mesh have different element shapes and ways to link elements together. So, each of them has its advantages and disadvantages (mesh time, geometry processing capabilities, solver convergence level, mesh quality and resolution accuracy, etc.)

The structured mesh includes the quadrilaterals elements in 2D and hexagons elements in 3D. The structured mesh has a simple algorithm and is applicable for both the finite difference method (FDM) and the finite volume method (FVM). This type of mesh is highly efficient, has better convergence [3][4]. However, generating a structured mesh for complex geometries is a time-consuming task as it may be necessary to manually subdivide the domain into multiple blocks depending on the nature of the geometry. Triangle mesh contains the triangle elements in 2D and the tetrahedral in 3D simulations. The triangle meshing process consists of two basic steps: creating nodes and defining connections between these nodes. Flexibility and automation make triangle mesh become an advantageous choice for meshing the complex geometry configuration although the accuracy is not as good as structured mesh due to the presence of skewed elements in sensitive areas such as layers boundary [5]. Recently, another alternative to triangle mesh is polyhedral mesh. Polyhedral meshes are converted from triangle meshes using commercial software (Ansys Fluent). They are linked by more adjacent nodes and faces, which makes the gradient approximation better than triangle mesh [6]. In case the meshing process cannot handle in complex geometries, Chimera mesh was developed as a meshing simplification tool. The use of structured mesh is divided independently and overlapping. This allows flexibility in the selection of elements in each mesh [7].

In this study, the effect above mesh types on numerical accuracy is investigated. The flow around the NACA0012 hydrofoil is selected for numerical benchmarking using commercial computational fluid dynamics (CFD) software Ansys Fluent 20R2. The simulation is performed for the wide range of attack angles and the result is quantitatively compared with Larson's experimental data of aerodynamic behavior on the hydrofoil.

II. NUMERICAL METHODOLOGY

A. Numerical Method

In this study, the flow aerodynamics around the NACA0012 hydrofoil is numerically analyzed using commercial CFD software ANSYS Fluent 2020R2. The flow field assumes incompressible steady. Hence, the Navier-Stokes equations are expressed as follows [2]:

$$\frac{\partial \overline{u_i}}{\partial x_i} = 0 \tag{1}$$

$$\frac{\partial \overline{u_i}}{\partial t} + \frac{\partial \overline{u_i u_j}}{\partial x_j} = \frac{-1}{\rho}\frac{\partial \bar{p}}{\partial x_i} + \frac{\partial}{\partial x_j}\left(\nu \frac{\partial \overline{u_i}}{\partial x_j} - \overline{u_i' u_j'}\right) \tag{2}$$

In these equations, $\bar{p}$ is the mean pressure. Besides, $\bar{u}$ is the mean velocity and u' is the fluctuation velocity; the subscript i and j denote the component directions and ν is the kinematic viscosity of the fluid. In addition, $u_i' u_j'$ is the Reynolds stress tensor, determined by Boussinesq hypotheses. For the turbulent effect, Spalart - Allmaras turbulence model is selected. Detail of this model can refer in the Ansys Fluent theory guide [2].

B. Calculation Domain and Boundary Condition

Figure 1 describes the boundary conditions and the computational domain for this study. where the airfoil length is set to *D* with the starting point being the center of the *16D* diameter inlet arc and 12*D* from the outlet position. In this study, a NACA 0012 airfoil with chord length *D* = 1 m is used for simulation. The uniform velocity of 52 m/s that corresponds to Mach number of 0.15 and Reynolds number Re = 6 x 10^6, the turbulent intensity *I* = 0.022%, and the turbulent length scale *l* = 0.07*D* is used at the inlet. Atmospheric pressure is specified at the outlet boundary. The angle of attack is changed from 0^o to 19^o. The numerical results are compared with Ladson's experiment in terms of lift coefficient C_L, drag coefficient C_d, and pressure coefficient C_p [1]. In this study, steady flow is used in conjunction with the Pressure base Coupled method. The Second-order upwind method is used for momentum and turbulent equations. The Second-order method is used for the pressure equation.

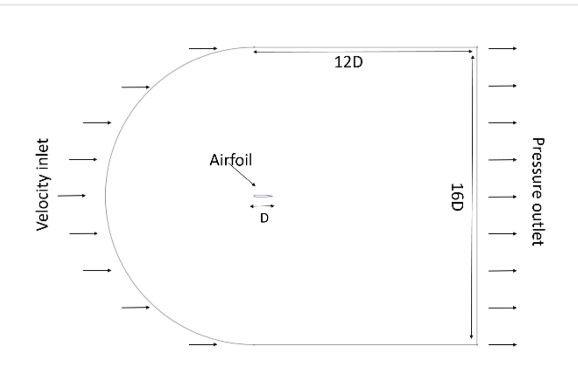

Fig. 1. Computational domain around airfoil NACA 0012

C. Mesh types

To investigate the effect of mesh on the numerical accuracy, four mesh types are performed, including the structured mesh, triangle mesh, chimera mesh, and polyhedral mesh. The mesh independence is performed for each mesh type. Then, the mesh of 296000 cells, 509770 cells, 328844 cells are used for the structured mesh, triangular mesh, chimera mesh respectively. The polyhedral mesh is converted from triangle meshes that have 285000 cells. The mesh detail in the simulation domain and around NACA0012 hydrofoil is shown in Fig.2 and Fig. 3.

For all mesh types, the mesh is clustered near the hydrofoil surface. The inflation mesh with 15 layers and the growth rate of 1.2 is generated. The first layer thickness is 0.000045 m to accurately predict the flow behavior in the boundary layer. In triangle mesh, polyhedral mesh, chimera mesh the cells are wrapped around the trailing edge resulting in the creation of few skewed cells inside the viscous padding at the trailing edge, while in structural mesh, the trailing edge has better mesh quality. The grid quality at the trailing edge is ideal in the structured mesh when compared to other meshes.

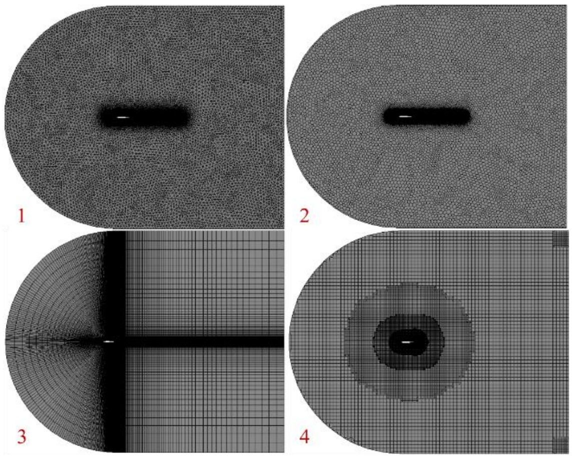

1/Triangle mesh *2/Polyhedral mesh*
3/Structured mesh *4/Chimera mesh*

Fig. 2. Mesh distribution in the domain

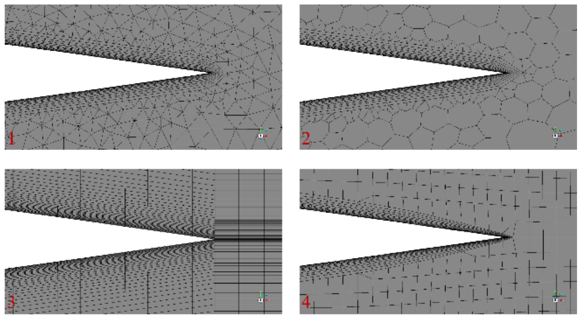

1/Triangle mesh *2/Polyhedral mesh*
3/Structured mesh *4/Chimera mesh*

Fig. 3. Mesh distribution near the trailing edge

III. RESULTS AND DISCUSSION

In this section, the effect of mesh on the numerical results is investigated through the comparison of flow aerodynamic parameters such as the lift coefficient C_L, the drag coefficient C_D, and the pressure coefficient C_P against the experimental data [8].

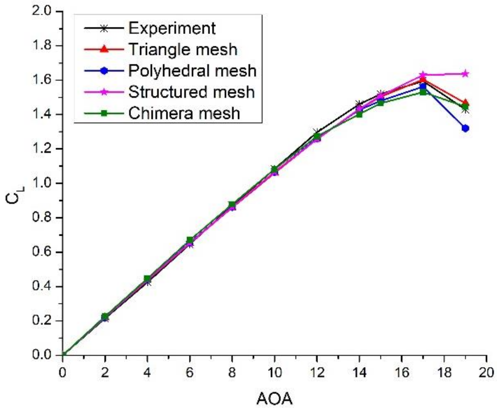

Fig. 4. Comparison C_L at a different angle of attack

Figure 4 illustrates the lift coefficient C_L between four mesh types and experimental data at different attack angles. A satisfactory prediction with experimental data reproduces by all mesh types at the attack angle of less than 10°. The discrepancy becomes large at the higher angle where the flow becomes stronger separation. The C_L decreases after the stall angle of around 17° and its tendency is predicted well by the triangle mesh, chimera mesh, and polyhedral mesh. On the other hand, this tendency is inaccurately predicted by the structured mesh.

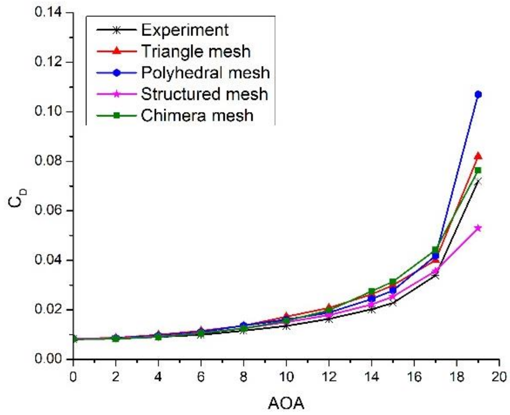

Fig. 5. Comparison C_D at a different angle of attack

Figure 5 depicts the drag coefficient between four mesh types and experimental data at different attack angles. The difference in the prediction of C_D becomes more clear at the attach angle greater than 10°. The experimental tendency is well predicted by all mesh types when the angle of attack is less than 10°. When the angle of attack is less than 17°, the structured mesh has the most accurate prediction but falls to predict the C_D at stall angle. At the same time, triangle and chimera mesh lead to better C_D results when the angle of attack is more than 17° while the polyhedral mesh is overestimated.

Figure 6 shows the pressure distribution on the NACA surface at different angles of attack (a) 0°, (b) 10°, and (c) 15°. A satisfactory prediction with Ladson's experimental data is produced by all mesh types. There is almost no difference in the predicted C_p between these meshes.

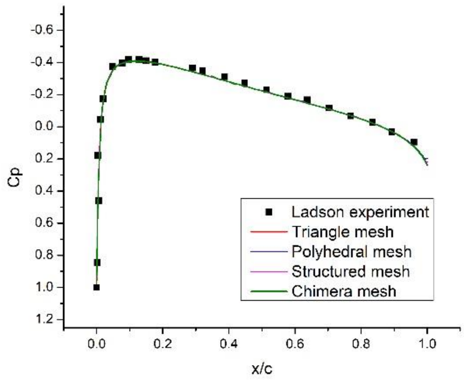

(a) 0^0

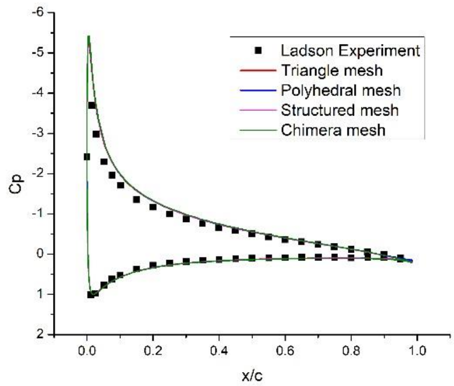

(b) 10^0

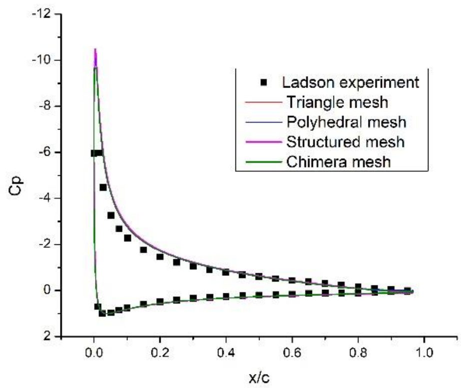

(c) 15°

Fig. 6. Comparison C_p at the angle of attack (a) 0°, (b) 10°, and (c) 15°

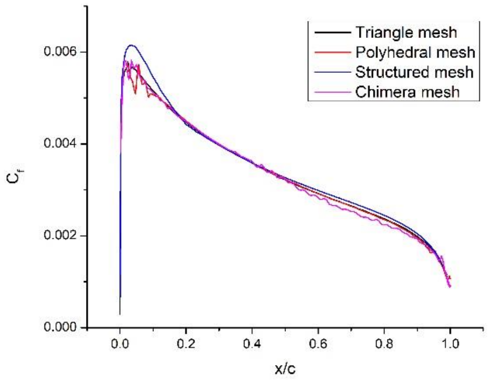

(a) 0^0

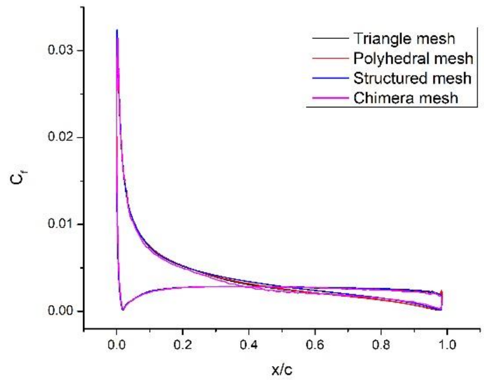

(b) 10^0

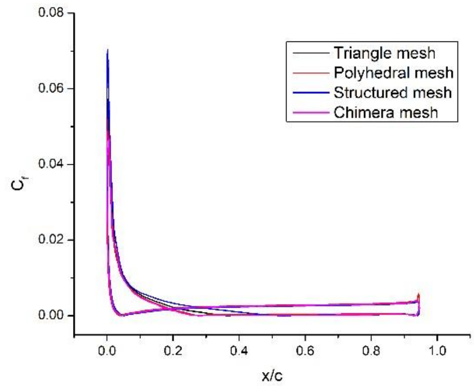

(c) 15^o

Fig. 7. Comparison C_f at the angle of attack (a) 0^o, (b) 10^o, and (c) 15^o

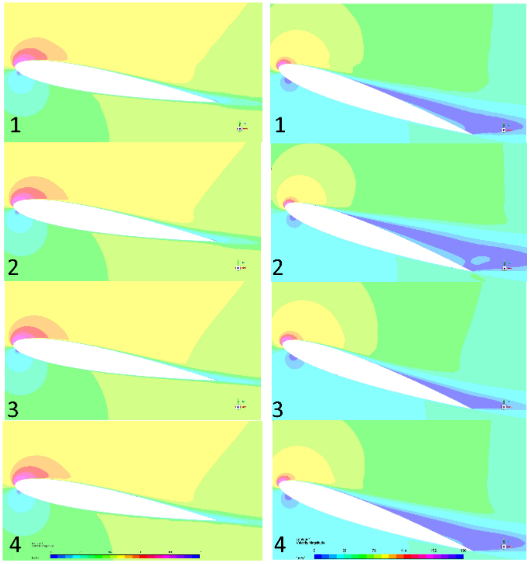

1/Triangle mesh *2/Polyhedral mesh*
3/Structured mesh *4/Chimera mesh*

Fig. 8. Flow velocity around NACA 0012 airfoil at the angle of attack 0^o, 10^o, and 19^o

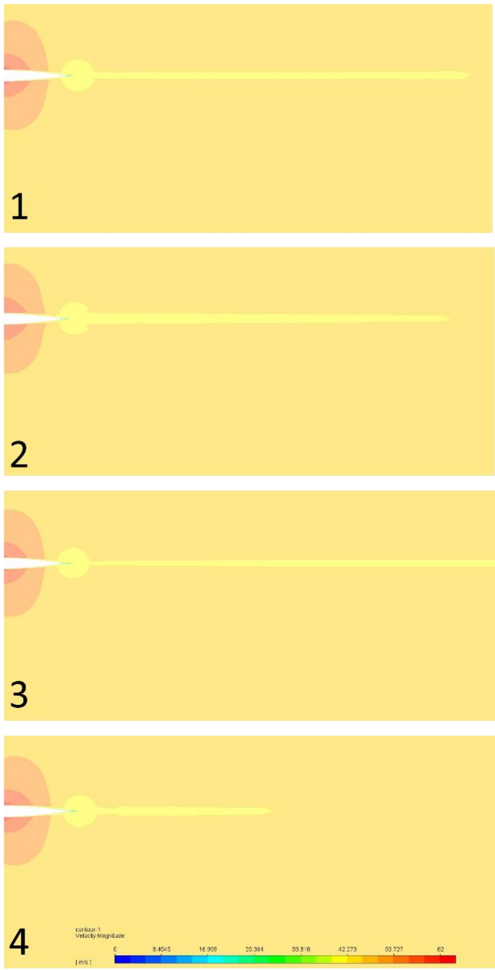

1/Triangle mesh *2/Polyhedral mesh*
3/Structured mesh *4/Chimera mesh*

Fig. 9. Velocity contour behind the trailing edge by various grids at the angle of attack of 0^o.

Figure 7 depicts the comparison of skin friction coefficient C_f on the hydrofoil surface with four mesh types at different attack angles (a) 0º, (b) 10°, and (c) 15º. At 0º, the difference between the C_f distributions of the mesh types is clear at the leading edge and region $x/c > 0.5$. In that, the fluctuation can be seen for the polyhedral mesh and chimera mesh. The reason may cause by the larger aspect ratio between the cell in the inflation region and outer region in polyhedral mesh and chimera mesh compared to the structured mesh. At a higher attack angle, the difference of the predicted C_f in the suction side is increased between four mesh, owing to the applicability in the prediction of the flow separation of each mesh that is discussed in detail below. In addition, the fluctuation of C_f that occurred at 0º is disappeared at a high attack angle for polyhedral mesh and chimera mesh. The region is still unclear.

Figure 8 shows the velocity contour distribution around the hydrofoil at a different angle of attack. The flow through the hydrofoil at an attack angle below 10º is almost the same for all mesh types. Meanwhile, the different side of the separation zone is observed for each mesh at an attack angle of 19º. For which, the largest separation results for the polyhedral mesh of 19º. The separation point is predicted earlier in triangle mesh, polyhedral mesh, and chimera mesh in comparison with the structured mesh. Because of the delay in flow separation, the friction on the surface is, therefore, higher for the structured mesh compared to the other meshes, as shown in Fig. 7(c).

Figure 9 shows the overview of the contour velocity behind the hydrofoil trailing edge attack angle of 0º. The weak velocity region is the longest for the structured mesh. This shows that the alignment and flow transition of structured mesh is better than the other 3 mesh types. This can be attributed to the differences in grid clustering around the trailing edge. The structured mesh has better resolutions of cells in this region.

IV. CONCLUSION

In this study, the effect of mesh type, which are the structured mesh, triangle mesh, polyhedral mesh, and chimera mesh, on the accuracy of the numerical result is investigated. The main result can be summarized as follow.

All meshes can well predict the flow mechanism around the hydrofoil in the absence of separation phenomenon. It can be seen that when the angle of attack is low (AOA < 10º), the C_L, C_D, C_p, and C_f are close to the experimental results. When the angle of attack is larger (AOA >10º), a different separation zone and position is predicted between the four meshes. The separation point is delayed in the structured mesh compared to the other mesh types. As the result, the structured meshes produce better results than other grids owing to the better aspect ratio in the separation region. After the stall, where the flow separation is large, the results of the structural mesh are halted significantly whereas the triangle and chimera grids would have been closer to the experiment.

REFERENCES

[1] NAS Technical Report: NAS – 2016 – 01.

[2] Ansys Fluent 12.0 Theory Manual.

[3] Castillo, J.E. (1991), "Mathematical aspects of grid Generation", Society for Industrial and applied Mathematics, Philadelphia.

[4] Jianfei, L. “Automatic mesh generation of 3-D geometric models”. Acta Mech Sinica 19, 285–288 (2003).

[5] Mavriplis, D.J. (1996), "Mesh Generation and adaptivity for complex geometries and flows", Handbook of Computational Fluid Mechanics.

[6] G. Balafas ,"Polyhedral Mesh Generation for CFD-Analysis of Complex Structures". Master’s thesis for the Master of Science program Computational Mechanics(2014).

[7] G. Houzeaux, B. Eguzkitza, R. Aubry, H. Owen1 and M. V´ azquez, “A Chimera Method for the Incompressible Navier-Stokes.Eq”. Int. J. Numer. Meth. Fluids 2013.

[8] Ladson et al. https://turbmodels.larc.nasa.gov/naca0012_val.html

The 6th International Conference on
Engineering Mechanics and Automation (ICEMA 2021)
Hanoi, November 14, 2021

Motion analyses of wave energy conversion dual buoys using ANSYS-AQWA

Nguyen Van Duc
Faculty of Mechaníc Engineering and Automation
VNU - Universit of Engineering and Technology
Hanoi, Vietnam

Dang The Ba*
Faculty of Mechaníc Engineering and Automation
VNU - Universit of Engineering and Technology
Hanoi, Vietnam
Email: badt@vnu.edu.vn

Do Huy Diep
Faculty of Mechaníc Engineering and Automation
VNU - Universit of Engineering and Technology
Hanoi, Vietnam

***Abstract* — To analyze the motion of the dual buoy mechanism and provide a theoretical basis for the design of wave energy conversion systems, AQWA hydrodynamic analysis software is used. The structural model of each buoy and the connection of two buoys through the PTO system has been built. The problem of simulating the movement of each buoy under the impact of waves has been analyzed. The simulation results show that the size of the buoy at the wave surface has a great influence on the effect of the waves on the buoy, causing the bouy to move with very different speeds, amplitudes and phases. These results are the basis to guide the calculation and design of the size and shape of the two buoys so that the relative motion between the two buoys is the largest.**

***Keywords*— ANSYS/AQWA software, wave energy conversion, dual buoys.**

I. Introduction

The concept of point absorption in wave energy conversion was developed in the late 1970s and early 1980s [1-3]. In general, this is a wave energy converter using an oscillating float whose transverse dimension is much smaller than the characteristic wave length. With the original simple design, the float is usually permanently connected to the bottom of the boundary via an energy converter [4-7]. In areas of deep water (greater than 50m) and high tide, this design may not work. Two-buoy system, later developed as an alternative, in which energy is converted from the relative motions between to different oscillating buoys [8-11].

One of the highly regarded, point-absorbing, two-float wave energy converter designs is the IPS float [9], invented by Sven A. Noren at Interproject Service (IPS), Sweden, of which, a The actual ½-scale prototype device was tested at sea in the early 1980s [4]. Another two-float wave energy converter is the AquaBuOY, developed in the 2000s, which combines IPS float concepts with a pair of tube pumps to pump water up to a high-pressure accumulator and then out to spinning the Pelton turbine [4]. A prototype of AquaBuOY was deployed and tested in 2007 in the Pacific Ocean, off the coast of Oregon. However, experimental evaluations of efficacy and industrial development have yet to be made.

The dynamic theory of wave energy conversion from the relative vertical oscillation of two buoys has been analyzed by Falnes and some other authors [6, 10, 11] and applied to a number of simulation problems with The transition energy is assumed to be linear of first order with respect to the relative displacement between the buoys. Then the system of equations is a linear differential system and is easily analyzed in the frequency domain. Analyzes were also performed and the heart was optimally configured corresponding to the maximum switching power. However, current calculations still use linear wave assumptions.

With the development of computational techniques, software now allows to simulate the interaction and motion of buoys under the action of complex ocean waves. In this report, we will refer to the problem of simulating the motion of two buoys in a wave energy converter under the action of ocean waves. To build a simulation model, a structural diagram of the system will be built. The structure of the buoys will be determined through geometric parameters. Modeling The conversion efficiency is calculated based on the difference in relative motion of the two floats. Simulation calculations are performed in the time domain with the assumption of linear waves. The model will be used to investigate the energy recovered through the generator according to the basic structural parameters of the device. The simulation results are theoretical orientation for the optimal design calculation of the device structure.

II. Designing

A. Device designing and basic assumptions

The device consists of two buoy (dual buoys) which the first buoy (buoy 1, see Fig. 1a) is large diameter and the second buoy is much smaller diameter. Two buoy are connected by a linear generator [12]. The relative motion in heaving mode between the buoys converts wave energy to electrical energy in the generator. The structure of generator is shown in Fig. 1.

The basic parameters of the device are shown in Table 1.

a) Buoy 1

b) Buoy 2

c) Dual-buoy

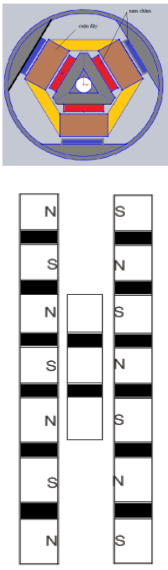

d) Linear generator

Fig.1. Structure design of dual buoy WEC

Tab.1. Basic design parameters of device

Name and unit	Value	Name and unit	Value
Sea water density kg/m^3	1030	Radius of generator case, m	0.1
Mass of buoy 1, kg	70.0	Lenth of Generator, m	2.0
Radius of buoy 1, m	0.40	Magnet bar dimension, cm	5x2.5x1
High of buoy 1, m	1.0	Br, T	0.2
Mass of magnet bars, kg	20.0	Number of magnet slices	3
Radius of buoy 2, m	0.024	Number of coils	9
Lenth of buoy 2, m	5.0	Radius of copper wire, mm	0.3
Mass of buoy 2, kg	30.0	Radius of a coil, m	0.12

B. Modeling

For simulation and analyzing the motion and performing of the device, we must take two parts that are mechanic simulation and electric simulation. A Hydrodynamic Diffraction and a hydrodynamic response analysis are our major two parts in the mechanical simulation, these analysis are held by ANSYS AQWA program. While an electric simulation implementations are held by MATLAB.

For the Ansys Aqwa, the calculated domain is set up in the form of a rectangular box with dimensions are 10x10x10 m. The coordinate system Oxyz with Oz is in vertical direction, Ox is in W-E and Oy is in S-N direction. (Figure 2). The general body motion is defined by six degrees of freedom; the movement in x, y, z directions and the rotations around the x, y, z axes.

By common notation we call these six degrees of freedom: surge, sway, heave, roll, pitch and yaw In this study, only heave motion is considered, although the inclusion of other degrees of freedom is straightforward. As the body of buoys is axisymmetric, the heave mode is independent of the other modes.

The 3D design of buoys is performed in NX and then imported in ANSYS AQWA as seen in Figure 2. The hydrodynamic diffraction analysis and the hydrodynamic response analysis done by ANSYS AQWA are applied for each buoy (Figure 2).

Defining the moments of inertia in ANSYS AQWA have been done by direct introducing the moments of inertia after introducing the mass. Defining the environment and its parameters is the first thing to do in ANSYS AQWA, environment parameters are like sea depth and water density.

The specific joints have been added to the device structure; ANSYS AQWA's hydrodynamic analysis allows structures to be connected by articulated joints. These joints do not permit relative translation of the two structures but allow relative rotational movement in a number of ways that can be defined by the user. There are different types of joints in AQWA: Ball and socket joint; Universal joint; Hinged joint; and rigid joint.

The mesh is automatically generated on the buoys in the model. These are the two main parameters in the meshing stage. The Defeaturing Tolerance controls how small details are treated by the mesh. If the detail is smaller than this tolerance then a single element may span over it, otherwise the mesh size willbe reduced in this area to ensure that the feature is meshed. The defeaturing tolerance can not be greater than 0.6 times max element size. Max Element Size controls the maximum size of the element that will be generated. In ANSYS AQWA this is explicitly related to the maximum wave frequency that can be utilized in the diffraction analysis.

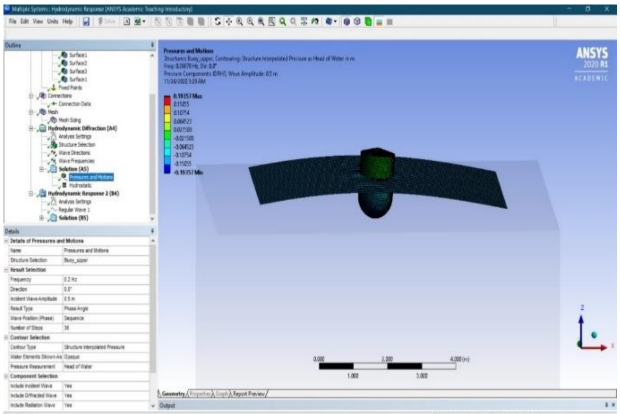

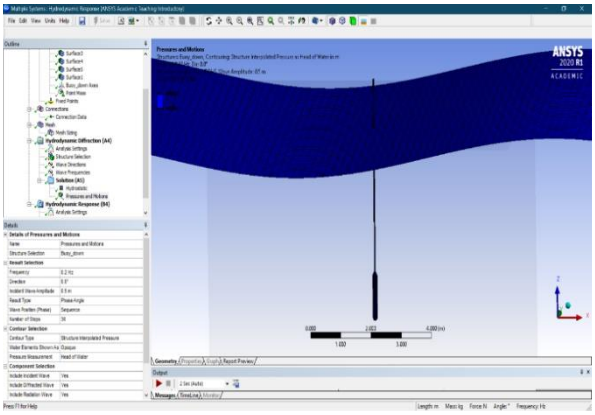

Fig.2. Simulation setting in AQWA

Adjusting the settings of the hydrodynamic diffraction analysis is the third step in the simulation process. First, we have to make sure that the buoys are selected. By selecting the buoys means that all the simulation parameters we are going to introduce will be applied on this selected structure. Second, the gravity input, as we know the gravity is a constant equals to 9.81 N/m. Third the wave direction selection, ANSYS AQWA permits selecting a number of wave directions but at least 4 wave directions must be applied, also you can choose the range between each direction. The results are calculated in each and every introduced wave but you have to choose one specific wave direction to view the results and the graphs. And to finish adjusting the hydrodynamic diffraction analysis settings, begins the part of choosing the adequate wave frequencies for this analysis, wave frequencies parameters depends on the environment, the structure settings and the mesh size. While adjusting the analysis settings we have to make sure of three main settings:

- Output ASCII Hydrodynamic Database -> Yes
- Calculate Full QTF Matrix ->No
- Ignore Modeling Rule Violations ->Yes

After designing the model we must introduce the hydrodynamic diffraction parameters needed to start this analysis and then start our analysis and generate the ".AH1" and ".LIS" files that are needed to generate the hydrodynamic data file used in the Matlab for calculation the output power from linear generator.

In this simulation, the linear wave was used and it has the form:

$$\eta(t) = \eta_a \cos(\omega t - kx) \ , \qquad (1)$$

Where □a(t) is wave height, □a is wave amplitude, ω is wave frequency, k is wave number. The wave force acting on the buoys is calculated inside AQWA based on this assumption other parameters of the device.

For generator simulation, we use the UDF to generate the code. The government equation are described as follow:

The relative movement between buoy 1 and 2 make the coils displacement relatively to magnets.

$$y(t) = s_b(t) - s_p(t) \quad (2)$$

Magnetic flux across the coil along magnets bar have the form:

$$\varphi_x(y) = \hat{\varphi}\sin(\frac{2\pi}{\lambda} y(t)) \qquad (2)$$

A displacement of a coil with N turn in that magnetic field will make a electromotive force as

$$e(t) = -Nl\hat{\varphi}\sin(\frac{2\pi y(t)}{\lambda})\dot{y}(t) \qquad (3)$$

The circuit of generator with a resistors has the form

$$L\frac{dI_L(t)}{dt} = -\left(\frac{R_L + R_i}{L}\right)R_L I_L(t) + \frac{R_L e(t)}{L} \ , \qquad (4)$$

Where L in (4) is the inductance (henry) of the coil, it has the form:

$$L = \mu_o.\mu.N^2.S.l_{\acute{o}ng} \ , \qquad (5)$$

With S cross section area of coil, □o is magnetic permeability of air í, □ is magnetic permeability of coil core, N is the number of turns, lống is the length of the coil.

The output power from one coil is calculated as follow:

$$P = I_L^2 R_L \qquad (6)$$

Electical-magnetic fore between coil and magnet (it is also the force between buoy 1 and buoy 2):

$$F_u = Nl\varphi_x I_L \ . \qquad (7)$$

In the formulas above, a local 2D coordinate system for generator has been used. In with Oy is along the generator center, OX is along the radius of cross section.

III. Results and discussions

With the wave condition in this simulation has a height of 1m and period of 5s, the results of simulation are obtained and presented as in Fig.3 to 6.

In Fig.3, the vertical displacement amplitude of buoy 1 is smaller but not so much than that of the wave. In the other hand, the vertical displacement amplitude of buoy 2 is much smaller to that of buoy 1. It is the same situation for the velocities (see Fig.4.).

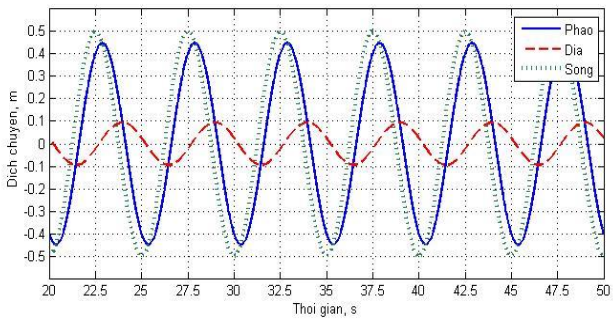

Fig.3 Vertical disp. of wave, buoy 1 and 2

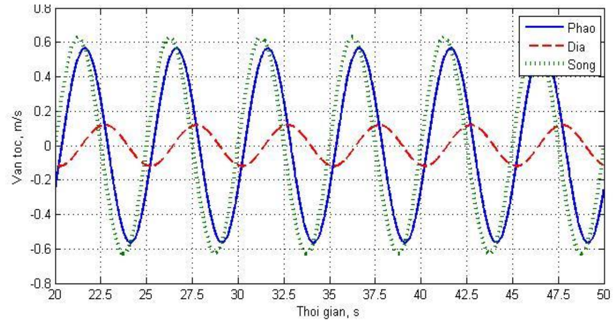

Fig.4 Vertical vel. of wave, buoy 1 and 2

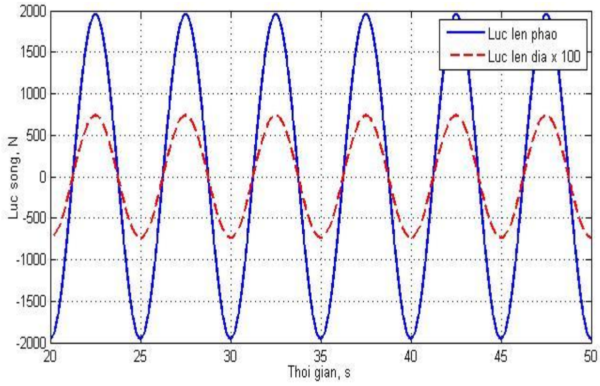

Fig.5. Diffraction forces on buoy 1 and 2

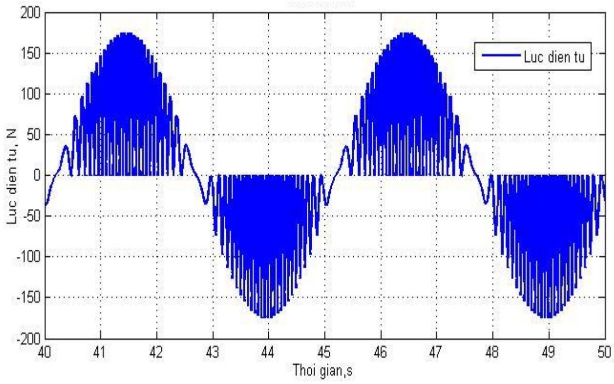

Fig.6. Relation reaction force between buoys

From this displacements and velocities, the output voltage and power are calculated as shown in Fig.7. and Fig.8.

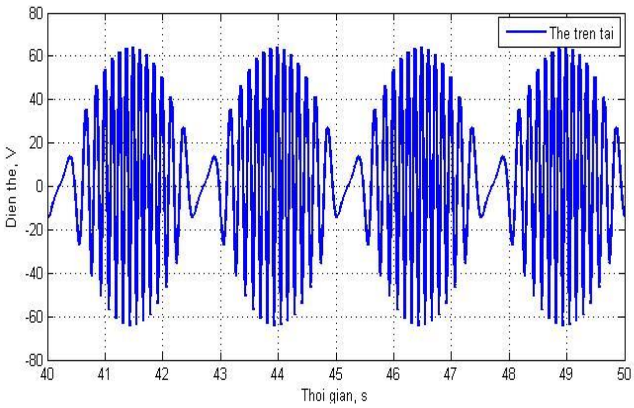

Fig.7. Generator output voltage

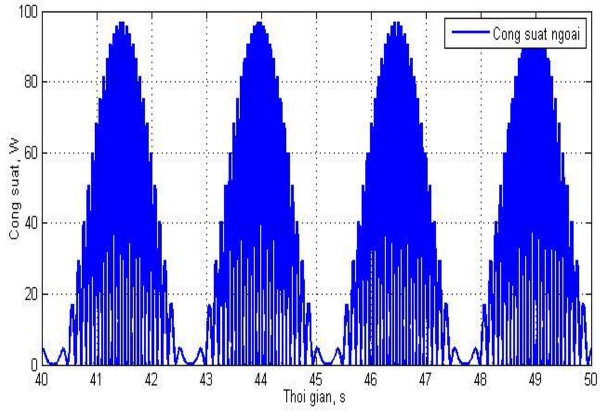

Fig.8. Output power

The simulations tools then used for investigating the output power of device depend on structure parameters.

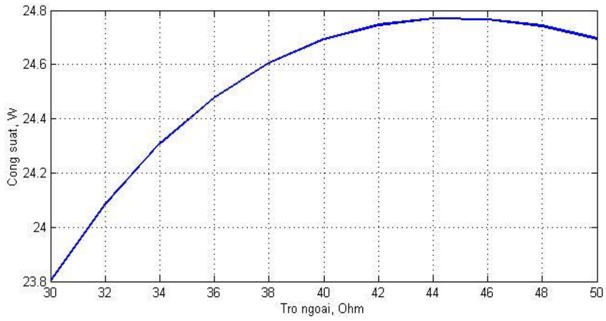

Fig.9. Power vs. generator resistance

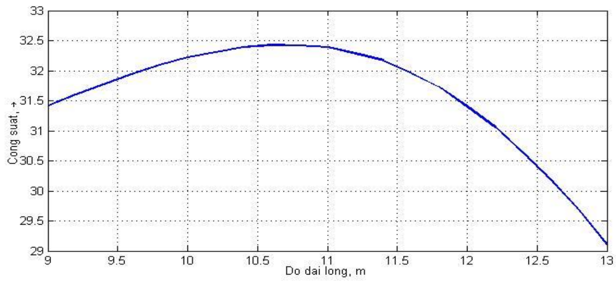

Fig.10. Power vs. length of buoy 2

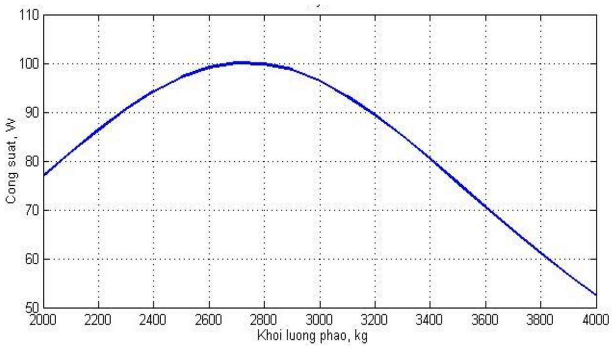

Fig.11. Power vs. mass of buoy 1

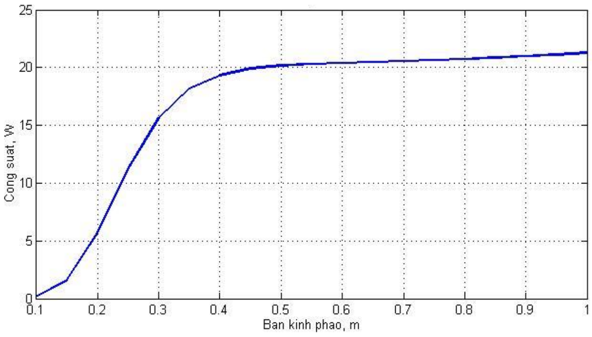

Fig.12. Power vs. radius of buoy 1

From the Fig, 9 – 12, we can find a collection of structure parameters to maximize the output power. This is a good guidance for next step for designing calculation.

IV Conclusion

On the basis of the principles of wave energy conversion, the wave energy converter has been analyzed and selected, and the configuration of a prototype wave energy convertor has been selected with dual buoy mechanism connected through a linear generator. This type of device has advantages for simple in fabrication and deployment because of its simple structure. It works regardless of the tide. It mak less energy loss for intermediate par in structures.

On the basis of the principle of structure and operation, a computational model has been built to simulate the operation of the device with the help of AQWA and Matlab. The results show the possibility of the next step for development calculation for a industrial-scale prototype. However, from the simulation results, we also recognize that the conversion efficiency is still very low, it is necessary to perform optimal calculation of the structure to achieve the higher efficiency.

In addition, when designing a linear generator for wave energy converters, it is necessary to optimize the windings to ensure slow motion (requires many turns of wire) and to ensure a small internal and external resistance. Moreover, in this research, the output power from the generator has it origin form (Fig.3 and 4), not yet ready for supporting to use in the real life. This is also the a need to be developed to realize using of direct-driven wave energy conversion mechanism in general, also in our project.

References

[1] J. Falnes, Ocean Waves and Oscillating Systems. Cambridge: Cambridge University Press, 2002.

[2] Y. Goda, Random Seas and Design of Maritime Structures. 2nd edition. Singapore: World Scientific, 2000.

[3] J. Falnes, "Optimum control of oscillation of wave-energy converters," International Journal of Offshore and Polar Engineering, vol. 12, pp. 147-155, 2002.

[4] A. F. de O. Falcão, "Phase control through load control of oscillating-body wave energy converters with hydraulic PTO system," Ocean Engineering, vol. 35, pp. 358-366, 2008.

[5] K. Budal and J. Falnes, "Interacting point absorbers with controlled motion," in B. Count (editor), Power from Sea Waves. London: Academic Press, pp. 381-399, 1980.

[6] J. Falnes, "Wave-energy conversion through relative motion between two single-mode oscillating bodies," Journal of Offshore Mechanics and Arctic Engineering, vol. 121, pp. 32-38, 1999.

[7] Dang The Ba, Numerical Simulation of a Wave Energy Converter Using Linear Generator, Vietnam Journal of Mechanics, Vol.35, No.2, P.103-111, 2013.

[8] A. F. de O. Falcão, "Modelling and control of oscillating-body wave energy converters with hydraulic power take-off and gas accumulator," Ocean Engineering, vol. 34, pp. 2021-2032, 2007.

[9] A. Weinstein, G. Fredrikson, M. J. Parks and K. Nielsen, "AquaBuOY, the offshore wave energy converter numerical modelling and optimization," in Proceedings of the MTTS/IEEE Techno-Ocean '04 Conference, Kobe, Japan, vol. 4, pp. 1854-1859, 2004.

[10] U. A. Korde, "Systems of reactively loaded coupled oscillating bodies in wave energy conversion," Applied Ocean Research, vol. 25, pp. 79-91, 2003.

[11] S. J. Beatty, B. J. Buckham and P. Wild, "Frequency response tuning for a two-body heaving wave energy converter," in Proceedings of 18th International Offshore and Polar Engineering Conference, Vancouver, p. 342-348, 2008.

[12] Dang The Ba, Nguyen Dong Anh, Phung Van Ngoc, Numerical simulation and experimental analysis for a linear trigonal double-face permanent magnet generator used in direct driven wave energy conversion, Procedia Chemistry , 14, 130 – 137, 2015.

SESSION 3.
SOLID MECHANICS

Effect of Structure Properties on Biped Locomotion

Van-Tinh Nguyen
School of Mechanical Engineering
Hanoi University of Science and Technology
Hanoi, Vietnam.
tinh.nguyenvan@hust.edu.vn

***Abstract*: This article addresses an effect of structure properties on walking behaviour of a humanoid robot. As you may know, the feet have an important role in bipedal walking since they directly interact with the environment. Thus, walking behaviour is sensitive to the foot features. In this paper, joint characteristics of the robot's foot have been investigated for our further understanding of locomotion mechanism. These properties are stiffness and damping factor of spring of passive toe joints. In addition, while considering the human walk, we discover that arm swing motion has a significant effect on angle of rotation, thus, the effect of the characteristic factor of shoulder joint has also been evaluated in the next stage. The study subject of this paper is a small humanoid robot named Kondo KHR-3HV belonging to the Kondo Kagaku company. The foot structure of the robot consists of a big toe and a tiptoe with passive joints using torsion spring. The arm swing mechanism using linear spring is applied to emulate arm swing motion of the humans. The results are collected and validated through dynamic simulation on Adams (MSC company, USA).**

Keywords: Biped walk, structure properties, toe mechanism, arm

I. INTRODUCTION

Humanoid robots have been developed for many decades with several state-of-art research [1-6]. One of the most challenge in this field is the control of the locomotion of the robot on the ground. This problem is much more difficult when the environment is uneven ground, since the robot will encounter the change of reaction and friction force in direction and magnitude. These forces have significant effect on the robust balance of the walk.

Literature review on the recent research, we witness very few publications dealing with humanoids walking on rough terrains. For instance, Majid Sadedel added low-cost passive toe joints to the feet structure of SURENA III humanoid robot [7]. Using passive toe joints reduces energy consumption of ankle and knee joints, thus, extending the working time of the robot. Shiqi Sun proposed adaptable compliant toe joints to improve the stability and energy efficiency [8], it could reduce the energy consumption of ankle joints. Jiang Yi et al. presented the control algorithm for robots walking on rough road. This algorithm redesigned the swing foot trajectory to adapt to change of terrain height [9]. Felix Sygulla and Daniel Rixen addressed a scheme with an early-contact method and direct force control for humanoid robot [10]. Boston Dynamics unveiled the Protection Ensemble Test Mannequin (PETMAN) which is a humanoid robot being developed for the US Army to test the special clothing used by soldiers for protection against chemical warfare agents. In addition, Boston Dynamics has developed Atlas robot which is based on PETMAN [11, 12], It is intended to aid emergency services in search and rescue operations. The robots of Boston Dynamics have outstanding performance when moving on rough road in the outdoor environment. These robots are both electrically powered and hydraulically actuated and consumes a lot of energy.

In my previous research [13], I introduced a foot structure for locomotion of biped robot on rough road. This structure was generated by applying topology optimization technique with four case studies. However, the prior paper fixed the characteristic factors of the joint with a certain value, thus, this research supposes that these factors have a significant effect on the walking behaviour of the robot and will present this relationship.

To this end, the rest of this paper is organized into five sections. Section 2 describes simulation model. Section 3 presents gait generation procedure. Section 4 addresses simulation result and discussions. Finally, Section 5 includes some brief conclusions.

II. SIMULATION MODEL

A. Subject

KHR-3HV robot is the subject of our research. From the real robot, we built two simulation models: no arm swing and arm swing mechanism in Adams environment as shown in Fig. 1. This research mainly focuses on the lower body with ten degrees of freedom.

B. Toe mechanism

As presented in [13], the foot structure of the robot consists of heel and toe mechanism as shown in Fig. 2. However, in motion, we recognize that the stiffness of torsion spring has a significant effect on walking behavior of the robot, thus, we will investigate this parameter in predefined range as described in Table I to witness its impact on the simulation result.

C. Arm swing mechanism

F. Naoki's research has proposed and modeled an arm swing mechanism using Adams [14] as shown in Fig. 3, the shoulder joint is linked to the hip joint by two linear springs, this mechanism is confirmed that the reaction moment from the arms to the trunk precludes ground reaction torque [15]. It makes the robot stable in motion. Our research applies this structure for the robot and the characteristic parameters of the linear spring is investigated in predefined range as described in Table II.

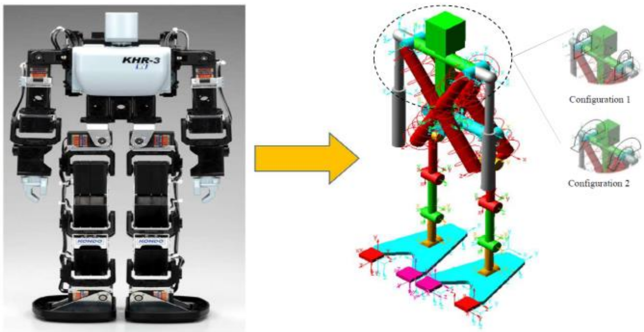

Figure 1. Simulation model.

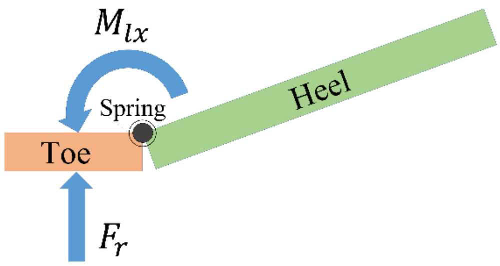

Figure 2. Toe mechanism.

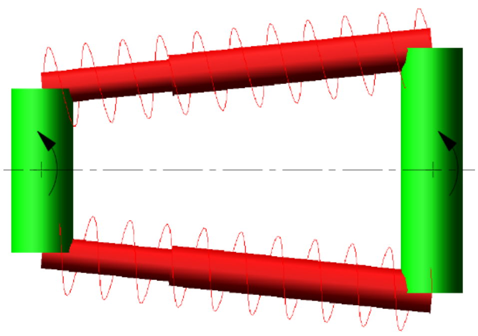

Figure 3. Arm swing mechanism.

TABLE I. CHARACTERISTIC FACTOR OF TORSION SPRING.

Factor		Level		
		1	*2*	*3*
Torsion spring	Stiffness (newton.mm/rad) (A)	1.5	2.0	2.5
	Damping (newton.mm.sec/rad) (B)	10	20	30

TABLE II. CHARACTERISTIC FACTOR OF LINEAR SPRING.

Factor		Level		
		1	*2*	*3*
Linear spring	Stiffness (newton.mm/rad) (C)	0.6	0.8	1.0
	Damping (newton.mm.sec/rad) (D)	0.004	0.008	0.012

III. GAIT GENERATION PROCEDURE

A. *Definition of Joint Angle*

The lower body of the robot has 10 controlled DoFs as depicted in Fig. 4 and range of joint angle are set in Table III.

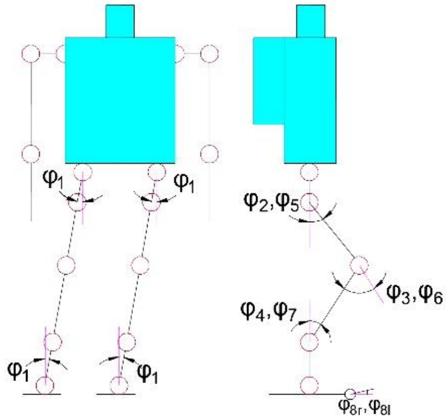

Figure 4. Robot linkage model.

TABLE III. RANGE OF JOINT ANGLE

Angle	Leg	Joint	Value (º)
φ_1	Both	Hip & ankle	-15º to 15º
φ_2	Right	Hip	-50º to 50º
φ_3	Right	Knee	0º to 60º
φ_4	Right	Ankle	-50º to 50º
φ_5	Left	Hip	-50º to 50º
φ_6	Left	Knee	0º to 60º
φ_7	Left	Ankle	-50º to 50º
φ_{8r}	Right	Proximal phalanx	0º to 30º
φ_{8l}	Left	Proximal phalanx	0º to 30º

B. *Gait function*

Joint angle is generated by a trigonometric function as Equation 1.

$$\varphi_i\,(t) = a_i + b_i.cos(\omega t) + c_i.sin(\omega t) + b_i.cos(\omega t) \qquad (1)$$

Where φ_i is the angle of i joint; a_i, b_i, c_i, b_i are coefficients, $i = 1 \div 4$; t is the time, and ω is the angular velocity. In motion, one cycle is set up to 1.2 seconds. Thus, the angular velocity is determined by below calculation.

$$\omega = \frac{2\Pi}{1.2} = 5.236 \text{ (rad/s)}$$

Optimization procedure is defined by Equation (2 – 5):
Design variables (DVs):

$$x = [a_i, b_i, c_i, d_i],\ i = 1 \div 4. \qquad (2)$$

Constraint functions:

$$g_1(x) = 20 - |X_f| \geq 0. \qquad (3)$$

$$g_2(x) = 5 - |R_f| \geq 0. \qquad (4)$$

Objective function:

$$f(x) = -Z_f \rightarrow min. \qquad (5)$$

Where X_f, Z_f, and R_f are lateral distance, walking distance, and angle of rotation, respectively. Values of X_f, Z_f, and R_f are approximated by response surface model with design variables *a*, *b*, *c*, *d*. The optimization process is described in below Pseudocode.

Pseudocode of algorithm is described as below:

1. Achieving the first simulation in Adams by Trial and Error method.
2 Design of experiment.
3. While termination condition is not reached.
   Making 3rd order response surface model.
   Applying ISADE with objective function (5) and constraint function (3), (4).
   Analysing the result through dynamic simulation in Adams.
4 The optimal value of design variable is achieved.

IV. SIMULATION RESULTS

Flat Surfaces shown in Fig. 5 is used to perform the locomotion of the robot. The first simulation is to confirm that arm swing behaviour enhances walking performance by reducing angle of rotation and increasing walking distance. The locomotion of the biped robot is considered in *4.8* seconds with *4* cycles.

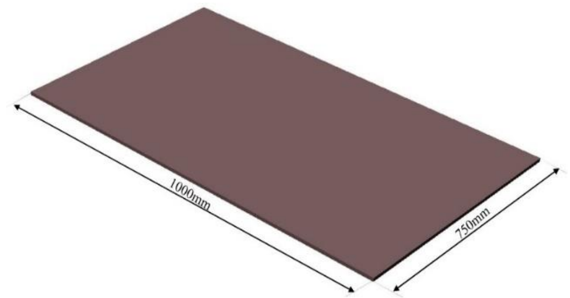

Figure 5. Flat ground for simulation.

To observe this point, the robot is considered in two configurations: At first, joint of shoulder is locked or in other words it has no joint. With second configuration, 1-DoF joint is designed for the shoulder. The robot locomotion is simulated on an above-mentioned environment. The simulation result is shown in Fig. 6.

The simulation result shows that X_f lateral distance, Z_f walking distance and R_f angle of rotation are *6.17mm*, *172.11mm*, and *9.19°*, respectively for configuration 1; *9.21mm*, *184.66mm*, and *3.98°*, respectively for configuration 2. To be specific, Fig. 6a shows that the trajectory of the robot's CoM, which is a periodical wave, is comparable to the humans as described in [16]. Fig. 6b illustrates the angle of the right foot rotation along the time axis in the walking process. We can see that this angle experiences a fluctuation about from *-25°* to *25°* around zero line, which means the feet rotate with a significant amplitude in the locomotion. However, from *3.0s* to *3.3s*, while the robot prepares to change into a stand, the angle of rotation quickly decreases, and this angle is constant in stability checking period. To compare performance of two configuration, we can see that the model having arm swing behavior has better performance. In detail, walking distance experiences an increase of about *7.29%*. In addition, the model having no shoulder joint adopts a little larger fluctuation of angle of rotation and account for *5%*, this angle at the final position is decreased by around *56.69%*.

(a)

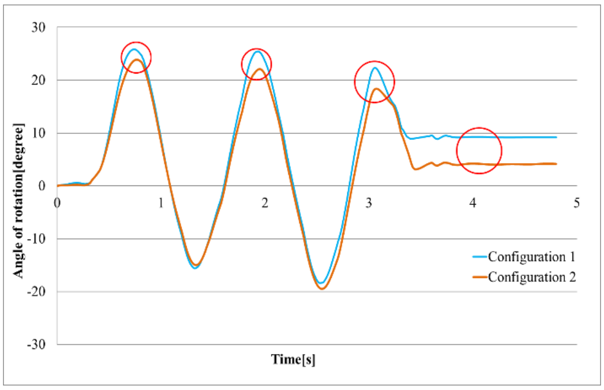

(b)

Figure 6. Simulation result: (a) CoM trajectory; (b) Angle of rotation.

In the next simulation, I will evaluate the effect of structure parameters on walking behaviour of the robot. The locomotion will be consider in *9.6* seconds with *8* cycles. I selected the orthogonal array of L9 for conducting the simulation. The result is shown in Table IV.

TABLE IV. DESIGN OF EXPERIMENT.

Orthogonal Array (L9)					Result	
No.	***A***	***B***	***C***	***D***	***X***	***R***
1	1.5	10	0.6	0.004	220.77	31.31
2	1.5	20	0.8	0.008	1.61	15.03
3	1.5	30	1.0	0.012	-202.36	-42.93
4	2.0	10	0.8	0.012	28.37	53.79
5	2.0	20	1.0	0.004	-208.73	-20.08
6	2.0	30	0.6	0.008	130.18	52.74
7	2.5	10	1.0	0.008	-184.83	-26.15
8	2.5	20	0.6	0.012	294.58	80.66
9	2.5	30	0.8	0.004	-22.96	29.06

Where A, B, C, D are characteristic factors.
X is lateral distance.
R is angle of rotation.

As can be seen that in case of X output in Table V, C has the most significant effect on lateral distance accounting for 45.23%, followed by D with 22.48% and A with 18.01%. B reveals the lowest number with 14.27%. Table VI shows that in case of R output, C also has the most significant effect on angle of rotation accounting for 83.54%followed by A with 10.72%, D with 4.11%. B reveals the lowest number with make up only 1.63%. Fig. 7-8 describe the relationship between output and four considered characteristic factors.

TABLE V. ANOVA WITH X OUTPUT.

Factor	f	S	V	S’	P
A	2	46114.80	23057.40	46114.80	18.01
B	2	36539.37	18269.68	36539.37	14.27
C	2	115798.87	57899.44	115798.87	45.23
D	2	57563.34	28781.67	57563.34	22.48
Total	8	256016.38			100.0

TABLE VI. ANOVA WITH R OUTPUT.

Factor	f	S	V	S’	P
A	2	1481.06	740.53	1481.06	10.72
B	2	225.62	112.81	225.62	1.63
C	2	11544.47	5772.23	11544.47	83.54
D	2	568.48	284.24	568.48	4.11
Total	8	13819.63			100.0

Where S: Sum of squares.
S’: Pure sum of squares.
V: Mean squares (variance).
P: Percentage by contribution.
f: Degrees of freedom.

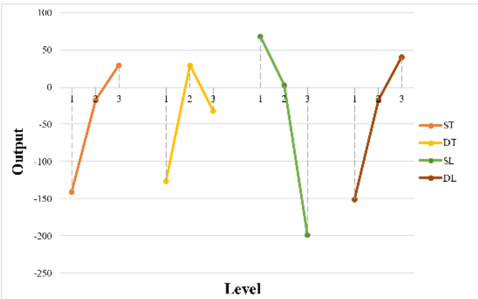

Figure 7. Relationship between X output and characteristic factors.

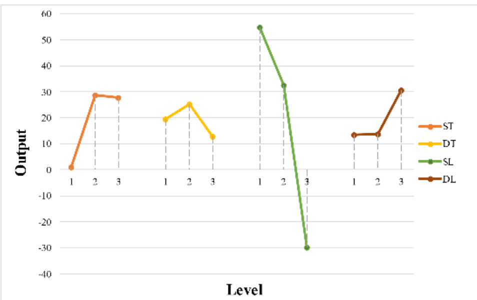

Figure 8. Relationship between R output and characteristic factors.

V. CONCLUSIONS

This research addresses the effect of characteristic factor of the structure on walking behaviour of the biped robot. Firstly, my research confirms that the arm swing mechanism enhances the walking performance by reducing the angle of rotation while the robot walks on the flat road. In the next stage, the Taguchi method is applied to evaluate the effect of four characteristic factors on the walking performance of the robot. The analysis results show that stiffness of linear spring has the most significant effect on biped walk.

REFERENCES

[1] K. Hirai, M. Hirose, Y. Haikawa, and T. Takenaka, "The Development of Honda Humanoid Robot", in Proc. IEEE Int. Conf. on Robotics and Automations, pp. 1321-1326, (1998).

[2] Y. Ogura, H. Aikawa, K. Shimomura, A. Morishima, H.o. Lim, and A. Takanishi, “Development of a new humanoid robot WABIAN-2”, Proceedings of IEEE International Conference on Robotics and Automation (2006), pp. 830-835.

[3] S. Lohmeier, T. Buschmann, and H. Ulbrich, “Humanoid robot LOLA”, Proceedings of IEEE international conference on robotics and automation (2009), pp. 775–780.

[4] T. Ishida, “Development of a Small Biped Entertainment Robot QRIO”, Proceedings of The Fourth Symposium Micro-Nanomechatronics for Information Based Society (2004), pp. 23-28.

[5] Oh JH, Hanson D, Kim WS, Han IY, Kim JY, Park IW., Design of android type humanoid robot albert HUBO. In: 2006 IEEE/RSJ international conference on intelligent robots and systems, pp 1428–1433 (2006).

[6] K. Kaneko, F. Kanehiro, M. Morisawa, K. Akachi, G. Miyamori, A. Hayashi, and N. Kanehira, “Humanoid robot HRP-4 - Humanoid robotics platform with lightweight and slim body”, Proceedings of IEEE/RSJ International Conference on Intelligent Robots and Systems (2011), pp. 4400-4407.

[7] Sadedel, M., Yousefi-Koma, A., Khadiv, M., & Mahdavian, M., Adding low-cost passive toe joints to the feet structure of SURENA III humanoid robot. Robotica, 35(11), 2099-2121 (2017). doi:10.1017/S026357471600059X

[8] Sun, S., Huang, Y. and Wang, Q., “Adding adaptable toe stiffness affects energetic efficiency and dynamic behaviours of bipedal walking,” J. Theoretical Biol. 388, 108–118 (2016).

[9] Yi J, Zhu Q, Xiong R and Wu J., Walking Algorithm of Humanoid Robot on Uneven Terrain with Terrain Estimation Int. J. Adv. Robot. Syst. 13 35 (2016).

[10] Sygulla F and Rixen D., A Force/Control Scheme for Biped Robots to Walk over Uneven Terrain Including Partial Footholds Prepr. Publ (2019).

[11] G. Nelson, A. Saunders, N. Neville, B. Swilling, J. Bondaryk, D. Billings, C. Lee, R. Play-ter, and M. Raibert, “PETMAN: A Humanoid Robot for Testing Chemical Protective Clothing”, Journal of the Robotics Society of Japan (2012), vol. 30, No. 4, pp. 372-377.

[12] T. Hornyak, “Be afraid: DARPA unveils Terminator-like Atlas robot”, CNET (2013)

[13] Van-Tinh Nguyen, Ngoc-Tam Bui, and Hiroshi Hasegawa, Gait-Behavior Optimization Considering Arm Swing and Toe Mechanism for Biped Walking on Rough Road, International Journal of Mechanical Engineering and Robotics Research, Vol. 9, No. 4, pp. 521-527 (2020)

[14] F. Naoki, “Energy saving of biped robots aiming for 24-hour continuous operation”, in master’s thesis, Shibaura Institute of Technology, Japan (2017).

[15] J. Park, “Synthesis of natural arm swing motion in human bipedal walking”, Journal of Biomechanics, vol. 41, No. 7, pp. 1417-1426, (2008).

[16] M. S. Orendurff, A. D. Segal, J. S. Berge, K. C. Flick, D. Spanier, and G. K. Klute, The kinematics and kinetics of turning: limb asymmetries associated with walking a circular path, Gait and Posture, vol. 23, pp. 106-111 (2006)

Exact receptance and receptance curvature functions of the axially load cracked beam carrying concentrated mass

Khoa Viet Nguyen
Institute of Mechanics, VAST
Graduate University of Science and Tecnology, VAST
Ha Noi, Viet Nam
nvkhoa@imech.vast.vn,

Thao Thi Bich Dao
Institute of Mechanics, VAST
Graduate University of Science and Tecnology, VAST
Ha Noi, Viet Nam
daothaohus@gmail.com

Long Vu Do
Hanoi University of Science, VNU
Ha Noi, Viet Nam
longvudo@gmail.com

Quang Nguyen Van
Institute of Mechanics, VAST
Ha Noi, Viet Nam
nvquang.imech@gmail.com

***Abstract*: This paper presents the derivation of the exact curvature receptance function of an axially loaded cracked beam carrying concentrated masses. The influence of the masses and axial force on the receptance curvature is investigated. When there are cracks, there are peaks in the receptance curvature. It is interesting that when concentrated masses are located at the crack positions the small peak in the receptance curvature is more significant than the case of where there is no attached mass. This result may be useful for crack detection: a mass can be applied to amplify small peaks in the receptance curvature to detect the small peak. However, these results are influenced by the axial force: the crack is detected better when the beam is tensioned, but it is more difficult to detect the crack when the beam is compressed.**

Keywords: Receptance, frequency response function, crack, axial force, concentrated mass

I. Introduction

The receptance function and its applications has been developed widely in mechanical system, structural dynamics, system identification etc. Milne [1] presented a general solution of the receptance function of isotropic homogeneous beams with uniform cross sections. Yang [2] derived the exact receptances of non-proportionally damped dynamic systems. Lin and Lim [3] presented the derivation of the receptance sensitivity with respect to mass modification and stiffness modification from the limited vibration test data. Gurgoze et al [4-5] focused on the receptance matrices of viscously damped systems carrying concentrated mass subject to unconstrained and constrained conditions. Karakas and Gurgoze [6] established a formulation of the receptance matrix of non-proportionally damped dynamic systems as an extension of [3] in which the receptance matrix was obtained directly without using the iterations. Arlaud et al. [7] presented the numerical and experimental approaches to study the receptance of railway tracks at low frequency. Burlon et al. [8-9] presented an exact frequency response function of axially loaded beams carrying massed with viscoelastic dampers.

Cracks may cause serious failure of mechanical system and civil engineering structures. Therefore, early crack detection is extremely important and this issue has attracted many researchers in the last three decades. Pandey et al. [10] and Abdel Wahab [11] applied the change in curvature mode shapes to determine the location of cracks in beam like structures. Zhang et al. [12] presented the crack identification method combining wavelet analysis with transform matrix using mode shapes of a cracked cantilever beam. The author of this paper [3] used 3D finite elements to calculate the mode shapes of a cracked beam. Caddemi and Calio [14-15] derived the exact closed-form solution for the vibration modes of the Euler-Bernoulli beam with multiple open cracks. However, the results of these papers showed that the change in mode shape is small and cannot be seen when the crack size is small, it can only be inspected visually when the crack size is very large. Recently, the author of this paper [16] presented a method to investigate the influence of crack using the receptance and its curvature. The results showed that the influence of the cracks on the receptance is very small when the crack size is small, but the influence of the cracks on the receptance curvature is much larger and this is useful for crack detection problem. However, the current researches have not investigated the influence of the axial force on the crack detection.

This work aims to establish the exact receptance curvature and its application for crack detection of a cracked beam carrying concentrated masses when the axial force is taken in account. When a concentrated mass is located at the crack positions the distortion of the receptance curvature at the crack position is more significant than when there is no masse attached, but this effect is dependent on the axial force. The proposed method is more effective for the compressed beam than the tensioned beam. In this study, the derivation of the receptance curvature of axially loaded cracked beam carrying concentrated masses is presented and numerical simulations are provided.

II. THEORETICAL BACKGROUND

In this work we consider the Euler-Bernoulli beam carrying lumped masses subjected to an axial force P and a vertical force $f(t)$ as presented in Fig. 1. The equation of forced vibration of the beam can be written as follows:

$$\frac{\partial^2}{\partial x^2}\left[EI.\frac{\partial^2 y}{\partial x^2}\right]-P\frac{\partial^2 y}{\partial x^2}+\left[\mu+\sum_{k=1}^{n}m_k\delta\left(x-x_{mk}\right)\right]\frac{\partial^2 y}{\partial t^2} = \delta\left(x-x_f\right)f\left(t\right) \tag{1}$$

Here: E is the Young's modulus, I is the moment of inertia of the cross sectional area of the beam, μ is the mass density, m_k is the k^{th} concentrated mass located at x_{mk}, $y(x, t)$ is the bending deflection of the beam at location x and time t, $f(t)$ is the force acting at position x_f, $\delta\left(x-x_f\right)$ is the Dirac delta function.

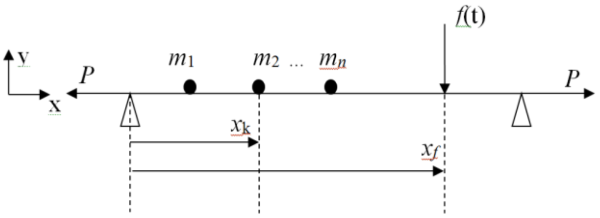

Fig. 1. A beam with concentrated masses

In order to simplify calculus, the non-dimensional coordinate $\xi = x/L$ is used. The differential Eq (1) takes the following form:

$$\frac{\partial^2}{\partial \xi^2}\left[EI\frac{\partial^2 y}{\partial \xi^2}\right]-L^4P\frac{\partial^2 y}{\partial \xi^2}+L^4\mu\frac{\partial^2 y}{\partial t^2} = L^4\delta\left(\xi-\xi_f\right)f\left(t\right)-L^4\sum_{k=1}^{n}m_k\delta\left(\xi-\xi_{mk}\right)\frac{\partial^2 y}{\partial t^2} \tag{2}$$

Eq. (2) can be considered as the equation of forced vibration of a beam without concentrated masses which is acted by the inertia forces of n concentrated masses and the external force $f(t)$. The solution of Eq. (2) can be found in the form:

$$y\left(\xi,t\right)=\sum_{i=1}^{\infty}\phi_i\left(\xi\right)q_i\left(t\right) \tag{3}$$

where ϕ_i is i^{th} mode shape of the beam without concentrated masses and q_i is the i^{th} generalized coordinate.

Substituting (3) into (2) and multiplying this equation by $\phi_j(\xi)$ and integrating from 0 to 1, one obtains:

$$\begin{aligned}&\int_0^1\left[EI\sum_{i=1}^{\infty}\phi_i''\left(\xi\right)\right]''\phi_j\left(\xi\right)q_i\left(t\right)d\xi-L^4P\int_0^1\sum_{i=1}^{\infty}\phi_i''(\xi)\phi_j\left(\xi\right)q_i\left(t\right)d\xi\\&+L^4\int_0^1\mu\sum_{i=1}^{\infty}\phi_i\left(\xi\right)\phi_j\left(\xi\right)\ddot{q}_i\left(t\right)d\xi\\&=-L^4\sum_{k=1}^{n}m_k\sum_{i=1}^{\infty}\phi_i\left(\xi_{mk}\right)\phi_j\left(\xi_{mk}\right)\ddot{q}_i\left(t\right)+L^4\phi_j\left(\xi_f\right)f\left(t\right)\end{aligned} \tag{4}$$

From the orthogonality of the normal mode shapes of the beam without concentrated masses, one has:

$$\int_0^1\phi_i\left(\xi\right)\left[EI\phi_j''''\left(\xi\right)-L^4P\phi_j''\left(\xi\right)\right]d\xi=0 \quad if\ i\neq j \tag{5}$$

$$\int_0^1\phi_i\left(\xi\right)\mu\phi_j\left(\xi\right)d\xi=0 \qquad if\ i\neq j \tag{6}$$

Integrating the first term of Eq. (5) twice by parts, yields:

$$\begin{aligned}&\left[\phi_i\left(\xi\right)EI\,\phi_j'''\left(\xi\right)-\phi_i'\left(\xi\right)EI\,\phi_j''\left(\xi\right)\right]\Big|_0^1\\&+\int_0^1 EI\phi_i''^2\left(\xi\right)d\xi=0 \qquad if\ i\neq j\end{aligned} \tag{7}$$

It is noted that, for general boundary conditions the first two terms in Eq. (7) will be zero:

$$\begin{cases}\phi_i\left(\xi\right)EI\,\phi_j'''\left(\xi\right)\Big|_0^1=0 & \forall i,j\\ \phi_i'\left(\xi\right)EI\,\phi_j''\left(\xi\right)\Big|_0^1=0 & \forall i,j\end{cases} \tag{8}$$

Therefore, from Eqs. (6)-(9) we have:

$$\begin{aligned}&\int_0^1\left[\phi_i''(\xi)EI\phi_j''(\xi)-L^4P\phi_i''(\xi)\phi_j\left(\xi\right)\right]d\xi\\&=\begin{cases}0 & if\ i\neq j\\ \int_0^1\left[EI\phi_i''^2\left(\xi\right)-L^4P\phi_i''(\xi)\phi_i\left(\xi\right)\right]d\xi & if\ i=j\end{cases}\end{aligned} \tag{9}$$

Applying Eqs. (5)-(9), Eq.(4) can be rewritten as:

$$\begin{aligned}&\left[\int_0^1\mu\phi_i^2\left(\xi\right)d\xi+\sum_{k=1}^{n}m_k\phi_i\left(\xi_{mk}\right)\phi_j\left(\xi_{mk}\right)\right]\ddot{q}_i\left(t\right)\\&+\int_0^1\left[\frac{1}{L^4}EI\phi_i''^2\left(\xi\right)-L^4P\phi_i''(\xi)\phi_i\left(\xi\right)\right]d\xi q_i\left(t\right)=\phi_j\left(\xi_f\right)f\left(t\right)\end{aligned} \tag{10}$$

Eq. (10) can be expressed in matrix form as follows:

$$\mathbf{M}\ddot{\mathbf{q}}\left(t\right)+\mathbf{K}\mathbf{q}\left(t\right)=\mathbf{\Phi}\left(\xi_f\right)f\left(t\right) \tag{11}$$

where:

$$\mathbf{M}=\begin{bmatrix}m_{11} & m_{12} & \cdots & m_{1N}\\ m_{21} & m_{22} & \cdots & m_{2N}\\ \vdots & \vdots & \ddots & \vdots\\ m_{N1} & m_{N2} & \cdots & m_{NN}\end{bmatrix}$$

$$\begin{aligned}&m_{ii}=\int_0^1\mu\phi_i^2d\xi+\sum_{k=1}^{n}m_k\phi_i^2\left(\xi_{mk}\right),\ i=1,...,N\\&m_{ij=}\sum_{k=1}^{n}m_k\phi_i\left(\xi_{mk}\right)\phi_j\left(\xi_{mk}\right),\ i,j=1,...,N,i\neq j\end{aligned} \tag{12}$$

$$\mathbf{K}=\begin{bmatrix}k_{11} & 0 & \cdots & 0\\ 0 & k_{22} & \cdots & 0\\ \vdots & \vdots & \ddots & \vdots\\ 0 & 0 & 0 & k_{NN}\end{bmatrix}$$

$$k_{ii=}\int_0^1\left[\frac{1}{L^4}EI\phi_1''^2\left(\xi\right)--P\phi_1''(\xi)\phi_1\left(\xi\right)\right]d\xi,i=1,...,N \tag{13}$$

$$\mathbf{\Phi}(\xi)=\left[\phi_1(\xi),...,\phi_N(\xi)\right]^T,\ \ddot{\mathbf{q}}(t)=\left[\ddot{q}_1(t),...,\ddot{q}_N(t)\right]^T$$
$$\mathbf{q}(t)=\left[q_1(t),...,q_N(t)\right]^T \tag{14}$$

If the force is zero, Eq (11) becomes:

$$\mathbf{M}\ddot{\mathbf{q}}(t)+\mathbf{K}\mathbf{q}(t)=\mathbf{0} \tag{15}$$

Eq. (15) is the free vibration equation of the beam-masses system. The natural frequency Ω of beam carrying concentrated masses can be derived by solving the eigenvalue problem associated with Eq. (14), that is:

$$\mathbf{det}\left[\mathbf{K}-\Omega^2\mathbf{M}\right]=0 \tag{16}$$

If the force is harmonic $f(t)=\bar{f}e^{i\omega t}$ then the solution of Eq. (11) can be found in the form:

$$\mathbf{q}(t)=\bar{\mathbf{q}}e^{i\omega t} \tag{17}$$

Substituting Eq. (18) into Eq. (12) yields:

$$\left(\mathbf{K}-\omega^2\mathbf{M}\right)\bar{\mathbf{q}}=\mathbf{\Phi}\left(\xi_f\right)\bar{f} \tag{18}$$

Left multiplying Eq. (19) with $\dfrac{\mathbf{\Phi}^T(\xi)}{\bar{f}}\left[\left(\mathbf{K}-\omega^2\mathbf{M}\right)\right]^{-1}$, the receptance at ξ due to the force at ξ_f is obtained:

$$\alpha\left(\xi,\xi_f,\omega\right)=\frac{\mathbf{\Phi}^T(\xi)\bar{\mathbf{q}}}{\bar{f}}=\mathbf{\Phi}^T(\xi)\left(\mathbf{K}-\omega^2\mathbf{M}\right)^{-1}\mathbf{\Phi}\left(\xi_f\right) \tag{19a}$$

The receptance curvature is defined as:

$$\frac{\partial^2}{\partial\xi^2}\alpha\left(\xi,\xi_f,\omega\right)=\left(\mathbf{\Phi}^T\right)''(\xi)\left(\mathbf{K}-\omega^2\mathbf{M}\right)^{-1}\mathbf{\Phi}\left(\xi_f\right) \tag{19b}$$

Here, the term $\mathbf{\Phi}^T(\xi)\bar{\mathbf{q}}$ and $\bar{f}$ are the amplitudes of the response at ξ and the force at ξ_f, respectively. If the integrals $\int_0^1\mu\phi_i^2 d\xi$ and $\int_0^1 EI\phi_i''^2 d\xi$ in Eqs. (12) and (13) are determined, the general form of the receptance function (19) will be derived. In this paper the receptance function of a cracked simply supported Euler-Bernoulli beam carrying concentrated masses will be presented.

The mode shape and its second derivative of the cracked simply supported Euler-Bernoulli beam is adopted from [17]:

$$\phi_k(\xi)=C_1\left\{\frac{1}{\alpha_k^2+\beta_k^2}\sum_{i=1}^{n}\lambda_i\mu_i s_k U_i+\sin\alpha_k\xi\right\}$$
$$C_3+\left\{\frac{1}{\alpha_k^2+\beta_k^2}\sum_{i=1}^{n}\lambda_i\varsigma_i s_k U_i+\sin\beta_k\xi\right\} \tag{20}$$

$$\phi_k''(\xi)=C_1\left\{\frac{1}{\alpha_k^2+\beta_k^2}\sum_{i=1}^{n}\lambda_i\mu_i s_k U_i+\sin\alpha_k\xi\right\}$$
$$+C_3\left\{\frac{1}{\alpha_k^2+\beta_k^2}\sum_{i=1}^{n}\lambda_i\varsigma_i s_k U_i+\sin\beta_k\xi\right\} \tag{21}$$

with: $s_k=\alpha_k\sin\alpha_k\tilde{\xi}_i+\beta_k\sinh\beta_k\tilde{\xi}_i$

However, in order to calculate the square of the mode shape of beam, the product of two Dirac's deltas need to be determined. According to the multiplication for distributions proposed by Bagarello [18] the product of two Dirac's deltas is expressed as follows:

$$\delta\left(\xi-\xi_{0i}\right)\delta\left(\xi-\xi_{0j}\right)=\begin{cases}A\delta\left(\xi-\xi_{0i}\right), & i=j\\ 0, & i\neq j\end{cases} \tag{22}$$

Constant A is calculated from the expression:

$$A=\frac{1}{\pi}\int_{-1}^{1}\frac{\phi(x)}{\xi^2}d\xi \tag{23}$$

Where

$$\phi(\xi)=\begin{cases}\dfrac{\xi^m}{\kappa}e^{\frac{1}{\xi^2-1}} & |\xi|<1\\ 0 & |\xi|\geq 1\end{cases} \tag{24}$$

Here m is an even natural number and κ is a normalization constant which gives:

$$\int_{-1}^{1}\phi(\xi)=1 \tag{25}$$

In order to guarantee the existence of the integral in Eq. (23) it is assumed m=2, leading to A=2.0132.

From (22) the square of the second derivative of the mode shape of beam is derived.

$$
\begin{aligned}
&\int_0^1 \left[\phi_k''(\xi)\right]^2 d\xi \\
&= \Phi^2 \sum_{i=1}^{n}\sum_{j=1}^{n} \lambda_i \lambda_j A_1 \Bigg\{ \frac{\alpha_k^5}{5}\Big[2\alpha_k \cos\alpha_k\left(\xi_{0i}-\xi_{0j}\right)\left(1-\xi_{0i}U_{ij}-\xi_{0j}U_{ji}+\xi_{0i}\delta_{ij}\right) \\
&\qquad -\sin\alpha_k\left(2-\xi_{0i}-\xi_{0j}\right)+\sin\alpha_k\left|\xi_{0i}-\xi_{0j}\right|\Big] \\
&\qquad +2\alpha_k^3\beta_k^3\Phi\Big[\alpha_k\cos\alpha_k\left(1-\xi_{0i}\right)\sinh\beta_k\left(1-\xi_{0j}\right)-\beta_k\sin\alpha_k\left(1-\xi_{0i}\right)\cosh\beta_k\left(1-\xi_{0j}\right) \\
&\qquad -\alpha_k\sinh\beta_k\left(\xi_{0i}-\xi_{0j}\right)U_{ij}-\beta_k\sin\alpha_k\left(\xi_{0i}-\xi_{0j}\right)U_{ji}\Big] \\
&\qquad +\frac{\beta_k^5}{5}\Big[-2\beta_k\cosh\beta_k\left(\xi_{0i}-\xi_{0j}\right)\left(1-\xi_{0i}U_{ij}-\xi_{0j}U_{ji}+\xi_{0i}\delta_{ij}\right) \\
&\qquad +\sinh\beta_k\left(2-\xi_{0i}-\xi_{0j}\right)-\sinh\beta_k\left|\xi_{0i}-\xi_{0j}\right|\Big] \\
&\qquad +2\left(\alpha_k^2+\beta_k^2\right)\Big[\alpha_k^3\sin\alpha_k\left(\xi_{0i}-\xi_{0j}\right)-\beta_k^3\sinh\beta_k\left(\xi_{0i}-\xi_{0j}\right)\Big]U_{ji}+\left(\alpha_k^2+\beta_k^2\right)^2 A\delta_{ij}\Bigg\} \\
&+\Phi\sum_{i=1}^{n}\lambda_i A_2\Big\{\alpha_k^5\left(1-\xi_{0i}\right)\cos\alpha_k\xi_{0i}+\frac{\alpha_k^4}{2}\left[\sin\alpha_k\xi_{0i}-\sin\alpha_k\left(2-\xi_{0i}\right)\right]-2\alpha_k^2\left(\alpha_k^2+\beta_k^2\right)\sin\alpha_k\xi_{0i} \\
&\qquad +2\alpha_k^2\beta_k^3\Phi\left[\beta_k\sin\alpha_k\xi_{0i}-\beta_k\sin\alpha_k\cosh\beta_k\left(1-\xi_{0i}\right)+\alpha_k\cos\alpha_k\sinh\beta_k\left(1-\xi_{0i}\right)\right]\Big\} \\
&+\Phi\sum_{i=1}^{n}\lambda_i A_3\Big\{-\beta_k^5\left(1-\xi_{0i}\right)\cosh\beta_k\xi_{0i}-\frac{\beta_k^4}{2}\left[\sinh\beta_k\xi_{0i}-\sinh\beta_k\left(2-\xi_{0i}\right)\right]+2\beta_k^2\left(\alpha_k^2+\beta_k^2\right)\sinh\beta_k\xi_{0i} \\
&\qquad +2\alpha_k^3\beta_k^2\Phi\left[-\alpha_k\sinh\beta_k\xi_{0i}+\alpha_k\sinh\beta_k\cos\alpha_k\left(1-\xi_{0i}\right)-\beta_k\cosh\beta_k\sin\alpha_k\left(1-\xi_{0i}\right)\right]\Big\}
\end{aligned} \tag{26}
$$

where:

$$
\begin{aligned}
&A_1=\mu_i\mu_j C_1^2+\zeta_i\zeta_j C_3^2+2\mu_i\zeta_j C_1 C_3; \\
&A_2=\mu_i C_1^2+\zeta_i C_1 C_3;\; A_3=\zeta_i C_3^2+\mu_i C_1 C_3; \\
&\Phi=\frac{1}{\alpha_k^2+\beta_k^2}
\end{aligned} \tag{27}
$$

III. NUMERICAL SIMULATION

Numerical simulations of a simply supported beam with two cracks is presented in this section. Parameters of the beam are: Mass density ρ=7800 kg/m^3; modulus of elasticity E=2.0x10^{11} N/m^2; L=1 m; b=0.02 m; h=0.01 m. The first three natural frequencies of the intact beam are calculated and listed in Table 1.

TABLE 1. THREE NATURAL FREQUENCIES OF THE INTACT BEAM

Mode	Natural frequency (Rad/s)
1	146.4
2	585.7
3	1317.8

A. Influence of the axial force on the receptance

a)

b)

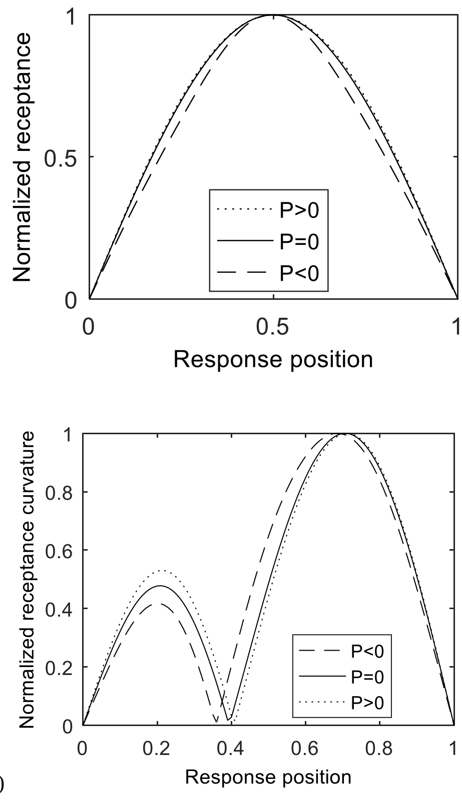

Fig. 2: Receptance curve of the intact beam: a) Receptance at the first natural frequency; b) Receptance at the second natural frequency

Figure 2a presents the receptance curve of the intact beam at the first natural frequency. It can be seen in this figure that the receptance of beam is lower when the beam is tensioned and it is higher when the beam is compressed. When there is a concentrated mass, the receptance curve of the beam is changed. Figure 2b presents the receptance curve when the forcing frequency is equal to the second frequency of the beam-mass system. As shown in Figure 2b, when the mass is located at 0.25*L*, the peak of receptane at the position of mass of the tensioned beam decreases. In addition, the receptance moves slightly to the left of the receptance of beam without axial force. In contrast, the receptane at the position of the compressed beam moves slightly to the right of the receptance of beam without axial force.

B. Simultanously influence of the mass and axial force on the receptance cuvature

In this section, in order to investigate the influence of the crack on the receptance curvature, two cracks with the same depths are made at arbitrary positions of 0.4*L* and 0.76*L* from the left end of the beam. Three crack depth levels ranging from 5% to 25% have been applied. The concentrated masses are $\bar{m}_1 = \bar{m}_2 = 0.6$, where $\bar{m}_k = \dfrac{m_k}{\mu}$.
The receptance curvature are calculated at 100 points spaced equally on the beam while the force is fixed at location of 0.75*L*. The forcing frequency is set equal to the first frequency.

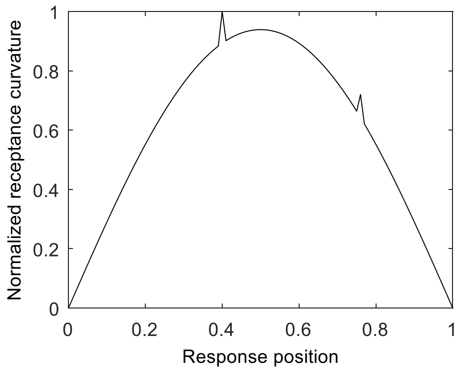

(a) Without mass

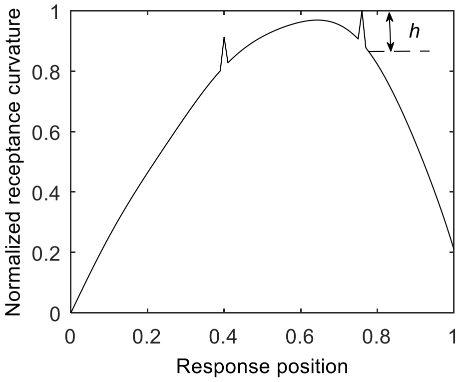

(b) P=-1x10^{3}N; Δh=33.7%

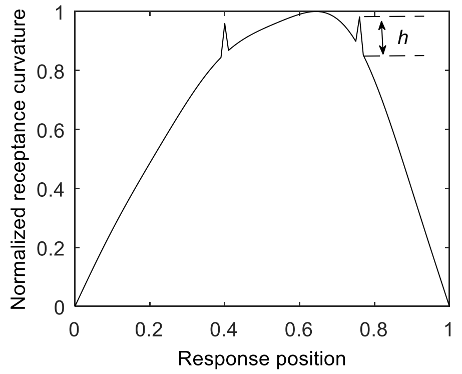

(c) P=0x10^{3}N; Δh=31.3%

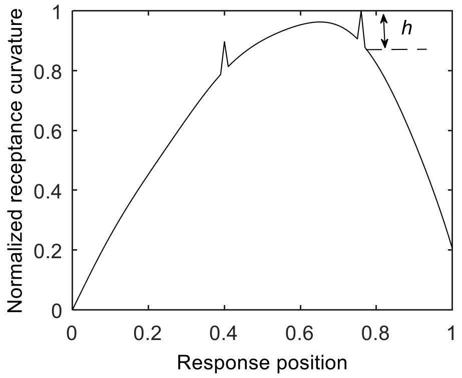

(d) P=1x10^{3}N; Δh=23.5%

Fig. 3: Receptance curvature, crack depth=5%; $\bar{m}_1 = 0; \bar{m}_2 = 0.6$

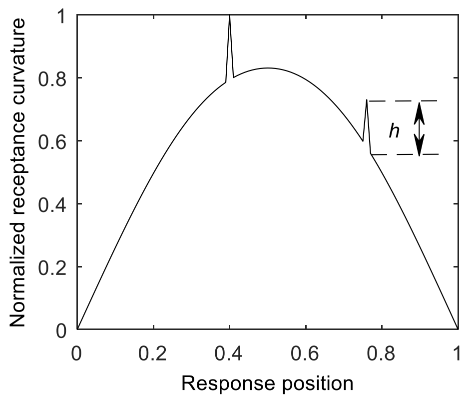

(a) Without mass

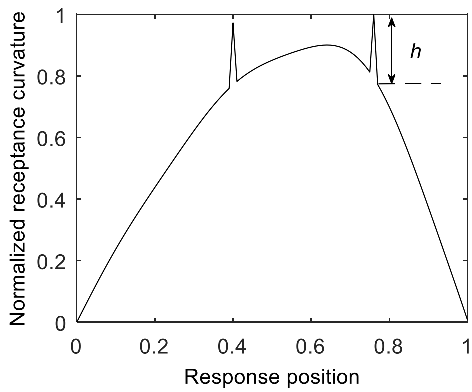

(b) P=-1x10^{3}N; Δh=37.1%

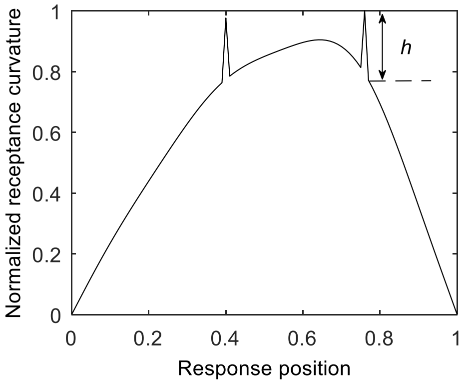

(c) P=0x10^{3}N; Δh=35.9%

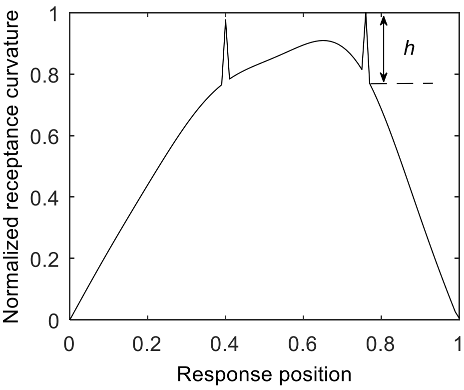

(d) P=1x10^{3}N; Δh=35.3%

Fig. 4: Receptance curvature, crack depth=10%: Δh=33.6%

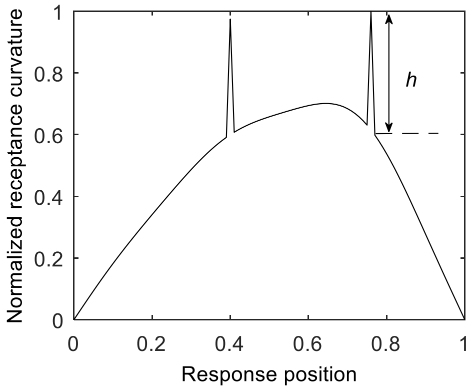

(c) P=0x10^{3}N; Δh=37.6%

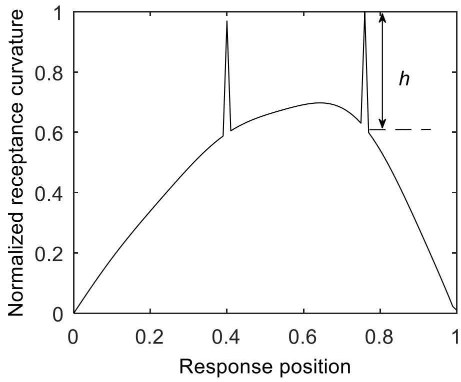

(d) P=1x10^{3}N; Δh=37.3%

Fig. 5: Receptance curvature, crack depth=20%: Δh=36.4%

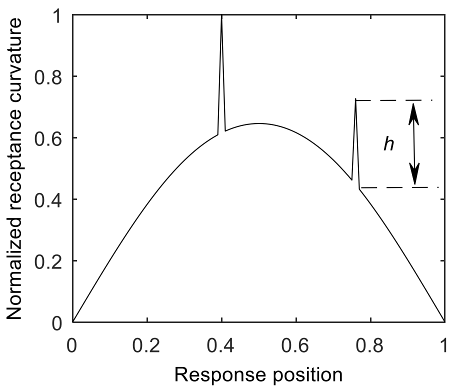

(a) Without mass

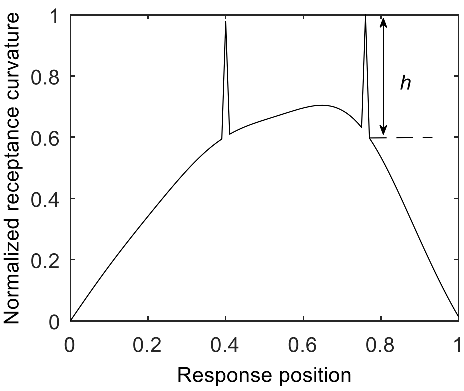

(b) P=-1x10^{3}N; Δh=37.9%

Figs. 3a, 4a, 5a present the graphs of normalized receptance curvature of the cracked beam without a concentrated mass. As can be observed from these figures, the positions of the sharp peaks are clearly detected at 0.4L and 0.76L which are the same with the crack positions. As can be observed from Figs. 3, 4, 5 when the crack depth increases from 5% to 20%, the height of sharp peaks in receptance curvature increase and becomes clearer.

When the crack depth is equal to 5% and there is one mass attached at the smaller peak at 0.76L, the height of the peak at that position in the receptance curvature increase significantly. As can be seen from Figs. 3b, 3c, 3d, the increase of the height of peak Δh is 33.7%, 31.3%, 23.5% when the axial force P=-1x10^{3}N, 0x10^{3}N, 1x10^{3}N, respectively. However, when the mass is attached at the location of 0.4L where the peak is larger, the influence of the mass is trivial. Our numerical simulation has pointed out that, the mass only has effect on the smaller peak. When the crack depth is 10% the Δh=37.1%, 35.9%, 35.3% for the cases P=-1x10^{3}N, 0x10^{3}N, 1x10^{3}N, respectively. Similarly, when the crack depth is 20% the Δh= 37.9%, 37.6%, 37.3% for the cases P=-1x10^{3}N, 0x10^{3}N, 1x10^{3}N, respectively.

Our simulation has shown that when there are two equal masses attached at two crack positions, the effects of the masses on the peaks of the receptance curvature are both small. This implies that the mass only amplifies the smaller peak in the receptance curvature. Therefore, in order to amplify the small peak in the receptance curvature of the cracked beam, only one mass is needed.

C. Influence of axial force on the crack detection

Simulation results show that the axial force has significant influence on the proposed method. Fig. 6 presents the relationship between the height of peak in the receptance curvature and the axial force when the crack depth is 20% of the beam height. As can be seen from this figure, the height of peak in the receptance curvature decreases when the axial force increases. It is noted that the rate of change of the peak height can be divided into two intervals: when the axial force ranges from $-1\text{x}10^3$N to $0\text{x}10^3$N, the height of peak decreases slowly; when the axial force ranges from 0N to $1\text{x}10^3$N, the height of peak decreases rapidly. This results suggest that the proposed method can be applied more effective for the tensioned beam than the compressed beam.

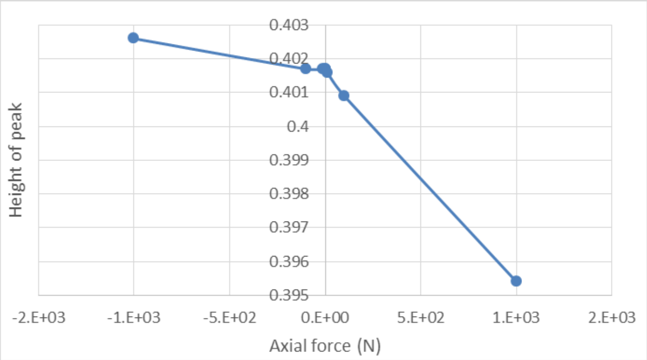

Fig. 6. Height of peak with different axial forces

IV. CONCLUSION

In this paper, the exact formula of the receptance curvature function of a simply supported cracked beam carrying masses is presented. The numerical simulations have been carried out to investigate the simultaneous influence of the crack and masses on the receptance curvature. The proposed method is useful for crack detection of axially loaded elements such as cables in cable stayed bridges.

When there are cracks, the receptance curvature is changed significantly at the crack positions and it can be used for crack detection. In addition, when there is a concentrated mass attached at crack position, the small peaks in the receptance curvature are amplified significantly. For the crack detection purpose, it is recommended that only one mass need to be attached on the beam in order to amplify the small peak in the receptance curvature of the cracked beam.

In this numerical simulation, the crack can be detected when the depth is as small as 5% of the beam height.

ACKNOWLEDGMENT

This research is funded by the Institute of Mechanics, Vietnam Academy of Science and Technology.

REFERENCES

[1] Milne HK. The receptance functions of uniform beams. *Journal of Soundand Vibration*, 131, (3), (1989), pp. 353-365.

[2] Yang B. Exact receptances of nonproportionally damped systems. *Transactions of American Society of Mechanical Engineers Journal of Vibration and Acoustics*, 115, (1993), pp. 47–52.

[3] In RM, Lim MK. Derivation of structural design sensitivities from vibration test data. *Journal of Sound and Vibration*, 201, (1997), pp. 613–631.

[4] Gurgoze M. Receptance matrices of viscously damped systems subject to several constraint equations. *Journal of Sound and Vibration*, 230, (5), (2000), pp. 1185-1190.

[5] Gurgoze M, Erol H. On the frequency response function of a damped cantilever simply supported in-span and carrying a tip mass. *Journal of Sound and Vibration*, 255, (3), (2002), pp. 489-500.

[6] Karakas A, Gurgoze M. A novel formulation of the receptance matrix of non-proportionally damped dynamic systems. *Journal of Sound and Vibration*, 264, (2003), pp. 733–740.

[7] Arlaud E, D'Aguiar SC, Balmes E. Receptance of railway tracks at low frequency: Numerical and experimental approaches. *Transportation Geotechnics*, 9, (2016), pp. 1–16.

[8] Burlon A, Failla G, Arena F. Exact frequency response analysis of axially loaded beams with viscoelastic dampers. *International Journal of Mechanical Sciences*, 115-116, (2016), pp. 370–384.

[9] Burlon A, Failla G, Arena F. Exact frequency response of two-node coupled bending-torsional beam element with attachments. *Applied Mathematical Modelling*, 63, (2018), pp. 508–537.

[10] A.K. Pandey M. Biswas, and M.M. Samman, Damage detection from changes in curvature mode shapes. *Journal of Sound and Vibration*, 145, (2), (1991), pp. 321-332.

[11] M.M. Abdel Wahab, Damage detection in bridges using modal curvature: application to a real damage scenario. *Journal of Sound and Vibration*, 226, (2), (1999), pp. 217-235.

[12] W. Zhang, Z. Wang, H. Ma, Crack identification of stepped cantilever beam combining wavelet analysis with transform matrix. *Acta Mechanica Solida Sinica*, 22, (4), (2009), pp. 360–368.

[13] K. V. Nguyen, Mode shapes analysis of a cracked beam and its application for crack detection. *Journal of Sound and Vibration*, 333, (2014), pp. 848–872.

[14] S. Caddemi and I. Calio, Exact closed-form solution for the vibration modes of the Euler–Bernoulli beam with multiple open cracks. *Journal of Sound and Vibration*, 327, (2009), pp. 473-489.

[15] S. Caddemi, I. Caliò. Exact reconstruction of multiple concentrated damages on beams. *Acta Mechanica*, 225, (11), (2014), pp. 3137-3156.

[16] K. V. Nguyen, M.V. Cao, Exact receptance function of cracked beams and Its application for crack detection. *Shock and Vibration Volume*, (2019), Article ID 9485351, 19 pages.

[17] B. Biondi, S. Caddemi, Closed form solutions of Euler–Bernoulli beams with singularities. *International Journal of Solids and Structures*, 42, (2005), pp. 3027–3044.

[18] F. Bagarello, Multiplication of distribution in one dimension: possible approaches and applications to d-function and its derivatives. *Journal of Mathematical Analysis and Applications*, 196, (1995), pp. 885–901.

Force Control of an Upper Limb Exoskeleton for Perceiving Reality and Supporting Human Movement Using Feed-forward Model

Nguyen Dong Anh
Department of Structural Mechanics
Institute of Mechanics, VAST
Hanoi, Vietnam
ndanh@imech.ac.vn

Manukid Parnichkun
School of Engineering and Technology
Asian Institute of Technology
Bangkok, Thailand
manukid@ait.asia

Phan Thi Tra My
Department of Structural Mechanics
Institute of Mechanics, VAST
Hanoi, Vietnam
tramypt86@gmail.com

Nguyen Cao Thang
Department of Structural Mechanics
Institute of Mechanics,VAST
Hanoi, Vietnam
caothang2002us@yahoo.com

Le Thi Hong Gam
Faculty of Physics
ThaiNguyen University of Education
ThaiNguyen, Vietnam
gamlth@tnue.edu.vn

Pham Ngoc Chung
Faculty of Basic Science
Hanoi University of Mining and Geology
Hanoi, Vietnam
chunghumg86@gmail.com

Nguyen Nhu Hieu
Faculty of Mechanical Engineering and Mechantronics
Phenikaa University
Hanoi, Vietnam
hieu.nguyennhu@phenikaa-uni.edu.vn

***Abstract*: There is much attraction in developing the upper limb exoskeleton in many applications such as supporting human movement, rehabilitation and training. This paper presents the dynamics analysis and control of the three degree of freedom (DOF) upper limb exoskeleton using the feed-forward model (FFM). In the upper limb exoskeleton, the interaction force between the human operator's hand and the end effector is uncertain and nonlinear due to the disturbance effect of Coriolis force, centrifugal force, gravitational force and friction force; it can be sensed by using a 3-axis force sensor placed at the end effector. In the feed-forward model, the interaction force is considered as an error or disturbance. The force control will reduce the error by using proportional integral derivative (PID) weight gains FMM. For stability, the derivative portion of the PID weight gains FFM is filtered by the low pass filter (LPF). The application of LPF-PID weight gains FFM in control of the 1 DOF upper limb exoskeleton is shown in an experiment.**

Keywords: 3 DOF upper limb exoskeleton, Proportional Integral Derivative (PID) weight gains FFM, feed-forward model (FFM), human machine interaction force, force sensor, servo motor, perceiving reality, and rehabilitation.

I. INTRODUCTION

The research aims to research and develop a three degree of freedom (3-DOF) upper limb exoskeleton. The 3-DOF upper limb exoskeleton is an external structure in the shape of human upper limb and is directly attached to human upper limb. It is equipped with force sensors for sensing the vector of forces exerted by the human operator at the end effector, and actuators for exerting necessary torques in revolute joints at wrist, elbow and shoulder. The controller regulates the interaction force to be a desired force reflection on the human operator. The control program is force feed-forward model. Kazerooni H. ([1], 1990) proposed an 1-DOF extender of upper extremity which used one set of piezoelectric load cell placed at the elbow link to sense the forces imposed by the human operator. The human operator is the center of controller, can receive physical feedback force from the extender; perceive a smaller amount of the force imposed by the environment and control the movement of the extender. Following this technique, Jing Tang et al. (2018), [2], proposed the direct force control of a 2-DOF upper limb exoskeleton for supporting human movement. In that direct force control model, there are two sets of force and torque sensors. The force sensor placed at the end effector measure the interaction force which is the force exerted by the human operator. The torque sensors placed at the joints measure the torque generated by the electrical motors. The measured forces and torques are utilized by a three closed-loop controller to control the 2 DOF upper limb exoskeleton. In the closed loop 1 (core loop), the human exerts force at the end effector to control the upper limb exoskeleton. The closed loop 2 is Proportional Derivative (PD) weight gains feed-forward controller and the closed-loop 3 is a Proportional Integral (PI) weight gains feed-back controller. In feed-forward model, the physical interaction force is considered as a force error or disturbance force. The target of the controller is to reduce the force exerted by the human operator at the end effector. In feed-back model, the torque generated by electrical motor is compared with the desired torque, thus the control voltage of electrical motor is controlled by the torque error. In [2], the force error can be sensed by a force sensor or is approximately considered by a spring model. In the spring model, the interaction force is modeled by the position error between the desired motion and current motion of the end effector. Developing this technique, Nguyen Cao Thang et al. (2019), [3], [4] have developed the Proportional Integral Derivative (PID) weight gains feed-forward model for a 3 DOF systems. In [3], the PI feed-forward model was proposed to control the torque of a 3-DOF upper limb exoskeleton. In [4], a three closed-loop controller including the human control model, PD weight gains feed-forward model and the PI weight gains feed-back model which was proposed in [2] was applied to control a 3-DOF upper limb exoskeleton to support human movement. However, in [4] the constant interaction force is not realistic. P.V.B. Ngoc et al. [5] promoted the PI weight gains feed-forward model to control a 3-DOF lower limb rehabilitation robot.

In this paper, the authors research and develop the PID weight gains feed-forward model for a 3 DOF upper limb exoskeleton to support human movement. The authors suggest that the novel PID weight gains feed-forward model will reduce the force exerted by the human operator at the end effector. This paper presents the modeling and simulation of a 3-DOF upper limb exoskeleton, and an experiment of a real 1-DOF upper limb exoskeleton. The aim of the controller is perceiving the vector of forces exerted by human operator and reducing them. In the paper, a scenario is considered in which there are two loops. Loop 1: the human operator exerts force at the end effector and can feels the external load or perceiving reality. The controller can track the orientation and magnitude of the physical interaction force between the human operator's hand and the end effector. The generalize moments exerted by the human operator at joints are derived by using transposed Jacobian matrix. In Loop 2, the PID weight gains FFM will utilize the human torque to control three motors located at joints to assist human operator to perform some tasks: moving freely and lifting some objects vertically and horizontally. By simulation and experiment, we can investigate the performance, stability, and smoothness of proposed controller. We can guarantee the stability of the system base on the low past filters (LPF) for derivative control, and adjust the control torque to avoid the chattering phenomenon. As the result, the human operator will naturally feel the external load first, after that he can be supported in a desired loading motion.

II. MODEL OF 3 DOF UPPER LIMB EXOSKELETON

The model of a 3 DOF upper limb exoskeleton is shown in figure 1.

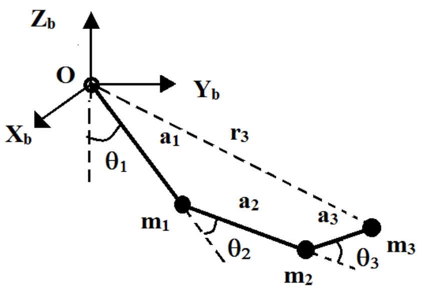

Fig.1. A three DOF upper limb exoskeleton

The upper limb exoskeleton system is a popular serial robotic chain including a joint at the shoulder (θ_1), a joint at the elbow (θ_2), and a joint at the wrist (θ_3), with 3 links namely: shoulder a_1, elbow a_2, and the wrist a_3. The length and masses of three links are a_1, a_2, a_3 and m_1, m_2, m_3 respectively.

Three geared servo motors are installed to power three links. In each servo motor, there is a position sensor used to measure rotation angle. At the end effector, a 3-axis force sensor is used to measure force exerted by the human operator's hand.

Denavite - Hartenberge (D-H) table is shown in Table 1.

TABLE 1. DENAVITE - HARTENBERGE (D-H) PARAMETERS FOR 3 DOF UPPER LIMB EXOSKELETON

Joint	a	α	d	θ
	0	$\pi/2$	0	$\pi/2$
1	a_1	0	0	$\theta_1-\pi/2$
2	a_2	0	0	θ_2
3	a_3	$-\pi/2$	0	θ_3
	0	0	0	$-\pi/2$

In Table 1, the parameters a_i are constant. Only the variables θ_i (i=1, 2, 3) vary by rotation around z_{i-1} axis. From D-H table, the homogeneous transformation matrices are obtained using equation (1), Spong MW, Hutchinson S, and Vidyasagar M. (2004) [6].

$$\mathbf{A}_i^{i-1} = Rot(z,\theta_i)Trans(0,0,d_i)Rot(x,\alpha_i)Trans(a_i,0,0) = \begin{bmatrix} \cos\theta_i, & -\sin\theta_i\cos\alpha_i, & \sin\theta_i\sin\alpha_i, & a_i\cos\theta_i, \\ \sin\theta_i, & \cos\theta_i\cos\alpha_i, & -\cos\theta_i\sin\alpha_i, & a_i\sin\theta_i, \\ 0, & \sin\alpha_i, & \cos\alpha_i, & d_i, \\ 0, & 0, & 0, & 1 \end{bmatrix} \quad (1)$$

The homogeneous transformation matrix that transforms the reference coordinate {3}, which is at the end effector to the reference coordinate {b}, or the fixed base, can be calculated by multiplying individual transformation matrices as follows.

$$\mathbf{A}_3^b = \mathbf{A}_1^b\mathbf{A}_2^1\mathbf{A}_3^2 \quad (2)$$

III. CONTROLLER DESIGN

The dynamics equation of motion is presented as the following equation. It can be conveniently constructed in matrix form, which is suitable for MDOF system (Do Sanh et al. [7]).

$$\mathbf{M}(\boldsymbol{\theta})\boldsymbol{\xi}+\mathbf{C}(\boldsymbol{\theta},\boldsymbol{\omega})+\mathbf{K}\boldsymbol{\theta}+\mathbf{G}(\boldsymbol{\theta})+\mathbf{F}(\boldsymbol{\omega}) = \mathbf{u}_S+\mathbf{J}(\boldsymbol{\theta})^T\mathbf{F}_{h\_global} \quad (3)$$

Where,

$\boldsymbol{\theta} = [\theta_1 \quad \theta_2 \quad \theta_3]^T$ - Vector of angles of rotation in joints 1, 2, 3.

$\boldsymbol{\omega} = [\omega_1 \quad \omega_2 \quad \omega_3]^T = \begin{bmatrix} \frac{d\theta_1}{dt} & \frac{d\theta_2}{dt} & \frac{d\theta_3}{dt} \end{bmatrix}^T$ - Vector of angular velocities in joints 1, 2, 3.

$\boldsymbol{\xi} = [\xi_1 \quad \xi_2 \quad \xi_3]^T = \begin{bmatrix} \frac{d^2\theta_1}{dt^2} & \frac{d^2\theta_2}{dt^2} & \frac{d^2\theta_3}{dt^2} \end{bmatrix}^T$ - Vector of angular accelerations in joints 1, 2, 3.

$\mathbf{u}_S = [u_{S1} \ u_{S2} \ u_{S3}]^T$ - Vector of supporting torques exerted by servo motors in joints 1, 2, 3.

$\mathbf{F}_{h\_global} = \left[F_{X_b}, \ F_{Y_b}, \ F_{Z_b}\right]^T$ - Vector of forces exerted by human operator at the end effector in the reference coordinate {b}, or the fixed base.

$\mathbf{A}_3^b$ - The homogeneous transformation matrix;

${}_{(b)}\mathbf{r}_3 = [x_3\ \ y_3\ \ z_3]^T = \mathbf{A}_3^b(1:3,4)$ - The end effector's position vector is defined by the first three rows and the last column of the homogeneous transformation matrix, given in equation (2);

$\mathbf{J}(\boldsymbol{\theta})$ - The Jacobian matrix.

The symbol (T) denotes the transpose of a matrix.

M(θ), C(θ,ω), G(θ), Kθ are matrix of inertia masses, vector of Coriolis and centrifugal forces, vector of gravity forces, and vector of elastic force, respectively, which are derived using Lagrange equation.

$\mathbf{F}(\boldsymbol{\omega})$ - Joint Friction force Vector

Friction modeling: The joint friction is modeled as the combination of both Coulomb and viscosity friction. The joint friction of joint *i (i=1,2,3)* can be expressed as follows.

$$F_i(\omega_i) = \tau_{Ci} sgn(\omega_i) + b_i \omega_i \tag{4}$$

$$sgn(\omega_i) = \begin{cases} 1 & \omega_i > 0 \\ 0 & \omega_i = 0 \\ -1 & \omega_i < 0 \end{cases} \tag{5}$$

In this paper, we consider a scenario:

Loop 1: At the beginning, a human operator moves the robot by exerting force at the end effector to guide the robot to follow a desired loading motion. At this stage, the human operator can feel the external load and the robot's weight. The angular sensors (encoders) installed at joints can measure the joints angles and the force sensor installed in the end effector can measure the forces exerted by the human operator.

Loop 2: After a delayed time, the human operator can feel a smaller amount of the external load and the robot's weight because the robot has been activated to support the movement of the joints.

The block scheme of controller system is shown in figure 2. In the loop 1, the human operator exerts the interaction force at the end effector to control the upper limb exoskeleton himself. The interaction force is considered as force error or a disturbance force. In this loop 1 of control process, the interaction force and the current positions of joints are sent to the Controller. In the Loop 2, the Controller will control torques in joints of the Exoskeleton. The target of the Feed-Forward Controller is to reduce the disturbance force.

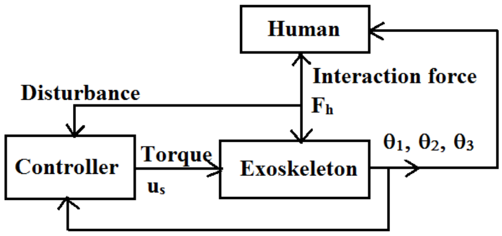

Fig. 2. Block scheme of feed-forward model system.

The interaction force is vector of forces exerted by the human operator at the end effector; it can be measured by using a 3 axis force sensor. For realistic simulation, the simulated interaction force $\mathbf{F}_{h\_global}$ that is exerted by the human operator at the end effector is approximately modeled by a spring model. It is proportional to the position error between the desired and current loading motion of the exoskeleton's end effector.

$$\mathbf{F}_{h\_global} = K_f(r_{3ds} - r_3) \tag{6}$$

Where, ${}_{(b)}\mathbf{r}_{3ds} = [x_{3ds}\ \ y_{3ds}\ \ z_{3ds}]^T$ is the desired position of the exoskeleton's end effector.

${}_{(b)}\mathbf{r}_3 = [x_3\ \ y_3\ \ z_3]^T$ is the current position of the exoskeleton's end effector,

K_f is the stiffness weight gain matrix of the interaction model. The forces and torques exerted by the human operator is also proportional to the stiffness weight gain matrix.

In Loop 1: the human operator applies some force to move the end effector in a desired loading motion using his own hand. The forces exerted by the human operator are directly transformed to the generalized torques at joints using transposed Jacobian matrix. At this stage, the human operator can feel the external load and the robot's weight.

$$\mathbf{u_H} = \mathbf{J}^T(\boldsymbol{\theta})\mathbf{F}_{h\_global} \tag{7}$$

Where, $\boldsymbol{\theta}$ - Vector of angles,

$\mathbf{F}_{h\_global}$ - Vector of global interaction forces.

In Loop 2: the upper limb exoskeleton (the robot) can supply the power in order to support the human operator's movement. At this stage, the human operator can still feel the smaller amount of the external load and the robot's weight.

In order to deal with this scenario, the proportional - integral - derivative (PID) weight gains FFM control will follow formula (8).

$$\mathbf{u}_{PID} = \mathbf{w}_P.\mathbf{u_H} + \mathbf{w}_I.\int_0^t \mathbf{u_H} d\tau + \mathbf{w}_D.\mathbf{u_K} \tag{8}$$

Where, $\mathbf{u_H} = [u_{H1}\ \ u_{H2}\ \ u_{H3}]^T$ is the vector of generalized torques exerted by the human operator at joints (the human operator's torque).

$\mathbf{u_K} = [u_{K1}\ \ u_{K2}\ \ u_{K3}]^T$ is the vector of derivative respect to time of human operator's generalized torque after the low pass filter.

$\mathbf{w}_P, \mathbf{w}_I, \mathbf{w}_D$ are the proportional - integral - derivative weight gains matrices.

In order to create the smoothness for the controlling process, we use a first order low pass filter (LPF) for controlling the derivative portion of PID formula (derivative control). The derivative respect to time of the human operator's generalized torques $d(u_{Hi})/dt$ $(i = 1,2,3)$ will be filtered by LPF leading to the smoothing derivative respect to time of generalized torques: u_{Ki} $(i = 1,2,3)$ following equation (9) or (10).

$$\tau_i \frac{d}{dt}(u_{Ki}) + u_{Ki} = \frac{d}{dt}(u_{Hi}) \tag{9}$$

Where, τ_i $(i = 1,2,3)$ are time constant of LPF *i*.

u_{Ki} $(i = 1,2,3)$ are smoothing derivative respect to time of the human operator's generalized torques after LPF.

$\frac{d}{dt}(u_{Hi})$ $(i=1,2,3)$ are derivative respect to time of the human operator's generalized torques before LPF.

Or one can use the Discrete Low Pass Filter (DLPF) for Derivative Control as follows.

$$u_{Ki}(t_k) = (1-r_i)*u_{Ki}(t_{k-1}) + r_i*\frac{d}{dt}(u_{Hi}(t_k)) \tag{10}$$

$$\frac{d}{dt}(u_{Hi}(t_k)) \approx u_{Hi}(t_k) - u_{Hi}(t_{k-1})$$

Where, $u_{Hi}(t_k)$ – Human torque at joint i ($i=1,2,3$)

$\frac{d}{dt}(u_{Hi}(t_k))$ – Derivative of human torque (approximated by current and previous human torque)

$u_{Ki}(t_k)$ - Derivative of human torque after LPF.

r_i – Smoothing factor.

For stably controlling of joint torques, the control torques at joints i ($i=1, 2, 3$) are adjusted as follows.

$$\begin{aligned} &\textit{if} \quad u_{PIDi} < -p_i \quad \textit{then} \quad u_{Si} = -s_i \\ &\textit{elseif} \quad u_{PIDi} > p_i \quad \textit{then} \quad u_{Si} = s_i \\ &\textit{else} \quad u_{Si} = 0 \end{aligned} \tag{11}$$

Where, $p_i, (i=1,2,3)$, (Nm) are perceiving parameters.

$s_i, (i=1,2,3)$, (Nm) are supporting parameters.

The perceiving parameters can delay the control torques to avoid chattering problem for the stability of proposed control system. The supporting parameters can create different levels of support.

IV. Simulation and Results

In this simulation of force control using Matlab software [8], the parameters of the mechanical system are:

$a_1 = 0.25$, $a_2=0.30$, $a_3= 0.1$ (m): length of links 1, 2, 3, respectively. $m_1 = 0.5$, $m_2 = 0.5$, $m_3 = 0.5$ (kg): the mass of links 1, 2, 3, respectively. $g = 9.81 \quad (\mathrm{m/s^2})$ (12)

Using the Proportional - Integral - Derivative weight gains FFM controller, The PID torques are the scale up versions of the human operator's torques. The weight gains matrices $\mathbf{w}_P$, $\mathbf{w}_I$, $\mathbf{w}_D$ and time constants of LPF are:

$$\mathbf{w}_P = \begin{bmatrix} 1 & 0 & 0 \\ 0 & 1 & 0 \\ 0 & 0 & 1 \end{bmatrix}, \mathbf{w}_I = \begin{bmatrix} 0.1 & 0 & 0 \\ 0 & 0.1 & 0 \\ 0 & 0 & 0.1 \end{bmatrix}, \tag{13}$$

$$\mathbf{w}_D = \begin{bmatrix} 0.1 & 0 & 0 \\ 0 & 0.1 & 0 \\ 0 & 0 & 0.1 \end{bmatrix}, \begin{bmatrix} \tau_1 \\ \tau_2 \\ \tau_3 \end{bmatrix} = \begin{bmatrix} 0.1 \\ 0.1 \\ 0.1 \end{bmatrix} \quad (s)$$

The interaction force and the stiffness weight gains matrix of the interaction model is set as follows.

$$\mathbf{F}_{\mathrm{h\_global}} = K_f(\mathrm{r}_{3d} - \mathrm{r}_3) \tag{14}$$

$$K_f = \begin{bmatrix} 0 & 0 & 0 \\ 0 & 100 & 0 \\ 0 & 0 & 100 \end{bmatrix} \quad (\mathrm{N/m})$$

The desired end effector's position vector is definitely following the three desired angles of joints. The desired angles of joints are below:

$$\begin{bmatrix} \theta_{1ds} \\ \theta_{2ds} \\ \theta_{3ds} \end{bmatrix} = \begin{bmatrix} \sin(t) \\ \sin(t) \\ 0.2*\sin(t) \end{bmatrix} \quad (\mathrm{rad}) \tag{15}$$

The initial position and speed of the joints are below:

$$\boldsymbol{\theta}_0 = \begin{bmatrix} 0 \\ 0 \\ 0 \end{bmatrix} (\mathrm{rad}); \quad \dot{\boldsymbol{\theta}}_0 = \begin{bmatrix} 0 \\ 0 \\ 0 \end{bmatrix} (\mathrm{rad/s}) \tag{16}$$

The joint friction coefficients are set as follows.

$$\tau_{Ci} = 0.1, b_i = 0.1, (i=1,2,3) \tag{17}$$

The joint stiffness coefficients matrix is set as follows.

$$K = \begin{bmatrix} 0 & 0 & 0 \\ 0 & 0 & 0 \\ 0 & 0 & 100 \end{bmatrix} \quad (\mathrm{Nm/rad}) \tag{18}$$

The perceiving parameters and supporting parameters of control torques are:

$$p_1 = 4, p_2 = 2, p_3 = 1, s_1 = 3, s_2 = 1.5, s_3 = 0.75 \quad (\mathrm{Nm}) \tag{19}$$

In the time axis, the duration of simulation is 10 seconds.

In the simulation program, the following equations (4) to (19) are simultaneously solved with the equation (3) by using ode solver ode45 in Matlab software.

In the simulation, the movement of the end effector in Y_bZ_b plane is shown in figure 3.

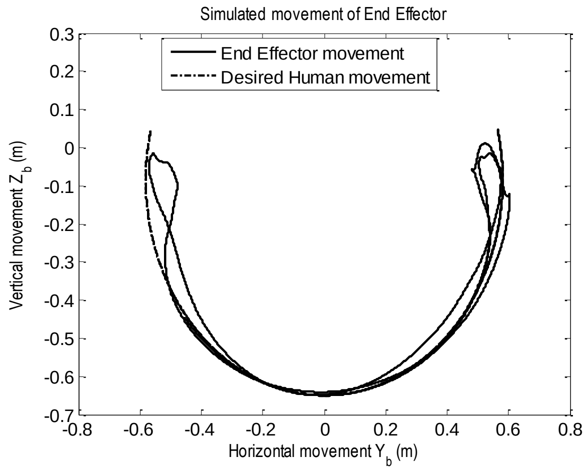

Fig. 3. Movement of end effector in Y_bZ_b plane

The interaction force exerted by human at the end effector is shown in figure 4.

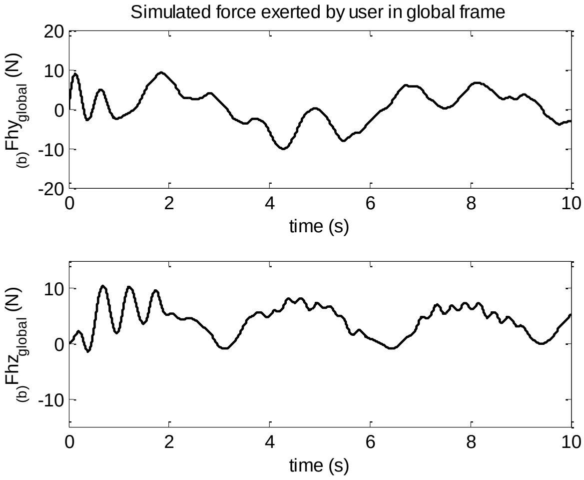

Fig. 4. Force exerted by human operator at the end effector in global frame {b} (attached to base)

The human torques, PID torques and Control torques at joint 1, 2, and 3 are shown in figures 5, 6, and 7.

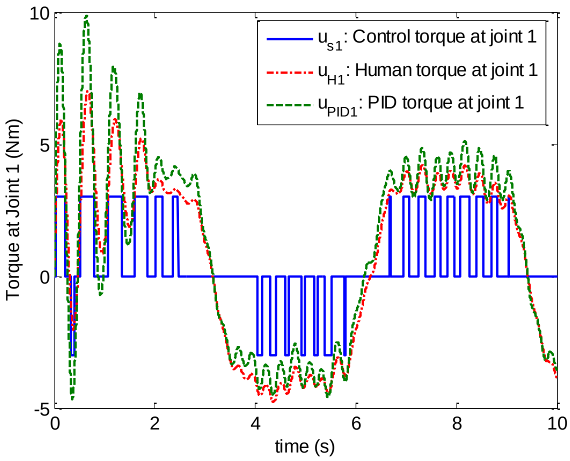

Fig. 5. Torque exerted by Human operator, and Controller in Joint 1

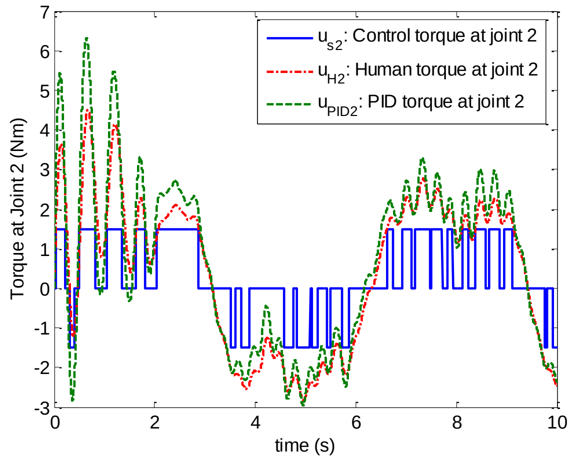

Fig. 6. Torque exerted by Human operator, and Controller in Joint 2

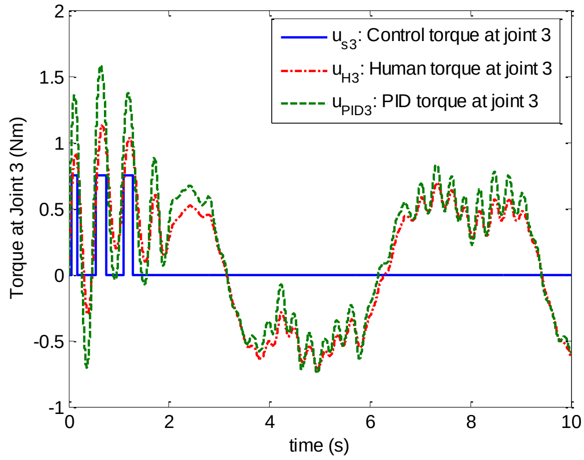

Fig. 7. Torque exerted by Human operator, and Controller in Joint 3

Since the supporting parameters s_1, s_2, s_3 can adjust the control torques, the strength of support depends on the supporting parameters. The control torques at joints can jointly support the human.

V. EXPERIMENT AND RESULTS

The experiment of PID weight gains feed-forward model to control a 1 DOF upper limb exoskeleton to support human operator's movement is shown in figure 8.

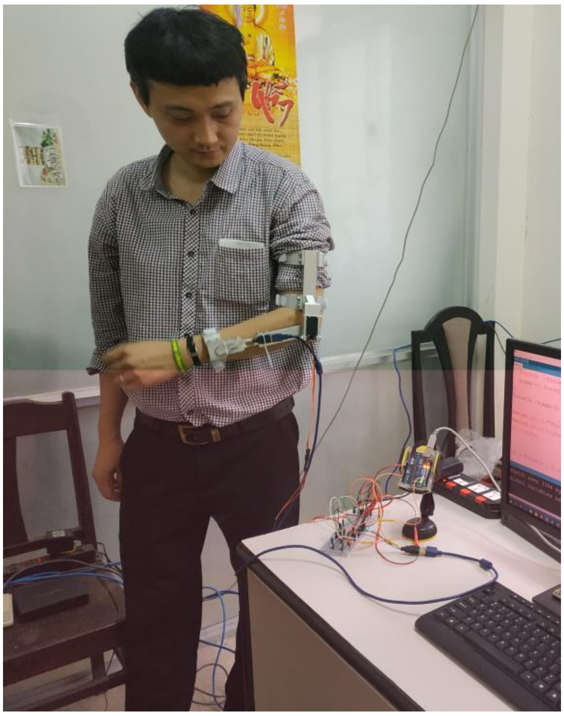

Fig. 8. An 1 DOF upper limb exoskeleton developed at Institute of Mechanics (VAST)

The 1 DOF exoskeleton has two links and one joint called elbow joint. The lengths of link 1 (shoulder link) and link 2 (elbow link) are l_1 = 0.16 (m) and l_2 = 0.2 (m), respectively. The single axis load cell whose max load is 9.8 (N) has very weak output voltage 0.001 (V), is placed at the link 2 to detect the physical interaction force. There is one servo motor whose max torque is approximately 1 (Nm), with very high gear ratio 280:1, in the elbow position of the exoskeleton.

In this experiment, we consider a scenario:

Loop 1: When the human operator moves his arm in flexion and in extension movement, the load cell will measure the interaction force between the human operator's arm and the elbow link of the exoskeleton.

Loop 2: The FFM will control the torque of the servo motor to support the user's elbow rotation and reduce the physical interaction force of the human operator.

The force control system is shown in figure 9.

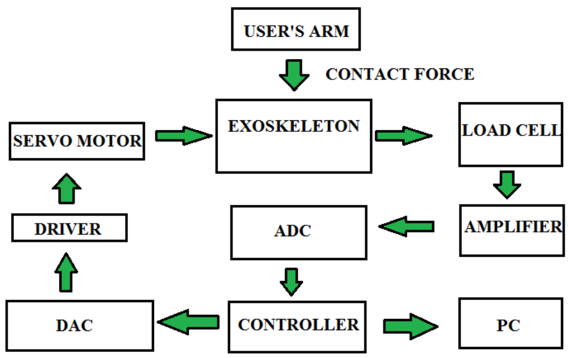

Fig. 9. Set up of the experiment

In figure 9, when the human hand moves, the interaction force F_{h_local} will be measured by the load-cell. The very weak measured voltage of the load-cell is amplified by the Operational Amplifier (OpAm). That amplified voltage will high enough so that the controller can input through the Analog to Digital Converter (ADC) channel. The controller will output the Pulse Width Modulation (PWM) signal through the Digital to Analog (DAC) channel to control a motor driver circuit (Driver) placed inside the Servo Motor. Since the control torque of the Servo Motor is geared up, the exoskeleton will support human movement. The PC is used for building source code and uploading the machine code to the controller; and displaying the results of the experiment.

When applying the FFM to control the motor mounted on Upper limb Exoskeleton's elbow, we use the PID weight gains with discrete LPF for derivative control as follows.

$$u_{PID}(t_k) = w_P * F_{h\_local}(t_k) * l_2 + w_I * \left[\sum_{k=1}^{n} F_{h\_local}(t_k) * l_2 \right] + w_D * F_K(t_k) * l_2 \qquad (20)$$

$$F_K(t_k) = (1-r) * F_K(t_{k-1}) + r \frac{d}{dt}\left(F_{h\_local}(t_k)\right)$$

$$\frac{d}{dt}\left(F_{h\_local}(t_k)\right) \approx F_{h\_local}(t_k) - F_{h\_local}(t_{k-1})$$

Where,

$F_{h\_local}(t_k)$ – The human force, measured by load cell at time t_k (k=1,2 ,3, ...n).

$\frac{d}{dt}\left(F_{h\_local}(t_k)\right)$ – Derivative of human force (approximated by current and previous human force)

$F_K(t_k)$ - Derivative of human force after LPF.

$w_P = 1$, $w_I = 1$, $w_D = 1$ - Constant PID weight gains.

$r = 1$ - smoothing factor

$l_2 = 0.2 \quad (m)$ - Length of link 2 (elbow link) .

u_{PID} - The filtered PID torque control.

In Equation (21), in order to avoid the chattering problem, we adjust the control torques as follows.

$$\begin{aligned} &if \quad u_{PID}(t_k) < -p \quad then \quad u_S(t_k) = -s \\ &else \quad if \quad u_{PID}(t_k) > p \quad then \quad u_S(t_k) = s \\ &else \quad u_S(t_k) = 0 \end{aligned} \qquad (21)$$

Where, p=0.75, s=0.1.

The human torque, PID torque, Control torque are displayed in Figure 10.

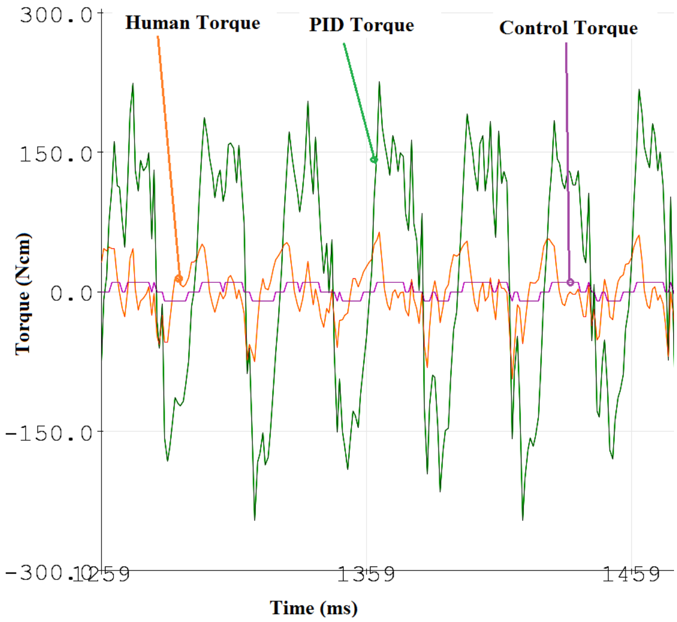

Fig. 10. The measurement of Human torque and control torque

Figure 10 shows the human torque, PID torque and the Control torque of servo motor which are controlled by Arduino UNO Single Board Computer (SBC). The control torque at elbow joint can support to fulfill the human movement.

VI. Conclusions

In this paper, we present kinematic and dynamic analysis of a 3-DOF upper limb exoskeleton using model force feed-forward model. In our experiment, the FFM is applied to control the real 1-DOF upper limb exoskeleton. We use a single axis load cell placed at the elbow link to measure the human machine physical interaction force. The force feed-forward model is applied to support human's torque by using the PID weight gains. In addition, we also have a LPF or a discrete LPF for derivative control. The proposed upper limb exoskeleton can smoothly and stably support human movement from the results of the simulation and experiment.

Acknowledgments

This paper is supported by Vietnam Academy of Science and Technology, code number: VAST01.09/20-21

REFERENCES

[1] Kazerooni Homayoon, Human robot interaction via the transfer of power and information signals, IEEE Transactions on Systems, Man, Cybernetics, Vol. 20, No. 2, March/April 1990, pp. 450-463, (1990).

[2] Jing Tang, Jianbin Zheng, Yang Wang, Direct force control of upper-limb exoskeleton based on fuzzy adaptive algorithm, Journal of Vibroengineering, Vol. 20, Issue 1, pp. 636-650, (2018).

[3] Nguyen Cao Thang, Manukid Parnichkun, Phan Thi Tra My, Le Thi Hong Gam, Pham Ngoc Chung, Nguyen Nhu Hieu, Force Control of an Upper Limb Exoskeleton for Perceiving Reality Using Force Feedforward Model, The 5th International Conference on Engineering Mechanics and Automation (ICEMA-5), pp. 337-344, Hanoi, Vietnam (2019).

[4] Nguyen Cao Thang, Manukid Parnichkun, Phan Thi Tra My, Nguyen Dong Anh, Pham Ngoc Chung, Nguyen Nhu Hieu, Force control of upper limb exoskeleton to support user movement, Journal of Mechanical Engineering, Automation and Control Systems, Vol. 1, Issue 2, pp. 89-101, (2020), https://doi.org/10.21595/jmeacs.2020.21689

[5] P.V.B. Ngoc, L.T.H. Gam, D.H. Quan, B.T. Thanh, N.L. Thien, Modeling and Simulation of 3-DOF Lower Limb Rehabilitation Robot using Force Feed Forward Control, Advances in Science, Technology and Engineering Systems Journal, Vol. 5, no. 4, (2020), pp. 626-632.

[6] Spong M.W., Hutchinson S., and Vidyasagar M., Robot dynamics and control, Wiley (2004).

[7] Do Sanh, Dinh Van Phong, Phan Dang Phong, Do Dang Khoa, Nguyen Cao Thang, Problem of determining reaction forces of mechanical constraints, Proceedings of International Symposium on Robotics and Mechatronics, Hanoi, Vietnam, (2009), pp. 129-135.

[8] Nguyen Quang Hoang, Matlab and Simulink for Engineer, Bach Khoa Publishing House, (2019).

The 6th International Conference on Engineering Mechanics and Automation (ICEMA 2021)
Hanoi, November 14, 2021

Free vibration of multi-span bi-directional functionally graded beams

Le Thi Ha

University of Transport and Communications, No 3 Cau Giay Street, Hanoi, Vietnam
lethiha@utc.edu.vn

Abstract: **Free vibration of multi-span bi-directional functionally graded material (2D-FGM) beams is presented by using a high-order deformation theory. The material properties of the beam are assumed to vary continuously in the thickness and longitudinal directions by a power-law distribution. The frequency parameter of the multi-span beam is computed with the finite element method. The accuracy of the derived formulation is confirmed by comparing the obtained results with the published data. The effects of material and number of spans on the frequency parameter of the beam are examined and discussed.**

Keywords: 2D-FGM, a high-order deformation theory, finite element method, multi-span

I. INTRODUCTION

The vibration problems of elastic beam are often meet in the design of bridges, railways, highways and many modern machining operations [1]. A large number of investigations concerning the dynamic analysis of beams subjected to moving load have been reported in the literature; only the main contributions related to the present work are briefly discussed herein. The early and excellent reference is the monograph of Frýba [2], in which several numbers of closed-form solutions for the vibration problems have been derived. Based on the analytical and finite element solutions to a fundamental moving load problem, Olsson [3] provided an interesting discussion and the reference data for studies of the moving load problem. Ichikawa et al. [4] investigated the dynamic behavior of a multi-span continuous beam subjected to a constant speed moving mass.

Functionally graded material, initiated by Japanese scientists in 1984 [5] has received much attention from engineers and researchers. FGM is formed by varying the percentage of constituent materials in certain desired spatial direction. FGM is being used widely as a structural material, and analysis of structures made of FGM is presently an important topic in the field of structural mechanics. A comprehensive list of publications on analyses of FGM structures subjected to different loadings is given in a review paper by Birman and Byrd [6].

There are practical circumstances, in which the unidirectional FGMs may not be so appropriate to resist multi-directional variations of thermal and mechanical loadings. On the other hand, a new type of functionally graded material (FGM) with material properties varying in two or three directions is needed to fulfill the technical requirements such as the temperature and stress distributions in two or three directions for aerospace craft and shuttles where the conventional FGMs (or 1D-FGM) with material properties which vary in one direction are not so efficient. Several models for bi-dimensional FGM beams and their mechanical behaviour have been considered recently. In this line of works, Simsek [7] considered the material properties vary in both the length and thickness directions, by an exponential function in vibration study of Timoshenko beam. Polynomials were assumed for the displacement field in computing natural frequencies and the dynamic response of the beam. Wang et al. [8] presented an analytical method for free vibration analysis of a 2D-FGM beam. The material properties are also assumed to vary exponentially in the beam thickness and length. The bending of a two-dimensional FGM sandwich (2D-FGSW) beam was investigated by Karamanli [9] using a quasi-3D shear deformation theory and the symmetric smoothed particle hydrodynamic method. Nguyen et al. [10] proposed a 2D-FGM beam model formed from four different constituent materials with volume fractions to vary by power-law functions in both the thickness and longitudinal directions. Timoshenko beam theory was adopted by the authors in evaluating the dynamic response of the beam to a moving load. Hao and Wei [14] assumed an exponential variation for the material properties in both the thickness and length directions in vibration analysis of 2D-FGM beams. Nguyen and Tran [15, 16] studied free vibration of bidirectional 2D-FGM beams using the shear deformable finite element formulations. The effects of longitudinal variation of cross-section and temperature rise have been taken into consideration in [15, 16], respectively. More, Anh el all [17] presented free vibration of bidirectional functionally graded sandwich (BFGSW) beams is studied by using a first-order shear deformation finite element formulation.

In this paper, a finite element procedure for vibration analysis of multi-span 2D- FGM beams is presented. The material properties of the beams are assumed to vary continuously in the thickness and longitudinal direction by a power-law distribution. Based on a third-order shear deformation theory, a beam element using the transverse rotation as an independent variable is formulated and employed to compute vibration characteristics. A parametric study is carried out to highlight the influence of the material heterogeneity, number of spans parameters on the vibration of the beam.

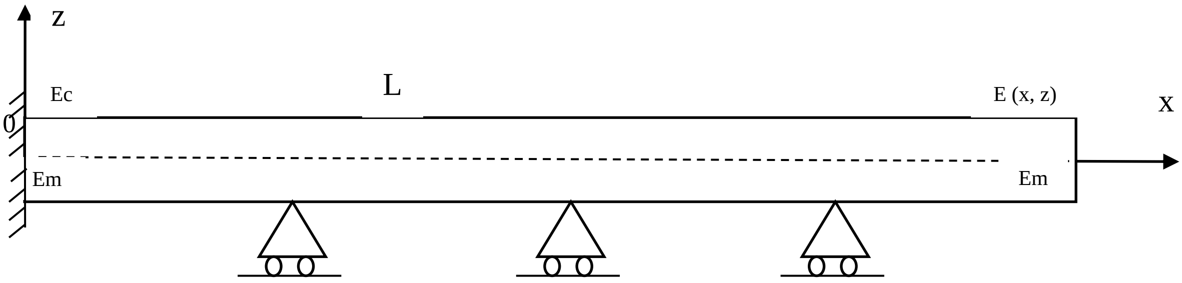

Figure 1. A multi-span 2D-FGM beam

II. PROBLEM AND FORMULATION

Figure 1 shows a multi-span beam with the boundary conditions: clamped at left end and free at the other. L is the length of a multi-span beam**,** L_s is the length of a span**.** The beam cross-section is assumed to be rectangular with width b and height h. The beam material is assumed to be a 2D-FGM composed from two constituent materials, and the effective properties of materials are graded in the thickness and longitudinal direction (x,***z***- direction) according to a power-law distribution as Karamanli [9]**:**

$$\begin{aligned} &V_c(x,z)=\left(1-\frac{x}{2L}\right)^{nx}\left(\frac{1}{2}+\frac{z}{h}\right)^{nz};\\ &V_c(x,z)+V_m(x,z)=1;\\ &P(x,z)=(P_c-P_m)\left(1-\frac{x}{2L}\right)^{nx}\left(\frac{1}{2}+\frac{z}{h}\right)^{nz}+P_m\\ &-\frac{h}{2}\le z\le\frac{h}{2};\\ &0\le x\le L \end{aligned} \tag{1}$$

Where V_c and V_m denote the volume fractions of ceramic and metal material, respectively; P(x,z) represents the effective material properties, including Young's modulus, shear modulus and mass density; the $()_c$ and $()_m$ subscripts respectively denote the ceramic and metal; *nz* and *nx* are the grading indexes, which dictate the variation of the constituent materials in the thickness and longitudinal directions, respectively.

Based on the third-order shear deformation theory [18], the axial and transverse displacements at any point of the beam, *u(x,z,t)* and *w(x,z,t)*, respectively, are given

$$\begin{aligned} u(x,z,t)&=u_0(x,t)+z(\gamma_0-w_{0,x})-\alpha z^3\gamma_0\\ w(x,z,t)&=w_0(x,t) \end{aligned} \tag{2}$$

Where t is the time variable and $\alpha = 4/3\, h^2$, $u_0(x, t)$ and $w_0(x,t)$ are, respectively, the axial and transverse displacements of the point on the x-axis, γ_0 is the transverse shear rotation. The axial strain and shear strain resulted from Eq. (2) are of the forms

$$\begin{aligned} \varepsilon_{xx}&=u_{0,x}+z\left(\gamma_{0,x}-w_{0,xx}\right)-\alpha z^3\gamma_{0,x}\\ \gamma_{xz}&=\gamma_0-3\alpha z^2\gamma_0 \end{aligned} \tag{3}$$

Based on the assumption of Hooke's law, the constitutive relation for 2D- FG beam is as follows

$$\begin{aligned} \sigma_{xx}&=E(x,z).\varepsilon_{xx}=E(x,z)[u_{0,x}+z(\gamma_{0,x}-w_{0,xx})-\alpha z^3\gamma_{0,x}]\\ \tau_{xz}&=G(x,z)\gamma_{xz}=\frac{E(x,z)}{2(1+\upsilon)}\left[\gamma_0-3\alpha z^2\gamma_0\right] \end{aligned} \tag{4}$$

where *E(x,z)* and *G(x,z)* are respectively the elastic modulus and shear modulus, which are functions of both the coordinates x, z, σ_{xx} and τ_{xz} are the axial stress and shear stress, respectively. The strain energy U of the beam resulted from Eqs. (3) and (4) is of the form

$$U=\frac{1}{2}\int_0^L\begin{bmatrix} A_{11}u_{0,x}^2+2A_{12}u_{0,x}(\gamma_{0,x}-w_{0,xx})\\ +A_{22}(\gamma_{0,x}-w_{0,xx})^2-2A_{34}\alpha u_{0,x}\gamma_{0,x}\\ -2\alpha A_{44}\gamma_{0,x}(\gamma_{0,x}-w_{0,xx})+\alpha^2A_{66}\gamma_{0,x}^2+B_{44}\gamma_0^2 \end{bmatrix}dx \tag{5}$$

where A_{11}, A_{12}, A_{22}, A_{34}, A_{44}, A_{66} and B_{44} are the beam rigidities, defined as:

$$\begin{aligned} &(A_{11},A_{12},A_{22},A_{34},A_{44},A_{66})(x,z)\\ &=\int_A E(x,z)(1,z,z^2,z^3,z^4,z^6)dA\\ &B_{44}(x,z)=\int_A G(x,z)(1-6\alpha z^2+9\alpha^2z^4)dA \end{aligned} \tag{6}$$

where *E(x,z)*, *G(x,z)* are respectively the elastic modulus and shear modulus of the beam. The kinetic energy (T) of the beam is then given by

$$T=\frac{1}{2}\int_0^L\begin{bmatrix} I_{11}(\dot u_0^2+\dot w_0^2)+I_{22}(\dot\gamma_0-\dot w_{0,x})^2+\alpha^2I_{66}\dot\gamma_0^2\\ +2I_{12}\dot u_0(\dot\gamma_0-\dot w_{0,x})-2\alpha I_{34}\dot u_0\dot\gamma_0\\ -2\alpha I_{44}\dot\gamma_0(\dot\gamma_0-\dot w_{o,x}) \end{bmatrix}dx \tag{7}$$

In Eqs. (7), I_{11}, I_{12}, I_{22}, I_{34}, I_{44}, I_{66} are the mass moments, defined as

$$\begin{aligned} &(I_{11},I_{12},I_{22},I_{34},I_{44},I_{66})(x,z)\\ &=\int_A \rho(x,z)(1,z,z^2,z^3,z^4,z^6)dA \end{aligned} \tag{8}$$

where, *ρ(x,z)* is the mass density of the beam.

Using the finite element method, the beam is assumed to be divided into numbers of two-node beam elements of length *l*. The vector of nodal displacements ***(*d*)*** for the element considering the transverse shear rotation γ_0 as an independent variable contains eight components as

$$\mathbf{d} = \left\{u_i, w_i, w_{i,x}, \gamma_i, u_j, w_j, w_{j,x}, \gamma_j\right\}^T \tag{9}$$

where $u_i, w_i, w_{i,x}, \gamma_i, u_j, w_j, w_{j,x}, \gamma_j$ are the values of u_0, w_0, $w_{0,x}$ and γ_0 at the node *i* and at the node *j*, respectively . In Eq. (9) and hereafter, a superscript '*T*' is used to denote the transpose of a vector or a matrix.

$$u_0 = N_u.\mathbf{d}; \quad w_0 = N_w.\mathbf{d}; \quad \gamma_0 = N_\gamma.\mathbf{d} \tag{10}$$

with *Nu*, *Nw* and *Nγ* denote the matrices of shape functions for u_0, w_0 and γ_0, respectively. In the present work, linear shape functions are used for the axial displacement and the shear rotation, using the above interpolation schemes, one can write the strain energy of the beam defined by Eqs. (5) as

$$U = \frac{1}{2}\sum^{ne} \mathbf{d}^T\mathbf{k}\mathbf{d} \tag{11}$$

where *ne* is the total number of the elements, and **k** is the element stiffness matrix with the following form

$$\mathbf{k} = \mathbf{k}_{11} + \mathbf{k}_{12} + \mathbf{k}_{22} + \mathbf{k}_{34} + \mathbf{k}_{44} + \mathbf{k}_{66} + \mathbf{k}_s \tag{12}$$

with

$$\begin{aligned}
\mathbf{k}_{11} &= \int_0^l N_{u,x}^T A_{11} N_{u,x} dx;\\
\mathbf{k}_{12} &= 2\int_0^l N_{u,x}^T A_{12} (N_{\gamma,x} - N_{w,xx}) dx;\\
\mathbf{k}_{22} &= \int_0^l (N_{\gamma,x} - N_{w,xx})^T A_{22} (N_{\gamma,x} - N_{w,xx}) dx;\\
\mathbf{k}_{34} &= -2\alpha \int_0^l N_{u,x}^T A_{34} N_{\gamma,x} dx;\\
\mathbf{k}_{44} &= -2\alpha \int_0^l N_{\gamma,x}^T A_{44} (N_{\gamma,x} - N_{w,xx}) dx;\\
\mathbf{k}_{66} &= \alpha^2 \int_0^l N_{\gamma,x}^T A_{66} N_{\gamma,x} dx;\\
\mathbf{k}_s &= \int_0^l N_\gamma^T B_{44} N_\gamma dx
\end{aligned} \tag{13}$$

Similarly, the kinetic energy in Eq. (7) can be rewritten as

$$T = \frac{1}{2}\sum^{ne} \left(\frac{\partial \mathbf{d}}{\partial t}\right)^T \mathbf{m} \left(\frac{\partial \mathbf{d}}{\partial t}\right) \tag{14}$$

where

$$\mathbf{m} = \mathbf{m}_{11} + \mathbf{m}_{12} + \mathbf{m}_{22} + \mathbf{m}_{34} + \mathbf{m}_{44} + \mathbf{m}_{66} \tag{15}$$

is the element consistent mass matrix, in which

$$\begin{aligned}
\mathbf{m}_{11} &= \int_0^l \left(N_u^T + N_w^T\right) I_{11} \left(N_u + N_w\right) dx;\\
\mathbf{m}_{12} &= 2\int_0^l N_u^T I_{12} \left(N_\gamma - N_{w,x}\right) dx;\\
\mathbf{m}_{22} &= \int_0^l \left(N_\gamma - N_{w,x}\right)^T I_{22} \left(N_y - N_{w,x}\right) dx;\\
\mathbf{m}_{34} &= -2\alpha \int_0^l N_u^T I_{34} N_\gamma dx;\\
\mathbf{m}_{44} &= -2\alpha \int_0^l N_{\gamma,x}^T \; I_{44} \left(N_y - N_{w,x}\right) dx;\\
\mathbf{m}_{66} &= \alpha^2 \int_0^l N_\gamma^T I_{66} N_\gamma dx;
\end{aligned} \tag{16}$$

are the element mass matrices stemming from axial, transverse translations, axial translation–sectional rotation coupling, and cross-sectional rotation, respectively.

Having the element stiffness and mass matrices derived, the equations of motion for the free vibration analysis in the context of the finite element analysis can be written in the form

$$\mathbf{M}\frac{\partial^2 \mathbf{D}}{\partial t^2} + \mathbf{K}\mathbf{D} = 0 \tag{17}$$

where **D**, **M**, and **K** are the structural nodal displacement vector, mass and stiffness matrices, obtained by assembling the element displacement vector **d**, mass matrix **m**, and stiffness matrix **k** over the total elements, respectively;

III. NUMERICAL RESULTS AND DISCUSSION

Using the derived finite element formulation, the vibration of multi-span 2D-FG beams is computed in this section. It is assumed that the beam is formed from spans of the same length. Otherwise stated, the beam is assumed to be composed of Steel and Alumina. The Young's modulus, mass density and Poisson's ratio of Steel are respectively 210 GPa, 7800 kg/m3, 0.3177, and that of Alumina are 390 MPa, 3960 kg/m3 and **0.3**, respectively. The beam with L_s=20 *m*, h=0.9 *m* and b=0.5 *m* used by Şimşek and his co-worker [12,13] is chosen in the computations reported below.

A. Formulation validation

Validation of the derived formulation is necessary to confirm the accuracy before computing the dynamic response of the beam. Firstly, the natural frequencies of a multi-span homogeneous beam are computed, and the obtained numerical results are listed in Table 1, where the corresponding results obtained by Ichikawa et al [4] are also given. The dimensionless natural frequency parameter, μ_i, in Table 1 is defined as

$$\mu_i^2 = \omega_i L_s^2 \sqrt{\frac{\rho_0 A}{E_0 I}} \tag{18}$$

where ω_i are the natural frequencies; L_s is the length of a span; E_0, ρ_0 are Young's modulus and mass density of the homogeneous beam, respectively; A =b.h; I=b.h^3/12. It should be noted that since the Bernoulli beam theory is used in Ichikawa et al [4], and in order to enable the numerical results comparable, the frequencies in Table 1 have been computed with an aspect ratio *Ls/h=100*, which is large enough to omit the effect of the shear deformation. As seen from the Table 1, a good agreement between the frequencies computed in the present work with that of Ichikawa et al [4] is noted.

TABLE 1. COMPARISON OF FIRST FIVE NATURAL FREQUENCIES OF MULTI-SPAN HOMOGENEOUS BEAMS (nx=0, nz=0).

Number of spans		μ_1	μ_2	μ_3	μ_4	μ_5
1	Present	3.1414	6.2817	9.4202	12.5567	15.6921
	Ichikawa [4]	π	2π	3π	4π	5π
2	Present	3.1414	3.9261	6.2817	7.0661	9.4202
	Ichikawa [4]	π	3.9266	2π	7.0686	3π
3	Present	3.1414	3.5560	4.2968	6.2817	6.7056
	Ichikawa [4]	π	3.5564	4.2975	2π	6.7076
4	Present	3.1414	3.3929	3.9261	4.4625	6.2817
	Ichikawa [4]	π	3.3932	3.9266	4.4633	2π

Secondly, the fundamental frequency of a one-span FGM beam composed of Aluminum (Al) and Alumina (Al_2O_3), previously studied in Sina et al [11] and Şimşek [12], is computed. The Young's modulus, mass density and Poisson's ratio of Alumina are *70 GPa, 2707 kg/m3* and *0.23*, respectively [12]. The computed fundamental frequency parameters of the present work are listed in Table 2 for various values of the aspect ratio, *L/h*. The corresponding values obtained by using an analytical method by Sina et al [11] and a numerical method by Şimşek [12] are also given in the table. The non-dimensional fundamental frequencies, μ, in Table 2 have been defined according to Sina et al [11] as

$$\mu = \omega L^2 \sqrt{\frac{I_{11}}{h^2 \int_0^L E(z)dz}} \tag{19}$$

where ω is the fundamental frequency of the FG beam**. As** seen from the Table 2**,** the fundamental frequencies computed in the present work are in good agreement with that of Sina et al [11] and Şimşek [12], regardless of the aspect ratios.

The numerical results listed in Tables 1-2 have been computed by using 14 elements for each span. More than 14 elements have been employed, but no improvement in the numerical results have been seen, and in this regard, 14 elements are used to discrete each span in the computations reported below.

TABΛE 2. COMPARISON OF NON-DIMENSIONAL FUNDAMENTAL FREQUENCY OF ONE-SPAN FGM BEAM (nx=0) .

nz		L/h=10	L/h=30	L/h=100
0.3	Present	2.7017	2.7382	2.7425
0.3	Sina et al [11]	2.695	2.737	2.742
0.3	Şimşek [12]	2.701	2.738	2.742

B. *Numerical results*

The dimensionless natural frequency parameter, μ_i, is chosen in the computations reported below.

$$\mu_i^2 = \omega_i L_s^2 \sqrt{\frac{\rho_m A}{E_m I}} \tag{20}$$

TABLE 3. THE FIRST FIVE NATURAL FREQUENCIES OF MULTI-SPAN 2D-FGM BEAMS (NX=0.5, 4 SPANS).

n_z	μ_1	μ_2	μ_3	μ_4	μ_5
0.2	4.2578	4.9192	5.5818	5.9084	6.5997
0.5	4.0490	4.6781	5.3084	5.6192	6.2932
1	3.8728	4.4746	5.0773	5.3745	6.0073
5	3.6017	4.1604	4.7198	4.9953	5.4736

TABLE 4. NON-DIMENSIONAL FREQUENCIES OF A MULTI-SPAN 2D-FGM BEAMS FOR DIFFERENT RATIOS L_S/H (NX=0.5, NZ=1).

Number of spans	L_s/h	μ_1	μ_2	μ_3
2	10	4.4172	5.2634	6.0070
	30	4.4857	5.3966	8.0482
	100	4.4939	5.4131	8.0882
3	10	4.0173	4.8133	4.9048
	30	4.0647	4.9069	5.3966
	100	4.0703	4.9183	5.4131
4	10	3.8404	4.2477	4.4172
	30	3.8790	4.4857	5.0949
	100	3.8836	4.4939	5.1079

The natural frequencies, as seen from Table 3, are smaller for a beam associated with a larger index nz. The effect of the aspect ratio on the natural frequencies of the beam is clearly seen from Table 4, where the frequencies slightly reduce for the beam having a lower aspect ratio, regardless of the number of span. In other word, the shear

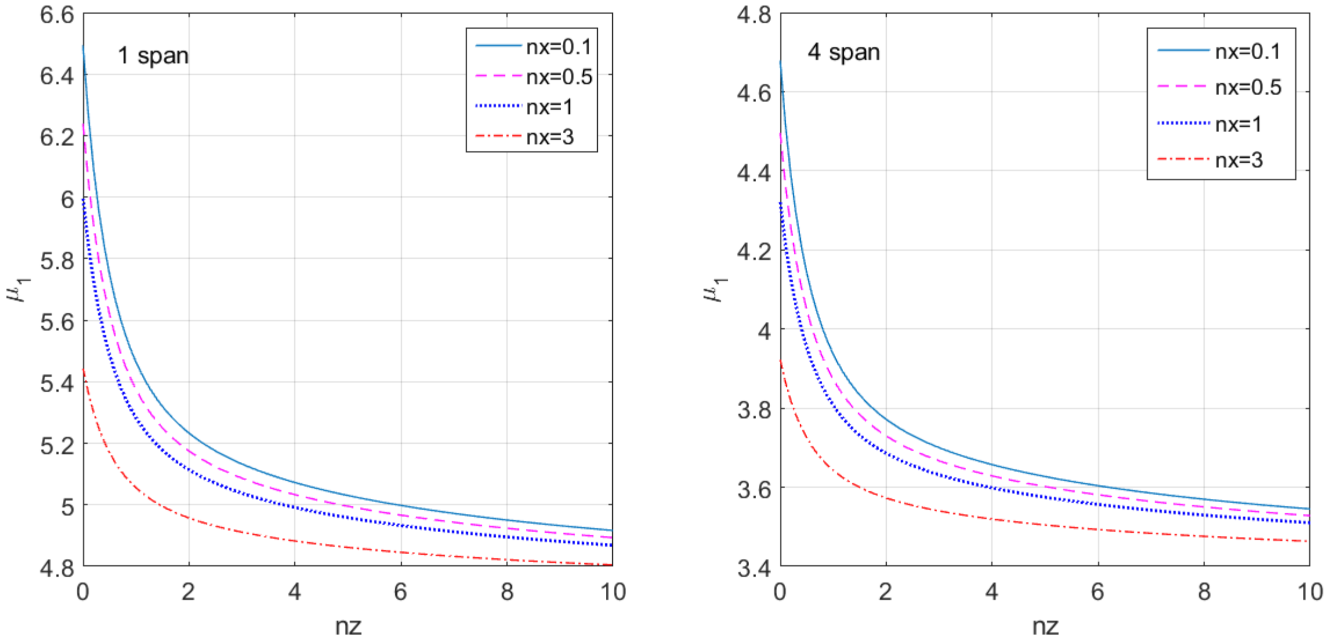

Figure 2. Variation of the fundamental frequency parameters of beam with grading indexes (*4 spans*)

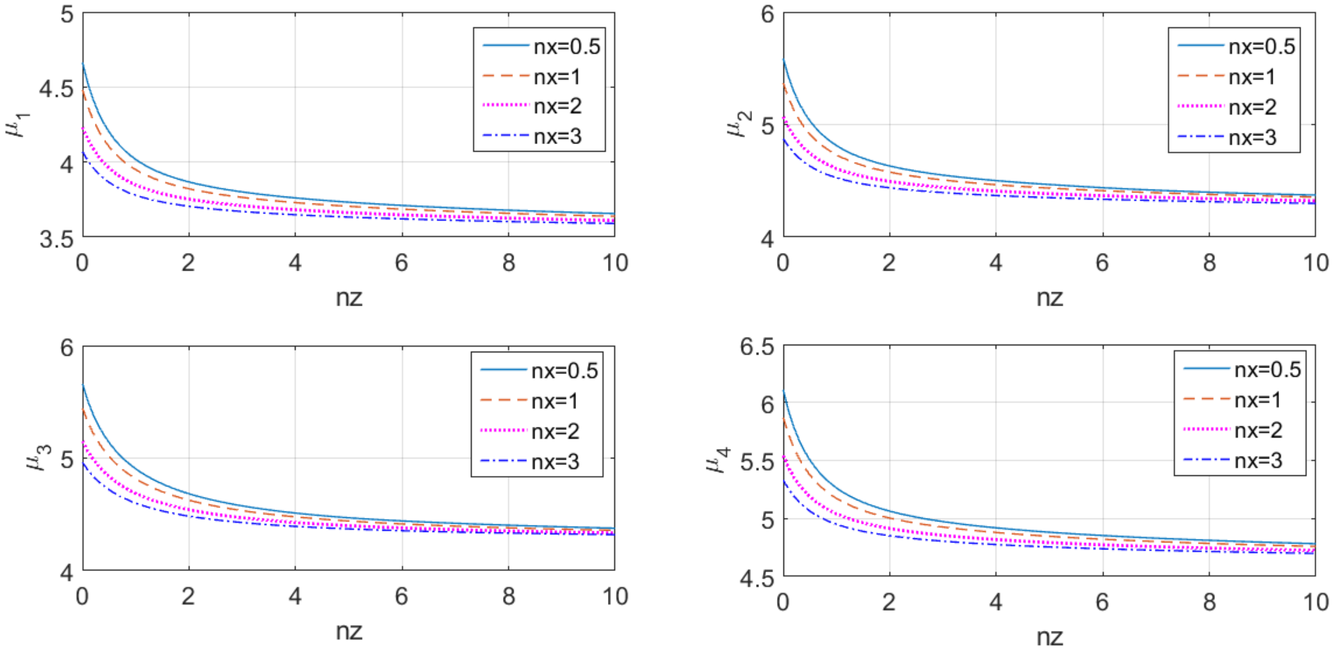

Figure 3. Variation of the first four frequency parameters of beam with grading indexes (*$L_s/h=10$, 3 spans*)

deformation slightly reduces the natural frequencies of the multi-span 2D-FGM beam.

The fundamental frequency parameters of the multi-span 2D-FGM beam with an aspect ratio $L_s/h = 20$ are given in figure 2 for the clamped at left end and free at the other beam. As seen from the figures, the frequency parameter decreases by the increase of the nx, nz, regardless of the number of span. The dependence of the frequency parameter upon the material grading index nz, nx can be explained by the change of the effective Young's modulus as shown by Eq. (1). The numerical result in figures reveals that the variation of the material properties in the thickness and the length direction play an important role in the frequencies of the 2D-FGM beams, and a desired frequency can be obtained by approximate choice of the material grading indexes.

The variation of the first four frequency parameters μ_i (i = 1, . . . , 4) with the material grading indexes is displayed in

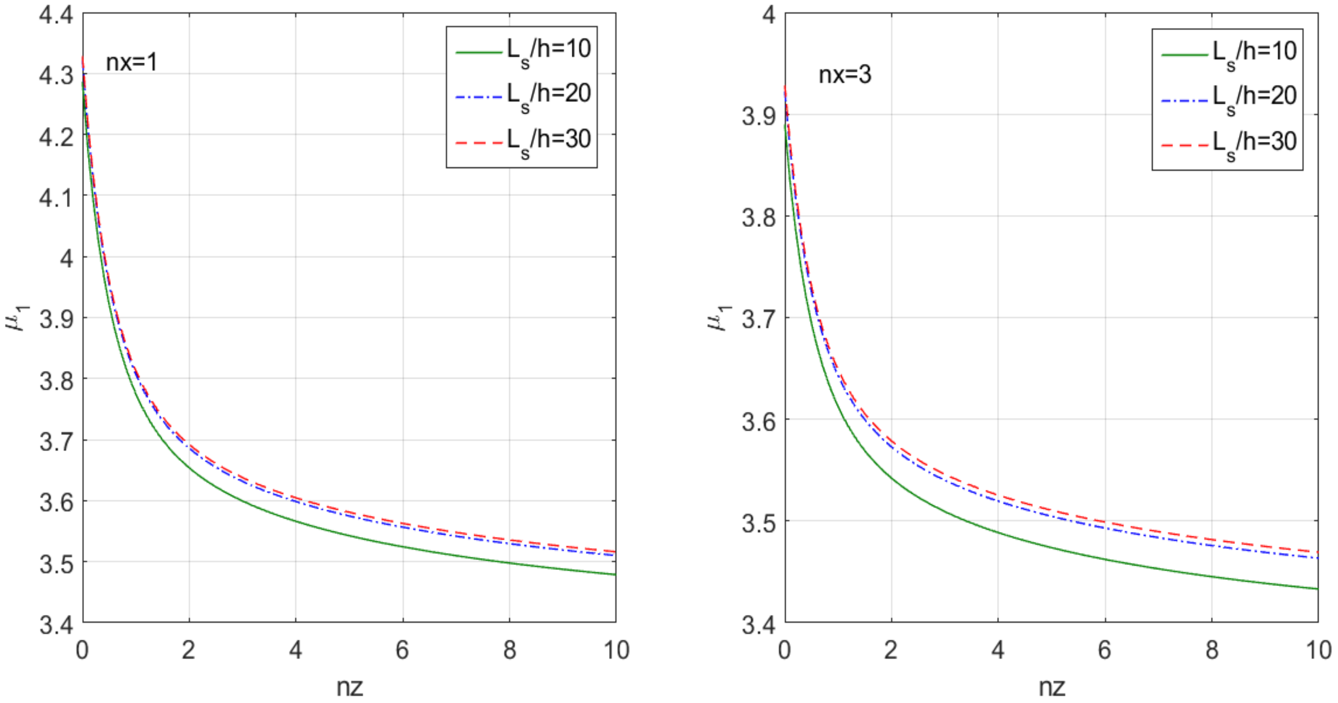

Figure 4. Fundamental frequency parameter of 2D-FGM beam with various values of aspect ratio (4 spans)

Figs. 3 for the clamped at left end and free at the other beams. The figures are obtained for the 3 spans beams with an aspect ratio $L_s/h = 10$. The dependence of the higher frequency parameters upon the grading indexes is similar to that of the fundamental frequency parameter. All the frequency parameters decrease by increasing the index nz, and they decrease by the increase of the index nx for all four frequency parameters.

The fundamental frequency parameters of the 2D-FGM beam with various values of aspect ratio computed with various values of the material parameters are shown in Fig. 4 for 4 spans, nx=1 and nx=3. As seen from the figure, seen from the figures the fundamental frequency parameter of the beam slightly increases by increasing the aspect ratio, regardless of the material index.

IV. CONCLUSION

A 2D-FGM beam model formed from two constituent materials its free vibration was studied. The material properties varying in both the thickness and longitudinal directions by the power gradation laws. Based on a third-order shear deformation theory, a beam element was formulated and employed in computing the vibration characteristics. It has been shown that the formulated element is accurate, and it is capable to model the effect of shear deformation on the frequencies of the beam. The obtained numerical result reveals that the variation of the material properties plays an important role in the frequencies of the beam. A parametric study has been carried out to highlight the effects of the material distribution and the numbers of spans on the frequencies of the beam. The influence of the aspect ratio on the vibration behaviour of the beam has also been examined and discussed.

REFERENCES

[1] W.H. Lin and M.W. Trethewey, “Finite element analysis of elastic beams subjected to moving dynamic loads”. J. Sound and Vibration, 2 , pp. 323-342, 1990.

[2] L. Fryba, “Vibration of solids and structures under moving loads”, Academia, Prague Garvan, The Maple book, Chapman & Hall/CRC, Florida, 1972.

[3] M. Olsson, “On the fundamental moving load problem”, J. Sound and Vibration, 2, pp. 299-307, 1991.

[4] M. Ichikawa, Y. Miyakawa and A. Matsuda, “Vibration analysis of the continuous beam subjected to a moving mass”, J. Sound and Vibration, 3, pp.611-628, 2000.

[5] M. Koizumi, “FGM activities in Japan”, Composites: part B, vol. 28, pp. 1-4, 1997.

[6] V. Birman and L.W. Byrd, “Modeling and analysis of functionally graded materials and structures”, Applied Mechanics Reviews, 5, pp. pp. 195-216. 2007.

[7] M. Simsek. “Bi-directional functionally graded materials (BDFGMs) for free and forced vibration of Timoshenko beams with various boundary conditions”, Composite Structures, 133, pp. 968-978, 2015.

[8] Z.-H. Wang, X.-H. Wang, G.-D. Xu, S. Cheng, and T. Zeng, “Free vibration of twodirectional functionally graded beams”, Composite Structures, 135, pp. 191-198, 2016.

[9] A. Karamanlı. “Bending behaviour of two directional functionally graded sandwich beams by using a quasi-3D shear deformation theory”, Composite Structures, 174, pp. 70-86, 2017.

[10] D. K. Nguyen, Q. H. Nguyen, T. T. Tran, and V. T. Bui,” Vibration of bi-dimensional functionally graded Timoshenko beams excited by a moving load”, Acta Mechanica, 1,pp. 141-155, 2017.

[11] S.A. Sina, H.M. Navazi, and H. Haddadpour, “An analytical method for free vibration analysis of functionally graded beams”, Materials & Design, 3, pp. 741-747, 2009.

[12] M. Şimşek, “Vibration analysis of a functionally graded beam under a moving mass by using different beam theories”, Composite Structures, 4,pp. 904-9, 2010.

[13] M. Şimşek, and T. Kocatürk, “Free and forced vibration of a functionally graded beam subjected to a concentrated moving harmonic load”, Composite Structures, 4, pp.465-473, 2009.

[14] H. Deng, W. Cheng, "Dynamic characteristics analysis of bi-directional functionally graded Timoshenko beams", Composite Structures, 141, pp. 253–263, 2016.

[15] D. K .Nguyen, T. T .Tran, " Free vibration of tapered BFGM beams using an efficient shear deformable finite element model". S teel and Composite Structures, 29(3), pp. 363–377, 2018.

[16] T. T .Thom, N. D. Kien, " Free vibration analysis of 2D - FGM beams in thermal environment based on a new third-order shear deformation theory", Vietnam Journal of Mechanics, 40(2):pp. 121–140, 2018.

[17] L.T.N. Anh, V.T.A.Ninh, T.V. Lang, N.D.Kien, "Free vibration of bidirectional functionally graded sandwich beams using a first-order shear deformation finite element formulation", Journal of Science and Technology in Civil Engineering, 14 (3): pp. 136–150, 2020.

[18] P. R. Heyliger and J. N. Reddy . A higher order beam finite element for bending and vibration problems. Journal of Sound and Vibration 126, 309–326, 1988.

Hopf bifurcation of a mass-spring system with LuGre friction model

Chung Ngoc Pham
Faculty of Basic Science
Hanoi University of Mining and Geology
Hanoi, Vietnam
chunghumg86@gmail.com

Hieu Nhu Nguyen
Faculty of Mechanical Engineering and Mechantronics
Phenikaa University
Hanoi, Vietnam
hieu.nguyennhu@phenikaa-uni.edu.vn

***Abstract*: In this study, we analyze Hopf bifurcation of a spring-mass system placed on a conveyor belt moving at constant velocity using LuGre model with the Stribeck effect. The Stribeck effect occurs when relative velocity between two surfaces is low (i.e. near-zero velocity) for which the friction force monotonically decreases as relative velocity is increasing. To check the existence of Hopf bifurcation of system motion, we use implicit algorithm criterion developed by Liu, called Liu's criterion, on the basis of the Routh-Hurwitz stability criterion, which is stated in terms of the coefficients of the characteristic equations instead of those of eigenvalues of Jacobian matrix corresponding to the system's equilibrium point. The bifurcated limit cycles can be observed in phase space of dynamical systems. We show that the system has undergone a supercritical Hopf bifurcation in an appropriate range of bifurcation parameters.**

Keywords:* *LuGre model, Stribeck effect, stability, Hopf bifurcation.

I. Introduction

Friction phenomenon is common in nature and in engineering systems [1]. One often uses two main friction models, namely, the static friction model and dynamic friction model, to represent the behavior of systems with two or more objects in contact and moving relatively to each other [2]. For the static friction model, the friction force is a function that depends only on the relative velocity of two bodies in contact. Coulomb and viscous frictions belong to the type of static friction model [3,4]. This model is only suitable for sliding motions between two objects in contact with large enough relative velocity. For low velocity motion, the static friction model is no longer suitable because it does not capture effects associated with micro-motion of contact surfaces. Hence, dynamic friction models need to be developed. The dynamic friction model proposed by Dahl [5] describes the spring-like behavior of surface asperities of two bodies in contact. The Dahl model, however, does not capture the Stribeck effect, i.e. the effect in which the friction force decreases as the velocity increases in the near-zero low velocity domain. To overcome this shortcoming, Canudas de Wit [6] proposed a new model, called LuGre model. In this model Canudas de Wit introduced a new variable, called the internal state variable, which describes the average deflection of asperities of the contact surface.

Stick-slip motion can occur when two objects slide over each other at low relative velocity [7]. The LuGre model is used to describe this phenomenon relatively well, in which the model can capture both stick motion phase with relatively small displacement at the micro-size of asperities, and gross sliding motion on the macro scale after stick phase [6,7]. The sliding motion can lead to the instability of the equilibrium point in the problem of moving objects on the conveyor belt at low speed. For a certain system parameter domain, the transition from stable to unstable state is called bifurcation [8]. The investigation on the parameter domain in which the bifurcation phenomenon occurs has an important meaning because it tells us the stable operating domain of the system, from which it is possible to design systems that can avoid the phenomenon of unexpected stick - slip motion.

In the framework of this paper, the authors proposed to use a relatively easy-to-use Hopf bifurcation criterion based on coefficients of the characteristic equation recieved from the Jacobian matrix of a linearized system in the neighborhood of the equilibrium point of the original nonlinear system with the LuGre friction model. This is the first time this bifurcation criterion has been used for the LuGre model applied to a mass - spring system moving on a conveyor belt at low relative velocity.

II. LuGre Dynamic Friction Model

In order to understand the the qualitative and quantitative mechanisms of friction behavior, investigations on both theoretical and experimental aspects are necessary. It is found that body surfaces reveal very irregular structures at the microscopic scale and thus two surfaces make contact at a number of asperities. Surface asperities are assumed to be elastic and are modeled as brush bristles. When subjected to a tangential force, the bristles will deflect and behave as spring-like elastic motions with damping which give rise friction. The model of friction force is represented as follows [6]

$$\begin{aligned} F_{fr} &= \sigma_0 z + \sigma_1 \dot{z} + \sigma_2 v \\ \dot{z} &= v - \frac{\sigma_0 |v|}{g(v)} z \\ g(v) &= F_C + (F_S - F_C)\exp\left\{-\frac{|v|}{v_S}\right\} \end{aligned} \tag{1}$$

where z is the average deflection of the bristles, called internal state variable; F_{fr} is the friction force; σ_0 is the contact stiffness; σ_1 is the damping coefficient of bristles;

σ_2 is the viscous friction coefficient; v is the relative velocity between two surfaces; $g(v)$ is the Stribeck function, F_C is the Coulomb friction force, F_S is the static friction force; v_S is the Stribeck velocity. The model described by Eq. (1) is known as the LuGre model [6] that exhibits the Stribeck effect, i.e. the effect that the friction force decreases as the relative velocity increases in the near-zero range. Because of the Stribeck effect, in this study, our attention is focused on the range of low-velocity with stick-slip phenomenon of a friction-induced vibrating system.

III. System Model

To study the phenomenon of friction-induced vibration, we consider a mass-spring system moving in a conveyor belt at a constant speed v_b as illustrated in Fig. 1. The contact surface between the mass and belt is modeled by the LuGre friction as presented in Eq. (1). Thus, the number of independent variables in our system is two: the first is displacement variable x and the second is internal state variable z.

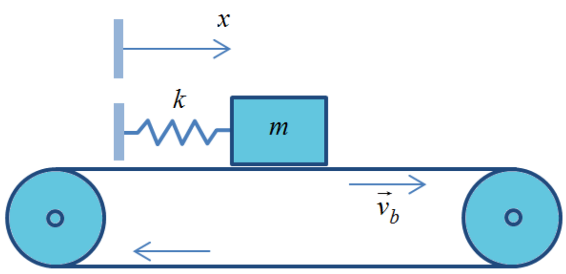

Fig. 1. A single-degree-of-freedom system placed on a conveyor belt

The governing equation of the system takes the following form:

$$\begin{aligned} m\ddot{x} &= -kx + F_{fr} \\ \dot{z} &= (v_b - \dot{x}) - \frac{\sigma_0 |v_b - \dot{x}|}{g(v_b - \dot{x})} z \end{aligned} \tag{2}$$

where m is the mass [kg], k is the spring stiffness [Nm^{-1}]. In Eq. (2), the friction force F_{fr} and the function g are determined as follows

$$\begin{aligned} F_{fr} &= \sigma_0 z + \sigma_1 \frac{dz}{dt} + \sigma_2 (v_b - \dot{x}) \\ g(v_b - \dot{x}) &= F_C + (F_S - F_C)\exp\left\{-\frac{|v_b - \dot{x}|}{v_S}\right\} \end{aligned} \tag{3}$$

where $v_r = v_b - \dot{x}$ is relative velocity.

3.1. Equilibrium point

The equilibrium point of the system is obtained when derivatives of all system state variables in time vanishes, i.e. $\dot{x} = 0$, $\ddot{x} = 0$, $\dot{z} = 0$. This leads to the following equation for finding equilibrium point $\{x_e, z_e\}$

$$\begin{aligned} -kx_e + \sigma_o z_e + \sigma_2 v_b &= 0 \\ v_b - \frac{\sigma_0 v_b}{g(v_b)} z_e &= 0 \end{aligned} \tag{4}$$

Solving system (4), we obtain:

$$\begin{aligned} x_e &= \frac{1}{k}[g(v_b) + \sigma_2 v_b] \\ z_e &= \frac{g(v_b)}{\sigma_0} \end{aligned} \tag{5}$$

It can be seen that the product of the deflection value of bristle at the equilibrium point of the system and stiffness coefficient σ_0 is equal to the value of the Stribeck function at the conveyor speed. The equilibrium displacement x_e is positive and depends on many factors such as the stiffness of spring k , the belt velocity v_b .

The equilibrium point in Eq. (5) can be stable or unstable depending on the determination range of system parameters. In the following subsection, the Routh-Hurwitz criterion is used to examine the stability of the equilibrium point.

3.2. Stability of equilibrium point via Routh-Hurwitz criterion

Eq. (2) can be rewritten as a system of the first-order derivative with three equations of state variables $x,\ y,\ z$:

$$\begin{aligned} \dot{x} &= Q_1(x,y,z) := y \\ \dot{y} &= Q_2(x,y,z) := -\frac{k}{m}x + \frac{\sigma_0}{m}z \\ &\quad + \frac{\sigma_1}{m}\left[(v_b - y) - \frac{\sigma_0 |v_b - y|}{g(v_b - y)} z\right] + \frac{\sigma_2}{m}(v_b - y) \\ \dot{z} &= Q_3(x,y,z) := (v_b - y) - \frac{\sigma_0 |v_b - y|}{g(v_b - y)} z \end{aligned} \tag{6}$$

where $Q_j = Q_j(x,y,z)$ (j=1,2,3) are nonlinear functions of state vector variable $\mathbf{w} = [x\ y\ z]^T$. To analyze the stability of the system (6), it is linearized in neighborhood of the equilibrium point of state vector variable, i.e. the point $\mathbf{w}_e = [x_e\ 0\ z_e]^T$. Denote $\tilde{x} = x - x_e$, $\tilde{y} = y - 0$, $\tilde{z} = z - z_e$ as disturbance elements of state vector around the equilibrium point $\mathbf{w}_e$. The linearized equation system takes the following form

$$\dot{\tilde{\mathbf{w}}}_e = \mathbf{J}(\mathbf{w}_e)\tilde{\mathbf{w}} \tag{7}$$

where $\mathbf{J}(\mathbf{w}_e)$ is the Jacobian matrix of nonlinear vector $\mathbf{Q} = [Q_1\ Q_2\ Q_3]^T$ calculated at the point $\mathbf{w}_e$:

$$\mathbf{J}(\mathbf{w}_e) = \begin{bmatrix} 0 & 1 & 0 \\ j_{21} & j_{22} & j_{23} \\ 0 & j_{32} & j_{33} \end{bmatrix} \tag{8}$$

where 5 elements of the matrix **J** are displayed in which they contain system parameters, other elements are either equal to zero or one:

$$
\begin{aligned}
& j_{21}=-\frac{k}{m},\; j_{22}=-\frac{\sigma_2}{m}+\frac{\sigma_1}{m}h\left(v_b\right)g'\left(v_b\right) \\
& j_{23}=\frac{\sigma_0}{m}-\frac{\sigma_0\sigma_1}{m}h\left(v_b\right) \\
& j_{32}=h\left(v_b\right)g'\left(v_b\right),\; j_{33}=-\sigma_0 h\left(v_b\right)
\end{aligned}
\tag{9}
$$

in which

$$
h\left(v_b\right)=v_b\,/\,g(v_b)\,,\; g'(v_b)=\frac{F_S-F_C}{v_S}\exp\left\{-\frac{v_b}{v_s}\right\}
$$

The characteristic polynomial of the matrix (8) is found to be:

$$
\lambda^3+l_2\lambda^2+l_1\lambda+l_0=0 \tag{10}
$$

where coefficients l_2 , l_1 , l_0 are determined as follows

$$
\begin{aligned}
& l_2=-j_{22}-j_{33} \\
& l_1=-j_{21}+j_{22}j_{33}-j_{23}j_{32}, \\
& l_0=j_{21}j_{33} \qquad .
\end{aligned}
\tag{11}
$$

Substituting elements j_{rs} from Eqs. (9) into Eqs. (11), we obtain

$$
\begin{aligned}
& l_2=\frac{\sigma_0 v_s}{F_C}\frac{\xi}{1+\mu_C\exp\{-\xi\}}\left[1-\frac{\sigma_1\mu_C F_C}{m\sigma_0 v_s}\exp\{-\xi\}\right]+\frac{\sigma_2}{m} \\
& l_1=\frac{k}{m}\left\{1+\frac{\sigma_0}{k}\frac{\sigma_2 v_s}{F_C}\frac{\xi}{1+\mu_C\exp\{-\xi\}}\right. \\
& \qquad\qquad \left.\times\left[1-\frac{F_C}{\sigma_2 v_s}\mu_C\exp\{-\xi\}\right]\right\} \\
& l_0=\frac{k^2}{m\sigma_2}\frac{\sigma_0}{k}\frac{\sigma_2 v_s}{F_C}\frac{\xi}{1+\mu_C\exp\{-\xi\}}
\end{aligned}
\tag{12}
$$

where $\xi=v_b/v_s$ is the ratio of belt velocity to Stribeck velocity; μ_C is the ratio of difference between the static and Coulomb friction forces to Coulomb frictio $\mu_C=\left(F_S-F_C\right)/F_C$. Because the static friction force is larger than the Coulomb friction, the value of ratio μ_C is larger than zero, i.e. $\mu_C>0$.

The stability condition of the system according to the Routh-Hurwitz criterion is

$$
\begin{aligned}
& \varsigma_1=l_0>0, \\
& \varsigma_2=l_2>0, \\
& \varsigma_3=l_1l_2-l_0>0.
\end{aligned}
\tag{13}
$$

We assume that the magnitude of parameter σ_0 is enough large such that the inequality $1-\frac{\sigma_1\mu_C F_C}{m\sigma_0 v_s}\exp\{-\xi\}>0$ holds. From that, we have $l_2>0$. The stability condition of equilibrium point of the system is now dependent on the third condition in (13), i.e. $l_1l_2-l_0>0$. This condition will be checked numerically in the Section 4.

3.3. Hopf bifurcation

A Hopf bifurcation gives the information on the appearance or disappearance of a periodic orbit through a local change in the stability properties of a fixed point of nonlinear dynamical systems [9]. In the traditional approach, the analysis on Hopf bifurcation is based on eigenvalues of Jacobian matrix in which a pair of complex conjugate eigenvalues will pass through the imaginary axis while all other eigenvalues have negative real parts. In case that the eigenvalues are found explicitly, this approach is convenient because we can evaluate the sign of all eigenvalues and can check the condition of Hopf bifurcation. However, the disadvantage of traditional method is that the expressions of eigenvalues may be complex if dimension of the Jacobian matrix is larger. To overcome this disadvantage, recently, Liu [10] developed a criterion on the basis of the Routh-Hurwitz stability criterion, which is stated in terms of the coefficients of the characteristic equations instead of those of eigenvalues. The Hopf analysis in our paper is based on the Liu's criterion for the system under consideration.

Applying the Liu's criterion [10] to the characteristic polynomial (10), we have the following conditions for the occurrence of Hopf bifurcation with bifurcation parameters v_b:

$$
\begin{aligned}
& \left(L_1\right):\quad l_0>0,\; l_2>0,\; l_1l_2-l_0=0 \\
& \left(L_2\right):\quad \frac{d}{dv_b}\left(l_1l_2-l_0\right)\neq 0
\end{aligned}
\tag{14}
$$

where the coefficients l_2 , l_1 , l_0 are determined from (12). It is noted that the condition (L_2) also can be applied to other bifurcation parameters. Two conditions $l_0>0,\; l_2>0$ are shown as similar to that in (13) for Routh-Hurwitz criterion. The third condition $l_1l_2-l_0=0$ in (L_1) and the condition (L_2) is checked by numerical calculation as presented in Section 4.

IV. Numerical Results and Discussions

4.1. Stable and unstable zones

Stable and unstable zones of equilibrium point in the plane of a certain pair of system parameters are formulated based on solving inequalities obtained from the Routh-Hurwitz criterion (13). Here, we are interested in two parameters: the belt velocity v_b and viscous damping coefficient σ_2. Calculation parameters are given in Table 1. As shown before in subsection 3.2, two inequalities $l_0>0$, $l_2>0$ in (13) are satisfied with appropriate assumptions. Fig. 2 illustrated the graph of $\varsigma_2=l_2$ with parameter values used in our simulations various values of belt velocity v_b from v_s to $3v_s$ with step $v_s/10$. It is seen that values of ς_2 are all positive, therefore the condition $\varsigma_2=l_2>0$ is satisfied. The inequalities $l_1l_2-l_0>0$ are also checked by numerical calculations for various values of system parameters.

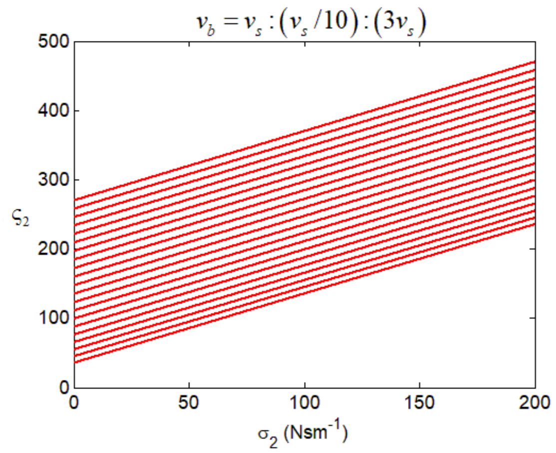

Fig. 2. Plots of curve ς_2 as function of the viscous damping coefficient σ_2 with various values of belt velocity v_b

Fig. 3 exhibits the behavior of function $\varsigma_3 = \varsigma_3(v_b, \sigma_2)$ as functions of the viscous damping coefficient σ_2 with various values of belt velocity v_b from v_s to $3v_s$ with step $v_s/10$. The function ς_3 is positive if v_b is larger than a value $v_{b,ZP}$ that is a zero-point of Eq. $\varsigma_3 = \varsigma_3(v_b, \sigma_2) = 0$. The solution $v_{b,ZP}$ is obtained using the Newton-Raphson method for Eq. $\varsigma_3 = \varsigma_3(v_b, \sigma_2) = 0$. The equilibrium point is stable if the belt velocity v_b is on the range $v_b > v_{b,ZP}$. In the following, the value $v_{b,ZP}$ is called the boundary velocity.

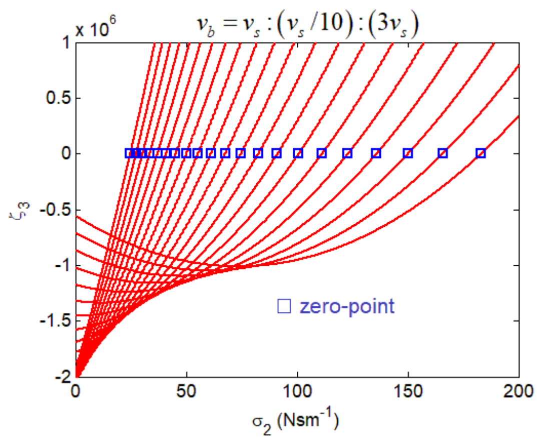

Fig.3. Plots of curve ς_3 as function of the viscous damping coefficient σ_2 with various values of belt velocity v_b

Fig. 4 displays the graph of zero-points in Fig.3. The curve of zero-point $v_{b,ZP}$ versus the damping coefficient σ_2 illustrates a boundary of stable zone (I) and unstable zone (II) for LuGre model. The increase of viscous damping leads to a result in which the boundary velocity $v_{b,ZP}$ will be pulled down to a lower level. That means the stable state can be reached at low velocity and large damping.

TABLE 1. PARAMETER VALUES USED IN OUR SIMULATIONS

Description/Unit	Notation	Value
Mass (kg)	m	1
Spring stiffness (Nsm^{-1})	k	100
Internal stiffness (Nsm^{-1})	σ_0	10^5
Internal damping (Nsm^{-1})	σ_1	$\sqrt{10^5}$
Viscous damping (Nsm^{-1})	σ_2	0.4
Coulomb friction (N)	F_C	1
Static Friction (N)	F_S	1.5
Stribeck velocity (sm^{-1})	v_s	0.001

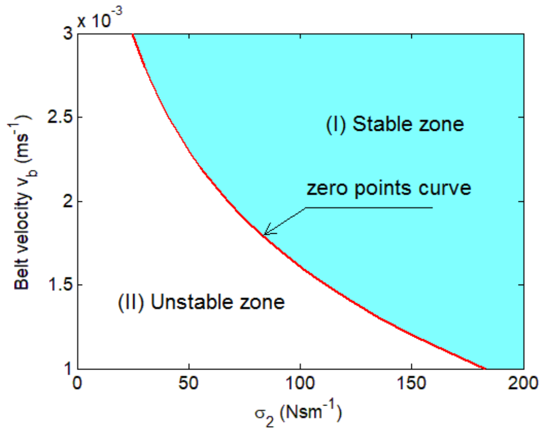

Fig. 4. Plot of zero-point curve of the function ς_3 versus the viscous damping coefficient σ_2. The stable zone (I) and unstable zone (II) are separated by the zero-point curve.

4.2. *Hopf bifurcation analysis*

The zero-point curve in Fig. 4 is obtained from the equation $l_1 l_2 - l_0 = 0$ of Hopf condition of bifurcation. If a point belonging to the stable zone (I) crosses the boundary curve, the stability of our system about the equilibrium point will change, i.e. the instability appears. To see the Hopf bifurcation, we select three points in the plane (σ_2 , v_b) in Fig. 4: S_1 (100, 1.75×10^{-3}), S_2 (86.76, 1.75×10^{-3}) and S_3 (50, 1.75×10^{-3}). The point S_1 belongs to the stable zone, the point S_2 lies on the boundary curve and S_3 drops on the unstable zone. The simulation results for phase trajectory corresponding to three points S_1, S_2, S_3 are portrayed on Figs. 5, 6, and 7. In Fig. 5, the phase trajectory starting from a given initial point $x(0) = 0.01$, $y(0) = v_b$, $z(0) = 1.1\times10^{-5}$ will approaches to the equilibrium point $\mathbf{w}_e$. Here, to see the asymptotically stable property of trajectory, we choose the phase plane is $(x - x_e, \dot{x})$ instead of $(x, \dot{x})$. This asymptotic behavior of phase trajectory shows that the selection of points belonging the stable zone will lead to the suppression of the system vibration. Fig. 6 exhibits a limit cycle of phase trajectory when the point S_2 lies on the boundary curve. A limit cycle is also observed in

Fig. 7 when the phase trajectory corresponding to the point S_3 is obtained after a long enough time.

In order verify the result of Hopf bifurcation obtained from the zero-point curve, we select $v_b = 1.75\times10^{-3}$ and explore the behavior of eigenvalues of Jacobian matrix (8) by solving numerically the characteristic equation (10) versus the parameter σ_2. Because Eq. (10) is a cubic polynomial form, it has a total of three solutions including imaginary ones. Each solution of Eq. 10 is separated into two parts, a real part and an imaginary part. The sign of the obtained solution will decide the the stability of the system. If all real parts of solutions are negative, the equilibrium point is stable. If at least a solution with positive real part, the equilibrium point is unstable. If all solutions have negative real parts except a pair of solutions with complex conjugate pure imaginary parts, a Hopf bifurcation occurs. Figs. 8 and 9 illustrate the real and imaginary parts of eigenvalues $\lambda_1, \lambda_2, \lambda_3$ of Eq. 10 as functions of parameter σ_2. In Fig. 8, starting from the point remarked by a squared shape, $\sigma_2 = 86.76$, the real parts of λ_2, λ_3 begin to receive negative values whereas the real part of λ_1 is always below the zero value. It is noted that the found value $\sigma_2 = 86.76$ associated with the considered value of belt velocity $v_b = 1.75\times10^{-3}$ is a Hopf bifurcation point. This result is the same as using the Liu's criterion (14).

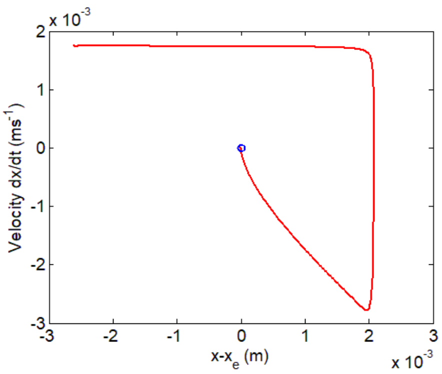

Fig. 5. Phase trajectory with belt velocity $v_b = 1.75\times10^{-3}$ and viscous damping $\sigma_2 = 100$

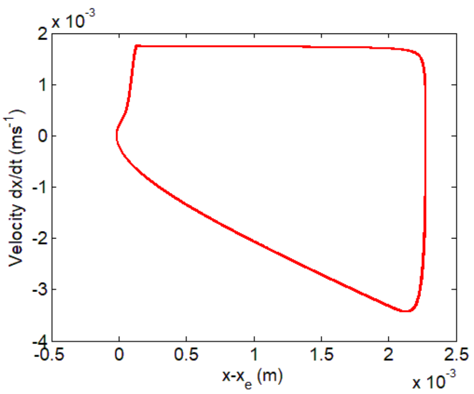

Fig. 6. Phase trajectory with belt velocity $v_b = 1.75\times10^{-3}$ and viscous damping $\sigma_2 = 86.76$

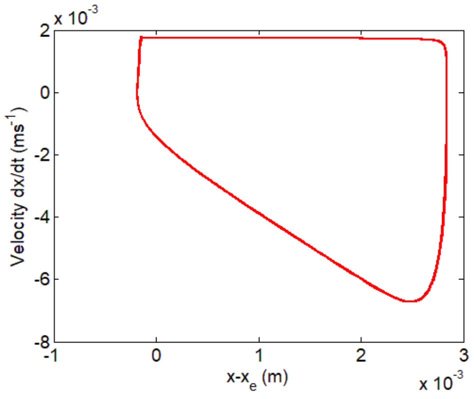

Fig. 7. Phase trajectory with belt velocity $v_b = 1.75\times10^{-3}$ and viscous damping $\sigma_2 = 50$

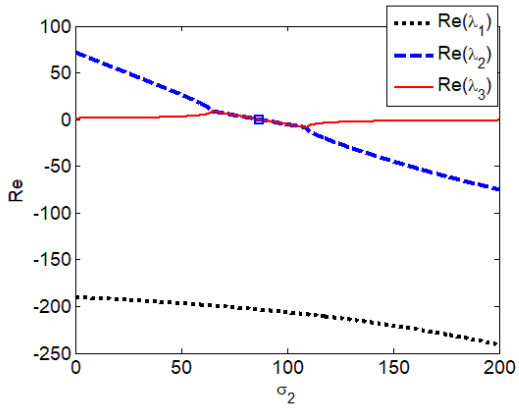

Fig. 8. Plots of real parts of eigenvalues $\lambda_1, \lambda_2, \lambda_3$ versus the parameter σ_2

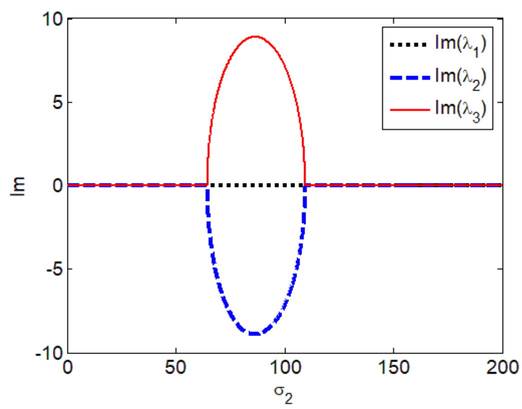

Fig. 9. Plots of imaginary parts of eigenvalues $\lambda_1, \lambda_2, \lambda_3$ versus the parameter σ_2

5. CONCLUSIONS

In the current study, using the Liu's criteiron, the authors have performed a Hopf bifurcation analysis for a mass-spring system moving on the conveyor belt with constant belt velocity in low velocity domain. Stick-slip phenomenon is observed through the Hopf bifurcation. If belt velocity falls on the boundary curve, the motion state of the system under consideration will change from the stable to the unstable zone. The boundary curve shows that, in the low velocity domain, the stability of equilibrium point can be achieved by increasing value of viscous damping. In the case of higher belt velocity, a stable level of equilibrium point can be attained with low viscous damping coefficient provided that damping coefficient value falls in the stable zone. The approach using Liu's criterion to find Hopf bifurcation has an advantage in comparison with the traditional approach, that is, it only uses the coefficient information of the characteristic equation instead of finding explicit solutions. Therefore, this study contributes to the understanding of the bifurcation of stick - slip motion systems in the low-velocity domain in a simpler way than the traditional approach.

REFERENCES

[1] Brian, A.H. (1991), Control of Machines with Friction, Springer Science+Bussiness Media, New York.

[2] Guran, A., Pfeiffer, F., Popp, K. (2001), Series on stability Dynamics with Friction: Modeling, Analysis and Experiment, World Scientific Publishing Company Pte Limited.

[3] Niranjan, P., Karinka, S., Sairam, K. (2017), Friction modeling in servo machines: a review. International Journal of Dynamics and Control, 6, pp. 893-906.

[4] Liang, J.W., Feeny B.F. (1998), Identifying coulomb and viscous friction from free-vibration decrements. Nonlinear Dynamics, 16, pp. 337–47. doi:10.1023/A:1008213814102

[5] Dahl, P.R. (1968), A solid friction model. Tech. rep.. Los Angeles, CA (USA): Space and Missile Systems Organization, Air Force System Command, ADA041920

[6] Canudas de Wit, C., Olsson, H., Åström, K.J., Lischinsky, P. (1995), A new model for control of systems with friction. IEEE Transactions on Automatic Control, 40, pp. 419–425.

[7] Pikunov, D., Stefanski, A. (2019), Numerical analysis of the friction-induced oscillator of Duffing’s type with modified LuGre friction model. Journal of Sound and Vibration, 440, pp. 23-33, DOI: 10.1016/j.jsv.2018.10.003

[8] Stender, M., Hoffmann, N., Papangelo, A. (2020), The basin stability of bistable friction-excited oscillators. Lubricants, 8, pp. 105, doi:10.3390/lubricants8120105

[9] Hassard, B.D., Kazarinoff, N.D., Wan, Y.H. (1980), Theory and Applications of the Hopf Bifurcation. Cambridge: Cambridge University Press.

[10] Liu, W.M. (1994), Criterion of hopf bifurcations without using eigenvalues. Journal of Mathematical Analysis and Applications, 182, pp. 250–256.

The 6th International Conference on
Engineering Mechanics and Automation (ICEMA 2021)
Hanoi, November 14, 2021

Influence of Technological Parameters on the Quality of Hydroforming Product from Tube Billet

Dinh Van Duy
Department of Metal forming
School of Mechanical Engineering,
Hanoi University of Science and Technology
Hanoi, Vietnam
duy.dinhvan@hust.edu.vn

Vu Duc Quang
Department of Machines &
Fundamentals of Machine Design
Faculty of Mechanical Engineering,
University of Economics - Technology for Industries
Hanoi, Vietnam
vuquang@uneti.edu.vn

Nguyen Dac Trung
Department of Metal forming
School of Mechanical Engineering,
Hanoi University of Science and Technology
Hanoi, Vietnam
trung.nguyendac@hust.edu.vn

***Abstract*: Hydroforming of products from tube billets is a process for forming complex parts of the automotive, bicycle, aircraft, shipbuilding, chemical, gas, oil, power plant construction industries, household appliances, etc. with fewer operations, lighter weight, better mechanical properties by using high pressure or low-pressure liquid punch. They are characterized by the use of tubes, thus allowing expansion to a variety of shapes. The quality of the hydroforming product from the tube billet depends on the key input technology parameters of the process. Product quality is characterized by accuracy in geometric dimensions, shape, surface quality (wrinkles, tears, etc.). There is a basis for optimal adjustment to improve product quality with great significance in practice. This paper presents the research results to determine the technological parameters and their influence on the quality of tube hydroforming products, such as liquid pressure - axial pressure - axial displacement, friction, and temperature. Research results help technologists to optimize technological parameters in the hydroforming process of the product from tube billet.**

Keywords: tube hydroforming, process parameters, metal forming

I. INTRODUCTION

Tube hydroforming is a unique metal forming process whereby complicated shapes are created by utilizing liquid pressure instead of (or in combination with) traditional mechanical forces. The tube hydroforming process has several advantages over other forming processes, which has helped establish it in a range of specific applications. These are the ability to create special geometrical profiles, reduced thinning, enhanced mechanical properties, better surface finish, fewer components required in an assembly, and less required rework due to the creation of geometries closer to the final shape [1]. These advantages primarily stem from the ability of the working fluid to exert pressure evenly over the entire surface of a material and for the equipment to vary this fluid pressure during the forming cycle based upon an optimized load path.

While tube hydroforming technology is currently used in the manufacturing sectors of many different industries, the development has been pushed most notably by the automotive industry (figure 1a) [2] and the aircraft industry (figure 1b) [3]:

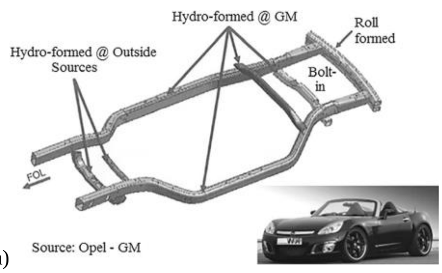

a)

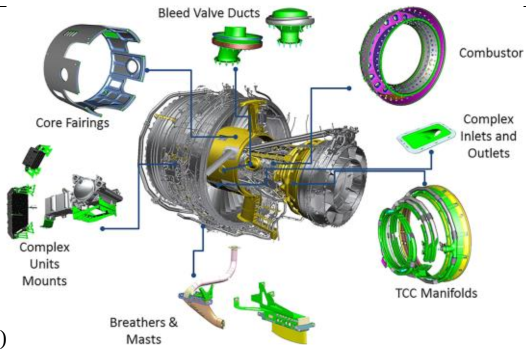

b)

Fig. 1 Tube hydroforming applications: a) automotive industry [2] and b) aircraft industry [3].

During any manufacturing process, certain technological parameters need to be set and controlled to ensure the specifications and quality of the product. Often in a manufacturing process, the more important of these parameters are known as key technology parameters. In tube hydroforming, key technological parameters can be used for both seamed and seamless tubes. In cases with more complicated shapes, performing operations such as bending must occur before the tubes can be loaded into the dies. The main technological parameters in tube hydroforming are liquid pressure - axial pressure - axial displacement, friction, and temperature. There is also a decision about whether or not upsetting or bending operations will perform before the hydroforming. Processes like axial upsetting can create some of the same features. They can also use axial feeding material similarly to tube hydroforming. This study investigates published works on the influence of important parameters in the process of hydrostatic forming of pipe blanks. The main technological parameters, affecting the geometrical and dimensional accuracy have been shown in this study.

II. RESEARCH RESULTS ON THE INFLUENCE OF KEY TECHNOLOGICAL PARAMETERS ON PRODUCT QUALITY

A. Influence of Fluid Pressure, Axial Pressure, and Axial Displacement

Tube hydroforming operations can either be carried out at high or low pressures. Higher pressures allow for more expansion, but material thinning increases in direct proportion to geometric expansion. Low-pressure hydroforming takes advantage of the tube crushing concept by first filling the tube with pressurized fluid and then using the closing force of the press to get the tube either close to or into its final shape. When compared by numerical simulation of high pressure and low-pressure pipe hydrostatic stamping, with pipe material using high strength steels, Nikhare C et al. found that a smaller press was needed for the low-pressure tube hydroforming operation. [4]. A similar result is also stated by Morphy et al., who present a comparison of two similar engine cradles, one made by high and one by low-pressure tube hydroforming. The results showed that low-pressure tube hydroforming was advantageous in processing steps, equipment, energy consumption, cycle time, and floor space [5].

A "process window" has a range of values that work for a given process and are displayed graphically. These windows are generated through simulation and experimentation. It is governed by the material properties and the geometry of the parts. In specific circumstances, companies can also set the physical limitations of their equipment as boundaries to the process window. Within reasonable work, the area can guarantee the quality of the hydroforming part (no wrinkles and breaks), and the desired forming area is defined in the middle of the working area [6].

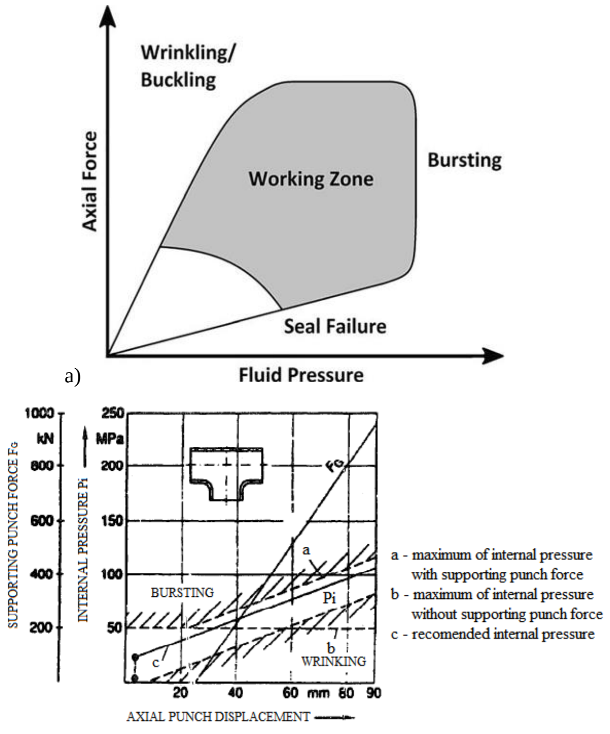

Fig. 2. a) Typical schematic of a tube hydroforming process window [6].

b) Working diagram for the forming of branch tube elements [7].

Load paths are similar to process windows. Instead of defining the range of viable technological parameters, they produce a specific sequence of values employed during a forming operation to produce the desired result. A load path is a statement of how much fluid pressure and axial force are applied at a given time through a forming process. Several studies cite process variability as a key difficulty in load path optimization and have proposed various means to take this into account.

B. Influence of Friction

The interaction of surfaces and lubricants is a key factor in the performance of a hydroforming process, the goal is to reduce friction to allow better material flow. Friction can be useful in controlling material flow by reducing thinning in important areas [2,8]. Fiorentino et al. investigated the lubrication conditions: dry, oil, Teflon, Teflon with oil, Teflon spray and graphitic oil by their friction coefficient to the formed parts such as bulge height, thickness distribution and surface finishing [9]:

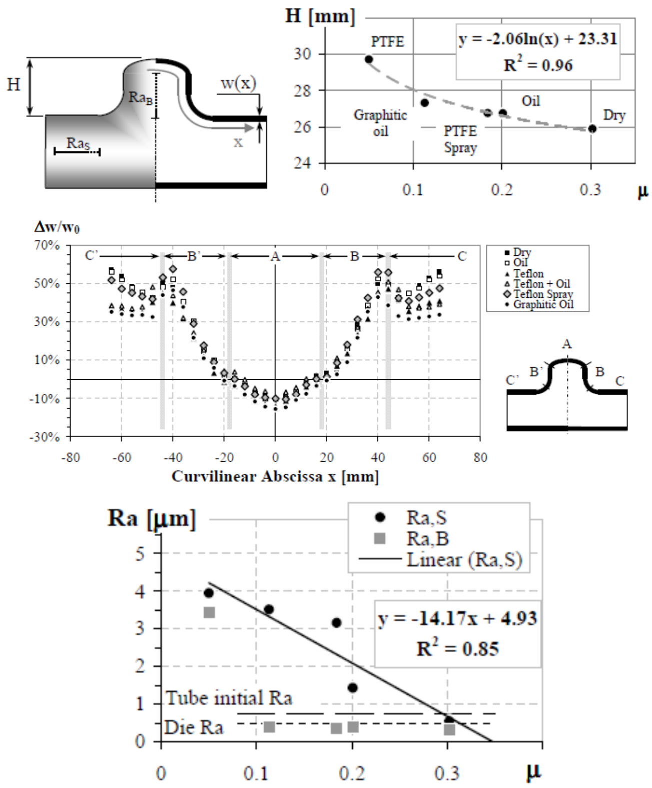

Fig. 3. Influence of friction on hydroforming tube results [9].

C. Influence of Forming Temperature

Heat-assisted tubular hydroforming studies have demonstrated that forming limits are extended considerably, especially for typically lightweight materials [2]. At the same time, it is possible to manufacture distinctly more complex component geometries featuring and improved mechanical properties. It is particularly true for manufacturing components made of light metals such as Aluminum, magnesium, and ferritic stainless steel. In the case of all these materials, the limits of forming have been significantly extended, such as reduced forming fluid pressure, reduced axial force, reduced counter-pressure, reduced spring back, reduced yield stress - increased strain, or their process chains can be considerably simplified or shortened due to omission of intermediate annealing operations [10]. Combining tempered forming with heat treatment, in particular, their use in conjunction with forming closed profiles made from Boron-Manganese alloyed steel materials opens up the possibility for a completely new category of components.

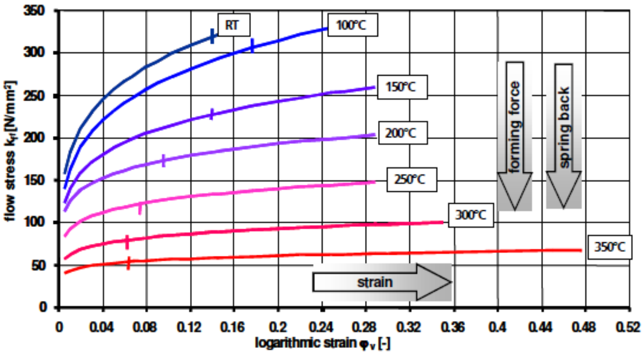

Fig. 4. Influence of temperature on flow curve for AZ31B [10].

III. Results and Discussion

Hydroforming has many advantages over competing for manufacturing processes as well as a few disadvantages. The first of these is increased formability. More complicated geometries can be created from a manufacturing perspective during hydroforming operations, which reduces weld lines, weight, and material waste. Also, the resulting mechanical properties can be stronger as an increase in stiffness, and the surface finish can be of higher quality because fluids will not scratch materials during forming.

The major disadvantage with the tube hydroforming process is the cycle times for the presses are much longer than conventional cold forming methods. Typical cycle times are around 20 to 60 s instead of just a few seconds in a traditional cold forming operation [5]. It takes more time to flood and increase fluid pressure inside a chamber than it does to press a set of dies together mechanically. The other disadvantage is difficult to produce sharp radii without using pressure intensifiers. Required pressure and the smallest radius on a part have an inversely proportional relationship. Lastly, all forming processes work-harden materials that have the effect of stiffening them and reducing their ductility. If a certain amount of flexibility is required in a hydroformed component, a heat treatment might be required post-forming or warm hydroforming.

Researches on tube hydrostatic forming technology just published the effect of one or two technological parameters but have not studied the aggregate effects of parameters on forming results, nor have studied the degree of influence of each parameter on the quality of forming product (wrinkling, thinning, rupturing). Regardless of these difficulties, the potential is so enormous that research on the tube hydroforming process is being carried out in various fields, such as in the automotive, aerospace, or rotating parts sectors.

IV. Conclusion

This paper presents the research results on the effects of key parameters in the tube hydroforming process. By synthesizing and analyzing published works, the effects of important technological parameters on the forming process are determined as fluid pressure - axial pressure - axial displacement, friction, and temperature. Researchers and applications have demonstrated that these parameters are crucial to success or failure. Friction parameter, calibrating pressure, temperature affect forming quality: bugle height, thinning, surface quality. This research helps technicians grasp the impact laws, determine the effects of key technology parameters in the tube hydroforming process, and choose the appropriate set of technological parameters that facilitates making quick and accurate decisions when calculating and designing to apply in practice.

References

[1] Pham, V.N., Tube hydrostatic forming technology. 1st ed., Bach Khoa Publishing House. Hanoi, Vietnam, 2007, pp.178-209.

[2] Tolazzi M., Hydroforming applications in automotive: a review, International Journal of Material Forming, vol. 3, no. 1, pp. 307-310, April. 2010, https://doi.org/10.1007/s12289-010-0768-2.

[3] Colin Bell1., Jonathan Corney., Nicola Zuelli., David Savings., A state of the art review of hydroforming technology, International Journal of Material Forming, Vol. 13 Iss.3, pp. 789-828, May. 2020, https://doi.org/ s12289-019-01507-1.

[4] Nikhare C, Weiss M, Hodgson PD., FEA comparison of high and low-pressure tube hydroforming of TRIP steel. Comput Mater Sci, vol. 47, no. 1, Pp. 146-152, 2009, https://doi.org/0.1016/j.commatsci.2009.06.024.

[5] Morphy, G., Tube hydroforming: dimensional capability analysis of a high volume automotive structural component production process, SAE Technical Paper 980450, pp. 1-10, 1998, https://doi.org/10.4271/980450.

[6] Hartl C., Micro-hydroforming. In micromanufacturing engineering and technology. 2nd edn. William Andrew, Oxford, England, 2015, pp 323-343. November. 1997, https://doi.org/10.1016/S0924-0136(97)00166-0.

[7] Dohmann F., Hartl Ch., Tube hydroforming-research and practical application. Journal of Materials Processing Technology vol. 71, no. 1, pp. 174-186, November. 1997, https://doi.org/10.1016/S0924-0136(97)00166-0.

[8] Wang C., Guo B., Shan D., Zhang M., Bai X., Tribological behaviors in micro forming considering microscopically trapped lubricant at contact interface. Int J Adv Manuf Technol vol. 71, no. 9-12, pp. 2083-2090, April. 2014, https://doi.org/10.1007/s00170-014-5657-2.

[9] Fiorentino A., Ceretti E., Attanasio A., Braga D., and Giardini C., Experimental study of lubrication influence in the production of hydroformed T-joint tubes. Key Engineering Materials vols. 410-41, pp 15-24, March 2009, https://doi.org/10.4028/www.scientific.net/KEM.410-411.15.

[10] Dirk Landgrebe and Frank Schieck., Hot gas-forming for advanced tubular automobile components-opportunities and challenges. ASME 2015 International Manufacturing Science and Engineering Conference vol. 1: Proceedings, 8 pages, September. 2015, Charlotte, North Carolina, USA, https://doi.org/10.1115/MSEC2015-9204.

The 6th International Conference on
Engineering Mechanics and Automation (ICEMA 2021)
Hanoi, November 14, 2021

Investigation of a sandwich plate with two MEE face sheets and FGM core layer from the nonlinear dynamic buckling point of view

Ngo Dinh Dat
Department of Engineering and Technology in Constructions and Transportation -University of Engineering and Technology, VNU Hanoi.
ngodinhdat0405@gmail.com

Nguyen Dinh Duc
Department of Engineering and Technology in Constructions and Transportation -University of Engineering and Technology, VNU Hanoi.
ducnd@vnu.edu.vn

Vu Dinh Giang
Faculty of Engineering Mechanics and Automation - University of Engineering and Technology, VNU Hanoi.
rangsut2k@gmail.com

Vu Thi Thuy Anh
Department of Engineering and Technology in Constructions and Transportation -University of Engineering and Technology, VNU Hanoi.
anhvutt@vnu.edu.vn

***Abstract*: A sandwich plate with two Magneto-Electro-Elastic (MEE) face sheets and Functionally Graded Materials (FGM) core layer resting on an elastic foundation and in a thermal environment will be studied in this paper for the nonlinear dynamic buckling problem. The hypothetical plate model above is formed from the fact that MEE materials have been receiving special attention from the research community owing to their specialized performance and coupled behavior under thermal, electric, magnetic, and mechanical loads, while FGM has been introducing for controlling material response to deformation, dynamic loading as well as to corrosion and wear, etc. The combination of these two materials in the sandwich plate model is expected to create a remarkable new sandwich model. The establishment of all basic equations for the nonlinear dynamic buckling problem of this novel sandwich model will be solved by analytical methods, and the effects of geometrical parameters, temperature, electric and magnetic potentials on the nonlinear dynamic buckling of the sandwich plate will be shown in the numerical results of this study.**

Keywords: *Smart materials, MEE, FGM, plate, dynamic, vibration, analytical method.*

I. INTRODUCTION

Many applications such as aerospace, automotive, power generation, microelectronics, structural, and bio-engineering demand properties that are unobtainable in conventional engineering materials. These applications require mutually exclusive properties to have resistance against thermo-mechanical stresses as well as chemical stability. The need for property distributions is found in a variety of common products that must have multiple functions, such as gears, which must be tough enough inside to withstand the fracture but must also be hard on the outside to prevent wear. similarly, a turbine blade should also possess a property distribution; the blade must be tough to withstand the loading, but it must also have a high melting point to withstand high temperatures on the outer surface...

MEE material is a new material that shows the full coupling between magnetic, electric, elastic fields, and the magneto-electric effect. In which, the magneto-electric effect is the phenomenon where a magnetic polarization occurs due to an electric field and vice versa. It is thanks to these properties that MEE is seen to be a smart material that has the ability to change reversibly their properties to respond to external environments such as stress, temperature, moisture, electric or magnetic fields. MEE has received considerable interest because of a wide variety of applications in sensors, civil structures, aerospace control systems, and medical devices [1].

Also, considered a new type of material, FGM exhibits many advantages compared to conventional alloys and composite materials. FGM may be used by the variation in composition and structure fought over volume, resulting in corresponding changes in the properties of the material, or otherwise, FGM gives the opportunity to take the benefits of different material systems e.g. ceramics and metals, simultaneously provide a thermal barrier and reduced residual stress coating [2].

If the experimental studies are not included, the theoretical studies of material can be divided into two groups: research by numerical methods and research by an analytic method. Each method has its own advantages and disadvantages. For the analytical method, the equations and the computation process will become very complex. However, the benefits of this method were that the obtained results are explicitly stated in terms of the input parameters of the material and the structure, so when we change these parameters, we can actively control the behaviors of the structures.

Research on MEE or FGM has received a lot of attention from scientists, including the authors or groups such as [3-10]. However, studies on MEE or FGM sandwich structure are still very limited. Some studies can be mentioned such as [11-13]. It is easy to see that most of the research mentioned above is solved by the numerical method, while the number of studies is solved by analytic methods is very limited. So, this suggests that more research on sandwich structures is still needed.

By using an analytical method based on classical plate theory, the report focuses on studying the nonlinear dynamic buckling of the sandwich plate with two MEE face sheets and FGM core layer subjected to the combination of external pressure, thermal, electric, and magnetic loads. In addition to the numerical survey results, the comparison results are also shown in the results section to assess the reliability of the research method in the article.

II. MATHEMATICAL MODEL

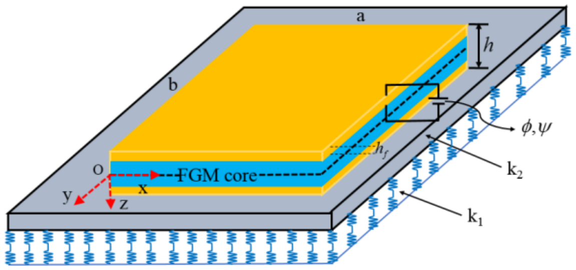

Fig. 1. The configuration and coordinate system of the sandwich plate

Consider a sandwich plate with two MEE face sheets and FGM core layer resting on elastic medium and subjected to the combination of external pressure, thermal, electric and magnetic loads with the size of the plate $a \times b \times h$ as shown in Fig. 1. A coordinate system (x, y, z) is established in which (x, y) plane on the middle surface of the sandwich plate and z on thickness direction.

A. Mechanical properties of MEE face sheets

TABLE I. MECHANICAL PROPERTIES OF MEE MATERIAL.

Material properties	Notation	Values
Elastic constants (GPa)	$C_{11}^f = C_{22}^f$	220
	$C_{12}^f = C_{13}^f = C_{23}^f$	120
	C_{33}	215
	$C_{44} = C_{55}$	45
	C_{66}	0
Piezoelectric constants (C/m^2)	e_{31}	-3.5
	e_{33}	9.0
	e_{15}	0
Dielectric constants $(C/\mathrm{N}m^2)$	$\eta_{11} = \eta_{22}$	0.85×10^{-9}
	η_{33}	6.3×10^{-9}
Magnetic permeability $(\mathrm{Ns}^2/\mathrm{C}^2)$	$\mu_{11} = \mu_{22}$	-2×10^{-4}
	μ_{33}	0.9×10^{-4}
Piezomagnetic constants $(N/\mathrm{A}m)$	q_{31}	350
	q_{33}	320
	q_{15}	200
Magneto-electric constants $(\mathrm{Ns/VC})$	$m_{11} = m_{22}$	5.5×10^{-12}
	m_{33}	2600×10^{-12}
Pyroelectric constant (C/m^2K)	p_3	7.8×10^{-7}
Pyromagnetic constant (C/m^2K)	λ_3	-23×10^{-5}
Thermal expansion coefficients (K^{-1})	$\alpha_1 = \alpha_2$	12.3×10^{-6}
	α_3	8.2×10^{-6}
Moisture expansion coefficients (m^3k^{-1})	β_1	0
	$\beta_2 = \beta_3$	1.1×10^{-4}
Density (kg/m^3)	ρ_f	5500

Two face sheets are made up of a combination of piezoelectric and piezomagnetic materials. The main constituents of the face sheet are Barium Titanate $(BaTiO_3)$ and Cobalt Ferric oxide $(CoFe_2O_4)$. In this study, the volume fraction of $BaTiO_3 - CoFe_2O_4$ in each face sheet is chosen to be 0.5 and the material properties of magneto-electro-elastic face sheet are given in Table 1 [3].

B. Material prorerties of FGM core layer

The FGM core layer is considered a mixture of ceramic and metal. According to the Voigt model, the property of functionally graded material may be expressed as

$$P = P_c V_c + P_m V_m. \tag{1}$$

where P_c and P_m are the corresponding properties of the ceramic and metal constituents, respectively. Here, V_c and V_m are the volume fractions of ceramic and metal that may be considered by power law distribution as [6]

$$V_c(z) = \left(\frac{2z+h}{2h}\right)^N, \quad V_m(z) = 1 - V_c(z). \tag{2}$$

where N is the volume fraction exponent. Thus, the property of functionally graded material, such as Young's modulus, the thermal conductivity, and the coefficient of thermal expansion, vary as a power form of the thickness coordinate [6]

$$P_{eff}(z) = \mathrm{Pr}_c V_c(z) + \mathrm{Pr}_m V_m(z) \tag{3}$$

Because of the weak variation of Poisson's ratio in the constituent materials, it is considered constant in this paper. The smart sandwich plate is assumed to rest on Pasternak-type elastic foundations. The interaction between elastic foundations and the sandwich plate is defined as follows

$$q_e = k_1 w - k_2 \nabla^2 w. \tag{4}$$

where $\nabla^2 = \frac{\partial^2}{\partial x^2} + \frac{\partial^2}{\partial y^2}$, w is the deflection of the smart sandwich plate, k_1 and k_2 are Winkler foundation stiffness and shear layer stiffness of Pasternak foundation, respectively.

C. Boundary condition

In this study, depending on the in-plane restraint at the edges, four edges of the plate are simply supported and immovable. The associated boundary conditions are

$$\begin{aligned} &w = u = M_x = 0, N_x = N_{x0}, x = 0, a \\ &w = v = M_y = 0, N_y = N_{y0}, y = 0, b \end{aligned} \tag{5}$$

with N_{x0}, N_{y0} are pre-buckling compressive force resultant in direction x.

III. FUNDAMENTAL FORMULATION

Establishing the basic equations means finding reciprocal relationships between stress, strain and displacement components. These relationships are expressed in the strain compatibility equations, the equilibrium equation and Hooke's law.

It is easy to see here, the plate is the sandwich structure with three layers, in which the middle layer (core layer) is of the properties of FGM material and the two outer layers are taking into account the coupling between elastic, electric and magnetic field. The factors of temperature also influence these two outer layers. Therefore, it is necessary to establish the stress, strain and displacement components in each layer first.

A. FGM core layer

In this study, the classical plate theory is used to establish the basic equations and investigate the nonlinear dynamic buckling of the smart sandwich plate. The normal and shear strain components across the plate thickness at a distance z from the mid-plane are defined as

$$\begin{Bmatrix} \varepsilon_x \\ \varepsilon_y \\ \gamma_{xy} \end{Bmatrix} = \begin{Bmatrix} \varepsilon_x^0 \\ \varepsilon_y^0 \\ \gamma_{xy}^0 \end{Bmatrix} + z \begin{Bmatrix} k_x \\ k_y \\ k_{xy} \end{Bmatrix} = \begin{Bmatrix} u_{,x} + 0.5w_{,x}^2 \\ v_{,y} + 0.5w_{,y}^2 \\ u_{,y} + v_{,x} + w_{xy} \end{Bmatrix} - z \begin{Bmatrix} w_{,xx} \\ w_{,yy} \\ 2w_{,xy} \end{Bmatrix}. \quad (6)$$

here $\varepsilon_x^o, \varepsilon_y^o, \gamma_{xy}^o, \gamma_{xz}^o, \gamma_{yz}^o$ are the normal and transverse shear strains on the mid-plane of plate, and u, v are displacement components along the x, y directions of plate.

For FGM core layer, the relationship between stress and strain components with the effect of temperature are expressed as Hooke law is defined as

$$\begin{Bmatrix} \sigma_x \\ \sigma_y \\ \sigma_{xy} \end{Bmatrix}_a = \begin{bmatrix} Q_{11}^a & Q_{12}^a & 0 \\ Q_{12}^a & Q_{22}^a & 0 \\ 0 & 0 & Q_{66}^a \end{bmatrix} \begin{Bmatrix} \varepsilon_x \\ \varepsilon_y \\ \gamma_{xy} \end{Bmatrix}_a - \begin{Bmatrix} \alpha_1 \\ \alpha_2 \\ 0 \end{Bmatrix} \Delta T, \quad (7)$$

where ΔT is temperature rise from stress free initial state or temperature difference, and E_a, v_a are elastic modulus and poisson's ratio of core layer,

$$Q_{11}^a = \frac{E_a}{1-v_a^2}, Q_{12}^a = \frac{v_a E_a}{1-v_a^2}, Q_{22}^a = Q_{11}^a, Q_{66}^a = \frac{E_a}{2(1+v_a)}.$$

B. MEE face sheets

The linear constitutive relations for magneto-electro-elastic face sheets taking into account the coupling between elastic, electric and magnetic fields can be represented as follows [1]

$$\begin{aligned}
\sigma_x^f &= \tilde{C}_{11}\varepsilon_x^f + \tilde{C}_{12}\varepsilon_y^f - \tilde{e}_{31}E_z - \tilde{q}_{31}H_z - \tilde{\alpha}_1\Delta T, \\
\sigma_y^f &= \tilde{C}_{12}\varepsilon_x^f + \tilde{C}_{22}\varepsilon_y^f - \tilde{e}_{32}E_z - \tilde{q}_{32}H_z - \tilde{\alpha}_2\Delta T, \\
\tau_{xy}^f &= \tilde{C}_{66}\gamma_{xy}^f, \\
D_x^f &= \tilde{\eta}_{11}E_x + \tilde{m}_{11}H_x + \tilde{p}_1\Delta T, \\
D_y^f &= \tilde{\eta}_{22}E_y + \tilde{m}_{22}H_y + \tilde{p}_2\Delta T, \\
D_z^f &= \tilde{e}_{31}\varepsilon_x + \tilde{e}_{32}\varepsilon_y + \tilde{\eta}_{33}E_z + \tilde{m}_{33}H_z + \tilde{p}_3\Delta T, \\
B_x^f &= \tilde{m}_{11}E_x + \tilde{\mu}_{11}H_x + \tilde{\lambda}_1\Delta T, \\
B_y^f &= \tilde{m}_{22}E_y + \tilde{\mu}_{22}H_y + \tilde{\lambda}_2\Delta T, \\
B_z^f &= \tilde{q}_{31}\varepsilon_x^f + \tilde{q}_{32}\varepsilon_y^f + \tilde{m}_{33}E_z + \tilde{\mu}_{33}H_z + \tilde{\lambda}_3\Delta T,
\end{aligned} \quad (8)$$

in which notation "f" represents for magneto-electro-elastic face sheets; $\sigma_x^f, \sigma_y^f, \tau_{xy}^f$, D_i^f $(i = x, y, z)$, and B_i^f $(i = x, y, z)$ are stress components, electric displacement and the magnetic flux respectively; C_{ij} $(ij = 11, 12, 22, 66)$, e_{kl} $(kl = 31, 32)$ and q_{kl} $(kl = 31, 32)$ are elastic coefficient, the piezoelectric coefficient and the magnetostrictive coefficient, respectively; $\alpha_i (i = 1, 2)$ and $\beta_i (i = 1, 2)$ are thermal expansion coefficients and moisture expansion coefficient, respectively. Further, η_{ij}, m_{ij} and μ_{ij} with $(ij = 11, 22, 33)$ are the dielectric constant, electromagnetic coefficient and the magnetic permeability constant, respectively; p_i, χ_i, λ_i $(i = 1, 2, 3)$ are the pyroelectric, hygroelectric, pyromagnetic and hygromagnetic material properties, respectively; E_i and $H_i\,(x, y, z)$ are respectively electric field and magnetic field, and the reduced form of the parameters appearing in Eq. (8) can be clearly presented in Appendix.

The components of electric and magnetic fields E_i and H_i can be expressed by gradients of the scalar electric and magnetic potentials Φ and Ψ as [11]

$$\{E_i, H_i\} = \{-\tilde{\Phi}_{,i}, -\tilde{\Psi}_{,i}\}, i = x, y, z. \quad (9)$$

in which the electric potential and magnetic potentials are assumed to have the form of combination of a cosine and linear function as follows

$$\begin{aligned}
\tilde{\Phi}(x, y, z, t) &= -\cos(\beta z)\Phi(x, y, t) + 2z\phi_0 / h_f, \\
\tilde{\Psi}(x, y, z, t) &= -\cos(\beta z)\Psi(x, y, t) + 2z\psi_0 / h_f,
\end{aligned} \quad (10)$$

where $\beta = \pi / h$, $\Phi(x,t), \Psi(x,t)$ are the spatial variation of the electric and magnetic potentials, respectively. Also, ϕ_0 and ψ_0 are the initial external electric and magnetic potentials, respectively.

Substituting Eq. (10) into Eq. (9) yields

$$\begin{aligned}
&E_i = \cos(\beta z)(\Phi_{,i}),\ H_i = \cos(\beta z)(\Psi_{,i}), i = x, y \\
&E_z = -\beta\sin(\beta z)\Phi - 2\phi_0 / h_f, H_z = -\beta\sin(\beta z)\Psi - 2\psi_0 / h_f.
\end{aligned} \quad (11)$$

C. The nonlinear motion and the deformation compatibility equation

With the stress, strain and displacement components calculated for each of the material layers above, the force and moment resultants of the smart magneto-electro-elastic sandwich plate are expressed as

$$\begin{aligned}
(N_i, M_i) = &\int_{-h_2/2-h_3}^{-h_2/2} \sigma_i^f(1,z)dz + \int_{-h_2/2}^{0} \sigma_i^C(1,z)dz \\
&+ \int_{0}^{h_2/2} \sigma_i^C(1,z)dz + \int_{h_2/2}^{h_2/2+h_1} \sigma_i^f(1,z)dz, \ (i = x, y, xy)
\end{aligned} \quad (12)$$

Replacing Eq. (6) into Eqs. (7) and (8) then the results into Eq. (12) leads to

$$\begin{aligned}
N_x &= F_{11}\varepsilon_x^0 + F_{12}\varepsilon_y^0 + G_{11}k_x + G_{12}k_y - F_{13}E_z - G_{13}H_z - \alpha_1\Delta T, \\
N_y &= F_{12}\varepsilon_x^0 + F_{22}\varepsilon_y^0 + G_{12}k_x + G_{22}k_y - F_{14}E_z - G_{14}H_z - \alpha_2\Delta T, \\
N_{xy} &= F_{66}\gamma_{xy}^0 + G_{66}k_{xy}, \\
M_x &= G_{11}\varepsilon_x^0 + G_{12}\varepsilon_y^0 + H_{11}k_x + H_{12}k_y - F_{23}E_z - G_{23}H_z - \alpha_3\Delta T, \\
M_y &= G_{12}\varepsilon_x^0 + G_{22}\varepsilon_y^0 + H_{12}k_x + H_{22}k_y - F_{24}E_z - G_{24}H_z - \alpha_4\Delta T \\
M_{xy} &= G_{66}\gamma_{xy}^0 + H_{66}k_{xy},
\end{aligned} \quad (13)$$

in which the detail of coefficients $A_{ij}\left(i = \overline{1,2}; \mathrm{j} = \overline{1,4}\right)$, A_{66} $(A = F, G)$, $\mathrm{H_{ij}}$ $(\mathrm{ij} = 11,12,22,66)$, $(\alpha, \beta)_i \left(i = \overline{1,4}\right)$ may be found in Appendix.

The nonlinear equilibrium equations of the sandwich plate using the Hamilton principle and the Volmir's assumption with $u << w, v << w, \rho_1 u_{,tt} \to 0, \rho_1 v_{,tt} \to 0$ are defined as [18]

$$N_{x,x} + N_{xy,y} = 0, \tag{14a}$$

$$N_{xy,x} + N_{y,y} = 0, \tag{14b}$$

$$\begin{aligned} &M_{x,xx} + 2M_{xy,xy} + M_{y,yy} + N_x \mathrm{w}_{,xx} + 2N_{xy}\mathrm{w}_{,xy} + N_y \mathrm{w}_{,yy} \\ &+ p - k_1 w + k_2\left(\mathrm{w}_{,xx} + \mathrm{w}_{,yy}\right) = \rho_1 \mathrm{w}_{,tt}. \end{aligned} \tag{14c}$$

$$\begin{aligned} &\int_{-h_c/2-h_f}^{-h_c/2} \left(\frac{\partial D_x}{\partial x}\cos(\beta z) + \frac{\partial D_y}{\partial y}\cos(\beta z) + D_z \beta \sin(\beta z) \right) dz \\ &+ \int_{h_c/2}^{h_c/2+h_f} \left(\frac{\partial D_x}{\partial x}\cos(\beta z) + \frac{\partial D_y}{\partial y}\cos(\beta z) + D_z \beta \sin(\beta z) \right) dz = 0 \end{aligned} \tag{14d}$$

$$\begin{aligned} &\int_{-h_c/2-h_f}^{-h_c/2} \left(\frac{\partial B_x}{\partial x}\cos(\beta z) + \frac{\partial B_y}{\partial y}\cos(\beta z) + B_z \beta \sin(\beta z) \right) dz \\ &+ \int_{h_c/2}^{h_c/2+h_f} \left(\frac{\partial B_x}{\partial x}\cos(\beta z) + \frac{\partial B_y}{\partial y}\cos(\beta z) + B_z \beta \sin(\beta z) \right) dz = 0 \end{aligned} \tag{14e}$$

in which, $p(Pa)$ is an external pressure uniformly distributed on the surface of the sandwich plate and

$$\rho_1 = \int_{-hf-hc/2}^{-hc/2} \rho_f(z)dz + \int_{-hc/2}^{hc/2} \rho_c(z)dz + \int_{hc/2}^{hc/2+hf} \rho_f(z)dz.$$

The deformation compatibility equation for a sandwich plate can be written as

$$\begin{aligned} \varepsilon^0_{x,yy} + \varepsilon^0_{y,xx} - \gamma^0_{xy,xy} &= \left(w_{,xy}\right)^2 - w_{,xx}w_{,yy} + \\ &+ 2w_{,xy}w^*_{,xy} - w_{,xx}w^*_{,yy} - w_{,yy}w^*_{,xx}. \end{aligned} \tag{15}$$

in which $w^*(x,y)$ is function of initial imperfection.

IV. SOLUTIONS TO THE PROBLEM

Base on the classical plate theory, the stress function method is applied to solve the problem, in which the chosen stress function Airy is introduced as

$$N_x = f_{,yy}, N_y = f_{,xx}, N_{xy} = -f_{,xy}. \tag{16}$$

Replace this stress function into Eqs. (14) and (15), while performing the necessary transformations, it can be seen that the four newly obtained equations are two nonlinear equations in terms of variables w, f, Φ and Ψ used to investigate the nonlinear vibration and dynamic of MEE-FGM-MEE sandwich plate surrounded on elastic foundations.

To solve four newly equations above and with the consideration of the boundary conditions (5), we assume the following approximate solutions:

$$\begin{aligned} &w(x,y,t) = W(t)\sin\lambda_m x \sin\delta_n y, \\ &\Phi(x,y,t) = \phi(t)\sin\lambda_m x \sin\delta_n y, \\ &\Psi(x,y,t) = \psi(t)\sin\lambda_m x \sin\delta_n y, \\ &w^*(x,y,t) = \mu h \sin\lambda_m x \sin\delta_n y, \\ &f(x,y,t) = A_1\cos 2\lambda_m x + A_2 \cos 2\delta_n y + \\ &\quad + A_3 \sin\lambda_m x \sin\delta_n y + 0.5N_{x0}y^2 + 0.5N_{y0}x^2 \end{aligned} \tag{17}$$

where $\lambda_m = m\pi/a$, $\delta_n = n\pi/b$, W is the amplitude of the deflection and m,n are odd natural numbers; ϕ and ψ are electric and magnetic potentials, respectively. The coefficients A_i $(i = 1 \div 3)$ are determined by substitution of Eq. (17) into the deformation compatibility equation, and:

$$A_1 = M_1 W(W + 2\mu h),\ A_2 = M_2 W(W + 2\mu h),\ A_3 = M_3 W,$$
$$M_1 = \delta_n^2 / 32F^*_{11}\lambda_m^2,\ M_2 = \lambda_m^2 / 32F^*_{22}\delta_n^2,$$
$$M_3 = -\frac{\left[G^*_{21}\lambda_m^4 + \left(G^*_{11} + G^*_{22} - 2G^*_{66}\right)\lambda_m^2\delta_n^2 + G^*_{12}\delta_n^4\right]}{\left[F^*_{11}\lambda_m^4 - \left(2F^*_{12} - F^*_{66}\right)\lambda_m^2\delta_n^2 + F^*_{22}\delta_n^4\right]}$$

Substitution of the approximate solutions (17) into the nonlinear motion equations and applying the Galerkin procedure for resulting equation yield

$$\begin{aligned} &h_{11}W + h_{12}W(W + \mu h) + h_{13}W(W + 2\mu h) + \\ &\quad + h_{14}W(W + \mu h)(W + 2\mu h) + h_{15}\phi + h_{16}\psi + \\ &\quad - \left(N_{x0}\lambda_m^2 + N_{y0}\delta_m^2\right)(W + \mu h) + n_5 p = \rho_1 W_{,tt}, \\ &h_{41}\mathrm{W} + h_{42}\phi + h_{43}\psi = 0, \\ &h_{51}\mathrm{W} + h_{43}\phi + h_{52}\psi = 0. \end{aligned} \tag{18}$$

where $h_{ij}\left(i = 1, j = 1 \div 6\right), h_{4l}\left(l = 1 \div 3\right), h_{51}, h_{52}, n_5$ are shown in Appendix.

The conditions expressing the immovability on four edges (i.e. $u = 0$ on $x = 0, a$ and $v = 0$ on $y = 0, b$) are satisfied on the average sense as

$$\int_0^b \int_0^a \frac{\partial u}{\partial x} dxdy = 0, \int_0^a \int_0^b \frac{\partial v}{\partial x} dydx = 0. \tag{19}$$

in which, the formulas of the normal and shear strains in the middle surface of the sandwich plate can be determine from Eq. (13) as

$$\begin{aligned} &\varepsilon^0_x = F^*_{22} f_{,yy} - F^*_{12} f_{,xx} + G^*_{11} w_{,xx} + G^*_{12} w_{,yy} + F^*_{13}\phi_0 + G^*_{13}\psi_0 + \alpha^*_1 \Delta T, \\ &\varepsilon^0_y = F^*_{11} f_{,xx} - F^*_{12} f_{,yy} + G^*_{21} w_{,xx} + G^*_{22} w_{,yy} + \\ &\quad + F^*_{14}\phi_0 + G^*_{14}\psi_0 + \alpha^*_2 \Delta T, \\ &\gamma^0_{xy} = -F^*_{66} f_{,xy} + 2G^*_{66} w_{,xy}, \end{aligned} \tag{20}$$

with: $\alpha^*_1 = F^*_{22}\alpha_1 - F^*_{12}\alpha_2, \alpha^*_2 = F^*_{11}\alpha_2 - F^*_{12}\alpha_1, F^*_{11} = F_{11}/\Delta,$

$$F^*_{22} = F_{22}/\Delta, F^*_{12} = F_{12}/\Delta, F^*_{66} = 1/F_{66}, G^*_{66} = G_{66}/F_{66},$$
$$\Delta = F_{11}F_{22} - F_{12}^2,\ G^*_{11} = F^*_{22}G_{11} - F^*_{12}G_{12}, G^*_{22} = F^*_{11}G_{22} - F^*_{12}G_{12},$$
$$G^*_{12} = F^*_{22}G_{12} - F^*_{12}G_{22}, G^*_{21} = F^*_{11}G_{12} - F^*_{12}G_{11},$$
$$F^*_{13} = -2\left(F^*_{22}F_{13} - F^*_{12}F_{14}\right)/h_f, G^*_{13} = -2\left(F^*_{22}G_{13} - F^*_{12}G_{14}\right)/h_f,$$
$$F^*_{14} = -2\left(F^*_{11}F_{14} - F^*_{12}F_{13}\right)/h_f, G^*_{14} = -2\left(F^*_{11}G_{14} - F^*_{12}G_{13}\right)/h_f.$$

From Eqs. (6) and (20), the derivative of displacements in the x and y directions are determined as

$$\begin{aligned} v_{,y} &= F^*_{11} f_{,xx} - F^*_{12} f_{,yy} + G^*_{21} w_{,xx} + G^*_{22} w_{,yy} + \\ &\quad + F^*_{14}\phi_0 + G^*_{14}\psi_0 + \alpha^*_2 \Delta T - \left(w_{,y}\right)^2/2 - w_{,y}w^*_{,y}, \\ u_{,x} &= F^*_{22} f_{,yy} - F^*_{12} f_{,xx} + G^*_{11} w_{,xx} + G^*_{12} w_{,yy} + \\ &\quad + F^*_{13}\phi_0 + G^*_{13}\psi_0 + \alpha^*_1 \Delta T - \left(w_{,x}\right)^2/2 - w_{,x}w^*_{,x}, \end{aligned} \tag{21}$$

Introducing Eq (17) into Eq. (21) then obtained results into Eq. (19) leads to

$$N_{x0} = g_1 W + g_2 (W + 2\mu h) W + g_3 \phi_0 + g_4 \psi_0 + g_5 \Delta T,$$
$$N_{y0} = f_1 W + f_2 (W + 2\mu h) W + f_3 \phi_0 + f_4 \psi_0 + f_5 \Delta T, \quad (22)$$

here $g_i, f_j \, (i, j = 1 \div 5)$ are shown in Appendix.

It is assumed that uniformly distributed transverse load has the form of $p = st$, the equations are used to study the nonlinear vibration of sandwich plate in the thermal environment is written as

$$\begin{aligned} &W_{,tt} + o_{11} W + o_{11}^* (W + \mu h) + o_{12} W (W + \mu h) + o_{15} \phi + o_{16} \psi \\ &+ o_{13}^* (W + \mu h)(W + 2\mu h) + + o_{14} W (W + \mu h)(W + 2\mu h) \\ &+ o_{13} W (W + 2\mu h) + o_{15}^* \phi (W + \mu h) + o_{16}^* \psi (W + \mu h) = n_5 st, \\ &h_{41} W + h_{42} \phi + h_{43} \psi = 0, \\ &h_{51} W + h_{43} \phi + h_{52} \psi = 0. \end{aligned} \quad (23)$$

where the $o_{1i} \, (i = 1 \div 6), o_{1j}^* \, (j = 1, 3)$ - coefficients, as shown in Appendix.

The fundamental frequency of natural vibration of the sandwich plate can be determined by finding the solution of under equation

$$\begin{vmatrix} o_{11} + o_{11}^* - \omega^2 & o_{15} & o_{16} \\ h_{41} & h_{42} & h_{43} \\ h_{51} & h_{43} & h_{52} \end{vmatrix} = 0 \quad (24)$$

To determine the value of the dynamic critical load, this study uses the the Budiansky–Roth criterion [17], with the time of instability as the time when the deflection amplitude - time curve reaches its maximum value first.

V. RESULTS AND DISCUSSION

A. Comparison results

In order to ensure the accuracy of present approach, the values of the dimensionless frequencies and fundamental frequencies of the FGM plate are calculated and compared with the results obtained by the other authors, such as Bich [14, 18], Alijani [15] and Kim [16]. The comparison results are shown in Tables 2, 3 with the following characteristic parameters: $\rho_m = 2702\, kg/m^3$, $\rho_c = 3800\, kg/m^3$ and $E_c = 380 \times 10^9 N/m^2$.

TABLE II. COMPARISON OF DIMENSIONLESS FREQUENCIES $\Omega = \omega_L a / \sqrt{c_{\max} / \rho_{\max}}$ OF FGM PLATE WITH $a/b = 1, a/h = 0.1,$

N	Present study	Bich [14]	Alijani [15]	Kim [16]
0	0.0581	0.0597	0.0579	0.0582
0.5	0.0505	0.0506	0.0506	0.0532
1	0.0447	0.0456	0.0456	0.0437
4	0.0389	0.0396	0.0396	0.0393
10	0.0363	0.0381	0.0380	0.0359

here $c_{\max}$, $\rho_{\max}$ are the maximum values of elastic constants and mass densities of piezoelectric and magnetostrictive layers, respectively.

TABLE III. COMPARISON OF FUNDAMENTAL FREQUENCIES OF NATURAL VIBRATION (rad/s) OF FGM PLATE WITH $a = b = 1.5, h = 0.008$.

N	0.2	1	5	10
Present study	197.114	162.112	139.794	135.384
Bich [18]	197.110	162.110	139.790	135.380

As can be seen, with the change of the volume fraction exponent N, the difference between the results shown in the table is not too large, or in other words, the present results agree very well with existing predictions, which indicates the reliability of present study.

B. Dynamic critical load

In this part, the influence of the parameters on the dynamic critical load value will be investigated.

Table 4 shows the effect of elastic foundations with two coefficients $k_1 (GPa/m), k_2 (GPa.m)$, modes of vibration (m,n) and the loading speed s on the dynamic critical load value of sandwich MEE-FGM-MEE plate with rectangular cross-section $a/b = 1$.

TABLE IV. EFFECTS OF ELASTIC FOUNDATIONS, MODES OF VIBRATION AND THE LOAD SETTING SPEED ON THE DYNAMIC CRITICAL LOAD VALUE

(k_1, k_2)	s	(m,n) (1,1)	(1,2)	(1,3)
(0,0)	3.5e11	8.1472e+7	8.9162e+7	9.7842e+7
	5e11	11.6389e+7	12.7374e+7	13.9748e+7
	7.5e11	17.4584e+7	19.1062e+7	20.9623e+7
(0.1e9,0)	3.5e11	8.1886e+7	8.9183e+7	9.7963e+7
	5e11	11.6980e+7	12.7405e+7	13.9947e+7
	7.5e11	17.5470e+7	19.1107e+7	20.9921e+7
(0.1e9, 0.02e9)	3.5e11	8.2589e+7	10.9986e+7	12.0764e+7
	5e11	11.7985e+7	15.6980e+7	17.2520e+7
	7.5e11	17.6977e+7	23.5470e+7	25.8780e+7

As can be observed, the value of the dynamic critical load of the sandwich plate with the support of elastic foundations is higher than one of sandwich plate without elastic foundations. The elastic foundations enhance the stiffness of the sandwich plate. Further, the value of the dynamic critical load increases significantly when the values of modes (m,n) and the loading speed s increase and vice versa with $(m,n), s$ decrease.

TABLE V. EFFECTS OF TEMPERATURE INCREMENT, THE RATIO b/h AND THE MAGNETIC POTENTIAL ϕ_0 ON THE DYNAMIC CRITICAL LOAD VALUE

$\Delta T\,(K)$	b/h	ϕ_0 -100	0	100
0	80	1.064876e+8	1.064873e+8	1.0648725e+8
	90	1.133963e+8	1.1339613e+8	1.133960e+8
	100	1.206422e+8	1.2064035e+8	1.2064032e+8
100	80	1.06594e+8	1.06592e+8	1.065918e+8
	90	1.134433e+8	1.134417e+8	1.134418e+8
	100	1.207651e+8	1.207647e+8	1.207646e+8
200	80	1.094731e+8	1.094725e+8	1.094713e+8
	90	1.135035e+8	1.135032e+8	1.1350315e+8
	100	1.20921e+8	1.209197e+8	1.209195e+8

The effects of temperature increment ΔT, the plate width to thickness ratio b/h and magnetic potential ϕ_0 on the dynamic critical load value of the sandwich plate with rectangular cross-section $a/b = 1$ resting on elastic foundation are given in Table 5. As expected, the increase of temperature increment ΔT, increase of ratio b/h and decrease of the magnetic potential value results in the increase of the dynamic critical load value. However, the difference of the dynamic critical load is not significant with the change of all three values examined.

TABLE VI. EFFECTS OF VOLUME FRACTION EXPONENT, THE RATIO a/b AND THE MAGNETIC POTENTIAL ψ_0 ON THE DYNAMIC CRITICAL LOAD VALUE OF SANDWICH PLATE

N	a/b	ψ_0 -200	0	200
0	0.5	7.51634e+7	7.51674e+7	7.51679e+7
	1	9.74085e+7	9.74157e+7	9.741621e+7
	1.5	10.45975e+7	10.46078e+7	10.46083e+7
1	0.5	8.26773e+7	8.26787e+7	8.267905e+7
	1	10.6592e+7	10.6594e+7	10.6596e+7
	1.5	11.36364e+7	11.36368e+7	11.36373e+7
2	0.5	8.49963e+7	8.49977e+7	8.49991e+7
	1	11.27222e+7	11.27276e+7	11.27331e+7
	1.5	11.93382e+7	11.93387e+7	11.93392e+7

The influences of volume fraction exponent N, ratio a/b and magnetic potentials $\psi_0\,(A)$ on the dynamic critical load value of the sandwich plate resting on elastic foundation are presented in Table 8. It is found that the effects of electric potentials are very small, the dynamic critical load value decreases as the electric potential decreases. Also, the ratio a/b and the volume fraction exponent have significant effect on the dynamic critical load of the smart sandwich plate. The value of the dynamic critical load increases significantly when the values of ratio a/b and the volume fraction exponent N increase.

C. The deflection amplitude - time curve

The influence of the parameters on the nonlinear dynamic response of sandwich plate will be investigated in this part.

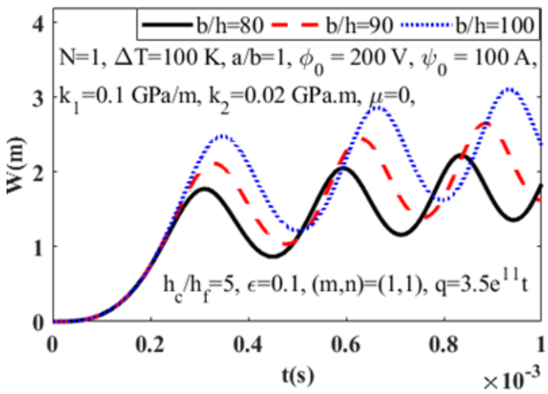

Fig. 2. Effects of initial imperfection on the nonlinear dynamic response of the sandwich plate.

Fig. 2 indicates the effects of length to thickness b/h on nonlinear dynamic response of the sandwich plate. As seen, an increase of ratios b/h results in a rise of the deflection amplitude of the sandwich plate.

The influences of the volume fraction exponent N and initial imperfection μ on the nonlinear dynamic response of the sandwich plate is given in Fig. 3 and Fig. 4. As can be seen, similar to the effect on the dynamic critical load value, the volume fraction exponent has very significantly effect on the deflection amplitude of the sandwich plate, while the imperfection has slightly effect.

Fig. 5 indicates the effects of temperature increment on the nonlinear dynamic response of the sandwich plate. Same as the results shown in Table 5, ΔT has very small effect on the deflection amplitude of the sandwich plate. An increase of temperature increment which is external impact reduce the stiffness of the sandwich plate results in a rise of the deflection amplitude of the smart sandwich plate.

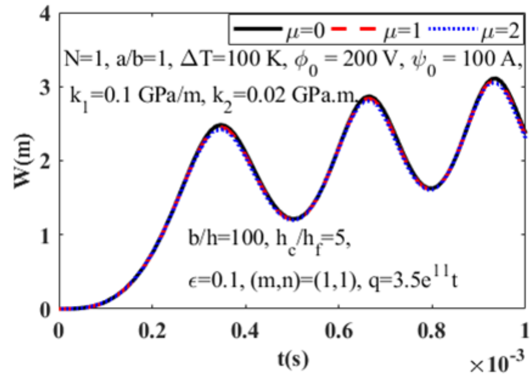

Fig. 3. Effects of ratio b/h on the nonlinear dynamic response of the sandwich plate.

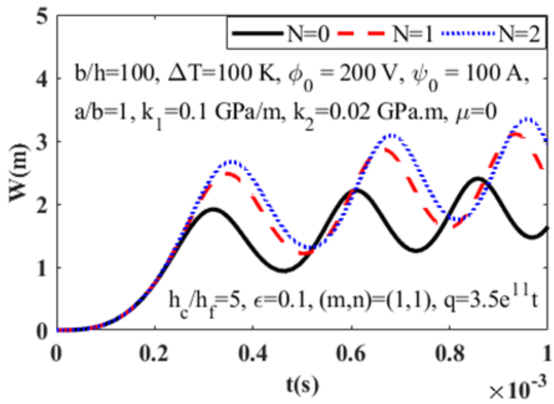

Fig. 4. Effects of volume fraction exponent on the nonlinear dynamic response of the sandwich plate.

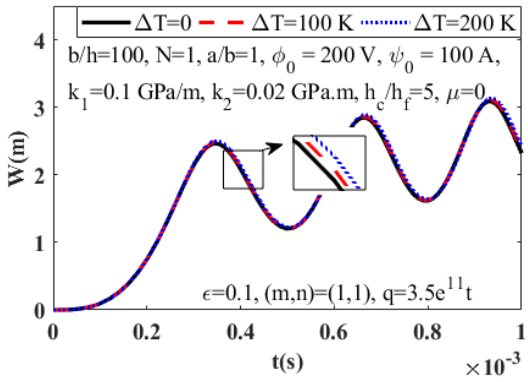

Fig. 5. Effects of temperature increment ΔT on the nonlinear dynamic response of the sandwich plate.

Figs. 6 and 7 illustrate the effect of elastic foundation on the nonlinear dynamic response of the sandwich plate, respectively. As can be seen, the deflection amplitude will become lower as two coefficients k_1 and k_2 increase. In other words, the elastic foundations increase the stiffness of the sandwich plate and the elastic modulus of the sandwich plate are increased due to the support of elastic foundations. Results from Figs. 6 and 7 also indicate that the effect of Pasternak foundation is more prominent than one of Winkler foundation.

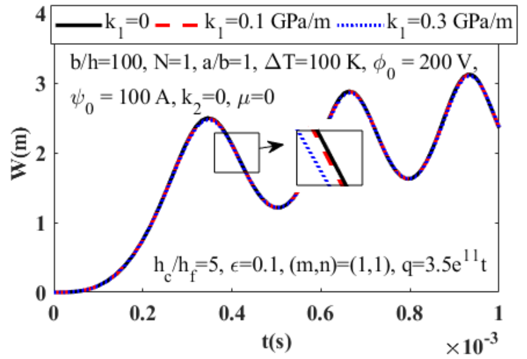

Fig. 6. Effects of the Winkler foundation stiffness on the nonlinear dynamic response of the sandwich plate.

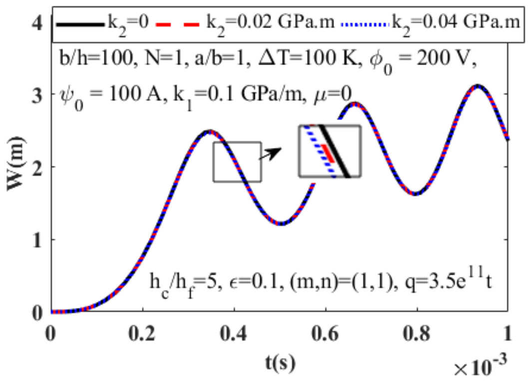

Fig. 7. Effects of the shear layer stiffness of Pasternak foundation on the nonlinear dynamic response of the sandwich plate.

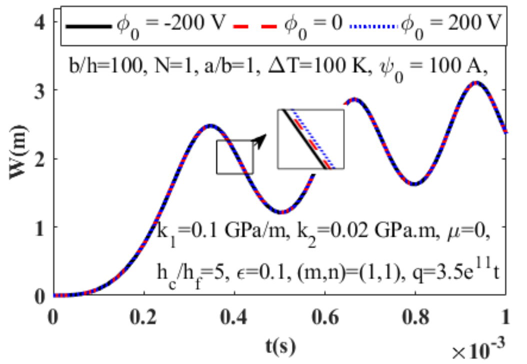

Fig. 8. Effects of electric potential on the nonlinear dynamic response of the sandwich plate.

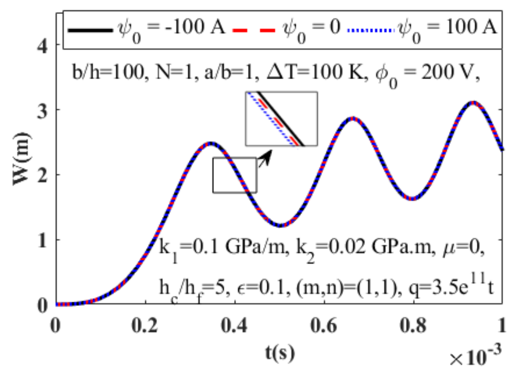

Fig. 9. Effects of magnetic potential on the nonlinear dynamic response of the sandwich plate.

The influences of magnetic and electric potentials on the deflection amplitude - time curve of the sandwich plate are depicted in Figs. 8 and 9, respectively. It is observed that both of electric and magnetic potentials have small effect on the nonlinear dynamic response of sandwich plate. The deflection amplitude of the sandwich plate with higher electric potential is higher than one with lower electric potential, whereas it becomes lower when the magnetic potential increases.

VI. Conclusions

By using an analytical method based on classical plate theory, the nonlinear dynamic buckling of the sandwich plate with two MEE face sheets and FGM core layer subjected to the combination of external pressure, thermal, electric, and magnetic loads were elucidated in this paper. In addition to surveys on the influence of geometrical and material parameters, a point worth noting here is by evaluating the influence of electric and magnetic potentials – the typical parameters of the MEE layer, it can be concluded that although both of them are considered to be external forces, they have small effect on the dynamic critical load of the sandwich plate with FGM core layer. In other words, the addition of MEE layers has little effect on the nonlinear dynamic buckling of sandwich plate with FGM core layer in the thermal environment, while they complement the plate with the advantages of magnetism and electrical properties, thereby expanding the scope of applications of FGM structures in sensors, civil structures, aerospace control systems and medical devices…

References

[1] M. Vinyas, "Computational Analysis of Smart Magneto – Electro – Elastic Materials and Structures: Review and Classifcation', Archives of Computational Methods in Engineering, 2020.

[2] B. Saleh, J. Jiang, A. Ma, D. Song, D. Yang, "Effect of main parameters on the mechanical and wear behaviour of functionally graded materials by centrifugal casting: a review". Met Mater Int., https://doi.org/10.1007/s12540-019-00273-8, 2019.

[3] M. Vinyas, S.C. Kattimani, "Static studies of stepped functionally graded magneto-electro-elastic beam subjected to different thermal loads", Compos. Struct 163, 216– 237, 2017.

[4] P. Zhang, C. Qi, H. Fang, C. Ma, Y. Huang, "Semi-analytical analysis of static and dynamic responses for laminated magneto-electro-elastic plates", Compos. Struct. 110933, 2019.

[5] M.C. Kiran, S.C. Kattimani, "Free Vibration of Multilayered Magneto-Electro-Elastic Plates With Skewed Edges Using Layer wise Shear Deformation Theory", Materials Today: Proceedings, 5(10), 21248–21255, 2018.

[6] N.D Duc, D.H Bich, V.T.T. Anh, "On the nonlinear stability of eccentrically stiffened functionally graded annular spherical segment shells", J. Thin-Walled Structures. Vol. 106, pp. 258-267, 2016.

[7] P.V. Vinh, N.T. Dung, N.C. Tho, D.V. Thom, L.K. Hoa, "Modified single variable shear deformation plate theory for free vibration analysis of rectangular FGM plates", Structures, 29, 1435-1444, 2021.

[8] D.H. Bich, D.G. Ninh. T.I. Thinh, "Nonlinear buckling analysis of FGM toroidal shell segments filled inside by an elastic medium under external pressure loads including temperature effects", Composites Part B: Engineering, 87, 75-91, 2016.

[9] V.H. Nam, N.T. Phuong, K.V. Minh, P.T. Hieu, "Nonlinear thermo-mechanical buckling and post-buckling of multilayer FGM cylindrical shell reinforced by spiral stiffeners surrounded by elastic foundation subjected to torsional loads". European Journal of Mechanics - A/Solids, 72, 393-406, 2018.

[10] M. Arefi, A.M. Zenkour, "Thermo-electro-magneto-mechanical bending behavior of size-dependent sandwich piezomagnetic nanoplates", Mechanics Research Communications, 84, 27–42, 2017.

[11] N.D. Dat, T.Q. Quan, V. Mahesh, N.D. Duc, "Analytical solutions for nonlinear magneto-electro-elastic vibration of smart sandwich plate

with carbon nanotube reinforced nanocomposite core in hygrothermal environment". Inter. J. of Mechan. Scien., 105906, 2020.

[12] D. Xiao, Q. Han, T. Jiang, "Guided wave propagation in a multilayered magneto-electro-elastic curved panel by Chebyshev spectral elements method" Compos. Struct. , 207, 701-710, 2019.

[13] V.T.T Anh, P.N. Thinh, V.D. Quang, N.D. Duc, "Impact of blast and mechanical loads on the shear deformable stiffened sandwich plate with an auxetic core layer in thermal environment", *J. Sandwich Struct. and Materials*, 0(0) 1–33, 2021.

[14] D.H. Bich, D.V. Dung, V.H. Nam, Nonlinear dynamical analysis of eccentrically stiffened functionally graded cylindrical panels, Compos. Struct. 94, 2465–2473, 2012.

[15] F. Alijani, M. Amabili, K. Karagiozis, F. Bakhtiari-Nejad, Nonlinear vibrations of functionally graded doubly curved shallow shells, J. Sound Vib. 330 (2011) 1432–1454.

[16] S.E. Kim, N.D. Duc, V.H. Nam, N.V. Sy, "Nonlinear vibration and dynamic buckling of eccentrically oblique stiffened FGM plates resting on elastic foundations in thermal environment", Thin-Walled Structures, 142, 287–296. doi:10.1016/j.tws.2019.05.013, 2019.

[17] B. Budiansky, and R. S. Roth, "Axisymmetric dynamic buckling of clamped shallow spherical shells", NASA technical note D_510, 1962, 597–609, 2012.

[18] D.H Bich; D.V Dung; V.H Nam, "Nonlinear dynamical analysis of eccentrically stiffened functionally graded cylindrical panels", 94(8), 2465-2473, 2012.

APPENDIX

$$\left(F_{ij},\,G_{ij},\,H_{ij}\right)=\int_{-h_f-h_c/2}^{-h_c/2}\tilde{C}_{ij}(1,\,z,z^2)\,dz+\int_{-h_c/2}^{0}Q_{ij}(1,\,z,\,z^2)\,dz+$$

$$+\int_{0}^{h_c/2}Q_{ij}(1,\,z,\,z^2)\,dz+\int_{h_c/2}^{h_c/2+h_f}\tilde{C}_{ij}(1,\,z,z^2)\,dz,\ \left(ij=11,12,22,66\right),$$

$$\left(F_{13},F_{23}\right)=\int_{-h_f-h_c/2}^{-h_c/2}\tilde{e}_{31}\left(1,z\right)dz+\int_{h_c/2}^{h_f+h_c/2}\tilde{e}_{31}\left(1,z\right)dz,$$

$$\left(F_{14},F_{24}\right)=\int_{-h_f-h_c/2}^{-h_c/2}\tilde{q}_{31}\left(1,z\right)dz+\int_{h_c/2}^{h_f+h_c/2}\tilde{q}_{31}\left(1,z\right)dz,$$

$$\left(G_{13},G_{23}\right)=\int_{-h_f-h_c/2}^{-h_c/2}\tilde{e}_{32}\left(1,z\right)dz+\int_{h_c/2}^{h_f+h_c/2}\tilde{e}_{32}\left(1,z,z^3\right)dz,$$

$$\left(G_{14},G_{24}\right)=\int_{-h_f-h_c/2}^{-h_c/2}\tilde{q}_{32}\left(1,z\right)dz+\int_{h_c/2}^{h_f+h_c/2}\tilde{q}_{32}\left(1,z\right)dz,$$

$$\alpha_i=\int_{-h_f-h_c/2}^{-h_c/2}\left(Q_{11}+Q_{12}\right)\tilde{\alpha}_1\left(1,z\right)dz+\int_{-h_c/2}^{0}Q_{11}\alpha_{11}\left(1,z\right)dz+\int_{0}^{h_c/2}Q_{11}\alpha_{11}\left(1,z\right)dz$$

$$+\int_{-h_c/2}^{0}Q_{12}\alpha_{22}\left(1,z\right)dz+\int_{0}^{h_c/2}Q_{12}\alpha_{22}\left(1,z\right)dz+\int_{h_c/2}^{h_f+h_c/2}\left(Q_{11}+Q_{12}\right)\tilde{\alpha}_1\left(1,z\right)dz,$$

$$\alpha_j=\int_{-h_f-h_c/2}^{-h_c/2}\left(Q_{12}+Q_{22}\right)\tilde{\alpha}_2\left(1,z\right)dz+\int_{-h_c/2}^{0}Q_{12}\alpha_{11}\left(1,z\right)dz+\int_{0}^{h_c/2}Q_{12}\alpha_{11}\left(1,z\right)dz$$

$$+\int_{-h_c/2}^{0}Q_{22}\alpha_{22}\left(1,z\right)dz+\int_{0}^{h_c/2}Q_{22}\alpha_{22}\left(1,z\right)dz+\int_{h_c/2}^{h_f+h_c/2}\left(Q_{12}+Q_{22}\right)\tilde{\alpha}_2\left(1,z\right)dz,$$

$$\tilde{C}_{11}=C_{11}-\frac{C_{13}^2}{C_{33}},\ \tilde{C}_{12}=C_{12}-\frac{C_{13}C_{23}}{C_{33}},\ \tilde{C}_{22}=C_{22}-\frac{C_{23}^2}{C_{33}},\tilde{C}_{66}=C_{66},\ \tilde{\lambda}_1=\lambda_1,$$

$$\tilde{\lambda}_2=\lambda_2,\ \tilde{e}_{31}=e_{31}-C_{13}\frac{e_{33}}{C_{33}},\ \tilde{e}_{32}=e_{32}-C_{23}\frac{e_{33}}{C_{33}},\tilde{q}_{31}=q_{31}-\frac{C_{13}q_{33}}{C_{33}},$$

$$\tilde{q}_{32}=q_{32}-\frac{C_{13}q_{33}}{C_{33}},\tilde{\mu}_{11}=\mu_{11}+\frac{q_{15}^2}{C_{55}},\ \tilde{\mu}_{22}=\mu_{22}+\frac{q_{24}^2}{C_{44}},\ \tilde{\mu}_{33}=\mu_{33}+\frac{q_{33}^2}{C_{33}},$$

$$\tilde{p}_2=p_2,\ \tilde{\eta}_{11}=\eta_{11}+\frac{e_{15}^2}{C_{55}},\ \tilde{\eta}_{22}=\eta_{22}+\frac{e_{24}^2}{C_{44}},\tilde{\eta}_{33}=\eta_{33}+\frac{e_{33}^2}{C_{33}},\ \tilde{p}_1=p_1,$$

$$\tilde{m}_{33}=m_{33}+\frac{e_{33}q_{33}}{C_{33}},\tilde{\alpha}_1=\alpha_1-\frac{C_{13}\alpha_3}{C_{33}},\tilde{m}_{11}=m_{11}+\frac{e_{15}q_{15}}{C_{55}},\tilde{m}_{22}=m_{22}+\frac{e_{24}q_{24}}{C_{44}},$$

$$\tilde{\alpha}_2=\alpha_2-\frac{C_{23}\alpha_3}{C_{33}},\ \tilde{p}_3=p_3+\frac{e_{33}\alpha_{33}}{C_{33}},\tilde{\lambda}_3=\lambda_3+\frac{q_{33}\alpha_{33}}{C_{33}}.$$

$$L_{11}^*=H_{11}-G_{11}^*G_{11}-G_{21}^*G_{12},\ L_{22}^*=H_{22}-G_{12}^*G_{12}-G_{22}^*G_{22},$$

$$L_{12}^*=H_{12}-G_{12}^*G_{11}-G_{22}^*G_{12},\ L_{21}^*=H_{12}-G_{11}^*G_{12}-G_{21}^*G_{22},$$

$$L_{66}^*=H_{66}-G_{66}^*G_{66},L_{31}^*=\left(-F_{23}\right)\beta\sin\left(\beta z\right),L_{32}^*=\left(-F_{24}\right)\beta\sin\left(\beta z\right),$$

$$L_{41}^*=\left(-G_{23}\right)\beta\sin\left(\beta z\right),L_{42}^*=\left(-G_{24}\right)\beta\sin\left(\beta z\right),$$

$$g_1=\frac{-4}{H^*ab\lambda_m\delta_n}\left[\left(F_{11}^*G_{11}^*+F_{12}^*G_{21}^*\right)\lambda_m^2+\left(F_{11}^*G_{12}^*+F_{12}^*G_{22}^*+M_3\left(F_{11}^*F_{22}^*-F_{12}^{*2}\right)\right)\delta_n^2\right],$$

$$H^*=F_{12}^{*2}-F_{11}^*F_{22}^*,\ g_2=-\frac{F_{11}^*\lambda_m^2+F_{12}^*\delta_n^2}{8H^*},g_3=\frac{F_{11}^*F_{13}^*+F_{12}^*F_{14}^*}{H^*},g_4=\frac{F_{11}^*G_{13}^*+F_{12}^*G_{14}^*}{H^*},$$

$$f_1=\frac{-4}{H^*ab\lambda_m\delta_n}\left[\left(F_{12}^*G_{11}^*+F_{22}^*G_{21}^*+M_3\left(F_{11}^*F_{22}^*-F_{12}^{*2}\right)\right)\lambda_m^2+\left(F_{12}^*G_{12}^*+F_{22}^*G_{22}^*\right)\delta_n^2\right],$$

$$f_2=-\frac{F_{12}^*\lambda_m^2+F_{22}^*\delta_n^2}{8H^*},\ f_3=\frac{F_{12}^*F_{13}^*+F_{22}^*F_{14}^*}{H^*},g_5=\frac{F_{11}^*\alpha_1^*+F_{12}^*\alpha_2^*}{H^*},\ f_4=\frac{F_{12}^*G_{13}^*+F_{22}^*G_{14}^*}{H^*},$$

$$f_5=\frac{F_{12}^*\alpha_1^*+F_{22}^*\alpha_2^*}{H^*}.$$

$$h_{11}=-\left[L_{11}^*\lambda_m^4+L_{22}^*\delta_n^4+\left(L_{12}^*+L_{21}^*+4L_{66}^*\right)\lambda_m^2\delta_n^2+k_1+k_2\left(\lambda_m^2+\delta_n^2\right)\right]+$$

$$+\left[G_{21}^*\lambda_m^4+G_{12}^*\delta_n^4+\left(G_{11}^*+G_{22}^*-2G_{66}^*\right)\lambda_m^2\delta_n^2\right]M_3,$$

$$h_{12}=\frac{-32\lambda_m\delta_nM_3}{3ab},\ h_{13}=-\frac{8\lambda_m\delta_n}{3ab}\left(\frac{G_{21}^*}{F_{11}^*}+\frac{G_{12}^*}{F_{22}^*}\right),\ h_{51}=-\left(T_{21}\lambda_m^2+T_{22}\delta_n^2\right),$$

$$h_{14}=-\frac{\left(\lambda_m^4/F_{22}^*+\delta_n^4F_{11}^*\right)}{16},\ h_{15}=L_{31}^*\lambda_m^2+L_{32}^*\delta_n^2,\ h_{16}=L_{41}^*\lambda_m^2+L_{42}^*\delta_n^2,$$

$$h_{52}=-\left(T_{23}\lambda_m^2+T_{24}\delta_n^2-\mu_{33}^*\right),\ h_{41}=-\left(T_{11}\lambda_m^2+T_{12}\delta_n^2\right),$$

$$h_{42}=-\left(T_{13}\lambda_m^2+T_{14}\delta_n^2-n_{33}^*\right),h_{43}=-\left(T_{15}\lambda_m^2+T_{16}\delta_n^2-m_{33}^*\right),$$

$$o_{11}^*=\frac{1}{\rho_1}\left(\left(g_3\lambda_m^2+f_3\delta_n^2\right)\phi_0+\left(g_4\lambda_m^2+f_4\delta_n^2\right)\psi_0+\left(g_5\lambda_m^2+f_5\delta_n^2\right)\Delta T\right),$$

$$o_{11}=\frac{-h_{11}}{\rho_1},o_{12}=\frac{1}{\rho_1}\left(-h_{12}+g_1\lambda_m^2+f_1\delta_n^2\right),\ o_{13}=\frac{-h_{13}}{\rho_1},o_{14}=\frac{-h_{14}}{\rho_1},$$

$$o_{15}=\frac{-h_{15}}{\rho_1},\ o_{16}=\frac{-h_{16}}{\rho_1},\ o_{13}^*=\frac{\left(g_2\lambda_m^2+f_2\delta_n^2\right)}{\rho_1},$$

$$T_{11}=-\int_{-h_f-h_c/2}^{-h_c/2}e_{31}z\beta\sin\left(\beta z\right)dz-\int_{h_c/2}^{h_c/2+h_f}e_{31}z\beta\sin\left(\beta z\right)dz,$$

$$T_{12}=-\int_{-h_f-h_c/2}^{-h_c/2}e_{32}z\beta\sin\left(\beta z\right)dz-\int_{h_c/2}^{h_c/2+h_f}e_{32}z\beta\sin\left(\beta z\right)dz,$$

$$T_{13}=\int_{-h_f-h_c/2}^{-h_c/2}\eta_{11}\cos^2\left(\beta z\right)dz+\int_{h_c/2}^{h_c/2+h_f}\eta_{11}\cos^2\left(\beta z\right)dz,$$

$$T_{14}=\int_{-h_f-h_c/2}^{-h_c/2}\eta_{22}\cos^2\left(\beta z\right)dz+\int_{h_c/2}^{h_c/2+h_f}\eta_{22}\cos^2\left(\beta z\right)dz,$$

$$T_{15}=\int_{-h_f-h_c/2}^{-h_c/2}m_{11}\cos^2\left(\beta z\right)dz+\int_{h_c/2}^{h_c/2+h_f}m_{11}\cos^2\left(\beta z\right)dz,$$

$$T_{16}=\int_{-h_f-h_c/2}^{-h_c/2}m_{22}\cos^2\left(\beta z\right)dz+\int_{h_c/2}^{h_c/2+h_f}m_{22}\cos^2\left(\beta z\right)dz,$$

$$\eta_{33}^*=-\int_{-h_f-h_c/2}^{-h_c/2}\eta_{33}\left(\beta\sin\left(\beta z\right)\right)^2dz-\int_{h_c/2}^{h_c/2+h_f}\eta_{33}\left(\beta\sin\left(\beta z\right)\right)^2dz,$$

$$m_{33}^*=-\int_{-h_f-h_c/2}^{-h_c/2}m_{33}\left(\beta\sin\left(\beta z\right)\right)^2dz-\int_{h_c/2}^{h_c/2+h_f}m_{33}\left(\beta\sin\left(\beta z\right)\right)^2dz.$$

$$T_{21}=-\int_{-h_f-h_c/2}^{-h_c/2}q_{31}z\beta\sin\left(\beta z\right)dz-\int_{h_c/2}^{h_c/2+h_f}q_{31}z\beta\sin\left(\beta z\right)dz,$$

$$T_{22}=-\int_{-h_f-h_c/2}^{-h_c/2}q_{32}z\beta\sin\left(\beta z\right)dz-\int_{h_c/2}^{h_c/2+h_f}q_{32}z\beta\sin\left(\beta z\right)dz,$$

$$\mu_{33}^*=-\int_{-h_f-h_c/2}^{-h_c/2}\mu_{33}\left(\beta\sin\left(\beta z\right)\right)^2dz-\int_{h_c/2}^{h_c/2+h_f}\mu_{33}\left(\beta\sin\left(\beta z\right)\right)^2dz$$

$$T_{23}=\int_{-h_f-h_c/2}^{-h_c/2}\mu_{11}\cos^2\left(\beta z\right)dz+\int_{h_c/2}^{h_c/2+h_f}\mu_{11}\cos^2\left(\beta z\right)dz,$$

$$T_{24}=\int_{-h_f-h_c/2}^{-h_c/2}\mu_{22}\cos^2\left(\beta z\right)dz+\int_{h_c/2}^{h_c/2+h_f}\mu_{22}\cos^2\left(\beta z\right)dz,$$

Nonlinear vibration in Dufing system subjected to narrow-bad colored noise excitation

N. D. Anh
Institute of Mechanics
Vietnam Academy of Science and Technology
Hà Nội, Việt Nam
ndanh@imech.vast.vn
Faculty of Mechanical Engineering and Automation
VNU University of Engineering and Technology
Hà Nội, Việt Nam
ndanh0403@gmail.com

Nguyen Ngoc Linh
Faculty of Mechanical Engineering
Thuyloi University
Hà Nội, Việt Nam
nnlinh@tlu.edu.vn

Nguyen Van Manh
Faculty of Mechanical
Hanoi University of Civil Engineering
Hà Nội, Việt Nam
manhnv@nuce.edu.vn

Anh Tay Nguyen
Department of Mechanical Engineering
SUNY Korea
South Korea
anh.nguyen.1@stonybrook.edu

***Abstract*: The Duffing system, which is widely used in various physical and engineering problems, has still been a popular area of research during the last few decades. Many investigations have been performed to understand the complex behavior of Duffing system taking into account of different effects such as chaotic, fractional and random ones [1-6]. For Duffing oscillator subject to random excitation the well-known averaging method, originally given by Krylov và Bogoliubov and then developed by Mitropolskii, is a useful tool for obtaining approximate solutions. Since the effect of some nonlinear terms is lost during the first order averaging procedure, the higher order stochastic averaging method is developed to overcome this deficiency and to obtain more accurate approximate solutions of nonlinear systems subject to random white noises. The higher order averaging method is also being successfully extended to the cases of colored noise excitation [11-12]. In this paper Duffing system subjected to a narrow-band colored noise is investigated. The paper shows that an approximate solution can be found by the second order stochastic averaging method. The accuracy of the approximate solution is confirmed by the Monte-Carlo method. The effects of the system parameters on the response are analyzed in detail. It is shown that the higher order averaging solution is more accurate than the one obtained by the traditional first order stochastic averaging method.**

Keywords: Stochastic system, Higher order averaging, Duffing oscillator, Colored excitation.

I. INTRODUCTION

The Duffing system, which is widely used in various physical and engineering problems, has still been a popular area of research during the last few decades. Many investigations have been performed to understand the complex behavior of Duffing system taking into account different effects such as chaotic, fractional, and random ones [1]-[6]. For Duffing oscillator subject to random excitation the well-known averaging method, originally given by Krylov and Bogoliubov and then developed by Mitropolskii, is a useful tool for obtaining approximate solutions. Since the effect of some nonlinear terms is lost during the first-order averaging procedure, the higher-order stochastic averaging method is developed to overcome this deficiency and to obtain more accurate approximate solutions of nonlinear systems subject to random white noises. A higher order stochastic averaging procedure using Fokker-Planck (FP) equation was developed by Anh [7], [8], and then applied to Van der Pol oscillator under white noise excitation [9], [10]. The higher-order averaging method is also being successfully extended to the cases of colored noise excitation [11]-[13]. However, in [13], only high order approximate solutions have been obtained, but the effects of the system's parameters on the response have not been analyzed yet.

Nonlinear random vibrations in dynamical systems subjected to the excitation of a white noise have often been investigated by many authors. It is well-known that the white noise process has a constant spectral density function and thus does not exist in the practice. Mean white, the random processes with linear-fractional spectral density functions of the frequency describe well many real environmental loadings. These processes contain an important class of colored noises which can be interpreted as the result of the passage of white noises through a certain linear system with constant parameters, called a forming filter.

In this paper Duffing system subjected to a narrow-band colored noise is investigated. The paper shows that the obtained approximate solution can be found by the second-order stochastic averaging method. The numerical simulations are carried out to verify that the accuracy of the higher-order averaging solution is better than the one of the first-order averaging solution. The effects of the system parameters on the response are analyzed in detail.

II. A FORM OF FORMING FILTER

Consider a mechanical system whose motion is described in the form

$$\ddot{x}+\omega^2 x=\varepsilon f(x,\dot{x})+\sqrt{\varepsilon}q(t) \quad (1)$$

The excitation $q(x)$ is a normal stationary random process, the result of the passage of a white noise through the linear forming filter

$$Lq(t)=\frac{d^n}{dt^n}q(t)+\sum_{s=0}^{n-1}\alpha_s\frac{d^s}{dt^s}q(t)=b\dot{\zeta}(t) \quad (2)$$

Where $\alpha_s;b=$ constants, $\dot{\zeta}(t)$ is a white noise of unit intensity. In Eq.(1), ω is the natural frequency, ε is a positive small parameter, $f(x,\dot{x})$ is a nonlinear function of displacement and velocity. The spectral density of the process $q(t)$ can be easy obtained from (2).

L

$$S_q(\omega)=\frac{1}{2\pi}\frac{b^2}{\ell(i\omega)\ell(-i\omega)} \quad (3)$$

where $$\mathscr{L}(\lambda)=\lambda^n+\sum_{s=0}^{n-1}\alpha_s\lambda^s \quad (4)$$

Consider a case when the linear filter (2) has only finite negative eigenvalue, i.e., all the roots λ_i of the characteristic equation

$$\mathscr{L}(\lambda)=0 \quad (5)$$

are distinct, real, negative, and

$$|\lambda|>\varepsilon \quad (6)$$

Eliminating now $q(t)$ from (1), (2) one obtains

$$L\left(\ddot{x}+\omega^2x\right)=\varepsilon Lf(x,\dot{x})+\sqrt{\varepsilon}b\dot{\zeta}(t) \quad (7)$$

Forming the characteristic equation of the generating linear equation $(\varepsilon=0)$

$$\left(\lambda^2+\omega^2\right)\mathscr{L}(\lambda)=0 \quad (8)$$

one gets the general solution in the form

$$x(t)=\sum_{i=1}^{n}C_ie^{\lambda_i t}+a\cos\varphi;\varphi=\omega t+\theta \quad (9)$$

Thus, according to the averaging method we make the replacement [12]

$$\frac{d^kx}{dt^k}=a(t)\frac{\partial^k}{\partial t^k}\cos(vt+\theta(t));k=0,1,\dots,n+1 \quad (10)$$

where $a(t),\theta(t)$ are Markov diffusion processes satisfying the equations

$$\begin{aligned}\dot{a}&=\varepsilon u_1(a,\theta)+\sqrt{\varepsilon}v_1(a,\theta)\dot{\zeta}(t)\\ \dot{\theta}&=\varepsilon u_2(a,\theta)+\sqrt{\varepsilon}v_2(a,\theta)\dot{\zeta}(t)\end{aligned} \quad (11)$$

or turning to the variable a,φ one gets

$$\begin{aligned}\dot{a}&=\varepsilon u_1(a,\varphi)+\sqrt{\varepsilon}v_1(a,\varphi)\dot{\zeta}(t)\\ \dot{\varphi}&=\omega+\varepsilon u_2(a,\varphi)+\sqrt{\varepsilon}v_2(a,\varphi)\dot{\zeta}(t)\end{aligned} \quad (12)$$

where one has

$$u_1(a,\varphi)=\begin{Bmatrix}-\dfrac{1}{\omega r}[Lf(x,\dot{x})]_0\sin\left(\varphi+\varphi_*\right)\\ +\dfrac{b^2}{2a\omega^2r^2}\cos^2\left(\varphi+\varphi_*\right)\end{Bmatrix};$$

$$u_2(a,\varphi)=\begin{Bmatrix}-\dfrac{1}{a\omega r}[Lf(x,\dot{x})]_0\cos\left(\varphi+\varphi_0\right)\\ -\dfrac{b^2}{a^2\omega^2r^2}\cos\left(\varphi+\varphi_*\right)\sin\left(\varphi+\varphi_*\right)\end{Bmatrix};$$

$$v_1(a,\varphi)=\frac{b}{\omega r}\sin\left(\varphi+\varphi_0\right),$$

$$v_2(a,\varphi)=\frac{b}{a\omega r}\cos\left(\varphi+\varphi_*\right);$$

$$[Lf(x,\dot{x})]_0=Lf(x,\dot{x})\frac{dx^k}{dt^k}=a\frac{\partial^k}{\partial t^k}\cos\varphi;$$

$$\varphi_*=\sum_{i=1}^{n}\varphi_i;\ r=\prod_{i=1}^{n}r_i;r_i=\sqrt{\lambda_i^2+\omega^2};$$

$$\sin\varphi_i=\frac{\omega}{r_i};\ \cos\varphi_i=-\frac{\lambda_i}{r_i};$$

$$D_i=\prod_{m>i>0}^{n}\left(\lambda_m-\lambda_i\right)\left(\lambda_i-\lambda_t\right) \quad (13)$$

For system(12), the corresponding Fokker-Planck equation for stationary probability function $W(a,\varphi)$ of amplitude and phase can be formed as follows

$$\omega\frac{\partial W}{\partial\varphi}=-\varepsilon L_1(W) \quad (14)$$

where the operator L_1 is defined as

$$L_1(W)=\begin{Bmatrix}\dfrac{\partial}{\partial a}\left(u_1W\right)-\dfrac{1}{2}\dfrac{\partial^2}{\partial a^2}\left(v_1^2W\right)\\ +\dfrac{\partial}{\partial\varphi}\left[u_2W-\dfrac{\partial}{\partial a}\left(v_1v_2W\right)-\dfrac{1}{2}\dfrac{\partial}{\partial\varphi}\left(v_2^2W\right)\right]\end{Bmatrix} \quad (15)$$

The solution $W(a,\varphi)$ of Eq. (14) is to be obtained in the form [13]: $$W(a,\varphi)=\sum_{i=0}^{\infty}\varepsilon^iW_i(a,\varphi) \quad (16)$$

Substituting (16) into (14) and comparing the coefficients of like powers of ε give:

$$\omega\frac{\partial W_0}{\partial\varphi}=0 \tag{17}$$

$$\omega\frac{\partial W_{i+1}}{\partial\varphi}=-L\left(W_i\right), i=0,1,2,\dots \tag{18}$$

Since the functions $W_i(a,\varphi)$ must be periodic ones of variable φ, one gets from (2.18)

$$\left\langle L_i\left(W_i\right)\right\rangle=0 \tag{19}$$

where $\langle\rangle$ is defined as the averaging operator

$$\langle.\rangle=\frac{1}{2\pi}\int_0^{2\pi}(.)d\varphi \tag{20}$$

Thus, one gets from (17) and (19) for $i=0$

$$\begin{gathered}W_0=W_0(a)\\ \left\langle L\left(W_0(a)\right)\right\rangle=0\end{gathered} \tag{21}$$

We expand into a series of Fourier

$$\begin{aligned}&u_i(a,\varphi)=\sum_{j=0}^{m}\left(S_{ij}(a)\sin 2j\varphi+C_{ij}(a)\cos 2j\varphi\right)\\&u_\ell(a,\varphi)u_k(a,\varphi)=\\&=\sum_{j=0}^{m}\left(S_{\ell k}(a)\sin 2j\varphi+C_{\ell kj}(a)\cos 2j\varphi\right); i,\ell,k=1,2\end{aligned} \tag{22}$$

Substituting (22) into (15) yield

$$L\left(W_0(a)\right)=\sum_{j=0}^{m}\left\{\begin{array}{l}\left[\frac{\partial}{\partial a}\left(S_{1j}W_0\right)-\frac{1}{2}\frac{\partial^2}{\partial a^2}\left(S_{11j}W_0\right)\right]\sin 2j\varphi+\\+\frac{\partial}{\partial a}\left(C_{1j}W_0-\frac{1}{2}\frac{\partial^2}{\partial a^2}\left(C_{11j}W_0\right)\right)\cos 2j\varphi\\+\frac{\partial}{\partial\varphi}\left(\begin{array}{l}S_{2j}W_0-\frac{\partial}{\partial a}\left(S_{12j}W_0\right)\\+jW_0C_{22j}\end{array}\right)\sin 2j\varphi\\+\left(\begin{array}{l}C_{2j}W_0-\frac{\partial}{\partial a}\left(C_{12j}W_0\right)\\-jW_0S_{22j}\end{array}\right)\cos 2j\varphi\end{array}\right\} \tag{23}$$

Substituting (23) into (21) gives the equation for $W_0(a)$

$$\frac{\partial}{\partial a}\left(C_{10}W_0\right)-\frac{1}{2}\frac{\partial^2}{\partial a^2}\left(C_{110}W_0\right)=0 \tag{24}$$

After finding $W_0(a)$ and substituting it into (18) for $i=0$ one gets

$$W_1(a,\varphi)=-\frac{1}{\omega}\int L\left(W_0\right)d\varphi \tag{25}$$

or noting (23)

$$\begin{aligned}&W_1(a,\varphi)=\\&=W_0(a)W_{10}(a)+\sum_{j=1}^{m}\left(W_{js}(a)\sin 2j\varphi+W_{jc}(a)\cos 2j\varphi\right)\end{aligned} \tag{26}$$

where it is denoted

$$\begin{aligned}&W_{js}(a)=-\frac{1}{\omega}\left\{\begin{array}{l}\frac{1}{2j}\left[\frac{\partial}{\partial a}\left(C_{1j}W_0\right)-\frac{1}{2}\frac{\partial^2}{\partial a^2}\left(C_{11j}W_0\right)\right]\\+S_{2j}W_0-\frac{\partial}{\partial a}\left(S_{12j}W_0\right)+jW_0C_{22j}\end{array}\right\}\\&W_{jc}(a)=-\frac{1}{\omega}\left\{\begin{array}{l}C_{2j}W_0-\frac{\partial}{\partial a}\left(C_{12j}W_0\right)-jS_{22j}W_0\\-\frac{1}{2}\left[\frac{\partial}{\partial a}\left(S_{1j}W_0\right)-\frac{1}{2}\frac{\partial^2}{\partial a^2}\left(S_{11j}W_0\right)\right]\end{array}\right\}\end{aligned} \tag{27}$$

The arbitrary integration function $W_1(a)$ in (26) will be defined by considering (18) and (19) for the case $i=1$

$$\omega\frac{\partial W_2}{\partial\varphi}=-L\left(W_1\right) \tag{28}$$

$$\left\langle L\left(W_1\right)\right\rangle=0 \tag{29}$$

Substituting (26) into (29) yields the differential equation for $W_{10}(a)$

$$\left\{\begin{array}{l}\left(C_{10}W_0W_{10}\right)-\frac{1}{2}\frac{\partial}{\partial a}\left(C_{110}W_0W_{10}\right)\\+\frac{1}{2}\sum_{j=0}^{m}\left[\begin{array}{l}\left(S_{1j}W_{js}+C_{1j}W_{jc}\right)\\-\frac{1}{2}\frac{\partial}{\partial a}\left(S_{11j}W_{js}+C_{11j}W_{jc}\right)\end{array}\right]\end{array}\right\}=0 \tag{30}$$

and using (24) one obtains the explicit form of $W_{10}(a)$

$$\begin{aligned}&W_{10}(a)=\\&=\sum_{j=1}^{m}\left\{\int\frac{1}{C_{10}(a)W_0(a)}\left[\begin{array}{l}S_{1j}(a)W_{js}(a)+C_{1j}(a)W_{jc}(a)\\-\frac{1}{2}\frac{\partial}{\partial a}\left(\begin{array}{l}S_{11j}(a)W_{jo}(a)\\+C_{11j}(a)W_{je}(a)\end{array}\right)\end{array}\right]da\right\}\end{aligned} \tag{31}$$

where the coefficients $C_{1k}(a)$, $S_{1k}(a)$, C_{1kj}, S_{1kj}, $W_0(a)$, $W_j(a)$, $W_{je}(a)$ are found from (22), (24) and (27), respectively. Thus, finally according to the averaging procedure the second approximate solution to the FP equation (14) is defined as

$$W(a,\varphi)=W_0(a)+\varepsilon\left[W_0(a)W_{10}(a)+W_{11}(a,\varphi)\right] \tag{32}$$

So, it is important that the second approximate solution can be obtained in explicit form as it is shown from (26), (27) and (31).

III. Application to the Exponentially Correlated Process

Let $q(t)$ be an exponentially correlated stationary random process, with following spectral density and correlation function

$$S_q(\omega)=\frac{\delta_1^2}{\pi}\frac{a}{a^2+\omega^2}, K_4(\tau)=\delta_1^2e^{-\alpha|r|}, \alpha\gg\varepsilon \tag{33}$$

The corresponding forming filter is

$$Lq=\dot{q}(t)+\alpha q(t)=\delta_1\sqrt{2\alpha}\dot{\zeta}(t) \tag{34}$$

According to the procedure described the solution of the system (1), (34) is defined in the form

$$x(t)=a\cos\varphi;\dot{x}=-a\omega\sin\varphi;\ddot{x}=-a\omega^2\cos\varphi \tag{35}$$

For the case (34) one has, see (13)

$$n=1;\lambda=-a;\sin\varphi_1=\frac{\omega}{\sqrt{\alpha^2+\omega^2}}$$

$$\cos\varphi_1=\frac{\alpha}{\sqrt{\alpha^2+\omega^2}};\varphi_*=\varphi_1,r=r_1=\sqrt{\alpha^2+\omega^2} \tag{36}$$

$$Lf=\frac{df}{dt}+\alpha f$$

The amplitude and phase differential equations are described by (12) where

$$u_1(a,\varphi)=$$

$$=\left\{-\frac{(df/dt+\alpha f)_0\sin(\varphi+\varphi_1)}{\omega\sqrt{\alpha^2+\omega^2}}+\frac{\delta_1^2\alpha^2\cos^2(\varphi+\varphi_1)}{\omega^2a(\omega^2+\alpha^2)}\right\};$$

$$u_2(a,\varphi)=$$

$$=\left\{-\frac{(df/dt+\alpha f)_0\cos(\varphi+\varphi_1)}{\alpha\omega\sqrt{\alpha^2+\omega^2}}-\frac{\delta_1^2\alpha^2\sin^2(\varphi+\varphi_1)}{\omega^2a^2(\omega^2+\alpha^2)}\right\}; \tag{37}$$

$$v_1(a,\varphi)=\frac{\delta_1\sqrt{2\alpha}\sin(\varphi+\varphi_1)}{\omega\sqrt{\alpha^2+\omega^2}};$$

$$v_2(a,\varphi)=\frac{\delta_1\sqrt{2\alpha}\cos(\varphi+\varphi_1)}{\omega a\sqrt{\alpha^2+\omega^2}}$$

Further, the solution to the corresponding FP equation can be performed as described above.

IV. DUFFING OSCILLATOR

It is well-known that the exact solution of the Duffing oscillator subject to colored noise it not available up to now. So, the approximate solutions are to be interested. So, consider the Duffing system

$$\ddot{x}+2\varepsilon h\dot{x}+\omega^2x+\varepsilon\gamma x^3=\sqrt{\varepsilon}q(t) \tag{38}$$

Where $q(t)$ is the exponentially correlated random process (33). For this case, one gets

$$f(x,\dot{x})=-2h\dot{x}-\gamma x^3;$$
$$\frac{df}{dt}+\alpha f=-2h\ddot{x}-2\alpha h\dot{x}-3\gamma x^2\dot{x}-\alpha\gamma x^3 \tag{39}$$

Substituting (35), (36), (39) into (37) gives

$$u_i(a,\varphi)=\sum_{j=0}^{2}\left(S_{ij}(a)\sin 2j\varphi+C_{ij}(a)\cos 2j\varphi\right);$$

$$u_\ell(a,\varphi)u_k(a,\varphi)= \tag{40}$$

$$=\sum_{j=0}^{\ell}\left(S_{\ell kj}(a)\sin 2j\varphi+C_{\ell kj}(a)\cos 2j\varphi\right)$$

Where:

$$r^2=a^2+\omega^2;$$

$$S_{10}(a)=0,C_{10}(a)=-ha+\frac{\delta_1^2\alpha}{2a\omega^2r^2};$$

$$S_{11}(a)=\frac{1}{\omega r^2}\left[\frac{\gamma a^3}{4}(\alpha^2-3\omega^2)-2\alpha ha\omega^2-\frac{\delta_1^2\alpha^2}{ar^2}\right]; \tag{41}$$

$$S_{12}(a)=S_{12}(a)=\left[\frac{\gamma a^3}{8\omega r^2}(\alpha^2-3\omega^2)\right],C_{12}(a)=\frac{\alpha\gamma a^3}{2r^2};$$

$$S_{20}(a)=0,C_{20}(a)=\frac{3}{8\omega}\gamma a^3;$$

$$S_{21}(a)=\frac{1}{r^2}\left[h(\omega^2-\alpha^2)-\alpha\gamma a^2-\frac{\delta_1^2\alpha(\alpha^2-\omega^2)}{a^2\omega^2r^2}\right];$$

$$C_{21}(a)=\frac{1}{r^2}\left[\frac{\alpha^2\gamma a^2}{2\omega}-2\alpha h\omega-\frac{2\delta_1^2\alpha^2}{a^2\omega r^2}\right];$$

$$S_{22}(a)=-\frac{\alpha\gamma a^2}{2r^2},C_{22}(a)=\frac{\gamma a^2}{8\omega r^2}(\alpha^2+3\omega^2);$$

$$S_{110}(a)=0,C_{110}(a)=\frac{\delta_1^2\alpha}{\omega^2r^2};$$

$$S_{111}(a)=\frac{2\delta_1^2a^2}{\omega r^4},C_{111}(a)=\frac{\delta_1^2\alpha(\omega^2-\alpha^2)}{\omega^2r^4};$$

$$S_{120}(a)=0,C_{120}(a)=0;$$

$$S_{121}(a)=\frac{\delta_1^2\alpha(\alpha^2-\omega^2)}{a\omega^2r^4},C_{121}(a)=\frac{2\delta_1^2\alpha^2}{\omega\omega r^4};$$

$$S_{220}(a)=0,C_{220}(a)=\frac{\delta_1^2\alpha}{a^2\omega^2r^2};$$

$$S_{221}(a)=-\frac{2\delta_1^2\alpha^2}{a^2\omega r^4},C_{221}(a)=\frac{\delta_1^2\alpha(\alpha^2-\omega^2)}{a^2\omega^2r^4}; \tag{42}$$

Substituting $C_{10}(a)$, $C_{110}(a)$ from (41) and (42) into (24) yields (with normalization coeficient $C=$ constant).

$$W_0(a)=Ca\exp\left\{-\frac{r^2\omega^2ha^2}{(\delta_1^2\alpha)}\right\} \tag{43}$$

Further, substituting (43), (42), (41) into (27) one gets.

$$W_{1s}=W_0(a)\left(\frac{\gamma h\omega}{2\delta_1^2}a^4\right);$$

$$W_{1c}=W_0(a)\left(-\frac{3\gamma}{2r^2}a^2-\frac{\gamma h(\alpha^2-3\omega^2)}{4\delta_1^2\alpha}a^4\right);$$

$$W_{2s}=W_0(a)\left(\frac{\gamma h\omega}{4\delta_1^2}a^4\right); \tag{44}$$

$$W_{2c}=W_0(a)\left(-\frac{3\gamma}{4r^2}a^2-\frac{\gamma h(\alpha^2-3\omega^2)}{16\delta_1^2\alpha}a^4\right)$$

Using (31) for $m=2$ and noting (42), (41), (44) after some calculations one has

$$W_{10}(a)=$$

$$=-\frac{3\gamma}{16\delta_1^2r^2}\left[\begin{gathered}\gamma\omega^2a^6+\left(4\alpha h\omega^2+h\alpha^3-\frac{h\omega^4}{\alpha}\right)a^4\\-\frac{6}{r^2}\delta_1^2(\omega^2-\alpha^2)a^2\end{gathered}\right] \tag{45}$$

Thus, the second approximate probability density function of amplitude and phase to the Duffing system (38) is found as

$$W(a,\varphi) = Ca\exp\left\{\frac{-\left(\alpha^2+\omega^2\right)\omega^2 ha^2}{\delta_1^2\alpha}\right\} x$$
$$x\left\{\begin{array}{l} 1-\dfrac{3\varepsilon\gamma}{16\delta_1^2\left(\alpha^2+\omega^2\right)}\left[\begin{array}{l}\gamma\omega^2a^6+\left(4\alpha h\omega^2+h\alpha^3-\dfrac{h\omega^4}{\alpha}\right)a^4\\ +\dfrac{6\delta_1^2\left(\alpha^2-\omega^2\right)a^2}{\left(\alpha^2+\omega^2\right)}\end{array}\right] \\ +\dfrac{\varepsilon\gamma h\omega}{2\delta_1^2}a^4\sin 2\varphi \\ -\left[\dfrac{3\varepsilon\gamma}{2\left(\alpha^2+\omega^2\right)}a^2+\dfrac{\varepsilon\gamma h\left(\alpha^2-3\omega^2\right)}{4\delta_1^2}a^4\right]\cos 2\varphi \\ +\dfrac{\varepsilon\gamma h\omega}{2\delta_1^2}a^4\sin 4\varphi \\ -\left[\dfrac{3\varepsilon\gamma}{4\left(\alpha^2+\omega^2\right)}a^2+\dfrac{3\varepsilon\gamma h\left(\alpha^2-3\omega^2\right)}{16\delta_1^2\alpha}a^4\right]\cos 4\varphi \end{array}\right\} \tag{46}$$

In the limit case when the colored noise $q(t)$ tends to the white noise $\delta\dot{\zeta}(t)$ i.e.

$$\alpha,\delta_1\to+\infty,\frac{2\delta_1^2}{\alpha}\to\delta^2 = \text{const} \tag{47}$$

the solution (46) tends to the following expression

$$W(a,\varphi)= \\ = Ca\exp\left\{-\frac{2\omega^2ha^2}{\delta^2}\right\}\left[1-\frac{\varepsilon\gamma h}{8\delta^2}a^4(3+4\cos 2\varphi+\cos 4\varphi)\right] \tag{48}$$

which is obtained in [11].

V. NUMERICAL RESULTS

In this section, numerical simulations for Duffing oscillator subject to colored noise system (38) are implemented where the probability density function $W(a,\phi)$ given by (46) will be analyzed, and then the accuracy of the corresponding approximate solution will be compared with the ones obtained by the Monte Carlo method ([14],[15]) and by the second order stationary joint probability density function. For the present investigation it is taken $\varepsilon=0.1; h=1; \omega_0=1;$ and various values of $\gamma;\delta^2{}_1$ and α are considered.

Fig. 1 and Fig. 2 show the joint probability density function $W(a,\phi)$ in two cases, $h;\delta_1^2=(1;20)$ and $h;\delta_1^2=(0.5;2)$ with $\varepsilon=0.1$, respectively.

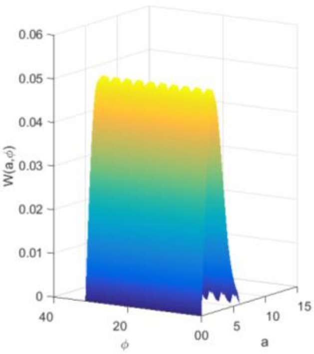

Fig. 1. $W(a,\phi)$ with $\alpha=2$ $\varepsilon=0.1; h=1; \omega_0=1; \gamma=0.1; \delta^2{}_1=20;$

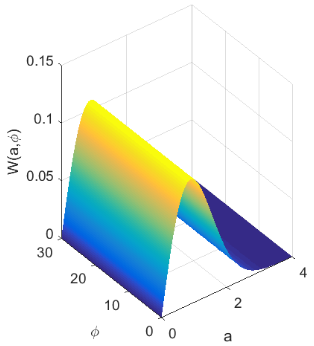

Fig. 2. $W(a,\phi)$ with $\alpha=2; \varepsilon=0.1; h=0.5; \omega_0=1; \gamma=0.02; \delta^2{}_1=2;$

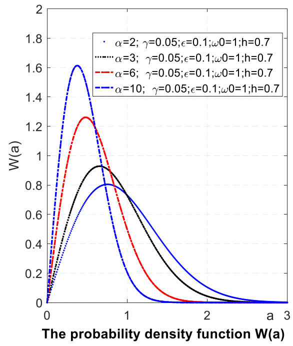

Fig. 3. $W(a)$ with $\alpha=2;3;6;10; h=0.7$ $\varepsilon=0.1; \omega_0=1; \gamma=0.05; \delta^2{}_1=2$

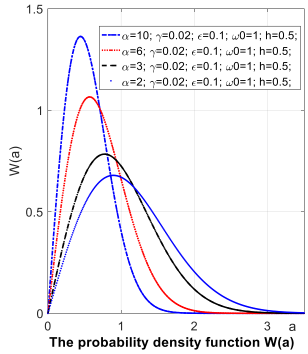

Fig. 4. $W(a)$ with $\alpha=2;3;6;10; h=0.5$ $\varepsilon=0.1; \omega_0=1; \gamma=0.05; \delta^2{}_1=2$

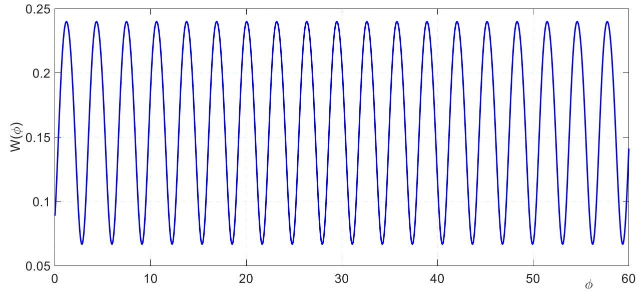

Fig. 5. $W(\phi)$ with $\alpha=2$ $\varepsilon=0.1; h=1; \omega_0=1; \gamma=0.1; \delta^2{}_1=20;$

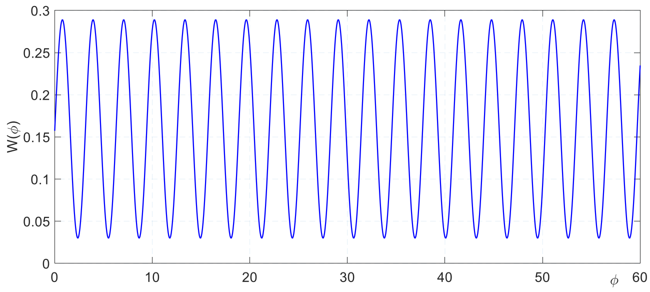

Fig. 6. $W(\phi)$ with $\alpha=2$ $\varepsilon=0.1; h=0.5; \omega_0=1; \gamma=0.05; \delta^2{}_1=2;$

Fig. 3 and Fig. 4 show the stationary probability density function of the response amplitude $W(a)$ in two cases, $\left(h;\delta_1^2\right)=(0.7;2)$ and $\left(h;\delta_1^2\right)=(0.5;2)$ with $\varepsilon=0.1$ and $\alpha=2;3;6;10;$ respectively. It shows that the peak of the stop probability density function of amplitude increases as the parameter α increases. And when having the same parameter α the peak of the stop probability density function of the amplitude with the larger h parameter will be higher. Figures 5 and 6 show the stationary probability density function of phase $W(\phi)$ in two cases, $\left(h;\delta_1^2,\gamma\right)=(1;20;0.1)$ and $\left(h;\delta_1^2;\gamma\right)=(0.5;2;0.05)$ with $\varepsilon=0.1$ and $\alpha=2;$ respectively. The probability density function $W(\phi)$ follows the trigonometric law, the amplitude peak of the stationary probability density function $W(\phi)$ increases when the nonlinearity is weak, with the same other system parameters.

TABLE I. MEAN –SQUARE AMPLITUDE OF DUFFING OSCILATIOR TO COLORED WITH $\varepsilon = 0.1; h = 1; \omega_0 = 1; \gamma = 0.1; \delta^2{}_1 = 20$

	Monte-Carlo Simulation	**2th Approximation**		**Linear**
α	$\langle x^2 \rangle_{MC}$	$\langle x^2 \rangle_2$	Error (%)	$\langle x^2 \rangle_{LN}$
2	3.5935	3.3639	6.3886	4.0000
2.5	3.0726	2.9099	5.2947	3.4483
3	2.7400	2.5309	7.6293	3.0000
4	2.1725	1.9802	8.8525	2.3529
5	1.7928	1.6158	10.01	1.9231
6	1.5314	1.3616	11.08	1.6216
8	1.1682	1.0336	11.52	1.2308
10	0.9508	0.8321	12.48	0.9901

TABLE II. MEAN –SQUARE AMPLITUDE OF DUFFING OSCILATIOR TO COLORED WITH $\varepsilon = 0.1; h = 0.7; \omega_0 = 1; \gamma = 0.05; \delta^2{}_1 = 2$

	Monte-Carlo Simulation	**2th Approximation**		**Linear**
α	$\langle x^2 \rangle_{MC}$	$\langle x^2 \rangle_2$	Error (%)	$\langle x^2 \rangle_{LN}$
2	0.5643	0.5659	0.28	0.5714
2.5	0.4848	0.4876	0.56	0.4926
3	0.4217	0.4240	0.54	0.4286
4	0.3286	0.3324	1.15	0.3361
5	0.2676	0.2716	1.52	0.2747
6	0.2278	0.2290	0.53	0.2317
8	0.1701	0.1738	2.17	0.1758
10	0.1389	0.1398	0.69	0.1414

In TABLE I. and TABLE II. the mean - square amplitudes of Duffing oscillator subject to colored noise (38) are given when the bandwidth parameter α varies. It is seen that the mean - square amplitude decreases when α increases from 2.0 to 10.0. In Tab. I and II the mean - square amplitude of corresponding linear system $\langle x \rangle_{LN}$ (γ=0), is also given. It is shown that in the case of colored noise the effect of cubic nonlinearity can be investigated by using the higher-order averaging procedure proposed. It shows that for weakly nonlinear systems, the error between the mean squared amplitude of the response and numerical simulation gives better results. With a random system subjected to color noise excitation, the error of the MC simulation is within the allowable range.

VI. CONCLUSION

The averaging method is a useful tool for investigating both deterministic and stochastic quasilinear systems. In stochastic problems, however, the method has often been developed only for white noise excitations. The obtained results show that the higher-order averaging method can be successfully extended to the cases of colored noise excitation.

ACKNOWLEDGMENT

Acknowledgement: The first author would like to thank the support from the project NCVCC 2021 of Vietnam Academy of Science and Technology.

REFERENCES

[1] G. Duffing, Erzwungene schwingungen bei veränderlicher eigenfrequenz. Vieweg u. Sohn Braunschweig **7**, 41–42 (1918)

[2] B. Ravindra and A. K. Mallik, Role of nonlinear dissipation in soft Duffing oscillators. Physical Review E, vol. 49, no. 6, pp. 4950–4954, 1994.

[3] J. Cao, C. Ma, H. Xie, Z. Jiang, Nonlinear Dynamics of Duffing System With Fractional Order Damping, Journal of Computational and Nonlinear Dynamics, 2010 5(4), 041012 (6 pages),

[4] A. Sharma, V. Patidar, G. Purohit, and K. K. Sud, Effects on the bifurcation and chaos in forced Duffing oscillator due to nonlinear damping. Communications in Nonlinear Science and Numerical Simulation, vol. 17, no. 6, pp. 2254–2269, 2012.

[5] Z. Li, D. Chen, J. Zhu, Y. Liu, Nonlinear dynamics of fractional order Duffing system, Chaos, Solitons & Fractals, Volume 81, Part A, 2015, Pages 111-116,

[6] L. Cilenti , B. Balachandran, Transient probability in basins of noise influenced responses of mono and coupled Duffing oscillators, Chaos **31**, 063117, (2021);

[7] Nguyen Dong Anh, Higher approximate solutions on stochastic averaging method, Proc. Of NCSR of Vietnam 5 (1) (1993) 19 – 26

[8] Nguyen Dong Anh, Higher order averaging method of coefficients in Fokker-Planck equation, Indian Journal SADHANA 20 (Parts 2-4) (1995) 373 – 387.

[9] Yu. A. Mitropolskii, N. D. Anh, N. D. Tinh: Random oscillations in the Van der Pol system under influence of wide-band stochastic process. Ucrainian Mathematical Journal 50 (11), 1517-1521, (in Russian), (1998).

[10] N. D. Anh, Nguyen Ngoc Linh, Nguyen Nhu Hieu, Nguyen Van Manh, Anh Tay Nguyen, Application of high order averaging method to Van der Pol oscillator, Proceeding of IFToMM Asian MMS 2021, topic Machinery and Machine Elements.

[11] Yu. A. Mitropolskii, Averaging Method in Nonlinear Mechanics , Naukova -Dumka, Kiev, 1971 (in Russian).

[12] Mitropolskii Iu. A., Dao N. V., Anh N. D. Nonlinear oscillations in systems of arbitrary order, Naukova-Dumka, Kiev, 1992 (in Russian).

[13] Nguyen Dong Anh, Higher approximate solutions on stochastic averaging method, Proc. Of NCSR of Vietnam 5 (1) (1993) 19 – 26

[14] K. Debrabant, A. Rößler: Families of efficient second order Runge–Kutta methods for the weak approximation of Itô stochastic differential equations. Applied Numerical Mathematics 59, 582–594 (2009).

[15] R. Valery Roy, Pol D. Spanos: Pade-Type Approach to Nonlinear Random Vibration Analysis. In: Stochastic Structural Dynamics 1: New Theoretical Developments, Y.K Lin, I.Elishakoff (Eds.) Springer, Berlin, Heidenberg, 155-172, (1991)

The 6th International Conference on Engineering Mechanics and Automation (ICEMA 2021)
Hanoi, November 14, 2021

Parameters analysis on the vibration of composite ring-stiffened cylindrical shells in interaction with elastic foundation

Tuan Hai Nguyen
Hanoi University of Science and Technology
School of Mechanical Engineering
Hanoi, Vietnam
hai.nt171258@sis.hust.edu.vn

Manh Cuong Nguyen
Hanoi University of Science and Technology
School of Mechanical Engineering
Hanoi, Vietnam
cuong.nguyenmanh1@hust.edu.vn

Quoc Hung Nguyen
Hanoi University of Science and Technology
School of Mechanical Engineering
Hanoi, Vietnam
hung.nq1395@gmail.com

***Abstract*: This study presents the continuous elements method (CEM) for the vibration parameters analysis of composite inner ring-stiffness cylindrical shells resting on Winkler elastic foundation. The dynamic stiffness matrix of the considered structure has been built by using a procedure of assembling continuous elements of cylindrical shells and annular shells in contact with elastic foundations. Solutions on natural frequencies and harmonic responses obtained by our formulation are compared to results of other approaches and to those of FEM to demonstrate the advantages of CEM: higher precision, time and resources of computing saved, size model reduced even in medium and high frequency range. In addition, the influences of shell and foundation parameters are also investigation.**

Keywords: Dynamics stiffness matrix, Continuous Element Method, composite shell, shells on elastic foundation, ring-stiffened cylindrical shells, vibration of shell

I. Introduction

Thick ring-stiffened shells resting on elastic foundation occupy leading civil, mechanical, architectural, aeronautical, and marine engineering positions, as they create optimal conditions, strength, and stability. Concerning the advancements of materials, laminate composite materials have superior properties, which have led to their widespread use in high-performance aircraft, spacecraft, automotive parts, and structures. ,etc space architecture, defense industry, electronics, and biomedicine. Various studies on composite shell structures as well as ring-stiffened cylinders have been performed using different methods: Sofiyev et al. applied Galerkin method to analyze laminated orthotropic shells surrounded by Pasternak foundation with different boundary conditions [1] and non-homogenous orthotropic shells surrounded by Pasternak elastic foundation under moving load [2]. Bagheziradeh et al. considered the dynamic behavior of FGM cylindrical shells surrounded by elastic foundation based on the Higher-order Shear Deformation Theory (HSDT) [3]. Al-Najaf and Warburton used the finite element method by axial symmetry to investigate the natural frequency and vibration modes of a thin circular cylindrical shell with ring-stiffeners [4]. Caresta M applied wave solution combining with power-serie solution [5]. Narita et al. employed the finite element method to analyze vibration of cylindrical shell [6].

Recently, the Continuous Element Method (CEM) or Dynamics Stiffness Method (DSM) has been developed to overcome the problems of other approaches in medium and high frequency analysis. Numerous Continuous Elements have been developed for metal and composite structures [7-8]. The CE models for composite cylindrical shells presented in [9] by Thinh and Cuong. The new research for thick laminated composite cylindrical and joined cylindrical-conical shells surrounded by Winkler elastic foundation by Cuong et al. [10] has highlighted CEM's strong capacity of assembling complex structures. Nevertheless, there is a lack on studies on the ring-stiffened shells resting on elastic foundation in the literature. The purpose of this paper is to present a ring-stiffened cylindrical shells made by composite material. The dynamic stiffness matrix of the investigated structure will be constructed basing on the FSDT. Obtained natural frequencies will be validated by comparing with those from the literature. Results on harmonic response of this approach compared to results of FEM programs to demonstrate the advantages of CEM: higher precision, time and resources of computing saved.

II. Theory of laminated composite shell of revolution on elastic foundation

A. Lamina constitutive relation

The plane stress-reduced stiffnesses of a laminate composite composed by N orthotropic layers are:

$$Q_{11} = \frac{E_1}{1-v_{12}v_{21}}, Q_{12} = \frac{v_{12}E_2}{1-v_{12}v_{21}}, \qquad (1)$$

$$Q_{22} = \frac{E_2}{1-v_{12}v_{21}}, Q_{44} = G_{23}, Q_{55} = G_{13}, Q_{66} = G_{12}$$

Where E_1, E_2 are Young's modulus, G_{12}, G_{13}, G_{23} are shear modulus and v_1, v_2 are poisson ratio, respectively and the laminate stiffness coefficients A_{ij}, B_{ij}, D_{ij} are defined by [10]:

$$A_{ij} = \sum_{k=1}^{n} \overline{Q_{ij}^{k}}\,(z_{k+1} - z_k)\ (i,j = 1,2,4,5,6)$$

$$B_{ij} = \frac{1}{2}\sum_{k=1}^{n} \overline{Q_{ij}^{k}}\,(z_{k+1}^2 - z_k^2) \qquad (2)$$

$$D_{ij} = \frac{1}{3}\sum_{k=1}^{n} \overline{Q_{ij}^{k}}\,(z_{k+1}^3 - z_k^3)\ (i,j = 1,2,6)$$

B. Kinematics of composite axis-symmetric shell

Consider a revolution shell is presented by a conical shell, as shown in Figure 1. R_1 is small radius and R_2 is large one, L is the length of generator line of the cone and α is its vertex angle. The radius at every point along its length is calculated by: $R(x) = R_1 + x sin\alpha$ (3).

If $\alpha \to 0$, the equation (1) presents cylindrical shells, if $\alpha \to \pi/2$ or $\alpha \to -\pi/2$, the equation (3) presents outer ring or inner ring stiffeners.

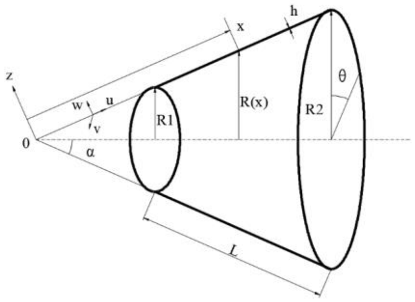

Figure 1. Geometry and coordinate system of conical shell

For our model composed by cylinders and inner rings only angles 0 and $-\dfrac{\pi}{2}$ are used

C. Equations of motion

The equations of motion using the first-order shear deformation shell theory (FSDT) for laminated circular conical shell on Winkler elastic foundation is written by:

$$\frac{\partial N_x}{\partial_x} + \frac{sin\alpha}{R}(N_x - N_\theta) + \frac{1}{R}\frac{\partial N_{x\theta}}{\partial_\theta} = I_0\ddot{u} + I_1\ddot{\varphi}_x\ ;$$

$$\frac{\partial N_{x\theta}}{\partial_x} + \frac{2sin\alpha}{R}N_{x\theta} + \frac{1}{R}\frac{\partial N_\theta}{\partial_\theta} + \frac{cos\alpha}{R}Q_\theta = I_0\ddot{v_0} + I_1\ddot{\varphi}_\theta$$

$$\frac{\partial M_x}{\partial_x} + \frac{sin\alpha}{R}(M_x - M_\theta) + \frac{1}{R}\frac{\partial M_{x\theta}}{\partial_\theta} - Q_x = I_1\ddot{u} + I_2\ddot{\varphi}_x\ ;$$

$$\frac{\partial M_{x\theta}}{\partial_x} + \frac{2sin\alpha}{R}M_{x\theta} + \frac{1}{R}\frac{\partial M_\theta}{\partial_\theta} - Q_\theta = I_1\ddot{v_0} + I_2\ddot{\varphi}_\theta \qquad (4)$$

$$\frac{\partial Q_x}{\partial_x} + \frac{1}{R}\frac{\partial Q_\theta}{\partial_\theta} + \frac{sin\alpha}{R}Q_x - \frac{cos\alpha}{R}N_\theta - k_w w$$
$$+k_p\left(\frac{\partial^2 w}{\partial_{x^2}} + \frac{sin\alpha}{R}\frac{\partial_w}{\partial_x} + \frac{1}{R^2}\frac{\partial^2 w}{\partial_{\theta^2}}\right) = I_0\ddot{w}$$

where u_0, v_0, w_0: displacement, φ_S, φ_θ : rotations of the point M_o at the median radius of the shell and:

$$[I_0, I_1, I_2] = \int_{-h/2}^{h/2}\rho(z)[1, z, z^2]dz\ \ (i = 1,2,3) \qquad (5)$$

D. Force resultants–displacement relationships

The force and moment resultants are written in terms of displacements for cross-ply axis-symmetric shell as follows [11]:

$$N_s = A_{11}\frac{\partial u_0}{\partial_s} + \frac{A_{12}}{R}\left(u_0 sin\alpha + \frac{\partial v_0}{\partial_\theta} + w_0 cos\alpha\right) + B_{11}\frac{\partial\varphi_s}{\partial_s} + \frac{B_{12}}{R}\left(\varphi_s sin\alpha + \frac{\partial\varphi_\theta}{\partial_\theta}\right)$$

$$N_\theta = A_{12}\frac{\partial u_0}{\partial_s} + \frac{A_{22}}{R}\left(\frac{\partial v_0}{\partial_\theta} + w_0 cos\alpha\right) + B_{12}\frac{\partial\varphi_s}{\partial_s} + B_{22}\left(\varphi_s sin\alpha + \frac{\partial\varphi_\theta}{\partial_\theta}\right)$$

$$N_{s\theta} = A_{66}\left(\frac{\partial v_0}{\partial_s} + \frac{1}{R}\left(\frac{\partial u_0}{\partial_\theta} - v_0 sin\alpha\right)\right) + B_{66}\left(\frac{1}{R}\frac{\partial\varphi_s}{\partial_\theta} + \frac{\partial\varphi_\theta}{\partial_s}\frac{sin\alpha}{R}\ \varphi_\theta - \frac{cos\alpha}{2R^2}\frac{\partial u_0}{\partial_\theta} + \frac{cos\alpha}{2R}\frac{\partial v_0}{\partial_s} + \frac{cos\alpha sin\alpha}{2R^2}v_0\right)$$

$$M_s = B_{11}\frac{\partial u_0}{\partial_s} + \frac{B_{12}}{R}\left(u_0 sin\alpha + \frac{\partial v_0}{\partial_\theta} + \frac{w_0 cos\alpha}{R}\right) + D_{11}\frac{\partial\varphi_s}{\partial_s} + \frac{D_{12}}{R}\left(\varphi_s sin\alpha + \frac{\partial\varphi_\theta}{\partial_\theta}\right)$$

$$M_\theta = B_{12}\frac{\partial u_0}{\partial_s} + \frac{B_{22}}{R}\left(u_0 sin\alpha + \frac{\partial v_0}{\partial_\theta} + w_0 cos\alpha\right) + D_{12}\frac{\partial\varphi_s}{\partial_s} + \frac{D_{22}}{R}\left(\varphi_s sin\alpha + \frac{\partial\varphi_\theta}{\partial_\theta}\right)$$

$$M_{s\theta} = B_{66}\left(\frac{\partial v_0}{\partial_s} + \frac{1}{R}\left(\frac{\partial u_0}{\partial_\theta} - v_0 sin\alpha\right)\right) + D_{66}\left(-\frac{cos\alpha}{2R^2}\frac{\partial u_0}{\partial_\theta} + \frac{cos\alpha}{2R}\frac{\partial v_0}{\partial_s} + \frac{1}{R}\frac{\partial\varphi_s}{\partial_\theta} + \frac{\partial\varphi_\theta}{\partial_s} + \frac{1}{R}sin\alpha\varphi_\theta + \frac{cos\alpha sin\alpha}{2R^2}v_0\right)$$

$$Q_\theta = kA_{44}\left(-\frac{cos\alpha}{R}v_0 + \frac{\partial w_0}{R\partial_\theta} + \varphi_\theta\right); Q_s\ kA_{55}\left(\frac{\partial w_0}{\partial_s}\right) + \varphi_s \quad (6)$$

where k is the shear correction factor (k=5/6)

III. DYNAMIC STIFFNESS FOR VIBRATION OF THICK LAMINATED COMPOSITE REVOLUTION SHELLS

A. State vectors

The state-vector for the investigated conical shells is $\mathbf{y}^T = \{u_0, v_0, w_0, \varphi_S, \varphi_\theta, N_S, N_{S\theta}, Q_S, M_S, M_{S\theta}\}^T$. Forces, moments and displacements can be expressed by Levi series expansions for natural symmetrical vibration mode m of revolution shells.

$$\{u_o(s,\theta,t), w_o(s,\theta,t), \phi_\theta(s,\theta,t), N_S(s,\theta,t), Q_S(s,\theta,t), M_S(s,\theta,t)\}^T$$
$$= \sum_{m=1}^{\infty}\{u(s), w(s), \phi_\theta(s), N_S(s), Q_S(s), M_S(s)\}^T cos(m\theta)e^{i\omega t}$$

$$\{v_o(s,\theta,t), \phi_s(s,\theta,t), N_\theta(s,\theta,t), Q_\theta(s,\theta,t), M_\theta(s,\theta,t)\}^T$$
$$= \sum_{m=1}^{\infty}\{v(s), \phi_s(s), N_\theta(s), Q_\theta(s), M_\theta(s)\}^T sin(m\theta) \qquad (7)$$

where m is circumferential mode of the shells.

By substituting (7) in equations (4) and (6), the derivations of state vectors (7) with respect to variable *s* are calculated from equations (6) and (7) as follows:

$$\begin{aligned}
\frac{dN_{xm}}{dx} &= f_6(u_m,\phi_{xm},N_{x\theta m},M_{x\theta m},\omega) \\
\frac{dN_{x\theta m}}{dx} &= f_7(v_m,w_m,\phi_{\theta m},N_{xm},M_{xm},\omega) \\
\frac{dQ_{mx}}{dx} &= f_8(v_m,w_m,\phi_{\theta m},N_{xm},M_{xm},\omega) \qquad (8)\\
\frac{dM_{xm}}{dx} &= f_9(u_m,\phi_{xm},Q_{xm},M_{x\theta m}) \\
\frac{dM_{m\theta x}}{dx} &= f_{10}(v_m,w_m,\phi_{\theta m},N_{xm},M_{xm},\omega) \\
\frac{du_m}{dx} &= f_1(v_m,w_m,\phi_{\theta m},N_{xm},M_{xm}) \\
\frac{dv_m}{dx} &= f_2(u_m,N_{x\theta m},M_{x\theta m}) \\
\frac{dw_m}{dx} &= f_3(\phi_{xm},Q_{xm}) \\
\frac{d\phi_m}{dx} &= f_4(v_m,w_m,\phi_{\theta m},N_{xm},M_{xm}) \\
\frac{d\phi_{\theta m}}{dx} &= f_5(\phi_{xm},N_{x\theta m},M_{x\theta m})
\end{aligned}$$

Equation (8) can be rewritten in matrix form as follows:

$$\frac{d\boldsymbol{y_m}}{dx} = \boldsymbol{A_m y_m} \qquad (9)$$

where $\boldsymbol{A_m}$ is a matrix 10×10

B. Dynamic stiffness matrix K

The dynamic transfer matrix $\boldsymbol{T_m^c}$ of cylindrical shells and $\boldsymbol{T_m^r}$ of ring stiffeners is calculated by:

$$\boldsymbol{T}_m^c = e^{\int_0^L \boldsymbol{A_m} ds} \qquad \boldsymbol{T}_m^r = e^{\int_0^{R_2-R_1} A_m ds} \qquad (10)$$

where R_1, R_2 are inner and outer radius of ring stiffeners.

To obtain dynamic stiffness matrix $\boldsymbol{K}(\omega)_m$, rewrite $\boldsymbol{T}_m$ as four blocks as:

$$\boldsymbol{T}_m = \begin{bmatrix} \boldsymbol{T}_{11} & \boldsymbol{T}_{12} \\ \boldsymbol{T}_{21} & \boldsymbol{T}_{22} \end{bmatrix}_m \qquad (11)$$

after some manipulations, the dynamic stiffness matrix $\boldsymbol{K}(\omega)_m$ is determined as:

$$\boldsymbol{K}(\omega)_m = \begin{bmatrix} \boldsymbol{T}_{12}^{-1}\boldsymbol{T}_{11} & -\boldsymbol{T}_{12}^{-1} \\ \boldsymbol{T}_{21} - \boldsymbol{T}_{22}\boldsymbol{T}_{12}^{-1}\boldsymbol{T}_{11} & \boldsymbol{T}_{22}\boldsymbol{T}_{12}^{-1} \end{bmatrix}_m \qquad (12)$$

IV. DYNAMIC STIFFNESS MATRIX FOR COMPOSITE INNER RING-STIFFENED CYLINDRICAL SHELLS RESTING ON WINKLER ELASTIC FOUNDATION

The model for analysis in this paper is presented in Figure 2. Here R_1 is the radius of cylindrical shells, R_2, R_3 are inner and outer radius of ring stiffeners. L_1, L_2 are lengths of cylindrical shells and h is the thickness of the cylindrical shell. The ring stiffeners has the width c_r and the thickness b_r. The reference surface is taken middle surface of the shells. The model is divided into 4 part as Figure 2. Each part has 3 continuous elements arranged in the following order cylindrical shell – ring stiffener – cylindrical shell.

These elements are represented by three dynamic stiffness matrix ***K1c(***ω***)***, ***Kr(***ω***)*** and ***K2c(***ω***)***,respectively. First, it is necessary to evaluate separately the dynamic stiffness matrix ***K1c(***ω***)***, ***Kr(***ω***)*** and ***K2c(***ω***)***. Then the assembling procedure of the dynamic stiffness matrix ***K(***ω***)*** for the ring-stiffened cylindrical shells can be constructed by employing the assembly procedure similar to those of FEM in Figure 3. Next, the dynamic stiffness matrix ***K(***ω***)*** for the ring-stiffened cylindrical shells is developed which satisfies the continuity conditions at the cylindrical-ring joint as follows [5] (α = 90° in this case):

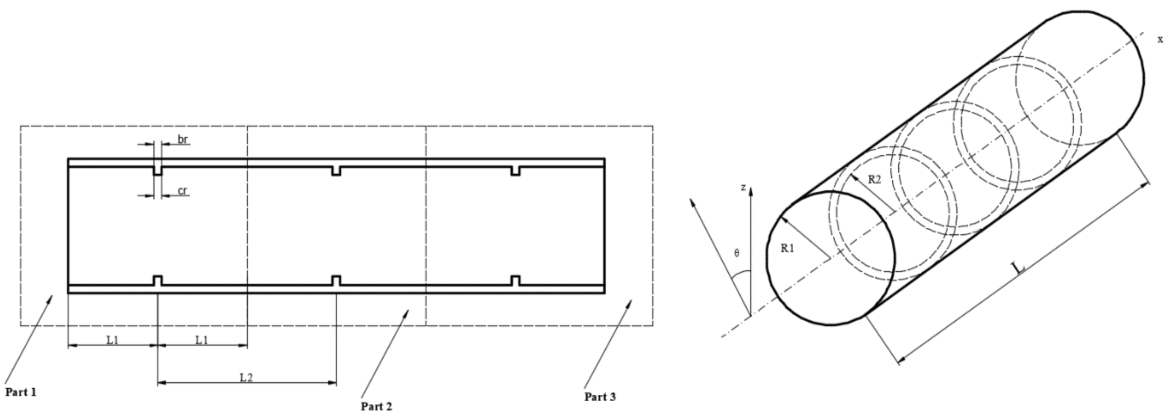

Figure 2. Continuous element of outer ring-stiffened cylindrical shells

$$
\begin{aligned}
&u_1 = u_r cos\alpha - w_r sin\alpha; && v_1 = v_r; \\
&w_1 = u_r sin\alpha + w_r cos\alpha && \frac{\partial w_1}{\partial x_1} = \frac{\partial w_r}{\partial x_r}; \\
&N_{x_1} = N_{x_r} cos\alpha - Q_{x_r} sin\alpha; && M_{x_{\theta 1}} = M_{x_{\theta r}}; \qquad (13) \\
&Q_{x_1} = N_{x_r} sin\alpha + Q_{x_r} cos\alpha; && M_{x_1} = M_{x_r}.
\end{aligned}
$$

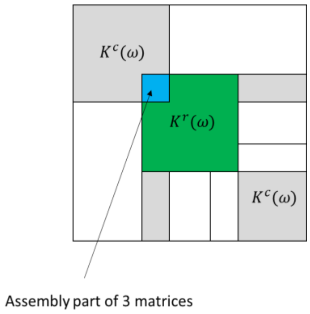

Figure 3. The assembling procedure of a ring-stiffened conical shell element

A. *Numerical results and discussion*

First, the developed formulations will be validated by comparing with other researches and by the Finite Element Methof (FEM). Due to the lack of available studies on composite ring-stiffened cylindrical shells resting on elastic foundation, the CE model will be compared with the solution of Narita [5] for composite cylinder without ring-stiffeners and then with composite ring-stiffened cylindrical shell surrounded by Winkler foundation model constructed in ANSYS software using two different meshes (60x40) and 120x80.

B. *Validation of the present model*

The study of Narita [5] using finite element method and ANSYS to analyze vibration of cylindrical shell will be used for validating our model. First, the result frequency parameters are defined as $\Omega = \omega R(\rho/E_2)^{1/2}$ would be compared to our solution. The material properties and dimensions of shells are as follows: h/R = 0.02, L/R = 4. The shell has three-layer cross-plies from outer to inner layer. All layers are of equal thickness and material properties used are (Material 1 – Graphite/Epoxy): $E_1 = 138GPa, E_2 = E_3 = 8.96Gpa, G_{12} = G_{13} = 7.1Gpa$, $G_{23} = 3.45Gpa, \nu_{12} = 0.3, \rho = 1645\ kg/m^3$.

The second test case concerns a clamped-clamped composite cylindrical shells with following properties: h = 0,0254m, R / h = 0.1, L = 4 R resting on Winkler foundation with K_w = 15x10$^4 (N/m^3)$. The shell and ring-stiffeners are made by the same material (Material 1) with layer scheme $[0°/90°/90°/0°]$. The frequencies of different vibration modes of the structure resting on elastic foundation is determined by CEM and by ANSYS and the obtained values are shown in Table 2. Table 1 and table 2 demonstrates the comparison of solutions obtained by CEM with Narita [5] and by ANSYS model respectively. Excellent discrepancies between the three models are obtained with small errors. This confirms that CE model is exact and can be used to study the dynamic behaviors of ring-stiffened composite cylindrical shells resting on Winkler foundation.

TABLE 1. THE COMPARISON OF FREQUENCY PARAMETERS $\Omega = \omega R(\rho/E_2)^{1/2}$ OF CROSS-PLY SHELL WITH BOUNDARY CONDITION CLAMPED-FREE (three layers, h/R = 0.02, L/R = 4, Material 1)

Lamination (outer/iner)	References	Ω_1	Ω_2	Ω_3 x(10^{-2})	Ω_4	Ω_5
0/0/0	Narita [5]	8.453	9.732	12.33	14.17	20.31
	CEM	8.454	9.719	12.30	14.13	20.49
	Error	0.01	0.13	0.24	0.28	0.89
0/90/0	Narita [5]	8.442	11.30	11.51	17.25	20.79
	CEM	8.427	11.28	11.49	17.20	20.75
	Error	0.18	0.18	0.17	0.29	0.19
90/90/90	Narita [5]	7.694	12.77	17.42	21.71	24.34
	CEM	7.672	12.73	17.34	21.62	24.25
	Error	0.29	0.31	0.46	0.41	0.37
90/0/90	Narita [5]	11.25	17.70	20.66	27.69	32.67
	CEM	11.23	17.61	20.65	27.57	32.36
	Error	0.18	0.51	0.05	0.43	0.95

TABLE 2. COMPARISON OF NATURAL FREQUENCIES (HZ) OF C-C CYLINDRICAL SHELL ON WINKLER FOUNDATION BY CEM AND BY FEM (ANSYS) (H=0.0254M, R/H=0.1, L=4R, LAYERS [0°/90°/90°/0°], MATERIAL 1)

Mode	ANSYS(60x40)	ANSYS (120x80)	CEM	Error(%)
1	530.68	530.68	530.2	0.09
2	661.08	661.07	660.4	0.10
3	735.82	735.82	734.9	0.13
4	1013.9	1013.9	1013.5	0.04
5	1045.0	1045.0	1043.8	0.11
6	1063.6	1063.6	1059.6	0.38
7	1295.7	1295.6	1292.9	0.21
8	1457.8	1457.8	1455.8	0.14
9	1527.2	1527.2	1525.0	0.14
10	1624.8	1624.5	1613.6	0.67

C. CEM for vibration analysis of composite ring-stiffened shells in interaction with elastic foundation

Ring-stiffened cylindrical shells have extremely important industrial applications, especially in the submarine industry. The next step of our study is obviously to confirm the advantage of the presented formula for this type of structure over FEM (Ansys). Consider a clamped-free (C-F) composite cylindrical shell have one ring-stiffened to the following dimensions: h = 0,0254m, R / h = 0.1, L = 4R,$L_1 = 2R, c_r = 0.02, b_r = 0.0254$, resting on Winkler foundation with kw = 15 x 104 (N/m^3). The shell is made by Material 1 with a layer composition of [0°/90°/0°]. Our results will be compared to FEM solutions with different meshes and the comparison is illustrated in Table 3. In this section, the effect of foundation stiffnesses and the number of layers on natural frequencies of shells is also under investigation. The results are presented in Table 4-5 and Figure 4-5.

TABLE 3. COMPARISON OF NATURAL FREQUENCIES (HZ) OF C-F RING-STIFFENED CYLINDRICAL SHELLS ON WINKLER FOUNDATION BY CEM AND BY FEM (ANSYS)

(h = 0,0254m, R / h = 0.1, L = 4R,$L_1 = 2R, c_r = 0.02, b_r = 0.0254$,kw = 15 x 10^4, layer [0°/90°/0°])

Mode	ANSYS(60x40)	ANSYS (120x80)	CEM	Error(%)
1	229.68	229.68	241.6	5.19
2	328.2	328.2	327.9	0.09
3	427.4	427.39	440.9	3.16
4	628.93	628.93	644.3	2.44
5	650.22	650.21	697.8	7.32
6	776.76	776.68	781.4	0.61
7	945.04	944.92	979.6	3.67
8	980.59	980.6	998	1.77
9	1088.5	1088.5	1092.5	0.37
10	1222.2	1222.0	1222.4	0.03

TABLE 4. EFFECTS OF FOUNDATION STIFFNESSES ON FREQUENCIES (HZ) OF C-F RING-STIFFENED CYLINDRICAL SHELLS

(h = 0,0254m, R / h = 0.1, L = 4R,$L_1 = 2R, c_r = 0.02, b_r = 0.0254$,kw = 15 x 10^4, layer [0°/90°/0°])

Mode	$k_w = 0$	$k_w = 15e4$	$k_w = 15e5$	$k_w = 15e6$	$k_w = 15e7$	$k_w = 15e8$	$k_w = 15e9$
1	241.5	241.6	243	255.9	360.3	740.2	1919.1
2	327.8	327.9	328.5	334.6	390.2	877.8	2015.9
3	440.8	440.9	441.7	449.9	524.4	1000.2	2454.9
4	644.3	644.3	644.8	649.7	696.3	1053.3	2592.8
5	697.8	697.8	698.3	703.4	751.8	1126.5	2633.1
6	781.3	781.4	781.9	786.7	833.5	1183	2791.8
7	979.6	979.6	979.8	981.9	1002.3	1205.6	2843.4
8	998	998	998.4	1002.7	1038.4	1348	2869.3
9	1092.5	1092.5	1092.8	1096.2	1128.9	1415.2	2926.6
10	1222.4	1222.4	1222.7	1225.4	1252.1	1492.7	2996.2

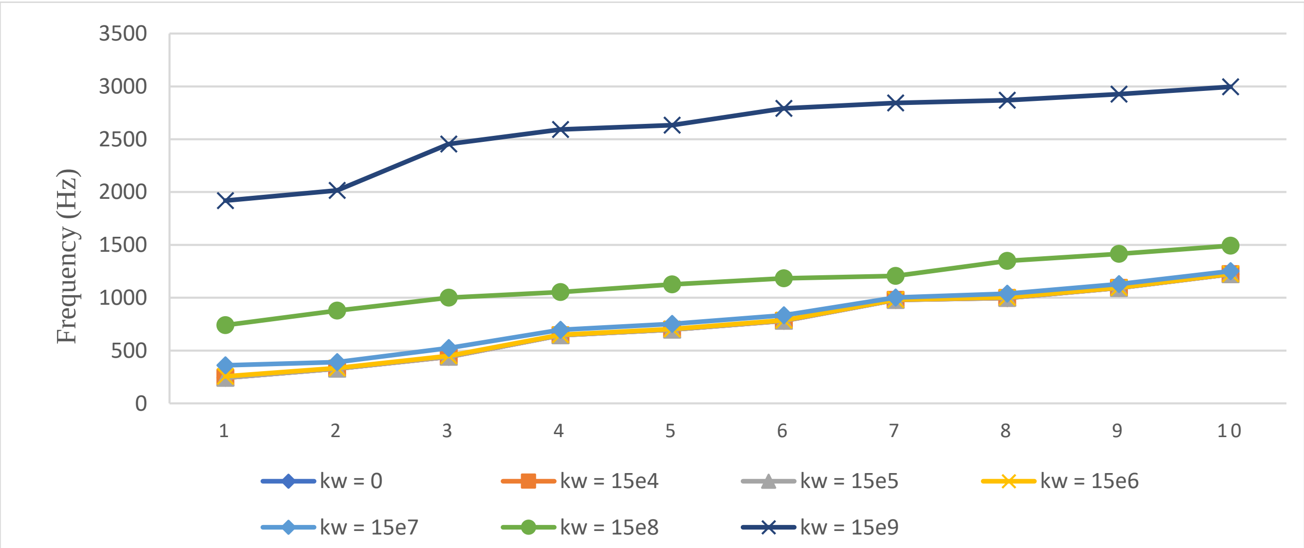

Figure 4. The variation of frequencies (Hz) for the C-F ring-stiffened cylindrical shells with different foundation stiffnesses
(h = 0,0254m, R / h = 0.1, L = 4R,$L_1 = 2R, c_r = 0.02, b_r = 0.0254$,kw = 15 x 10^4, layer [0°/90°/0°])

TABLE 5. EFFECTS OF number OF LAYERS ON FREQUENCIES (HZ) OF C-F RING-STIFFENED CYLINDRICAL SHELLS

(h = 0,0254m, R / h = 0.1, L = 4R, $L_1 = 2R, c_r = 0.02, b_r = 0.0254$, kw = 15 x 10^4, layer [0°/90°/0°])

Mode	0/90	0/90/0/90	0/90/0/90/0/90	0/90/0/90/0/90/0/90	0/90/0/90/0/90/0/90/0/90
1	272.8	314	315.3	315.9	316.3
2	309.4	341.7	353.7	358.1	360.2
3	591.9	649.6	660.6	664.9	667.2
4	596	813.4	849.6	862.6	868.9
5	766.3	938.1	942.6	944.7	945.9
6	921.2	952.8	984.5	996	1001.6
7	1005	1160.6	1176.4	1182.8	1186.1
8	1071.3	1196.6	1232	1245.4	1252.1
9	1084.8	1477.4	1541.5	1564.6	1575.7
10	1205.3	1581.3	1629.8	1632.6	1632.6

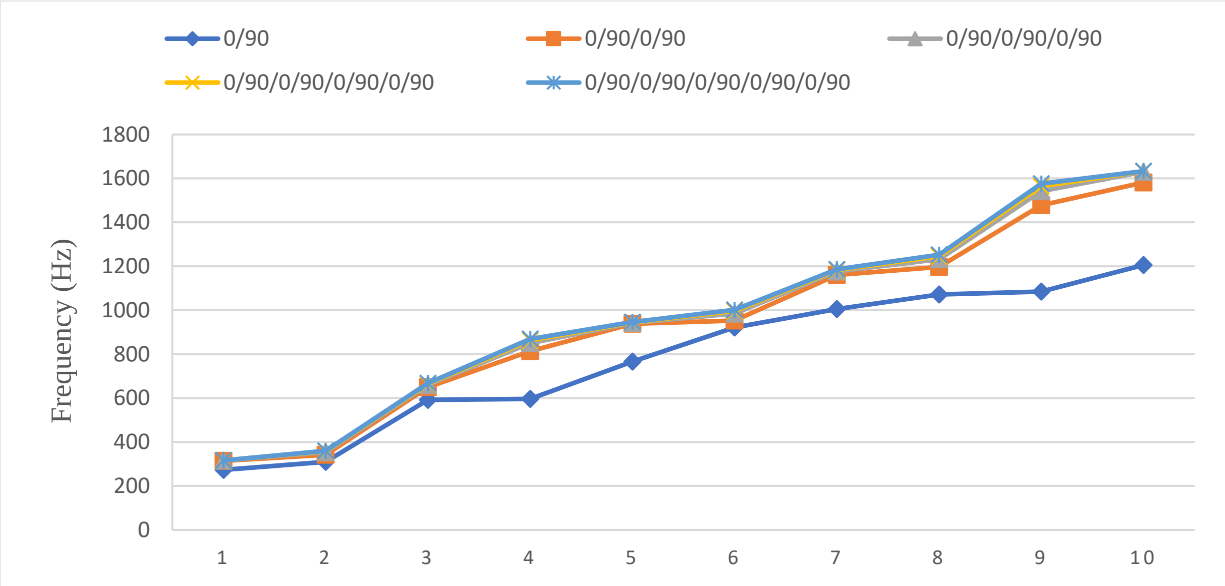

Figure 4. The variation of frequencies (Hz) for the C-F ring-stiffened cylindrical shells with different number of layers (h = 0,0254m, R / h = 0.1, L = 4R, $L_1 = 2R, c_r = 0.02, b_r = 0.0254$, kw = 15 x 10^4, layer [0°/90°/0°])

Table 3 shows that the present model for inner ring-stiffened cylindrical shells resting on Winkler foundation is validated. Errors varies from 0.03 to 7.32 and the large error of 7.32% (for the coarse and fine meshing) indicate that CEM has a higher accuracy than ANSYS model because FEM is an approximate method and the coupling of the rings and shell elements has strongly affected the accuracy of the results. It can be seen that CEM gives better results than current simulation software using FEM because it is necessary to have a very finer mesh of FEM to reach the exact value of CEM. Concerning the influence of foundation stiffnesses, from Table 4 and Figure 4 it is noted that when the stiffness of the Winkler elastic foundation is small from 0 to 15x10^6(N/m^3), it does not significantly affect the vibration frequency of the shell. When increasing the foundation stiffness to 15x10^8, 15x10^9 (N/m^3) it can be seen that the foundation affects greatly the natural vibration frequencies of the shell. With the same shell thickness, when the number of layers increases from 2 to 4, the frequency of the shell has a slight augmentation. However, if the shell thickness is made by more than 4 composite layers, shell natural frequencies remain almost unchanged.

V. CONCLUSION AND DEVELOPMENTS

The Continuous Element Method has successfully been used to study the free vibration analysis of composite ring-stiffenend cylindrical shells in contact with Winkler elastic foundation. The continuous element assembling algorithm presented satisfies the kinematic and physical compatibility. Results obtained by our formulation are in close agreement with those issued from other researches and FEM which confirms the precision and the validity of CE model. Throughout numerous test cases, it is shown that CEM allows to calculate the natural frequency vibration of the composite ring-stiffened shell in any frequency range with high accuracy, saving time and computing resources. The effects of the elastic foundation stiffness as well as the composite layer number have also been taken into account in this study.

This CE model can be expanded to solve the problem of ring-stiffened conical shell on elastic foundation and composite joined cylindrical-conical-ring shells on elastic foundation

REFERENCES

[1] A. H. Sofiyev and N. Kuruoglu. Natural frequency of laminated orthotropic shells with different boundary conditions and resting on the Pasternak type elastic foundation. Composites Part B: Engineering, 42, (6), (2011), pp. 1562–1570.
[2] A. H. Sofiyev, H. Halilov, and N. Kuruoglu. Analytical solution of the dynamic behavior of non-homogenous orthotropic cylindrical shells on elastic foundations under moving loads. Journal of Engineering Mathematics, 69, (4), (2011), pp. 359–371
[3] E. Bagherizadeh, Y. Kiani, and M. R. Eslami. Mechanical buckling of functionally graded material cylindrical shells surrounded by Pasternak elastic foundation. Composite Structures, 93, (11), (2011), pp. 3063–3071
[4] A.M. Al-Najafi, G.B. Warburton, Free vibration of ring-stiffened cylindrical shells. Journal of Sound and Vibration 13 (1970),pp. 9–25.
[5] Caresta M, Kessissoglou NJ. Free vibrational characteristics of isotropic coupled cylindrical–conical shells. Journal of Sound and Vibration, 329, (6), (2010): pp. 733–751.
[6] Narita Y., Ohta Y., Saito M., Finite element study for natural frequencies of cross-ply lami-nated cylindrical shells,Composite structures, 26, (1993), 55-62.
[7] J. R. Banerjee and A. J. Sobey. Dynamic stiffness formulation and free vibration analysis of a three-layered sandwich beam. International Journal of Solids and Structures, 42, (8), (2005), pp. 2181–2197.
[8] J. R. Banerjee and A. J. Sobey. Dynamic stiffness formulation and free vibration analysis of a three-layered sandwich beam. International Journal of Solids and Structures, 42, (8), (2005), pp. 2181–2197.
[9] Tran Ich Thinh, Nguyen Manh Cuong. Dynamic stiffness matrix of continuous element for vibration of thick cross-ply laminated composite cylindrical shells. Compos Struct 2013;98:93–102
[10] N. M. Cuong, L. Q. Vinh, T. I. Thinh, and N. T. T. Hoan. Continuous element formulation for composite combined conical-cylindrical shells on elastic foundations. In Proceeding of the 12th National Conference on Mechanics, Da Nang, Vietnam, (2015). pp. 281–288.
[11] Reddy J. N. - Mechanics of Laminated Composite Plates and Shells: Theory and Analysis, 2nd edn, CRC press, New York, 2003.
[12] Kouchakzadeh M. A., Shakouri M. - Free vibration analysis of joined cross-ply laminated conical shells, International Journal of Mechanical Sciences 78 (2014) 118-125.

Research for Static Stability of the Conical Shells Including Foundation Effects

Nguyen Dang Bich
Institute for Building Science and Technology
Hanoi, Vietnam
ndbich.ibst@gmail.com

Nguyen Hoang Tung
Construction Technical College Number 1
Hanoi, Vietnam
nguyenhoangtung2104@gmail.com

Le Xuan Tung
Hoa Binh Corporation
Hanoi, Vietnam
letungpdu@gmail.com

Abstract: **This paper introduces how to establish and solve the linear static stability of the conical shells and the circular plate. The linear static stability equation system is the partial differential equation system with functional coefficient. This coefficient has infinite value at the the apex of cone and center of the circular plate. Therefore, the integrals that need to be computed during the resulting process are the singular integrals. The problem is that preselected solution must be appropriate, to satisfy the boundary condition and the singular integrals are converged and computed. This paper introduces the form of a preselected solution responsing such requirements. With the preselected solution, we can solve the linear static stability problem of the conical shells subjected to uniformly distributed load, including foundation effects, based on the Pasternak foundation model with two parameters on the elastic foundations. The linear static stability equation describing the proximity equilibrium state has been established, therefore the critical load has been found. The effect of material parameters and other parameters on the critical load was investigated.**

Keywords: **conical *shell*, preselected solution, linear static stability equation, singular integrals.**

I. INTRODUCTIONS

The linear static stability problem of the conical shell made of different materials, subjected to different mechanical - thermal load, is a problem that scientists are interested in researching. But most of the publications until now have selected the truncated conical shells or the circular plate as the studied subjects, because choosing the conical shell or the circular plate as the research object have met many difficulties in the process of solving. The following evidences will prove that.

A finite element formulation based on first order shear deformation theory was used to study the thermal buckling and vibration behavior of truncated functionally graded materials (FGM) conical shells in a high - temperature environment, presented in [1, 2].

A linear buckling analysis was presented for nano composite truncated conical shells reinforced with single walled carbon nanotubes subjected to lateral thermal pressure, seen in [3, 4].

The vibration and stability analyses were presented for axially compressed three - layered truncated conical shells with a functionally graded middle layer surrounded by elastic media. The governing equations were solved by using the Galerkin method, seen in [5, 6]. An improved high - order theory was presented for temperature - dependent buckling analysis of sandwich conical shell with thin functionally graded face sheets and homogenous soft core, studied in [7, 8].

The buckling of thin truncated conical shells made of functionally graded materials with simply supported boundary conditions subjected to hydrostatic pressure was investigated by using Galerkin method, these equations were transformed to pairs of time - dependent differential equations and then hydrostatic buckling pressure expression was obtained, seen in [9, 10]; subjected to axial compressive load and resting on Winkler - Pasternak foundations [11, 12].

Nonlinear buckling of an FGM truncated conical shell surrounded by an elastic medium, presented in [13].

The result of an investigation on the buckling of functionally graded truncated conical shells under axial load resting on elastic foundations within the third order shear deformation theory could be seen in [14, 15]; under nonlinear temperature rise across the thickness in the framework could be seen in [16].

The thermo mechanical instability of truncated conical shells made of functionally graded material under different uniform temperature rises was studied in [17]; reinforced by eccentrically functionally graded stiffeners was analyzed in [18, 19];

An investigation on mechanical buckling of FGM truncated conical shells reinforced by orthogonal stiffeners based on FSDT was analyzed in [20, 21]; The thermal and mechanical stability of a functionally graded composite truncated conical shell reinforced by carbon nanotube fibers and surrounded by the elastic foundations were studied by using Galerkin method, therefore the closed form expression for determining the linear thermal and mechanical buckling load was obtained, seen in [22, 23].

In the linear static stability equation system of the conical shells and the circular plate with functional coefficient, the functional coefficient has infinite value at the the apex of cone and center of the circular plate. Therefore, studying the stability of the conical shells is more difficult and complicated than of the truncated conical shells.

The purpose of this study is to establish and solve the problem of the linear static stability of the conical shells and circular plates, to propose a preselected solution that satisfies the boundary conditions and the singular integrals encountered during the solution process are converged and calculated. The linear static stability problem is solved for the conical shells, the truncated conical shells.

II. PROBLEM STATEMENT

A. Functionally Graded Material (FGM)

Functionally graded material (FGM) has elastic modulus and variable density according to the law:

$$E(z)=E_mV_m+E_cV_c=E_m+(E_m\text{-}E_c)\left(\frac{2z+h}{2h}\right)^{k_0}$$

$$\rho(z)=\rho_mV_m+\rho_cV_c=\rho_m+(\rho_m\text{-}\rho_c)\left(\frac{2z+h}{2h}\right)^{k_0}$$

$$\nu(z)=\nu=const,\; k_0\geq 0$$

The FGM normally consists of ceramic and metal materials for which each respective fraction volume (k_0) is selected reasonably and continuously from side to side. The FGM structure avoids from the formation of concentrate stresses at the interface between material layers, the formation splitting and cracks in the material microstructure. FGM therefore usually has high strength and high thermal resistance. In practice, FGM can be used in rocket shells and space structures. It can also be used in tank shells for civil structures. Above expressions for the Young modulus and mass density of elastic material such as steel or reinforced concrete when: $E_m = E_c = E,\ \rho_m = \rho_c = \rho$

in which:

E Young modulus of steel or reinforced concrete,

ρ mass density of steel or reinforced concrete.

Thus, the conical shells made of FGM is generalized, the case of the conical shells made of steel or reinforced concrete can be inferred.

B. The Conical Shell Model

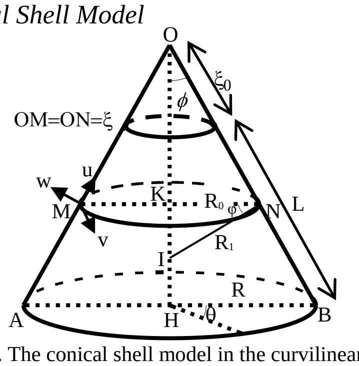

Figure 1. The conical shell model in the curvilinear coordinate

$R_0=KN$ distance from generator to the OH axis;

$R_1 = IN$ in which IN perpendicular with OB and create with KN an angle is φ;

$R_0 = \xi\sin\phi;$

$R_1 = R_0/\cos\varphi = \xi\sin\phi/\cos\varphi;$

ϕ semi vertex angle;

w displacement in the direction that is perpendicular to the generator;

u displacement in the generatrix direction;

v displacement in the direction that is tangent to MN arc.

For conical shells: $\phi=\varphi,\ \xi_0=0,\ 0\leq\xi\leq L.$

For truncated conical shells:

$\phi=\varphi,\ \xi_0\neq 0,\ \xi_0\leq\xi\leq\xi_0+L.$

C. The Strain - Displacement Relations [10]

$$\left.\begin{aligned}
\varepsilon_\xi^0 &= \frac{\partial u}{\partial\xi}+\frac{1}{2}\left(\frac{\partial \mathrm{w}}{\partial\xi}\right)^2\\
\varepsilon_\theta^0 &= \frac{1}{\xi\sin\phi}\frac{\partial v}{\partial\theta}+\frac{u}{\xi}+\frac{\mathrm{w}}{\xi}\frac{\cos\varphi}{\sin\phi}+\frac{1}{2\xi^2\sin^2\phi}\left(\frac{\partial \mathrm{w}}{\partial\theta}\right)^2\\
\gamma_{\xi\theta}^0 &= \frac{1}{\xi\sin\phi}\frac{\partial u}{\partial\theta}+\frac{\partial v}{\partial\xi}-\frac{v}{\xi}+\frac{1}{\xi\sin\phi}\frac{\partial \mathrm{w}}{\partial\xi}\frac{\partial \mathrm{w}}{\partial\theta}
\end{aligned}\right\}\quad(1)$$

where $\varepsilon_\xi^0,\varepsilon_\theta^0$ are the normal strains and $\gamma_{\xi\theta}^0$ is the shear strain at the middle surface of the shell, respectively.

$$\left.\begin{aligned}
\chi_\xi &= \frac{\partial^2 w}{\partial\xi^2}\\
\chi_\theta &= \frac{1}{\xi^2\sin^2\phi}\frac{\partial^2 w}{\partial\theta^2}+\frac{1}{\xi}\left(\frac{\partial \mathrm{w}}{\partial\xi}\right)\\
\chi_{\xi\theta} &= \frac{1}{\xi\sin\phi}\frac{\partial^2 w}{\partial\xi\partial\theta}-\frac{1}{\xi^2\sin\phi}\frac{\partial \mathrm{w}}{\partial\theta}
\end{aligned}\right\}\quad(2)$$

where χ_ξ , χ_θ and $\chi_{\xi\theta}$ are bending and twisting curvatures with respect to the u- and v-axes, respectively.

D. The Equilibrium Equation [18]

$$\xi\frac{\partial N_\xi}{\partial\xi}+\frac{1}{\sin\phi}\frac{\partial N_{\xi\theta}}{\partial\theta}+N_\xi-N_\theta=0\quad(3)$$

$$\frac{1}{\sin\phi}\frac{\partial N_\theta}{\partial\theta}+\xi\frac{\partial N_{\xi\theta}}{\partial\xi}+2N_{\xi\theta}=0\quad(4)$$

$$\begin{aligned}
&\frac{\partial^2 M_\xi}{\partial\xi^2}+\frac{2}{\xi\sin\phi}\frac{\partial M_{\xi\theta}}{\partial\xi\partial\theta}+\frac{1}{\xi^2\sin^2\phi}\frac{\partial^2 M_\theta}{\partial\theta^2}+\frac{2}{\xi}\frac{\partial M_\xi}{\partial\xi}\\
&-\frac{1}{\xi}\frac{\partial M_\theta}{\partial\xi}+\frac{2}{\xi^2\sin\phi}\frac{\partial M_{\xi\theta}}{\partial\theta}-\frac{1}{\xi}N_\theta\frac{\cos\varphi}{\sin\phi}+N_\xi\chi_\xi+2N_{\xi\theta}\chi_{\xi\theta}\quad(5)\\
&+N_\theta\chi_\theta-K_1w+K_2\left(\frac{\partial^2 w}{\partial^2\xi}+\frac{1}{\xi}\frac{\partial w}{\partial\xi}+\frac{1}{\xi^2\sin^2\phi}\frac{\partial^2 w}{\partial\theta^2}\right)-q=0
\end{aligned}$$

in which:

K_1 (N/m^3) is the Winkler foundation stiffness and K_2 (N/m) is the shear subgrade modulus of the Pasternak foundation model;

N_i, N_{ij}, M_i, M_{ij} are the force resultants and moment resultants, respectively.

E. The Force Resultants and Moment Resultants of The Conical Shells Calculated according to The Strains

$$\left.\begin{aligned} N_\xi &= \frac{E_1}{1-v^2}(\varepsilon_\xi^0 + v\varepsilon_\theta^0) - \frac{E_2}{1-v^2}(\chi_\xi + v\chi_\theta) \\ N_\theta &= \frac{E_1}{1-v^2}(\varepsilon_\theta^0 + v\varepsilon_\xi^0) - \frac{E_2}{1-v^2}(\chi_\theta + v\chi_\xi) \\ N_{\xi\theta} &= \frac{E_1}{2(1+v)}\gamma_{\xi\theta}^0 - \frac{E_2}{1+v}\chi_{\xi\theta} \end{aligned}\right\} \tag{6}$$

$$\left.\begin{aligned} M_\xi &= \frac{E_2}{1-v^2}(\varepsilon_\xi^0 + v\varepsilon_\theta^0) - \frac{E_3}{1-v^2}(\chi_\xi + v\chi_\theta) \\ M_\theta &= \frac{E_2}{1-v^2}(\varepsilon_\theta^0 + v\varepsilon_\xi^0) - \frac{E_3}{1-v^2}(\chi_\theta + v\chi_\xi) \\ M_{\xi\theta} &= \frac{E_2}{2(1+v)}\gamma_{\xi\theta}^0 - \frac{E_3}{1+v}\chi_{\xi\theta} \end{aligned}\right\} \tag{7}$$

in which:

$$\left(E_1, E_2, E_3\right) = \int_{-h/2}^{h/2} E\left(z\right)\left(1, z, z^2\right) dz .$$

F. The Membrane State

The conical shells problem is a symmetric problem, in the membrane state the terms do not depend on the angle θ.

$$N_\xi^0 \neq 0,\ N_\theta^0 \neq 0,\ N_{\xi\theta}^0 = 0,\ w^0 = 0$$

$$M_\xi^0 = M_\theta^0 = M_{\xi\theta}^0 = 0$$

In the membrane state Eq. (4) satisfies itself, Eqs. (3), (5) leads to two equations for determining the membrane force N_ξ^0, N_θ^0.

$$\xi\frac{\partial N_\xi^0}{\partial \xi} + N_\xi^0 - N_\theta^0 = 0 \tag{8}$$

$$-\frac{1}{\xi}N_\theta^o\frac{\cos\varphi}{\sin\phi} - q = 0 \tag{9}$$

Solving the system of Eqs. (8), (9) with q=*constant* find:

$$N_\xi^0 = -\frac{1}{2}q\xi\frac{\sin\phi}{\cos\varphi} \tag{10}$$

$$N_\theta^0 = -q\xi\frac{\sin\phi}{\cos\varphi} \tag{11}$$

G. The Linear Static Stability Equation

For static stability analysis of the conical shells, uses the proximity equilibrium standard to linearize the nonlinear relations of the conical shells. Suppose under the external forces, the conical shells is in the fundamental equilibrium state (membrane state) determined by the displacement field: u^0, v^0, w^0 and the force resultants of the conical shells N_i^0, the moment resultants M_i^o, M_{ij}^o in which $i = \xi,\ ij = \xi\theta$ when the buckling, the conical shell changes to the proximity equilibrium that determined by the displacement field:

$$u = u^0 + u^1$$
$$v = v^0 + v^1$$
$$w = w^0 + w^1$$

With the corresponding force resultants and moment resultants:

$$N_\xi = N_\xi^0 + N_\xi^1,\ N_\theta = N_\theta^0 + N_\theta^1,\ N_{\xi\theta} = N_{\xi\theta}^0 + N_{\xi\theta}^1$$

$$M_\xi = M_\xi^0 + M_\xi^1,\ M_\theta = M_\theta^0 + M_\theta^1,\ M_{\xi\theta} = M_{\xi\theta}^0 + M_{\xi\theta}^1$$

in which:

u^1, v^1, w^1 infinitesimal incremental displacements,

N_i^1, M_i^1, M_{ij}^1 incremental force resultants and moment resultants corresponding to u^1, v^1, w^1.

The linear static stability equation system is obtained as follows:

$$A \equiv \xi\frac{\partial N_\xi^1}{\partial\xi} + \frac{1}{\sin\phi}\frac{\partial N_{\xi\theta}^1}{\partial\theta} + N_\xi^1 - N_\theta^1 = 0 \tag{12}$$

$$B \equiv \frac{1}{\sin\phi}\frac{\partial N_\theta^1}{\partial\theta} + \xi\frac{\partial N_{\xi\theta}^1}{\partial\xi} + 2N_{\xi\theta}^1 = 0 \tag{13}$$

$$\begin{aligned} C \equiv\ & \frac{\partial^2 M_\xi^1}{\partial\xi^2} + \frac{2}{\xi\sin\phi}\frac{\partial^2 M_{\xi\theta}^1}{\partial\xi\partial\theta} + \frac{1}{\xi^2\sin^2\phi}\frac{\partial^2 M_\theta^1}{\partial\theta^2} + \frac{2}{\xi}\frac{\partial M_\xi^1}{\partial\xi} \\ & -\frac{1}{\xi}\frac{\partial M_\theta^1}{\partial\xi} + \frac{2}{\xi^2\sin\phi}\frac{\partial M_{\xi\theta}^1}{\partial\theta} - \frac{1}{\xi}N_\theta^1\frac{\cos\varphi}{\sin\phi} + N_\xi^0\frac{\partial^2 w^1}{\partial^2\xi} \\ & +\frac{1}{\xi}N_\theta^0\frac{\partial w^1}{\partial\xi} + N_\theta^0\frac{1}{\xi^2\sin^2\phi}\frac{\partial^2 w^1}{\partial\theta^2} - K_1 w^1 \\ & +K_2\left(\frac{\partial^2 w^1}{\partial^2\xi} + \frac{1}{\xi}\frac{\partial w^1}{\partial\xi} + \frac{1}{\xi^2\sin^2\phi}\frac{\partial^2 w^1}{\partial\theta^2}\right) = 0 \end{aligned} \tag{14}$$

The linear relation between the incremental strains and the incremental displacements:

$$\left.\begin{aligned} \varepsilon_\xi^1 &= \frac{\partial u^1}{\partial\xi} \\ \varepsilon_\theta^1 &= \frac{1}{\xi\sin\phi}\frac{\partial v^1}{\partial\theta} + \frac{u^1}{\xi} + \frac{w^1}{\xi}\frac{\cos\varphi}{\sin\phi} \\ \gamma_{\xi\theta}^1 &= \frac{1}{\xi\sin\phi}\frac{\partial u^1}{\partial\theta} + \frac{\partial v^1}{\partial\xi} - \frac{v^1}{\xi} \end{aligned}\right\}$$

$$\left.\begin{aligned}
\chi_{\xi}^{1} &= \frac{\partial^2 w^1}{\partial \xi^2} \\
\chi_{\theta}^{1} &= \frac{1}{\xi^2 \sin^2\phi}\frac{\partial^2 w^1}{\partial \theta^2} + \frac{1}{\xi}\left(\frac{\partial w^1}{\partial \xi}\right) \\
\chi_{\xi\theta}^{1} &= \frac{1}{\xi\sin\phi}\frac{\partial^2 w^1}{\partial \xi \partial \theta} - \frac{1}{\xi^2\sin\phi}\frac{\partial w^1}{\partial \theta}
\end{aligned}\right\}$$

The relation between the incremental force resultants, moment resultants and the incremental strains:

$$\left.\begin{aligned}
N_{\xi}^{1} &= \frac{E_1}{1-\nu^2}(\varepsilon_{\xi}^{1} + \nu\varepsilon_{\theta}^{1}) - \frac{E_2}{1-\nu^2}(\chi_{\xi}^{1} + \nu\chi_{\theta}^{1}) \\
N_{\theta}^{1} &= \frac{E_1}{1-\nu^2}(\varepsilon_{\theta}^{1} + \nu\varepsilon_{\xi}^{1}) - \frac{E_2}{1-\nu^2}(\chi_{\theta}^{1} + \nu\chi_{\xi}^{1}) \\
N_{\xi\theta}^{1} &= \frac{E_1}{2(1+\nu)}\gamma_{\xi\theta}^{1} - \frac{E_2}{1+\nu}\chi_{\xi\theta}^{1}
\end{aligned}\right\}$$

$$\left.\begin{aligned}
M_{\xi}^{1} &= \frac{E_2}{1-\nu^2}(\varepsilon_{\xi}^{1} + \nu\varepsilon_{\theta}^{1}) - \frac{E_3}{1-\nu^2}(\chi_{\xi}^{1} + \nu\chi_{\theta}^{1}) \\
M_{\theta}^{1} &= \frac{E_2}{1-\nu^2}(\varepsilon_{\theta}^{1} + \nu\varepsilon_{\xi}^{1}) - \frac{E_3}{1-\nu^2}(\chi_{\theta}^{1} + \nu\chi_{\xi}^{1}) \\
M_{\xi\theta}^{1} &= \frac{E_2}{2(1+\nu)}\gamma_{\xi\theta}^{1} - \frac{E_3}{1+\nu}\chi_{\xi\theta}^{1}
\end{aligned}\right\}$$

H. The Boundary Condition

$$\frac{\partial \mathrm{w}}{\partial \xi},\ w = 0 \ \text{when}\ \xi = \xi_o,\ \xi = \xi_o + L \tag{15}$$

K. The Form of Preselected Solution

$$\left.\begin{aligned}
u^1 &= U\sin\left[\frac{m\pi(\xi - \xi_0)}{L}\right]\cos\frac{n\theta}{2} \\
v^1 &= V\sin\left[\frac{m\pi(\xi - \xi_0)}{L}\right]\sin\frac{n\theta}{2} \\
w^1 &= W\sin^2\left[\frac{m\pi(\xi - \xi_0)}{L}\right]\cos\frac{n\theta}{2}
\end{aligned}\right\} \tag{16}$$

With the preselected solution (16) we have:

$$u^1 = v^1 = w^1 = 0;\ \frac{\partial w^1}{\partial \xi} = 0 \quad \text{when} \quad \xi = \xi_o;\ \xi = \xi_o + L$$

From that inferred:

$$w = 0,\ \frac{\partial w}{\partial \xi} = 0 \quad \text{when} \quad \xi = \xi_o,\ \xi = \xi_o + L$$

Because in the membrane state $w^0 = 0$ and so the boundary condition (15) is satisfied.

III. THE RESULTING METHOD

Substituting Eq. (1), (2) into Eq. (6), (7), with incremental displacements u^1, v^1, w^1 just take into account the linear terms. Found $N_{\xi}^{1},\ N_{\theta}^{1},\ N_{\xi\theta}^{1},\ M_{\xi}^{1},\ M_{\nu}^{1},\ M_{\xi\theta}^{1}$ then substituting these terms into Eqs. (12), (13), (14) we get the equation system with three unknowns *U, V, W*.

$$\left.\begin{aligned}
&\int_0^{2\pi}\int_{\xi_0}^{\xi_0+L} A\sin\left[\frac{m\pi(\xi - \xi_0)}{L}\right]\cos\frac{n\theta}{2}\,d\xi d\theta = 0 \\
&\int_0^{2\pi}\int_{\xi_0}^{\xi_0+L} B\sin\left[\frac{m\pi(\xi - \xi_0)}{L}\right]\sin\frac{n\theta}{2}\,d\xi d\theta = 0 \\
&\int_0^{2\pi}\int_{\xi_0}^{\xi_0+L} A\sin^2\left[\frac{m\pi(\xi - \xi_0)}{L}\right]\cos\frac{n\theta}{2}\,d\xi d\theta = 0
\end{aligned}\right\} \tag{17}$$

In which *A, B, C* are the left - hand side of Eqs. (12), (13), (14) after substituting u^1, v^1, w^1 that calculated according to Eq. (16). Integral coefficients, Eq. (17) has the form:

$$\begin{cases}
a_{11}U + a_{12}V + a_{13}W = 0 \\
b_{11}U + b_{12}V + b_{13}W = 0 \\
c_{11}U + c_{12}V + c_{13}W = 0
\end{cases} \tag{18}$$

Coefficient a_{ij}, b_{ij}, c_{ij} that were calculated numerically from non - primitive singular integrals. To *u, v, w* is not trivial solution, the determinant of the coefficients of Eq. (18) must be zero.

$$\begin{vmatrix} a_{11} & a_{12} & a_{13} \\ b_{11} & b_{12} & b_{13} \\ c_{11} & c_{12} & c_{13} \end{vmatrix} = 0 \tag{19}$$

Solving the Eq. (19) we find $q_{critical}$.

Researching the static stability of conical shells by analytical method has the following difficulties:

-The fundamental relations and the static stability equations in proximity state that were set up in curvilinear coordinate and it's coefficient is the function of the coordinate.

-By applying the Galerkin method, the integrals are non - primitive singular integrals, therefore, numerical integration must be calculated by applying the Mathematica 7.0 software.

The above has introduced in principle to establish the resulting equations. In fact, establishing the resulting equation is quite complex. First of all, the explicit formulas of the strains $\varepsilon_{ij}\left(i, j = \varphi, \theta\right)$ and their derivatives $\partial\varepsilon_{ij}/\partial\varphi,\ \partial\varepsilon_{ij}/\partial\theta\ \left(i, j = \varphi, \theta\right)$ according to the form of functions at the Eq. (16) need to be established. Based on that, the explicit formulas of the force resultants and moment resultant N_{ij}, $M_{ij}\left(i, j = \varphi, \theta\right)$ and their derivatives according to the form of functions expressed by Eq. (16) can be established.

IV. EXAMPLES

A. Example 1: Effect of The Form on The Linear Static Stability of The FGM Conical Shells, FGM Truncated Conical Shells

Case 1: Investigation on the linear static stability of the conical shells made of FGM, bottom radius *R*=5m, generatrix length 15m, thickness of shell *h*, semi vertex angle ϕ; rest on Pasternak foundation model with two parameters: $K_1=184.10^6\ N/m^3$;$K_2=19.10^6\ N/m$

Other parameters:

$k_0=9$; $\nu=0,3$;$n=2$;$m=3$;$E_m=70.10^9 N/m^2$;$E_c=380.10^9 N/m^2$;

$h=0,025$m.

From the bottom radius and the generatrix length we calculated: $\phi=\varphi=0,339837$; $\xi_0=0$; $0\le\xi\le15$

With the above data, applying Mathematica 7.0 to calculate the coefficients of the linear static stability Eq. (18) we obtain:

$-8,18635.10^7u-1,97584.10^7v+2,61894.10^6w=0$

$1,63434.10^7u-6,49045.10^7v-6,83796.10^6w=0$

$-4,57619.10^6u-1,24155.10^7v-1,15145.10^9w+7,84674qw=0$

To *u, v, w* is not trivial solution, the determinant of the coefficients of Eq. (18) must be zero. From that calculation $q_{critical}=1,46629.10^8$

Case 2: Investigation on the linear static stability of the truncated conical shells made of FGM, bottom radius *R*=5m, generatrix length 10m, the distance according to generator from the apex of cone to the above bottom is 5m, thickness of shell *h*, semi vertex angle ϕ; rest on Pasternak foundation model with two parameters:

$K_1=184.10^6\ N/m^3$;$K_2=19.10^6\ N/m$. Other parameters:

$k_0=9$; $\nu=0,3$;$n=2$;$m=3$;$E_m=70.10^9 N/m^2$;$E_c=380.10^9 N/m^2$;

$h=0,025$m.

From the bottom radius and the generatrix length we calculated: $\phi=\varphi=0,339837$; $\xi_0=0$; $0\le\xi\le15$

With the above data, applying Mathematica 7.0 to calculate the coefficients of the linear static stability Eq. (18) we obtain:

$-1,29506.10^8u-6,1202.10^6v+537803w=0$

$5,06239.10^6u-5,65562.10^7v-1,43489.10^6w=0$

$-231526u-621280\ v-8,09031.10^8w+9,14819qw=0$

To *u, v, w* is not trivial solution, the determinant of the coefficients of Eq. (18) must be zero. From that calculation $q_{critical}= 8,84346.10^7$

TABLE I. VALUES $q_{critical}$ IN THE FGM CONICAL SHELLS, FGM TRUNCATED CONICAL SHELLS

The form of shells	Conical shells	Truncated conical shells
The parameters of shells	$\phi=\varphi=0,339837$	$\phi=\varphi=0,339837$
	$\xi_0=0,\ 0\le\xi\le15$	$\xi_0=5,\ 5\le\xi\le15$
$q_{critical}$	$1,46629.10^8$	$8,84346.10^7$

Comments: With the same semi vertex angle and the same FGM material, value $q_{critical}$ descending order to conical shells, truncated conical shells. Thus the conical structure is more stable and durable than the truncated conical ones.

B. Example 2: Effect of The Shape on The Linear Static Stability of The Reinforced Concrete (RC) Conical Shells, RC Truncated Conical Shells

Case 1: Investigation on the linear static stability of the conical shells made of RC, bottom radius *R*=5m, generatrix length 15m, thickness of shell *h*, semi vertex angle ϕ; rest on Pasternak foundation model with two parameters:

$K_1=184.10^6\ N/m^3$;$K_2=19.10^6\ N/m$. Other parameters:

$\nu=0,3$;$n=2$;$m=3$;$E_m=E_c=44.10^9 N/m^2$;

$h=0,08$m.

From the bottom radius and the generatrix length we calculated: $\phi=\varphi=0,339837$; $\xi_0=0$; $0\le\xi\le15$

With the above data, applying Mathematica 7.0 to calculate the coefficients of the linear static stability Eq. (18) we obtain:

$-1,14123.10^8u-2,75444.10^7v+3,73977.10^6w=0$

$2,27837.10^7u-9,04807.10^7v-9,34942.10^6w=0$

$-6,28371.10^6u-1,71374.10^7v-1,1474.10^9w+7,84674qw=0$

To *u, v, w* is not trivial solution, the determinant of the coefficients of Eq. (18) must be zero. From that calculation $q_{critical}=1,46074.10^8$

Case 2: Investigation on the linear static stability of the truncated conical shells made of RC, bottom radius *R*=5m, generatrix length 10m, the distance according to generator from the apex of cone to the above bottom is 5m, thickness of shell h, semi vertex angle ϕ; rest on Pasternak foundation model with two parameters:

$K_1=184.10^6\ N/m^3$;$K_2=19.10^6\ N/m$. Other parameters:

$\nu=0,3$;$n=2$;$m=3$;$E_m=E_c=44.10^9 N/m^2$;

$h=0,08$m.

From the bottom radius and the generatrix length we calculated: $\phi=\varphi=0,339837$; $\xi_0=0$; $0\le\xi\le15$

With the above data, applying Mathematica 7.0 to calculate the coefficients of the linear static stability Eq. (18) we obtain:

$-1,80539.10^8u-8,53193.10^6v+778761w=0$

$7,05728.10^6u-7,88427.10^7v-1,9469.10^6w=0$

$-314945u-858941v-8,0864.10^8w+9,14819qw=0$

To *u, v, w* is not trivial solution, the determinant of the coefficients of Eq. (18) must be zero. From that calculation $q_{critical}=8,83913.10^7$

TABLE II. VALUES $q_{critical}$ IN THE RC CONICAL SHELLS, RC TRUNCATED CONICAL SHELLS

The form of shells	Conical shells	Truncated conical shells
The parameters of shells	$\phi=\varphi=0,339837$	$\phi=\varphi=0,339837$
	$\xi_0=0;\ 0\le\xi\le15$	$\xi_0=5;\ 5\le\xi\le15$
$q_{critical}$	$1,46074.10^8$	$8,83913.10^7$

Comments: With the same semi vertex angle and the same RC material, value $q_{critical}$ descending order to conical shells, truncated conical shells. Comparing parameters, especially is $q_{critical}$ in Example 1 and 2, when the thickness of FGM shell is 0,025m and the thickness of RC shell is 0,08m that the stability and strength of conical shells are same.

C. Example 3: Effect of Semi Vertex Angle on The Linear Static Stability of The FGM Conical Shells

Case 1: Investigation on the linear static stability of the FGM conical shells, bottom radius R=5m, generatrix length 15m, thickness of shell h, semi vertex angle ϕ; rest on Pasternak foundation model with two parameters: $K_1=184.10^6\ N/m^3;K_2=19.10^6\ N/m$. Other parameters:

k_0=9; $\nu = 0,3$; n=2; m=3; E_m=70.10^{9}N/m^2; E_c=380.10^{9}N/m^2;

h=0,025m.

From the bottom radius and the generatrix length we calculated: $\phi = \varphi = 0,339837;\ \xi_0 = 0;\ 0 \le \xi \le 15$

With the above data, applying Mathematica 7.0 to calculate the coefficients of the linear static stability Eq. (18) we obtain:

$-8,18635.10^7u-1,97584.10^7v+2,61894.10^6w=0$

$1,63434.10^7u-6,49045.10^7v-6,83796.10^6w=0$

$-4,5761910^6u-1,24155.10^7v-1,15145.10^9w+7,84674qw=0$

To u, v, w is not trivial solution, the determinant of the coefficients of Eq. (18) must be zero. From that calculation $q_{critical}$=1,46629.10^8

Case 2: Investigation on the linear static stability of the FGM conical shells, bottom radius R=5m, generatrix length 15m, thickness of shell h, semi vertex angle ϕ; rest on Pasternak foundation model with two parameters:

$K_1=184.10^6\ N/m^3;K_2=19.10^6\ N/m$. Other parameters:

k_0=9; $\nu = 0,3$; n=2; m=3; E_m=70.10^{9}N/m^2; E_c=380.10^{9}N/m^2;

h=0,025m.

From the bottom radius and the generatrix length we calculated: $\phi = \varphi = \pi / 6;\ \xi_0 = 0;\ 0 \le \xi \le 15$

With the above data, applying Mathematica 7.0 to calculate the coefficients of the linear static stability Eq. (18) we obtain:

$-7,33259.10^7u-1,31723.10^7v+1,5927.10^6w=0$

$9,75725.10^6u-4,10805.10^7v-4,17113.10^6w=0$

$-4,21897.10^6u-7,62026.10^6v-8,26481.10^8w+9,25636qw=0$

To u, v, w is not trivial solution, the determinant of the coefficients of Eq. (18) must be zero. From that calculation $q_{critical}$=8,92293.10^7

Case 3: Investigation on the linear static stability of the FGM conical shells, bottom radius R=5m, generatrix length 15m, thickness of shell h, semi vertex angle ϕ; rest on Pasternak foundation model with two parameters:

K_1=184.10^{6}N/m^3; K_2=19.10^{6}N/m. Other parameters:

k_0=9; $\nu = 0,3$; n=2; m=3; E_m=70.10^{9}N/m^2; E_c=380.10^{9}N/m^2;

h=0,025m.

From the bottom radius and the generatrix length we calculated: $\phi = \varphi = \pi / 3;\ \xi_0 = 0;\ 0 \le \xi \le 15$

With the above data, applying Mathematica 7.0 to calculate the coefficients of the linear static stability Eq. (18) we obtain:

$-6,87726.10^7u-7,60502.10^6v+502868w=0$

$4,18999.10^6u-2,93209.10^7v-1,39912.10^6w=0$

$-2,50458.10^6u-2,58489.10^6v-6,09662.10^8w+22,0773qw=0$

To u, v, w is not trivial solution, the determinant of the coefficients of Eq. (18) must be zero. From that calculation $q_{critical}$=2,76109.10^7

TABLE III. VALUES $q_{critical}$ IN THE FGM CONICAL SHELLS THAT CHANGE THE SEMI VERTEX ANGLE ϕ

The semi vertex angle	$\phi = 0,339837$	$\phi = \pi / 6$	$\phi = \pi / 3$
$q_{critical}$	1,46629.10^8	8,92293.10^7	2,76109.10^7

Comments: With the same FGM material, when the semi vertex angle increases then values $q_{critical}$ decreases.

D. Example 4: Effect of Elastic Foundations on The Linear Static Stability of The RC Conical Shells

Case 1: Investigation on the linear static stability of the RC conical shells, bottom radius R=5m, generatrix length 10m, thickness of shell h, semi vertex angle ϕ; rest on Pasternak foundation model with two parameters: K_1=184.10^{6}N/m^3; K_2=19.10^{6}N/m. Other parameters:

$\nu = 0,3$; n=2; m=3; E_m=E_c=44.10^{9}N/m^2;

h=0,08m.

From the bottom radius and the generatrix length we calculated: $\phi = \varphi = \pi / 6;\ \xi_0 = 0;\ 0 \le \xi \le 15$

With the above data, applying Mathematica 7.0 to calculate the coefficients of the linear static stability Eq. (18) we obtain:

$-1,02221.10^8u-1,8363.10^7v+2,29013.10^6w =0$

$1,36022.10^7u-5,72687.10^7v-5,72533.10^6w =0$

$-5,77196.10^6u-1,04945.10^7v-8,24221.10^8w+9,25636qw=0$

To u, v, w is not trivial solution, the determinant of the coefficients of Eq. (18) must be zero. From that calculation $q_{critical}$=8,89651.10^7

Case 2: Investigation on the linear static stability of the RC conical shells, bottom radius R=5m, generatrix length 10m, thickness of shell h, semi vertex angle ϕ; rest on Pasternak foundation model with two parameters:

K_1=10^{7}N/m^3; K_2=2.10^{5}N/m. Other parameters:

$\nu = 0,3$; n=2; m=3; E_m=E_c=44.10^{9}N/m^2;

h=0,08m.

From the bottom radius and the generatrix length we calculated: $\phi = \varphi = \pi / 6;\ \xi_0 = 0;\ 0 \le \xi \le 15$

With the above data, applying Mathematica 7.0 to calculate the coefficients of the linear static stability Eq. (18) we obtain:

-1,02221.10^{8}u-1,8363.10^{7}v+2,29013.10^{6}w =0

1,36022.10^{7}u-5,72687.10^{7}v-5,72533.10^{6}w =0

-5,77196.10^{6}u-1,04945.10^{7}v-3,08883.10^{7}w+9,25636qw =0

To *u, v, w* is not trivial solution, the determinant of the coefficients of Eq. (18) must be zero. From that calculation $q_{critical}$=3,25821.10^6

Case 3: Investigation on the linear static stability of the RC conical shells, bottom radius *R*=5m, generatrix length 10m, thickness of shell *h*, semi vertex angle ϕ; rest on Pasternak foundation model with two parameters:

K_1=5.10^{5}N/m^3;K_2=3.10^{4}N/m. Other parameters:

$\nu = 0,3$;*n*=2;*m*=3;E_m=E_c=44.10^{9}N/m^2;

h=0,08m.

From the bottom radius and the generatrix length we calculated: $\phi = \varphi = \pi / 6;\ \xi_0 = 0;\ 0 \le \xi \le 15$

With the above data, applying Mathematica 7.0 to calculate the coefficients of the linear static stability Eq. (18) we obtain:

-1,02221.10^{8}u-1,8363.10^{7}v+2,29013.10^{6}w =0

1,36022.10^{7}u-5,72687.10^{7}v-5,72533.10^{6}w =0

-5,77196.10^{6}u-1,04945.10^{7}v+6,01015.10^{6}w+9,25636qw =0

To *u, v, w* is not trivial solution, the determinant of the coefficients of Eq. (18) must be zero. From that calculation $q_{critical}$ =-728082

TABLE IV. VALUES $q_{critical}$ IN THE RC CONICAL SHELLS THAT CHANGE THE PARAMETERS K_1, K_2

The parameters	K_1=184.10^{6}N/m^3 K_2=19.10^{6}N/m	K_1=10^{7}N/m^3 K_2=2.10^{5}N/m	K_1=5.10^{5}N/m^3 K_2=3.10^{4}N/m
$q_{critical}$	8,89651.10^7	3,25821.10^6	-728082

Comments: With the same RC material, when the foundation parameters decreases then value $q_{critical}$ decreases, even reduced to the value $q_{critical}$<0, that time the conical shells were buckling due to the earth pressure.

V. CONCLUSIONS

Based on the content and the results of the study, some conclusions can be represented:

- Establishing the linear static stability equation system by displacements of the conical shells. Based on this equation system, the conical shells and truncated conical shells problem can be solved.

- Proposing the form of function (16) satisfying the clamped boundary condition and ensuring that the singular integrals can be converged and numerically solved.

- Solving the linear static stability problem of the structures with singular points. Finding the critical loads in the cases: the FGM shells, the RC shells, changed the semi vertex angle for FGM conical shells and changed the foundation parameters for RC conical shells. Thereby the technical signification comments are derived.

REFERENCES

[1] R.Bhangale, N.Ganesan and C.Padmanabhan, "Linear thermo elastic buckling and free vibration behavior of functionally graded truncated conical shells", Journal of Sound and Vibration 292(1), pp. 341-371, 2006.

[2] R.Naj, M.S.Boroujerdy and M.R.Eslami, "Thermal and mechanical instability of functionally graded truncated conical shells", Thin-Walled Structures 46(1), pp. 65-78, 2008.

[3] J.E.Jam and Y.Kiani, "Buckling of pressurized functionally graded carbon nanotube reinforced conical shells," Compos. Struct., Vol.25, pp. 586-595, 2015.

[4] M.Mirzaei and Y.Kiani, "Thermal buckling of temperature dependent FG-CNT reinforced composite conical shells", Aerospace Science and Technology 47(9), pp. 42-53, 2015.

[5] A.Najafov, A.Sofiyev, P.Ozyigit and K.T.Yucel, "Vibration and stability of axially compressed truncated conical shells with functionally graded middle layer surrounded by elastic medium", Journal of Vibration and Control 20(2), pp. 303-320, 2012.

[6] A.H.Sofiyev, Z.Zerin and A.Korkmaz, "The stability of a thin three-layered composite truncated conical shell containing an FGM layer subjected to non-uniform lateral pressure", Composite Structures 85(2), pp. 105-115, 2008.

[7] A.Deniz, "Non-linear stability analysis of truncated conical shell with functionally graded composite coatings in the finite deflection", Composites: Part B 51, pp. 318-326, 2013.

[8] J.Seidi, S.M.R.Khalili and K.Malekzadeh, "Temperature-dependent buckling analysis of sandwich truncated conical shells with FG face sheets", Composite Structures 131, pp. 682-691, 2015.

[9] A.H.Sofiyev, "The vibration and stability behavior of freely supported FGM conical shells subjected to external pressure", Composite Structures 89, pp. 356-366, 2009.

[10] A.H.Sofiyev, N.Kuruoglu and M.Turkmen, "Buckling of FGM hybrid truncated conical shells subjected to hydrostatic pressure", Thin Walled Structures 47(1), pp. 61-72, 2009.

[11] A.H.Sofiyev, "Thermoelastic stability of functionally graded truncated conical shells", Journal of Composite Structures 77(1), pp. 56-65, 2007.

[12] A.H.Sofiyev, "The buckling of FGM truncated conical shells subjected to axial compressive load and resting on Winkler-Pasternak foundations", International Journal of Pressure Vessels and Piping 87, pp. 753-761, 2010.

[13] A.H.Sofiyev and N.Kuruoglu, "Nonlinear buckling of an FGM truncated conical shell surrounded by an elastic medium", International Journal of Pressure Vessels and Piping 107, pp. 38-49, 2013.

[14] A.H.Sofiyev, F.Kadioglu and N.Kuruoglu, "Influences of elastic foundations and shear deformations on the buckling behavior of FGM truncated conical shells under axial compression", Mechanics of Advanced Materials and Structures 24(16), pp. 01-14, 2016.

[15] A.H.Sofiyev and N.Kuruoglu, "Combined effects of elastic foundations and shear stresses on the stability behavior of functionally graded truncated conical shells subjected to uniform external pressures", Thin-Walled Structures 102, pp. 68-79, 2016.

[16] A.H.Sofiyev, Z.Zerin and N.Kuruoglu, "Thermoelastic buckling of FGM conical shells under non-linear temperature rise in the framework of the shear deformation theory", Composites Part B Engineering 108, pp. 279-290, 2017.

[17] DH.Bich, N.T.Phuong and H.V.Tung, "Buckling of functionally graded conical panels under mechanical loads", Composite Structures 94(4), pp. 1379-1384, 2012.

[18] D.V.Dung, L.K.Hoa and N.T.Nga, "On the stability of functionally graded truncated conical shells reinforced by functionally graded stiffeners and surrounded by an elastic medium", Composite Structures 108, pp. 77-90, 2014.

[19] D.V.Dung, L.K.Hoa, N.T.Nga and L.T.N.Anh, "Instability of eccentrically stiffened functionally graded truncated conical shells under mechanical loads", Composite Structures, Vol.106, pp. 104-113, 2013.

[20] D.V.Dung and D.Q.Chan, "Analytical investigation on mechanical buckling of FGM truncated conical shells reinforced by orthogonal stiffeners based on FSDT", Composite Structures 159, pp. 827-841, 2016.

[21] D.V.Dung, B.Hoai and L.K.Hoa, "Post buckling nonlinear analysis of FGM truncated conical shells reinforced by orthogonal stiffeners

resting on elastic foundations", Acta Mechanica 228(4), pp. 1457-1479, 2017.

[22] N.D.Duc, P.H.Cong, N.D.Tuan, P.Tran and N.V.Thanh, "Thermal and mechanical stability of functionally graded carbon nanotubes (FG CNT)-reinforced composite truncated conical shells surrounded by the elastic foundations", Thin-Walled Structures, Vol.115, pp. 300-310, 2017.

[23] N.D.Duc, P.H.Cong, V.M.Anh, V.D.Quang, P.Tran, N.D.Tuan and N.H.Thinh, "Mechanical and thermal stability of eccentrically stiffened functionally graded conical shell panels resting on elastic foundations and in thermal environment", J. Composite Structures, Vol.132, pp. 597-609, 2015.

The 6th International Conference on
Engineering Mechanics and Automation (ICEMA 2021)
Hanoi, November 14, 2021

Self-Supervised Depth Estimation with Vision Transformer

Xuan-Quang Ma
Vingroup AI Engineer Training Program
Vingroup Big Data Institute
Hanoi, Vietnam.

Van-Tinh Nguyen
School of Mechanical Engineering
Hanoi University of Science and Technology
Hanoi, Vietnam.
Email: tinh.nguyenvan@hust.edu.vn

***Abstract*: While convolutional neural network can extract local features of image, Vision Transformer can process global features. In this work, we propose to apply self-supervised monocular depth estimation pipeline to train a network composes of Vision Transformer, which integrates local features and global features of input image to improve quality of predicted depth map. In addition, we propose a method of choosing loss weights in multi components self-supervised loss to improve the performance of depth prediction. Our work achieves a competitive result among other self-supervised depth estimation methods. Our code is available at: https://github.com/maxuanquang/SfMLearner-ViT/**

Keywords: Depth estimation, self-supervised, vision transformer, convolutional neural networks, multi-loss balancing.

I. Introduction

Per-pixel depth estimation is a low-level task in computer vision which has application in various fields such as autonomous vehicles [1], augmented reality [2], robotics [3], etc. Deep Learning based Dense Depth Estimators in recent years became successful with the advances in deep neural networks.

Deep Learning based Dense Depth Estimators can be separated into supervised methods and self-supervised methods. For supervised methods, the ground truth label of depth can be collected from LiDAR sensors [4], then images are paired with depth maps become the input for depth estimation network [5]. On the other hand, self-supervised methods integrate depth prediction and ego-motion estimation into a framework and take the supervision signals from view synthesis [6]. Self-supervised methods do not need ground truth for learning depth, the pipeline setting is also simpler compared to supervised methods.

While self-supervised methods have several strengths compared to supervised methods, they still perform worse than supervised methods on benchmark datasets. These weaknesses come from several reasons that violate image reconstruction assumptions such as: there are occluded pixels and pixels that do not satisfy the Lambertian assumption in image pairs; there are pixels belong to moving objects. These pixels inhibit training process and make network output poor quality depth maps. In addition, with normally used photometric reconstruction error, a low error does not guarantee accurate predicted depths and poses. This is because reconstructing pixels in the textureless regions could make loss value low even with inaccurate predictions.

Previous methods [7][8][9][10] use encoder-decoder architecture to predict depth maps on several scales and use smooth loss [11] to force depths propagation from

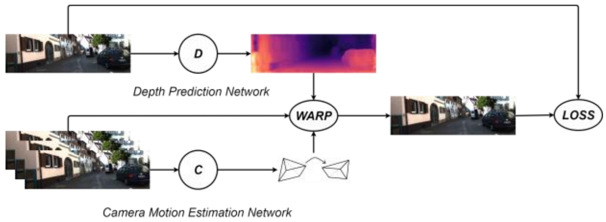

Figure 1. Self-supervised Depth Estimation Pipeline

discriminative regions to textureless regions, which partially solved above problems. However, this propagation has a limited range because convolutional neural network is lack of ability to process global features of image, it can only process global features on low resolution feature maps. We believe that if the depth network can process image's global features at high resolution feature maps, it can reason better about textureless regions as well as regions belong to moving objects and improves performance of depth estimation.

In recent years, Vision Transformer [12] is emerging as a potential approach for many Computer Vision problem as it has a good ability of processing global features of image. AdaBins [13] specified that integrating local features extracted by convolutional neural network and global features processed by Vision Transformer at high resolution feature maps helped increase overall supervised depth estimation framework's performance.

Inspired from the idea of AdaBins [13], we pose the question of integrating local features extracted from CNN encoder-decoder architecture and global features extracted from Vision Transformer in self-supervised depth estimation pipeline. Previous works [13][14] found ways to apply Vision Transformer in supervised setting for problems such as Image Segmentation, Depth Estimation, etc. Self-supervised methods with Vision Transformer has also been researched in [15][16][17] for Image Segmentation, Image Reconstruction,

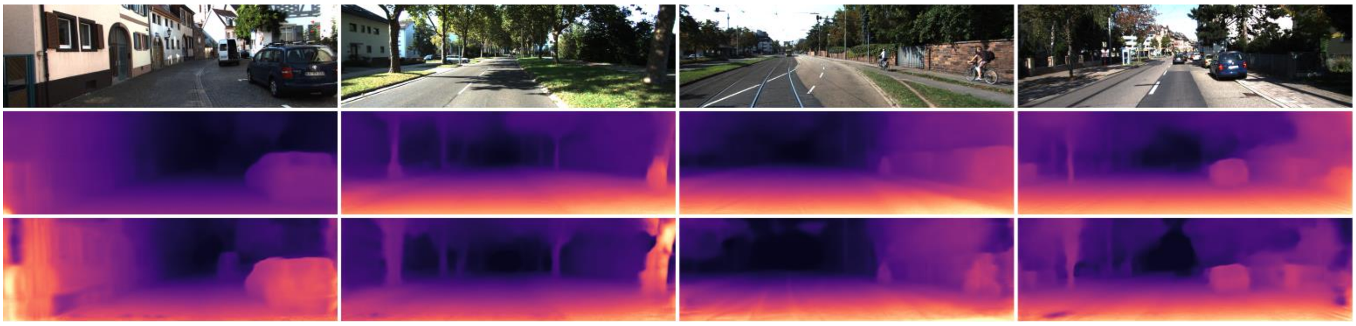

Figure 2. Qualitative comparison between CC [2] (second row) and our method (last row). It can be seen that we achieve better performance on the low-texture regions like walls and finer details are present like silhouette of humans and trees.

etc. To the best of our knowledge there isn't any work had applied Vision Transformer for self-supervised depth estimation. In this work, we propose a self-supervised pipeline that uses convolutional encoder-decoder architecture and Vision Transformer to estimate dense depth map.

In a self-supervised depth estimation pipeline, the loss function usually used composes of multi components e.g. L1-loss, Structural Similarity loss, Smooth loss, etc. Normally the final objective function is a weighted sum of these components [6][7][9]. However, weighting these components is problematic due to several reasons. First, each loss has a different order of magnitudes, which makes some losses suppressed if total loss is not weighted properly. Second, the contribution of each loss to the overall performance is hard to evaluate. Therefore, in this work, we propose a method of choosing loss weights that finds normalized value of each loss component and choose weights based on these normalized values. Extensive experimental results show that our proposed loss weighting method improves the performances of monocular depth estimators meaningfully.

In summary, our main contributions include:

1. A self-supervised depth estimation pipeline is proposed that uses convolutional encoder-decoder architecture and Vision Transformer to integrate local features and global features of input images.

2. A method of choosing weights in multi-loss is proposed to improve performance of overall pipeline.

II. Related works

Self-supervised depth estimation methods. SfmLearner [6] was one of the first works that used view synthesis as the supervisory signal for depth estimation. Competitive Collaboration [7] used geometry constraint to combine learning of different tasks (Depth Estimation, Pose Estimation, Optical Flow Estimation, Motion Segmentation) into a framework and saw improvements in all tasks. Monodepth2 [8] added occlusion masking into its framework by using a minimum photometric loss for adjacent frames instead of a mean photometric loss. Depth from Video in the Wild [9] addressed static scene assumption by removing pixels belong to moving objects with an additional instance segmentation network. Feature Depth [18] avoided textureless regions by representing image by its features and reconstructed feature representation of image instead of the image itself.

Multi-loss weighting methods. In previous depth estimation works [6][7][8], the weight of each component in total loss was chose heuristically. Kendal et al. [19] proposed a loss weighting method based on the uncertainty of each loss function. Groenendijk et al. [20] defined a hypothesis that a loss component had been satisfied when its variance had decreased towards zero. They used adaptive weights for loss components and calculated loss's weight based on its coefficient of variation. Chen et al. [21] relied on another hypothesis that contribution of each loss depended on its gradient magnitudes. They balanced contribution of each loss term by directly tuning gradient magnitudes. Lee et al. [22] chose loss weights by continuously rebalancing value of each loss component in total loss.

III. Methodology

In this section, we firstly introduce the warping image process, then we introduce the self-supervised depth estimation pipeline with Vision Transformer. Finally, we present our weights choosing method for self-supervised loss function.

A. Warping image process

Camera model. The camera model that projects a $3D$ point $P=(X,Y,Z)$ in camera coordinate to a $2D$ pixel $p=(u,v)$ on image plane given the camera intrinsics $K=(f_x,f_y,c_x,c_y)$:

$$p=(u,v)=\left(f_x\frac{X}{Z}+c_x,\ f_y\frac{Y}{Z}+c_y\right) \quad (1)$$

Backprojecting a $2D$ pixel $p=(u,v)$ on image plane to a $3D$ point $P=(X,Y,Z)$ given its depth $D(p)$ follows below equation:

$$P=(X,Y,Z)=D(p)\left(x-\frac{c_x}{f_x},y-\frac{c_y}{f_y},1\right) \quad (2)$$

Warping source image to target image. A target image I_t can be reconstructed from a source image I_s via:

$$\hat{I}_{s\to t}(p)=I_s(\hat{p}) \quad (3)$$

where $\hat{p}$ is the corresponding pixel on source image I_s of a pixel p on target image I_t. We need to find $\hat{p}$ via p.

Given a pixel $p=(u,v)$ in target image, the corresponding $3D$ point of it in target image coordinate is:

$$P=D(p)\left(x-\frac{c_x}{f_x},y-\frac{c_y}{f_y},1\right) \quad (4)$$

The coordinate of P in source image coordinate is calculated as:

$$P_s = RP + t = (X_s,\ Y_s,\ Z_s) \tag{5}$$

where R and t are the rotational transformation matrix and transitional transformation vector respectively.

The corresponding pixel $\hat{p}$ of p is:

$$\hat{p} = \left(f_x \frac{X_s}{Z_s} + c_x,\ f_y \frac{Y_s}{Z_s} + c_y\right) \tag{6}$$

$I_s(\hat{p})$ and $I_t(p)$ should be similar with these assumptions: the corresponding $3D$ point is static and visible in both frame, it lies on a Lambertian surface; the predicted depth and pose are both correct.

B. *Self-supervised Depth Estimation Pipeline with Vision Transformer*

The Self-supervised Depth Estimation training pipeline is shown in Figure 1.

Monocular Depth Estimation Network. Our work use AdaBins [13] network architecture which composes of a modern encoder-decoder and a AdaBins module as the Depth Prediction Network. The AdaBins module includes a Vision Transformer architecture to perform global statistical analysis at the output of encoder-decoder architecture which is a high resolution feature map, and then it refines the output Range-Attention Maps to get the final depth prediction. This module divides depth interval $D = (d_{min}, d_{max})$ into N bins and adaptively computes bin widths b for each image. Therefore, it predicts depth values as a linear combination of bin centers.

Camera Motion Estimation Network. The camera motion network consists of several stacked convolutional layers and followed by adaptive average pooling layers to process image features to get the relative camera motion between frames.

Overall pipeline. The self-supervised depth estimation training pipeline includes 2 networks: Depth Prediction Network (D) and Camera Motion Estimation Network (C). The D network inputs target image and output predicted depth map. The C network inputs target image and source images, it outputs relative camera poses from target image to source images. The depth map and camera poses are used for reconstructing the target image follows Section 3.A. The target image I_t and reconstructed image $\hat{I}_{s\to t}$ are then fed to loss function to get the error, which is the training signal to backpropagate and update both D and C networks.

C. *Method of Choosing Loss Function Weights*

The self-supervised loss function used in this work is:

$$L = \lambda_{L1}\mathcal{L}_{L1} + \lambda_{SSIM}\mathcal{L}_{SSIM} + \lambda_s\mathcal{L}_{smooth} \tag{7}$$

Through experiments, we saw that the pipeline achieved the best result with weights as SSIM loss, L1 loss and smoothness loss contributed 36%, 63% and 1% respectively in terms of value in total loss. Our method of experiment for choosing best weights for self-supervised loss function is described as follows:

- Firstly, we trained D network and C network with loss weights of SSIM loss, L1 loss and smoothness loss were 1, 1 and 1 respectively to watch their original values without scaling. We trained the networks for 20 epochs until it converged and plotted SSIM loss, L1 loss and smoothness loss values in the final 3 epochs to watch theirs distributions. We would use these mean values of the distributions for calculating approximate contributed proportions of each loss components in terms of value in the total loss.
- Secondly, we conducted experiments on choosing smoothness loss weight.
- Thirdly, we conducted experiments on choosing L1 and SSIM losses weights.

1) *Choosing Smoothness Loss Weight*

We used the Edge Aware Smoothness Loss [11] for our work. This loss forces the network to predict smooth disparity map according to edges of the input RGB image. While smoothness loss improves continuities of depth map, a too large weight for smoothness loss makes depth maps too smooth and erases objects' edges. In contrast, a too small weight for smoothness loss cannot enforce relevant between neighboring super-pixels which creates artifacts and infinite-depth holes in depth maps. Because of all above reasons, choosing a suitable weight for smoothness loss is very important to overall performance of the network.

Our method of experiment for weighting smoothness loss is described as follows:

- Firstly, we fixed L1 loss and SSIM loss weights as in CC [7]. Secondly, based on mean values of the distributions found above, we changed weight value of smoothness loss therefore its contribution to total loss varied from 99% to 0%.
- We realized that when training network from scratch, a larger than 12% smoothness loss contribution made network predict trivial solutions, where predicted disparity maps were all the same value at every pixels to minimize smoothness loss.
- The network could learn and predict non-trivial solutions at smoothness loss contribution less than 12%. With the contribution of smoothness loss larger than 5%, the predicted disparity maps were too smooth. The predicted disparity maps could preserve objects and scenes' edges when proportion of smoothness loss was under 5%. The best performance achieved when the smoothness loss contribution was approximate 1% in terms of value in the total loss.

2) *Choosing L1-loss and SSIM-loss Weights*

L1 and SSIM losses are used for calculating the difference between reconstructed target image from source image. Both L1 and SSIM can be used individually for this purpose, but several works [7][8] specified that combining them help improves network performance. Previous works chose weight ratios between L1 and SSIM heuristically. Some other works [20][21][22] chose weighting between losses automatically based on some hypotheses.

Instead of choosing loss weights heuristically or automatically without control of the weights, we conducted experiments on choosing the best weights for L1 and SSIM manually.

Our experiment is described as follows:

- Based on mean values found from the distributions of L1 loss, SSIM loss and Edge Aware Smoothness loss, we fixed the proportion of smoothness loss to 1% - the best value for smoothness loss we found above.

TABLE 1. COMPARISON OF PERFORMANCES REPORTED ON EIGEN ET AL.'S TEST SPLIT [23].

Method	*AbsRel*	*SqRel*	*RMSE*	*RMSE log*	δ_1	δ_2	δ_3
SfMLearner [11]	0.208	1.768	6.958	0.283	0.678	0.885	0.957
GeoNet [24]	0.155	1.296	5.857	0.233	0.793	0.931	0.973
DF-Net [25]	0.150	1.124	5.507	0.223	0.806	0.933	0.973
Struct2Depth [10]	0.141	1.036	5.291	0.215	0.816	0.945	0.979
CC [7]	**0.140**	1.070	5.326	0.217	0.826	0.941	0.975
Monodepth2 [8]	0.155	**0.882**	**4.701**	**0.190**	**0.879**	**0.961**	**0.982**
Ours	0.176	1.467	6.607	0.261	0.768	0.913	0.962

TABLE 2. COMPARISON OF PERFORMANCES (ATE) REPORTED ON KITTI ODOMETRY DATASET [4].

Method	*Sequence 09*	*Sequence 10*
ORB-SLAM (full)	0.014 ± 0.008	0.012 ± 0.011
ORB-SLAM (short)	0.064 ± 0.141	0.064 ± 0.130
Mean Odometry	0.032 ± 0.026	0.028 ± 0.023
SfmLearner [11]	0.016 ± 0.009	0.013 ± 0.009
Mahjourian et al. [26]	0.013 ± 0.010	0.012 ± 0.011
Geonet [24]	$\mathbf{0.012} \pm 0.007$	0.012 ± 0.009
DF-Net [25]	0.017 ± 0.007	0.015 ± 0.009
Ours	$0.013 \pm \mathbf{0.007}$	$\mathbf{0.011} \pm \mathbf{0.007}$

- We changed the contribution percentage of L1 and SSIM losses, L1 varied from 99% to 0% and SSIM varied from 0% to 99%.
- After several experiments, we saw that the network output the best quality depth maps with L1, SSIM and smoothness losses accounted for 63%, 36% and 1% respectively.

In final, the total loss is:

$$L = \lambda_{L1}\mathcal{L}_{L1} + \lambda_{SSIM}\mathcal{L}_{SSIM} + \lambda_s\mathcal{L}_{smooth} \tag{7}$$

Where:

$$\mathcal{L}_{L1} = \sum_p |I_t(p) - I_s(\hat{p})| \tag{8}$$

$$\mathcal{L}_{SSIM} = \sum_p 1 - SSIM\big(I_t(p), I_s(\hat{p})\big) \tag{9}$$

$$SSIM(x,y) = \frac{(2\mu_x\mu_y + c_1) + (2\,\sigma_{xy} + c_2)}{{\mu_x}^2 + {\mu_y}^2 + c_1)\,(\sigma_x^2 + \sigma_y^2 + c_2)} \tag{10}$$

$$\mathcal{L}_{smooth} = \sum_p \|e^{-\nabla I_t}\nabla d\|^2 \tag{11}$$

with μ_x, σ_x are the local mean and variance over the pixel neighborhood with $c_1 = 0.01^2, c_2 = 0.03^2$; ∇ is the first derivative along spatial directions; $\lambda_{L1} = 1.0, \lambda_{SSIM} = 0.12, \lambda_{smooth} = 0.21$.

IV. NUMERICAL EXPERIMENTS AND DISCUSSIONS

A. Depth Evaluation

Evaluation metrics. The standard metrics for depth evaluation are presented as follows:

$$AbsRel\colon \frac{1}{|D|}\sum_{d\,\in D}\frac{|d^* - d|}{|d^*|} \tag{12}$$

$$RMSE\colon \sqrt{\frac{1}{|D|}\sum_{d\,\in D}\|d^* - d\|^2} \tag{13}$$

$$SqRel\colon \frac{1}{|D|}\sum_{d\,\in D}\frac{\|d^* - d\|^2}{d^*} \tag{14}$$

$$RMSE\ log\colon \sqrt{\frac{1}{|D|}\sum_{d\,\in D}\|\log d^* - \log d\|^2} \tag{15}$$

$$\delta_t\colon \frac{1}{|D|}|\{d\ \in D \mid max\left(\frac{d^*}{d}, \frac{d}{d^*}\right) < 1.25^t\}| \tag{16}$$

where d and d^* are predicted depth and ground truth depth, D is a set of all the predicted depth values of an image, $|\,.\,|$ returns the number of the elements in the input set.

During evaluation, the depth is capped at 80m. Similar to SfmLearner [6], our predicted depth is defined up to a scale factor which is calculated by:

$$\hat{s} = \frac{median(D_{gt})}{median(D_{pred})} \tag{17}$$

where D_{gt} is the ground-truth depth and D_{pred} is the predicted depth maps.

Comparison to other works. Table 1. shows performances of several methods on KITTI Eigen et al.'s test split. Our work achieved a competitive result compared to other self-supervised method.

Compared to CC [7], although our result is not as good as CC on KITTI Eigen et al.'s test split, we still see that the impact of Vision Transformer in extracting global features with the clear representation of textureless regions in Figure 2. CC [7] predicts depth maps on 6 scales to widen effective range of smoothness loss, which derives depths propagation from discriminative regions to textureless regions. In contrast, our work just predicts depth map on one scale but the representation of textureless regions in depth map is still clear, which indicates that global features (the combination representation of the whole image including textureless regions and discriminative regions) are processed properly. It clearly shows that our hypothesis is accurate that incorporating local features and global features with the help of Vision Transformer in self-supervised setting helps network predict better depth map.

B. Odometry Evaluation

Evaluation metrics. The common error metric Absolute trajectory error (ATE) is used in this work for odometry evaluation.

TABLE 3. RESULTS OF OUR WORK ON EIGEN ET AL.'S TEST SPLIT [23] WITH DIFFERENT CHOICES OF LOSS FUNCTION WEIGHTS

Weight Values of Method	*Percentage of L1*	*Percentage of SSIM*	*Percentage of Smooth*	*AbsRel*	δ_1
SfMLearner	89%	0%	11%	0.195	0.729
CC	17%	81%	2%	0.189	0.743
Ours	63%	36%	1%	0.176	0.768

TABLE 4. PERCENTAGES OF CONTRIBUTION TO TOTAL LOSS AFTER NETWORKS CONVERGED

Experiment name	*Preset Percentage of L1*	*Preset Percentage of SSIM*	*Preset Percentage of Smooth*	*Percentage of L1 after training*	*Percentage of SSIM after training*	*Percentage of Smooth after training*
Experiment 1	89%	0%	11%	89.36%	0%	10.64%
Experiment 2	63%	36%	1%	62.55%	36.29%	1.16%
Experiment 3	17%	81%	2%	16.73%	80.72%	2.55%
Experiment 4	0%	89%	11%	0%	89.80%	10.20 %

Comparison to other works. Our Camera Motion Network is evaluated on KITTI Odometry dataset, the result is shown in Table 2.

Our work achieves a high result compared to other methods. It is the second best method on Sequence 09 and the best on Sequence 10. The improvements come from optimal weights chose by our method, where L1 loss, SSIM loss and Smoothness loss cooperate properly to help supervisory signal be more meaningful.

C. Evaluation of Loss Function Weight Choosing Method

Table 3. compares results on KITTI Eigen et al.'s test split of our framework with our optimal loss weights and loss weights chose heuristically by other methods. Our choosing method achieves highest result among other heuristic methods.

Table 4. shows the contribution in terms of value of each loss in total loss after the networks converged. The percentage of contribution of each loss converges to preset parameters after the networks converged. This specifies that our choosing method based on percentage of distribution is stable and meaningful.

D. Implementation Details

We use raw KITTI sequences [4] for training using Eigen et al.'s split [23]. The networks are trained with a batch size of 4 and learning rate of 10^{-4} using ADAM optimization. The images are scaled to 256 × 832 for training. The data is augmented with random scaling, cropping and horizontal flips. For all results presented we train for 20 epochs with each epoch takes 120 minutes on a Nvidia V100-SMX2 16GB GPU.

V. CONCLUSIONS

In this work, Vision Transformer is used in self-supervised depth estimation pipeline, which concatenates local features and global features of image to help predicted depth map be more precise. A new method for choosing loss weights in self-supervised multi-loss function is proposed, which increases networks' performance and can be widely used for every type of multi-loss function. The whole framework can be trained end-to-end in self-supervised setting and achieves competitive depth estimation result on benchmark dataset.

REFERENCES

[1] Menze, Moritz, and Andreas Geiger. "Object scene flow for autonomous vehicles." Proceedings of the IEEE conference on computer vision and pattern recognition. 2015.

[2] DeSouza, Guilherme N., and Avinash C. Kak. "Vision for mobile robot navigation: A survey." IEEE transactions on pattern analysis and machine intelligence 24.2 (2002): 237-267.

[3] Newcombe, Richard A., Steven J. Lovegrove, and Andrew J. Davison. "DTAM: Dense tracking and mapping in real-time." 2011 international conference on computer vision. IEEE, 2011.

[4] Geiger, Andreas, Philip Lenz, and Raquel Urtasun. "Are we ready for autonomous driving? the kitti vision benchmark suite." 2012 IEEE conference on computer vision and pattern recognition. IEEE, 2012.

[5] Lee, Jin Han, et al. "From big to small: Multi-scale local planar guidance for monocular depth estimation." arXiv preprint arXiv:1907.10326 (2019).

[6] Zhou, Tinghui, et al. "Unsupervised learning of depth and ego-motion from video." Proceedings of the IEEE conference on computer vision and pattern recognition. 2017.

[7] Ranjan, Anurag, et al. "Competitive collaboration: Joint unsupervised learning of depth, camera motion, optical flow and motion segmentation." Proceedings of the IEEE/CVF Conference on Computer Vision and Pattern Recognition. 2019.

[8] Godard, Clément, et al. "Digging into self-supervised monocular depth estimation." Proceedings of the IEEE/CVF International Conference on Computer Vision. 2019.

[9] Gordon, Ariel, et al. "Depth from videos in the wild: Unsupervised monocular depth learning from unknown cameras." Proceedings of the IEEE/CVF International Conference on Computer Vision. 2019.

[10] Casser, Vincent, et al. "Depth prediction without the sensors: Leveraging structure for unsupervised learning from monocular videos." Proceedings of the AAAI conference on artificial intelligence. Vol. 33. No. 01. 2019.

[11] Wang, Chaoyang, et al. "Learning depth from monocular videos using direct methods." Proceedings of the IEEE Conference on Computer Vision and Pattern Recognition. 2018.

[12] Dosovitskiy, Alexey, et al. "An image is worth 16x16 words: Transformers for image recognition at scale." arXiv preprint arXiv:2010.11929 (2020).

[13] Bhat, Shariq Farooq, Ibraheem Alhashim, and Peter Wonka. "Adabins: Depth estimation using adaptive bins." Proceedings of the IEEE/CVF Conference on Computer Vision and Pattern Recognition. 2021.

[14] Ranftl, René, Alexey Bochkovskiy, and Vladlen Koltun. "Vision transformers for dense prediction." arXiv preprint arXiv:2103.13413 (2021).

[15] Caron, Mathilde, et al. "Emerging properties in self-supervised vision transformers." arXiv preprint arXiv:2104.14294 (2021).

[16] Atito, Sara, Muhammad Awais, and Josef Kittler. "Sit: Self-supervised vision transformer." arXiv preprint arXiv:2104.03602 (2021).

[17] Li, Chunyuan, et al. "Efficient Self-supervised Vision Transformers for Representation Learning." arXiv preprint arXiv:2106.09785 (2021).

[18] Shu, Chang, et al. "Feature-metric loss for self-supervised learning of depth and egomotion." European Conference on Computer Vision. Springer, Cham, 2020.

[19] Kendall, Alex, Yarin Gal, and Roberto Cipolla. "Multi-task learning using uncertainty to weigh losses for scene geometry and semantics." Proceedings of the IEEE conference on computer vision and pattern recognition. 2018.

[20] Groenendijk, Rick, et al. "Multi-loss weighting with coefficient of variations." Proceedings of the IEEE/CVF Winter Conference on Applications of Computer Vision. 2021.

[21] Chen, Zhao, et al. "Gradnorm: Gradient normalization for adaptive loss balancing in deep multitask networks." International Conference on Machine Learning. PMLR, 2018.

[22] Lee, Jae-Han, and Chang-Su Kim. "Multi-loss rebalancing algorithm for monocular depth estimation." Computer Vision–ECCV 2020: 16th European Conference, Glasgow, UK, August 23–28, 2020, Proceedings, Part XVII 16. Springer International Publishing, 2020.

[23] Eigen, David, Christian Puhrsch, and Rob Fergus. "Depth map prediction from a single image using a multi-scale deep network." arXiv preprint arXiv:1406.2283 (2014).

[24] Yin, Zhichao, and Jianping Shi. "Geonet: Unsupervised learning of dense depth, optical flow and camera pose." Proceedings of the IEEE conference on computer vision and pattern recognition. 2018.

[25] Zou, Yuliang, Zelun Luo, and Jia-Bin Huang. "Df-net: Unsupervised joint learning of depth and flow using cross-task consistency." Proceedings of the European conference on computer vision (ECCV). 2018.

[26] Mahjourian, Reza, Martin Wicke, and Anelia Angelova. "Unsupervised learning of depth and ego-motion from monocular video using 3d geometric constraints." Proceedings of the IEEE Conference on Computer Vision and Pattern Recognition. 2018.

The 6th International Conference on
Engineering Mechanics and Automation (ICEMA 2021)
Hanoi, November 14, 2021

Simulation of crack propagation in FG-GPLRC structures and its application in dataset generation

Mai Van Trung
Faculty of Engineering Mechanics and Automation - University of Engineering and Technology, VNU Hanoi.
maitrungsky.td@gmail.com

Vu Dinh Giang
Faculty of Engineering Mechanics and Automation - University of Engineering and Technology, VNU Hanoi.
rangsut2k@gmail.com

Nguyen Dinh Duc
Department of Engineering and Technology in Constructions and Transportation -University of Engineering and Technology, VNU Hanoi.

Vu Thi Thuy Anh*
Department of Engineering and Technology in Constructions and Transportation -University of Engineering and Technology, VNU Hanoi.
*Corresponding author: *anhvutt@vnu.edu.vn*

***Abstract*: The major challenge in Artificial Intelligence applications is the difficulty in dataset collection, especially in the case of advanced materials. The reason for this matter is not only the availability of these materials but also the constraints in human resources, time, and space for the collection. This report aims to develop a method to generate data for the application of AI through the investigation of crack propagation in the structure made of advanced materials: Functionally Graded Graphene Nano-platelet Reinforced composite (FG-GPLRC). The combined knowledge of eXtended Finite Element Method (XFEM) and MATLAB is used to simulate crack propagation in structure, as well as create a dataset with the desired number of data about the crack of FG-GPLRC structure will be a novel, interdisciplinary approach of this study, which is expected to have many useful points for an area of research where data collection is still difficult. In addition, a method for improvement of the simulation results has been proposed in this study too, where meshing is carried out to achieve the convergence between simulation and analytical results.**

Keywords: Advanced materials, FG-GPLRC, Crack propagation, XFEM, MATLAB, Dataset.

I. INTRODUCTION

The development of science and technology leads to increasing demand for the use of new materials. Many applications in aerospace technology, submarines, microelectronics... require mutually exclusive mechanical properties of the material to have resistance against thermo-mechanical stresses as well as chemical stability. For example, a turbine blade, which must be tough to withstand the loading, but must also have a heat resistance on the outer surface. The gears, which must be tough enough inside to withstand the fracture but must also be hard on the outside to prevent wear. The structural and properties in conventional materials are unobtainable, but only properties in new materials or advanced materials (such as FGM, Graphene, auxetic...) can meet these requirements.

Advanced materials are the basis of many applications, including sensors and actuators, or artificial muscles, particularly as electroactive polymers... With the continuous development of science and technology, it requires more attention from scientists to study this material. According to the understanding of the authors, except for experimental and applied researches, theoretical studies on advanced materials mostly focused on studying the behavior of structures under the influence of load, i.e. on studying the structure prior to fracture. Theoretical studies on structures with cracks appearing or research on crack propagation are scarce and can be divided into the main directions: i) group uses the theory of Fracture Mechanics [1, 2], ii) Group using molecular dynamics simulation [3, 4], iii) And a few other methods [5, 6].

However, it can be seen that there is no method developed based on the investigation of crack propagation, as well as there is no universal method to study problems of structures made of advanced materials with cracks or simply simulate crack propagation in structures made of advanced materials.

Nowadays, with the advances in science and technology, research and application of AI in surveying and detecting cracks using computer vision is increasingly attracting the attention of many research groups based on the outstanding advantages in terms of execution time and safety when compared with the surveying of human especially on the structure located in hard-to-reach locations or large infrastructures. However, to be able to apply AI, it is necessary to have a large enough dataset, and this will be a huge difficulty if the above structures are made of advanced materials, due to limitations on the popularity of these materials stemming from their cost, as well as the importance of material selection on important details. Therefore, it is very important to study and collect data on the occurrence of cracks in structures made of advanced materials at this time. To cope with the challenge in lacking quality datasets of real-crack in this field, simulations can be considered as an alternative.

This report will focus on developing a dataset through a surveying of crack propagation in beams made of FG-GPLRC material - a new kind of material that contains multiple graphene single layers has been regarded as the strongest reinforcing nano-fillers in polymer composites [7, 8] with many applications in various fields such as electronics, energy storage, and sensors... The combined knowledge of XFEM and MATLAB is used to simulate crack propagation in the beam and then creating a dataset with the desired number of data about the crack of FG-GPLRC structure would be a new approach of this study…Related to the idea of combining Finite Element Method (FEM) or XFEM and MATLAB, an interface named

Abaqus2MATLAB (A2M), connecting Abaqus and MATLAB, has been developed in [9]. Although A2M has provided a framework for finite element post-processing, two aspects are still untouched when dealing with crack analysis: only fixed cracks are simulated, and coordinates of crack tips are not extractable. Inspired by A2M and to overcome the mentioned challenges, we propose in this paper an automatic simulation approach where the propagation path of the simulated crack is taken into consideration and coordinates of crack tips can be extracted for creating the dataset.

II. THEORETICAL BASIS AND XFEM IMPLEMENTATION

Hitherto, many methods have been developed to determine the characteristic quantities for the fracture strength of different materials [1-8], in which, most of the methods are developed on the basis of FEM. However, due to some limitations in the process of crack simulation analysis in complex structures, especially when the crack grows, it creates discontinuous regions in the model. To overcome this phenomenon, Belytschko and Black proposed the XFEM method [11, 12], in which the space of the finite element is enhanced by the Jump Function and the asymptotic functions near the top of the crack. This solution helps to simulate cracks of any form without having to perform a re-mesh. This paper presents a method of applying the XFEM method in Abaqus software to build a simulation model of crack propagation.

A. Stress distribution in the vicinity of the crack

The crack is assumed to have similar properties to the V-notch. Due to the characteristic geometry, the stress concentration is concentrated at the crack crests. In addition, the high-stress concentration at the crack edges can cause the appearance of material subjected to plastic deformation. The stress state of the material region surrounding the crack crest is depicted in Fig. 1. However, when the crack hypothesis is in the ideal state, the influence of plastic deformation and crack characteristics can be ignored according to the theory of linear elastic fracture mechanics [13].

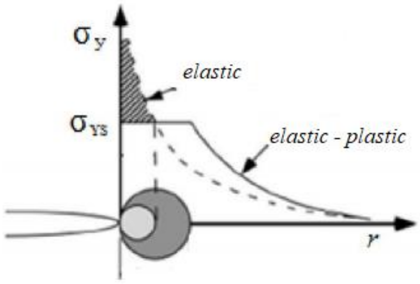

Fig. 1. The real and hypothetical states of cracks

When the structure is subjected to an external force and is in a linear elastic state, the stress of the material area surrounding the crack is determined [12]:

$$\sigma_{ij} = \left(\frac{k}{\sqrt{r}} \right) f_{ij}(\theta) + \sum_{m=0}^{\infty} A_m r^{\frac{m}{2}} g_{ij}^{(m)}(\theta) \tag{1}$$

here, the polar coordinate system (r, θ) has the origin at the vertex of crack, k is a constant, f_{ij} is a function of θ, A_m is the intensity of the higher order function g_{ij}.

Although the load on a crack can be arbitrary, however, crack development in a solid is usually studied according to three basic modes (Fig. 2): i) mode I – opening mode (tensile stress normal to the plane of the crack), ii) mode II – sliding mode (a shear stress acting parallel to the plane of the crack and perpendicular to the crack front), and iii) mode III – tearing mode (a shear stress acting parallel to the plane of the crack and parallel to the crack front).

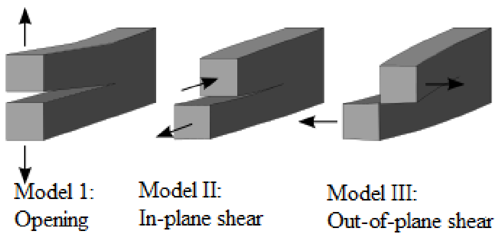

Fig. 2. The basic load states

In case the structure is loaded in mode I and in the elastic deformation state, the width of the structure is considered to be very large compared to the crack length (*a*), Eq. (1) can be rewritten below form [12]:

$$\sigma_{ij} = \left(\frac{K_I}{\sqrt{2\pi r}} \right) f_{ij}(\theta), K_I = \sigma\sqrt{\pi a}, \tag{2}$$

where K_I is the stress strength coefficient when the structure is loaded in mode I; σ is the applied stress at the edge of the beam. It is clear that, if K_I is calculated, it is possible to determine the entire stress field surrounding the top of the crack. However, in practice, all parts have a limited size, so in order to take into account the finiteness of the body a correction factor Y given in Ewalds and Wanhill is used and the K_I is usually determined by the expression [12, 13]:

$$K_I = Y\sigma\sqrt{\pi a}, \tag{3}$$

with

$$Y = 1{,}12 - 0{,}231\frac{a}{W} + 10{,}55\frac{a^2}{W^2} - 21{,}72\frac{a^3}{W^3} + 30{,}38\frac{a^4}{W^4}, \tag{4}$$

B. XFEM implementation

XFEM allows the existence of discontinuities in elements by increasing degrees of freedom by displacement functions [14]:

$$u = \sum_{i=1}^{N} N_i(x) \left[u_i + H(x)a_i + \sum_{\alpha=1}^{4} F_\alpha(x) b_i^\alpha \right], \tag{5}$$

with u is the displacement vector; u_i are node displacement vectors; a_i, b_i are the advanced node degrees of freedom of the freedom vector; $N_i(x)$ are surface functions; $H(x)$ is the step function and $F(x)$ are the crack vertex asymptotic functions.

III. EFFECTIVE MATERIAL PROPERTIES OF FG-GPLRC

Fig. 3. The UD-GPLRC type of distribution pattern

In this study, the cracked FG-GPLRC structure is a multilayer isotropic polymer material reinforced by GPLs, which are uniformly or randomly distributed in each layer. The edge crack with *a* depth of a is located at a distance of L_1 from the left end. It is assumed that each GPLRC layer has equal thickness, and is well bonded with its adjacent layers. There are many different distribution patterns of FG-GPLRC, but in order to focus on the main research problem, this paper only considers the distribution where all layers have the same GPL composition: UD-GPLRC. Four distribution patterns of FG-GPLRC are shown in Fig. 3.

In each GPLRC layer, graphene platelets act as effective rectangular solid fiber randomly orientated and uniformly distributed in the matrix. The Halpin-Tsai model is used to evaluate its effective Young's modulus [10] as:

$$E^{GRA} = \frac{3}{8}\left(\frac{1+\xi_L\eta_L V_{GPL}}{1-\eta_L V_{GPL}}\right)E_m + \frac{5}{8}\left(\frac{1+\xi_T\eta_T V_{GPL}}{1-\eta_T V_{GPL}}\right)E_m, \quad (6)$$

$$\eta_L = \frac{E_{GPL}/E_m - 1}{E_{GPL}/E_m + \xi_L}, \quad \eta_T = \frac{E_{GPL}/E_m - 1}{E_{GPL}/E_m + \xi_T}, \quad (7)$$

$$\xi_L = 2\left(a_{GPL}/h_{GPL}\right), \quad \xi_T = 2\left(b_{GPL}/h_{GPL}\right). \quad (8)$$

in which,

$$\rho^{GRA} = \rho_{GPL}V_{GPL} + \rho_m V_m, \quad V_m = 1 - V_{GPL},$$

$$\nu_{12}^{GRA} = \nu_{21}^{GRA} = \nu_{GPL}V_{GPL} + \nu_m V_m.$$

here V_{GPL}, V_m is the volume fraction of GPL and matrix, E_{GPL}, E_m are the Young's moduli of the matrix and GPL; $a_{GPL}, b_{GPL}, h_{GPL}$ are the average length, with and thickness of GPL respectively; ν_{GPL}, ν_m are the Poisson's ratio of the matrix and GPL respectively.

For U-GPLRC distribution pattern, the total GPL volume fraction V_{GPL} is expressed by:

$$V_{GPL} = \frac{W_{GPL}\cdot\rho_m}{W_{GPL}\cdot\rho_m + \rho_{GPL}\left(1-W_{GPL}\right)}, \quad (9)$$

where W_{GPL} represents the total GPL weight fraction of the beam.

In this study, the total UD-GPLRC layer is $\chi_L = 10$, which was shown by Yan and Yang as being sufficiently large to obtain accurate results for an ideal FG beam [16]. Each GPLRC layer is a GPL-reinforced epoxy composite. The length, width and thickness of GPLs are assumed as $a_{GPL} = 2.5\mu m, b_{GPL} = 1.5\mu m,$ and $t_{GPL} = 1.5nm$ respectively. The material properties of the GPL and epoxy used in the simulations are listed in Table I.

TABLE I. MATERIAL PROPERTIES OF EPOXY AND GPL

	Young's modulus (GPa)	Mass density (kg/m3)	Poisson's ratio
Epoxy	3	1200	0.186
GPL	1010	1062.5	0.34

IV. SIMULATION OF CRACK PROPAGATION IN FG-GPLRC STRUCTURE IN ABAQUS

Abaqus commercial software with integrated XFEM was selected to simulate crack propagation in the FG-GPLRC beam in this paper because of its ability to connect with MATLAB programming software. This combination is extremely important because as mentioned above, this study aims to generate a large enough number of simulations to generate a dataset for ML or DL so that the simulation "by hand" with such a large number is not possible. In other words, simulation operations cannot be repeated over and over, but instead, an interaction between Abaqus and MATLAB needs to be established so that operations can be performed automatically in MATLAB. Solving this problem during the implementation of the research will also be an important contribution of this study.

Two structure models, which are loaded in mode I, were considered here to give results on crack in structures made of GPL materials. The elastic modulus of GPL material was selected and calculated above. In addition, to be able to simulate the crack propagation in the structure using Abaqus, a parameter to pay attention to here is the value of tensile modulus. Usually, this value can only be calculated experimentally. For the convenience of the survey, in this report, this value is taken based on the experimental results of Manta in [15].

A. Edge crack in the middle in a FG-GPLRC plate under uniaxial tension

Skills as well as meshing solutions for simulation models using a software integrated with FEM or XFEM have important role and great influence on the accuracy of calculation results. If the meshing solution is given appropriately, the number of analytical calculations required in the process of producing results will reduce, thereby shortening the simulation time.

For the purpose of making a comparison results between the simulation used in this study and the analytical method to evaluate the reliability of the solution selection, in this section, by selecting the solution meshing C3D8R [18], in which, in the area surrounding the crack, the elements are smaller in size, while in the area outside the crack, the elements have an increasing size in the direction of the boundary, the plate model with the crack at the edge is meshing and simulating, thereby evaluating the difference between the value of stress intensity factor K_I according to the simulation method and the analytical method.

The FG-GPLRC plate configuration with a crack in the middle available is shown in Fig. 4 and the simulation solution C3D8R for the FG-GPLRC plate is shown in Fig. 5. The error in the stress intensity factors is calculated as:

$$error = \left|\frac{K_I^{Abaqus} - K_I^{analytical}}{K_I^{analytical}}\right|. \quad (10)$$

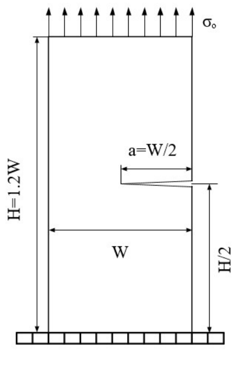

Fig. 4. The FG-GPLRC plate with center edge crack

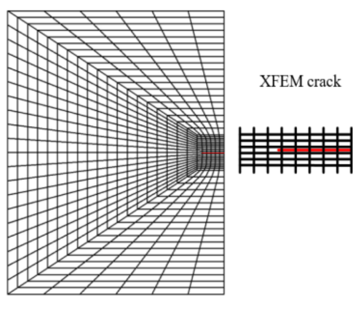

Fig. 5. The solution of mesh C3D8R for the FG-GPLRC plate with center edge crack

The survey process was carried out in 5 cases with the ratio between the initial notch crack of length and the width of the beam a/W as 0.05, 0.1, 0.2, 0.3 and 0.4, respectively. In which, corresponding to each case, the mesh size in the crack appearing area is also changed in order to achieve the best fit between the simulation results and the calculated results.

The meshing and simulation are performed on Abaqus, where the stress intensity factors K_I are extracted in Abaqus/Viewer. The comparison results are shown in Table II below.

TABLE II. COMPARISON RESULTS FOR THE STRESS INTENSITY FACTOR OF THE CRACKED FG-GPLRC PLATE

Methods / a/W	Analytics	Numerical methods
0.05	10.034	10.035
0.1	14.832	14.854
0.2	24.343	24.482
0.3	36.084	36.332
0.4	52.720	52.998

From Table II, it can be seen that the meshing solution C3D8R improves simulation results clearly. In the case without applying this solutions, can be easily guessed that, only when the crack propagates in the plate a short distance, i.e. the ratio between the crack length and the width of the plate is small, the numerically computed results are well in agreement with the analytical solution, but as the ratio increases, the error value also increases too. This can be explained by the opening of the crack mouth, leading to the formation of an angle deviation from the original position of the plate, so the analytic formula is no longer completely accurate.

In other words, if the comparison results are made between the simulation results and the results from the actual experiments, the meshing solution will help select the most appropriate number of elements in the mesh, thereby giving the most accurate simulation model with the realistic. Unfortunately, in this study, this comparison has not been made, because there is no published document of experimental results of the crack structures made of FG-GPLRC.

B. Three point bending test under the effect of the load placed at any position

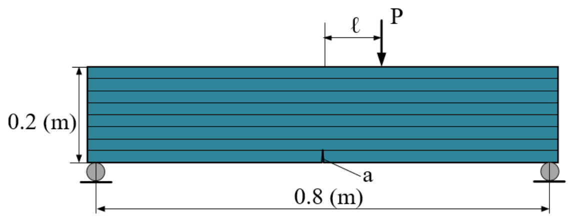

Fig. 6. Geometry of an FG-GPLRC beam with an initial notch crack at the lower surface and subjected to load at the upper surface

In this section, a beam with the geometry problem is shown in Fig. 6 is considered for testing the crack propagation in the FG-GPLRC structure. To conventionally initiate the crack propagation, an initial notch crack of length a was made at the opposite surface of the beam where the load P is applied, and for convenience of surveying, the beam was considered to be very thin, and the load was placed at an initial position with distance l from the center of the beam.

The material properties and tensile modulus of GPL are used as the previous example. Figs. 7, 8 and 9 illustrated segmentation results when the load is placed respectively at the center of the beam ($l = 0$) and at $l = 10, 30$ cm from the center position. Notably, when the load is placed at the initial position, the crack propagation is in the same direction (vertical) as per the load direction since the shear force is negligible (Fig. 7). In contrast, when the load is placed at 10 cm from the middle of the beam, a change in propagation direction occurred due to the appearance of the shear force (Fig. 8). And last, at the position $l = 30$ cm - the position closest to the support, it is clear that the crack length propagates a very short distance, this is consistent with the mechanical properties of the structure, that the structure will show more stability at when the force is close to the support position. In addition, all the cracks have all started from the original crack position and have grown gradually towards the direction of the force position.

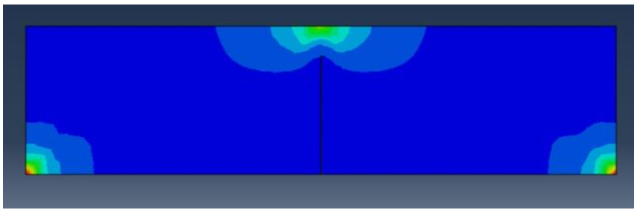

Fig. 7. Crack propagation in beams when the load is placed at $l = 0$

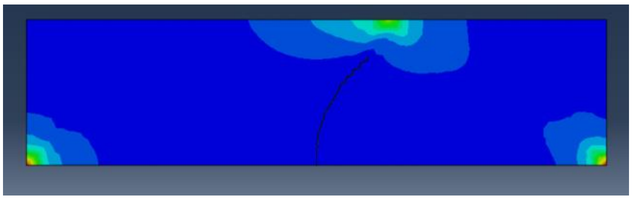

Fig. 8. Crack propagation in beams when the load is placed at $l = 10$

Fig. 9. Crack propagation in beams when the load is placed at $l = 30$

The accuracy of XFEM in modeling the propagation of crack will be next investigated in this section. Due to the ease that, XFEM doesn't require the mesh to be aligned with the geometry of the crack, it offers an elegant, computationally inexpensive, and easy way of analyzing problems with curved crack propagation. The geometry problem is considered as the same beam model used for the three-point bending test in Fig. 6 above, with the load is placed at $l = 8$ cm from the center of the beam. The analysis was carried out using three different mesh discretizations in order to see the effect of mesh refinement on tracking crack paths using XFEM. Three mesh discretizations, used in the analysis, mesh A: 756 nodes, mesh B: 1221 nodes, and mesh C: 1701 nodes.

Since no comparison is made here with the actual crack of the FG-GPLRC beam (true crack), so from the results shown in Figs. 10 and 11 no comment can be made about the convergence in meshing here. However, some formative remarks that can be shown here are:

i) First, Figs. 10 and 11 show the crack paths obtained with different mesh discretization; XFEM is well able to predict the curved crack path without the need for mesh alignment with the crack. Further, the obtained crack path is qualitatively representing the expected crack pattern for shear cracks in beams.

ii) secondly, it can be seen from Fig. 11 that the crack path seems to be smoother when the mesh was coarse (mesh A), however, the crack propagation pattern becomes more complicated (zigzag lines) with the mesh refinement (mesh B, C).

The example demonstrated that the crack growth pattern is also affected by the mesh discretization.

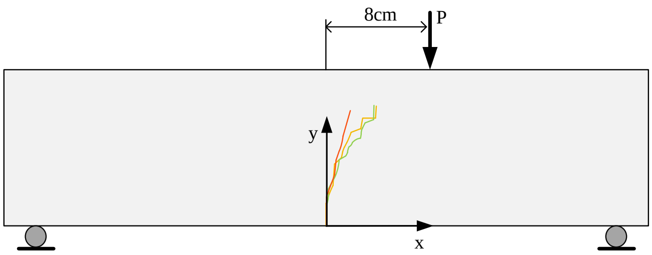

Fig. 10. Shear crack propagation in beams when the load is placed at the position $x = 8$

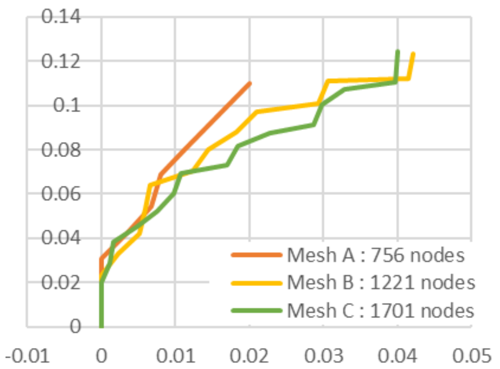

Fig. 11. Effect of mesh discretization on crack propagation path when the load is placed at the center position $x = 8$

Another interesting feature that can also be observed from the crack paths is that, the crack direction becomes unstable and shows oscillations near the end of the beam. In the authors opinion this is due to the fact that, in that zone the body is in compression and under compression loading the crack direction tends to become unstable as the crack nears arrest.

V. DATASET CREATION PROCESS

As described above, an interaction between Abaqus and MATLAB needs to be established to generate a large enough number of simulations. In MATLAB, this operation can be performed automatically by setting up a MATLAB script containing a for loop that will execute a predefined number of Abaqus analyses. In each repetition of the loop, the following processes are done:

i) The Abaqus input file of the *i-th* analysis is generated

ii) The Abaqus input file is run from MATLAB with the above specific commands

iii) The results of the Abaqus analysis are read from the results (*.dat) file that is generated after the Abaqus analysis is terminated. Then, two-level sets are obtained.

iv) Based on these level sets, the crack figure is calculated and the results are stored appropriately for future use.

v) Modify the position of load into file input and continue with the next repetition of them for a loop by returning step 2.

In the first step in the above algorithm, the simulation results in path B above of section IV with the load is placed at $l = 8$ cm from the center of beam will be used as the Abaqus input file (inp file) to serve to create the dataset. The result and simulation process of inp file requires accuracy because it will be determined the simulation results of the next simulation result generated.

The two-level sets obtained in the 3-th step in the above algorithm are the two typical values for one crack tip. Within the framework of XFEM discontinuities are often represented using the Level Set Method (LVM). LVM is a numerical technique for tracking moving interfaces. It allows treatment of internal boundaries and interfaces without explicit treatment of interface geometry. The key idea is to construct iso-contours such that the interface is represented as a zero iso-contour.

By using the LVM in XFEM, for a crack, requires two level sets: the first describes the crack surface, Φ (phi) and the second, Ψ (psi), is constructed so that the intersection of two level sets gives the crack front. As such, to describe the crack geometry can use a signed distance functions and the crack is entirely described by nodal data. For calculating Φ and Ψ, it must be noted: The nodal value of the function Φ is the signed distance of the node from the crack face, positive value on one side of the crack face, negative on the other. The nodal value of the function Ψ is the signed distance of the node from an almost-orthogonal surface passing through the crack front and the function Ψ has zero value on this surface and is negative on the side towards the crack. This can be easily visualized through the following example in Fig. 12 of the correspondence between the values of Φ and Ψ with nodes.

Node	Φ	Ψ
1	+0.25	-1.5
2	+0.25	-1.0
3	-0.25	-1.5
4	-0.25	-1.0

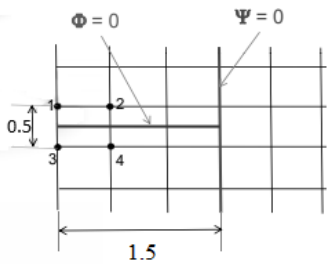

Fig. 12. Example of the correspondence between the values of Φ and Ψ with nodes.

By applying LVM in Abaqus, the two-level sets value of each crack tip will be obtained, then applying a coordinate system transformation from the polar coordinate system (representing the value of the two-level sets) to the Cartesian coordinate system (representing the vertex coordinates (x, y) of the crack), connecting all the crack tips we will obtain a characteristic crack line representing the crack propagation in the beam structure in MATLAB. The set of all these curves is the result dataset of the study.

A. Automatic conversion results

By connecting between Abaqus and MATLAB, the results of the simulation of the crack propagation in beams using Abaqus are also shown in the output of MATLAB. This correlation result is shown in Fig. 13. It can be seen that the results of the crack propagation in beam displayed in both Abaqus and MATLAB are completely similar. This demonstrates the reliability in converting simulation results from simulation software to programming software mentioned in the report.

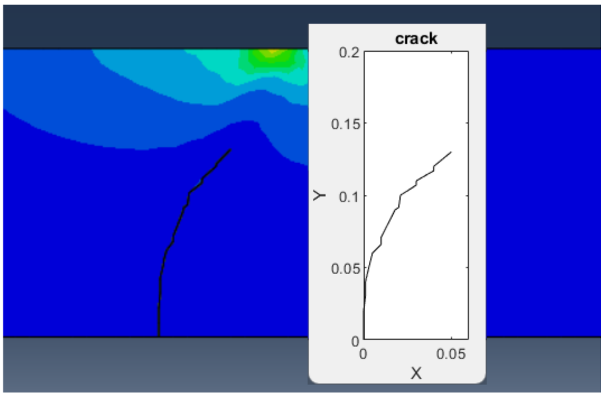

Fig. 13. Simulation results of crack propagation in beams using Abaqus and MATLAB

In addition, as can be seen, the result is shown in Fig. 13 is the result of one simulation, corresponding to the result at one load location. By changing the position of the load within an allowed range on MATLAB will result in a dataset of the coordinates of the crack tips in the crack propagation path. The number of data corresponding to the step number of iterations in the loop created in MATLAB. The resulting data is shown in Fig. 14. This dataset about the coordinates of all the crack tips in each crack propagation path of all simulations will be stored in a file with file format ".txt" - a popular file format, which is convenient for various purposes by applying ML or DL of the following user's.

x_output	y_output
-0.193059698	-0.0890298488
-0.193059698	-0.0772651436
-0.193059698	-0.0655004384
-0.191869927074492	-0.0549255042255078
-0.189821588230087	-0.0452091378699132
-0.187228614517951	-0.0358618105820493
-0.186970144992983	-0.0243555712070166
-0.186970144992983	-0.0125908660070166
-0.185916246331663	-0.00188005946833704
-0.179909160356322	0.00387756042132199
-0.175408731814105	0.0113174178791054
-0.175029844140078	0.022703235640078
-0.174650956446701	0.0340890540467011
-0.163362368706672	0.034740766306672
-0.163089557998111	0.0462326625981106
-0.162816747332655	0.0577245571326545
0,0	
-0.193059698	-0.0890298488
-0.193059698	-0.0772651436
-0.193059698	-0.0655004384
-0.191869028319121	-0.0549264029808788

Fig. 14. The resulting data

Here are a few notes, in particular:

i) the "+" or "-" of coordinates sign in Fig. 15 depends on the initial coordinate system, and the row with character (0,0) in Fig. 15 is to distinguish between the crack propagation paths of the different simulations,

ii) the range of change in force should not be too close to the position of bearing support in order to meet the uniformity of the propagation crack lengths of the simulations.

The research results in this section show that after finishing the loop in MATLAB with a predefined number of steps (N) which is also the number of simulations to be performed automatically in Abaqus, a dataset of N crack propagation paths is obtained and stored as coordinates with two parameters x and y corresponding to the coordinates of the tips in the crack propagation path. Depending on the length as well as the number of crack tips in each propagation path, the number of (x, y) value pairs in each propagation path is more or less. And this obtained data set is also the obtained result data set of this paper about the crack propagation path in the structure made of FG-GPLRC material.

Depending on the purpose of the problem, the number of crack data to be required, as well as the object, size, or model of the structure, the Programmer chooses suitable algorithms for the training of purpose. When there are actual experimental results on crack development in the structure made of FG-GPLRC material, based on the results of the survey on the mesh discretization (Fig. 12), the number of nodes mesh is selected accordingly to achieve convergence between simulation results and experimental results, thereby improving the accuracy of the simulation method. Simultaneously with the more exactly obtained dataset obtained after having more exactly simulation results, for example, by using algorithms in image detection, the appropriate mathematical models by training the data obtained base on the dataset generation method above can be given. This is an area of great significance in modern life, contributing to warning about failure or assessing the safety level of structures made of FG-GPLRC.

VI. CONCLUSIONS

By providing a simulation solution in the Abaqus, the crack propagation in the FG-GPLRC structure is simulated and represented clearly in this report. To the best of our knowledge, there is currently no actually experiment results in this field. However, a method for improvement of the simulation results has been proposed in this study, where meshing is carried out to achieve the convergence between simulation and analytical results. And, to some extent, the conducted comparison and selection of meshing solutions to enhance the similarity with the analytical results proposed in this work has suggested another solution for simulation methods of the FG-GPLRC material.

Another major contribution of this work is the automatic generation of crack propagation, leading to the establishment of a quality dataset. A comparison with real-world cracks to verify its correlation will be conducted in our future work.

REFERENCES

[1] A. Emdadi, M.A. Zaeem, “Phase-field modeling of crack propagation in polycrystalline materials”. Comput. Mater. Sci., 186, 110057, 2021. doi:10.1016/j.commatsci.2020.110057.

[2] M. Tam, Z. Yang, S. Zhao, H. Zhang, Y. Zhang, J. Yang, “Nonlinear bending of elastically restrained functionally graded graphene nanoplatelet reinforced beams with an open edge crack”. Thin-Walled Structures, 156, 106972, 2020.

[3] J. Yao, Y. Xia, S. Dong, P. Yu, J. Zhao, “Finite element analysis and molecular dynamics simulations of nanoscale crack-hole interactions in chiral graphene nanoribbons”, Eng. Frac. Mech., 10657, 2019, doi:10.1016/j.engfracmech.2019.106571

[4] A.C. Hansen-Dörr, L. Wilkens, A. Croy, A. Dianat, G. Cuniberti, M. Kästner, “Combined molecular dynamics and phase-field modelling of crack propagation in defective graphene”, Comput. Mater. Sci., 163, 117–126, 2019, doi:10.1016/j.commatsci.2019.03.028

[5] H. Kimura, Y. Akiniwa, K. Tanaka, H. Tanaka, Y. Okumura, “Smart structure for suppression of mode I and II crack propagation in CFRP laminates by shape memory alloy TiNi actuator”, Inter. J. Fatig., 28(10), 1147–1153, 2006, doi:10.1016/j.ijfatigue.2006.02.002

[6] B. Engel, J.P. Rouse, C.J. Hyde, W. Lavie, D. Leidermark, S. Stekovic, H. Li, “The prediction of crack propagation in coarse grain RR1000 using a unified modelling approach”, Inter. J. Fatig., 137, 105652, 2020. doi:10.1016/j.ijfatigue.2020.105652.

[7] M. Rafee, F. Nitzsche, M.R. Labrosse, “Modeling and mechanical analysis of multiscale fber-reinforced graphene composites: nonlinear bending, thermal postbuckling and large amplitude vibration”, Int. J. Non. Lin. Mech., 103, 104–112, 2018.

[8] K.S. Novoselov, A.K. Geim, S.V. Morozov, D. Jiang, Y. Zhang, S.V. Dubonos, I.V. Grigorieva, A.A. Firsov, “Electric feld effect in atomically thin carbon films”, Science 306, 666–669, 2004.

[9] G. Papazafeiropoulos, M. Muñiz-Calvente, E. Martínez-Pañeda, “Abaqus2MATLAB: a suitable tool for finite element post-processing”, Adv. Eng. Soft., 105, 9-16, 2017, DOI:10.1016/j.advengsoft.2017.01.006.

[10] M.A. Rafee, J. Rafee, Z. Wang, H. Song, Z.Z. Yu, N. Koratkar, “Enhanced mechanical properties of nanocomposites at low graphene content, ACS Nano 3, 3884–3890, 2009.

[11] T. Belytschko, T. Black, “Elastic crack growth in finite elements with minimal remeshing”. Int. J. Numer. Methods Eng., 45, 601–620, 1999.

[12] J. Shi, D. Chopp, J. Lua, N. Sukumar, T. Belytschko, “Abaqus implementation of extended finite element method using a level set representation for three-dimensional fatigue crack growth and life predictions”. Eng. Fract. Mechan., 77(14), 2840–2863, 2010. doi:10.1016/j.engfracmech.2010.06.009.

[13] H. Ewalds and R. Wanhill. Fracture Mechanics. 1984.

[14] D. Broek, “Elementary engineering fracture mechanics”. Matinus Nijhoff, Boston, London, 1982.

[15] A. Manta, M. Gresil, G. Soutis, “Tensile and flexural behaviour of a graphene/epoxy composite: experiments and simulation”. J. Phys.: Mater. 3 (2020) 014006.

[16] N.A. Tu, “research on crack in structures using xfem”, Sci. and Tech. J. Hanoi Industrial University, 42, 1-5, 2017.

[17] C. Feng, S. Kitipornchai, J. Yang, “Nonlinear bending of polymer nanocomposite beams reinforced with non-uniformly distributed graphene platelets (GPLs)”, Compos. Part B-Eng. 110,132 – 140, 2017.

[18] R.M María and M.G.A. José, “Stress Intensity Factors Calculation of Cracks in Bolted Joints with XFEM”, ICEMM S.L, Parque Científico Universidad Carlos III de Madrid, 28918 Leganés, Spain, www.icemm.es.

The 6th International Conference on
Engineering Mechanics and Automation (ICEMA 2021)
Hanoi, November 14, 2021

Simulation superelastic behavior of shape memory alloy and applications reduce oscillations

Hoang Ngoc Quy
VNU University of Engineering and Technology
Institute of Mechanics
144 Xuan Thuy, Cau Giay, Hanoi, Vietnam
Email: ngocquyk52@gmail.com

Nguyen Truong Giang
VNU University of Engineering and Technology
Institute of Mechanics
144 Xuan Thuy, Cau Giay, Hanoi, Vietnam
Email: ntgiang@imech.vast.vn

***Abstract*: Shape memory alloys (SMA) remember their shape due to thermoelastic martensitic phase transformation. These alloys have advantages in terms of large recoverable strain and these alloys can exert continuous force during use. The shape memory effect and superelasticity are two important properties of SMA. This paper addresses a one-dimensional model able to reproduce the shape memory alloy superelastic behavior, taking into account the different elastic properties between austenite and martensite. The model is based on a single scalar internal variable, the martensite fraction, for which evolutionary equations in rate form are proposed. The model's ability to simulate one-dimensional experimental data is evaluated. Finally, the superelastic property of SMA is used to reduce oscillations in cable-stayed cables. The results were compared for the case with and without SMA. The problem of the optimal design of the device is studied. The maximum dissipation energy depends on the cross-sectional area, the length, and the location of the SMA on the cable.**

Keywords: Shape memory alloy, matensitic phase transformation, stay cable, superelastic

I. INTRODUCTION

Shape memory alloys (SMA) are materials able to change their crystallographic structure depending on the temperature and the state of stress [1]. These changes are, in general, interpreted as martensitic transformations, that is, solid-solid, diffusionless transformations between a crystallographically more-ordered parent phase (austenite) and a crystallographically less-ordered product phase (martensite) [2]. For shape memory alloys, the transformation is reversible and, in many cases, rate-independent. At the macroscopic level shape memory solids present the superelastic effect (the recovery of large deformations in loading-unloading cycles, occurring at sufficiently high temperatures) and the shape memory effect (the recovery of large deformations by a combination of mechanical and thermal processes). Both the superelastic and the shape memory effects are in general not present in traditional materials. Hence, shape memory alloys lend themselves to be successfully adopted in a broad set of advanced applications [3-4], one of which is to reduce the vibration of cable-stayed bridge cables.

The stay cable is a very flexible construction, lightweight, and has a low damping rate. They are subjected to static and dynamic loads that cause large fluctuations, resulting in fatigue damage that shortens bridge construction life and can even damage the structure. In order to minimize the above effects, there have been many useful studies for improving the life of cables. The mechanical method based on the use of mechanical dampers is also a method that significantly reduces vibrations and is easy to fabricate and install. One of the types of mechanical dampers is the shape memory alloy dampers with the advantages of large damping capacity, self-centering ability, high fatigue-resistant performance, and good corrosion resistance.

In the present work, the attention is focused on an inelastic framework recently proposed, well suited for the modeling of complex material behaviors, such as those occurring in materials undergoing solid-solid phase transitions. The rest of the paper is structured as follows: Section II gives a brief introduction about the shape memory effect and superelastic of shape memory alloy. In section III we address a one-dimensional (1D) model able to reproduce the SMA superelastic behavior and to take into account the non-negligible differences between the martensite and the austenite elastic properties. The numerical simulation and comparison with experimental data are presented in section IV. The results of the application reduce oscillations of cable-stayed bridge cables is developed and shown in section V. The conclusion will be presented in section VI.

II. SHAPE MEMORY EFFECT AND SUPERELASTICITY OF SMA

Shape memory alloys have two phases, each phase has different crystal structures and therefore, has different properties. One is the high temperature phase called austenite (A) and the other is the low temperature phase called martensite (M). Austenite (generally cubic) has a different crystal structure from martensite (tetragonal, orthorhombic or monoclinic). The transformation from one structure to the other does not occur by diffusion of atoms, but rather by shear lattice distortion. Such a transformation is known as martensitic transformation. The reversible phase transformation from austenite (parent phase) to martensite (product phase) and vice versa forms the basis for the unique behavior of SMAs [5].

A. *Shape memory effect*

An SMA exhibits the shape memory effect (SME) when it is deformed while in the twinned martensitic phase and then unloaded while at a temperature below A_f. When it is subsequently heated above A_f, the SMA will regain its original shape by transforming back into the parent austenitic phase [5]. The nature of the SME can be better understood by following the thermomechanical loading path in a combined stress-strain temperature space as shown in Fig 1.

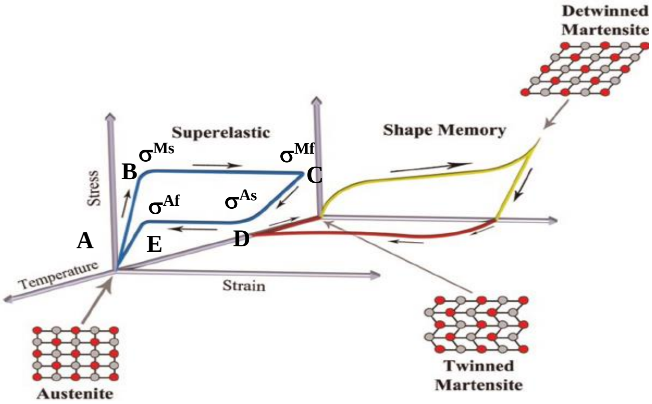

Fig. 1. Stress-strain-temperature data exhibiting the shape memory effect and superelastic for a typical NiTi SMA [5].

In this paper we consider the superelastic effect, ie the behavior of the SMA under the applied load.

B. *Superelasticity*

When a mechanical load is applied, the parent phase (austenite) undergoes elastic loading (A → B). When the stress is reached (σ^{Ms}) start transformation martensite as shown in Fig 1. The transformation proceeds (B → C), to the stress level (σ^{Mf}), indicating the end of the transformation [5]. When the stress is released gradually by unloading, the martensite elastically unloads along the path (C → D). When the incident stress (σ^{As}) marks the martensite to revert to austenite. The process is accompanied by the recovery of the strain due to phase transformation at the end of unloading. The end of the transformation back into austenite is denoted by the point at which the σ-ε unloading curve rejoins the elastic region of austenite (point E corresponding to stress σ^{Af}). The material then elastically unloads to A. The forward and reverse phase transformation during a complete pseudoelastic cycle results in a hysteresis, which, in the σ-ε space, represents the energy dissipated in the transformation cycle. The transformation stress levels and the size of the hysteresis vary depending on the SMA material and testing conditions. The inversion phase transition described above is called the superelastic behavior.

III. CONTITUTIVE MODEL FOR SUPERELASTIC SHAPE MEMORY ALLOYS

In the following we present a uniaxial model able to describe the superelastic behavior of shape memory materials. The model is cast within the generalized plasticity framework [4]. Other applications of the theory to the case of shape memory solids can be found in [6].

A. *Time-continuous model*

We assume to work with one scalar internal variable, ξ_S, representing the martensite fraction, and with two processes which may produce variations of the martensite fraction: the conversion of austenite into martensite (A→M) and the conversion of martensite into austenite (M→ A).

Following experimental evidence [7], for both the processes we choose linear kinetic rules in terms of the uniaxial stress σ. In particular, the activation conditions for the conversion of austenite into martensite are:

$$\sigma^{Ms} < |\sigma| < \sigma^{Mf} \text{ and } \dot{\overline{|\sigma|}} > 0 \tag{1}$$

Where σ^{Ms} and σ^{Mf} are material parameters |•| is the absolute value and a superpose dot indicates a time-derivative. The corresponding evoiution equation is set equal to:

$$\dot{\xi}_S = -(1-\xi_S)\frac{\dot{\overline{|\sigma|}}}{|\sigma| - \sigma^{Mf}} \tag{2}$$

On the other hand, the activation conditions for the conversion of martensite into austenite are:

$$\sigma^{Af} < |\sigma| < \sigma^{As} \text{ and } \dot{\overline{|\sigma|}} < 0 \tag{3}$$

With σ^{As} and σ^{Af} material parameters. The corresponding evolution equation is set equal to:

$$\dot{\xi}_S = \xi_S \frac{\dot{\overline{|\sigma|}}}{|\sigma| - \sigma^{Af}} \tag{4}$$

B. *Free energy*

We improved the free energy of shape memory alloy based on the suggestion by Auricchio and Sacco [8]. We consider the following free energy:

$$\begin{aligned}\psi &= \left[(u_A - T\eta_A) - \xi(\Delta u - T\Delta\eta)\right] + C\left[(T-T_0) - T\log\frac{T}{T_0}\right] \\ &+ \frac{1}{2}(1-\xi+\tau)L\left[\varepsilon - \varepsilon_L \xi \,\mathrm{sgn}(\sigma)\right]^2 \\ &- (T-T_0)\left[\varepsilon - \varepsilon_L\xi\,\mathrm{sgn}(\sigma)\right](1-\xi+\tau)L\alpha\end{aligned} \tag{5}$$

$$\begin{cases}(1-\xi+\tau)L = E_A & \text{with} \quad \xi = 1 \\ (1-\xi+\tau)L = E_M & \text{with} \quad \xi = 0\end{cases} \tag{6}$$

Where u_A and η_A are the internal energy and entropy of the austenite, Δu and $\Delta\eta$ are the internal energy difference and the entropy difference between the austenite and the martensite, C is the material heat capacity, T_0 is the natural or reference state temperature, ξ is a variable with value in the range [0:1], L is constant modulus, τ is a constant, σ is the uniaxial stress, α is the thermal expansion factor.

C. *Stress-strain relationship*

The stress is defined as the partial derivative of the free energy with respect to the total strain:

$$\sigma = \frac{\partial\psi}{\partial\varepsilon} = (1-\xi+\tau)L\left[\varepsilon - \varepsilon_L\xi\,\mathrm{sgn}(\sigma)\right] - (1-\xi+\tau)L\alpha(T-T_0) \tag{7}$$

In an isothermal setting, the free energy can be written:

$$\sigma = \left(1-\xi+\tau\right)L\left[\varepsilon-\varepsilon_L\xi\,\mathrm{sgn}(\sigma)\right] \quad (8)$$

Limiting the discussion to a small deformation regime, we assume an additive decomposition of the total strain ε:

$$\varepsilon = \varepsilon^e + \varepsilon_L\xi\,\mathrm{sgn}(\sigma) \quad (9)$$

Where ε^e is the elastic strain, ε_L is the maximum residual strain and sgn(•) is the sign function. The maximum residual strain ε_L, regarded as a material constant, is a measure of the maximum deformation obtainable only by multiple-variant martensite detwinning, hence, a measure of the maximum deformation obtainable aligning all the single-variant martensites in one direction [9]. Moreover, the presence of sgn(σ) in (8) indicates that the direction of the effect relative to the martensite fraction ξ_S is governed by the stress.

The elastic strain is assumed to be linearly related to the stress:

$$\sigma = E\varepsilon^e \quad (10)$$

With $E = \left(1-\xi+\tau\right)L$ the elastic modulus.

D. Time-discrete model

The While during the development of the time-continuous model we assumed the stress as control variable, during the development of the time-discrete model we assume the strain as control variable. This choice is consistent with the fact that, from the point of view of the integration scheme, the time-discrete problem is considered strain-driven. Accordingly, we consider two time values, say t_n and $t_{n+1}>t_n$ such that t_{n+1} is the first time value of interest after t_n. Then, knowing the strain at time t_{n+1} and the solution at time t_n, we should compute the new solution at time t_{n+1}. To minimize the appearance of subscripts (and to make the equations more readable), we introduce the convention: $a_n=a(t_n)$ and $a=a(t_{n+1})$; where a is any generic quantity. Therefore, the subscript n indicates a quantity evaluated at time t_n, while no subscript indicates a quantity evaluated at time t_{n+1}.

We use a backward-Euler scheme to integrate the time-continuous evolutionary equations (2) and (4). Written in residual form and after clearing fractions, the time-discrete evolutionary equations specialize to:

$$R^{AM} = \lambda_s\left(|\sigma|-\sigma^{Mf}\right)+\left(1-\xi_s\right)\left(|\sigma|-|\sigma_n|\right)=0 \quad (11)$$

$$R^{MA} = \lambda_s\left(|\sigma|-\sigma^{Af}\right)+\xi_s\left(|\sigma|-|\sigma_n|\right)=0 \quad (12)$$

where the martensitic fraction increment λ_s is defined as:

$$\xi_s = \xi_s^n + \lambda_s \text{ or } \lambda_s = \int_{t_n}^{t_{n+1}} \dot{\xi}_s dt \quad (13)$$

The quantity λ_s can be computed expressing the stress σ as a function of λ_s and requiring the satisfaction of the evolutionary equation corresponding to the active phase transformation.

Introduction (9) into (8) indicates that *sgn(σ)=sgn(ε)*; hence, (8) can be rewritten:

$$\varepsilon = \varepsilon^e + \varepsilon_L\xi\,\mathrm{sgn}(\varepsilon) \quad (14)$$

Making use (14), substitution of expression (10) into (11) and (12) transforms the time-discrete evolutionary equations in two equations which can be solved in terms of λ_s.

E. Solution algorithms

To solve the time-discrete evolutionary equations, we can either adopt an iterative strategy or a closed-form solution approach, as briefly discussed in the following.

- Solution by iterative strategy. As an iterative scheme, we select the Newton Raphson strategy. To guarantee the method a quadratic convergence, the derivatives of the evolutionary equations written in residual form are required to obtain the tangent modulus consistent with the time-discrete model.

- Solution in closed form. The elastic modulus of Reuss and Tanaka, which may be found in [10], is substituted into the time-discrete evolutionary equations (11) and (12) written in residual form, returns expressions of the following type: $A\xi^2+B\xi+C=0$ and $A\xi^3+B\xi^2+C\xi+D=0$, where A, B, C and D are the quadratic and cubic equation coefficients defined as in [10]. Whose roots can be easily found in closed-form.

Due to the complexity of the coefficients and non-generality in solution closed-form, in this paper, we will proceed to solve the time-discrete evolutionary equations (11) and (12) by the solution iterative strategy.

F. Algorithmic tangent modulus

The construction of the tangent modulus consistent with the time-discrete model is discussed further below. The use of a consistent tangent modulus preserves the quadratic convergence of the Newton method. From the linearization (9) we get:

$$d\sigma = E\left[d\varepsilon-\varepsilon_L\,\mathrm{sgn}(\varepsilon)d\lambda_s\right] \quad (15)$$

Assuming that

$$d\lambda_s = Hd\varepsilon \quad (16)$$

we can solve (15) in terms of $d\sigma$, obtaining the relation:

$$d\sigma = E^T d\varepsilon \quad (17)$$

where the tangent elastic modulus E^T is given by:

$$E^T = E\left[1-\varepsilon_L H\,\mathrm{sgn}(\varepsilon)\right] \quad (18)$$

The quantity H is computed from the linearization of the discrete evolutionary equation corresponding to the active phase transformation. Then, from equations (11) and (12) we get:

$$dR^{AM} = \left(1-\xi_{s,n}\right)d|\sigma|+d\lambda_s\left(|\sigma_n|-\sigma^{Mf}\right)=0 \quad (19)$$

$$dR^{MA} = -\xi_{s,n}d|\sigma|+d\lambda_s\left(|\sigma_n|-\sigma^{Af}\right)=0 \quad (20)$$

Since $d|\sigma|=sgn(\sigma)d\sigma=sgn(\varepsilon)d\,\sigma$, relation (15) allows to solve (19) and (20) in terms of $d\lambda_s$, obtaining:

$$H = H^{AM} = \frac{-\mathrm{sgn}(\varepsilon)\left(1-\xi_{s,n}\right)E}{\left(1-\xi_{s,n}\right)\left[-\mathrm{sgn}(\varepsilon)E\varepsilon_L\right]+\sigma_n-\mathrm{sgn}(\varepsilon)\sigma^{Mf}} \quad (21)$$

$$H = H^{MA} = \frac{\mathrm{sgn}(\varepsilon)\left(\xi_{s,n}\right)E}{\left(\xi_{s,n}\right)\left[\mathrm{sgn}(\varepsilon)E\varepsilon_L\right]+\sigma_n-\mathrm{sgn}(\varepsilon)\sigma^{Af}} \quad (22)$$

A return-map algorithm is used as the solution algorithm for the time-discrete model. Algorithm scheme solves the time-discrete evolutionary equations as in Fig. 2.

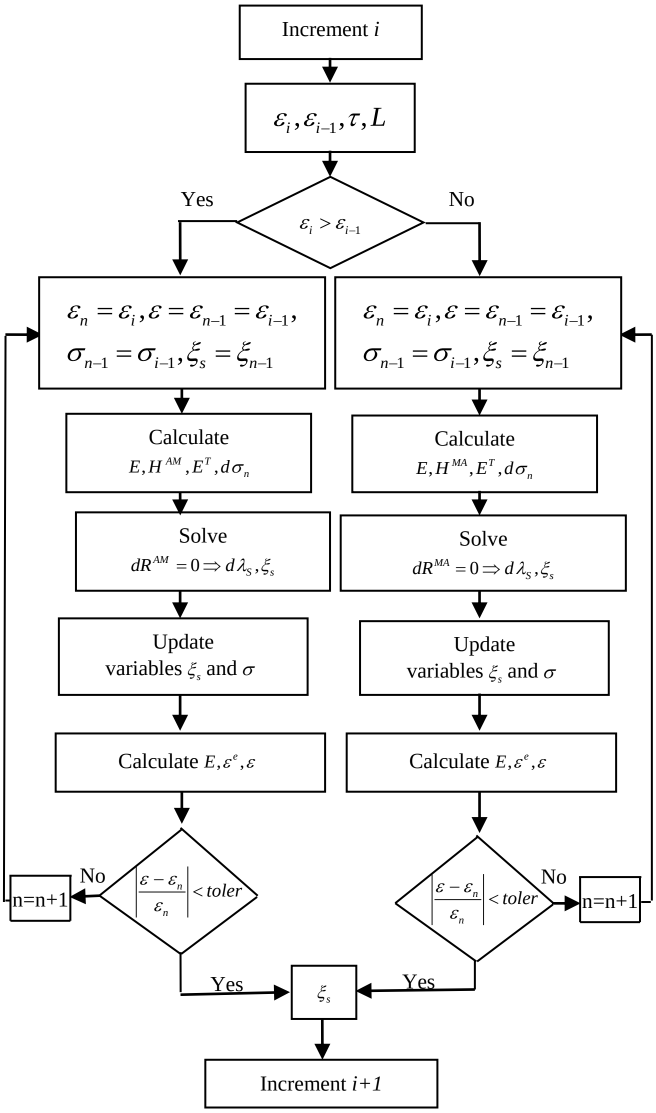

Fig. 2. Algorithm scheme.

IV. NUMERICAL SIMULATION AND COMPARISON WITH EXPERIMENTAL DATA

We now want to assess our ability to simulate typical SMA superelastic stress-strain responses. We consider the experimental data presented as in [11] and we have defined a bar of constant cross-section A and length L subjected to uniaxial tension by the displacement function u(x,t) as shown in Fig. 3 and Fig. 4.

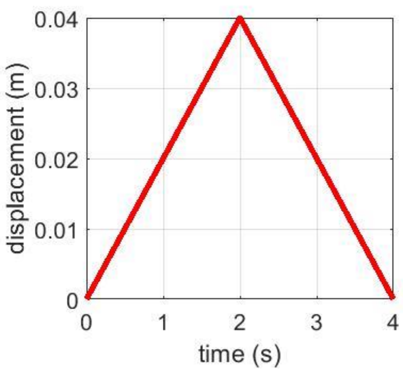

Fig. 3. Displacement function u(x,t)

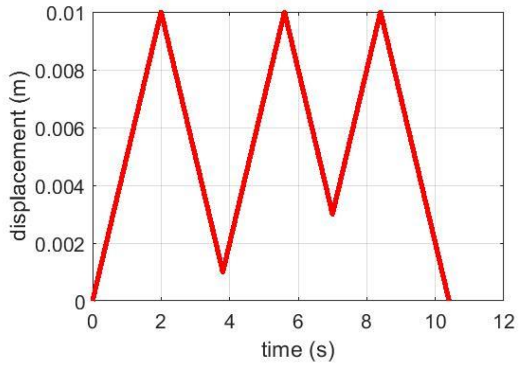

Fig. 4. Displacement function u(x,t)

From the inspection of the experimental stress-strain curves the following material parameters are chosen for the model:

TABLE I. MATERIAL PARAMETTERS

E_A (Mpa)	E_M (Mpa)	σ^{As} (Mpa)	σ^{Af} (Mpa)	σ^{Ms} (Mpa)	σ^{Mf} (Mpa)	ε_L (%)
60000	7500	520	600	240	200	8

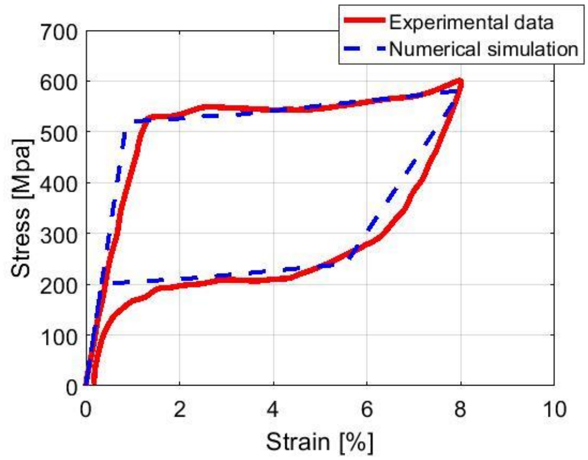

Fig. 5. Uniaxial tension stress-strain response. Experimental data [11] and numerical simulation.

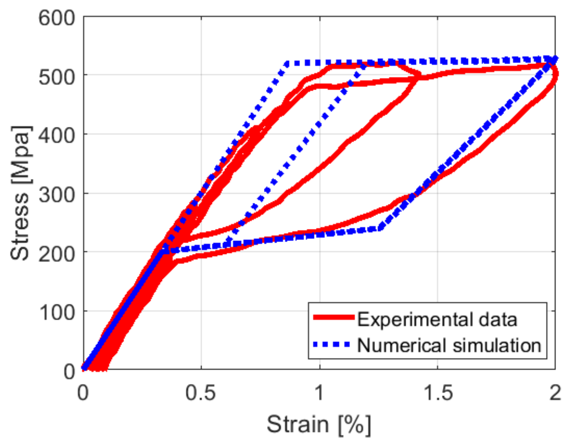

Fig. 6. Uniaxial tension stress-strain response. Experimental data [11] and numerical simulation

The numerical simulations show a good capacity of the model to fit experimental data Fig. 5. Moreover, Fig. 6 shows the model ability to reproduce the hysteresis behavior during any loading path and, in particular, internal hysteresis loops, as experimentally observed [12].

V. APPLICATION SHAPE MEMORY ALLOY SUPERELASTIC BEHAVIOR TO CONTROL A STAY CABLE IN CABLE-STAYED BRIDGES

In the following, we present an oscillating inclined stay cable model taking into account the influence of SMA damping and simulation results to evaluate the influence of SMA damping on the vibration of cable-stayed bridge cables. The Dynamic equations formulation of a sag stay cable has been presented by Nguyen and Hoang [13].

A. Dynamic equations formulation of a sag stay cable

We start considering a cable connecting two points denoted as A and B and placed to a distance L. The segment connecting A and B defines an angle θ versus horizontal axis. For the case of only body load, the cable configuration is planar and we indicate with Axy an orthogonal reference system defined within such a plane. The planar oscillations can occur in the transverse direction (y-axis) as shown in Fig. 7 and non-planar oscillations can occur in direction Az, so that Axyz forms a direct orthogonal frame [14].

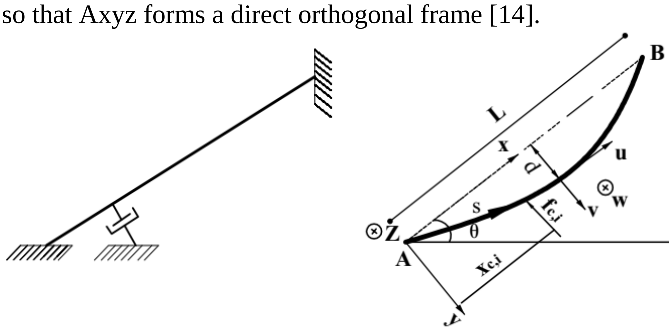

Fig. 7. Schematic diagram of an inclined stay cable

The dynamic equation for the oscillating inclined cable, according to Nguyen and Hoang [13], takes the following form:

$$m_{ii}\ddot{\alpha}_i(t)+\left(k_{ii}+\lambda^2 m_{ii}\right)\alpha_i(t)=F_{yi}-f_c(t)\varphi_i(x_c) \tag{23}$$

Where:

$$\begin{cases} \lambda^2=\dfrac{EA}{L}\left(\dfrac{mg\cos\theta}{T}\right)^2 \\ m_{ii}=m\displaystyle\int_0^L\varphi_i(x)\varphi_i(x)dx=m\dfrac{L}{2} \\ k_{ii}=-T\displaystyle\int_0^L\varphi_i''(x)\varphi_i(x)dx+\lambda^2\int_0^L\varphi_i(x)dx\int_0^L\varphi_i(x)dx \\ \quad=\dfrac{T\pi^2 i^2}{2L}+\lambda^2\dfrac{4L^2}{i^2\pi^2} \\ F_{yi}=\displaystyle\int_0^L F_y(x,t)\varphi_i(x)dx \\ \varphi_i(x_c)=\sin\left(\dfrac{i\pi x_c}{L}\right) \end{cases} \tag{24}$$

We observe that the system of dynamical equations (23) are decoupled in all terms except than the term $f_c(t)$ induced by the presence of the SMA damper. So the SMA damper introduces non-linearity into combined linear cable-damper system and Newmark numerical method is used to compute the dynamic response of the cable. The damping force $f_c(t)$, the form of which will be clearly dependent on the SMA constitutive behavior.

B. Optimization of the cross-sectional area, the length of the SMA wires and position of SMA damper

In order to give an optimal parameters for the SMA, such as for the cross-sectional area and the length of wires, different criteria may be followed. The most useful criterion design refers to energy based methods [15]. The idea is that the SMA performs at its best if it is capable of dissipating as much as possible of the total energy of the structure. The energy balance of the equilibrium equation (24) for one mode is defined as follows:

$$E_k(t)+E_e(t)=E_i(t)+E_c(t) \tag{25}$$

where $E_k(t)$ is the stay cable kinetic energy defined as:

$$E_k(t)=\frac{1}{2}m_{ii}\dot{\alpha}_1(t) \tag{26}$$

$E_e(t)$ is the stay cable elastic energy defined as:

$$E_e(t)=\frac{1}{2}(k_{11}+\lambda^2 m_{11})\alpha_1^2(t) \tag{27}$$

$E_i(t)$ is the input energy defined as:

$$E_i(t)=\int_0^t F_{y1}(t)\dot{\alpha}_1(t)dt \tag{28}$$

$E_c(t)$ is the energy associated with the SMA device defined as:

$$E_c(t)=E_{ec}(t)+E_{dc}(t) \tag{29}$$

This energy term can be considered as the sum of an elastic term, $E_{ec}(t)$, and of a dissipative term, $E_{dc}(t)$. The dissipative term is the area of hysteresis loop.

The optimal device in free-vibration is chosen when the maximum value of the energy dissipated in the SMA device, $E_{dc}(t)$, is considered. For a fixed position of the SMA, we decided to maximize the force exerted by SMA $f_c(t)$ with the hope that this should load also to augmentation of dissipated energy. The force exerted by SMA has this expression

$$f_c(t)=EA_{SMA}\left(\frac{v(x_c,t)}{L_{SMA}}-\xi_s\varepsilon_L sign(\varepsilon)\right) \tag{30}$$

where A_{SMA} and L_{SMA} are respectively the cross-sectional area and the length of the SMA device, and $v(x_c,t)$ is the cable transverse displacement at location x_c. For one mode $v(x_c,t)=\alpha_1(t)\varphi_1(x_c)$. From (30), it is clear that to maximize the value of force damper the cross-sectional area of the SMA device should be chosen as big as possible and the length of the SMA device should be chosen as short as possible. Therefore, the appropriate SMA device length should be determined by the following condition: $\varepsilon_{SMA}^{\max}=\varepsilon^{Mf}$; where ε^{Mf} is the strain corresponds to the stress finish of the martensite transformation σ^{Mf}. Thus, the optimal length of the SMA device is

$$L_{SMA}^{opt}=\frac{\left|v^{\max}(x_c,t)\right|}{\varepsilon^{Mf}} \tag{31}$$

$v^{\max}(x_c,t)$ is the maximum desired displacement of transversal displacement of the stay cable with the SMA damper. It is necessary to select $v_{max}(x_c)$ reasonable so that L_{SMA}^{opt} is suitable for the installation on the stay-cable bridge and $v^{max}(x_c)$ satisfies the conditions $v^{max}(x_c) < y(x_c)$.

C. Numerical simulations

In this example, we assume that the external load is zero (F = 0) and consider only the first mode of vibration. The cable length is L=4m, mass m=0.6 kg/m per unit length, diameter D=0.004m, elastic modulus E = 9x10^{10} N/m^2, of inclination angle = 30° with respect to horizontal. The SMA, installed at a distance x_c = 0.1L, has the following parameters: D_{SMA} = 0.0005m and the SMA length is L_{SMA} = 0.116m chosen from (31).

Fig. 8 shows the role of the SMA damper in the free vibration of the cable. With SMA damper, the cable's vibration amplitude is smaller (~ 0.06) compared to the amplitude without the SMA (~0.003), corresponding to 95%.

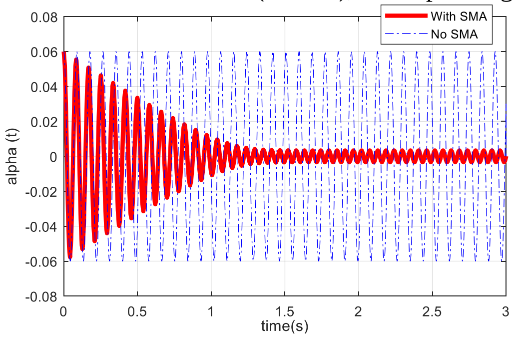

Fig. 8. The vibration of cable with and without SMA dampers

1) Effect of the SMA damper cross-sectional area

To analyse the effect of the SMA cross-sectional area, α_1 for the first mode of the stay cable is plotted by solving (23) and considering that the SMA damper is located at x_c = 0.1L and the SMA length is L_{SMA} = 0.116m chosen from (31), SMA diameter changes D_{SMA} = 0.00025m, D_{SMA} = 0.0004m, D_{SMA} = 0.0006m. The results are shown in Fig. 9. The change in diameter of the SMA wire shows that with diameter D_{SMA} = 0.0006m, it has the smallest amplitude of vibration compared to the other two diameters of D_{SMA} = 0.00025m and D_{SMA} = 0.0004m on the left of Fig. 9, and, on the right, the force damper is piloted versus the transversal displacement of stay cable for each D_{SMA}. These results are correct with the analytical conclusion from (30).

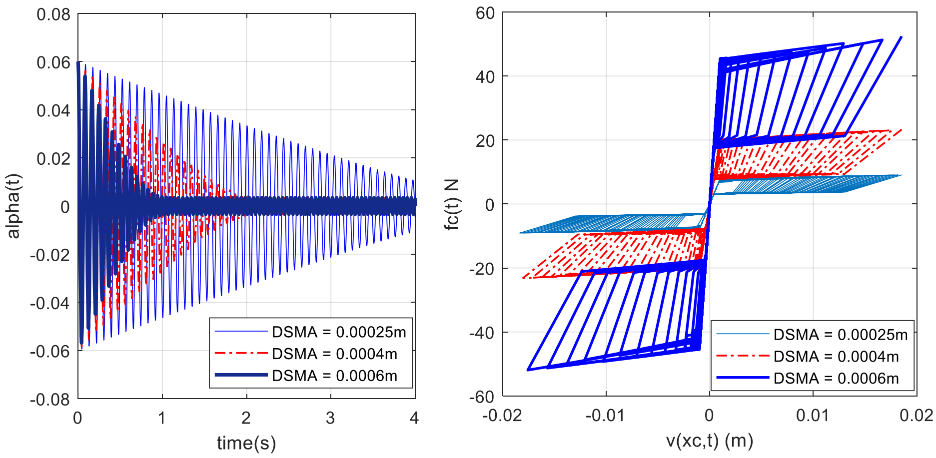

Fig. 9. Cross-sectional area effect of the SMA damper.

2) Effect of the length of the SMA damper

In this example the wire diameter of the SMA damper and the location of the SMA damper are fixed at D_{SMA}=0.0005m and x_c = 0.1L, respectively while the length of the SMA is varied as 0.116, 0.25 and 0.5 m. The results are shown in Fig. 10. The damping of the stay cable transverse vibration increases while decreasing the length of the SMA damper. The wire SMA length has more important effect on the small vibrations.

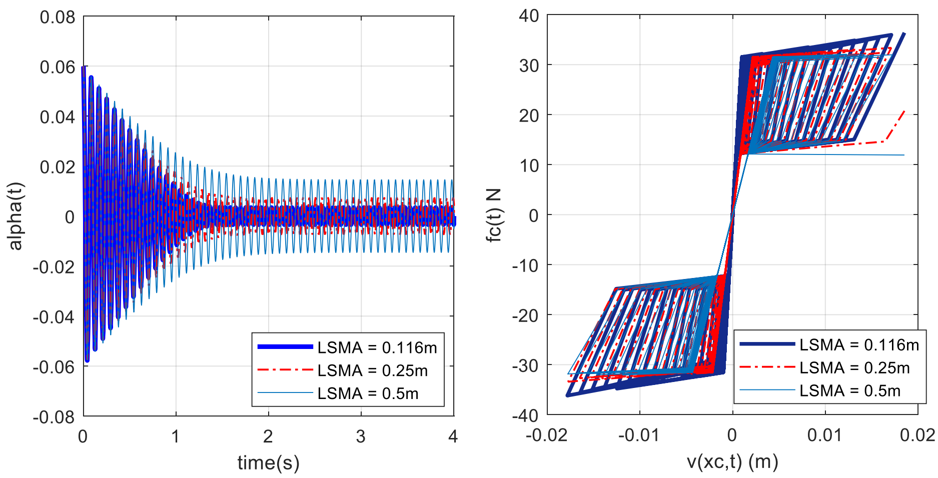

Fig. 10. Length effect of the SMA damper

3) Effect of the SMA damper position on the cable

In this example, the wire diameter of the SMA damper and the length of the SMA are fixed at D_{SMA}=0.0005m and L_{SMA} = 0.116 chosen from (30), respectively, while the location of the SMA damper is varied as x_c = 0.1L, 0.25L and 0.5 L. The results are shown in Fig. 11. The change of the position of the SMA damper also affects the vibration amplitude of the stay cable in Fig. 11, the position with the largest amplitude is x_c = 0.5L compared to the other two cases.

In practice, the choice of the location where the damper is installed on the stay-cable bridge is necessary. The middle position of the cable-stayed bridge gives better damping ability but is difficult to install or the SMA length is too long. In contrast, at the bridgehead, although the vibration reduction is less but easier to install, the length of the SMA is more reasonable. Thus choosing the right position and diameter so that the force SMA f_c is maximum is shown in Fig. 12. Based on Fig. 12, we can choose the appropriate installation position and diameter to give maximum SMA force which corresponds to the known optimal length L_{SMA}^{opt} in (30). That way the design of the damping will become easier.

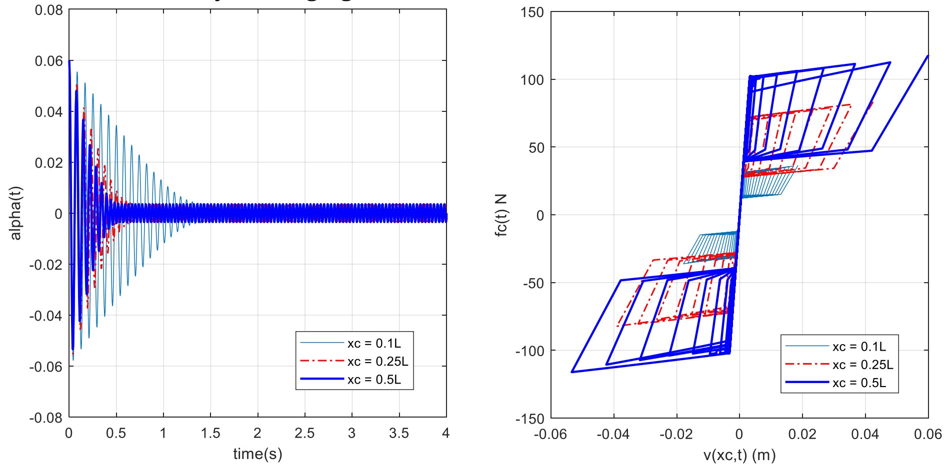

Fig. 11. Effect of the SMA damper position change on the cable

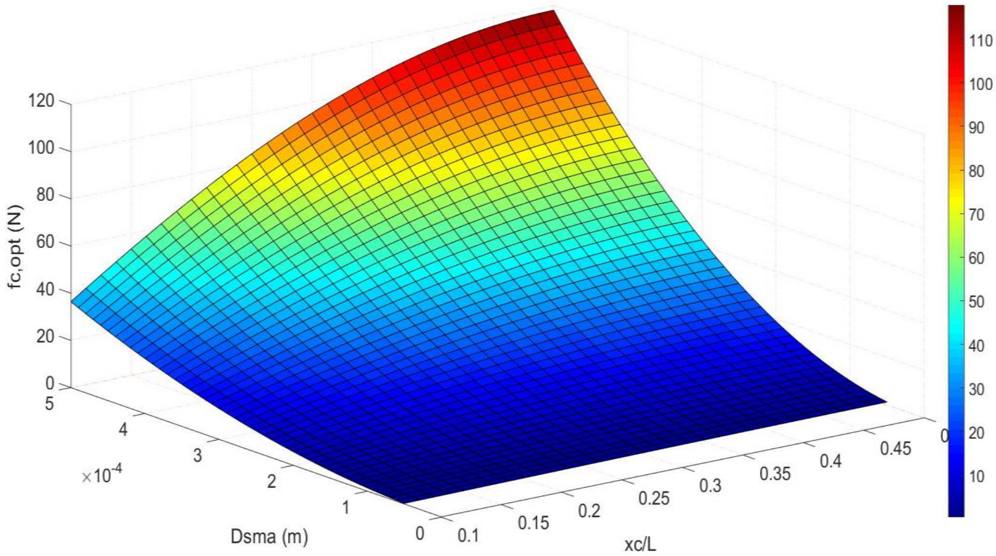

Fig. 12. Relationship between diameter, position and force SMA corresponding $L_{SMA}^{opt} = 0.116m$

VI. CONCLUTIONS

In this study, we presented a one-dimensional (1D) model able to reproduce the superelastic effect. The model is based on a single scalar internal variable, the martensite fraction, we improved the free energy function suggested by Auricchio and calculated the dependence of the elastic modulus on the martensitic fraction. The model's ability to reproduce experimental data related to materials has also been demonstrated. Its ability to describe the material response for complex loading histories (full forward and reverse phase transformations, partial loading-unloading patterns with the description of internal hysteresis loops) has been numerically tested.

The simulation on a cable model with SMA damper showed the excellent property of energy dissipation of the SMA and their ability to suppress the cable vibration. The performance of the SMA damper is notably dependent on the cross-sectional area, the length and the position of the SMA. The formula for calculating the optimal SMA wire length has been proposed. Based on this calculation, a diagram of the relationship between the SMA diameter, the damping installation position and the optimal force SMA was developed. Therefore, it is useful to search for the suitable dimensional parameters of the SMA device.

ACKNOWLEDGMENT

This work has been supported by VNU University of Engineering and Technology under project number CN21.10.

REFERENCES

[1] C. M. Wayman, Shape memory alloys, MRS Bull. April, 49-56 (1993).

[2] A. G. Khachaturyan, "Theory of Structural Transformations in Solids", Wiley (1983).

[3] T. W. Duerig, K. N. Melton, D. Stake1 and C. M. Wayman (Eds), "Engineering Aspects of Shape Memory Alloys", Butterworth-Heinemann (1990).

[4] J. Lubliner and F. Auricchio, "Generalized plasticity and shape memory alloys", Int. J. Solids Structures 33, 991-1003 (1996).

[5] Dimitris C. Lagoudas (2008), "Shape memory alloy Modeling and Engineering Applications", Department of Aerospace Engineering Texas A&M, University College Station TX, USA.

[6] F. Auricchio, R. L. Taylor and J. Lubliner, "Shape-memory alloys: macromodelling and numerical simulations of the superelastic behavior", Comput. Meths Appl. Mech. Engng 146 (1997) 281-312.

[7] A. A. Likhachev and Yu.N. Koval, "On the differential equation describing the hysteretic behavior of shape memory alloys", Scripta Met. Mater. 27, 223-227 (1992).

[8] F.Auricchio and E.Sacco, "Thermo-mechanical modelling of a superelastic shapememory wire under cyclic stretching-bending loadings", International Journal of Solids and Structures, Vol. 38, pp. 6123–6145(2001).

[9] C. M. Wayman, Introduction to the Crystallography of Martensitic Transformations, Macmillan (1964).

[10] F. Auricchio and E. Sacco, "A one-dimensional model for superelastic shape-memory alloys with different elastic properties between martensite and austenite", International Journal of Non-Linear Mechanics, 32:1101-1114, 1997.

[11] F. Auricchio, SHAPE-MEMORY ALLOYS: Applications, micromechanics, macromodelling and numerical simulations, Ph.D. dissertation, Department of Civil Engineering, University of California at Berkeley (1995).

[12] I. Muller and H. Xu, "On the pseudo-elastic hysteresis", Acta Met. Mater. 39, 263-271 (1991).

[13] Nguyen Truong Giang, Hoang Ngoc Quy, "Evaluate the effectiveness of shape memory alloy in the cable-stayed bridge dampers", Hội nghị Khoa học 45 năm Viện Hàn lâm Khoa học và Công nghệ Việt Nam 1975-2020, Hà Nội, pp 118-129.

[14] O. Ben Mekki, F. Auricchio, "Performance evaluation of shape-memory-alloy superelastic behavior to control a stay cable in cable-stayed bridges", International Journal of Non-Linear Mechanics, (2010).

[15] G.W. Housner, L.A. Bergaman, T.K. Caughey, A.G. Chassiakos, R.O. Claus, S.F. Masri, R.E. Skelton, T.T. Soong, B.F. Spencer, J.T.P. Yao, "Structural control: past, present, and future", Journal of Engineering Mechanics 123 (9) (1997) 897–971.

The 6th International Conference on
Engineering Mechanics and Automation (ICEMA 2021)
Hanoi, November 14, 2021

Vibration analysis of FGM ring-stiffened conical shells by Continuous Element Method

Cong Vinh Pham
Hanoi University of Science and Technology
School of Mechanical Engineering
Hanoi, Vietnam
phamcongvinh06041997@gmail.com

Manh Cuong Nguyen
Hanoi University of Science and Technology
School of Mechanical Engineering
Hanoi, Vietnam
cuong.nguyenmanh1@hust.edu.vn

Tuan Hai Nguyen
Hanoi University of Science and Technology
School of Mechanical Engineering
Hanoi, Vietnam
hai.nt171258@sis.hust.edu.vn

Abstract: **This research presents the continuous element (CE) formulation for the vibration analysis of FGM ring-stiffened conical shells. Using the solutions of the shell differential equations, the dynamic stiffness matrix of the investigated structure is evaluated. An algorithm of assembling conical and annular shells is introduced in order to compute the natural vibrational frequencies of FGM ring-stiffened conical shells. The CE solutions will be compared to those from other researches to emphasize the advantages of the continuous element method in terms of higher accuracy, saving computer time and resources and especially, the possibility to investigate the medium and high frequency ranges. The influences of shell and material parameters are also in consideration.**

Keywords: *Dynamics stiffness matrix, Continuous Element Method, FGM shell, conical shell, ring-stiffened conical shells, vibration of shell.*

I. Introduction

Thick conical shells, especially ring-stiffened conical shells occupy leading positions in civil, mechanical, architectural, aeronautical, and marine engineering. In relevance with the advancements of materials, the Functionally graded materials (FGM) are a special class of composites that exhibit smooth and continuous variation of material properties from one surface to another and can thus alleviate stress concentrations present in multilayer composites. Due to the complexity of those structures as well as the difficulties of modeling the FGM material, the determining of correct frequencies and vibration modes is of considerable importance for the engineering design of these structures.

Abundant studies have been conducted on metal, composite and FGM conical shell structures using different approaches: a power series solution combining with Donnell–Mushtari and Flügge equations [1], a four-parameter power-law distribution [2], FSDT and Rayleigh-Ritz procedure [3], Haar wavelet method [4], meshless method [5], superposition method combining with Galerkin method and Harmonic balance method [6]. However, these solutions meet difficulties with the construction of complex formulations representing the FGM ring-stiffened shells if the number of rings becomes important or if the structure are composed by various kinds of shells: cylinders, cones…especially in medium and high frequency range.

The Continuous Element Method (CEM) or Dynamics Stiffness Method (DSM) has been developed to overcome such difficulties of other approaches. Various types of continuous elements have been introduced for composite shells [7], composite ring-stiffened cylindrical shells [8], FGM conical shells on elastic foundation [9] and FGM annular plates [10]. Nevertheless, the studies on CEM of FGM complex ring-stiffened conical shells have never been mentioned before. In this study, the ring-stiffened conical shells made by FGM ceramic-metallic material are under investigation. The dynamic stiffness matrix of the studied structure will be constructed basing on the FSDT. Obtained natural frequencies will be validated by comparing with those from the literature in order to validate the precision and reliability of the present formulations. The effects of the power-law exponent and cone angles on the free frequencies of the studied structures has also been examined and discussed.

II. Theoretcal Fomulations

A. Description of the model

Consider a revolution FGM shell presented by a conical shell, as shown in Figure 1. R_1 is small radius and R_2 is large one, L is the length of generator line of the cone and α is its vertex angle. The radius at every point along its length is calculated by $R(x) = R_1 + x sin\alpha$ (1)

If $\alpha \to 0$, the equation (1) presents cylindrical shells, if $\alpha \to \pi/2$ or $\alpha \to -\pi/2$, the equation (1) corresponds to the case of outer ring or inner ring-stiffeners.

Typically, FGM shells are created from mixture of two materials M_1 and M_2. In this research, FGM shells are made from mixture of ceramic and metal Young's modulus $E(z)$, density $\rho(z)$ and Poisson's ratio $\mu(z)$ are assumed to vary continuously with the shell thickness and can be expressed as a linear combination:

$$E(z) = (E_c - E_m).V_c + E_m$$
$$\mu(z) = (\mu_c - \mu_m).V_c + \mu_m \quad (2)$$
$$\rho(z) = (\rho_c - \rho_m).V_c + \rho_m$$

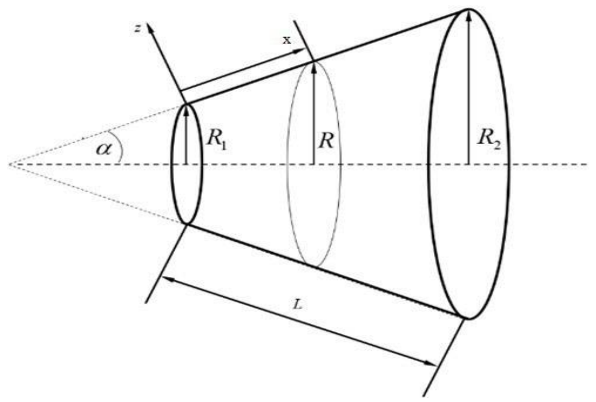

Fig. 1. Geometry and coordinate system of conical shells

Where the symbol c and m represent ceramic and metal components, respectively.

The volume fraction V_c follows two generalized four-parameter power-law distributions [1]:

$$V_c = \left[1 - a\left(\frac{1}{2} + \frac{z}{h}\right) + b\left(\frac{1}{2} + \frac{z}{h}\right)^c\right]^p \quad (3)$$

In which, the exponent of the power p is a positive real number ($0 < p < \infty$) and the parameters a, b,c defined contour variation material through the thickness of the crust is graded according to function power. Assuming that the sum of the volumes of the two components is essentially uniform, i.e. $V_c + V_m = 1$.

Therefore, according to the relationship defined in equation (2), when the exponent laws of powers p is set to 0 (p = 0) or extremely ($p = \infty$), the FGM material becomes a homogeneous isotropic data, expressed by: $p = \infty \rightarrow V_c = 0$ $V_m = 1 \rightarrow E(z) = E_m,\ \mu(z) = \mu_m, \rho(z) = \rho_m$ (4)

When p = 1, the components of ceramic (M_1) and metal (M_2) will become linear.

B. Kinematic relations and stress resultants

The displacements of a point in the FGM shell for the first-order shear deformation theory (FSDT) are expressed in terms of the displacements and rotation components of the middle surface as:

$$u(x,\theta,z,t) = u_0(x,\theta,t) + z\varphi_x(x,\theta,t);$$

$$v(x,\theta,z,t) = v_0(x,\theta,t) + z\varphi_\theta(x,\theta,t); \quad (5)$$

$$w(x,\theta,z,t) = u_0(x,\theta,t)$$

Where u, v, w are the displacements following x, θ, z directions; u_0, v_0, w_0 are displacement of the middle surface of the shell in the longitudinal direction, circumference and radial directions. φ_x and φ_θ represent linear rotations of the reference surface about the θ and x,-axis respectively. t is time variable.

The linear strain-displacement relations in the shell space are defined as:

$$\varepsilon_x = \frac{\partial_{u_0}}{\partial_x};$$

$$k_x = \frac{\partial_{\varphi_x}}{\partial_x};$$

$$\varepsilon_\theta = \frac{1}{R}\left(u_0 sin\alpha + \frac{\partial_{v_0}}{\partial_\theta} + w_0 cos\alpha\right)$$

$$k_{x\theta} = \frac{1}{R}\frac{\partial_{\varphi_x}}{\partial_\theta} + \frac{\partial_{\varphi_\theta}}{\partial_x} - \frac{sin\alpha}{R}\varphi_\theta \quad (6)$$

$$\varepsilon_{x\theta} = \frac{\partial_{v_0}}{\partial_x} + \frac{1}{R}\frac{\partial_{u_0}}{\partial_\theta} - \frac{sin\alpha}{R}v_0;$$

$$k_\theta = \frac{1}{R}\left(\varphi_x sin\alpha + \frac{\partial_{\varphi_\theta}}{\partial_\theta}\right);$$

$$\gamma_{xz} = \frac{\partial_{w_0}}{\partial_x} + \varphi_x;$$

$$\gamma_{xz} = -\frac{cos\alpha}{R}v_0 + \frac{1}{R}\frac{\partial_{w_0}}{\partial_\theta} + \varphi_\theta$$

Based on Hook's law, the relationship between strains and stress is written as:

$$\begin{Bmatrix} \sigma_x \\ \sigma_\theta \\ \tau_{x\theta} \\ \tau_{xz} \\ \tau_{\theta z} \end{Bmatrix} = \begin{bmatrix} Q_{11}(z) & Q_{12}(z) & 0 & 0 & 0 \\ Q_{12}(z) & Q_{11}(z) & 0 & 0 & 0 \\ 0 & 0 & Q_{66}(z) & 0 & 0 \\ 0 & 0 & 0 & Q_{66}(z) & 0 \\ 0 & 0 & 0 & 0 & Q_{66}(z) \end{bmatrix} \begin{Bmatrix} \varepsilon_x \\ \varepsilon_\theta \\ \gamma_{x\theta} \\ \gamma_{xz} \\ \gamma_{\theta z} \end{Bmatrix} \quad (7)$$

Where the elastic constants $Q_{ij}(z)$ are functions of thickness variable z and defined by:

$$Q_{11}(z) = \frac{E(z)}{1-\mu^2(z)};\quad Q_{12}(z) = \frac{\mu(z)E(z)}{1-\mu^2(z)};\quad Q_{66}(z) = \frac{E(z)}{2[1+\mu(z)]} \quad (8)$$

The relationships between forces, moments and stress are expressed as:

$$(N_x, N_\theta, N_{x\theta}, Q_x, Q_\theta) = \int_{-h/2}^{h/2}(\sigma_{xx}, \sigma_{\theta\theta}, \tau_{x\theta}, \tau_{xz}, \tau_{\theta z})dz \quad (9)$$

$$(M_x, M_\theta, M_{x\theta}) = \int_{-h/2}^{h/2}(\sigma_{xx}, \sigma_{\theta\theta}, \tau_{x\theta})zdz \quad (10)$$

Where N_x, N_θ and $N_{x\theta}$ are the in-place force resultants, M_x, M_θ and $M_{x\theta}$ are moment resultants, Q_x , Q_θ are transverse shear force resultants

Equation (7) - (9) can be rewritten in matrix form as follows:

$$\begin{Bmatrix} N_x \\ N_\theta \\ N_{x\theta} \\ M_x \\ M_\theta \\ M_{x\theta} \\ Q_x \\ Q_\theta \end{Bmatrix} = \begin{bmatrix} A_{11} & A_{12} & 0 & B_{11} & B_{12} & 0 & 0 & 0 \\ A_{12} & A_{11} & 0 & B_{12} & B_{11} & 0 & 0 & 0 \\ 0 & 0 & A_{66} & 0 & 0 & B_{66} & 0 & 0 \\ B_{11} & B_{12} & 0 & D_{11} & D_{12} & 0 & 0 & 0 \\ B_{12} & B_{11} & 0 & D_{12} & D_{11} & 0 & 0 & 0 \\ 0 & 0 & B_{66} & 0 & 0 & D_{66} & 0 & 0 \\ 0 & 0 & 0 & 0 & 0 & 0 & k.F_{44} & 0 \\ 0 & 0 & 0 & 0 & 0 & 0 & 0 & k.F_{55} \end{bmatrix}$$

$$= \begin{Bmatrix} \varepsilon_x \\ \varepsilon_\theta \\ \varepsilon_{x\theta} \\ k_x \\ k_\theta \\ k_{x\theta} \\ \gamma_{xz} \\ \gamma_{\theta z} \end{Bmatrix} \quad (11)$$

The materials used in this study are assumed to be functional grade and linear in recovery. So, extensional stiffness A_{ij}, the bending stiffness D_{ij} and the extensional-bending coupling stiffness B_{ij} stretch respectively are expressed by:

$$A_{ij} = \int_{-h/2}^{h/2} Q_{ij}(z)dz\,;\ B_{ij} = \int_{-h/2}^{h/2} z.Q_{ij}(z)dz\,;$$

$$D_{ij} = \int_{-h/2}^{h/2} z^2.Q_{ij}(z)dz\,; \quad (12)$$

$$F_{ij} = \int_{-h/2}^{h/2} Q_{ij}(z)dz\,; \quad i,j = 4,5$$

Where k is the shear correction factor (k = 5/6)

C. Equations of motion

The equations of motion using the FSDT for a conical shell are determined by:

$$\frac{\partial N_x}{\partial_x} + \frac{sin\alpha}{R}(N_x - N_\theta) + \frac{1}{R}\frac{\partial N_{x\theta}}{\partial_\theta} = I_0\ddot{u} + I_1\ddot{\varphi}_x\,;$$

$$\frac{\partial N_{x\theta}}{\partial_x} + \frac{2sin\alpha}{R}N_{x\theta} + \frac{1}{R}\frac{\partial N_\theta}{\partial_\theta} + \frac{cos\alpha}{R}Q_\theta = I_0\ddot{v}_0 + I_1\ddot{\varphi}_\theta$$

$$\frac{\partial Q_x}{\partial_x} + \frac{1}{R}\frac{\partial Q_\theta}{\partial_\theta} + \frac{sin\alpha}{R}Q_x - \frac{cos\alpha}{R}N_\theta - k_w w + k_p\left(\frac{\partial^2 w}{\partial_{x^2}} + \frac{sin\alpha}{R}\frac{\partial_w}{\partial_x} + \frac{1}{R^2}\frac{\partial^2 w}{\partial_{\theta^2}}\right) = I_0\ddot{w} \quad (13)$$

$$\frac{\partial M_x}{\partial_x} + \frac{sin\alpha}{R}(M_x - M_\theta) + \frac{1}{R}\frac{\partial M_{x\theta}}{\partial_\theta} - Q_x = I_1\ddot{u} + I_2\ddot{\varphi}_x\,;$$

$$\frac{\partial M_{x\theta}}{\partial_x} + \frac{2sin\alpha}{R}M_{x\theta} + \frac{1}{R}\frac{\partial M_\theta}{\partial_\theta} - Q_\theta = I_1\ddot{v}_0 + I_2\ddot{\varphi}_\theta$$

Where $[I_0, I_1, I_2] = \int_{-h/2}^{h/2} \rho(z)[1, z, z^2]dz$

D. Force resultant

The force and moment resultants of FGM revolution shells are determined by: formula (14) in appendix

III. Dynamic Stiffness Matrix For Vibration of FGM Revolution Shells

A. State vectors

The chosen state-vector for the conical shells is:

$$y^T = \{u_0, v_0, w_0, \varphi_x, \varphi_\theta, N_x, N_{x\theta}, Q_x, M_x, M_{x\theta}\}^T \quad (15)$$

Forces, moments and displacements can be expressed by Lévi series expansions for natural vibration mode m of revolution shells as:

$$\{u_o(x,\theta,t), w_o(x,\theta,t), \varphi_x(x,\theta,t), N_x(x,\theta,t), Q_x(x,\theta,t), M_x(x,\theta,t)\}^T$$

$$= \sum_{m=1}^{\infty}\{u_m(x), w_m(x), \varphi_{xm}(x), N_{xm}(x), Q_{xm}(x), M_{xm}(x)\}^T cos(m\theta)$$

$$\{v_o(x,\theta,t), \varphi_\theta(x,\theta,t), N_{x\theta}(x,\theta,t), M_{x\theta}(x,\theta,t)\}^T =$$

$$\sum_{m=1}^{\infty}\{v_m(x), \varphi_{\theta m}(x), N_\theta(x), M_\theta(x)\}^T sin(m\theta)e^{i\omega t} \quad (16)$$

Where m is circumferential mode of the shell.

Equation (14) can be rewritten in matrix form as follows:

$$\frac{dy_m}{dx} = A_m y_m \quad (17)$$

With A_m is a 10x10 matrix.

B. Dynamic stiffness matrix of a FGM conical shell continuous element

The dynamic transfer matrix T_m is evaluated as:

$$T_m(\omega) = e^{\int_0^L A_m(\omega)dx} = \begin{bmatrix} T_{11} & T_{12} \\ T_{21} & T_{22} \end{bmatrix} \quad (18)$$

After some manipulations, the dynamic stiffness matrix is determined as:

$$K_m(\omega) = \begin{bmatrix} T_{12}^{-1}T_{11} & -T_{12}^{-1} \\ T_{21} - T_{22}T_{12}^{-1}T_{11} & T_{22}T_{12}^{-1} \end{bmatrix} \quad (19)$$

C. Dynamic stiffness matrix of FGM ring-stiffened conical shells

The Continuous Elements (represented by the Dynamic Stiffness Matrix) of a FGM conical shell will be evaluated using (19) with $0^o < \alpha < 90^o$ Similarly, by applying the value $\alpha = 90^o$ or $\alpha = -90^o$ in (19), the Continuous Element for a FGM outer or inner ring can be obtained. Next, these two elementary Continuous Elements will be assembled in order to model and to analyze the free vibration of FGM ring-stiffened conical shell

Let's investigate the FGM conical shells with one outer ring stiffener (see Fig. 2). Using CE model, this complex structure is divided into three continuous elements: one conical shell element with length *a*, one ring element and another conical shell element having the length *L-a*. These elements are represented by three dynamic stiffness matrix ***K1c(*ω*)***, ***Kr(*ω*)*** and ***K2c(*ω*)***,respectively. First, it is necessary

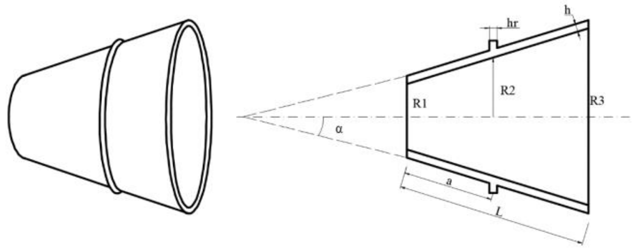

Figure 2. FGM ring-stiffened conical shell

to evaluate separately the dynamic stiffness matrix ***K1c(ω)***, ***Kr(ω)*** and ***K2c(ω)***. Then the assembling procedure of the dynamic stiffness matrix ***K(ω)*** for the ring-stiffened conical shells is developed which satisfies the continuity conditions at the conical-ring joint as follows [1] (α = 90° in this case):

$$u_1 = u_r \cos\alpha - w_r \sin\alpha; \qquad v_1 = v_r;$$

$$w_1 = u_r \sin\alpha + w_r \cos\alpha; \qquad \frac{\partial w_1}{\partial x_1} = \frac{\partial w_r}{\partial x_r}$$

$$N_{x1} = N_{xr} \cos\alpha - Q_{xr} \sin\alpha;$$

$$Q_{x1} = N_{xr} \sin\alpha + Q_{xr} \cos\alpha;$$

$$M_{x\theta 1} = M_{x\theta r}; \quad M_{x1} = M_{xr} \qquad (20)$$

From this dynamic stiffness matrix ***K(ω)***, natural frequencies of FGM ring-stiffened cylindrical shells will be extracted from harmonic responses [7-10].

IV. Numerical results and discussion

First, our formulation will be validated by comparison with solutions from other studies. Due to the lack of studies on FGM ring-stiffened conical shells, CE solutions are compared to the research of Rahimi [2] on FGM cylinder with one ring-stiffener and to those of Tornabene [3] and Zhu Su [4] on FGM conical shells. Here, shell structures and ring-stiffeners are made by the same FGM material described in Table 1.

TABLE 1. MATERIAL PROPERTIES OF THE STUDIED SHELLS

Material	E(GPa)	υ	$\rho(kg/m^3)$
Si_3N_4	322.27	0.24	2370
Nickel	205.98	0.31	8900
Zirconia	244.27	0.28	5700
Strainless Steel	201.04	0.3262	8166

A. *Validation of the present model*

Table 2 presents the comparison of CE solutions with those of Rahimi et al. [2] using Ritz method and thin Sander shell theory for a FGM cylindrical shell with one ring support. The shell and ring dimensions are: L = 51.12 cm, R = 21.62 cm, R_r=h_r=h = 0.15 cm, Free-Clamped (F-C) boundary condition is under investigation. The shell and ring are made of Zirconia/ Strainless Steel FGM with following properties: $(a = 1/b = 0.5/c = 2/p = 5)$ (FGM_I). (Material 1). L_1 is the distance from the left end of the shell to the position of the ring. In this case, our developed continuous element for FGM ring-stiffness conical shells can be used for modeling ring-stiffness cylindrical shells by setting a very small value of α and α=1° is chosen in this study. Very tiny errors obtained by two solutions (under 1%) confirm the exactness and the reliability of our formulation for studying the vibration of FGM ring-stiffened shell structures.

Next, To confirm the proposed formulation, the frequency parameter $\Omega = \omega R_2 \sqrt{\rho\,(1-\mu^2)/E}$ of a C-C isotropic conical shell without ring support compared with previously published analytical results from Shu[5] using the global method of generalized differential quadrature (GDQ) and Zhu Su [6] employing using the first-order shear deformation theory and Rayleigh–Ritz procedurein Table 3. The power-law p is set to 0 so that the FGM material becomes homogeneous isotropic data. FSDT solutions obtained by Tornabene et al. [3] and Zhu Su et al. [4] are used for validating our continuous element model for the case of FGM conical shell without ring-stiffeners.Table 4 shows the first four frequencies for FGM conical shells with F–C boundary condition, which made of aluminum and zirconia and have $R_1 = 0.5, h = 0.1, L\cos\alpha = 2, \alpha = 45°$. The Material 1 is used for comparison except three values of *p* (*p*=0.6, 5, 20) are examined. It is seen that the CE results are in good agreement with those of [3] and [4] for different power-series exponents *p*. From this comparison, it can be certainly identified that the present results agree well with those in the literature.

TABLE 2. COMPARISON OF NATURAL FREQUENCIES (HZ) FOR A FGM CYLINDRICAL SHELL WITH ONE RING SUPPORT (M=1, N=1)

(L = 51.12 cm, R = 21.62 cm, R_r=h_r=h = 0.15 cm , B.C. : F − C), Material 1

L_1/L	Rahimi[2]	Present	Errors (%)
0	120.8574	119.7276	0.93
0.2	158.7590	158.3592	0.25
0.5	294.2014	293.8351	0.12
0.8	533.7894	533.0724	0.13
1	415.6396	414.9329	0.17

B. *Influences of power-law exponents*

In this section, the variation of frequencies for the $FGM_{I(a=1/b=0.5/c=2/p)}$ conical shells having one ring-stiffened with respect to different power-law exponent values will be examined. The shell parameters are: $R_1 = 1m, H = 2m, h = 0{,}1m, a/H = 0.5$ and for the ring $R_r = 0.1m, h_r = 0.1m$. The same FGM material (Si3N4, Nickel) is used for both ring and shell and the Free-Clamped boundary condition are in investigation. Obtained results are exhibited in Table 5 and Figure 3. It is shown in Table 5 and Figure 3 that when *p* increases, natural frequencies decrease. It is obvious that when *p* augments, the rate of change in material composition changes, resulting in a shift in the ratio between ceramic and metal. As *p* rises, the material ratio changes from rich ceramic components to rich metal ones. As a result, rich ceramic FGM has higher rigidity than rich metal- rich materials.

C. *Effects of semi-vertex cone angle*

Next, the free vibrations of FGM (Si3N4, Nickel) ring-stiffened conical shells with different semi-vertex angles α are studied. The geometrical parameters of the FGM conical shells are taken to be: $R_1 = 1m, H = 2, a/L = 0.5, R_r = 0.1m, h = h_r = 0.1m$ and boundary condition: F-C is applied. Results are given in Table 6 and Figure 4. It is shown that the fundamental frequencies of the FGM conical shells also increase as semi-vertex angle α decreases. It is obvious that the stiffness of a ring-stiffened FGM conical shell reduces when α augments, thus the natural frequencies decrease.

TABLE 3. COMPARISON OF FREQUENCY PARAMETERS $\Omega = \omega R_2\sqrt{\rho(1-\mu^2)/E}$ FOR A C-C ISOTROPIC CONICAL SHELL WITHOUT RING SUPPORT ($\alpha = 45°, h/R_2 = 0.01, Lsin\alpha/R_2 = 0.5, m = 1$)

	n							
	0	1	2	3	4	5	6	7
Shu [2]	0.8732	0.8120	0.6696	0.5428	0.4566	0.4089	0.3963	0.4143
Zhu Su [3]	0.8726	0.8117	0.6694	0.5427	0.4564	0.4086	0.3958	0.4133
Present	0.8358	0.7938	0.6834	0.5674	0.4814	0.4306	0.4151	0.4295

TABLE 4. COMPARISON OF THE FIRST FOUR FREQUENCIES (HZ) FOR FGM CONICAL SHELL WITHOUT RING SUPPORT ($\alpha = 45°, h/R_2 = 0.01, Lsin\alpha/R_2 = 0.5, m = 1, BC: F-C$)

Type FGM	$p = 0,6$			$p = 5$			$p = 20$		
	[3]	[4]	Present	[3]	[4]	Present	[3]	[4]	Present
$FGM_{I(a=1/b=0.5/2/p)}$	208.92	208.58	225.6	204.81	203.36	221.6	204.89	203.29	221.0
	230.11	230.06	236.0	223.84	223.72	230.1	227.33	227.17	232.8
	284.73	284.67	283.8	275.52	275.26	275.1	282.68	282.35	281.6
	321.51	321.28	345.8	316.64	315.48	340.2	312.5	311.15	335.9
	208.49	208.74	225.1	202.87	203.30	219.2	202.6	203.89	218.2
	229.65	229.61	235.4	221.78	222.16	227.5	224.87	224.73	229.8
	284.17	284.21	283.1	273.02	273.47	272.0	279.65	279.80	277.9
	321.18	321.33	345.6	315.18	315.81	339.3	310.83	311.39	334.9

TABLE 5. THE INFLUENCE OF THE POWER-LAW EXPONENTS p ON NATURAL FREQUENCIES OF $FGM_{I(a=1/b=0.5/c=2/p)}$ RING-STIFFENED CONICAL SHELLS ($\alpha = 30°, R_1 = 1m, H = 2, a/L = 0.5, R_r = 0.1m, h = 0.1m$, B.C.: F – C)

p	Frequency (Hz)											
0.5	113	125	160	162	199	203	221	223	240	264	275	277
2	83	91	117	118	146	149	162	163	176	194	200	203
5	69	76	98	99	122	124	135	137	147	163	166	168
20	62	68	88	89	109	111	121	122	132	146	149	151
100	60	66	85	87	105	108	117	118	127	140	145	147

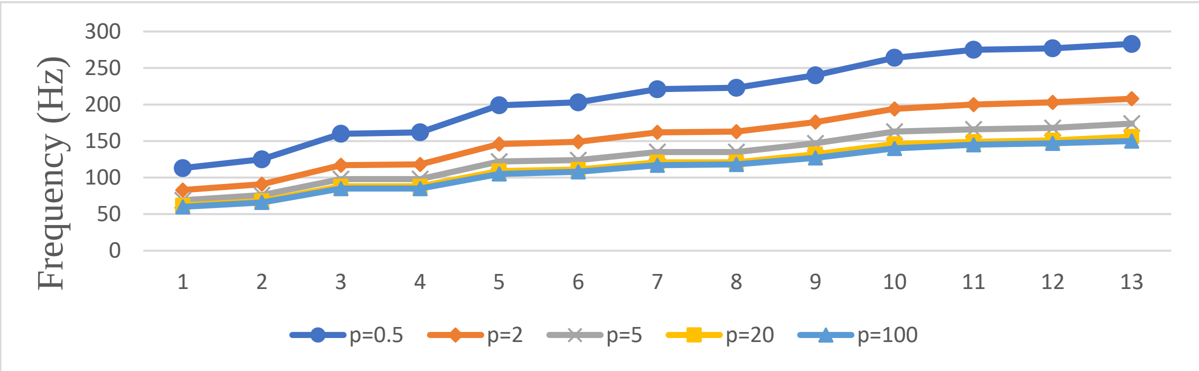

Figure 3. The variation of frequencies for the $FGM_{I(a=1/b=0.5/2/p)}$ ring-stiffened conical shells with different power-law exponents ($R_1 = 1m$, $H = 2m, R_r = 0.1m, h = h_r = 0.1m, a/L = 0.5$ B.C.: F – C)

TABLE 6. THE INFLUENCE OF SEMI-VERTEX ANGLE α ON NATURAL FREQUENCIES OF $FGM_{I(a=1/b=0.5/c=2/p=1)}$ RING-STIFFENED CONICAL SHELLS ($R_1 = 1m, H = 2, a/L = 0.5, R_r = 0.1m, h = h_r = 0.1m$, B.C.: F – C)

α	Frequency (Hz)											
15°	134	136	200	248	259	260	276	311	328	347	403	416
30°	98	108	138	140	172	176	191	193	208	229	237	240
45°	65	72	76	90	105	107	113	115	125	126	129	145
60°	37	41	42	47	54	56	58	59	62	63	64	68

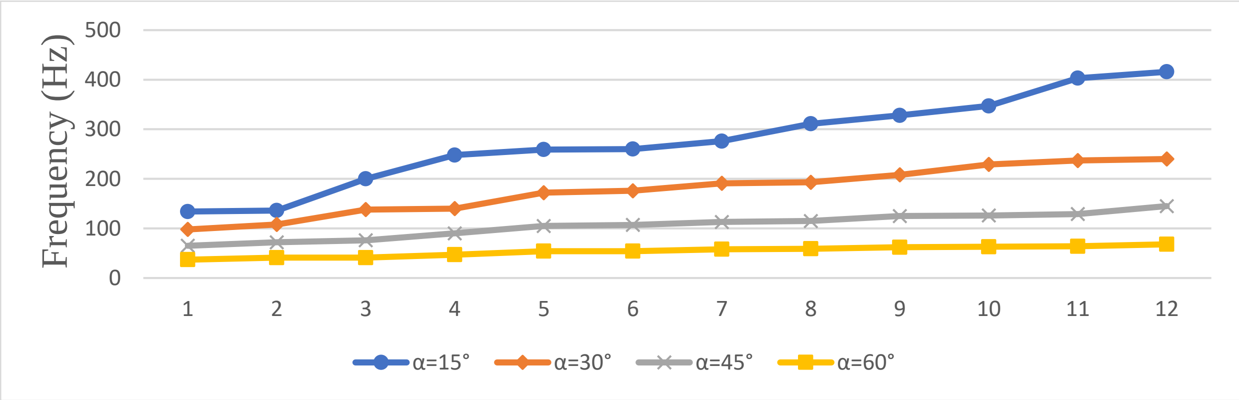

Figure 4. The variation of frequencies for the $FGM_{I(a=1/b=0.5/2/p)}$ ring-stiffened conical shells with different semi-vertex angle α

$(R_1 = 1m,\ H = 2m, R_r = 0.1m, h = h_r = 0.1m, a/L = 0.5$ B.C.: F – C)

V. Conclusion And Developments

In this research, a new Dynamic Stiffness Matrix has been successfully constructed for analyzing FGM ring-stiffened conical shells. The obtained results indicate that CEM allows computing the natural frequencies of vibration analysis FGM ring-stiffened conical shells with high accuracy for any frequency range. Through various test case, it is noted that the Continuous Element Method can effectively be employed for the analysis of FGM ring-stiffened conical shells where almost all other current methods meet grand difficulties due to the important number of meshing elements as well as the complexity of the studied structures. The influences of the power-law exponent and semi-vertex cone angles have also been envisaged in details.

The developments of the CE model can be developed to deal with the problem of FGM joined cylindrical-conical-ring shell structure and FGM ring-stiffened conical shells in interaction with elastic foundations.

References

[1] Caresta M, Kessissoglou NJ. Free vibrational characteristics of isotropic coupled cylindrical–conical shells. Journal of Sound and Vibration, 329, (6), (2010): pp. 733–751.

[2] G.H. Rahimi, R. Ansari and M. Hemmatnezhad. (1981). Vibration of functionally graded cylindrical shells with ring support. Scientia Iranica, 18(6), (2011), pp. 1313-132

[3] Francesco Tornabene. Free vibration analysis of functionally graded conical, cylindrical shell and annular plate structures with a four-parameter power-law distribution. Comput Methods Appl Mech Engrg,198, (2009), pp. 37 – 40

[4] Zhu Su, Guoyong Jin, Shuangxia Shi, Tiangui Ye, Xingzhao Jia. A unified solution for vibration analysis of

Keep your text and graphic files separate until after the text has been formatted and styled. Do not use hard tabs, and limit use of hard returns to only one return at the end of a paragraph. Do not add any kind of pagination anywhere in the paper. Do not number text heads-the template will do that for you.

[5] Xiang Xie, Guoyong Jin, Tiangui Ye, Zhigang Liu. Free vibration analysis of functionally graded conical shells and annular plates using the Haar wavelet method. Applied Acoustics, 85, (2014), pp.130-142.

[6] X. Zhao, K.M. Liew. Free vibration analysis of functionally graded conical shell panels by a meshless method. Composite Structures, 93, (2011), pp. 649 – 664.

[7]. J.B. Casimir, M.A. Khadimallah, M.C. Nguyen. Formulation of the dynamic stiffness of a cross-ply laminated circular cylindrical shell subjected to distributed loads, Computers and Structures 166 (2016) 42–50.

[8]. Nam L. T. B, Cuong N. M, Thinh T. I, Dat T. T, Trung V. D. Continous Element Formulation for Composite Ring-Stiffened Cylindrical Shells, Vietnam Journal of Science and Technology **56** (4) (2018) 515-530.

[9]. Nguyen Dong Anh, Le Quang Vinh, Nguyen Manh Cuong and Vu Quoc Hien. Dynamic analysis of FGM conical shells surrounded by Pasternak elastic foundations. The 3rd Int. Conf. on Transport Infrastructure & Sustainable Development, (2019)

[10]. Nguyen Manh Cuong, Le Quang Vinh and Nguyen Dong Anh. Dynamic analysis of functionally graded annular plates via Continuous Element Method. Tuyển tập công trình Hội nghị khoa học toàn quốc Cơ học Vật rắn lần thứ XIV, TPHCM, 7-2018. Pp. 105-112

APPENDIX:

$$N_S = A_{11}\frac{\partial u_0}{\partial s} + \frac{A_{12}}{R}\left(u_0 \sin\alpha + \frac{\partial \upsilon_0}{\partial \theta} + w_0 \cos\alpha\right) + B_{11}\frac{\partial \phi_S}{\partial s} + \frac{B_{12}}{R}\left(\phi_S \sin\alpha + \frac{\partial \phi_\theta}{\partial \theta}\right)$$

$$N_\theta = A_{12}\frac{\partial u_0}{\partial s} + \frac{A_{22}}{R}\left(\frac{\partial v_0}{\partial \theta} + w_0 \cos\alpha\right) + B_{12}\frac{\partial \phi_S}{\partial s} + B_{22}\left(\phi_S \sin\alpha + \frac{\partial \phi_\theta}{\partial \theta}\right)$$

$$N_{S\theta} = A_{66}\left(\frac{\partial v_0}{\partial s} + \frac{1}{R}\left(\frac{\partial u_0}{\partial \theta} - \upsilon_0 \sin\alpha\right)\right) + B_{66}\left(\frac{1}{R}\frac{\partial \phi_S}{\partial \theta} + \frac{\partial \phi_\theta}{\partial s}\frac{\sin\alpha}{R}\phi_\theta - \frac{\cos\alpha}{2R^2}\frac{\partial u_0}{\partial \theta} + \frac{\cos\alpha}{2R}\frac{\partial \upsilon_0}{\partial s} + \frac{\cos\alpha \sin\alpha}{2R^2}\upsilon_0\right)$$

$$M_S = B_{11}\frac{\partial u_0}{\partial s} + \frac{B_{12}}{R}\left(u_0 \sin\alpha + \frac{\partial v_0}{\partial \theta} + \frac{w_0 \cos\alpha}{R}\right) + D_{11}\frac{\partial \phi_S}{\partial s} + \frac{D_{12}}{R}\left(\phi_S \sin\alpha + \frac{\partial \phi_\theta}{\partial \theta}\right)$$

$$M_\theta = B_{12}\frac{\partial u_0}{\partial s} + \frac{B_{22}}{R}\left(u_0 \sin\alpha + \frac{\partial v_0}{\partial \theta} + w_0 \cos\alpha\right) + D_{12}\frac{\partial \phi_S}{\partial s} + \frac{D_{22}}{R}\left(\phi_S \sin\alpha + \frac{\partial \phi_\theta}{\partial \theta}\right) \quad (14)$$

$$M_{S\theta} = B_{66}\left(\frac{\partial v_0}{\partial s} + \frac{\partial u_0}{R\partial \theta} - \frac{\sin\alpha}{R}\upsilon_0\right) + D_{66}\left(-\frac{\cos\alpha}{2R^2}\frac{\partial u_0}{\partial \theta} + \frac{\cos\alpha}{2R}\frac{\partial \upsilon}{\partial s} + \frac{1}{R}\frac{\partial \phi_S}{\partial \theta} + \frac{\partial \phi_\theta}{\partial s} + \frac{1}{R}\sin\alpha\phi_\theta + \frac{1}{2R^2}\cos\alpha\sin\alpha\upsilon_0\right)$$

$$Q_\theta = KA_{44}\left(\frac{-\cos\alpha}{R}\upsilon_0 + \frac{1}{R}\frac{\partial w_0}{\partial \theta} + \phi_\theta\right), Q_S = KA_{55}\left(\frac{\partial w_0}{\partial s} + \phi_S\right)$$

Here $A_{16} = A_{26} = A_{45} = B_{16} = B_{26} = D_{16} = D_{26} = 0$

Transform the formula 17:

$$y_k = T.y_0$$

$$T = \frac{y_k}{y_0}$$

$$\frac{dy_m}{dx} = A_m y_m$$

$$\frac{d_{y_m}}{y_m} = A_m dx$$

$$\int_0^L \frac{d_{y_m}}{y_m} = \int_0^L A_m dx$$

$$\ln\frac{y_{mL}}{y_{m0}} = \int_0^L A_m dx$$

$$\frac{y_{mL}}{y_{m0}} = e^{\int_0^L A_m dx}$$

$$T = e^{\int_0^L A_m dx}$$

The 6th International Conference on Engineering Mechanics and Automation (ICEMA 2021)
Hanoi, November 14, 2021

Finite element modeling for free vibration behaviors of piezoelectric cracked nanoplates with flexoelectric effects

Doan Hong Duc
University of Engineering and Technology
Vietnam National University
Hanoi, Vietnam
doan.d.aa.eng@gmail.com

Do Van Thom
Faculty of Mechanical Engineering
Le Quy Don Technical University
Hanoi, Vietnam
thom.dovan.mta@gmail.com

Phung Van Minh
Faculty of Mechanical Engineering
Le Quy Don Technical University
Hanoi, Vietnam
minhpv.mta@gmail.com

Nguyen Dinh Duc
University of Engineering and Technology
Vietnam National University
Hanoi, Vietnam
ducnd@vnu.edu.vn

***Abstract*: For the first time, the finite element technique is used to investigate the free vibrations of fractured nanoplates where linearly changing plate thickness and the flexoelectric effect are taken into account. Mindlin's first-order shear deformation theory is used to establish mechanical behavior relations and equilibrium equations for nanoplates. Because the phase-field variable is employed to describes the crack, it forms a continuum that is simple to compute and integrated. The present theory is reviewed for accuracy by comparing the computed data of this paper with those of published findings. The effects of geometric and material properties on natural frequencies, vibration mode shapes, and charge polarization of fractured and variable thickness nanoplates are then investigated in this study.**

Keywords: vibration, nanoplates, finite element method, flexoelectricity, first-order shear deformation, variable thickness

I. INTRODUCTION

The flexoelectric effect arises in dielectric materials as a result of a combination of charge polarization and strain variation [1-4]. This phenomenon was detected by Kogan in 1964, and it was not of significant concern to researchers for many periods afterward, mostly because the material technology level, as well as the applications of this influence, had not developed to the same stage. However, since the mid-2000s, when nanoscience advanced so rapidly that scientists discovered numerous coefficients linked to the flexoelectric effect of materials with high capacitance coefficients, and structures as tiny as nanometers are widely utilized, this tendency has shifted dramatically. Researchers all around the globe discovered that the flexoelectric effect would be visible for nano-scale structures since only these structures would exhibit the phenomena of deformation variations [5-7]. Materials having the flexoelectric effect have been extensively utilized in various sectors and areas because of this polarization effect.

Mechanical reactions, as well as free vibration of structures, have been discovered by researchers all around the globe, with notable results. Using Kirchhoff plate theory and the Ritz approximation technique, Zhang et al. [8] examined the flexoelectric impact on the electroelastic responses and free vibrational behaviour of a piezoelectric nanoplate. Another group of researchers, led by Yang and associates, investigated the flexoelectric effect and provided an accurate solution for free vibration and static bending of nanoplates, which includes the flexoelectric effect. When taking into consideration the flexoelectric effect, Shingare and Kundalwal [10] studied the static and forced vibration response of graphene reinforced nanocomposite plates. The theory for shear deformation of the first-order was used by Amiret al. [11] to study the free vibration behavior of flexoelectric sandwich plates based on the elastic medium of two parameters. The Kirchhoff plate theoretical approach, the modified flexolelectric theory, and disruptive techniques were used by Ghobadi and his collaborators [12] to investigate the nonlinear FG flexoelectric nano-plates' thermo-electromechanical vibration behaviour. Arani and coworkers [13] used first-order shear deformation plate theory and a differential quadrature method to investigate the impacts of flexoelectricity and surface effects on the nonlocal vibration of annular nanoplates. The works [14-17] also investigated the mechanical responses of nanoplates taking into account piezoelectric and flexoelectric effects. Cracks may occur during the manufacturing process or during operation; one of the most frequent defects in plate structure is cracking. Cracks have a major effect on the overall mechanical reaction and vibration response of these structures, decreasing their performance in application. The investigation of cracked plate structures aids in the identification of failures as well as the most efficient design and exploitation. Scientists have explored the overall mechanical behavior and vibration behavior of fractured plates and have obtained specific findings. The projects [21–31] demonstrated the vibration characteristics of cracked plates using a wide range of applications and methods, including the Ritz method [21, 27, 28, 30], phase-field concept and the finite difference method [22], analytical solutions [23, 24, 26, 29], peridynamic ideas [25], and the finite element analysis [31].

Only a few studies [31] are reported for the free vibration issue of fractured nanoplates. As can be seen, the free vibration issue of fractured nanoplates in general, and the flexoelectricity effect, in which the plate thickness may be altered, in particular, has not been reported; nevertheless, this is an intriguing mathematical topic. At the same time, it has a suitable orientation for the most efficient exploitation and usage of nanostructures when the flexoelectricity effect is taken into consideration. As a result, this study employs phase-field theory in conjunction with the finite element technique to investigate the free vibration of fractured nanoplates of varying thickness, including the impact of flexoelectricity.

The body of this work is as follows: Section 2 provides finite element formulas for calculating the free vibration issue of fractured nanoplates while taking the flexoelectric effect into consideration. Section 3 includes verification examples that demonstrate the correctness of the suggested methodology and mathematical model. Section 4 introduces numerical findings and comments on the free vibration responses of fractured nanoplates in detail. Part 5 offers several new findings linked to the paper's substance.

II. Finite element model of flexoelectric cracked nanoplate with variable thickness

A nanoplate with dimensions of length a, width b, and thickness h is considered in the Cartesian coordinate system $Oxyz$, as illustrated in Figure 1, and the crack has a length of c (the thickness h varies linearly along the x-axis).

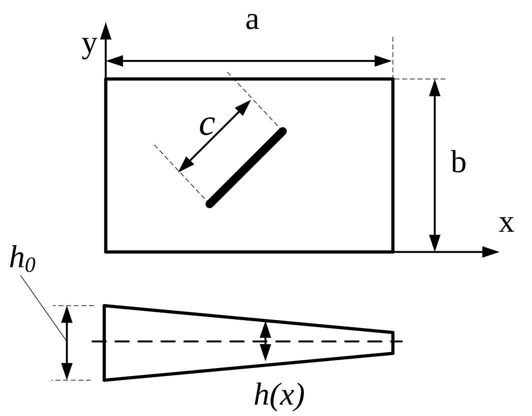

Fig. 1. A flexoelectric cracked nanoplate model

This study is based on Mindlin plate theory and the three-dimensional displacement field (u, v, w) is

$$\begin{aligned}&\left\{u_x,u_y\right\}(x,y,z)=\left\{u_0,v_0\right\}\left(x,y,0\right)\\&+z\left\{\phi_x,\phi_y\right\}\left(x,y\right);\ u_z(x,y,z)=w_0(x,y,0)\end{aligned}\tag{1}$$

in which u_0, v_0 and w_0 denote displacements in the x, y, and z directions at the mid-plane of the nanoplate, respectively, whereas ϕ_x and ϕ_y represent the transverse normal rotations of the y- and x-axes, respectively.

This study used the finite element technique in conjunction with phase-field theory, with every single element consisting of mechanical displacement components and a phase-field component S. These variables in each element are computed as follows from the displacement at the element nodes:

$$\begin{aligned}&u_0=\sum_{i=1}^{n}N_iu_{0i};\ v_0=\sum_{i=1}^{n}N_iv_{0i};\ \phi_x=\sum_{i=1}^{n}N_i\phi_{xi}\\&\phi_y=\sum_{i=1}^{n}N_i\phi_{yi};\ w_0=\sum_{i=1}^{n}N_iw_{0i};\ s=\sum_{i=1}^{n}N_i^ss_i=\boldsymbol{N}^s\boldsymbol{s}\end{aligned}\tag{2}$$

in which n = 3 is the number of nodes in each element (triangle plate element), N_i and N_i^s are the shape functions of the quadratic polynomial and the first-degree polynomial, respectively.

The bending strain field is defined as:

$$\begin{aligned}\boldsymbol{\varepsilon}=\begin{Bmatrix}\varepsilon_{xx}\\\varepsilon_{yy}\\\gamma_{xy}\end{Bmatrix}&=\begin{Bmatrix}\dfrac{\partial u_0}{\partial x}+z\dfrac{\partial\phi_x}{\partial x}\\\dfrac{\partial v_0}{\partial y}+z\dfrac{\partial\phi_y}{\partial y}\\\dfrac{\partial u_0}{\partial y}+\dfrac{\partial v_0}{\partial x}+z\left(\dfrac{\partial\phi_x}{\partial y}+\dfrac{\partial\phi_y}{\partial x}\right)\end{Bmatrix}\\&=\underbrace{\begin{Bmatrix}\varepsilon_{0x}\\\varepsilon_{0y}\\\gamma_{0xy}\end{Bmatrix}}_{\boldsymbol{\varepsilon}_0}+z\underbrace{\begin{Bmatrix}\varepsilon_{1x}\\\varepsilon_{1y}\\\gamma_{1xy}\end{Bmatrix}}_{\boldsymbol{\varepsilon}_1}=\boldsymbol{\varepsilon}_0+z\boldsymbol{\varepsilon}=\boldsymbol{B}_0\boldsymbol{q}_e+z\boldsymbol{B}_1\boldsymbol{q}_{e1}\end{aligned}\tag{3}$$

where $\boldsymbol{q}_e=\left\{u_0,v_0,w_0,\phi_x,\phi_y\right\}^T$ and

$$\boldsymbol{B}_0=\sum_{i=1}^{n}\begin{bmatrix}\dfrac{\partial N_i}{\partial x}&0&0&0&0\\0&\dfrac{\partial N_i}{\partial y}&0&0&0\\\dfrac{\partial N_i}{\partial y}&\dfrac{\partial N_i}{\partial x}&0&0&0\end{bmatrix};\ \boldsymbol{B}_1=\sum_{i=1}^{n}\begin{bmatrix}0&0&0&\dfrac{\partial N_i}{\partial x}&0\\0&0&0&0&\dfrac{\partial N_i}{\partial y}\\0&0&0&\dfrac{\partial N_i}{\partial y}&\dfrac{\partial N_i}{\partial x}\end{bmatrix}\tag{4}$$

The shear strain field is calculated as:

$$\boldsymbol{\gamma}=\left\{\gamma_{xz};\ \gamma_{yz}\right\}=\left\{\phi_x+\frac{\partial w_0}{\partial x};\phi_y+\frac{\partial w_0}{\partial y}\right\}=\boldsymbol{B}_\gamma\boldsymbol{q}_e\tag{5}$$

with $$\boldsymbol{B}_\gamma=\sum_{i=1}^{n}\begin{bmatrix}0&0&\dfrac{\partial N_i}{\partial x}&1&0\\0&0&\dfrac{\partial N_i}{\partial y}&0&1\end{bmatrix}.$$

This study makes the assumption that the electric field is applied solely in the thickness direction, ignoring the

x- and y-axes. As a result, the nanoplate's strain gradient is denoted as: the strain gradients along the thickness direction

$$\boldsymbol{\eta}=\left\{\eta_{xxz}=\frac{\partial\varepsilon_x}{\partial z}=\frac{\partial\phi_x}{\partial x};\eta_{yyz}=\frac{\partial\varepsilon_y}{\partial z}=\frac{\partial\phi_y}{\partial y}\right\} = \boldsymbol{B}_\eta\boldsymbol{q}_e;$$

$$\boldsymbol{B}_\eta=\sum_{i=1}^{n}\begin{bmatrix}0 & 0 & 0 & \frac{\partial N_i}{\partial x} & 0\\ 0 & 0 & 0 & 0 & \frac{\partial N_i}{\partial x}\end{bmatrix} \tag{6}$$

This study makes no attempt to account for the influence of nonlocal parameters. Because this study takes into account the impact of flexoelectricity, the stress and electric displacement vectors for a nanoscale dielectric material have the following detail form [2]:

$$\begin{aligned}&\sigma_{ij}=c_{ijkl}\varepsilon_{kl}-e_{kij}E_k;\ \chi_{ijm}=-f_{kijm}E_k;\\ &P_i=c_{ijk}\varepsilon_{jk}+\kappa_{ij}E_k+f_{ijkl}\eta_{jkl}\end{aligned} \tag{7}$$

in which σ_{ij} is the stress tensor, E_k is the electrical field, χ_{ijm} is the moment stress tensor or higher-order stress tensor, P_i is the electric displacement vector, c_{ijkl}, e_{kij}, f_{kijm}, and κ_{ij} are elastic, piezoelectric, flexoelectric, permittivity constant tensor components. The polarization $f_{ijkl}\eta_{jkl}$ of the charge as a result of the flexoelectric effect is the third component in the expression of P_i.

The following is how equation (7) is represented in matrix form:

$$\boldsymbol{\sigma}=\begin{bmatrix}c_{11} & c_{12} & 0\\ c_{12} & c_{11} & 0\\ 0 & 0 & c_{66}\end{bmatrix}\begin{Bmatrix}\varepsilon_x\\ \varepsilon_y\\ \gamma_{xy}\end{Bmatrix}-e_{31}\begin{Bmatrix}1\\1\\0\end{Bmatrix}E_z=\boldsymbol{F}_\sigma\boldsymbol{\varepsilon}\text{-}\boldsymbol{E}_{3z};$$

$$\boldsymbol{\sigma}_\tau=\begin{Bmatrix}\sigma_{xz}\\ \sigma_{yz}\end{Bmatrix}=\begin{bmatrix}c_{66} & 0\\ 0 & c_{66}\end{bmatrix}\boldsymbol{\gamma}=\boldsymbol{F}_\tau\boldsymbol{\gamma}; \tag{8}$$

$$\boldsymbol{\chi}=\begin{Bmatrix}\chi_{xxz}\\ \chi_{yyz}\end{Bmatrix}=-f_{14}\begin{Bmatrix}1\\1\end{Bmatrix}E_z$$

$$P_z=e_{31}\left(\varepsilon_x+\varepsilon_y\right)+\kappa_{33}E_z+f_{14}\left(\eta_{xxz}+\eta_{yyz}\right) \tag{9}$$

in which $f_{14}=f_{3113}$ and $f_{14}=f_{3223}$ [12], and

$$\boldsymbol{F}_\sigma=\begin{bmatrix}c_{11} & c_{12} & 0\\ c_{12} & c_{11} & 0\\ 0 & 0 & c_{66}\end{bmatrix};\ \boldsymbol{E}_{3z}=e_{31}\begin{Bmatrix}1\\1\\0\end{Bmatrix}E_z;$$

$$\boldsymbol{F}_\tau=\begin{bmatrix}c_{66} & 0\\ 0 & c_{66}\end{bmatrix} \tag{10}$$

Electric displacement may be calculated using Gaussian's law in electrostatics, which is represented by the following formula: $\frac{\partial P_z}{\partial z}=0$

The following is the expression for the internal electric field expressed under the open-circuit condition:

$$\begin{aligned}E_z&=-\frac{e_{31}}{\kappa_{33}}\left\{\left(\varepsilon_{0x}+\varepsilon_{0y}\right)+z\left(\varepsilon_{1x}+\varepsilon_{1y}\right)\right\}-\frac{f_{14}}{\kappa_{33}}\left(\varepsilon_{1x}+\varepsilon_{1y}\right)\\ &=-\frac{e_{31}}{\kappa_{33}}\left\{\boldsymbol{B}_{0xy}\boldsymbol{q}_e+z\boldsymbol{B}_{1xy}\boldsymbol{q}_e\right\}-\frac{f_{14}}{\kappa_{33}}\boldsymbol{B}_{1xy}\boldsymbol{q}_e\end{aligned} \tag{11}$$

where

$$\boldsymbol{B}_{0xy}=\sum_{i=1}^{n}\begin{bmatrix}\frac{\partial N_i}{\partial x} & \frac{\partial N_i}{\partial y} & 0 & 0 & 0\end{bmatrix};$$

$$\boldsymbol{B}_{1xy}=\sum_{i=1}^{n}\begin{bmatrix}0 & 0 & 0 & \frac{\partial N_i}{\partial x} & \frac{\partial N_i}{\partial y}\end{bmatrix}$$

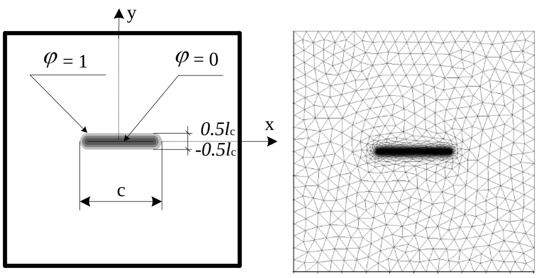

Fig. 2. The top view model of crack appeared in the nanoplate

According to the phase-field theory [32-37], the crack region in this study is determined by spreading out the fracture area across the domain with the use of a scalar field [32-37]. The phase-field parameter s has a range of 0 to 1, with $s = 1$ indicating that the material is undamaged, $s = 0$ indicating that the material is completely damaged, $0 < s < 1$ indicating that the material is softening. It indicates that the material is undergoing micro-fracture progression. The crack is represented by a narrow area, and it is presumed that the phase-field variable s influences the elastic energy, leading to reduced stiffness and addition of s^2 to the energy function in equation (12). The length scale parameter l_c controls the width of the crack, with a rise in l_c causing the crack area to expand.

Considering the open-circuit state, the electric Gibbs free energy may be expressed as follows:

$$\begin{aligned}\Pi &= \frac{1}{2}\int_V s^2\left(\boldsymbol{\varepsilon}^T\boldsymbol{\sigma}+\boldsymbol{\gamma}^T\boldsymbol{\sigma}_\tau+\boldsymbol{\eta}^T\boldsymbol{\chi}\right)dV\\ &= \frac{1}{2}\int_V s^2\left(\boldsymbol{\varepsilon}^T\boldsymbol{F}_\sigma\boldsymbol{\varepsilon}+\boldsymbol{\gamma}^T\boldsymbol{F}_\tau\boldsymbol{\gamma}-\boldsymbol{\varepsilon}^T\boldsymbol{E}_{3z}+\boldsymbol{\eta}^T\boldsymbol{\chi}\right)dV\\ &+\int_A G_C\left[\frac{(1-s)^2}{4l_c}+l_c\left|\nabla s\right|^2\right]dA\end{aligned} \tag{12}$$

The critical energy release rate G_C is determined by Griffith's theory, and it is given by the following equation.

$$\begin{aligned}\Pi &= \frac{1}{2}\boldsymbol{q}^T\left\{\int_V s^2\begin{pmatrix}\boldsymbol{B}_0^T\boldsymbol{F}_\sigma\boldsymbol{B}_0+\boldsymbol{B}_0^T z\boldsymbol{F}_\sigma\boldsymbol{B}_1\\ +\boldsymbol{B}_1^T z\boldsymbol{F}_\sigma\boldsymbol{B}_0+\boldsymbol{B}_1^T z^2\boldsymbol{F}_\sigma\boldsymbol{B}_1\\ +\boldsymbol{B}_\gamma^T\boldsymbol{F}_\tau\boldsymbol{B}_\gamma\end{pmatrix}dV\right\}\boldsymbol{q}\\
&= -\frac{1}{2}\boldsymbol{q}^T\left\{\int_A s^2\int_{h_x}\begin{pmatrix}\boldsymbol{B}_0^T\frac{e_{31}^2}{\kappa_{33}}\boldsymbol{I}_3\boldsymbol{B}_{0xy}\\ +\boldsymbol{B}_0^T z\frac{e_{31}^2}{\kappa_{33}}\boldsymbol{I}_3\boldsymbol{B}_{1xy}\\ +\boldsymbol{B}_1^T z\frac{e_{31}^2}{\kappa_{33}}\boldsymbol{I}_3\boldsymbol{B}_{0xy}\\ +\boldsymbol{B}_1^T z^2\frac{e_{31}^2}{\kappa_{33}}\boldsymbol{I}_3\boldsymbol{B}_{1xy}\end{pmatrix}dzdA\right\}\boldsymbol{q}\\
&-\frac{1}{2}\boldsymbol{q}^T\left\{\int_A s^2\int_{h_x}\begin{pmatrix}\boldsymbol{D}_0^T\frac{f_{14}e_{31}}{\kappa_{33}}\boldsymbol{I}_3\boldsymbol{D}_{1xy}+3\boldsymbol{D}_0^T z^2\frac{f_{14}e_{31}}{\kappa_{33}}\boldsymbol{I}_3\boldsymbol{D}_{3xy}\\ +\boldsymbol{D}_1^T z\frac{f_{14}e_{31}}{\kappa_{33}}\boldsymbol{I}_3\boldsymbol{D}_{1xy}+3\boldsymbol{D}_1^T z^3\frac{f_{14}e_{31}}{\kappa_{33}}\boldsymbol{I}_3\boldsymbol{D}_{3xy}\\ +\boldsymbol{D}_3^T z^3\frac{f_{14}e_{31}}{\kappa_{33}}\boldsymbol{I}_3\boldsymbol{D}_{1xy}+3\boldsymbol{D}_3^T z^5\frac{f_{14}e_{31}}{\kappa_{33}}\boldsymbol{I}_3\boldsymbol{D}_{3xy}\end{pmatrix}dzdA\right\}\boldsymbol{q}\\
&-\frac{1}{2}\boldsymbol{q}^T\left\{\int_A s^2\int_{h_x}\left(\boldsymbol{B}_\eta^T\frac{f_{14}e_{31}}{\kappa_{33}}\boldsymbol{I}_2\boldsymbol{B}_{0xy}+\boldsymbol{B}_\eta^T z\frac{f_{14}e_{31}}{\kappa_{33}}\boldsymbol{I}_2\boldsymbol{B}_{1xy}\right)dzdA\right\}\boldsymbol{q}\\
&-\frac{1}{2}\boldsymbol{q}^T\left\{\int_A s^2\int_{h_x}\left(\boldsymbol{B}_\eta^T\frac{f_{14}^2}{\kappa_{33}}\boldsymbol{I}_2\boldsymbol{B}_{1xy}\right)dzdA\right\}\boldsymbol{q}\\
&+\int_A G_C\left[\frac{(1-s)^2}{4l_c}+l_c\left|\nabla s\right|^2\right]dA\\
&= \left\{\frac{1}{2}\boldsymbol{q}^T\left\{\int_A s^2\int_{h_x}UdzdA\right\}\boldsymbol{q}+\int_A G_C\left[\frac{(1-s)^2}{4l_c}+l_c\left|\nabla s\right|^2\right]dA\right\}\end{aligned} \tag{13}$$

where $\boldsymbol{I}_3=\{1;1;0\}$ and $\boldsymbol{I}_2=\{1;1\}$;

The following is the formula for calculating the kinetic energy of the plate element:

$$D=\frac{1}{2}\int_A\rho\int_{h_x}\begin{pmatrix}\left(\frac{\partial\dot{u}}{\partial t}\right)^T\left(\frac{\partial\dot{u}}{\partial t}\right)\\ +\left(\frac{\partial\dot{v}}{\partial t}\right)^T\left(\frac{\partial\dot{v}}{\partial t}\right)\\ +\left(\frac{\partial\dot{w}}{\partial t}\right)^T\left(\frac{\partial\dot{w}}{\partial t}\right)\end{pmatrix}dzdA=\frac{1}{2}\dot{\boldsymbol{q}}^T\boldsymbol{M}\dot{\boldsymbol{q}} \tag{14}$$

where $\boldsymbol{M}$ is the mass matrix. According to kinetic energy and potential energy, the Lagrange function is expressed as follows:

$$\begin{aligned}L(\dot{\boldsymbol{q}},\boldsymbol{q},s)&=D-\Pi=\frac{1}{2}\dot{\boldsymbol{q}}^T\boldsymbol{M}\dot{\boldsymbol{q}}-\frac{1}{2}\boldsymbol{q}^T\left\{\int_A s^2\int_{h_x}UdzdA\right\}\boldsymbol{q}\\ &-\int_A G_C\left[\frac{(1-s)^2}{4l_c}+l_c\left|\nabla s\right|^2\right]dA\end{aligned} \tag{15}$$

Using the Lagrange function expression, one may get the minimal equation, which looks like this:

$$\begin{cases}\delta L(\dot{\boldsymbol{q}},\boldsymbol{q},s,\delta\boldsymbol{q})=0\\ \delta L(\dot{\boldsymbol{q}},\boldsymbol{q},s,\delta s)=0\end{cases} \tag{16}$$

According to the matrix representation of the preceding equation, it is as follows:

$$\left\{\boldsymbol{K}-\omega^2\boldsymbol{M}\right\}\boldsymbol{q}=0 \tag{17}$$

$$\begin{aligned}&\boldsymbol{s}^T\left\{\int_A 2\left(\boldsymbol{N}^s\right)^T H(\boldsymbol{q})\boldsymbol{N}^s dA\right\}\\ &+\boldsymbol{s}^T\left\{\int_A 2G_C\left[\frac{-\left(\boldsymbol{N}^s\right)^T\boldsymbol{N}^s}{4l_c}+l_c\left(\boldsymbol{B}_s\right)^T\boldsymbol{B}_s\right]dA\right\}\\ &=-\sum_e\left\{\int_A 2G_C\left[\frac{\boldsymbol{N}^s}{4l_c}\right]dA\right\}\end{aligned} \tag{18}$$

As a result, the stiffness matrix of the nanoplate contains components that are related to the coefficient f_{14}, which clearly demonstrates the influence of the flexoelectric effect on the stiffness of the nanoplate, and this results in a free vibration response of cracked nanoplates that is distinct from that of conventional plates. The phase-field parameter will be acquired by solving equation (18), and then the frequencies and vibration mode shapes will be obtained by substituting them into equation (17) above, which will be obtained.

The determination of the function $H(\boldsymbol{q})$ according to the crack length and crack width is calculated as shown in the work [32-34, 36].

III. VERIFICATION EXAMPLES

Problem 1: The SSSS nanoplate has: h=20 nm, $a=b=50h$, c_{11}=102 GPa; c_{12}=31 GPa; c_{33}=35.50 GPa; e_{31}=-

DHD gratefully acknowledges the support of the Vietnam National Foundation for Science and Technology Development (NAFOSTED) under grant number 107.02-2020.18.

17.05 C/m^2; k_{33}=1.76.10^{-8} C/(Vm); f_{14}=10^{-7} C/m, ρ=7600 kg/m^3. Table 1 shows the first fundamental frequencies derived from the analytical formulation of Yang et al. [38] and this study (incremental mesh size). As can be seen, the results are extremely close; therefore, the suggested model and computation software are validated.

TABLE I. COMPARISON OF THE CURRENT FINDINGS TO THE ANALYTICAL RESULTS FOR THE FIRST FREQUENCY (10^8 RAD/S)

	The total number of components			
	4449	4645	4691	5097
Present work	4.790	4.790	4.790	4.790
Analytical solution [38]	4.813			

Problem 2: The natural frequencies of a cantilever plate with one crack are compared in this problem. The plate measures a = b = 24 cm, h = 2.75 cm, E= 67 MPa, ν =0.33, ρ = 2800 kg/m^3 [39-40]. The crack's center appears in the coordinates x = 9cm, y = 9cm, c/a=0.1416. Table 4 shows the natural frequencies of this plate as determined by experimental, theoretical, and FE approaches, as well as this study. The findings in Table 2 show that it provides the required dependability with 4691 elements, therefore the computations in the following sections will utilize this mesh.

TABLE II. NATURAL FREQUENCIE OBTAINED FROM SOME METHODS

ω_i	Mesh	This work	Theoretical [39]	Experiment [39]	FE solution [40]
1	4449	0.9854	0.9931	0.9917	0.9891
	4645	0.9857			
	4691	0.9901			
	5097	0.9975			
	4645	0.9918			
	4691	0.9987			
	5097	0.9989			

IV. NUMERICAL RESULTS AND DISCUSSIONS

The nanoplate has h_0=20 nm, a=b=50h_0, c_{11}=102 GPa; c_{12}=31 GPa; c_{33}=35.50 GPa; e_{31}=-17.05 C/m^2; k_{33}=1.76.10^{-8} C/(Vm); f_{14}^0 =10^{-7} C/m, and mass density ρ =7600 kg/m^3. The linear variable thickness is denoted by the letter $h = h_0(1-\psi x/a)$. The flexo parameter and the non-dimensional natural frequency are defined as follows: $\omega_i^* = \omega_i a\sqrt{\frac{\rho}{c_{11}}}; f_{14}^* = \frac{f_{14}}{f_{14}^0}$. Furthermore, the calculations show that the charge polarization is distributed throughout the plane of the plate as $\left[P_{xxz}, P_{yyz}, 0\right] = \left[f_{14}\eta_{xxz}, f_{14}\eta_{yyz}, 0\right]$.

- Effect of the crack length c

This is an intriguing issue since monitoring the specific vibrational responses of the nanoplate will tell us about the impact of crack length on the response. The crack length c grows in value from zero to about 0.6. Table 3 presents the calculation results of the first five natural frequencies of the nanosheets, which vary depending on the crack length, in order to provide the readers an idea of how the natural frequencies change. Table 3 gives the findings of the first five natural frequencies of the nanoplate as a function of the crack length c.

The findings indicate that as the fracture length c increases, the natural vibration frequencies of the plate all drop, which is explained by the fact that as the crack length increases, the surface area of energy release increases, and the plate softens, lowering the natural frequency of the plate.

Figure 2 depicts the first five natural vibration mode shapes of the nanoplate, which correspond to three different instances of crack length c, and Figure 3 depicts the charge polarization of the five plate-specific vibrations. One can observe that the crack length has a considerable effect on the free vibration mode shapes of the nanoplate; furthermore, the polarization is greatly affected by the presence of crack; polarization is seen around the crack.

TABLE III. THE FIRST FIVE FUDAMENTAL FREQUENCIES OF THE CCCC CRACKED NANOPLATE, ψ = 0.5, $f_{14}^* = 1$

c/a	ω_i^*				
	1	2	3	4	5
0	0.1818	0.3672	0.3706	0.5466	0.6486
0.2	0.1710	0.3618	0.3662	0.5436	0.5930
0.3	0.1632	0.3447	0.3607	0.5352	0.5612
0.4	0.1562	0.3069	0.3527	0.5150	0.5390
0.6	0.1475	0.3341	0.4596	0.5143	0.5395

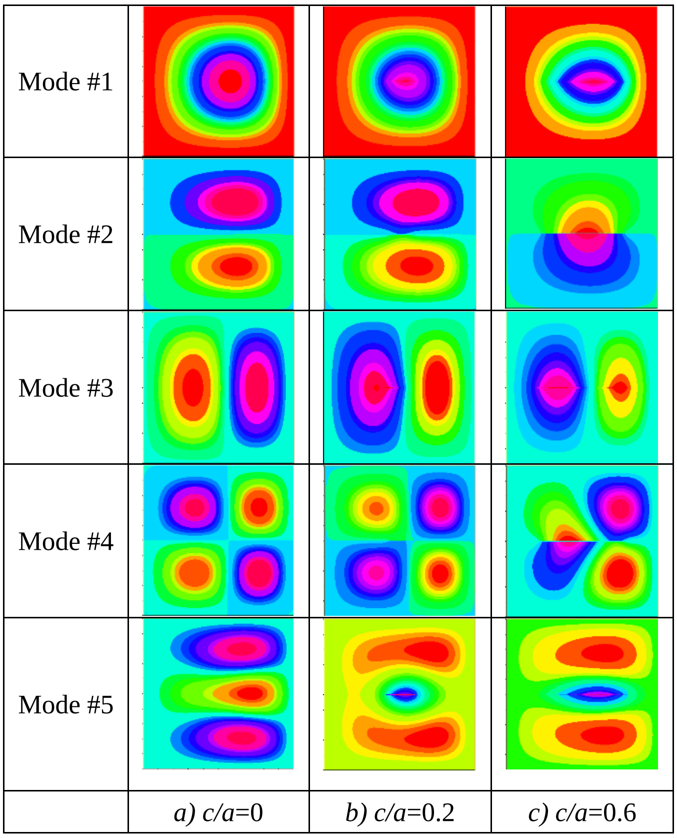

Fig. 3. The first five vibration mode shapes of the CCCC cracked nanoplate, a = b, h_0 = a/50

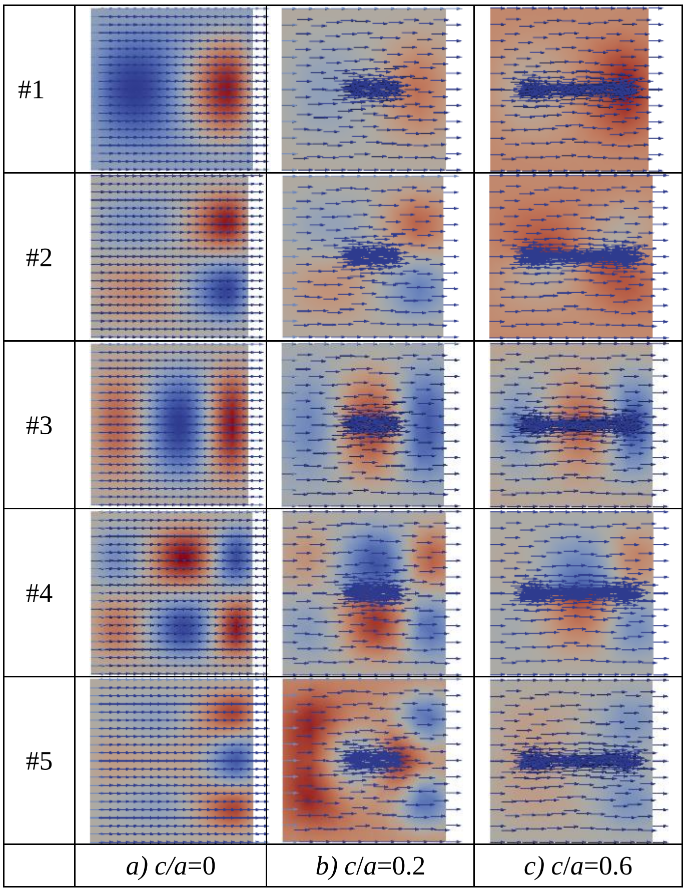

Fig. 4. The first five polizations of the CCCC cracked nanoplate depend on c/a ratio, $a = b$, $h_0 = a/50$

- *Effect of variable thickness*

To investigate how the variation law of plate thickness impacts the nanoplate's free vibration response in the situation of the flexoeltric effect, the study changes the parameter ψ from 0 to 0.6. The findings of the computation of the first three natural frequencies are given in Table 4. The reader can easily observe that when the parameter ψ is increased, the natural frequency of the plate drops for both CCCC and SSSS boundary conditions.

TABLE IV. THE FIRST THREE NATURAL FREQUENCIES OF THE CRACKED NANOPLATE, H_1= A/50, C/A=0.5, $f_{14}^{*} = 1$

ψ	$\bar{\omega}_1$		$\bar{\omega}_2$		$\bar{\omega}_3$	
	CCCC	SSSS	CCCC	SSSS	CCCC	SSSS
0	0.1970	0.1068	0.3345	0.2595	0.4480	0.3086
0.1	0.1879	0.1018	0.3197	0.2481	0.4277	0.2946
0.2	0.1788	0.0968	0.3048	0.2364	0.4071	0.2805
0.3	0.1695	0.0919	0.2897	0.2246	0.3861	0.2662
0.4	0.1602	0.0869	0.2744	0.2127	0.3647	0.2518
0.5	0.1509	0.0821	0.2589	0.2005	0.3430	0.2372
0.6	0.1415	0.0773	0.2432	0.1883	0.3211	0.2227

- *Effect of boundary conditions*

Finally, the paper examines the impact of boundary circumstances on the vibration mode shapes of the structure. The nanoplate has a crack with a ratio of *c*/a=0.5, $h_1 = a/50$, and parameter $\psi = 0.5$. The plate is exposed to four distinct boundary conditions, namely SSSS, CCCC, SCSC, CFFF, and SSCC. Table 5 contains the results of the computation of the nanoplate's five natural frequencies. The CCCC nanoplate has the greatest natural frequency, while the CFFF nanoplate has the lowest.

TABLE V. THE FIRST FIVE FUNDAMENTAL FREQUENCIES OF THE CRACKED NANOPLATE, $f_{14}^{*} = 1$, ψ =0.5

BC	$\bar{\omega}_i$				
	1	2	3	4	5
SSSS	0.0821	0.2005	0.2372	0.3772	0.3905
CCCC	0.1509	0.2589	0.3430	0.4901	0.5243
SCSC	0.1272	0.2154	0.3285	0.4094	0.4328
CFFF	0.0240	0.0438	0.1014	0.1174	0.1405
SSCC	0.1177	0.2316	0.2900	0.4014	0.4492

V. CONCLUSIONS

This paper analyzes free vibration responses of the cracked nanoplates taking into consideration the flexoelectric effect. The formulae for the calculations are derived from Mindlin's first-order shear deformation theory and the finite element technique. The paper examines the effect of a variety of factors on natural frequencies and vibration mode shapes of cracked nanoplates. The following observations may be made as:

- As the length of the crack grows, the nanoplate's natural frequency drops. Additionally, the length of the crack has a substantial effect on the vibration mode shapes and charge polarization of the structure.

- When varying the variation ratio of the thickness and boundary conditions, natural frequencies and the vibration mode shapes of the cracked plate change significantly..

- When the thickness is varied at a different pace and boundary conditions changes, natural frequencies and vibration mode shapes of the cracked plate vary considerably.

The findings of the calculations presented in this study may be utilized as a guideline in the design and use of nanoplates in practical applications.

ACKNOWLEDGMENT

DHD gratefully acknowledges the support of Vietnam National Foundation for Science and Technology Development (NAFOSTED) under grant number 107.02-2020.18.

REFERENCES

[1] Aifantis EC. Chapter One - Internal Length Gradient (ILG) Material Mechanics Across Scales and Disciplines. Advances in Applied Mechanics 2016, 49, pp. 1-110.

[2] Longlong S, Renhong L, Zhenggang R, Linfeng F, Shanming K, Yu W. Flexoelectric materials and their related applications: A focused review. Journal of Advanced Ceramics 2019, 8, pp. 153–173.

[3] Pavlo Z, Gustau C, Alexander KT. Flexoelectric Effect in Solids: Annual Review of Materials Research 2013, 43, pp. 387-421.

[4] Qian D, Sihao L, Zhaoqi L, Kai T, Xu L, Shengping S. The impact of flexoelectricity on materials, devices, and physics editors-pick. Journal of Applied Physics 2020, 128, 080902.

[5] Nguyen BH, Nanthakumar SS, Zhuang X, Wriggers P, Jiang X, Rabczuk T. Dynamic flexoelectric effect on piezoelectric nanostructures. European Journal of Mechanics - A/Solids 2018, 71, pp. 404-409.

[6] Oates WS. Flexoelectricity, strain gradients, and singularities in ferroelectric nanostructures. Journal of Intelligent Material Systems and Structures 2017, 28 (20), pp. 3091-3105.

[7] Xiaoning J, Fuh-Gwo Y. Flexoelectricity in Nanostructures: Theory, Nanofabrication and Characterization. Technical Final Report 2017, North Carolina State University, Raleigh NC27695.

[8] Zhang Z, Yan Z, and Jiang L. Flexoelectric effect on the electroelastic responses and vibrational behaviors of a piezoelectric nanoplate. Journal of Applied Physics 2014, 116, 014307.

[9] Yang W, Liang X, and Shen S. Electromechanical responses of piezoelectric nanoplates with flexoelectricity. Acta Mechanica 2015, 226, 3097–3110.

[10] Shingare KB, Kundalwal SI. Static and dynamic response of graphene nanocomposite plates with flexoelectric effect. Mechanics of Materials 2019, 134, 69-84.

[11] Amir S, Zarei HBA, Khorasani M. Flexoelectric vibration analysis of nanocomposite sandwich plates. Mechanics Based Design of Structures and Machines: An International Journal 2020, 48 (2), 146-163.

[12] Shu LL, Wei XY, Pang T, Yao X, Wang CL. Symmetry of flexoelectric coefficients in crystalline medium. Journal of Applied Physics 2011, 110, 104106.

[13] Arani AG, Arani AHS, Haghparast E. Flexoelectric and surface effects on vibration frequencies of annular nanoplate. Indian Journal of Physics 2020.

[14] Yue Y. Nonlinear Vibration of the Flexoelectric Nanoplate with Surface Elastic Electrodes Under Active Electric Loading. Acta Mechanica Solida Sinica 2020, 33, 864–878.

[15] Wang B, Xian-Fang L. Flexoelectric effects on the natural frequencies for free vibration of piezoelectric nanoplates. Journal of Applied Physics 2021, 129, 034102.

[16] Yan Z and Jiang LY. Vibration and buckling analysis of a piezoelectric nanoplate considering surface effects and in-plane constraints. Proceedings of the Royal Society A: Mathematical, Physical and Engineering Sciences 2012, 468 (2147), 3458-3475.

[17] Reza A, Raheb G. Size-Dependent Nonlinear Vibrations of First-Order Shear Deformable Magneto-Electro-Thermo Elastic Nanoplates Based on the Nonlocal Elasticity Theory. International Journal of Applied Mechanics 2016, 08 (4), 1650053.

[21] Jian X, Wang Y, Chen L. Nonlinear vibration of cracked rectangular Mindlin plate with in-plane preload. Journal of Sound and Vibration 2020, 481, pp.115437

[22] Jalal T, Reza A. Numerical phase-field vibration analysis of cracked functionally graded GPL-RC plates. Mechanics Based Design of Structures and Machines-An International Journal. Published online: 26 Aug 2020, pp.1-21.

[23] Chenghui X, Dalun R, Zhenhuan Z, Zichen D, Lim CW. Vibration and buckling characteristics of cracked natural fiber reinforced composite plates with corner point-supports. Engineering Structures 2020, 214, pp. 110614.

[24] Rjoub YSA, Alshatnawi JA. Free vibration of functionally-graded porous cracked plates. Structures 2020, 28, pp. 2392-2403.

[25] Jeeyeon H , Zhenghao Y , Wenxuan X , Selda O, Erkan O. Free vibration analysis of cracked plates using peridynamics. Ships and Offshore Structures 2020, 15(1), pp. S220-S229.

[26] Zhaoyang H, Yushi Y, Chao Z, Xinran Z, Rui L. On the symplectic superposition method for new analytic free vibration solutions of side-cracked rectangular thin plates. Journal of Sound and Vibration 2020, 489, pp.115695.

[27] Zhang LW, Pan ZZ, Chen X. Vibration characteristics of matrix cracked pretwisted hybrid composite blades containing CNTRC layers. Journal of Sound and Vibration 2020, 473, pp. 115242.

[28] Jian X, Yuefang W, Lihua C. Buckling and free vibration of a side-cracked Mindlin plate under axial in-plane load. Archive of Applied Mechanics 2020, 90, pages1811–1827.

[29] Zhaoyang H, Xinran Z, Dongqi A, Chao Z, Yushi Y, Rui L. New analytic buckling solutions of side-cracked rectangular thin plates by the symplectic superposition method. International Journal of Mechanical Sciences 2021, 191, pp. 106051

[30] Maryam A, Payam A. Free vibration analysis of flexible rectangular fluid tanks with a horizontal crack. Applied Mathematical Modelling 2021, 91, pp. 93-110.

[31] Zaouagui B, Belalia SA, Boukhalfa A. h-p finite element vibration analysis of side cracked rectangular nano-plates based on nonlocal elasticity theory. The European Physical Journal Plus 2019, 134, Article number: 336.

[32] Josef K, Marreddy A, Lorenzis LD, Hector G, and Alessandro R. Phase-field description of brittle fracture in plates and shells. Computer Methods in Applied Mechanics and Engineering 2016, 312, pp. 374-394.

[33] Bourdin B, Francfort GA, and Marigo JJ. The variational approach to fracture. Journal of Elasticity 2008, 91, 5–148.

[34] Michael JB, Clemens VV, Michael AS, Thomas JRH, and Chad ML. A phase-field description of dynamic brittle fracture. Computer Methods in Applied Mechanics Engineering 2012, 217–220, pp. 77–95.

[35] Thom VD, Duc HD, Duc ND, and Tinh QB. Phase-field thermal buckling analysis for cracked functionally graded composite plates considering neutral surface. Composite Structures 2017, 182, pp. 524-548.

[36] Duc HD, Thom VD, Phuc MP, and Duc ND. Validation simulation for free vibration and buckling of cracked Mindlin plates using phase-field method. Mechanics of Advanced Materials and Structures 2018, 0, pp. 1-10.

[37] Thom DV, Zenkour AM, Duc HD. Buckling of cracked FG plate resting on elastic foundation considering the effect of delamination phenomenon. Composite Structures, 2021, 273, 114278.

[38] Yang W, Liang X, and Shen S. Electromechanical responses of piezoelectric nanoplates with flexoelectricity. Acta Mechanica 2015, 226, pp. 3097–3110.

[39] Krawczuk M. Natural vibrations of rectangular plates with a through crack. Archive of Applied Mechanics, 63, 1993, pp.491-504.

[40] Qian GL, Gu S.N, Jiang JS. A finite element model of cracked plates application to vibration problems. Composite Structures, 39, 1991, pp. 483-487.

The 6th International Conference on
Engineering Mechanics and Automation (ICEMA 2021)
Hanoi, November 14, 2021

Optimum buckling analysis of laminated composite plates reinforced by multiple stiffeners

Pham Dinh Nguyen*
Department of Engineering and Technology in Constructions and Transportation
University of Engineering and Technology, VNU Hanoi.
144 Xuan Thuy Street, Cau Giay District, Hanoi, Vietnam
*Corresponding author: nguyenpd@vnu.edu.vn

George Papazafeiropoulos
Department of Structural Engineering
National Technical University of Athens
Zografou, Athens 15780, Greece
Email: gpapazafeiropoulos@yahoo.gr

Quang-Viet Vu
Faculty of Civil Engineering
Vietnam Maritime University.
484 Lach Tray Street, Hai Phong City, Vietnam
Email: vietvq@vimaru.edu.vn

Nguyen Dinh Duc
Department of Engineering and Technology in Constructions and Transportation
University of Engineering and Technology, VNU Hanoi.
144 Xuan Thuy Street, Cau Giay District, Hanoi, Vietnam
Email: ducnd@vnu.edu.vn

Abstract: **This paper presents an optimization procedure developed in Abaqus2Matlab to obtain the optimum locations of stiffeners, fiber angles of the laminated composite plates subjected to compression, bending, and shear. Abaqus2Matlab is a computational tool that supports automatic linking between Abaqus and Matlab by transferring and creating the necessary files for the optimization procedure. In this procedure, a gradient-based interior-point optimization algorithm is employed to maximize the buckling coefficients until achieving the optimum design variables (locations, fiber angles) of the problem. The results of specific cases that used this method are compared with results found in the literature. The results of the maximum buckling coefficient with the optimum design variables of the laminated composite plates subjected to different types of loads and boundary conditions are studied in a detail.**

Keywords: Buckling analysis, Abaqus2Matlab, Optimum design, Laminated composite plates, Stiffened plates

I. INTRODUCTION

Composite materials are lightweight and they have low density, high strength and high stiffness. In recent years, many studies have been published for the buckling analysis of the laminated composite structures using finite element methods or analytical methods. For the free vibration and buckling analysis of laminated composite plates, Wang et al. [1] used the meshless approach based on the reproducing kernel particle method. Nguyen-Van et al. [2] developed the smoothed quadrilateral flat shell element with in-plane rotations. Thai et al. [3] presented the isogeometric approach utilizes non-uniform rational B-splines to implement for the quadratic, cubic, and quartic elements. Khdeir and Librescu [4] presented the higher-order plate theory and the technique based on the state space concept. Fares and Zenkour [5] presented Hamilton–Reissner's mixed variational principle to deduce a consistent first-order theory. Chakrabarti and Sheikh [6] presented a new triangular element based on higher order shear deformation theory.

Optimizing the composite structures in order to increase the load capacity and make the most of the material properties. In the last decade, most of researches is mainly concerned about the optimization problem of fiber angles using the analytical method with a single variable of the layers. For one design variable, Hu and Lin [7] presented the results of optimum fiber angles for the buckling optimization of the laminated plates subjected to uniaxial compression with various geometries and boundary conditions. Chai et al. [8] studied the optimization procedure using the Complex technique in conjunction with the finite strip method to find the optimum ply angle in antisymmetric laminated composite plates subjected to in-plane compression. Riche and Haftka [9] presented the optimization of the laminate stacking sequence for the maximum critical buckling load using the genetic algorithm. For two design variables, Huang and Kroplin [10] presented the optimization problem of the composite laminated plates with fiber angles and ply thicknesses are design variables. Akbulut abd Sonmez [11] proposed the optimization procedure for minimizing weight of laminated composite plates using the direct search simulated annealing algorithm. Jing et al. [12] presented the permutation search algorithm to reduce the evaluations in stacking sequence optimization of laminated composite plates. Almeida [13] used the harmony search algorithm to maximize the critical buckling load of the symmetric laminated plates. Bargh and Sadr [14] applied the particle swarm optimization (PSO) algorithm to the lay-up design of symmetrically laminated composite plates for maximization of the fundamental frequency. Ho-Huu et al. [15] used the improved differential evolution and smoothed finite element method for the laminated composite plates for maximization of the critical buckling load. Chandrasekhar et al. [16] presented the topology optimization of laminated composite plates with two different objective functions namely strain energy and fundamental frequency. Matsuzaki et al. [17] presented the optimization of curvilinear fiber orientation of composite plates based on the fracture criterion for the multi-objective functions. Keshtegar et al. [18] applied the adaptive Kriging-improved partial swarm optimization algorithm for maximizing the buckling load of the laminated composite plates.

Stiffeners is often used to increase the load carrying capacity and avoid instability of the structure. Some studies on the optimization problem with the location of stiffeners as design variables of the plates can be mentioned as follows Alinia and Moosavi [19] studied the stability of longitudinally stiffened web plates under interactive shear and bending forces. Issa-El-Khoury et al. [20] presented the location of curved and longitudinal stiffeners of the plates under shear and bending. Vu et al. [21] presented the results of the location of stiffeners for the buckling analysis of longitudinally multi-stiffened steel plates subjected to combined bending and shear.

From the above literature review, this paper proposes a new optimization procedure for the laminated composite plates reinforced stiffeners subjected to biaxial compression, shear and bending to obtain maximizing buckling coefficient with design variables are fiber angles and location of stiffeners. The optimization procedure is implemented by using Abaqus2Matlab [22] which is designed for transferring model and/or results data from Abaqus to Matlab and vice versa to generate the necessary Abaqus input files, run the analysis and extract the analysis results in Matlab.

II. METHODOLOGY

A. Buckling analysis

Consider a laminated composite plate with the total thickness h, length a and width b as shown in Figure 1. A coordinate system (x,y,z) is derived in which (x,y) plane on the middle surface of the shell and z on thickness direction. The composite plate consists of n laminae which has own fiber orientation θ_i and ply thickness t_i.

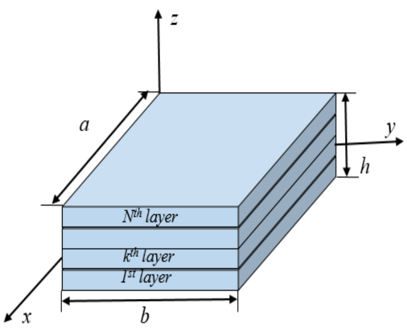

Fig. 1. Model of a laminate composite plate

In the buckling analysis, the following algebraic equation is used to solve the eigenvalue problem to determine eigenvalues λ_i and eigenvectors (ϕ_i):

$$\left(\left[K_L\right]+\lambda_i\left[K_\sigma\right]\right)\phi_i=0 \tag{1}$$

in which, λ_{cr} is lowest eigenvalue corresponding to the critical buckling load, eigenvectors (ϕ_i) are corresponding to buckling mode shapes, $\left[K_L\right]$ is a linear stiffness matrix and $\left[K_\sigma\right]$ is a stress stiffness matrix

The critical buckling load (F_{cr}) is obtained from the following equation:

$$F_{cr}=\lambda_{cr}P \tag{2}$$

with P is an applied load.

In this study, the various loading conditions are presented as uniform compression, pure shear, pure bending. The elastic critical buckling stress is obtained by the classical elastic plate theory (Timoshenko 1936 [23]). The elastic critical buckling stress is given by:

$$\sigma_{cr}^{i}=K_i\frac{\pi^2E_2}{12\left(1-\upsilon_{12}^2\right)}\left(\frac{h}{b}\right)^2 \tag{3}$$

in which, $i=c,b,s$ represent uniform compression, bending and shear, respectively.

B. Proposed optimization procedure

The purpose of the problem is to determine the value of the maximum critical buckling coefficient of laminated composite plates. The variable designs of the problem is stiffener location of the plates. The objective function is defined as follows:

$$K\left(X_i\right)=\frac{12\left(1-v_m^2\right)b}{\pi^2E_2h^3}F_{cr}\left(X_i\right) \tag{4}$$

with $0\le X_i\le b$, X_i is stiffener location of the plates

In the case, The variable designs are stiffener location and fiber angles, the objective function is defined as follows:

$$K\left(X_i,\theta_j\right)=\frac{12\left(1-v_m^2\right)b}{\pi^2E_2h^3}F_{cr}\left(X_i,\theta_j\right) \tag{5}$$

in which, $-90^0\le\theta_i\le 90^0,\ i=\overline{1\div n}$.

An effective optimization procedure using Abaqus2Matlab [22] is proposed for the computation of the optimum location and fiber angles of the composite plates shown in Figure 2.

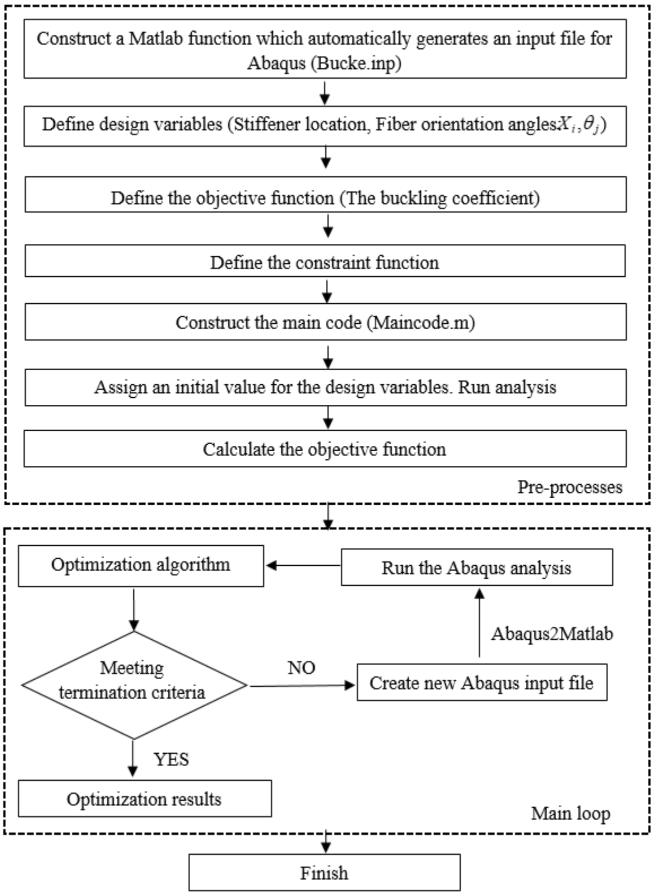

Fig 2. Flowchart of the optimization procedure

III. NUMERICAL RESULTS AND DISCUSSIONS

A. Validation

The nondimensional buckling load $\bar{N} = \dfrac{\lambda_{cr} a^2}{E_2 h^3}$ of the laminated composite plates under uniaxial compression are compared with previous works in Table 1. The material properties of the laminated composite plates is given as follows: $a = b = 1, a / h = 10,$

$$E_1 / E_2 = 40, G_{12} = G_{13} = 0.6E_2, G_{23} = 0.5E_2, v_{12} = 0.25.$$

Table 2 compares the buckling coefficients of the stiffened steel plates subjected to pure bending. Table 3 presents the comparison results of the optimization of fiber angles and thickness of the laminated composite plates. From the results of comparisons in those tables, it can be concluded that the FE models and the optimization procedure are reliable.

TABLE I. COMPARISON OF THE NONDIMENSIONAL BUCKLING LOAD OF $[0/90]_5$ LAMINATED PLATES UNDER UNIAXIAL COMPRESSION

BCs	SSSS	SSCC	SSSC	SSFC	SSFS	SSFF
Ref. [1]	25.703	35.162	32.95	14.495	12.658	12.224
Ref. [3]	25.534	34.531	32.874	14.356	12.543	12.131
Ref. [4]	25.527	35.178	32.6882	14.483	12.617	12.234
Ref. [15]	25.256	35.094	32.759	14.343	12.493	-
Present	25.241	34.057	31.955	14.225	12.417	11.992

TABLE II. COMPARISON OF BUCKLING COEFFICIENTS k OF THE PLATE SUBJECTED TO PURE BENDING

	Alinia and Moosavi [19]	Present
Without stiffeners	25.53	25.60
With stiffeners	154	154.03

TABLE III. COMPARISON OF THE OPTIMUM PLY-ANGLE OF SSSS SQUARE COMPOSITE PLATES UNDER BIAXIAL COMPRESSION

	Case I			Case II			
	$[\theta_i^o]$	$\bar{N}$	NSA	$[\theta_i^o]$	$[t_i^o]$	$\bar{N}$	NSA
Ref. [15]	[-45/45]s	15.661	520	[45/-45]s	$[10.24/39.76]_s$	19.491	1260
Present	[-45/45]s	14.871	68	[45/-45]s	$[9.60/40.40]_s$	19.504	84

B. Results of optimum stiffened location

In this section, the material properties of the square plates is chosen as $a = b = 1, b / h = 10, t_s = h / 10, b_s = 4t_s,$ $E_1 / E_2 = 40, G_{12} = G_{13} = 0.6E_2, G_{23} = 0.5E_2, v_{12} = 0.25$.

Table 4 shows the optimum fiber orientation angles of the laminated composite plate subjected to combined shear and bi-compression using three optimization algorithms: the gradient-based interior-point algorithm (IPA), the genetic algorithm (GA), and the differential evolution algorithm (DE). The results show that the optimization procedure with the IPA is more appropriate and effective than others in the buckling analysis case of the composite plates.

TABLE IV. THE EFFICIENCY OF THE OPTIMIZATION PROCESS USING THE IPA

Algorithms	$\bar{N}$	$[\theta_i^o]$	Time (hours)	NSA
IPA	15.2616	[45/-45]s	0.667	76
GA	15.2616	[45/-45]s	12	1715
DE	15.2616	[45/-45]s	12	1700

Table 5 presents the effect of boundary conditions on the buckling coefficient of the laminated composite plates subjected to biaxial compression and mode shapes of the stiffened composite plates in this case are shown in Figure 3. It can be observed that, the value of buckling coefficient of the plate with CCCC boundary condition is the highest with optimum location of two stiffeners is X_1=0.6112 and X_2=0.7083, respectively.

TABLE V. OPTIMUM LOCATION OF STIFFENERS OF $[0/90]_S$ COMPOSITE PLATES UNDER BIAXIAL COMPRESSION

BCs	X_1	X_2	K_c	NSA
SSSS	0.5870	0.6735	56.041	90
CCCC	0.6112	0.7083	91.477	99
SSCC	0.5915	0.6807	70.422	95
CCSS	0.6096	0.6964	77.365	34
CCFF	0.583	0.670	41.954	39

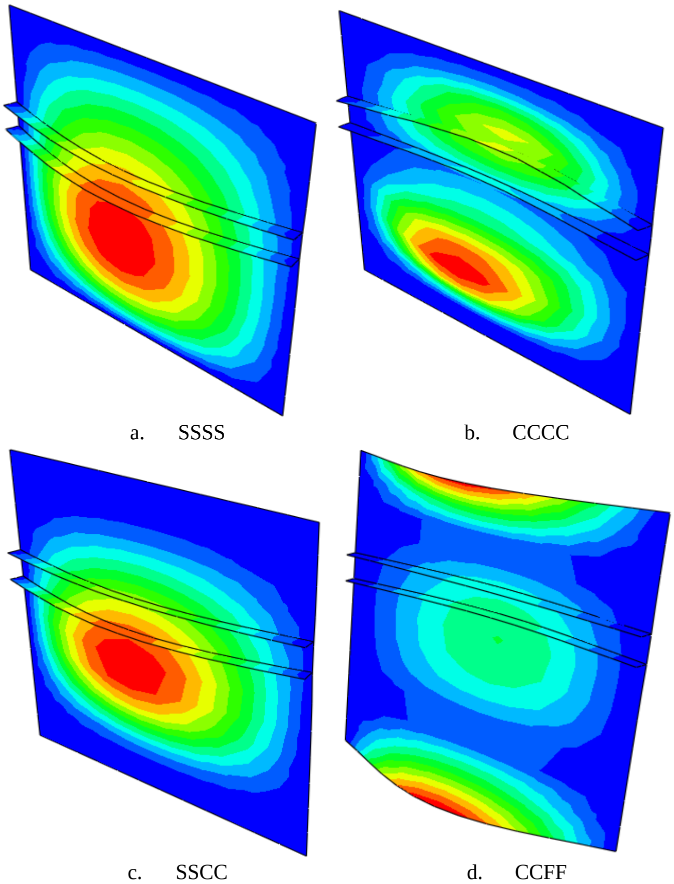

Fig. 3. Mode shapes of the stiffened composite plates

The results of optimum location of stiffeners of the SSSS composite plates subjected to biaxial compression with various length to thickness ratios in Table 6 and aspect ratios in Table 7. From Tables 6 and 7, it can be seen that that the optimum location of the stiffener 1 and 2 is 0.58D and 0.68D, respectively.

TABLE VI. EFFECT OF *A/H* RATIOS ON THE CRITICAL BUCKLING LOAD OF THE [0/90]S COMPOSITE PLATES UNDER BIAXIAL COMPRESSION ($a = b = 1$)

a/h	X_1	X_2	F_{cr}	NSA
10	0.5870	0.6735	49.115	90
20	0.5000	0.5832	9.484	69
30	0.5757	0.6620	3.084	51
50	0.5000	0.7594	0.795	128

TABLE VII. EFFECT OF *A/B* RATIOS ON THE BUCKLING COEFFICIENT OF THE [0/90]S COMPOSITE PLATES UNDER BIAXIAL COMPRESSION ($a = 1, h = 0.1$)

b/a	X_1	X_2	K_c	NSA
0.5	0.2929	0.4217	12.263	39
1	0.5870	0.6735	56.041	90
2	1.2024	1.3803	212.628	115

Tables 8 and 9 present the effects of the length to thickness ratios of the SSSS laminated composite plates subjected to pure bending and shear, respectively. As can be seen, the optimum location of stiffeners are slightly changed between 0.5D and 0.7D when *a/h* ratios are increased. The critical buckling load of the laminated plates is decreased when *a/h* ratio increases.

TABLE VIII. EFFECT OF *a/h* RATIOS ON THE BUCKLING COEFFICIENT OF THE $[0/90]_S$ COMPOSITE PLATES UNDER PURE BENDING

a/h	X_1	X_2	F_{cr}	NSA
10	0.6250	0.7083	61.967	259
20	0.5856	0.6666	22.175	43
30	0.5871	0.6680	8.203	35
50	0.5048	0.6661	2.292	306

TABLE IX. EFFECT OF *A/H* RATIOS ON THE BUCKLING COEFFICIENT OF THE [0/90]S COMPOSITE PLATES UNDER PURE SHEAR

a/h	X_1	X_2	F_{cr}	NSA
10	0.6250	0.7123	36.610	105
20	0.7917	0.7119	16.079	161
30	0.5799	0.6632	7.971	44
50	0.5000	0.6638	2.1872	58

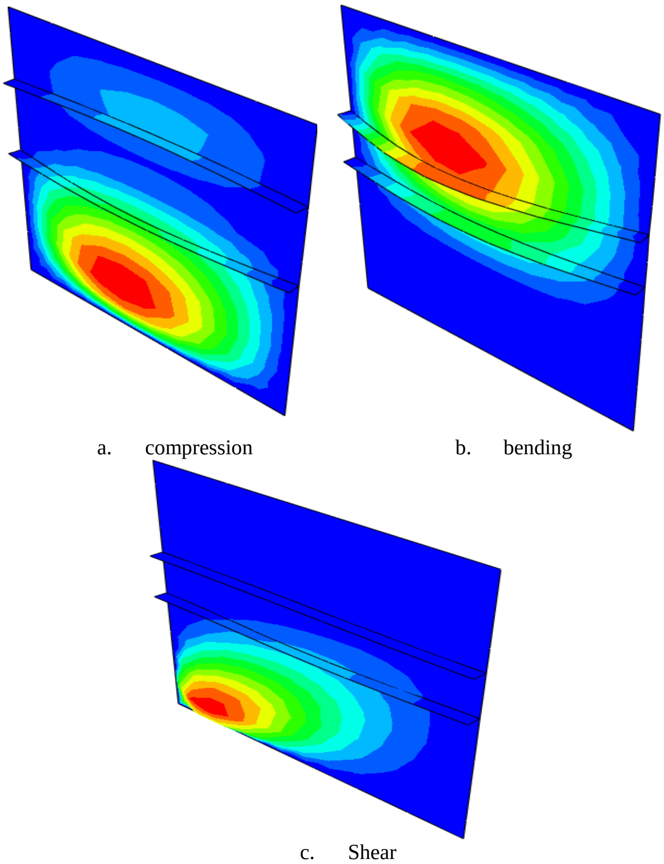

Fig. 4. Mode shapes of the stiffened composite plates subjected to various types of loads

C. Results of optimum stiffeners and fiber angles

Tables 10, 11 and 12 illustrate the optimum results of the location of stiffeners and fiber angles (X_i, θ_j^0) of the [0/90]s laminated composite plates under biaxial compression with various BCs, length to thickness ratios (*a/h*), and aspect ratios (*b/a*), respectively. As can be seen, the values of the critical buckling load and buckling coefficient of the laminated composite plates with two design variables (fiber angles and location of stiffeners) is higher than that of the plate with one design variable (location of stiffeners). Specifically, for the SSSS BCs, the buckling coefficient of the plate fixed fiber angles [0/90]s with design variables of stiffened location is $K_c = 56.041$ and the optimum location is X_1=0.5870D, X_2= 0.6735D in Table 5, while that value is $K_c = 71.746$ for the plate with two design variables are location of stiffeners (X1=0.5D and X2=0.5788) and fiber angles ([-37.95/40.32]s) in Table 10.

The convergence histories of the laminated composite plates with various BCs and length to thickness ratios are presented in Figures 5 and 6.

TABLE X. OPTIMUM LOCATION OF STIFFENERS AND FIBER ANGLES OF [0/90]S COMPOSITE PLATES UNDER BIAXIAL COMPRESSION

BCs	$[\theta_i^o]$	X_1	X_2	K_c	NSA
SSSS	[-37.95/40.32]s	0.500	0.579	71.746	247
CCCC	[-80.42/11.14]s	0.668	0.583	101.777	167
SSCC	[-69.6/26.34]s	0.580	0.750	89.839	163
CCSS	[29.1/59.65]s	0.752	0.587	87.734	351
CCFF	[-42.22/40.97]s	0.774	0.9	50.649	281

TABLE XI. OPTIMUM LOCATION OF STIFFENERS AND FIBER ANGLES OF SSSS COMPOSITE PLATES UNDER BIAXIAL COMPRESSION WITH VARIOUS a/h RATIOS

a/h	$[\theta_i^o]$	X_1	X_2	F_{cr}	NSA
10	[-37.95/40.32]s	0.5000	0.5788	62.878	247
20	[-40.1/40.58]s	0.5781	0.6602	11.708	229
30	[-41.34/39.81]s	0.6618	0.5785	4.138	251
50	[-49.89/34.56]s	0.6163	0.5417	1.126	278

TABLE XII. OPTIMUM LOCATION OF STIFFENERS AND FIBER ANGLES OF SSSS COMPOSITE PLATES UNDER BIAXIAL COMPRESSION WITH VARIOUS *b/a* RATIOS

b/a	$[\theta_i^o]$	X_1	X_2	K_c	NSA
0.5	[-65.5/50.61]s	0.3958	0.4169	35.846	308
1	[-37.95/40.32]s	0.5000	0.5788	71.746	247
2	[-30/42.42]s	1.0833	1.2520	238.996	219

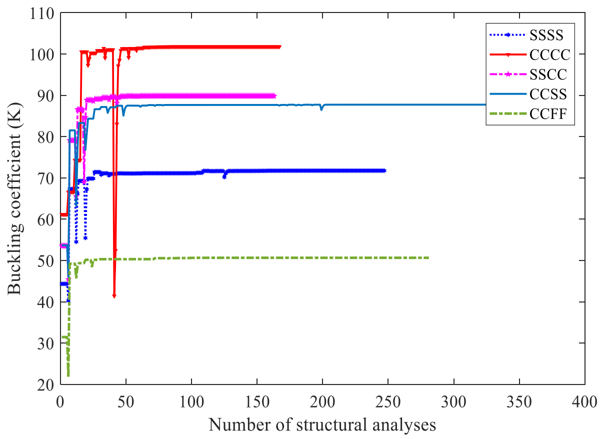

Fig. 5. Convergence histories of the buckling coefficient for the laminated composite plates with various BCs

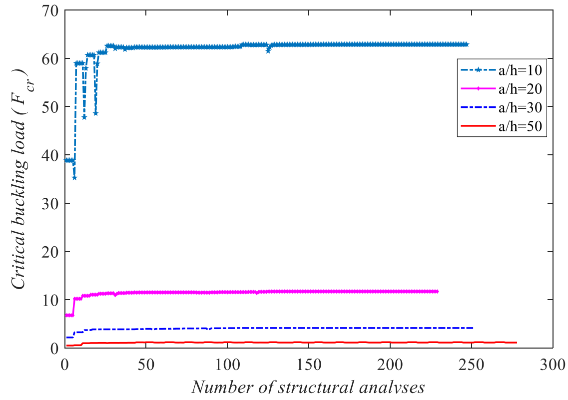

Fig. 6. Convergence histories of the critical buckling load for composite plates with different *a/h* ratios

Tables 13 and 14 present the optimum positions of two single stiffeners and the optimum fiber angles for the laminated composite plates subjected to bending and shear, respectively. The optimal values of the stiffener location are between 0.7D and 0.8D for the plate under pure bending and for the plate under pure shear, these values are between 0.55D and 0.7D.

TABLE XIII. OPTIMUM LOCATION OF STIFFENERS AND FIBER ANGLES OF COMPOSITE PLATES UNDER PURE BENDING WITH VARIOUS BCS

BCs	$[\theta_i^o]$	X_1	X_2	K_b	NSA
SSSS	[0.28/31.15]s	0.6935	0.7578	75.122	300
CCCC	[-1.41/33]s	0.7152	0.7917	77.280	233
SSCC	[-1.76/31.77]s	0.7149	0.7917	77.248	292
CCSS	[-0.68/32.95]s	0.6900	0.8408	77.250	217

TABLE XIV. OPTIMUM LOCATION OF STIFFENERS AND FIBER ANGLES OF COMPOSITE PLATES UNDER PURE SHEAR WITH VARIOUS BCS

BCs	$[\theta_i^o]$	X_1	X_2	K_s	NSA
SSSS	[-37.81/47.67]s	0.6420	0.690	154.621	434
CCCC	[-6.29/23.63]s	0.5939	0.6792	157.276	190
SSCC	[-13.16/36.55]s	0.6885	0.5695	156.706	214
CCSS	[-14.32/34.46]s	0.6914	0.5855	161.271	289

IV. CONCLUSIONS

In this paper, a new optimization procedure for the laminated composite plates reinforced by two stiffeners under various types of loads is proposed by using the Abaqus2Matlab toolbox combined to the gradient-based interior point algorithm (IPA) to obtain the maximum buckling coefficient considering the fiber angles and location of stiffeners as design variables. Some conclusions are drawn from this study as follows:

The optimum location of stiffeners and the optimum fiber angles help the plates have the maximum critical buckling load. The optimum results are recommended to design the composite plates in the particular cases.

The optimum position of two longitudinal stiffeners subjected to compression is between 0.5D and 0.6D, shear 0.5D and 0.7D

The variations of the length to thickness ratio (a / h) have slightly affect the optimum fiber angles and location of stiffeners of the laminated composite plates.

ACKNOWLEDGMENT

Pham Dinh Nguyen was funded by Vingroup Joint Stock Company and supported by the Domestic Master/ PhD Scholarship Programme of Vingroup Innovation Foundation (VINIF), Vingroup Big Data Institute (VINBIGDATA), code VINIF.2020.TS.17.

REFERENCES

[1] J. Wang, K.M. Liew, M.J. Tan and S. Rajendran, “Analysis of rectangular laminated composite plates via FSDT meshless method,” Int. J. Mech. Sci. vol. 44, pp. 1275-93, 2002.

[2] H. Nguyen-Van, N. Mai-Duy, W. Karunasena and T. Tran-Cong, “ Buckling and vibration analysis of laminated composite plate/shell structures via a smoothed quadrilateral flat shell element with in-plane rotations,” Comput. Struct. vol. 89, pp. 612-25, 2011.

[3] C.H. Thai, H. Nguyen-Xuan, N. Nguyen-Thanh, T.H. Le, T. Nguyen-Thoi and Rabczuk T, “Static, free vibration, and buckling analysis of laminated composite Reissner–Mindlin plates using NURBS-based isogeometric approach,” Int. J. Numer. Meth. Eng, vol. 91, pp. 571-603, 2012.

[4] A.A. Khdeir and L. Librescu L, “Analysis of symmetric cross-ply elastic plates using a higher-order theory: part II: buckling and free vibration,” Compos. Struct, vol. 9, pp. 259-277, 1988.

[5] M.E. Fares and A.M. Zenkour, “Buckling and free vibration of non-homogeneous composite cross-ply laminated plates with various plate theories,” Compos. Struct, vol. 44, pp. 279-287, 1999.

[6] A. Chakrabarti and A.H. Sheikh, “Buckling of laminated composite plates by a new element based on higher order shear deformation theory,” Mech. Adv. Mater. Struct, vol. 10, pp. 303-17, 2003.

[7] H.T. Hu and B.H. Lin, “Buckling optimization of symmetrically laminated plates with various geometries and end conditions,” Compos. Sci. Technol, vol. 55, pp. 277-285, 1998.

[8] G.B. Chai, K.T. Ooi and W. Khong, “Buckling strength optimization of laminated composite plates,” Compos. Struct, vol. 46:1, pp. 77-82, 1993.

[9] R.L. Riche and R.T. Haftka, “Optimization of laminate stacking sequence for buckling load maximization by genetic algorithm,” AIAA J, vol. 31: 5, pp. 951-956, 1993.

[10] C. Huang and B. Kroplin, “On the optimization of composite laminated plates,” Eng. Computation, vol. 12: 5, pp. 403-414, 1995.

[11] M. Akbulut and F.O. Sonmez, “Optimum design of composite laminates for minimum thickness,” Compos. Struct, vol. 86: 21-22, pp. 1974-1982, 2008.

[12] Z. Jing, X. Fan and Q. Sun, “Stacking sequence optimization of composite laminates for maximum buckling load using permutation search algorithm,” Compos. Struct, vol. 121, pp. 225-236, 2015.

[13] F.S. Almeida, “Stacking sequence optimization for maximum buckling load of composite plates using harmony search algorithm,” Compos. Struct, vol. 14, pp. 287-299, 2016.

[14] H.G. Bargh and M.H. Sadr, “Stacking sequence optimization of composite plates for maximum fundamental frequency using particle swarm optimization algorithm,” Meccanica, vol. 47, pp. 719-730, 2012.

[15] V. Ho-Huu, T.D. Do-Thi, H. Dang-Trung, T. Vo-Duy and T. Nguyen-Thoi, “Optimization of laminated composite plates for maximizing buckling load using improved differential evolution and smoothed finite element method,” Compos Struct, vol. 146, pp. 132-147, 2016.

[16] K.N.V. Chandrasekhar, V. Bhikshma and K.U. Bhaskara Reddy, “ Topology optimization of laminated composite plates and shells using optimality criteria,” J Appl Comput Mech, vol 7: (1), 2021.

[17] R. Matsuzaki, K. Mitsui, Y. Hirano, A. Todoroki and Y. Suzuki, “Optimization of curvilinear fiber orientation of composite plates and its experimental validation,” Compos. Struct, vol. 255, pp. 112956, 2021.

[18] B. Keshtegar, T.N. Thoi, T. T. Truong and S.P. Zhu, “Optimization of buckling load for laminated composite plates using adaptive Kriging-improved PSO: A novel hybrid intelligent method,” Defence. Techno, vol. 17, pp. 85-99, 2021.

[19] M.M. Alinia and S.H. Moosavi, “Stability of longitudinally stiffened web plates under interactive shear and bending forces,” Thin-Walled. Struct, vol. 47, pp. 53-60, 2009.

[20] G. Issa-El-Khoury, D.G. Linzell and L.F. Geschwindner, “Flexure-shear interaction influence on curved, plate girder web longitudinal stiffener placement,” J. Constr. Steel. Res, vol. 120, pp. 25-32, 2016.

[21] Quang Viet Vu, George Papazafeiropoulos, Carlos Graciano and Seung Eock Kim, “Optimum linear buckling analysis of longitudinally multi-stiffened steel plates subjected to combined bending and shear,” Thin Walled Structures, vol. 136, pp. 235-245, 2019.

[22] G. Papazafeiropoulos, M. Muñiz-Calvente and E. Martínez-Pañeda, “Abaqus2Matlab: A suitable tool for finite element post-processing,” Adv. Eng. Softw, vol. 105, pp. 9-16, 2017.

[23] S. Timoshenko, Theory of Elastic Stability, Engineering Societies Monograph, McGraw-Hill Book Company, 1936.

The 6th International Conference
on Engineering Mechanics and Automation (ICEMA 6)
Hanoi, November 13-14, 2021

Determination of Aerodynamic Coefficients of Drone Propeller by 3D Scanning Technology and Blade Element Momentum Method

Nguyen Hoang Quan
School of Aerospace Engineering
University of Engineering and Technology
Vietnam National University, Hanoi
144 XuanThuy, CauGiay, Hanoi, VietNam
nhquan@vnu.edu.vn

Tran Dang Huy
University of Engineering and Technology
Vietnam National University, Hanoi
144 XuanThuy, CauGiay, Hanoi, VietNam
danghuycn7k63uet@gmail.com

Duong Viet Dung
School of Aerospace Engineering
University of Engineering and Technology
Vietnam National University, Hanoi
144 XuanThuy, CauGiay, Hanoi, VietNam
duongdv@vnu.edu.vn

Abstract: **The inspection and evaluation of the aerodynamic characteristics of propellers suitable for the drone design process is currently of interest to the UAV community in Vietnam. In this report, the research team presents the method of digital reconstruction of the small-sized propeller based on the laser scanning technology with high accuracy, reliable, robust and nondestructive manner. The aerodynamic coefficients C_L, C_D of the drone propeller are identified by the Blade Element Momentum (BEM) method, which is a combination of momentum theory, blade element theory and vortex theory. The simulation results obtained in the JBLADE software, which characterize the propeller performance, show an acceptable agreement with experimental results.**

Keywords: 3D scanner, reverse engineering, propeller, blade element momentum theory

1. INTRODUCTION

Nowadays, flying devices are more and more popular. Assembling and integrating a drone from separate parts is no longer strange to the UAV community in Vietnam. However, for the drone to fly stably, the selection and testing of the aerodynamic parameters of the propeller becomes an important matter. From this fact, the research team has built a process to determine the aerodynamic parameters of the propeller based on 3D scanning equipment and JBLADE aerodynamic calculation software. This is a process developed at School of Aerospace Engineering, University of Engineering and Technology, VNU, which helps students check the quality of the wings before assembling the flying device.

In order to reconstruct the propeller in 3D from the actual blade, various measurement methods have been developed. Reverse engineering of a propeller blade complex 3D shape requires measuring of its geometrical parameters. There are various techniques for measuring geometry of solid bodies, and for propeller geometrical measurement there are conventional and non-conventional methods. Most of the conventional methods used for identifying propeller parameters are difficult, destructive, in-accurate and time consuming methods [1]. These conventional methods include: Pitch Gauge, Tracing the Edges, Slicing the Propeller into sections and Using Templates [2].

New technologies have been developed to measure surface details for reverse engineering processes using accurate and non-destructive methods, starting with the use of probe supports for surface measurement, which has problems maintaining suitable environment conditions to ensure measurement accuracy, and then came the use of three-dimensional laser scanners, which have effectively improved measurement accuracy. The new progress in the applications of Laser technology has created a new production of three dimensional scanners capable of measuring the geometry of intricate shapes like propellers [3, 4]. In this study, the Shining3D EinScan Pro 2X Plus equipment was utilized to reconstruct the propeller shape (Fig. 1).

Fig. 1. Shining3D EinScan Pro 2X Plus 3D scanner

After reconstructing the propeller using 3D scanning technology to determine the aerodynamic parameters of the propeller, instead of the CFD method, the research team adopted the open source JBLADE software, a computation engine based on the Blade Element Momentum (BEM) method [5-8]. The BEM model, which is actually a 2D method extrapolated to the third dimension, applies semi-empirical corrections, derived from experimental measurements or CFD calculations in order to take into account the three-dimensional effects. With the powerful analytical capabilities and low computational cost of the BEM method, we can quickly design and test various propellers suitable for drone motor.

In this report, the process of scanning objects using 3D scanning technology will be introduced. To determine the aerodynamic coefficients of the propeller, the JBLADE tool is used. In order to prove the accuracy of the computational model, a propeller sample is scanned, aerodynamically calculated and compared with the test results.

2. PROCEDURE FOR DETERMINING THE AERODYNAMIC COEFFICIENTS OF PROPELLERS

A. Method of rendering by 3D scanning technology

In this section, the research team presents a measurement method using 3D scanning technology that facilitates reduces dimensional errors. The EniScan Pro 2x Plus 3D scanner from SHINING3D is used to examine and scan objects. This scanner has characteristic parameters which are described in TABLE 1.

TABLE 1. CHARACTERISTIC PARAMETERS OF THE 3D ENISCAN PRO 2X PLUS SCANNER

Scan Speed	30fps 1,500,000 points/s
Scan Accuracy	0.04mm
Volumetric Accuracy	0.1+0.3mm/m
Minimum Point Distance	0.2mm

3D scanning technology is the technology for measuring and reconstructing object shapes based on laser scanning technology. This is a technology that measures object structures in a non-contact, non-destructive manner and digitally records object shapes based on the principle of laser operation. The scanner projects the laser onto the surface of the object, a laser sensor that picks up the reflection and locates the point on the surface of the object and generates data from cloud points that describe the surface of the object. This technology is the ideal approach to measure and examine surfaces with complex contours, dark or reflective objects at a mild level.

The procedure of 3D scanning of objects is carried out as follows:

- Prepare the surface for the 3D scanned object to have the best ray reflection and the most optimal object rendering conditions.
- Acquisition of scan data in pixels, point cloud (Fig. 2 [a]).
- Edit the pixel data to match reality.
- Use special CAD software to create object surfaces (Fig. 2[c]) and STL formats (Fig. 2[b]).

The shape of the object obtained in the CAD file format is used for the aerodynamic computation or for the manufacturing process of the sample product. In the next section the aerodynamic calculation method of the reconstructed propeller is presented.

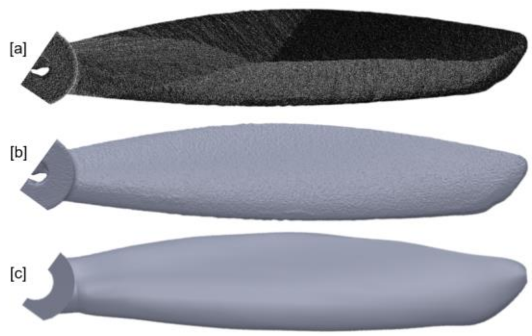

Fig. 2. Object model data types [a] point cloud (scan data), [b] STL (polygon), [c] CAD (surface)

B. Determination of the aerodynamic coefficients using the XFOIL and BEM methods

The aerodynamic coefficient of the propeller is an essential characteristic parameter to help design and select the right propeller for the drone. In this part, the research team uses the XFOIL method in combination with the BEM method to determine the lift coefficient and the wing drag coefficient depending on the angle of attack.

The lift coefficient is a number that aerodynamicists use to model all of the complex dependencies of shape, inclination, and some flow conditions on lift. The lift coefficient $\mathbf{C_L}$ is equal to the lift **L** divided by the quantity: density **ρ** times half the velocity **v** squared times the wing area **A**. It is given by following expression:

$$C_L = \frac{L}{1/2\rho v^2 A}$$

The drag coefficient is a number to model all the complex dependencies of shape, inclination, and flow conditions on aircraft drag. The drag coefficient $\mathbf{C_D}$ is equal to the drag **D** divided by the amount: density **ρ** times half the velocity **v** squared times the reference area **A**. It is given by following formula:

$$C_D = \frac{D}{1/2\rho v^2 A}$$

To determine the aerodynamic coefficients of the scanned wings, we can use the CFD method to calculate. However, this method requires computers with high computing speed, large memory and a long time. In this report, the research team uses the XFOIL method, written by Dr. Mark Drela, an aerodynamics professor at the Massachusetts Institute of Technology. It uses a high order panel method and a fully coupled viscous/inviscid interaction approach to evaluate drag, boundary layer transition and separation [5-6]. XFOIL is a reliable tool that is widely used in the aircraft industry.

In order to apply the XFOIL method, the examined propeller needs to be cut into many faces (2D), from the parameters of thickness, camber line of each section, we obtain the airfoil shape of each section and calculate the coefficients C_L and C_D of each section (Fig. 3- 4). In this study, the team examined the propeller of 10 inches x 4.5° twist. For the calculation results to be acceptable, the number of blade cross-sections must be large enough. The more the wings are cut into segments, the more precise the calculation results will be (Fig. 5).

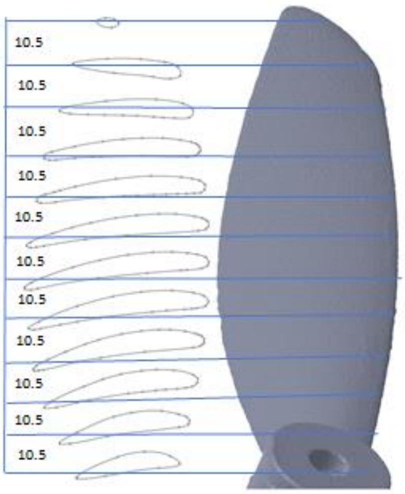

Fig. 3. Cut the cross section in the face at the same distance

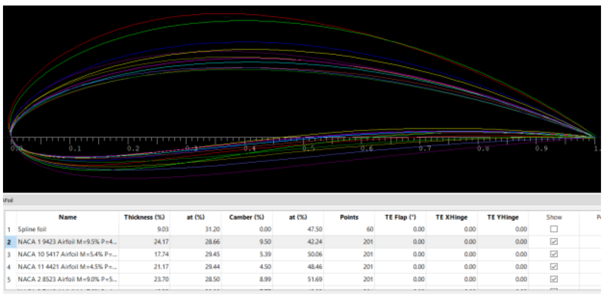

Fig. 4. Modeling to determine the aerodynamic parameters of the propeller after 3D scanning.

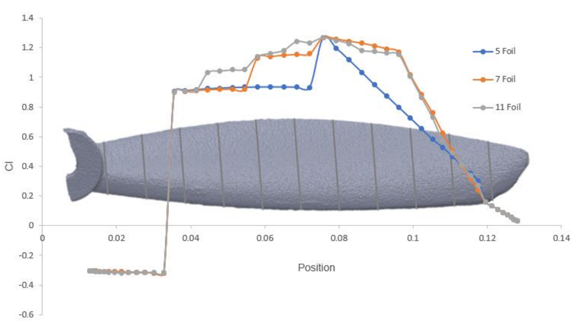

Fig. 5. The curve shows the lift coefficient as a function of the number of wing cross-sections.

The XFOIL method is integrated into the JBLADE software [7]. It is an open source propeller design and analysis code written in the Qt® programming language. The code is based on David Marten's QBLADE and André Deperrois' XFLR5 [8].

The airfoil performance figures required for the blades simulation come from QBLADE's coupling with the open-source code XFOIL. This integration, which is also being improved, allows the fast design of custom airfoils and computation of their polars.

JBLADE uses the Blade Element Momentum (BEM) theory to account for the 3D flow equilibrium [9]. The BEM theory is one of the first and still most widely used methods for studying rotor aerodynamics and it is described in many studies in the literature. The BEM theory is a theory that combines both the blade element theory and the momentum theory. It is used to calculate the local forces on a propeller or wind turbine blade. The blade element theory is combined with momentum theory to mitigate some of the difficulties in calculating the induced velocities on the rotor.

There are different approaches to calculating the aerodynamic coefficients of the propeller, CFD is the most commonly used, the major advantage of BEM over CFD is the time savings and significantly less computational effort. Thanks to the BEM model, it is possible to rapidly develop experimental propeller designs with different engines, easily change and retest the steps and make a preliminary design and then it is possible to do more detailed work using the CFD method.

3. RESULTS AND DISCUSSION

In this part, the research team used modern 3D scanning technology with the Shining 3D EinScan Pro 2X Plus Scanner with an accuracy of 0.04mm to reconstruct the shape of a drone propeller with a diameter parameter of 10 inches and the twist angle at 75 % of the blade radius is 45°.

After the wing shape has been reconstructed, the file format must be converted from a pixel cloud to a CAD file before the JBLADE software is called up to calculate the aerodynamic coefficient. In order to select the required number of sections to get good results, the team had to calculate the convergence of the number of blade sections.

Fig. 5 shows that a cross section count of 11 gives acceptable results. Therefore, the research team chose the number of cross-sections with 11, the surfaces are 10.5mm apart. After the calculation process, the research team received the following results. Fig. 6 shows the influence curve of the angle of attack on the lift coefficient when the air flow reaches $Re=10^5$, Mach=0.3. Fig. 7 shows the relationship between the lift coefficient and the drag coefficient when $Re=10^5$, Mach=0.3.

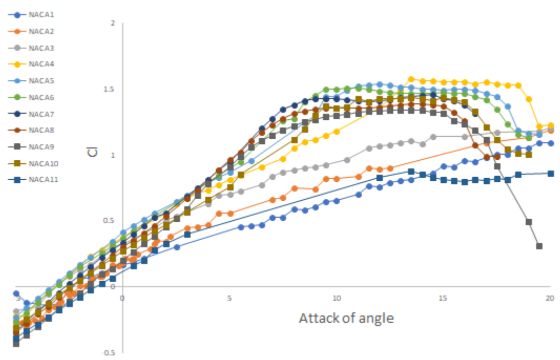

Fig. 6. The curve shows the relationship between the lift coefficient and the angle of attack with $Re=10^5$, Mach=0.3

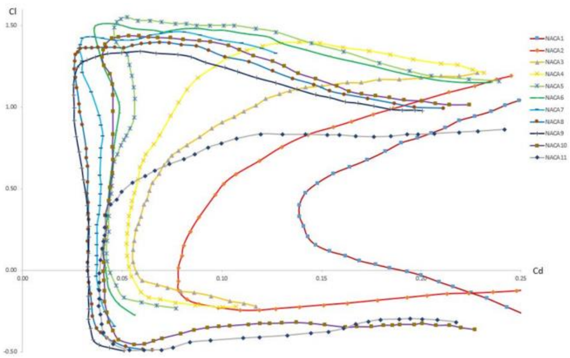

Fig. 7. The curve showing the relationship between C_L and C_D with $Re=10^5$, Mach=0.3

To test the calculation results, the team calculated the wing lift force as a function of the propeller rotation speed and compared it with the experimental results. Experimental components include a 10 inches x 4.5° twist blade, a brushless motor that can reach 7200rpm, power meter, bench scale, and a motor mount that can be mounted on the scale (Fig. 8). The deviation of the scale measure compared to the original is the lift of the wing at each instant of the engine's rotational speed. Fig. 9 shows that the software's calculation results are similar to the experimental results [10]. This proves that the method for determining the aerodynamic coefficient can be applied in practice.

Fig. 8. Test to measure the lift force of the propeller [10]

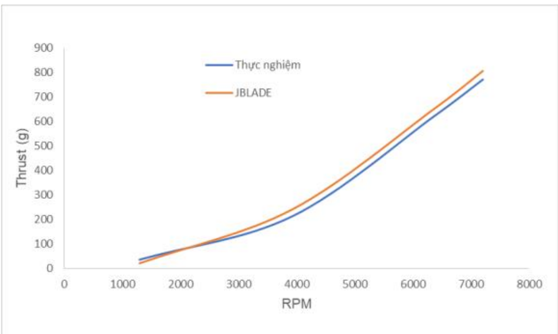

Fig. 9. Calculation results with the JBLADE software and experimental results

4. CONCLUSION

In this article, the propeller was scanned using 3D laser scanning technology. It is a successful means of measuring and exporting measured geometry data for complex scanned surfaces with high accuracy, reliably, robustly and non-destructively. This is of great help in reverse engineering of a propeller from the scanned data. The propeller geometry is measured with a 3D laser scanner, a 3D CAD model is numerically tested with the JBLADE tool. This result is confirmed by experimental results showing that the method can be used to determine the aerodynamic coefficient of the research group.

ACKNOWLEDGMENTS

This research has been done under the research project QG.21.27 "Research and manufacture of Unmanned Aerial Vehicles for transporting 2 kg items" of Vietnam Nation University, Hanoi.

REFERENCES

[1] M. Y. Anwar, S. Ikramullah, and F. Mazhar,"Reverse Engineering in Modeling of Aircraft Propeller Blade - First Step To Product Optimization," IIUM Engineering Journal, Vol. 15, No. 2, (2014).

[2] P. K. Johnson, "Model Aircraft Propellers," http://www.Air Field Models.com, (2004).

[3] K. H. Lee, and H. Woo, "Direct integration of reverse engineering and rapid prototyping," Computers & Industrial Engineering, 38:21-38, (2000).

[4] Y. Senai, Y. Burak, and B. Mazlum, "optical 3D scanner technology," 3rd international congress on 3D printing technologies and digital industry, Turkey (2018).

[5] L. L. Erickson, "Panel methods – an Introduction," NASA Ames Research Center Moffett Field, CA, United States (1990).

[6] D. Mark, "Xfoil an analysis and design system for low reynolds airfoils," Conference on Low Reynolds Number Airfoil, France (1989).

[7] M. A. R. Silvestre, J. Morgado, and J. C. Páscoa, "JBLADE: a Propeller Design and Analysis Code," International Powered Lift Conference, Los Angeles, CA (2013).

[8] M. David, and W. Juliane, "QBlade Guidelines v0.6," Technical Report (2013).

[9] L. Jeremy, R. Sebastián, and S. Julien, "Analysis of the Blade Element Momentum Theory," Computer Science, Mathematics, (2020).

[10] Experimentaltechnik.com, A2212 Motor and 10x4.5 Propeller on the Test Stand; Thrust, Current and Speed Measurement (2014).

NHÀ XUẤT BẢN
ĐẠI HỌC QUỐC GIA HÀ NỘI
16 Hàng Chuối - Hai Bà Trưng - Hà Nội

Giám đốc – Tổng biên tập: (024)39715011
Hành chính: (024)39714899; Fax: (024)39724736
Quản lý xuất bản: (024) 39728806
Biên tập: (024) 39714896

Chịu trách nhiệm xuất bản: Giám đốc: TS. PHẠM THỊ TRÂM
Chịu trách nhiệm nội dung: Tổng Biên tập: TS. NGUYỄN THỊ HỒNG NGA

Biên tập xuất bản: NGUYỄN THỊ THỦY
Biên tập chuyên môn: PHAN THỊ CẨM LY
Chế bản: VÕ SINH VIÊN
Trình bày bìa: NGUYỄN NGỌC ANH

Đối tác: Trường Đại học Công nghệ - ĐHQGHN
Địa chỉ: 144 Xuân Thủy - Cầu Giấy - Hà Nội

PROCEEDINGS OF THE 6TH INTERNATIONAL CONFERENCE ON
ENGINEERING MECHANICS AND AUTOMATION
(ICEMA 2021)

Mã số: 2L - 259ĐH2021
In 100 bản, khổ 19x27 tại Công ty Cổ phần in và Thương mại Ngọc Hưng
Địa chỉ: Số 296 đường Phúc Diễn, tổ dân phố số 1, P. Xuân Phương, Q. Nam Từ Liêm, Hà Nội
Số xác nhận đăng ký xuất bản: 6807-2021/CXBIPH/05-334/ĐHQGHN, ngày 30/11/2021.
Quyết định xuất bản số: 1696LK-XH/QĐ - NXB ĐHQGHN ngày 07/12/2021.
In xong và nộp lưu chiểu năm 2021.